The Stratification of Sporadic Parkinson's Disease Patients by Cellular Mechanism.

Toby James Burgess

Thesis submitted for the degree of Doctor of Philosophy (PhD)

Sheffield Institute of Translational Neuroscience

Division of Neuroscience

September 2024

Abstract

Parkinson's Disease (PD) is an incurable neurodegenerative disease that is widely recognised to be heterogeneous both mechanistically and clinically. Several dysfunctional mechanisms have been identified, including mitochondrial and lysosomal dysfunction. Disease-modifying therapeutics target specific mechanisms of disease to repair dysfunction. A key reason why neuroprotection trials have failed in PD is that clinical trials select participants without considering mechanism heterogeneity.

We investigated mitochondrial and lysosomal dysfunction in patient-derived fibroblasts from a new cohort of sporadic PD patients and healthy controls; these two key mechanisms are promising targets for therapeutics. Imaging and biochemical assays assessed organelle health and mitochondrial and lysosomal dysfunction scores were generated for each cell line. The patients were stratified by identifying distinct patterns of dysfunction within their cells. Further investigation of mitochondria and lysosome function was conducted in the subgroup's fibroblasts to validate stratification. Some fibroblast lines from the subgroups were reprogrammed into induced neuronal progenitor cells and differentiated into induced dopaminergic neurons to identify defining mechanisms of dysfunction in a disease-relevant cell type.

85 % of the organelle health parameters showed significantly more variation in the patient population demonstrating mechanism heterogeneity. Stratification identified four distinct subgroups defined by either mitochondrial dysfunction, lysosomal dysfunction or a combination of dysfunction in both organelles. Further investigation of the lysosomal dysfunction subgroup showed a reduction in Cathepsin D activity in the fibroblasts and significant enlargement of lysosomes in induced dopaminergic neurons. A lack of oxidative phosphorylation flexibility was observed in the fibroblasts from mitochondrial dysfunction subgroup and elevated complex V activity was observed in one of the mixed dysfunction subgroups. This study outlines a new method of stratification that can produce more homogenous groups of PD patients. This method could be used to improve clinical trial design, identify new biomarkers and discover new mechanisms to target mechanistically.

Acknowledgements

Many people helped and supported me throughout this PhD and I am incredibly grateful for everyone. Firstly, I would like to thank my primary supervisor Professor Heather Mortiboys. It is very clear working in academia that not all supervisors were created equally and I cannot state how lucky and grateful I am to have had Heather. Heather is an excellent mentor and scientist, who sets the standard for us to aspire to and she challenges us to achieve everything we can. Secondly, I would like to thank my secondary supervisor Professor Oliver Bandmann. The enthusiasm Oliver has for science and Parkinson's is always a great source of motivation. His knowledge and experience, particularly from a clinical perspective, have helped broaden my understanding of disease and provided an appreciation for a bench-to-bedside approach to research.

I am thankful for the Sheffield Alumni Foundation, which funded this project. Their dedication to raising funds throughout COVID enabled me to stay in Sheffield and work on a project I was truly excited about.

I would like to thank the many past and present members of the Mortiboys team for all their help, support and friendship. It has been a pleasure to work with each and every member and I will always appreciate the time we have spent inside the lab and out. I am particularly thankful for all the help from Katy Barnes, who taught me so much when I started, and Rachel Hughes, who helped with the reprogramming. I am grateful to Dr Tom Payne, who is a fantastic clinician, TC assistant and whose patience is second to none when teaching me R. I would also like to thank Dr Sarah Roscoe and Stephen Bradley who conducted some of the initial screening of the fibroblasts. SITraN has been a fantastic environment to complete my PhD in and I would like to thank everyone for their scientific guidance.

I would like to thank my family for their continuous support and love. I cannot begin to express how much they have helped me throughout this PhD. They have always been there for me when I needed them and were always interested in the work I was doing.

Finally, thank you to my wife Jodie. Jodie has been my rock. We have been through so much together throughout our PhDs but we did it. You have been through all the emotions with me from frustration at cells to the highs of generating my first neurons. I could not have done it without your love and support.

Contents

List of Figures

List of Tables

List of Abbreviations

AD	Autosomal dominant
ADP	Adenosine diphosphate
AR	Autosomal resessive
a-syn	a-synuclein
ATG	Autophagy-related protein
ATP	Adenosine triphosphate
ATP13A2	ATPase cation transporting 13A2
BMP	Bis (monoacylglycero)phosphate
BNIP3	BCL2 interacting protein 3
BRUCE	BIR repeat containing ubiquitin-conjugating enzyme
CatB	Cathepsin B
CatD	Cathepsin D
CatL	Cathepsin L
CCCP	Carbonyl cyanide m-chlorophenyl hydrazone
CoA	Co-enzyme A
CSF	Cerebrospinal fluid
CTSB	Cathepsin B gene
CTSD	Cathepsin D gene
DAT	Dopamine transporter
DMSO	Dimethyl sulphoxide
DNM2	Dynamin 2
DRP1	dynamin-related protein 1
ECAR	Extracellular acidification rate
ETC	Electron transport chain
$FAD/FADH_2$	Flavin adenine dinucleotide
FIS1	Mitochondrial fission 1
fPD	Familial Parkinson's Disease
FUNDC1	FUN14 domain containing 1
GCases	Glucocerebrosidase
GD	Gaucher Disease
GDP	Guanosine triphosphate
GRASP	Golgi reassembly and stacking protein
GTP	Guanosine diphosphate
GWAS	Genome-Wide Association Studies
HOPs	Homotypic fusion and vacuole protein sorting
iDA neurons	Induced dopamingeric neurons
IMM	Inner mitochondria membrane
iNeurons	Induced neurons
iNPC	Induced neuronal progenitor cell
iPSC	Induced pluripotent stem cell
Klf4	Krüppel-like factor 4
LAMP1/2	Lysosomal associated membrane protein 1/2
LC3	Microtubule-associated protein 1A/1B-light chain 3
LIMP2	Lysosomal integral membrane protein 2

Llome	L-leucyl-L-leucine methyl ester
LRRK2	Leucine-rich repeat kinase 2
M6P	Mannose-6-phosphate
MAP2	Microtubule associated protein 2
MDS-UPDRS	Movement Disorder Society Unified Parkinson's Disease Rating Scale
MFF	Mitochondrial fission factor
MFN-1/2	Mitofusin 1/2
MID49/51	Mitochondrial dynamics proteins of 49 kDa and 51 kDa
Miro1	Mitochondrial rho GTPase 1
MMP	Mitochondria membrane potential
MPTP	1-methyl-4-phenyl-1,2,3,6-tetrahydropyridine
mtDNA	Mitochondrial DNA
NAD+/NADH	Nicotinamide adenine dinucleotide
NLRP3	Nucleotide-binding oligomerization domain (NOD)-leucine-rich repeat (LRR)-pyrin domain (PYD)-containing
NPC1	Niemann-Pick C1
NSF	N-ethylmaleimide sensitive factor
OCR	Oxygen consumpstion rate
Oct	Octamer-binding transcription factor 4
OMA1	Overlapping with the M-AAA protease 1
OMM	Outer mitochondria membrane
OPA1	Optic atrophy 1
OSCP	Oligomycin sensitivity conferral protein
PBMC	Peripheral blood mononuclear cell
PBS	Phosphate buffered saline solution
PD	Parkinson's Disease
PFB-Fdglu	5-(Pentafluorobenzoylamino) fluorescein di-β-D-glucopyranoside
PFC	Prefrontal cortex
PIGD	Postural instability and gait disturbance
PINK1	Phosphatase and tensin homolog (PTEN)-induced putative kinase protein 1
RBD	Rapid eye movement sleep behaviour disorder
RF	Risk Factor
ROS	Reactive oxygen species
SENS-PD	Severity of predominantly Non-dopaminergic Symptoms in PD
SN	Substantia nigra
SNAP	Soluble NSF attachment proteins
SNARE	Soluble N-ethylmaleimide-sensitive factor attachment protein receptor
Sox2	SRY-box transcription factor 2
sPD	Sporadic Parkinson's Disease
TBC1D15	Tre-2/Bub2/Cdc16 domain family member 15
TH	Tyrosine hydroxylase
TMEM175	Transmembrane protein 175
TMRM	Tetramethylrhodamine, methyl ester
UDCA	Ursodeoxycholic acid
USP30	Ubiquitin-specific protease 30
VAMP	Vesicle-associated membrane protein

v-ATPase	Vacuolar-ATPase
VPS	Vacuolar protein sorting

1 Introduction

1.1 Parkinson's Disease

Parkinson's Disease (PD) is the second most common neurodegenerative disease in the world (Feigin *et al.*, 2017; Erkkinen, Kim and Geschwind, 2018; Ray Dorsey *et al.*, 2018; Ou *et al.*, 2021). Prevalence increased by over 26 % between 1990 and 2016 (Ray Dorsey *et al.*, 2018) and is predicted to continue increasing. Unfortunately, no disease-modifying therapies have been successful in clinical trials. The rapidly growing population and no disease-modifying therapies mean that the socioeconomic burden of PD will continue to grow putting strain on already stretched healthcare systems (Findley *et al.*, 2011; Albarmawi *et al.*, 2022).

1.1.1 Clinical Presentation

PD was first clinically described in 1817 by James Parkinson (Parkinson, 1817). Today's clinical understanding has built on this description. PD is a movement disorder characterised by four motor symptoms: bradykinesia (slowness of movement), tremor at rest, rigidity (a restriction of movement in all joint directions) and postural instability (an inability to maintain balance when stationary or moving) (Jankovic, 2008). Assessment of these features is the main method for diagnosing PD, although the presentation of these symptoms varies greatly between patients, for example, a subset of PD patients never present with tremor symptoms (Martin *et al.*, 1973). Other motor symptoms that are commonly observed include gait disturbance, speech disorders, dysphagia (swallowing difficulties) and respiratory disturbance (Jankovic, 2008), but these may result from the four main symptoms. However, non-motor symptoms are commonly described and are often more debilitating than the defining motor symptoms. Non-motor symptoms often manifest prior to motor symptoms, (Chaudhuri, Healy and Schapira, 2006) but the majority are not associated with PD until motor symptom onset. These prodromal symptoms include hyposmia, rapid eye movement sleep behaviour disorder (RBD), depression and constipation (Schapira, Chaudhuri and Jenner, 2017). RBD, dream enactment, is the only symptom that can indicates an increased probability of PD; studies have shown that 41-91% of people manifesting RBD are diagnosed with neurodegenerative disease later in life, predominantly synucleinopathies (St Louis and Boeve, 2017). Non-motor symptoms are not limited to prodromal manifestation, extremely debilitating symptoms, such as dementia, hallucinations, pain and orthostatic hypotension, are associated with later stages of PD (Schapira, Chaudhuri and Jenner, 2017). Clinical symptoms are measured using clinical score rating scales, such as the Movement Disorder Society Unified Parkinson's Disease Rating Scale (MDS-UPDRS) and Severity of predominantly Non-dopaminergic Symptoms in PD (SENS-PD). These rating scales rank symptoms based on clinician

observation and patient reporting, compressing the results into one score. MDS-UPDRS is currently the main assessment used to determine clinical trial efficacy outcomes and is separated into four parts: part I assesses the patients' experience of non-motor symptoms in daily life, part II measures the patients' experience of motor symptoms in daily life, part III is a clinical assessment of motor symptoms and part IV assesses motor complications (Parkinson's UK, 2025). SENS-PD predominantly rates non-motor symptoms and was designed to provide a more informative overview of the symptom itself because the MDS-UPDRS scale mainly assesses the impact the symptom is having on a patient's quality of life (van der Heeden *et al.*, 2016).

1.1.2 Hallmarks of Parkinson's Disease

Pathologically PD is defined by the loss of dopaminergic neurons in the midbrain, which project from the substantia nigra pars compacta (SN) to the putamen (Dickson, 2012). Although the exact cause of neuron death is currently unknown, Lewy bodies, caused by the aggregation of α-synuclein (α-syn), are commonly observed in patient neurons (Baba *et al.*, 1998). These aggregates begin to form long before the loss of neurons and subsequent onset of symptoms (Fearnley and Lees, 1991; Nandhagopal *et al.*, 2011) and occur in the cell body, neurite and synaptic compartments of the neurons (Irizarry *et al.*, 1998; Schulz-Schaeffer, 2010). One theory is that α-syn dysregulation first occurs in the synapse resulting in impairment, followed by axonal degeneration and then cell body death in a dying-back mechanism (Calo *et al.*, 2016).

α-syn is a 140 amino acid cytosolic protein that localises to the pre-synaptic terminal in mammalian neurons (Jakes, Spillantini and Goedert, 1994; Iwai *et al.*, 1995; Kahle *et al.*, 2000). It has three domains, an N-terminal domain that is amphipathic enabling membrane and lipid interactions, a central core consisting of the non-amyloid-β component (NAC) region and the acidic C-terminus that enables nuclear localisation and interactions with other molecules (Calo *et al.*, 2016). It is hypothesised that the C-terminus protects against aggregation; C-terminally truncated forms of α-syn aggregate more readily (Serpell *et al.*, 2000; Murray *et al.*, 2003; Levitan *et al.*, 2011; Iyer *et al.*, 2017; Ma *et al.*, 2018) and are found within Lewy bodies in postmortem tissue (Baba *et al.*, 1998). The NAC region is responsible for aggregation, deletion of this hydrophobic motif reduces oligomerisation and fibril formation. Despite these three domains having various interacting capabilities, α-syn is generally an unfolded monomer in healthy conditions (Eliezer *et al.*, 2001). Functionally α-syn is proposed to be involved in the fusion of synaptic vesicles with the synaptic membrane. It interacts with the soluble N-ethylmaleimide-sensitive factor attachment protein receptor (SNARE) complex enhancing its formation and acting as a chaperone. The SNARE complex forms when the vesicle-SNARE proteins vesicle-associated membrane protein-2 (VAMP2) and synaptobrevin tether to target-SNARE proteins

soluble NSF attachment protein 25 (SNAP25) and Syntaxin-1. α-syn's C-terminus interacts with VAMP2 and possibly synaptobrevin (Burré, Sharma and Südhof, 2014) while its N-terminus interacts with the plasma membrane bringing the v-SNARE proteins and t-SNARE proteins into close proximity (Liu *et al.*, 2021). Despite this proposed function and extensive research, the exact role of α-syn is still unclear (Calo *et al.*, 2016). α-syn is the most researched aspect of PD pathology but α-syn aggregation does not occur in a subset of PD patients (Hasegawa *et al.*, 2009; Kalia *et al.*, 2015).

Other hallmarks of PD have also been identified, including mitochondrial dysfunction, lysosomal dysfunction, oxidative stress and neuroinflammation. It can be argued that dysfunction in these systems is interlinked (McGeer and McGeer, 2004; Hornung *et al.*, 2008; Rajamäki *et al.*, 2010; Bauernfeind *et al.*, 2011; Nakahira *et al.*, 2011; Zhou *et al.*, 2011; Salminen *et al.*, 2012; Shimada *et al.*, 2012; Sliter *et al.*, 2018; He *et al.*, 2020) and even a result of α-syn (Fellner *et al.*, 2013). Mitochondrial dysfunction, lysosomal dysfunction and oxidative stress will be reviewed later in the chapter.

The role of inflammation in PD, like many other hallmarks, remains unclear (Tan *et al.*, 2020). However, immune activation has been observed in PD models and patients in many studies that utilised post-mortem tissue, positron emission tomography, cerebrospinal fluid (CSF) and blood (McGeer *et al.*, 1988; Müller *et al.*, 1998; Selikhova *et al.*, 2002; Hofmann *et al.*, 2009; Bartels *et al.*, 2010; Qin *et al.*, 2016; Kustrimovic *et al.*, 2018; Tansey and Romero-Ramos, 2019). Furthermore, individuals with autoimmune disease have an increased risk of PD (Li, Sundquist and Sundquist, 2012), while those on immunosuppressants have a reduced risk (Racette *et al.*, 2018). It is understood that over-activation of the immune system, particularly microglia can lead to brain inflammation and neuronal damage (Duffy *et al.*, 2018). This may be a consequence of or the cause of elevated inflammatory cytokines in the CSF (Mogi *et al.*, 1996; Zhang *et al.*, 2016; Wijeyekoon *et al.*, 2020) and blood (Qin *et al.*, 2016; Wijeyekoon *et al.*, 2020). However, changes in these cytokines do not correlate with α-syn levels in the CSF (Wijeyekoon *et al.*, 2020). Nucleotide-binding oligomerization domain (NOD)-leucine-rich repeat (LRR)-pyrin domain (PYD)-containing (NLRP3) inflammasome activation has been observed in many PD models, other inflammasomes show no differences (as reviewed by Nguyen *et al.*, 2022). The role that NLRP3 plays, and the cause of its specific activation, is unknown, but higher protein levels are found in later stages of disease suggesting an association with severity (von Herrmann *et al.*, 2018). Studies even show that specific variants of NLRP3 reduce the risk of PD (von Herrmann *et al.*, 2018). This suggests a form of heterogeneity within the population.

1.1.3 Genetics of Parkinson's Disease

The genetics of PD has been widely studied in recent years. It must be noted that the majority of these studies are ethnically uniform, mainly selecting participants with European ancestry. Several groups

such as African, South Asian and Latino must be extensively explored to gain a global understanding of PD genetics (Khani *et al.*, 2024). Genetic risk loci and risk small nucleotide polymorphisms are generally found by large Genome-Wide Association Studies (GWAS) studies and mutations are found by investigations into families with inherited PD (Billingsley *et al.*, 2018). GWAS studies can identify protective variants as well, but few have been described. One example is the combination of Leucine-rich repeat kinase 2 (LRRK2) N551K, R1398H K1423K variants, which is surprisingly common, occurring in 10 % of people of Asian ethnic origin (Tan *et al.*, 2010; Ross *et al.*, 2011; Heckman *et al.*, 2014). This is possibly due to a reduction in kinase activity (Tan *et al.*, 2010).

Due to the vast range of genetic mutations associated with PD (Table 1), this chapter will discuss a few of the more common variants that are associated with mitochondria and lysosome function, namely LRRK2, GBA, PRKN and PINK1. Others such as CTSB and CTSD are discussed in later chapters (4.1 Introduction4.1).

Table 1: A non-exhaustive summary of the genes associated with PD. Reporting the gene, the proteins function in health, known mutations, its penetrance/mendelian inheritance and prevalence. Autosomal dominant (AD), Autosomal recessive (AR) and Risk factor (RF).

Gene	Function	Mutations/ variants	Penetrance/ Mendelian Inheritance	Percentage of the population	Reference
SNCA	Encodes synuclein	A53T, G51D, A30P, E46K, H50Q, triplication	AD	< 1 %	(Polymeropoulos *et al.*, 1997; Krüger *et al.*, 1998; Zarranz *et al.*, 2004; Appel-Cresswell *et al.*, 2013; Lesage *et al.*, 2013)
LRRK2	Unknown kinase	G2019S, R1441C/G/S/H, Y1699C, R1628P, I2020T, N1437H	RF, AD	1-5%	(Paisán-Ruíz *et al.*, 2004; Zimprich *et al.*, 2004)
GBA1	Lysosomal enzyme	L444P, N370S, E326K	RF	5-15 %	(Smith and Schapira, 2022)
VPS35	Endosome trafficking	D620N and others	AD	< 0.1 %	(Zimprich *et al.*, 2011)

PRKN	Mitophagy	Many, often deletions	AR	1 %	(Kitada *et al.*, 1998)
PINK1	Mitophagy	G309D, truncation nonsense mutation	AR	< 1 %	(Valente *et al.*, 2001)
DJ-1	Mitochondria related but function unknown	L166P	AR	< 1 %	(Bonifati *et al.*, 2003)
VPS13C	Phospholipid transporter	Multiple truncations	AR	< 0.1 %	(Lesage *et al.*, 2016)
ATP13A2	Lysosome ATPase cation transporter	Exon 13 deletion	AR	rare	(Ramirez *et al.*, 2006)
PLA2G6	Phospholipase A2, controlling membrane homeostasis	R741Q, 53 more	AR	rare	(Magrinelli *et al.*, 2022)
FBX07	Degradation of PINK1	Missense, splice site and nonsense reported	AR	rare	(Fonzo *et al.*, 2009)
DNAJC6	Synaptic vesicle formation	Nonsense and missense mutations	AR	rare	(Edvardson *et al.*, 2012)
DNAJC13	Synaptic vesicle formation	R903K, R1516H, G394V, R1382H, N855S	Predicted RF	rare	(Gagliardi *et al.*, 2018)
TMEM230	Synaptic vesicle formation	R141K	AD	rare	(Deng *et al.*, 2016)
SYNJ1	Synaptic vesicle formation	R258Q, S1422R	AR, AD predicted	rare	(Krebs *et al.*, 2013; Quadri *et al.*, 2013)
CHCHD2	Mitochondria intermembrane space, function unknown	T61I, R145Q and 4 others	AD	rare	(Funayama *et al.*, 2015)

CTSB	Lysosome enzyme	G284V	-	rare	(Milanowski *et al.*, 2022)
CTSD	Lysosome enzyme	V95I, G145V, A239V, R266H	-	rare	(Robak *et al.*, 2017)
ATXN2	Post-Transcriptional regulator	CAG repeat expansion	-	rare	(Laffita-Mesa, Paucar and Svenningsson, 2021)

1.1.3.1 LRRK2

LRRK2 mutations account for the largest proportion of genetic PD cases, although mutations are not completely penetrant (Marder *et al.*, 2015; Lee *et al.*, 2017). Carriers of the LRRK2 G2019S mutation, the most common variant, have a risk of developing PD between 25-74 % depending on the study (Healy *et al.*, 2008; Marder *et al.*, 2015; Lee *et al.*, 2017). Most studies report LRRK2 mutations to account for between 1-5 % of the PD population, but specific ethnic groups, Ashkenazi Jewish and North African Berber populations, have much higher prevalences at 14 % and 37 % (Healy *et al.*, 2008). LRRK2's exact role in PD is currently unclear. It is known that LRRK2 is expressed in the brain and the cytoplasm of neurons (Miklossy *et al.*, 2006), where it can associate with mitochondria (Neethling *et al.*, 2019) and plays a role in cellular dynamics, immune response and autophagy. LRRK2 expression is high in microglia, which contribute to the induction of neuroinflammation in PD (Rui *et al.*, 2018). Studies show that LRRK2 mutations reduce α-syn clearance and result in the heightened release of pro-inflammatory cytokines, leading to dopaminergic neuron death (Rui *et al.*, 2018). LRRK2 mutations occur within the guanosine triphosphatases (GTPase) and kinase domains and result in elevated kinase activity, but the exact targets of kinase activity that cause PD eludes researchers (Sosero and Gan-Or, 2023).

LRRK2 mutations have a deleterious impact on mitochondria in PD. LRRK2 G2019S patient-derived fibroblasts and iDopaminergic neurons (iDA neurons) display reduced mitochondrial respiration, MMP and ATP levels, along with the decreased activity of complex III and complex IV (Mortiboys *et al.*, 2010, 2015; Papkovskaia *et al.*, 2012; Su and Qi, 2013; Grünewald *et al.*, 2014). Mitochondrial morphology is altered in the LRRK2 G2019S models, including animals, SH-SY5Y transfected cells and patient-derived fibroblasts (Mortiboys *et al.*, 2010; Niu *et al.*, 2012; Wang *et al.*, 2012; Su and Qi, 2013; Grünewald *et al.*, 2014; Juárez-Flores *et al.*, 2018). However, the exact mechanism that causes mitochondrial abnormalities in LRRK2 mutants remains unclear. It is suggested that LRRK2 mutations may slow mitophagy resulting in the accumulation of defective mitochondria, possibly through the

delayed removal of mitochondrial rho GTPase 1 (Miro1), which is required for mitophagy initiation (Hsieh *et al.*, 2016). However, other researchers have described direct interactions with DRP1, which result in elevated fission (Niu *et al.*, 2012; Wang *et al.*, 2012; Su and Qi, 2013). Increased fission was associated with increased mitophagy (Smith *et al.*, 2016), further complicating the understanding of LRRK2 mechanisms. Dysregulated mitochondrial dynamics could account for increased mitochondrial ROS production due to an increase in defective mitochondria. A study using induced pluripotent stem cell (iPSC)-derived iDA neurons showed an increase in oxidative stress response gene expression and a lack of adaptability in response to oxidative stress-inducing toxins, such as 6-hydroxydopamine and hydrogen peroxide (Nguyen *et al.*, 2011).

LRRK2 mutations impact on lysosomes and autophagy has been widely studied in PD. LRRK2 mutations have a detrimental effect on autophagy as shown by overexpression of LRRK2 or expression of LRRK2 G2019S in mice or HEK293 cells, which results in the accumulation of un-degraded substrates, such as α-syn, due to the inhibition of proteolysis in the chaperone-mediated autophagy (Orenstein *et al.*, 2013). Contradictory to this, elevated degradation by lysosomes and an increased number and size of autophagosomes and autolysosomes have been shown in LRRK2 G2019S patient-derived fibroblasts (Bravo-San Pedro *et al.*, 2013). The elevation in autophagosomes and lysosomes may be due to a compromised maturation, which has been highlighted by reduced LC3-II colocalization and reduced acidification of lysosomes in LRRK2 G2019S iDA neurons and mouse brain tissue (Sánchez-Danés *et al.*, 2012; MacLeod *et al.*, 2013). LRRK2 may cause dysfunction through a dysregulation of Rab-mediated retrograde transport of lysosome contents to the golgi or a dysregulation of contents release, causing lysosome swelling (MacLeod *et al.*, 2013; Pang *et al.*, 2022). Despite extensive research, further work is required to fully understand LRRK2's involvement in PD and its role in mitochondrion and lysosome functions.

1.1.3.2 GBA

GBA1 mutations are the largest risk factor for PD. Homozygous mutations lead to Gaucher's Disease (GD). GD-affected families have higher incidence rates of PD, leading to the association of GBA1 mutations with PD (Goker-Alpan *et al.*, 2004). Studies found that heterozygous mutations are present in 2.3 % to 9.4 % of patients depending on the ethnic group (Sidransky and Lopez, 2012). Homozygous and heterozygous mutation carriers have the same risk of developing PD (Anheim *et al.*, 2012; Alcalay *et al.*, 2014). Like LRRK2, GBA mutations are far more common in the Ashkenazi Jewish population (Alcalay *et al.*, 2014). Eleven mutations are associated with PD; the most commonly researched are GBA N370S, GBA L444P and GBA E326K. Interestingly, different GBA mutations are associated with different PD severities. N370S leads to mild PD, L444P and E326K lead to severe PD and unexpectedly E326K homozygotes do not develop GD (Smith and Schapira, 2022).

GBA1 encodes glucocerebrosidase (GCase), the lysosomal enzyme that cleaves glucosylceramide and glucosylsphingosine. Mutations result in misfolding in the endoplasmic reticulum preventing the transport of GCase to the lysosome (Smith and Schapira, 2022). The specific mutation and whether it is homozygous or heterozygous affects the level of GCase activity (Gegg *et al.*, 2012; McNeill *et al.*, 2014; Migdalska-Richards and Schapira, 2016), however, activity does not correlate with PD risk (Smith and Schapira, 2022). Reduced GCase activity was observed in the brains, blood, patient-derived fibroblasts and iPSCs of carriers and reduced activity has also been observed in sporadic non-carrier patients as well (Gegg *et al.*, 2012; Schöndorf *et al.*, 2014; Alcalay *et al.*, 2015; Rocha *et al.*, 2015; Huebecker *et al.*, 2019; Thomas *et al.*, 2021). Reduced activity, by approximately 30 %, in the sPD group significantly correlates with the levels of LIMP-2, the GBA trafficking receptor (Thomas *et al.*, 2021), suggesting that mislocalisation of GCase and subsequently lysosomal dysfunction plays a crucial role in the development of sPD as well as fPD. However, one study using the live GCase substrate 5-(Pentafluorobenzoylamino) fluorescein di-β-D-glucopyranoside (PFB-FDGlu) observed no differences in GCase activity between controls, sPD and GBA mutation carrier iPSCs, but the differing results may be due to differing techniques (Labrador-Garrido *et al.*, 2023).

Much of the research in GBA1 mutations has focused on GCase activity, however, some studies have assessed lysosome content. *GBA1* mutant iPSCs and SH-SY5Y cells show altered lysosomes and autophagy with increased lysosomal size and number, increased LC3-II levels and increased P62 levels suggesting a blockage in lysosomal degradation leading to the accumulation of autophagosomes and swollen, cargo filled lysosomes (Schöndorf *et al.*, 2014; Fernandes *et al.*, 2016; Kuo *et al.*, 2022). This was also supported by electron microscopy showing electron-dense lysosomes, suggesting they are full of undegraded waste (Fernandes *et al.*, 2016). García-Sanz *et al.* (2017) showed that patient-derived fibroblasts from GBA carriers had elevated lysosome mass. Whereas, other studies observed no change in lysosome content in patient-derived fibroblasts from GBA mutation carriers (McNeill *et al.*, 2014; Yang *et al.*, 2020; Thomas *et al.*, 2021). This variation has not been explored and may be due to differences in mutations, methodology, tissue or patient heterogeneity.

Table 2: A summary of the main GBA literature outlined above showing the results, disease model and authors. Where multiple models were used, numbers indicate the results found in each. The method of measuring GCase activity is highlighted in brackets.

Findings	Disease Model	Reference
GBA1 mutations occur in 2.3-9.4 % of the PD cases	PD patients	(Sidransky and Lopez, 2012)
Reduced GCase activity, and other hydrolases (4-methylumbelliferone (4-Mu)	Postmortem SN, GBA carriers	(Huebecker *et al.*, 2019)
Reduced GCase activity in hippocampus and cerebellum, but only in the 60-year-old group in the SN due to an age dependent decrease in controls (4-Mu)	Postmortem brain tissue, GBA carriers	(Rocha *et al.*, 2015)
Reduced GCase activity in SN and other brain regions. The reduction was greater in GBA-PD than sPD (4-Mu)	Postmortem brain tissue, sPD and GBA carriers	(Gegg *et al.*, 2012)
Reduced GCase activity in sPD and GBA carriers, sPD had reduced LIMP2 levels (4-Mu)	Patient-derived fibroblasts	(Thomas *et al.*, 2021)
Reduced GCase activity, the reduction is greater in GBA carriers than sPD	Patient blood samples, sPD and GBA	(Alcalay *et al.*, 2015)
Reduced chaperone-mediated autophagy, GCase mutants accumulate on the lysosome surface and showed increased α-syn. Increased lysosome content was also observed	1. iPSCs from GBA carrier 2. Patient-derived fibroblasts 3. SH-SY5Y transfected with mutant	(Kuo *et al.*, 2022)
Enlarged lysosomes, altered lipid profiles and increased extracellular α-syn	iPSCs from GBA N370S patients	(Fernandes *et al.*, 2016)
Reduced Gcase activity and increased α-syn (4-Mu)	iPSC derived neurons	(Schöndorf *et al.*, 2014)
No difference in GCase activity was found between any of the PD patient groups and controls (PFB-FDGlu)	Patient-derived iPSCs WT, LRRK2 G2019S, GBA N370S and sPD	(Labrador-Garrido *et al.*, 2023)
Descreased GCase activity, increase lysosome clustering, increased CatB and CatD protein levels and elevated cholesterol colocalization with lysosomes (4-Mu)	Patient-derived fibroblasts GBA N370S heterozygote	(García-Sanz *et al.*, 2017)
Reduced GCase activity but no difference in lysosome content (4-Mu)	Patient-derived fibroblasts mixed mutations	(McNeill *et al.*, 2014)
Reduced GCase activity, reduced CatD activity, no difference in lysosome content or CatB activity and increased α-syn levels (4-Mu)	Differentiated dopaminergic neurons from human neural crest stem cells from GBA N370S and sPD patient postmortem putamen.	(Yang *et al.*, 2020)

1.1.3.3 PRKN and PINK1

Parkin and Phosphatase and tensin homolog-induced kinase 1 (PINK1) mutations occur in 8.6 % and 3.7 % of early-onset PD respectively (Kitada *et al.*, 1998; Valente *et al.*, 2001; Lill, 2016). PINK1/Parkin PD normally manifests before 40 years old and can even manifest in juveniles (Pickrell and Youle, 2015). Missense, nonsense and deletion *PRKN* mutations have all been reported in PD, whereas PINK1

mutations are more commonly missense and nonsense mutations: Q129X, P196K, G309D, W437X, G440E, Q456X (Lill, 2016). Both proteins are involved in the initiation of one pathway of mitophagy, which is the clearance of dysfunctional mitochondria. In brief, PINK1 is a threonine/serine kinase that is normally transported to the inner mitochondrial membrane (IMM), where it is cleaved and degraded. Upon damage, this transport is prevented by depolarisation of the mitochondrial membrane potential (MMP) and PINK1 stabilises on the outer mitochondrial membrane (OMM). PINK1 auto-phosphorylates resulting in Parkin recruitment and subsequent PINK1 phosphorylation of Parkin to activate it. Parkin is an E3 ubiquitin ligase that tags damaged mitochondria with poly-ubiquitin chains, which PINK1 phosphorylates. These poly-ubiquitin tags are recognised by autophagy machinery and the mitochondria are degraded (Narendra *et al.*, 2008, 2010; Geisler *et al.*, 2010; Palikaras, Lionaki and Tavernarakis, 2018).

Mutations in PINK1 and Parkin cause mitochondrial dysfunction. Evidence from mutant animal models shows a reduction in complex I activity, lower mitochondrial respiration and abnormal mitochondrial morphology (Greene *et al.*, 2003; Flinn *et al.*, 2013; Stauch *et al.*, 2016). Other studies utilised patient-derived fibroblasts, identifying reduced MMP and ATP levels and decreased activity of complex I (Mortiboys *et al.*, 2008; Grünewald *et al.*, 2010; van der Merwe *et al.*, 2014; Zanellati *et al.*, 2015). However, several papers have shown no difference in MMP (Grünewald *et al.*, 2010; Haylett *et al.*, 2016). This conflict may be due to different media conditions and assaying methods, or an inherent heterogeneity within Parkin patients, possibly due to the wide variety of mutations.

1.1.4 Therapeutics

No disease-modifying therapies have been approved for use in PD and therefore PD is currently managed with symptomatic treatments. There are currently several symptomatic treatments on the market for PD, these include both pharmacological and non-pharmacological therapies. Discovered in 1970, Levodopa is the “gold standard” treatment (Abbott, 2010). Since then, the discovery of new treatments has been disappointing (McFarthing *et al.*, 2023). Levodopa is metabolised in the brain to form dopamine and replenish the loss caused by dopaminergic neuron loss (Fahn, 2008). There are two other types of pharmacological treatment: dopamine agonists, such as apomorphine, and monoamine oxidase type B (MAO-B) or catechol-O-methyltransferase (COMT) inhibitors, such as selegiline and co-careldopa (The Michael J Fox Foundation, 2024). Dopamine agonists directly target dopamine receptors but have unpleasant side effects, such as hallucinations, fatigue (which is already a problem in PD) and impulse control issues. MAO-B inhibition prevents the breakdown of dopamine in glial cells, thus increasing the levels left in the synaptic cleft, enhancing signalling (Tan, Jenner and Chen, 2022). COMT catalyses Levodopa into 3-O-methyldopa which has a long half-life and competes

with Levodopa for transport across the blood-brain barrier, inhibition reduces 3-O-methyldopa and thus increases the delivery of Levodopa to the brain (Nissinen and Männistö, 2010).

Despite the immense effort of the research community to discover effective disease-modifying therapies, treatments continually fail at clinical trials. Likely reasons for treatment failure are the lack of mechanism understanding and the assumption that the targeted mechanism is the driving mechanism in most of the trial's participants (Lang and Espay, 2018). However, it is well-documented that PD is a heterogeneous disease (Van Rooden *et al.*, 2010; Marras and Lang, 2013; Simuni *et al.*, 2016; Von Coelln and Shulman, 2016; De Pablo-Fernández *et al.*, 2019; Lee *et al.*, 2019; Milanese *et al.*, 2019; Carling *et al.*, 2020; Berg *et al.*, 2021). As of the 31st of January 2024, there were 60 active clinical trials assessing small molecule disease-modifying therapies registered on the ClinicalTrials.gov website (McFarthing *et al.*, 2024). Of these 37 % are in Phase I, 58 % in Phase II and 5 % in Phase III. They have a range of mechanisms, including antioxidants, anti-inflammatories, kinase inhibitors and mitochondria-targeting compounds. Those in Phase III are Ambroxol, a GBA chaperone, Exenatide, a GLP-1 agonist and Lactobacillus acidophilus, a probiotic with prebiotic fibres (McFarthing *et al.*, 2024). Other studies are trialling cell therapies, for example, TED-A9 cells (NCT05887466) are embryonic stem cell-derived A9 dopaminergic neuronal precursor cells that are transplanted into the putamen of the patient and mature into dopaminergic neurons and replace lost neurons (Lee, 2024).

1.2 Mitochondrial Biology

1.2.1 Healthy Mitochondria

Mitochondria were once bacteria that evolved to form a symbiotic relationship with cells, eventually becoming organelles essential to cell survival and metabolism in all human cells (Martin, 2010), except erythrocytes (Zhang *et al.*, 2011). These organelles are membrane-bound and consist of an intermembrane space trapped between the IMM and OMM and the mitochondrial matrix within the IMM (Telser, 2002). The matrix contains circular double-stranded mitochondrial DNA (mtDNA) strands that encode 13 proteins, which are key components of the electron transport chain (ETC) that is situated on the IMM (Cooper and Hausman, 2007). Although mitochondria contain their own DNA the nucleus still encodes the vast majority of the proteins identified within mitochondria, of which studies have found 615 proteins (Boengler, Heusch and Schulz, 2011). Mitochondria form networks within the cell's cytoplasm, the shape and distribution are finely regulated to ensure optimal function.

1.2.1.1 Initial Stages of ATP Production

The primary function of mitochondria is to produce adenosine triphosphate (ATP) via oxidative phosphorylation. During metabolism, substrates are broken down and transported into the

mitochondria by a variety of pathways. The majority of ATP is produced via glucose metabolism. The process of glycolysis in the cell cytosol transforms glucose into two pyruvate molecules. Pyruvate travels into the mitochondria, where it is converted into carbon dioxide (CO_2) and an acetyl molecule which binds with Coenzyme A (CoA). The acetyl group of acetyl-CoA is transferred to oxaloacetate in the mitochondrial matrix to start the citric acid cycle, reducing nicotinamide adenine dinucleotide (NADH) and flavin adenine dinucleotide ($FADH_2$) molecules, which are crucial to oxidative phosphorylation, the final process of aerobic respiration.

1.2.1.2 Oxidative Phosphorylation

Oxidative Phosphorylation occurs at the IMM using the five complexes (I-V) of the ETC. In summary, the transfer of electrons along the ETC drives conformational changes in complexes I, III and IV pumping protons across the IMM into the intermembrane space. This creates an electrostatic gradient across the IMM resulting in a flow of protons through complex V to drive the synthesis of ATP.

1.2.1.2.1 Complex I

Complex I is the first proton pump in the chain. The combination of forty-four subunits forms a hydrophobic arm inserted into IMM and a hydrophilic arm located in the matrix. The complex consists of three domains: a dehydrogenase, hydrogenase and a hydrogen ion translocation domain. To initiate oxidative phosphorylation complex I oxidises NADH, which was either produced in the citric acid cycle or glycolysis. The NADH molecule donates an electron pair to the flavin mononucleotide subunit of complex I, reducing it. The electrons are then passed along the iron-sulphur cluster chain to ubiquinone transforming it into ubiquinol. This transfer of electrons causes a conformational change which opens complex I's proton pore and drives the transfer of four protons, from the matrix into the mitochondrial intermembrane space (reviewed by Zhao *et al.*, 2019; Nolfi-Donegan, Braganza and Shiva, 2020).

1.2.1.2.2 Complex II

Complex II can also initiate oxidative phosphorylation. Complex II is formed of four subunits. Like complex I, a portion of the complex is embedded in the IMM and the rest protrudes into the matrix. Complex II is not a proton pump, however, it is part of the citric acid cycle where it catalyses the conversion of succinate to fumarate reducing the FAD molecule to $FADH_2$. This creates a constant supply of $FADH_2$, which releases its electrons to the iron-sulphur cluster chain within complex II, resulting in the transfer of electrons to ubiquinone to form ubiquinol (reviewed by Zhao *et al.*, 2019; Nolfi-Donegan, Braganza and Shiva, 2020).

1.2.1.2.3 Complex III

Complex III is the second proton pump and facilitates the transfer of electrons from ubiquinol to cytochrome c. Complex III fully resides within the IMM and consists of eleven subunits. Ubiquinol first binds to the Q0 (ubiquinol oxidation site) on the intermembrane space side of complex III, triggering the release of two protons, through complex III, into the mitochondrial intermembrane space. This oxidises ubiquinol causing the transfer of one electron to the iron-sulphur cluster in complex III, and subsequently to cytochrome c, via the intermediate cytochrome c1. The second electron of ubiquinol quickly transfers to cytochrome b low affinity, followed by cytochrome b high affinity, both within complex III. Where the electron then transfers to a ubiquinone molecule bound at the Q1 site, in the matrix, forming ubisemiquinone. A second ubiquinol molecule binds to Q0 and undergoes the same process, releasing two more protons into the intermembrane space and transferring an electron to cytochrome C and the reduced ubisemiquinone transforming it to ubiquinol and releasing it back into the matrix. This all happens because cytochrome c can only accept one electron, while ubiquinol donates two (reviewed by Zhao *et al.*, 2019; Nolfi-Donegan, Braganza and Shiva, 2020).

1.2.1.2.4 Complex IV

Complex IV is the final proton pump in the chain. Like complex III, it spans the IMM and consists of thirteen subunits. Cytochrome c is a mobile electron carrier that transports the electrons from complex III to complex IV. Electron static attraction guides cytochrome c to subunit II of complex IV where two molecules transfer two electrons to a copper ion (CuA) at the same time. The first electron travels along a chain from CuA to heme a, then heme a3, stopping at CuB. The second stops at heme a3. An oxygen molecule forms a bridge between heme a3 and CuB accepting the electrons from each metal. A second pair of cytochrome c molecules transfer two more electrons which travel down the metal chain to the oxygen bridge reducing it further and causing two protons to bind forming two OH groups. Two more cytochrome c molecules then donate electrons to the OH group, via the same mechanism, enabling another pair of protons to bind to the OH groups forming water molecules. This process drives four protons into the intermembrane space (reviewed by Zhao *et al.*, 2019; Nolfi-Donegan, Braganza and Shiva, 2020).

1.2.1.2.5 Complex V

Complex V is the last complex of the ETC and is an F_0F_1 ATP synthase. It consists of sixteen subunits that form the F_0 and F_1 domains. The F_1 domain contains three α subunits, three β subunits, a γ subunit, a δ subunit and a ε subunit. The γ, δ and ε subunits form a central stalk, δ and ε at the base above the c-ring of the F_0 domain. The γ subunit protrudes into the matrix where it is surrounded by the ring of six alternating α and β subunits. The F_0 domain is bound to the IMM and formed from a ring of 8 c

subunits, a peripheral stalk (one b subunit, d subunit, F_6 subunit and an oligomycin sensitivity conferral protein (OSCP), one a subunit and accessory subunits (e, f, g, A6L) (Figure 1).

The proton gradient created by the transfer of protons into the mitochondrial intermembrane space enables protons to flow down the gradient through complex V. They travel through the F_0 c-ring back into the mitochondrial matrix. This transfers energy to the F_1 domain causing a conformational change and rotation of the γ subunit which drives the synthesis of ATP from adenosine diphosphate (ADP) and phosphate (Figure 1). The peripheral arm stabilises the structure and prevents the α/β ring from spinning (reviewed by Jonckheere, Smeitink and Rodenburg, 2012; Neupane *et al.*, 2019).

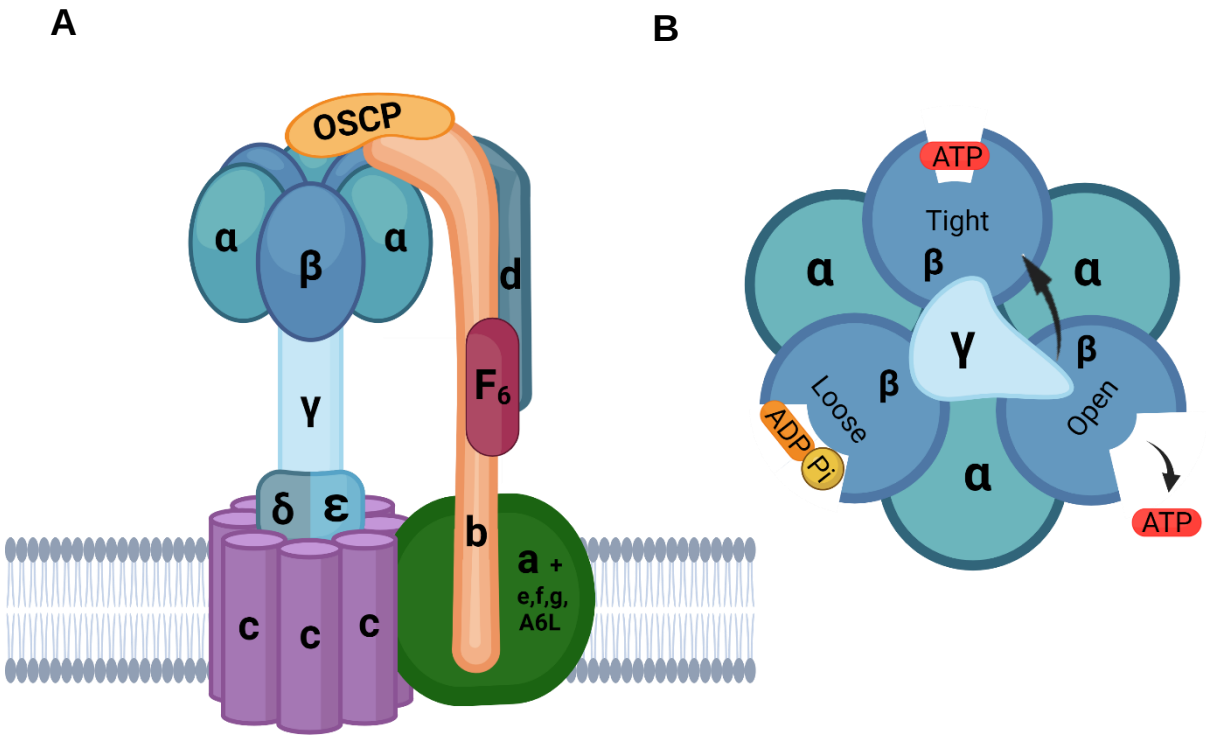

Figure 1: Complex V structure and ATP synthesis. A) Structure of complex V showing all subunits. **B)** A view from the matrix side of the α/β ring with the γ subunit rotating causing conformational changes that enable the production of ATP from ADP + phosphate (adapted from Neupane et al., 2019).

1.2.1.3 Fuel Usage during ATP Production

Aerobic respiration is the most commonly used method for producing ATP. It uses glucose generated from carbohydrates as a chemical energy source. Anaerobic respiration also uses glucose through glycolysis. Lactate dehydrogenase converts pyruvate into lactate by the oxidation of NADH to NAD+. This does not require the involvement of mitochondria. Other chemical energy sources can be used

by mitochondria when glucose levels are low, these include fatty acids, amino acids, DNA and RNA. For the purpose of this study, fatty acid and amino acid oxidation will be reviewed below.

1.2.1.3.1 Fatty Acids

Fatty acids are the main source of chemical energy during nutrient stress because they store large amounts of energy, particularly compared to glucose. For example, a 16-carbon fatty acid stores over double the energy per gram. Fatty acids are generated by lipolysis, which will not be reviewed. Like pyruvate these are processed before transport into the mitochondria; acyl-CoA synthetases bind CoA with the fatty acid to form fatty CoA in an ATP-dependent manner. There are five groups of acyl-CoA synthetases, each specialised to specific length fatty acids (Ma *et al.*, 2021).

Long-chain fatty acids do not pass through the mitochondria membranes, therefore carnitine palmitoyl transferase 1 processes the fatty CoA into acylcarnitine, which can be shuttled across the IMM by carnitine-acylcarnitine translocase. In the matrix, carnitine palmitoyl transferase 2 releases the fatty CoA from carnitine enabling fatty acid β-oxidation to begin. Mitochondrial β-oxidation is a repeated four step process and produces one NADH, one $FADH_2$ and one acetyl-CoA per round, leaving the fatty CoA two carbons shorter. Chain-specific acyl-CoA dehydrogenase oxidises the bond between the α and β carbons in the fatty acid chain reducing FAD to $FADH_2$. Then enoyl CoA hydratase hydrates this bond site to attach an OH^- group to the β carbon and an H^+ to the α carbon. Next, β-hydroxyl acyl CoA dehydrogenase removes two protons and electrons from the hydroxyl group and β carbon to reduce NAD+ to NADH. Finally, the bond between the carbons is cleaved by β-keto thiolase with a second CoA to produce acetyl-CoA and a fatty CoA with two fewer carbons. This process is repeated until the fatty CoA is left with two carbons, so for a sixteen-carbon fatty CoA, eight rounds of β-oxidation occur. Unsaturated double bonds cannot undergo β-oxidation and must be isomerised to form a single bond by either enoyl CoA isomerase or 2,4-dienoyl CoA reductase. Fatty acids with an odd number of carbons are not processed as fully and the repeated process of β-oxidation stops at a five-carbon length chain. Each round of β-oxidation can produce four ATP molecules from the NADH and $FADH_2$, while the acetyl-CoA enters the citric acid cycle described above (reviewed by Spinelli and Haigis, 2018; Adeva-Andany *et al.*, 2019; Talley and Mohiuddin, 2020).

1.2.1.3.2 Amino Acids

Mitochondria can oxidise a variety of amino acids to produce ATP, however, this review will focus on glutamine. Glutamine is the most abundant amino acid; it can be transported into the mitochondria. Some cell types can form glutamine from glutamate and ammonia in the mitochondrial matrix by glutamine synthetase, but localisation of the enzyme to mitochondria is weak and does not occur in astrocytes (Matthews *et al.*, 2010). The reverse of this process is the first step of glutamine catabolism,

glutamine is converted into glutamate and ammonia by glutaminase. Glutamate is converted to α-ketoglutarate by glutamate dehydrogenase, reducing NADP+ to NADPH. α-ketoglutarate is a component of the citric acid cycle and glutamine/glutamate catabolism replenishes it during nutrient deficiency (DeBerardinis *et al.*, 2007; Yang *et al.*, 2014; and reviewed by Plaitakis *et al.*, 2017).

1.2.1.4 Other Functions

Mitochondria have other roles within the cell such as involvement in calcium signalling, immune response, cell death and reactive oxygen species (ROS) production. These have been extensively reviewed by Murphy *et al.*, (2016), Nguyen *et al.*, (2019), Osellame *et al.*, (2013) and Wang and McLean (2022) respectively and hence here only a short overview is provided.

1.2.1.4.1 Calcium Signalling

Mitochondria play a crucial role in calcium homeostasis. Mitochondrial calcium uniporter transports calcium into the mitochondria where it signals for upregulated ATP production by downstream pathways and even mitochondrial biogenesis. During calcium overload, the mitochondria are capable of sweeping up substantial amounts of calcium from the cytosol to temporarily maintain health.

1.2.1.4.2 Immune Response

The role of mitochondria in the immune response is twofold. Firstly, metabolic reprogramming is vital to determine an immune cell's fate, this is the reliance on specific fuel metabolism or the use of oxygen. For example, inflammatory macrophages rely heavily on anaerobic glycolysis, but memory T-cells prefer oxidative phosphorylation for ATP production. Immune cells undergo metabolic reprogramming when they change between active and resting states. The second role is regulating the innate immune response with signalling molecules. Mitochondrial ROS triggers NLRP3 activation and pro-inflammatory cytokine production. mtDNA can activate the same systems when released from dysfunctional mitochondria, but it is also recognised by pattern recognition receptors and GMP/AMP synthase that mediate downstream immune responses. In some cases, mtDNA is released into the circulatory system leading to systemic inflammation.

1.2.1.4.3 Cell Death

Cell death occurs by necrosis or apoptosis, both of which mitochondria are involved in. Its role in necrosis is to open its mitochondrial permeability transition pore resulting in a loss of calcium homeostasis, dissipation of the MMP and ATP production, causing rapid cell death. Apoptosis can be mitochondrially triggered. In health, cytochrome c is sequestered in the intermembrane space. To trigger apoptosis, a complex path of molecular interactions on the OMM enables the release of cytochrome c into the cytosol, resulting in the formation of the apoptosome and subsequent caspase-3 activation.

1.2.1.4.4 ROS Signalling

ROS are unwanted bioproducts of oxidative phosphorylation. They are formed by the leakage of electrons. If unchecked vast qualities of ROS lead to damage within the cell, cell death and associated pathologies. Mitochondria and the cytoplasm contain antioxidants which scavenge ROS but ensure low levels are maintained. These low levels are important for signalling within the cell, regulating processes such as protein phosphorylation, self-defence mechanisms after injury and transcription regulation.

1.2.1.5 Fission and Fusion

Mitochondria form a network throughout cells which is carefully maintained by continuous fusion and fission. Fusion involves the combining of mitochondria and is thought to enable the sharing of mtDNA and distribution of other mitochondrial components, as well as acting as a buffer against temporary deleterious effects. Fission on the other hand enables the transport of mitochondria to distribute healthy mitochondria or remove dysfunctional segments. Fission allows for the segmentation of mtDNA creating heteroplasmy and the release of cytochrome c during apoptosis. It is sometimes stated that connected mitochondria are highly functional but fragmented mitochondria are dysfunctional. However, mitochondria are the Goldilocks of the cell, both excessive connectivity or fragmentation by a disequilibrium in fission and fusion results in dysfunction. The amount of connectivity is tightly controlled and must be kept just right for cellular health (reviewed by Osellame, Blacker and Duchen, 2012; Friedman and Nunnari, 2014; Murphy *et al.*, 2016; Adebayo *et al.*, 2021; Kraus *et al.*, 2021).

The process of mitochondria fusion involves three GTPases: Mitofusin 1 and 2 (MFN1/2) and optic atrophy protein 1 (OPA1). MFN1 and MFN2 first accumulate at mitochondria contact sites, where they promote docking by oligomerisation and subsequent fusion of the OMMs. OPA-1 then mediates IMM fusion. Long isoform OPA1 (L-OPA1) is tethered to the IMM and hangs in the intermembrane space. It is hypothesised that this tail binds to cardiolipin enabling the fusion of the IMM. There are eight splice variants of OPA1 and cleavage at site S1 by overlapping with the M-AAA protease 1 (OMA1) determines if they are L-OPA1 or short isoform OPA1 (S-OPA1). The involvement of S-OPA1 is debated with studies showing that fusion can or cannot occur without S-OPA1 (reviewed by Friedman and Nunnari, 2014; Adebayo *et al.*, 2021).

Mitochondria fission is mediated by dynamin-related protein 1 (DRP1), dynamin 2 (DNM2), human mitochondrial dynamic proteins 49 and 51 (MID49/51), mitochondria fission 1 protein (FIS1) and mitochondria fission factor (MFF). DRP1 occurs in the cytosol and localises to the mitochondria by

recruitment from MID49, MID51, FIS1 and MFF. DRP1 forms an oligomeric ring around the mitochondria. DRP-1 is a GTPase and once the ring is formed GTP hydrolysis occurs to cause conformational changes and a constriction of the ring. This is followed by DNM2 recruitment to cleave the site, although this is debated (reviewed by Friedman and Nunnari, 2014; Adebayo *et al.*, 2021).

1.2.1.6 Mitophagy

Mitophagy is the process of recycling dysfunctional mitochondria to maintain a functional network. Mitophagy removes small, fragmented mitochondria that have been cleaved from the network by fission and targeted for degradation. Once a mitochondrion is damaged beyond repair, mitophagy receptors initiate mitophagy. Several receptor pathways utilise different initiation factors such as B-cell lymphoma 2 Interacting Protein 3 (BNIP3), FUN14 Domain Containing 1 (FUNDC1) or PINK1/Parkin. These receptors recruit autophagosome machinery, including Microtubule-associated protein 1A/1B-light chain 3 (LC3), to form a vesicle that carries the mitochondrion to a lysosome. PINK1/Parkin involvement in PD highlights this crucial mechanism in mitochondrial quality control (Onishi *et al.*, 2021). Mitophagy regulation, pathways and involvement in PD have been extensively reviewed elsewhere (Malpartida *et al.*, 2021; Onishi *et al.*, 2021; Li *et al.*, 2022).

1.2.2 Mitochondria in Parkinson's Disease

Mitochondrial dysfunction was first identified as a mechanism of PD in the 1980s when drug users took synthetic heroin containing 1-methyl-4-phenyl-1,2,3,6-tetrahydropyridine (MPTP) and displayed a Parkinsonian phenotype (Ballard, Tetrud and Langston, 1985). It was discovered, using animal models, that MPTP is metabolised to form a 1-methyl-4-phenylpyridinium ion, which is a complex I inhibitor and results in SN neuron loss (Langston *et al.*, 1984; Ballard, Tetrud and Langston, 1985). Inhibition of complex I resulted in reduced ATP levels and harmful ROS production (Ramsay, Salach and Singer, 1986; Hasegawa *et al.*, 1990; Chan *et al.*, 1991). Other toxins, which were commonly used without protection, have since been associated with PD and implicated in mitochondrial dysfunction, such as rotenone (Sherer *et al.*, 2003), paraquat (Mollace *et al.*, 2003) and trichloroethylene (Gash *et al.*, 2008).

Subsequently, genetic screening identified multiple genetic variants that are associated with PD and mitochondrial functions. Some variant genes encode proteins that directly interact with mitochondria, including *PINK1* (Valente *et al.*, 2001), *PRKN* (Kitada *et al.*, 1998) and *DJ-1* (Matsumine *et al.*, 1997).

Other genetic variants occur in genes encoding proteins that do not directly interact with mitochondria but result in mitochondrial dysfunction. These include *LRRK2* (Paisán-Ruíz *et al.*, 2004; Zimprich *et al.*, 2004), *VPS35* (Zimprich *et al.*, 2011) and *SNCA* (Polymeropoulos *et al.*, 1997). Mitochondria in sporadic PD (sPD) display some phenotypes similar to LRRK2 and Parkin PD (Chai and

Lim, 2013; Macdonald *et al.*, 2018). Complex I, and in some studies complex IV, activity is decreased in the SN, platelets and patient-derived fibroblasts of sporadic PD patients (Bindoff *et al.*, 1989; Schapira *et al.*, 1990; Benecke, Strümper and Weiss, 1993; Winkler-Stuck *et al.*, 2004; Keeney *et al.*, 2006). This decrease was not observed in all studies, suggesting variability in methodology, tissue or heterogeneity within sPD patients (Subrahmanian and LaVoie, 2021). An increase in mtDNA aberrations was shown in postmortem SN samples (Gu *et al.*, 2002; Dölle *et al.*, 2016); this is due to a depletion in wildtype mtDNA and the normal age-related accumulation of mutations (Dölle *et al.*, 2016).

Carling *et al.* (2020), was the first study to stratify a mitochondrial dysfunction-driven subgroup. They analysed the differences between a cohort of 100 sPD patients and 50 controls. There was no significant difference in ATP or MMP between the patient and controls. However, they found a subgroup of patients with ATP and MMP levels that were 2 standard deviations lower than the control group. Fibroblasts from this group were converted to induced Neuronal Progenitor Cell (iNPC) derived iDA neurons, which showed far greater depletions in ATP and MMP compared to controls. Interestingly, they also found several patients with increased mitochondrial activity (Carling *et al.*, 2020). This result was supported by another large sporadic cohort study that showed increased mitochondrial respiration as well (Milanese *et al.*, 2019). However, both groups show mitochondrial function variability is greater in the PD population than in the controls (Milanese *et al.*, 2019; Carling *et al.*, 2020). Postmortem brain tissue shows similar heterogeneity. A study using ninety-two sPD patient tissue found no difference between patients and controls in complex I positive neurons in the SN, but a proportion of the sPD patients had significantly lower complex I. They classified this group as a specific subgroup of PD. Further investigation showed the group had an elevated number of mtDNA deletions and distinct transcriptomic profiles compared to complex I normal patients (Fløtnes *et al.*, 2024).

Overall, there is strong evidence supporting the contribution of mitochondrial dysfunction in sPD and the heterogeneity of the mechanism. Additionally, the findings by Carling *et al.* (2020) and Fløtnes *et al.* (2024) suggest that it is possible to stratify sPD patients based on cellular mechanisms, particularly for the mitochondria dysfunction phenotype.

1.3 Lysosomal Biology

1.3.1 Healthy Lysosomes

Almost 70 years have passed since Christian de Duve first described small compartments containing hydrolytic enzymes within cells (de Duve *et al.*, 1955). Since then, our understanding of lysosomes has

advanced greatly; however, their role in PD has yet to be untangled from other dysfunctional pathways.

Lysosomes are integral to cell maintenance, recycling and removal of cellular and extracellular material. Structurally, lysosomes are membrane-enclosed organelles that contain hydrolytic enzymes capable of degrading substrates from simple proteins, carbohydrates and lipids to complex structures such as organelles (Cooper and Hausman, 2007). This membrane is called the limiting membrane because it protects the cell from the lysosome's contents and consists of a lipid bilayer and many membrane-bound proteins. The lysosome also contains intraluminal vesicles, which are thought to play a role in lipid degradation. It is unclear what prevents the lipolysis of the limiting membrane. The lysosome has a unique lipid signature, namely an enrichment of sphingomyelin and bis(monoacylglycerol)phosphate (BMP), but low levels of cholesterol (Brotherus and Renkonen, 1977; Möbius *et al.*, 2003). In fact, increased levels of lysosome cholesterol are a marker of lysosomal storage disorders. However, BMP is scarce within the cell, aside from the lysosome, and its precursors, phosphatidylglycerol and cardiolipin, originate in the mitochondria. Its unique stereochemical configuration means it cannot be degraded by lysosomal enzymes. BMP is enriched in the intraluminal vesicles; it is theorised that BMP is a binding site and cofactor of lipases, such as sphingomyelinase and phospholipase A_2. The fact that BMP is almost absent from the limiting membrane may be the reason why lipases cannot bind and degrade the lipid bilayer (reviewed by Schulze, Kolter and Sandhoff, 2009; Cockcroft, 2021; Rudnik and Damme, 2021). There are over 120 lysosomal membrane proteins (Braulke and Bonifacino, 2009), which play a role in acidification, membrane transport, organelle trafficking, signalling and vesicle fusion. Lysosomal membrane proteins are heavily glycosylated, forming a glycocalyx. The glycocalyx's function is still unidentified but it may be another protective mechanism maintaining the limiting membrane's integrity (Kosicek *et al.*, 2018). Lysosome-associated membrane proteins 1 and 2 (LAMP1/2) account for 50 % of the membrane protein content (Eskelinen, 2006). The lumen of these organelles contains roughly 60 hydrolases, which require an acidic environment of pH 4.5-5.5 to function optimally (Cooper and Hausman, 2007; Ballabio and Bonifacino, 2020; Muthukottiappan and Winter, 2021). The recycled cellular components are then transported into the cytosol by over 30 transporter proteins highlighting the complexity of this organelle (Muthukottiappan and Winter, 2021).

1.3.1.1 Lysosome Biogenesis

Lysosomes are formed by the fusion of a vesicle that buds off from the golgi apparatus or plasma membrane and either an endosome, phagosome or autophagosome (Cooper and Hausman, 2007). Although some proteins are initially packed into the golgi vesicle lumen, the majority are transported to the lysosome. Hydrolases are synthesised and transported to the lumen of the endoplasmic

reticulum. Glycosylation and cleavage processing occurs before transport to the golgi apparatus. During transport through the golgi, further processing of the oligosaccharide occurs to bind mannose-6-phosphate (M6P). The M6P is recognised by M6P receptors, resulting in the clathrin-coated vesicle packaging and fusion with endosomes. In the endosome, the hydrolases dissociate from the M6P receptor. The endosome then travels to the lysosome and fuses to load the lysosome. Other receptors have also been implicated in transport, such as sortilin, lysosomal integral membrane protein 2 (LIMP-2) and low-density lipoprotein receptor-related protein. Lysosomal membrane proteins cannot be tagged with M6P and transport is mediated by sorting signal sequences in their C-terminus. This can take two routes, the first is via endosomes packaged in the golgi that fuse with the lysosome and the second is via the secretory network where they are transported to the plasma membrane before being re-internalised and transported to the lysosome (extensively reviewed by Bonifacino and Traub, 2003; Janvier and Bonifacino, 2005; Braulke and Bonifacino, 2009; Xu and Ren, 2015; Yang and Wang, 2021).

1.3.1.2 Acidification

Lysosomal acidification is controlled by vaculolar-type ATPase (v-ATPase), a proton pump that transects the limiting membrane. It hydrolyses ATP to provide the energy required to transport protons into the lumen (Ohkuma, Moriyama and Takano, 1982). It is a rotatory proton transporter with a similar structure to complex V of the ETC (Nelson, 1992), hydrolysis of ATP in the cytosolic F_1 domain drives the rotation of the central stalk which is attached to a c-subunit rotor. Protons travel through the c-subunit rotor (Hirata *et al.*, 2003; Yokoyama *et al.*, 2003). Proton transport increases the voltage difference across the membrane which must be dissipated to maintain the transport of protons. Strong evidence suggests voltage is reduced by an influx of anions (Dell'Antone, 1979; Ohkuma, Moriyama and Takano, 1982; Cuppoletti, Aures-Fischer and Sachs, 1987; Van Dyke, 1993; Graves *et al.*, 2008) but there is some evidence stating that the efflux of cations is required (Steinberg *et al.*, 2010), transporters for both are present in the limiting membrane (Kornak *et al.*, 2001; Graves *et al.*, 2008; Majumdar *et al.*, 2011; Xu *et al.*, 2014). Acidification controls degradation in the lysosome by enabling hydrolase maturation (Richo and Conner, 1994), dissociation of lipids and proteins from receptor carriers (Yamashiro and Maxfield, 1984; Singh *et al.*, 2009) and metal ions (Yamashiro and Maxfield, 1984; Asano *et al.*, 2011). Acidification has been extensively reviewed by Mindell (2012) and Colacurcio and Nixon (2016).

1.3.1.3 Lysosomal Fusion

There are four main ways that cargo is delivered to the lysosome: maturation, vesicular, kiss-and-run and hybrid. Vesicular is the most commonly known, where a vesicle fuses with the lysosome to form one structure. Kiss-and-run is a similar method; however, the vesicle is transiently fused and buds off from the lysosome after exchanging contents (Bright, Gratian and Luzio, 2005). The hybrid method is

where large endosomes fuse with lysosomes forming a hybrid organelle, which often reforms a lysosome by minor maturation (Bright *et al.*, 1997). Lastly maturation, this occurs in endosomes that bud off from the plasma membrane and are loaded with lysosomal proteins in a form of biogenesis.

The process of endosomal fusion is well documented. Docking requires the proteins N-ethylmaleimide sensitive factor (NSF), SNAPs and GTPase Rabs (Rab7 most likely) to tether the endosome and lysosome within 25 nm of one another (Bright *et al.*, 1997; Mullock *et al.*, 1998). Tethering may also include the homotypic fusion and vacuole protein sorting (HOPS) complex. This enables the formation of a trans-SNARE complex consisting of syntaxin-7, syntaxin-8, vacuolar protein sorting (VPS) 10 protein tail interactor-1B and VAMP-7. VAMP-7 wraps around the three other proteins forming a parallel helix bundle called a SNARE-pin that draws the membranes tightly together (Antonin *et al.*, 2002; Pryor *et al.*, 2004). Lastly, Ca^{2+} efflux and Calmodulin activation facilitate final membrane fusing in some way but this is yet to be described (Jaconi *et al.*, 1990; Pryor *et al.*, 2000). Autophagosome fusion with lysosomes is more complicated; a recent review by Ke (2024) outlines the various mediators. The complex array of mediators includes three different SNARE complexes with different tethering factors, such as HOPS complex, Autophagy-related protein 14 (ATG14), Golgi Reassembly and Stacking Protein 55 (GRASP55) and BIR repeat containing ubiquitin-conjugating enzyme (BRUCE). LAMP2, Rab7 and ATG8/LC3 may also play a role in some cases.

1.3.1.4 Hydrolases

There are 60 different hydrolases in the lumen of the lysosome. These are sub-classed into phosphatases, nucleases, sulfatases, proteases, lipases and glycosidases (Trivedi, Bartlett and Pulinilkunnil, 2020; Bouhamdani, Comeau and Turcotte, 2021). Deficiencies or loss-of-function of hydrolases are the cause of many rare diseases, of which most involve neurodegeneration (Lübke, Lobel and Sleat, 2009). This suggests that neurons are incredibly sensitive to loss of hydrolase function.

1.3.1.4.1 Proteases

The most characterised hydrolases are the cathepsins. These are a family of fifteen proteases that are classified based on a specific amino acid in their active site. There are serine proteases (A and G), aspartyl proteases (D and E) and cysteine proteases (B, C, F, H, K, L, O, S, V, X and W). Cathepsin activity is tightly regulated by pH; some can even autoactivate when the pH is acidic enough (Yadati *et al.*, 2020). For example, Cathepsin D (CatD) is optimally active at pH 4.0 (Yadati *et al.*, 2020) but autoactivates at pH 4.5 (Richo and Conner, 1994), whereas Cathepsin B (CatB) is optimally active at pH 6.0 (Werle *et al.*, 1997; Colacurcio and Nixon, 2016). This may be linked to the roles they play in the cytosol when they are incorrectly packaged. For example, CatB is involved in apoptosis, NLRP3 inflammasome activation, TGF-β signalling and lipid metabolism (Yadati *et al.*, 2020).

1.3.1.4.2 Lipases

An example of a lipase is lysosomal acid lipase that catalyses cholesteryl esters and triglycerides into cholesterol and fatty acids, respectively.

1.3.1.4.3 Sulfatases

Eight sulfatases are specifically localised to the lysosome, where they mainly catalyse sulfatides, specifically sphingolipids with galactose-3S head groups, and glycosaminoglycans. Deficiencies in sulfatases are the cause of seven lysosomal storage diseases (Hanson, Best and Wong, 2004).

1.3.1.4.4 Nucleases

Nucleases are specialised to degrade either RNA or DNA. DNAase-II, for example, can degrade double-stranded DNA without specificity. It is specially glycosylated to optimally function in acid conditions. Its main function is to degrade pathogen DNA upon phagocytosis or cellular DNA during apoptosis (Evans and Aguilera, 2003; Fujiwara, Wada and Kabuta, 2017).

1.3.1.4.5 Glycosidases

Glycosidases cleave glycosidic bonds, often these are attached to lipids or proteins (Cecioni *et al.*, 2022). GCase is the most relevant to PD, as reviewed above. Glycosidases are the second largest group of hydrolases in the lysosome and deficiencies are responsible for a myriad of genetically inherited diseases that lead to neurological degeneration, such as Fabry disease, Schindler disease and Tay–Sachs disease, to name a few (Lübke, Lobel and Sleat, 2009).

1.3.1.4.6 Phosphatases

Phosphatases are a small family of lysosomal hydrolases. One example is lysosomal acid phosphatase, which cleaves the M6P tag off cargo when it is transported to the lysosome. This is crucial to the transport of almost all hydrolases (Ashtari *et al.*, 2016).

Table 3: A summary of all the lysosomal hydrolases, their function, transport mechanism and associated diseases. (Main souce: Lübke, Lobel and Sleat, 2009; with additions from Evans and Aguilera, 2003; Hanson, Best and Wong, 2004; Yadati et al., 2020; Bouhamdani, Comeau and Turcotte, 2021)

Enzyme Function	Enzyme	Related disease	Transport method
Protease	Cathepsin A	Neuraminidase deficiency with beta-galactosidase deficiency	M6P receptor-mediated

	Cathepsin B		M6P receptor-mediated or LRP1
	Cathepsin C	Papillon–Lefèvre syndrome	M6P receptor-mediated
	Cathepsin D	Neuronal ceroid lipofuscinosis (type 10)	M6P receptor or sortilin or LRP1
	Cathepsin E		M6P receptor-mediated
	Cathepsin F	Neuronal ceroid lipofuscinosis (type 10)	M6P receptor-mediated
	Cathepsin G		M6P receptor-mediated
	Cathepsin H		M6P receptor-mediated or sortilin
	Cathepsin K	Pycnodysostosis	M6P receptor-mediated
	Cathepsin L		M6P receptor-mediated
	Cathepsin O		M6P receptor-mediated
	Cathepsin S		M6P receptor-mediated
	Cathepsin V		M6P receptor-mediated
	Cathepsin W		M6P receptor-mediated
	Cathepsin X		M6P receptor-mediated
	Cathepsin Z		M6P receptor-mediated
	Dipeptidyl-peptidase I	Papillon-Lefevre syndrome	M6P receptor-mediated
	Carboxypeptidase, vitellogenic-like		M6P receptor-mediated
	Gamma-glutamyl hydrolase		M6P receptor-mediated
	Legumain		M6P receptor-mediated
	Tripeptidyl-peptidase I	Ceroid lipofuscinosis	M6P receptor-mediated
Lipase	Acid ceramidase	Farber disease	M6P receptor-mediated
	Acid lipase	Wolman disease	M6P receptor-mediated
	Palmitoyl-protein thioesterase 1	Ceroid lipofuscinosis	M6P receptor-mediated
	Palmitoyl-protein thioesterase 2		M6P receptor-mediated
	Sphingomyelin phosphodiesterase	Niemann-Pick disease (type a and b)	M6P receptor-mediated
	N-acylsphingosine amidohydrolase (acid ceramidase)-like (NAAA)		-

	Acyloxyacyl hydrolase		M6P receptor-mediated
Glycosidase	Alpha-galactosidase A	Fabry disease	M6P receptor-mediated
	Alpha-L-iduronidase	Mucopolysaccharidosis type I	M6P receptor-mediated
	Alpha-N-acetylgalactosaminidase	Schindler disease (type I)	M6P receptor-mediated
	Alpha-N-acetylglucosaminidase	Mucopolysaccharidosis type IIIb	M6P receptor-mediated
	Beta-galactosidase	Mucopolysaccharidosis type IVb	M6P receptor-mediated
	Beta-glucuronidase	Mucopolysaccharidosis type VII	M6P receptor-mediated
	Beta-hexosaminidase	Tay–Sachs disease or Sandhoff disease	M6P receptor-mediated
	Beta-mannosidase	Mannosidosis	M6P receptor-mediated
	Galactocerebrosidase	Krabbe disease	M6P receptor-mediated
	Glucocerebrosidase	Gaucher's Disease and Parkininson's Disease	LIMP-2 mediated
	Glycosylasparaginase	Aspartylglucosaminuria	M6P receptor-mediated
	Hyaluronidase	Mucopolysaccharidosis type IX	M6P receptor-mediated
	Lysosomal alpha-glucosidase	Glycogen storage disease II	M6P receptor-mediated
	Lysosomal alpha-mannosidase	Mannosidosis, alpha b	M6P receptor-mediated
	Sialic acid 9-O-acetylesterase		M6P receptor-mediated
	Sialidase 1	Mucolipidosis I	M6P receptor-mediated
	Sialidase 4		M6P receptor-mediated
	Tissue alpha-L-fucosidase	Fucosidosis	M6P receptor-mediated
Sulfatase	Arylsulfatase A	Metachromatic leukodystrophy	M6P receptor-mediated
	Arylsulfatase B	Mucopolysaccharidosis type VI	M6P receptor-mediated
	Arylsulfatase G		M6P receptor-mediated
	Arylsulfatase K		M6P receptor-mediated
	heparan N-sulfatase	Mucopolysaccharidosis type IIIa	M6P receptor-mediated
	Iduronate 2-sulfatase	Hunter syndrome	M6P receptor-mediated

	N-acetylgalactosamine-6-sulfatase	Mucopolysaccharidosis type IVa	M6P receptor-mediated
	N-acetylglucosamine-6-sulfatase	Mucopolysaccharidosis type IIId	M6P receptor-mediated
Phosphatase	Tartrate-resistant acid phosphatase		M6P receptor-mediated
	Lysosomal acid phosphatase		LAP pathway, trafficking via the plasma membrane
Nuclease	Ribonuclease T2		-
	Deoxyribonuclease II (DNAase II)		M6P receptor-mediated

1.3.1.5 Recycling Building Blocks

Once degradation is finished, the products must be redistributed around the cell because they are often valuable building blocks. Lysosomes are involved in nutrient sensing and, in times of stress, collect in the perinuclear region and swell. It is hypothesised to increase autophagy for metabolite production (Ballabio and Bonifacino, 2020; Bouhamdani, Comeau and Turcotte, 2021). Ten lysosome membrane transporters that export metabolites exist, exporting amino acids, dipeptides, small lipids and monosaccharides (Pisoni and Thoene, 1991; Rudnik and Damme, 2021). Unlike hydrolases, mutations are rarely associated with disease. This may be due to other mechanisms enabling release or that loss of function mutations are not compatible with life, resulting in death before birth (Rudnik and Damme, 2021). One example is Niemann-Pick C1 (NPC1), an exporter of cholesterol, defects cause cholesterol accumulation seen in Niemann Picks Disease (Lu, 2022). Transporters are large proteins with six or more transmembrane domains and are heavily glycosylated to protect the protein domains from proteases (Rudnik and Damme, 2021). The mechanism of export by many of these proteins is still unclear, although some are dependent on ATP hydrolysis and others require H^+ symport (Sagné and Gasnier, 2008).

1.3.1.6 Mitochondria and Lysosome Contact Sites

Lysosomes form contacts with multiple organelles, such as mitochondria (Wong *et al.*, 2019). It is proposed that the contacts enable signalling between organelles without degradation, particularly between mitochondria and lysosomes. Importantly, the fusion of membranes does not occur; a 10 nm gap between the membranes is observed (Wong, Ysselstein and Krainc, 2018). Mitochondria-lysosome contacts are generally transient, existing for an average of 60 seconds but can last for over 10 minutes.

Despite being short-lived, contacts are relatively common, with roughly 15 % of lysosomes contacting mitochondria at any one time (Wong, Ysselstein and Krainc, 2018).

Mitochondria-lysosome contact tethering currently eludes researchers. It is known that Rab7-GTP is required but further work is required to understand the other players. Untethering is better understood. Tre-2/Bub2/Cdc16 domain family member 15 (TBC1D15) is recruited to the mitochondria by FIS1. TBC1D15 triggers Rab7-GTP hydrolysis to form guanosine diphosphate (GDP)-bound Rab7 which can no longer interact with effectors and dissociates from the lysosome membrane (Wong, Ysselstein and Krainc, 2018). There is no bulk transfer of material and contacts do not initiate mitophagy.

There are three proposed reasons for contact sites. Contact sites mediate lysosome dynamics by causing the dissociation of Rab7 from the lysosome membrane, preventing functions like fusion (Wong, Ysselstein and Krainc, 2018). The opposite may also be true as mitochondria fission sites are co-localised with LAMP1-positive contact sites (Itoh *et al.*, 2018; Wong, Ysselstein and Krainc, 2018). Both these functions are supported by the untethering process. During untethering, MID51 and FIS1 can form an oligomer resulting in the recruitment of TBC1D15 to FIS1 and DRP1 to MID51. DRP1 is then transferred to MFF leading to DRP1-mediated fission by GTP hydrolysis and TBC1D15-mediated GTP hydrolysis of Rab7, which then dissociates (Wong, Ysselstein and Krainc, 2018; Leisten, Woods and Wong, 2023). Finally, despite the lack of bulk transfer, there may be a selective transfer of ions, such as calcium or iron, amino acids or lipids between organelles (Wong *et al.*, 2019; Peng, Wong and Krainc, 2020; Peng *et al.*, 2023). Mitochondria-lysosome contact duration and number are reduced in Parkin mutant HeLa cells and iDA neurons from iPSCs. Overexpressing TBC1D15 rescued this phenotype in the iDA neurons (Peng *et al.*, 2023).

1.3.2 Lysosomes in Parkinson's Disease

Research into defective lysosomal systems in PD has mainly focused on subgroups of genetically driven or associated PD. GWAS studies have linked multiple gene loci associated with lysosomes and the endo-lysosomal pathways to PD. Lysosome-associated genes *LRRK2* (Funayama *et al.*, 2002), *PARK9* (ATPase cation transporting 13 A2 (ATP13A2) (Ramirez *et al.*, 2006), *VPS35* (Zimprich *et al.*, 2011), *VPS13C* (Lesage *et al.*, 2016) and *CTSB* (Milanowski *et al.*, 2022) have shown various disruptions within lysosomes, however, there is no consistent clinical presentation. Mutations in endo-lysosomal genes associated with the packaging and transport of endosomes to the lysosome are also associated with PD but are much rarer with only a few families carrying the mutations, these include *DNAJC6* (Edvardson *et al.*, 2012), *RAB39B* (Wilson *et al.*, 2014) and *SYNJ1* (Quadri *et al.*, 2013). Interestingly, the most common genetic risk factors for PD are mutations in *GBA1* (Sidransky *et al.*, 2009; Duran *et*

al., 2013), which encodes GCase. Due to these driving genes, it is suggested that lysosomal dysfunction is a primary mechanism of disease.

Dysfunction in three specific hydrolases, GCase, CatD and CatB, has been observed in PD. GCase's involvement in PD was reviewed above (GBA1.1.3.2 GBA). While GCase degrades lipids with carbohydrate heads, cathepsins degrade proteins. Three cathepsins are highly expressed in the brain: CatB, CatD and Cathepsin L (CatL) (Yadati *et al.*, 2020). Genetic mutations that cause PD have been identified in *Cathepsin B* (*CTSB*), the gene encoding cathepsin B proenzymes. Investigation of two related patients' fibroblasts carrying *CTSB* PD-associated variants showed no alterations in mRNA or protein level or activity of CatB (Milanowski *et al.*, 2022). Several GWAS studies have suggested that variants of *CTSB* can be used as a biomarker of PD as they elevate risk, especially in *GBA1* mutants (Chang *et al.*, 2017; Nalls *et al.*, 2019; Blauwendraat *et al.*, 2020). A recent two-sample mendelian analysis of two GWAS cohorts claims that increased levels CatB, predicted genetically by the presence of specific small nucleotide polymorphisms, decrease the risk of PD, although this is a very small reduction (Lu *et al.*, 2024). Observations of CatB within cells have noted differences as well. Most of the work investigating CatB has been conducted using KO lines or inhibition with a CatB-specific inhibitor, CA074me, rather than patient-derived cell lines. Inhibition and KO of CatB in neurons from iPSCs treated with PFFs show increased lysosome number, impaired GCase activity and increased α-syn levels compared to PFF-treated WT iNeurons (Jones-Tabah *et al.*, 2024). This matches previous literature reporting lysosome phenotypes without investigating CatB (García-Sanz *et al.*, 2017; Carling *et al.*, 2020). Not only does CatB appear to alter GCase activity but GBA N370S patient-derived iPSCs have reduced active CatB protein levels, suggesting that they modulate one another (Blauwendraat *et al.*, 2020). Other familial mutations have shown an effect on CatB activity. Transgenic mouse primary astrocytes carrying the LRRK2 G2019S had a reduction in CatB activity and a reduced pH from 5.5 to 5.0 (Henry *et al.*, 2015). LRRK2 G2019S macrophages from engineered iPSCs had a reduction in CatB protein levels, which could be rescued by inhibition of LRRK2 (Yadavalli and Ferguson, 2023). However, it is still unclear whether LRRK2 G2019S causes a reduction in pH leading to less activity or whether it actively modulates CatB protein levels and expression.

Only one genetic study has identified an association between PD and specific *Cathepsin D* (*CTSD*) variants, this identified four point mutations that increase the risk of PD (CTSD V95I, G145V, A239V and R266H) (Robak *et al.*, 2017). These variants were introduced into *CTSD* KO SH-SY5Y cells. No changes in lysosome size or number were identified, while CatB activity was slightly reduced in all mutants. A239V significantly reduced α-syn levels, while the other mutants showed small increases. Surprisingly, A239V significantly elevates CatD activity and protein. G145V reduced protein and activity but not significantly (Bunk *et al.*, 2021). CatD activity is also altered in fPD and sPD. Similar to

CatB, LRRK2 G2019S macrophages have reduced CatD protein, which is rescued by inhibition of LRRK2 (Yadavalli and Ferguson, 2023). An extensive study of GBA N370S dopaminergic neurons showed reduced CatD and pro-CatD protein levels, corresponding with reduced CatD activity. GCase replacement therapy or treatment with Ambroxol restored GCase activity, CatD protein levels and CatD activity. The reduction in activity was associated with increased α-syn monomer levels (Yang *et al.*, 2020), however, it is unclear if this is due to CatD activity or GCase function. It is possible that GCase production of ceramide is the crucial step as ceramide is theorised to activate CatD (Heinrich *et al.*, 2000). The study further confirmed the reduction of CatD protein in PD by assessing levels in sPD and GBA N370S patients' putamen (Yang *et al.*, 2020). Transmembrane protein 175 (TMEM175) KO in Hela cells caused reduced cathepsin activity, specifically CatB and CatD, but no reduction in their protein was observed. Further exploration showed that *Tmem175 (-/-)* mice have reduced CatB activity and increased lysosomal acidification from pH 4.5 to 4.0 (Hu *et al.*, 2022). CatD has been highly studied in lysosomal storage disorders as well. *CTSD* mutations resulting in the inactivation of CatD cause Neuronal Ceroid Lipofuscinoses type 10, a neurodegenerative disorder that results in death within days of birth (Koike *et al.*, 2000; Siintola *et al.*, 2006). Some cases with less severe inactivation can result in late infantile/ juvenile versions of the disease (Rosenberg *et al.*, 2019). However, this CatD deficiency has been associated with severe α-syn aggregation in the brain of these patients, as well as in sheep and mice (Qiao *et al.*, 2008; Cullen *et al.*, 2009). This resulted in further investigation of CatD in α-syn clearance.

As highlighted above, CatB and CatD are active in α-syn clearance, as is CatL. Multiple reports have shown that CatB and CatD form truncated forms of α-syn (Sevlever, Jiang and Yen, 2008; Cullen *et al.*, 2009; R. P. McGlinchey and Lee, 2015; McGlinchey *et al.*, 2019). CatD forms C-terminally truncated versions of α-syn by cleaving the protein at F4/M5 and F94/V95, resulting in a 90 amino acid sequence and at A124/Y125 resulting in a 124 amino acid sequence (Figure 2) (R. P. McGlinchey and Lee, 2015; McGlinchey *et al.*, 2019). It is likely that some reports missed the C-terminal truncation by CatD (Bunk *et al.*, 2021) due to the use of antibodies with C-terminal epitopes (R. P. McGlinchey and Lee, 2015). CatB cleaves at several sites throughout α-syn, the main sites being N122/E123 in fibrillar α-syn and A90/A91 in monomer α-syn (Figure 2), which results in 122 and 90 amino acid sequences that account for the majority of α-syn truncation identified by western blotting (McGlinchey *et al.*, 2019). Although full-length α-syn can aggregate under the right conditions, truncated forms aggregate more readily (Serpell *et al.*, 2000; Murray *et al.*, 2003; Levitan *et al.*, 2011; Iyer *et al.*, 2017; Ma *et al.*, 2018), particularly under acidic conditions (Uversky, Li and Fink, 2001). This is further supported by the identification of truncated forms of α-syn in Lewy Bodies in postmortem patient brain tissue (Baba *et al.*, 1998) and a report that the C-terminus plays no role in aggregation (Qin *et al.*, 2007). Aggregation

is enhanced by truncations after amino acids 85-90, this corresponds with the end of the NAC region of α-syn (amino acids 61-95), which is required for aggregation (Giasson *et al.*, 2001). Further truncation into the NAC region results in reduced α-syn aggregation (Giasson *et al.*, 2001; Murray *et al.*, 2003) suggesting that further proteolysis would result in less aggregation. These results coincide with key SNCA mutations associated with PD occurring in the N-terminal region; A53T (Polymeropoulos *et al.*, 1997), G51D (Lesage *et al.*, 2013), A30P (Krüger *et al.*, 1998), E46K (Zarranz *et al.*, 2004), H50Q (Appel-Cresswell *et al.*, 2013). This data suggests that CatB and CatD actively drive PD progression.

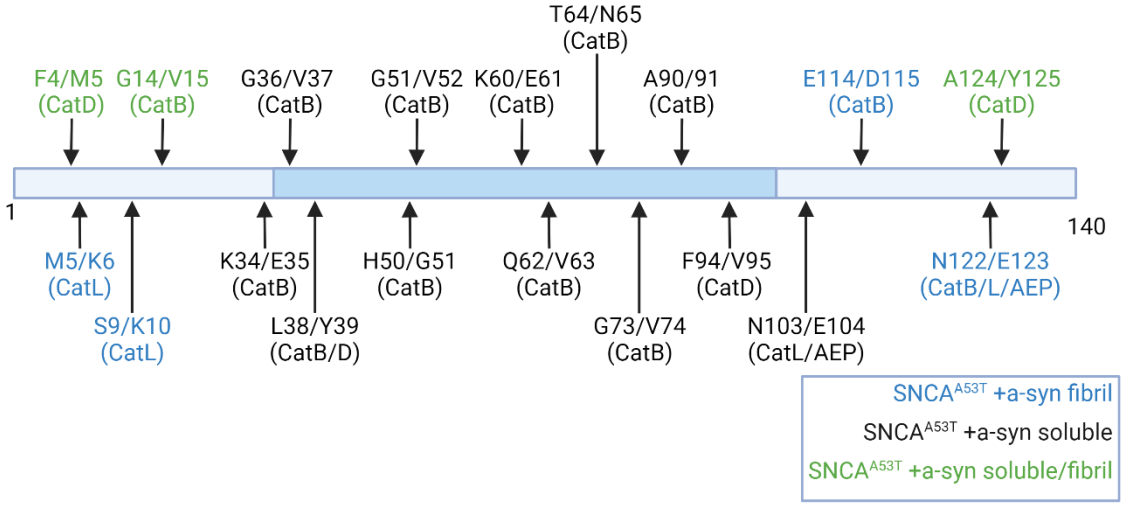

Figure 2: The reported cleavage sites on α-syn by CatB, CatD and CatL. Cuts marked black were identified in soluble α-syn, those in blue occur in fibrillar α-syn and those in green occur in both forms (adapted from McGlinchey *et al.*, 2019).

Table 4: A summary of the cathepsin literature showing results, disease model and authors. The results start with genetic characterisation and then findings in further in-depth studies. Where multiple models were used, numbers indicate the results found in each.

Hydrolase	Findings	Disease Model	Reference
Cathepsin B	CTSB genetic variant for CatB G284V. No reduced activity of CatB.	Patient family, fibroblasts.	(Milanowski *et al.*, 2022)
	1. CTSB [rs1293298] variant reduced CatB mRNA expression. 2. GBA N370S reduced CatB protein levels.	1. GWAS of GBA populations. 2. Patient-derived GBA iPSCs.	(Blauwendraat *et al.*, 2020)
	CTSB [rs2740594c] variant associated with PD.	GWAS of PD populations.	(Chang *et al.*, 2017)

	CTSB variant association with PD.	GWAS of PD populations.	(Nalls *et al.*, 2019)
	CTSB variants that increase expression reduce disease risk mildly.	Mendelian analysis of two GWAS cohorts.	(Lu *et al.*, 2024)
	Inhibition and knockout of CatB increased lysosome number, impaired GCase activity and increased α-syn aggregation.	iPSC KO lines/ CA074me were treated with PFFs.	(Jones-Tabah *et al.*, 2024)
	LRRK2 G2019S astrocytes had reduced CatB activity and reduced pH (5.5 in WT to 5.0 in mut).	Mouse primary astrocytes transgenic LRRK2 G2019S.	(Henry *et al.*, 2015)
	LRRK2 G2019S macrophages have reduced protein levels of CatB, inhibition of LRRK2 elevates CatB protein levels.	LRRK2 G2019S CRISPR iPSC (Beylina *et al.*, 2021).	(Yadavalli and Ferguson, 2023)
	CatB, CatD and CatL cleave α-syn forming truncated α-syn, but CatB and CatL form α-syn absent of the C-terminus.	A53T OE mouse brain lysosomal extracts.	(McGlinchey *et al.*, 2019)
	1. CatB cannot completely degrade α-syn monomers, however, assays were conducted at pH 5.0. It could not clear fibrils either. 2. CatB cleaves sites on α-syn form truncated forms absent of the C-terminus.	1. Isolated human CatB with PFF. 2. Mouse brain lysosome extract.	(R. P. McGlinchey and Lee, 2015)
	Inhibition of CatB causes α-syn aggregation. This begins in LAMP1 lysosomes that are not acidified.	HEK293F/Syn-enhanced cyan fluorescent protein cells + PFF.	(Tsujimura *et al.*, 2015)
Cathepsin D	CatD inhibition did not affect α-syn aggregation.	iPSC KO were treated with PFFs.	(Jones-Tabah *et al.*, 2024)
	1. CatD alone cannot prevent aggregate formation, however, assays were conducted at pH 5.0. It could not completely clear fibrils either. 2. CatD causes α-syn truncation by F4/M5 and F94/V95 cuts or A124/Y125.	1. Mouse lysosomal extract inhibited with Leupeptin or Pepstatin A. 2. Isolated human CatD with PFF.	(R. P. McGlinchey and Lee, 2015)
	1. OE of inactive CatD decreased endogenous CatD activity by 50%. Increased α-syn monomer/ oligomer levels and CatB activity but did not alter mRNA levels of either. 2. Inhibition with Pepstatin A had the same effect.	1. Differentiated SH-SHY5Y CatD G295 transgenic. 2. Differentiated SH-SHY5Y.	(Crabtree *et al.*, 2014)
	LRRK2 G2019S macrophages have reduced protein levels of CatD and inhibition of LRRK2 elevates CatD protein levels.	LRRK2 G2019S CRISPR iPSC (Berlina et al., 2021).	(Yadavalli and Ferguson, 2023)
	1. Increased α-syn aggregation in the neurons from mouse tissue despite α-syn mRNA downregulation. α-syn aggregates were outside lysosomes/autophagosomes. CatB protein and activity were elevated. 2. Transfection of CatD protected neurons against aggregation and α-syn-induced death.	1. *Ctsd (-/-)* mouse. 2. SH-SY5Y transfected with α-syn (mutant or WT) and syntaphilin and CatD.	(Qiao *et al.*, 2008)
	1. CatD co-expression reduced α-syn aggregation, including with SNCA mutations A30P, A53T or E46L. 2. CatD KO reduces soluble α-syn and increases aggregation and fibril formation. 3. CatD KO elevates α-syn aggregation in the brain of sheep. 4. A-syn aggregation in several brain regions. 5. The absence of endogenous CatD enhanced retina neurodegeneration.	1. MES23.5 cells transfected with SNCA and CTSB. 2. *Ctsd (-/-)* mouse brain lysate and tissue sections. 3. *CTSD (-/-)* sheep brain sections. 4. Three human newborns, one carrying the *CTSD (c.764 dupA),* one related sibling with the same symptoms and one unrelated individual with	(Cullen *et al.*, 2009)

	It is important to note that these results were not quantified.	no detectable CatD protein but no genetic investigation. postmortem brain sections. 5. Drosophila *ctsd (-/-) or (+/+)* expressing human α-syn.	
	1. A-syn is cleaved to form 12 kDa length C-terminally truncated forms of α-syn. 2. A-syn is cleaved to form 12 kDa length C-terminally truncated forms of α-syn by endogenous CatD. Pepstatin A and CatD KD prevented truncation formation and reduction of α-syn. It is important to note that this result was not quantified.	1. A-syn transfected 3D5 cell lysate incubated with bovine CatD. 2. A-syn transfected 3D5 cell lysosomal fractionation.	(Sevlever, Jiang and Yen, 2008)
	1. Ceramide, a product of GCase cleaving glucosylceramide, activates CatD.Reduced ceramide decreased CatD activity. 2. Elevated ceramide increased CatD activity.	1. Niemann Pick cells (Sphingomyelin phosphodiesterase deficient) reduced ceramide. 2. Farber disease cells (A-ceramidase) elevated ceramide.	(Heinrich *et al.*, 2000)
	1. CatD and pro-CatD protein levels and CatD activity are reduced in GBA N370S het. A-syn monomers increased. GCase replacement therapy restores CatD protein levels/ activity and α-syn monomer levels. Ambroxol treatment restored GCase and CatD activity and reduced α-syn monomer levels. 3. CatD and pro-CatD protein levels are reduced in GBA N370S and sPD.	1. Differentiated dopaminergic neurons from human neural crest stem cells. 1. GBA N370S and sPD patient postmortem putamen.	(Yang *et al.*, 2020)
	1. TMEM175 KO reduces Cathepsin activity, CatB activity and CatD activity without altering protein levels. 2. TMEM175 KO reduced CatB activity and increased acidification (pH 4.5 to 4.0)	1. TMEM175 KO Hela cells. 2. *Tmem175 (-/-)* mouse.	(Hu *et al.*, 2022)

ATP13A2 encodes a lysosomal ATPase transporter of heavy metals, polyamines and Ca2+ (van Veen *et al.*, 2020). Mutations in ATP13A2 are very rare and cause juvenile onset. Patient-derived fibroblasts of ATP13A2 mutants show decreased autophagosome clearance and impaired lysosomal acidification and proteolysis (Dehay *et al.*, 2013; Tsunemi and Krainc, 2014). ATP13A2 levels are also reduced in sporadic PD (Dehay *et al.*, 2012), further suggesting that lysosomal dysfunction may be a primary mechanism of sPD.

As mentioned, deleterious lysosomal phenotypes have been associated with sPD. Components of the autophagy-lysosomal system were identified within Lewy Bodies in post-mortem tissue (Bourdenx, Bezard and Dehay, 2014). It was hypothesised that the origin of Lewy Bodies is autophagosomes and Lewy Bodies develop as more un-degraded autophagosomes are deposited. Compounding the issue could be the favourable environment for the aggregation of α-syn that vesicles provide (Lee, Patel and Lee, 2005; Wu *et al.*, 2009). Studies observed reduced numbers of lysosomes, lysosome-associated

proteins and lysosomal activity in postmortem tissue and rodent models (Chu *et al.*, 2009; Alvarez-Erviti *et al.*, 2010; Dehay *et al.*, 2010; Boman *et al.*, 2016). Another study identified an increased number of lysosomes in a subgroup of sporadic patient fibroblasts and iDA neurons. This subgroup displayed a decrease in CatD activity (Carling *et al.*, 2020). Furthermore, the accumulation of autophagosomes was observed in iDA neurons generated from sporadic and genetic patient-derived fibroblasts (Sánchez-Danés *et al.*, 2012), similar to the phenotype observed in LRRK2 mutation carriers.

Overall, the evidence observed across multiple genotypes and sPD suggests that an unbalanced auto-lysosome system likely leads to cellular dysfunction and possibly causes cell death. Furthermore, the stratification of a subgroup of sporadic patients displaying excessive lysosomal dysfunction (Carling *et al.*, 2020) supports the idea that lysosomal dysfunction is a primary mechanism in a proportion of the PD population.

1.4 Stratification

One of the proposed reasons for pharmaceutical stagnation is the heterogeneity of PD (Lang and Espay, 2018). PD is both clinically and mechanistically diverse. Although there are four key identifying symptoms of PD, there are many more motor and non-motor symptoms and these present differently depending on the patient. The exact symptoms and time that they manifest in the progression of the disease can vary, as well as the severity and response to treatment (Jankovic, 2008; Schapira, Chaudhuri and Jenner, 2017; Tolosa *et al.*, 2021). This makes it hard to diagnose PD with estimates of between 10-24 % of cases being misdiagnosed (Tolosa *et al.*, 2021). Due to heterogeneity, several attempts have been made to stratify PD to enable a more accurate prognosis or more effective clinical trial designs for therapeutic assessment. In this context, patient stratification is the arrangement of patients into smaller, more homogenous subgroups based on defined criteria, such as specific symptoms or disease phenotypes.

1.1.1. Clinical Stratification

Several studies have tried to stratify patients using clinical measures, demographics or the presence of specific symptoms. Many clinical studies use cluster analysis to stratify patients. Cluster analysis is a statistical approach that organises patients into groups based on their similarity without prior information. Clinical scores, which rate observations like motor severity, motor complication and non-motor symptoms, are often used in cluster analysis studies (Van Rooden *et al.*, 2010; Marras and Lang, 2013; Mu *et al.*, 2017; Campbell *et al.*, 2020; R. Hendricks and Khasawneh, 2021). One cluster analysis found that clinical stratification often clustered patients into two categories defined by old age-at-onset and rapid progression or young age-at-onset and slow progression (Van Rooden *et al.*, 2010). Other higher-powered studies using cluster analysis found three groups: mild-predominant motor,

intermediate and diffuse malignant (De Pablo-Fernández *et al.*, 2019). These groups show no difference in Lewy Body pathology. De Pablo- Fernández *et al.* (2019) also utilised biomarkers in an attempt to validate these groups, however, the combined genetic risk score found that genetics did not determine which group the patients fell into. This is most likely due to a weakness in the genetic risk scoring method or too few patients as previous work has described different clinical manifestations in different genetic mutants (Brüggemann and Klein, 1993; Chahine *et al.*, 2013; Li, Tan and Yu, 2014; Tolosa *et al.*, 2021; Nishioka *et al.*, 2022). Other clinical subtypes have also been described, such as tremor-dominant PD or postural instability and gait disturbance (PIGD) subtypes (Fereshtehnejad *et al.*, 2017). These differ based on key defining symptoms and are linked with varying progression rates. However, longitudinal follow-up visits resulted in patients changing categories (Simuni *et al.*, 2016; Lee *et al.*, 2019). Clinical stratification has been widely explored, and as cluster analysis and cohort sampling size become greater, distinct groups may become evident. However, one large flaw in many of these studies is the lack of resampling to validate techniques or the use of biomarkers to determine their cellular relevance (Mestre *et al.*, 2021). It could be argued that clinical subtyping is only applicable to disease prognosis and should not influence disease-modifying therapy assessment or the production of precision medicine treatment approaches (Mestre *et al.*, 2021; R. M. Hendricks and Khasawneh, 2021). The use of cluster analysis could be utilised to produce clearer, defined clinical descriptions would enable faster and more accurate diagnosis (Berg *et al.*, 2014).

1.1.2. Genetic Stratification

Genetic stratification is the most established method for stratifying PD. GWAS and familial studies have identified over 20 genes that have been classed as causes of fPD and over 90 risk loci for sPD. With advancements in tools, such as the NeuroChip platform, hundreds of thousands of small nucleotide polymorphisms can be assessed rapidly from a blood sample and at a low cost (Blauwendraat *et al.*, 2017). For clinical trials targeting specific genotypes of PD, this is the perfect stratification method. However, genetic variants are rare in PD, which combined with strict exclusion criteria, makes it difficult to recruit for late-stage clinical trials requiring large numbers of participants. In a large genetic study of mostly European ancestry, 3 % of patients carried a *LRRK2* mutation, the most common genetic cause of PD. Less than 1 % carried *PRKN* mutations and only 0.07 % carried *PINK1* mutations (Westenberger *et al.*, 2024). Clinical trials targeting *GBA* mutations can use genetic stratification as over 10 % of patients carry a risk variant (Westenberger *et al.*, 2024), enabling trial recruitment. The Ambroxol to Slow Progression in Parkinson Disease (ASPro-PD, NCT05778617) and GRoningen Early-PD Ambroxol Treatment (GREAT, NCT05830396) trials are assessing the efficacy of Ambroxol, a GCase chaperone, in PD. The GREAT trial is using genetics to exclude any patients without

a GBA variant (Siemeling, 2023). In contrast, the ASPro-PD trial is screening for variants but not excluding patients, suggesting that GBA status will be involved in result analysis (Ikeji, 2024).

Polygenic risk scores provide a broader approach to genetic stratification. Polygenic risk scores have been established to predict disease onset, however, several studies have attempted to stratify PD (Dehestani, Liu and Gasser, 2021). Mitochondrial and autophagy-lysosomal polygenic risk scores accurately predict PD manifestation; however, they do not correlate with MDS-UPDRS scores, and only the mitochondrial polygenic risk score correlates with age-at-onset (Billingsley *et al.*, 2019; Dehestani *et al.*, 2022). However, these scores were developed to segment disease mechanisms for clinical trials and not clinical features. A recent study assessed stratified PD patients based on high or low oxidative phosphorylation mitochondrial risk scores. Patients in the high group responded more effectively to ursodeoxycholic acid (UDCA) and had lower mitochondrial respiration than the low group (Arena *et al.*, 2024). This shows their potential utility in clinical trial selection and personalised treatment plans to enable the cost-effective selection of patients.

1.1.3. Biomarkers

Biomarkers to diagnose PD during the prodromal stage are a vast area of research and may enable the stratification of PD in the future. The α-syn seed amplification assay is the first accurate method for detecting α-syn (Concha-Marambio *et al.*, 2023; Siderowf *et al.*, 2023). This assay has multiple applications when considering subgrouping. It is accurate at detecting the presence of α-syn in sporadic and GBA mutant patients, suggesting that it could be utilised by clinical trials to confirm pathology before the trial begins. Due to the specificity in GBA-PD (Siderowf *et al.*, 2023), it would be reasonable to exclude α-syn negative patients from GBA-targeting clinical trials. In contrast, LRRK2 patient assessment was only accurate in 67.5% of patients, suggesting possible subgroups within this genetic population of PD and the need for different targeted therapeutics (Siderowf *et al.*, 2023). However, the selection of α-syn positive patients for clinical trials does little to improve trials for prospective compounds. Other biomarkers are being investigated in blood, CSF and urine.

CSF can be obtained by a lumbar puncture, which is a highly invasive technique, so is not an ideal method for stratification. Although, due to the lack of biomarkers to date it may provide the best method. In contrast, blood and urine are non-invasive but are peripheral samples limiting their association with brain biomarkers. Lysosomal enzyme activity in CSF provides a possible biomarker for stratification. GCase activity is reduced in GBA-PD patients and sPD patient CSF (Parnetti *et al.*, 2014, 2017). Examination of the data shows large variation in the sPD group, indicative of heterogeneity and a cluster of patients with exceptionally low activity. Levels of other lysosomal enzymes, such as CatD and β-hexosaminidase, are reduced in sPD (Parnetti *et al.*, 2017), suggesting that the evaluation of a

lysosome enzyme profile may indicate stratification methods. GCase activity can be measured in blood (Sosero *et al.*, 2021). Development of lysosome enzyme activity stratification methods using blood rather than CSF may be possible.

Mitochondrial dysfunction groups have also been stratified by biomarkers. mtDNA copy number and damage are biomarkers that have been explored. However, in peripheral blood, copy number did not correlate with cognitive symptoms or severity (Pyle *et al.*, 2015) and was not elevated in sPD or LRRK2 G2019S carriers (Gonzalez-Hunt *et al.*, 2020). However, mtDNA damage is elevated in sPD and LRRK2 G2019S carriers peripheral blood mononuclear cells (PBMCs) and lymphoblastoid cell lines (Gonzalez-Hunt *et al.*, 2020; Qi *et al.*, 2023). Interestingly, LRRK2 kinase inhibition dramatically reduced mtDNA damage suggesting this biomarker could be used as a measure of efficacy (Gonzalez-Hunt *et al.*, 2020; Qi *et al.*, 2023). Other studies have investigated inflammation markers such as cytokines. Higher pro-inflammatory markers and lower anti-inflammatory markers correlate with faster disease progression (Williams-Gray *et al.*, 2016). Possible methods assessing inflammatory markers for mechanism stratification rather than symptom correlation may enable stratification for clinical trials.

1.1.4. Phenotypic Stratification

Phenotypic stratification is the classification of patients based on the dysfunctional mechanism within their cells. To our knowledge, three studies have proposed methods (Carling *et al.*, 2020; Barnhoorn *et al.*, 2024; Fløtnes *et al.*, 2024) but further work is being conducted to develop new methods (Stige *et al.*, 2024). Carling *et al.* (2020) assessed mitochondrial dysfunction and lysosomal dysfunction in patient-derived fibroblasts from one hundred patients. Two distinct subgroups were identified, a mitochondrial dysfunction group defined by reduced ATP levels and a lysosomal dysfunction group defined by increased lysosome counts. Further work in the fibroblasts identified specific dysfunction including respiratory complex dysfunction and lower CatD activity in the respective groups. The groups were also reprogrammed into iNPCs and differentiated into iDA neurons. Dysfunction in the neurons was more extreme than in the fibroblasts for both groups (Carling *et al.*, 2020).

Fløtnes *et al.* (2024) assessed mitochondrial function in postmortem tissue of PD patients. Complex I protein levels, specifically subunit NDUFS4, were assessed in the SN and prefrontal cortex (PFC) postmortem tissue from ninety-two patients. Little variation was observed in the controls' PFC samples and due to the loss of neurons in the SN, the PFC was chosen for stratification. A proportion of sPD patients had a reduced number of complex I positive cells, these were clustered based on the severity of the reduction into mild or severe complex I groups. Single nucleotide RNA sequencing confirmed different transcriptomic profiles between the complex I group and sPD patients. Lower transcription of respiratory complex machinery was observed suggesting a failure to respond. This

method utilises postmortem samples and thus cannot be used for clinical trial selection. However, complex I patients were significantly more likely to have non-tremor dominant PD (Flønes *et al.*, 2024). Non-tremor dominant PD could be used as a classifier in trials to reduce heterogeneity until further research on biomarkers and phenotypic screening in biosamples discovers a more accurate identifier. It should be noted that postmortem tissue enables the observation of late stages of PD and therefore, these deficits may not be present at early stages of pathology when clinical trials are attempting to modify disease.

Another research group developed a hybrid clinical and phenotypic stratification by assessing mitochondrial respiration in fibroblasts, erythroblasts and iPSC-derived iDA neurons from the same patients. In the fibroblasts, increasing respiration correlated with increasing severity of clinical symptoms (Milanese *et al.*, 2019). Therefore, the cohort was stratified into four subgroups based on clinical severity, which was assessed by the MDS-UPDRS and SENS-PD scales. Maximal respiration reduced with clinical severity. Further investigation in the iDA neurons showed that maximal respiration was elevated in the more clinically severe subgroups (Barnhoorn *et al.*, 2024). Stratification based on severity would be a cost-effective method of selecting trial participants and allude to likely mechanistic dysfunction. Phenotypic assessment of erythroblasts would be better at selecting mechanistically homogenous subgroups; however, this would be more time-consuming and expensive. One caveat is that the duration of disease correlated with increasing respiration (Milanese *et al.*, 2019). Longer disease duration is often an exclusion factor for clinical trials because trials aim to prevent further neuron loss as early as possible.

Stratification by phenotype would provide homogenous groups affected by specific mechanisms of disease. Disease-modifying therapies target specific dysfunctional pathways, thus phenotypic trial selection would greatly increase the likelihood of compound efficacy in each patient. This method would be more costly, however, compared to the economic burden of PD, stratification using these methods would be insignificant.

1.5 Project Rational

There is clear evidence of mechanistic heterogeneity in sPD patients. This mechanistic heterogeneity may be one of the main reasons why all neuroprotection trials have failed in PD. Stratification of sPD is crucial to improving the success of clinical trials. Therefore, this project aimed to build upon the foundation set by Carling *et al*. (2020) and produce a detailed screening and stratification method in a new cohort of sPD patients. This method will enable further research into disease-driving mechanisms and selection for clinical trials. Fibroblasts are a poor model for investigating detailed

inflammatory mechanisms, oxidative stress and α-syn. Due to this, these mechanisms were not assessed in the fibroblasts and therefore, not included in the stratification method.

1.5.1 Model Selection for sPD Stratification

It is widely recognised that every model of disease has advantages and limitations. Due to the heterogeneous and complex nature of sporadic PD, model selection is difficult. Many studies utilise simple cell or animal models using toxins or introduce genetic mutations to model PD, these models are homogeneous and excellent for understanding disease mechanisms and genetic forms of PD. However, they cannot model heterogeneity or the causes of individual patients' PD. For this patient-derived tissue and cells are the only accurate models and thus the only models that can be used for stratification studies. Toxin and genetic mutation-induced disease models can elude possible subgroups (D'Sa *et al.*, 2023), but patient cells must be used to confirm the groups.

PD is a systemic disorder, meaning that multiple patient-derived models could be used for this stratification study, such as fibroblasts, blood, CSF, brain tissue and iNPC/iPSC-derived cells to name a few. CSF and blood could be used for large stratification studies but their use in investigating mitochondria and lysosomes is limited. CSF does not contain lysosomes or mitochondria but could be useful for identifying a biomarker for subgroups because it contains secreted components of these organelles, such as mtDNA and lysosome enzymes (Mullin *et al.*, 2020; Puigròs *et al.*, 2024). However, collecting CSF is invasive for the patient (Kim, 2022) and therefore it would be beneficial to the patients to identify biomarkers in other less invasive samples, such as blood and urine. Blood stratification methods with biomarkers would be a cost-effective method of stratification for the clinic and should be investigated by subsequent studies to identify biomarkers in already defined subgroups.

Fibroblasts on the other hand are a good model for investigating mitochondria and lysosomes using imaging techniques because they are flat and have a large cytoplasm for visualising the networks. Despite fibroblasts being derived from the participant's dermis, they are commonly utilised to research systemic neurological disorders (Trushina, 2019), such as PD and their use in PD research is well-established (Mytilineou *et al.*, 1994; Mortiboys *et al.*, 2008, 2015; Grünewald *et al.*, 2010; Auburger *et al.*, 2012; Dehay *et al.*, 2012; Manzoni *et al.*, 2013; Ambrosi *et al.*, 2014; Haylett *et al.*, 2016; Teves *et al.*, 2018; Carling *et al.*, 2020). Fibroblasts provide a model of disease that represents a patient's polygenic predisposition and cumulative biological ageing phenotypes, such as environmental damage and epigenetic signatures (Auburger *et al.*, 2012; Teves *et al.*, 2018; Olesen, Villavicencio-Tejo and Quintanilla, 2022). These characteristics combined with the relatively low invasiveness of the biopsy (Auburger *et al.*, 2012) make fibroblasts a key model for assessing heterogeneity in the patient population. Biopsies can be taken within three years of disease diagnosis

in order to capture early stages of dysfunction compared to post-mortem tissue analysis (Olesen, Villavicencio-Tejo and Quintanilla, 2022). However, it should be noted that fibroblasts do have some limitations as well. They have low protein levels of α-syn (Hoepken *et al.*, 2008), a point which should be considered when interpreting any results because α-syn aggregation is a key component of PD pathology (Bourdenx, Bezard and Dehay, 2014; Hattori and Sato, 2024). However, this offers the unique advantage of identifying disparate deleterious mechanisms that are involved in PD progression and initiation. To validate stratified groups other models that express α-syn should be utilised alongside fibroblasts to confirm their results with the presence of α-syn. Fibroblasts are also bioenergetically distinct from dopaminergic neurons, relying on glycolysis to primarily produce ATP. Therefore, culturing in galactose is required to unmask deficits in oxidative phosphorylation. Despite this limitation many groups have identified similar defects in fibroblasts and other patient-derived models of PD, such as iNPCs, iPSCs and brain tissue (Schapira *et al.*, 1990; McNeill *et al.*, 2014; Carling *et al.*, 2020; Yang *et al.*, 2020; Arena *et al.*, 2024).

iPSCS, iNPCs and brain-derived tissue and cells provide disease-relevant information and are also the best models to reveal the vulnerability of the affected cell type, in PD's case, Dopaminergic neurons (Hartmann, 2004; Chia, Tan and Chao, 2020; Schwartzentruber *et al.*, 2020). Primary dopaminergic neurons can only be extracted postmortem and therefore, would not fit within project time constraints and would only demonstrate late stages of diseases as the majority of patients live many years with PD (Hartmann, 2004).

iPSC and iNPC-induced neurons and glia are valuable models of disease that maintain the dysfunction phenotypes and polygenic risk of the patient. iPSCs are the most common model; produced from hair follicles, fibroblasts or blood cells and are pluripotent (Takahashi and Yamanaka, 2006; Cerneckis, Cai and Shi, 2024). iNPCs are produced from skin fibroblasts using the same Yamanaka factors as iPSCs, however, the cells do not reach pluripotency because they are forced down the neuronal progenitor cell route early in reprogramming (Meyer *et al.*, 2014). This is possible due to the fibroblasts and neuronal cells shared ectodermal origin. Prevention from reaching pluripotency maintains the cells' ageing phenotype and cumulative lifestyle damage (Gatto *et al.*, 2021; Bell *et al.*, 2024). Gatto et al. (2021) demonstrated that iNPC-derived astrocytes from older individuals had transcriptome profiles similar to older postmortem-derived astrocytes and infant-derived iNPC-derived astrocytes more closely resembled foetal-derived astrocytes. Further investigation of the transcriptome profiles showed reduced levels of RAN binding protein 17 (RANBP17) and laminin subunit alpha 3A (LAMA3A), which is consistent with ageing (Mertens *et al.*, 2015; Godin *et al.*, 2016), whereas iPSCs do not retain the aged transcriptomic profile of aged fibroblasts (Mertens *et al.*, 2015, 2018). Gatto et al. (2021) also showed that the iNPCs had larger nuclei, laminin fragmentation, reduced histone methylation and

reduced telomere length, which have been previously reported as ageing characteristics (Pienta, Getzenberg and Coffey, 1992; Haithcock *et al.*, 2005; Scaffidi, Gordon and Misteli, 2005; Maleszewska, Mawer and Tessarz, 2016; Fasching, 2018). Other advantages include non-clonal generation, unlike iPSCs, which prevents clonal bias (Willmann *et al.*, 2013) and a shorter iDA neuron differentiation protocol compared to iPSCs (Schwartzentruber *et al.*, 2020), which greatly improved throughput and reduced cost. However, iNPCs have some disadvantages compared to iPSCs. iNPCs are tripotent and can only differentiate into central nervous system neurons (Schwartzentruber *et al.*, 2020), astrocytes (Meyer *et al.*, 2014) and oligodendrocytes (Ferraiuolo *et al.*, 2016), compared to iPSCs that can form any cell type (Cerneckis, Cai and Shi, 2024). Furtehrmore, despite the extensive ageing study by Gatto et al. (2021), no study has reported the ageing characteristics being retained in neurons. iNPCs have not been characterised to the same extent as iPSCs, mainly due to their lack of use globally compared to iPSCs. iPSC models have been extensively assessed to produce a set of standards that should be adhered too, this includes but is not limited to karyotyping and fingerprinting/purity tests (*Standards for Human Stem Cell Use in Researc*). Karyotyping throughout use ensures that the cell lines genetic integrity is maintained (chromosome number and morphology) and further genetic testing ensures that genetic alterations do not influence results. Fingerprinting and purity tests use stem cell markers to determine the percentage of stem cells that are within the culture and confirm that the pluripotency state is maintained. This can be conducted using flow cytometry or high-content imaging (Nazareth *et al.*, 2013; Suresh Babu *et al.*, 2023). A global set of standards should bedeveloped for iNPCs and this drawback should be considered when evaluating the results of this study. Despite these drawbacks iNPCs were selected because PD is an age-related disorder and thus retention of the ageing characteristics was very important. Validation of the subgroups and further investigation of unique dysfunctional mechanism was conducted in iNPC derived dopaminergic neurons.

1.5.2 Project Hypothesis and Aims

Hypothesis:

We hypothesise that mitochondrial and lysosomal dysfunction heterogeneity within the patient-derived fibroblasts from a new cohort of sPD patients will be greater than the control population and will enable the stratification of distinct, homogeneous subgroups defined by organelle dysfunction.

Aim 1: To investigate mitochondrial and lysosomal heterogeneity in patient-derived fibroblasts and stratify the patients into subgroups defined by dysfunction.

Objective:

- To measure mitochondrial and lysosomal dysfunction in the cohort and determine heterogeneity.
- To identify and define distinct subgroups.
- To assess mitochondrial and lysosomal dysfunction within fPD patients to compare the sPD subgroups with genetically stratified groups.

Aim 2: To deeply investigate the lysosome function in fibroblasts and iDA neurons from the lysosomal dysfunction subgroup.

Objectives:

- To validate initial screening results.
- To investigate lysosome pH, hydrolase activity and morphology in the fibroblasts from patients in the subgroup.
- To investigate lysosome pH, hydrolase activity and morphology in induced dopaminergic neurons from patients in the subgroup.
- To screen some lysosomal modulators and assess the effect on lysosomal morphology, pH and hydrolase activity.

Aim 3: To deeply investigate mitochondrial and lysosomal dysfunction in fibroblasts and iDA neurons from the mitochondrial dysfunction subgroup and low mixed group.

Mitochondrial dysfunction subgroup objectives:

- To validate the mitochondrial phenotype observed in the initial screen with new controls.
- To assess respiration and ATP production in the patient-derived fibroblasts.
- To assess mitophagy, mitochondrial function, morphology and ROS production in the iDA neurons.

Low mixed group objectives:

- To validate the mitochondrial and lysosomal phenotype observed in the initial screen.
- To assess mechanisms of mitochondrial and lysosomal dysfunction in detail in the patient-derived fibroblasts.
- To assess mitochondrial and lysosomal function in iDA neurons.

2 Chapter 2: Methods

2.1 Recruitment

Participants were recruited from the movement disorder clinic at Sheffield Teaching Hospitals NHS Foundation Trust and through the Parkinson's UK Research Network. Written consent was provided by all participants and the study was approved by the local Research Ethics Committee (REC 18/NW/0328). Patient diagnosis was completed by a movement disorder specialist in accordance with the Queen Square Brain Bank Criteria. Exclusion criteria included evidence of significant cognitive impairment (Mini Mental State Examination score <25) or an impairment to MRI or skin biopsy, such as ferromagnetic implants or anticoagulation treatments. In total, 35 patients, within 3 years of diagnosis, and 25 healthy controls with similar age and sex distribution were selected (Table 5). The cohort size was determined by a balance of cost, time and the minimum number of patients required to observe heterogeneity. This study was performed in conjunction with the assessment of the cohort using ^{31}Phosphorus magnetic resonance spectroscopy, which was the main restriction to cohort size due to its cost. This study was the largest assessment of sporadic PD patients using ^{31}Phosphorus magnetic resonance spectroscopy (Payne *et al.*, 2023).

The Modified Hoehn and Yahr Staging, MDS-UPDRS Part III and Movement Disorders Society Non-Motor Symptom Scale were used to assess participants along with a detailed clinical history and neurological examination. For all patients, a predictive disease progression score was calculated based on a validated prognostic model estimating the risk of an unfavourable outcome in PD (the presence of postural instability or dementia within 5 years).

2.2 Genetic Assessment

All participants supplied an EDTA blood sample for genetic analysis. This was assayed using the NeuroChip platform, which detects known pathogenic mutations in monogenic genes as well as any *GBA1* variants with an increased risk of PD manifestation (Blauwendraat *et al.*, 2017). These variants were cross-referenced with the Single Nucleotide Polymorphism Database and then classified based on published guidelines (Payne *et al.*, 2023). Dr Thomas Payne and Stephen Bradley processed the samples.

2.3 Tissue Culture

2.3.1 Biopsy

A 3mm punch biopsy needle was utilised to collect a skin biopsy from the upper forearm of all participants, unfortunately, COVID-19 restrictions impaired the collection of biopsies from one participant, who was excluded from all analysis. Once collected fibroblast lines were established according to previously reported protocols (Allen *et al.*, 2014). Biopsying and cell line establishment was carried out by Dr Thomas Payne and Dr Sarah Roscoe.

Table 5: Age, sex, age at diagnosis and genotype of all participants.

Cell Line	Status	Sex (M/F)	Age (years)	Time Between Diagnosis and Biopsy (months)	Initial Screen Group
ATP001	Sporadic PD	F	68	16	13
ATP005	Sporadic PD	M	53	13	1
ATP007	Sporadic PD	M	60	25	6
ATP010	Sporadic PD	M	66	27	12
ATP012	Sporadic PD	M	63	21	6
ATP014	Sporadic PD	M	78	32	2
ATP016	Sporadic PD	M	50	8	3
ATP017	Sporadic PD	M	72	12	2
ATP019	Sporadic PD	M	73	18	2
ATP020	Sporadic PD	M	52	13	3
ATP021	Sporadic PD	M	82	19	5
ATP023	Sporadic PD	F	71	25	2, 11
ATP025	Sporadic PD	F	54	17	1
ATP026	Sporadic PD	F	59	7	4
ATP027	Sporadic PD	M	61	12	12
ATP028	Sporadic PD	F	53	8	1
ATP029	Sporadic PD	F	53	22	3
ATP030	Sporadic PD	F	55	11	4
ATP031	Sporadic PD	F	60	4	1
ATP032	Sporadic PD	F	68	2	6
ATP033	Sporadic PD	M	69	3	11

ATP034	Sporadic PD	F	63	12	6
ATP035	Sporadic PD	M	76	16	2
ATP036	Sporadic PD	F	69	14	11
ATP037	Sporadic PD	M	66	12	12
ATP038	Sporadic PD	M	59	4	7
ATP039	Sporadic PD	F	60	16	4
ATP040	Sporadic PD	M	51	5	7, 12
ATP041	Sporadic PD	M	53	6	3, 10
ATP043	Sporadic PD	F	53	7	10
ATP046	Sporadic PD	F	42	26	8
ATP047	Sporadic PD	M	58	8	8
ATP048	Parkin PD	F	50	16	10
ATP049	SNCA PD	F	28	11	9
ATP002	Control	M	71	N/A	2
ATP003	Control	M	53	N/A	3, 7
ATP004	Control	F	52	N/A	1, 3
ATP006	Control	F	49	N/A	3, 4, 8
ATP008	Control	F	66	N/A	1, 4, 6
ATP009	Control	F	71	N/A	2
ATP011	Control	F	74	N/A	2
ATP013	Control	F	59	N/A	1, 4, 7
ATP015	Control	F	67	N/A	11, 13
ATP018	Control	M	75	N/A	2
ATP022	Control	F	81	N/A	5
ATP024	Control	M	72	N/A	2
ATP042	Control	M	61	N/A	6, 7
ATP044	Control	M	62	N/A	6
ATP045	Control	F	64	N/A	6
ATP050	Control	F	28	N/A	9
ATP051	Control	M	58	N/A	12
ATP052	Control	M	62	N/A	11
ATP053	Control	F	56	N/A	12
ATP054	Control	M	61	N/A	12

ATP055	Control	F	53	N/A	10
ATP056	Control	M	52	N/A	12
ATP057	Control	F	55	N/A	10
ATP058	Control	M	50	N/A	10
ATP059	Control	M	64	N/A	-

2.3.2 Fibroblast Maintenance

All lines were maintained in T75 flasks (Nunclon; 156499) once established. They were cultured in EMEM media (.

Table 6) at 37 °C and 5 % CO_2. Cells were fed every 3-4 days and once confluent were divided for further culture. All media was removed and the cells were washed twice with phosphate buffered saline solution (PBS). Cells were detached using 1X 0.5 % trypsin with EDTA (Thermofisher; 25300-054) for 5 minutes at 37 °C. Trypsin was neutralised using EMEM media. The cell suspension was centrifuged at 550 g for 4 minutes, followed by the supernatant being removed. The cell pellet was resuspended in EMEM media and added to new flasks (1:3 dilution to maintain passage consistency), plates or assayed. For plating the cell number was estimated using a haemocytometer and the suspension was diluted to dispense the correct number of cells per well. All cells used in assays were between passage 6 and 15. The fPD lines were culured in the same fashion, however, the biopsies were established in DMEM media (.

Table 6), so the cells were maintained and assayed in DMEM media.

Fibroblasts were stored long term at -80 °C or in liquid nitrogen. The cells were collected in the same manner as splitting. The pellet for each flask was resuspended in 2 mL EMEM media, supplemented with an addition 10 % FBS and 10 % Dimethyl Sulphoxide (DMSO) (Sigma) and divided into two cryovials (Thermofisher; 368632). The vials were frozen in CoolCell freezing containers (Corning; 432000) for a minimum of 2 hours to ensure a -1 °C per minute freezing rate, before being transferred to boxes for long term storage.

Cells were recovered from long term storage by dripping room temperature EMEM media onto the frozen pellet until the vial was full, then transferring this suspension into 5 mL of room temperature EMEM media. This process was repeated until the entire vial had thawed. The solution was transferred to a new T75 flask and media was topped up to 10 mL. The following day the media was removed and replaced with fresh EMEM media.

2.3.3 Fibroblast Reprogramming

Fibroblasts from subgrouped patients or corresponding controls were reprogrammed to iNPCs following the Meyer *et al.* (2014) protocol. Reprogramming was completed by myself and Professor Heather Mortiboys. Fibroblasts were cultured in DMEM media for a week before plating. Fibroblasts were plated in a 10 µg/mL fibronectin (R&D; 1918-FN-02M) coated 6-well plate (Greiner BIO-ONE; 657160) at several densities, between 75,000-150,000 cells per well, in DMEM media. Two days later the optimally dense well for each cell line was transduced with VSV-G pseudotype retroviral vectors (Alstem; RF101) carrying Octamer-binding transcription factor 4 (Oct4), SRY-box transcription factor 2 (Sox2), Krüppel-like factor 4 (Klf4) and c-myc with a Transplus virus transduction enhancer. The cells were incubated overnight at 37 °C and 5 % CO_2. The viral media was removed and the well was washed twice with PBS, then 2 mL DMEM media was added. After 3 days the DMEM media was removed and replaced with Pre-iNPC media (.

Table 6). The cells were cultured in Pre-iNPC media until an iNPC culture was established, no longer than 12 days. They are then switched to reprogramming iNPC media (.

Table 6). iNPC status was confirmed by positive immunocytochemistry for Pax6 and Nestin.

2.3.4 iNPC Maintenance

All cell lines are cultured in 10 cm dishes (Thermofisher; 181466) coated with 10 µg/mL fibronectin (R&D) for 30 minutes at room temperature. The cells were cultured in complete iNPC media (.

Table 6) at 37 °C and 5 % CO_2. When dishes reached confluency, the cells were split based on growth rate. Confluency was determined by the maximum percentage of the dish that the cell line will fill before detaching, it varies between 80 % and 100 %. When splitting the media was aspirated and kept. 1 mL accutase (Corning-Fisher; 15323609) was added and incubated at 37 °C and 5 % CO_2 for 5 minutes. The accutase was quenched using the reserved media and the cell solution was spun at 200 g for 4 minutes. The supernatant was removed and the cells resuspended in fresh complete iNPC media and added to the coated dish so the final volume of complete iNPC media was 10 mL.

For neuronal differentiation cells are plated into 6-well plates coated with 10 µg/mL fibronectin. The plating density was optimised for each cell line. Differentiation was started when the cells reached between 70 % and 90 % confluency depending on the cell line. All cells used for assays and differentiation were passage 20 or below and control and patient pairs are within 3 passages.

iNPCs are stored long term at -80 °C or in liquid nitrogen. Cells are detached and pelleted as described above. The pellet was resuspended in complete iNPC media containing 10 % DMSO and 1 mL was

added to each cryovial. The vials are frozen in CoolCell freezing containers in the same fashion as fibroblasts.

iNPCs are recovered from long term storage using the dropwise method described above and complete iNPC media. The cell solution was added to a 10 cm dish coated with 10 µg/mL fibronectin. The media was completely changed the following day to remove the DMSO and dead cells.

2.3.5 Induced Dopaminergic Neuron Differentiation

On day 0 the complete iNPC media was removed and 2 mL DAPT iDA neuron media (.

Table 6) was added to each well. On day 2 the media was exchanged for FGF iDA neuron media (.

Table 6), the cells were fed with this media every day by aspirating the media and adding 1 mL of fresh media until day 12. On day 12 the cells were replated into a fibronectin-coated black 96-well plate (Agilent; 204626-100) at a density of 10,000-20,000 cells per well depending on the cell line. For plating the cell number was estimated using a haemocytometer and the suspension was diluted to dispense the correct number of cells per well. Each well contains 100 µL FGF iDA neuron media. On day 13 the cells are switched into TGF iDA neuron media (.

Table 6) by aspirating the FGF iDA neuron media and adding 90 µL TGF iDA neuron media. The media was changed every day until day 27 when the plate was assayed. On day 27 the cells were assayed.

Patient 3 from the low mixed group did not survive the 10 days of FGF iDA neuron media. Therefore, it was cultured on a shortened protocol. Patient 3 and the corresponding control were cultured in FGF media from day 2 to day 6 when the cells were replated into a black 96-well plate. The media was exchanged to TGF iDA neuron media on day 7 and cultured for 15 days. The media was exchanged every day.

Table 6: Composition of cell culture media.

Media	Components
EMEM media	Eagle's Minimum Essential Media (Corning; 10-010-CV) supplemented with 10% FBS (Labtech; FCS-SA/500), 100 IU/mL penicillin, 100 µg/mL streptomycin (Sigma; P0781), 1X MEM vitamins (Corning; 25-020-CI), 1 mM sodium pyruvate (Sigma; S8636), 0.1 mM non-essential amino acids (Hyclone; HYCLSH30238.01) and 50µg/mL uridine (Sigma; U3003)
DMEM media	Dulbecco's Modified Eagle Medium (VWR; 392-0414) supplemented with 10% FBS (Labtech; FCS-SA/500), 100 IU/mL penicillin, 100 µg/mL

	streptomycin (Sigma; P0781), 1 mM sodium pyruvate (Sigma; S8636) and 50µg/mL uridine (Sigma; U3003)
Galactose media	Dulbecco's Modified Eagle Medium, no glucose (Thermofisher; 11966025) supplemented with 5 mM galactose (Sigma; G0750) 10% FBS (Labtech; FCS-SA/500), 100 IU/mL penicillin, 100 µg/mL streptomycin (Sigma; P0781), 1 mM sodium pyruvate (Sigma; S8636) and 50 µg/mL uridine (Sigma; U3003)
Pre-iNPC media	Dulbecco's modified essential media/Ham's F12 nutrient mixture (DMEM/F12) (Gibco, 10565018) supplemented with 1 % N2 (Gibco; 17502001), 1 % B27 (Gibco; 17504001), 20 ng/mL recombinant human Herparin binding Embryonic growth factor (Peprotech, 100-47), 20 ng/mL Recombinant human FGF-basic (Peprotech, AF-100-18B)
Reprogramming iNPC media	Dulbecco's modified essential media/Ham's F12 nutrient mixture (DMEM/F12) (Gibco, 10565018) supplemented with 1 % N2 (Gibco; 17502001), 1 % B27 (Gibco; 17504001), 40 ng/mL Recombinant human FGF-basic (Peprotech, AF-100-18B)
Complete iNPC media	Dulbecco's modified essential media/Ham's F12 nutrient mixture (DMEM/F12)(Gibco, 10565018) supplemented with 1 % N2 (Gibco; 17502001), 1 % B27 (Gibco; 17504001), 100 IU/mL penicillin, 100 µg/mL streptomycin (Sigma; P0781), 40 ng/mL Recombinant human FGF-basic (Peprotech, AF-100-18B)
DAPT iDA neuron media	Dulbecco's modified essential media/Ham's F12 nutrient mixture (DMEM/F12)(Gibco, 10565018) supplemented with 1 % N2 (Gibco; 17502001), 2 % B27 (Gibco; 17504001), 100 IU/mL penicillin, 100 µg/mL streptomycin (Sigma; P0781), 2.5 µM N-[N-(3,5-Difluorophenacetyl)-L-alanyl]-S-phenylglycine t-butyl ester (DAPT) (Sigma; D5942)
FGF iDA neuron media	Dulbecco's modified essential media/Ham's F12 nutrient mixture (DMEM/F12)(Gibco, 10565018) supplemented with 1 % N2 (Gibco; 17502001), 2 % B27 (Gibco; 17504001), 100 IU/mL penicillin, 100 µg/mL streptomycin (Sigma; P0781), 50 ng/mL Recombinant human FGF-8a (Peprotech, 100-25A) and 1 µM Smoothened agonist (SAG) (Sigma-566660)
TGF iDA neuron media	Dulbecco's modified essential media/Ham's F12 nutrient mixture (DMEM/F12)(Gibco, 10565018) supplemented with 1 % N2 (Gibco;

	17502001), 2 % B27 (Gibco; 17504001), 100 IU/mL penicillin, 100 µg/mL streptomycin (Sigma; P0781), 33ng/mL Recombinant human Transforming Growth Factor-β (TGF)(Peprotech, 100-21), 127 µM N6,2′-O-Dibutyryladenosine 3′,5′-cyclic monophosphate sodium salt (Sigma; D0627), 25 ng/mL Recombinant human Brain-Derived Neurotrophic Factor (BDNF) (Peprotech, 450-02), 25 ng/mL Recombinant human Glial-Derived Neurotrophic Factor (GDNF) (Peprotech, 450-10), 1 µg/mL ciprofloxacin (Merck; PHR1044)

2.3.5.1 Treatment with Therapeutic Compounds

The iDA neurons were treated 24 hours before the end of differentiation. Ambroxol, Venglustat and Cardiolipin, DMSO and Methanol were diluted to working concentrations in TGF iDA neuron media. The media in the neuron plate was removed and replaced with the treatment media like a normal feed. Each dosing condition was completed in duplicate wells. DMSO was the vehicle treatment for Ambroxol and Venglustat. Methanol was the vehicle treatment for Cardiolipin. Both vehicles were dosed at the highest concentration. Ambroxol was dosed at 1 µM, 10 µM and 30 µM. Venglustat was dosed at 1 µM, 10 µM, 100 µM. Cardiolipin was dosed at 10 ng/mL and 100 ng/mL.

2.4 Initial Screening

2.4.1 Participant Grouping

To enable screening the fibroblast lines were separated into thirteen groups of age- and sex-matched patients and controls (Table 5). Several lines were assayed in groups consisting of one control and one patient due to slow growth or because age and sex did not allow for multiple participants in the groups. Some groups were assayed by Stephen Bradley and Dr Sarah Roscoe.

2.4.2 Live Immunofluorescent Imaging

Fibroblast lines were seeded into 6 wells of a black 96-well plate (Agilent; 204626-100) at a density of 1000 cells per well, as described above 2.3.2 Fibroblast Maintenance). The next day, three wells were fed with EMEM media and three with galactose media (.

Table 6) and cultured for 72 hours. Cells were incubated for 1 hour with Phenol Free Minimum Essential Medium (Gibco; 51200-038) containing 80 nM tetra-methylrhodamine methyl ester (TMRM, Sigma; T5428), 1 µM lysotracker green DND-26 (Thermofisher; L-7526) and 20 µM Hoechst 33528 (Sigma; B2883). The media was changed to Phenol Free MEM only and the cells were imaged on the

Opera Phoenix (PerkinElmer) using the 40X magnification water lens or InCell Analyzer 2000 using the 60X magnification lens (GE Healthcare). Imaging exposures and Z-plane positions were optimised per plate for the Cy3 (Excitation 530-560/Emission 570-650), FITC (Excitation 460-490/Emission 500-550) and DAPI channels (Excitation 355-385/Excitation 430-500). Images were subsequently analysed using Columbus (PerkinElmer, Figure 4) or InCell Developer Toolbox (GE Healthcare, Figure 3). This enabled the segmentation of mitochondria, nuclei and lysosomes. MMP, mitochondria count, mitochondria form factor, lysosome count, lysosome area and lysosome form factor were quantified for each segmented population (lysosomes, long mitochondria, small mitochondria, perinuclear mitochondria and mitochondria). Small mitochondria and long mitochondria were defined by a form factor threshold during image analysis. This was established by previous work in the lab but classifies 55 % of control fibroblast mitochondria as small and 45 % as long.

TMRM accumulates in mitochondria in a MMP-dependent manner. The concentration of TMRM was carefully optimised to ensure that the fluorescent intensity was dependent on MMP as high concentrations of TMRM can cause the aggregation of TMRM in mitochondria, quenching the fluorescence and thus affecting the measurement of MMP. CCCP was used as a negative control as uncoupling prevents TMRM accumulation in the mitochondria as the mitochondria depolarise. This was all optimised by Professor Mortiboys prior to the project.

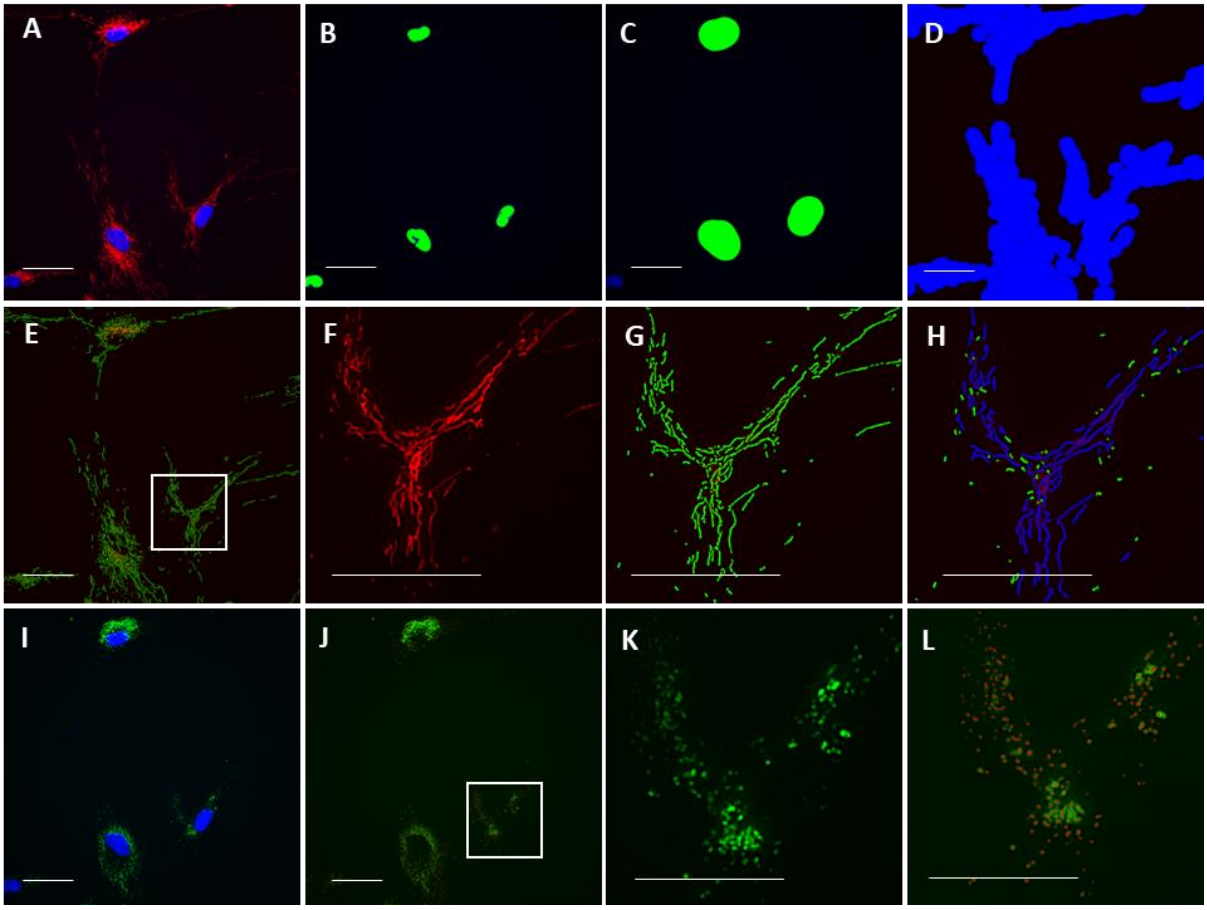

Figure 3: Representative images of the initial screen live imaging assay image analysis using the Incell Developer Toolbox. A) Mitochondria and nuclei stained with TMRM (red) and Hoechst (blue), **B)** Nuclei segmentation (green), **C)** Perinuclear region segmentation (green), **D)** Cell region segmentation (blue), **E)** Segmentation of mitochondria (green) using TMRM (red), **F)** Magnified image of mitochondria stained using TMRM (red), **G)** Magnified image of the segmentation of mitochondria (green) using TMRM (red), **H)** Magnified image of the segmentation of long (blue) and small mitochondria (green) using TMRM (red), **I)** Lysosomes and nuclei stained with lysotracker green (green) and Hoechst (blue), **J)** Segmentation of the lysosomes (red) using lysotracker green (green), **K)** Magnified image of lysosomes stained using lysotracker green (green), **L)** Magnified image of the segmentation of lysosomes (red) using lysotracker green (green). The white boxes in **E** and **J** show the location of the images used for **F/G/H** and **K/L**. Scale bar = 40 µm.

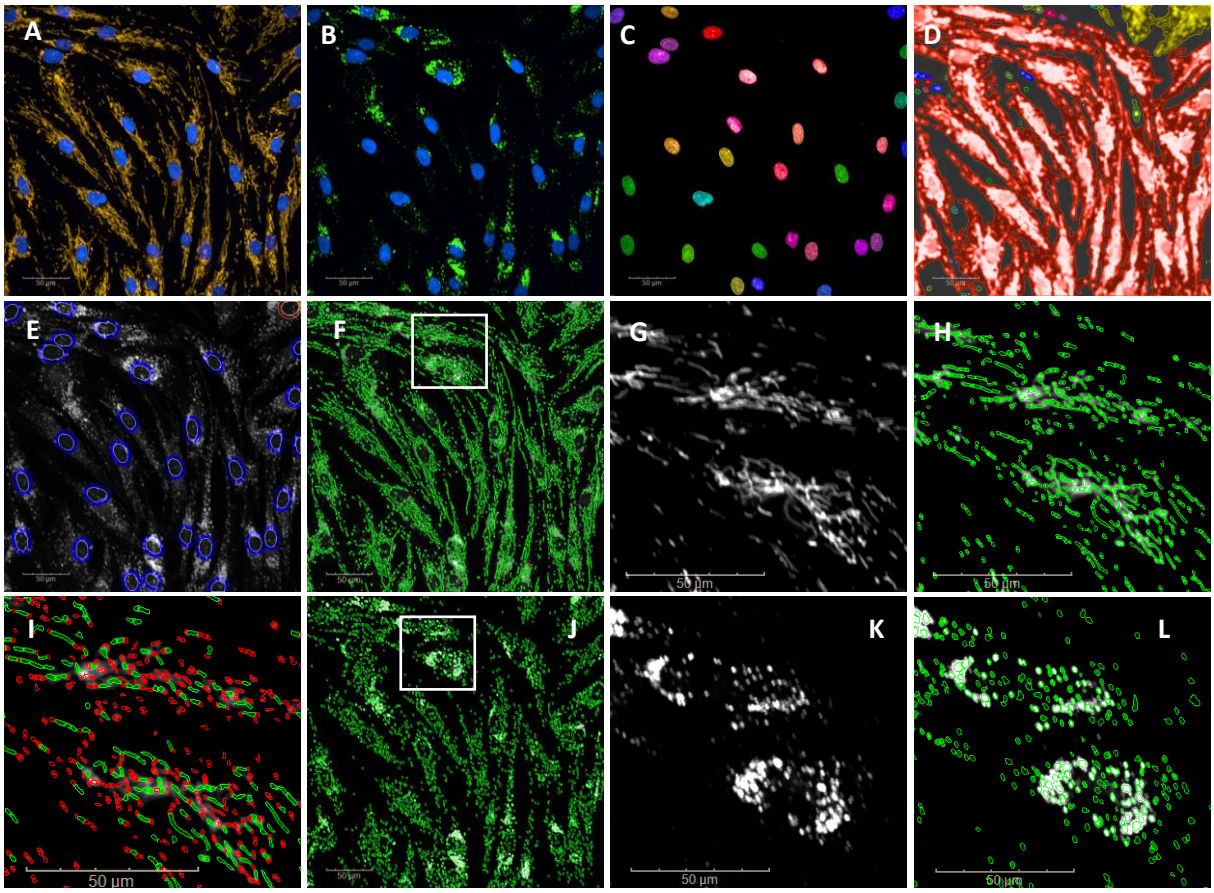

Figure 4: Representative images of the initial screen live imaging assay image analysis using Columbus analysis software. A) Mitochondria and nuclei stained with TMRM (orange) and Hoechst (blue), **B)** Lysosomes and nuclei stained with lysotracker green (green) and Hoechst (blue), **C)** Nuclei segmentation (coloured), **D)** Cell region segmentation (coloured), **E)** Perinuclear region segmentation (blue), **F)** Segmentation of mitochondria (green) using TMRM (white), **G)** Magnified image of mitochondria stained using TMRM (white), **H)** Magnified image of the segmentation of mitochondria (green) using TMRM (white), **I)** Magnified image of the segmentation of long (green) and small mitochondria (red) using TMRM (white), **J)** Segmentation of the lysosomes (green) using lysotracker green (white), **K)** Magnified image of lysosomes stained using lysotracker green (white), **L)** Magnified image of the segmentation of lysosomes (green) using lysotracker green (white). The white boxes in **F** and **J** show the location of the images used for **G/H/I** and **K/L**. Scale bar = 50 µm

2.4.3 Total ATP levels

Fibroblast lines were seeded into 6 wells of a white 96-well plate (Greiner Bio-One; 165306) at a density of 4000 cells per well 2.3.2 Fibroblast Maintenance). The following day, three wells were fed with EMEM media and three with galactose media. 72 hours later ATP levels were determined using the ATPlite kit from PerkinElmer (6016949). The cells were lysed using 100 µl PBS mixed with 50 µL ATPlite lysis buffer and agitated on an orbital shaker for 5 minutes. 50 µL ATPlite substrate solution

was added immediately and the plate was agitated for 5 minutes. The plate was incubated at room temperature in the dark for 10 minutes before measuring luminescence. 50 µL cyquant solution, consisting of PBS with 20 % HBSS and 0.2 % cyquant dye (Thermofisher; C7026), was added after the measurement and the plate was incubated at 37 °C for 1 hour. The fluorescent intensity was measured using the Excitation 480 nm/ Emission 520 nm channel. This assesses total DNA content for normalisation.

2.4.4 Statistical Analysis

Results from the image analysis and ATP assay were combined and analysed using R. Scoring begins by normalising the result for each well to the mean of the control wells on the plate. A mean was calculated from the three wells for each line and media condition. The standard deviation for the control line means was then calculated for each repeat and media condition and used to generate a z-score, using the equation $z = (i - \mu) / \sigma$ (where i is the mean for a cell line in one repeat and media condition, µ is the mean of all the controls in the cohort in the repeat and media condition, σ is the standard deviation of the controls in that repeat and media condition). This produced one z-score for each line per media condition per repeat. The z-scores for each repeat were combined using the equation $cz = \sum(w * z)$ (where w is the weighting and z is the individual repeat z-score). The weighting was calculated using the coefficient variance of the controls, this was calculated using the equation $3\sqrt{2 * (\text{coef1} + \text{coef2} + \text{coef3})}$ (where coef is the coefficient variance between the controls in two repeats, there are three coef values to consider the three pairs of repeats). The coefficient variance was calculated using the Pearson Correlation Coefficient in a pairwise manner. A composite z-score combining the media condition z-scores per cell line was calculated in a similar fashion, this produced one z-score per parameter for each line.

Finally, we combined all the parameters for mitochondrial dysfunction to form one composite z-score for mitochondrial dysfunction, and likewise for lysosomal dysfunction. We weighted the mitochondrial dysfunction score to ensure that functional parameters accounted for 45 % of the final score, morphology parameters accounted for 45 % of the score and localisation accounted for 10 % (Table 7). All z-scores were converted to absolute numbers to prevent opposite scores from cancelling each other out. Functional parameters included MMP and ATP of which each accounted for 22.5 %, with MMP being broken down further into overall MMP (7.5 %), small mitochondria MMP (7.5 %) and long mitochondria (7.5 %), this allowed us to account for dysfunction in one type of mitochondria as well as the entire population (Table 7). Morphology parameters include form factor (FF), which was also divided into overall FF (7.5 %), small mitochondria FF (7.5 %) and long mitochondria FF (7.5 %), and mitochondrial count, which was divided into the number of mitochondria per cell (11.25 %) and the

long vs small mitochondria ratio (11.25 %, Table 7). The localisation parameter was the percentage of perinuclear mitochondria (10 %, Table 7).

Parameters were selected and weighting was assigned based on previous literature in Parkin, LRRK2 and sPD fibroblasts, which reported significant abnormalities in function parameters (MMP and ATP) and morphology (count and form factor) (Mortiboys *et al.*, 2008, 2010, 2015; Grünewald *et al.*, 2010, 2014; Papkovskaia *et al.*, 2012; van der Merwe *et al.*, 2014; Zanellati *et al.*, 2015; Haylett *et al.*, 2016; Juárez-Flores *et al.*, 2018; Carling *et al.*, 2020). Further investigation of small and long mitochondria populations was included because mitochondrial shape and size can vary with their function and role. For example, small, fragmented mitochondria can be produced by fission to counter dysfunction and are targeted for degradation, but fusion can occur to enable a transfer of the matrix contents and possible repair (reviewed by Adebayo *et al.*, 2021). Due to dysfunctional mitochondrial dynamics being identified in certain forms of genetic PD (PINK1/Parkin mutations), this study wanted to observe whether different mitochondria subpopulations were affected in different sPD patient subgroups. Equal weighting for function and morphology was assigned to prevent bias towards one or the other. Likewise, the parameters that measured function and morphology were equally weighted to prevent bias towards a specific parameter, for example, ATP and MMP were both assigned a weighting of 22.5 %. Finally, the total mitochondrial populations, long mitochondria and small mitochondria were equally weighted for MMP and form factor to prevent bias for one population. Previous literature reported that dysfunctional mitochondria are transported to the perinuclear region for degradation (Geisler *et al.*, 2010; C. Kim *et al.*, 2021), therefore, to further include mitochondrial dynamics into the stratification method we included the percentage of perinuclear mitochondrial. Mitochondria localisation has been investigated less in PD and consequently was assigned a smaller weighting than function and morphology.

We also calculated a lysosomal dysfunction composite z-score using an even weighting for each morphological parameter, lysosomes per cell (33.3 %), lysosomal area (33.3 %) and lysosomal FF (33.3 %). An unbiased approach with equal weighting for each parameter was selected due to the limited research consensus on lysosome morphology in PD (reviewed above in 1.1.3.2 GBA and 1.3.2 Lysosomes in Parkinson's Disease) and therefore a limited understanding of the significance of each parameter on disease.

A z-score describes the position of a raw result from the population's mean and is measured in standard deviation units. This method of scoring dysfunction was selected because it enables the combination of scores from tests with different ranges without introducing bias towards the parameter with the greater range. For example, the standard deviation for ATP in the control

population was 17.9 %, whereas the mitochondrial form factor's standard deviation was 1.4 %. Combining the scores from these tests would bias the weighting towards the ATP result. Likewise combining scores between media conditions would bias results towards the more variable data set. Thus, z-scoring enabled a defined weighting of all parameters, conditions and repeats. However, it has several weaknesses, these include losing meaningful raw results and magnifying small differences (Wiesen, 2006). In this instance, both were deemed acceptable. The aim was to identify patterns of dysfunction and highlight individuals with highly dysfunctional organelle, therefore, raw values were less important. Furthermore, statistical assessment of the populations used normalised data as well as z-scores to prevent the loss of meaningful raw results. The purpose of the method was to equalise differences between parameters with different results ranges, thus it was inevitable that differences in parameters with small ranges were magnified. This was expected and the raw results were assessed during the stratification process to confirm a meaningful difference was occurring.

Statistical analysis comparing population means used an unpaired T-test with Welch correction for normally distributed parameters or Mann-Whitney U test for non-normally distributed data. To assess variation a Fisher's F-test was used for normally distributed parameters and a Levene's test for non-normally distributed data. Normality was assessed using a Shapiro-Wilks test, significance ($p < 0.05$) indicated that the data was not normally distributed.

The composite z-scoring method combining repeats and media conditions was mainly established by Professor Heather Mortiboys and Dr Thomas Payne, while I provided some assistance. The final mitochondrial and lysosomal dysfunction scores were established by Professor Mortiboys and again I provided some assistance.

Table 7: A table showing the parameter weighting that was used for the mitochondrial dysfunction score composite z-score calculation.

Type of Parameter	Parameter	Weighting in Mitochondrial Dysfunction Score (%)
Function	MMP	7.5
	Small Mitochondria MMP	7.5
	Long Mitochondria MMP	7.5
	ATP	22.5
Morphology	Mitochondria per Cell	11.25
	Long vs Small Mitochondria Ratio	11.25

	Form Factor	7.5
	Small Mitochondria Form Factor	7.5
	Long Mitochondria Form Factor	7.5
Localisation	Perinuclear Mitochondria Percentage	10

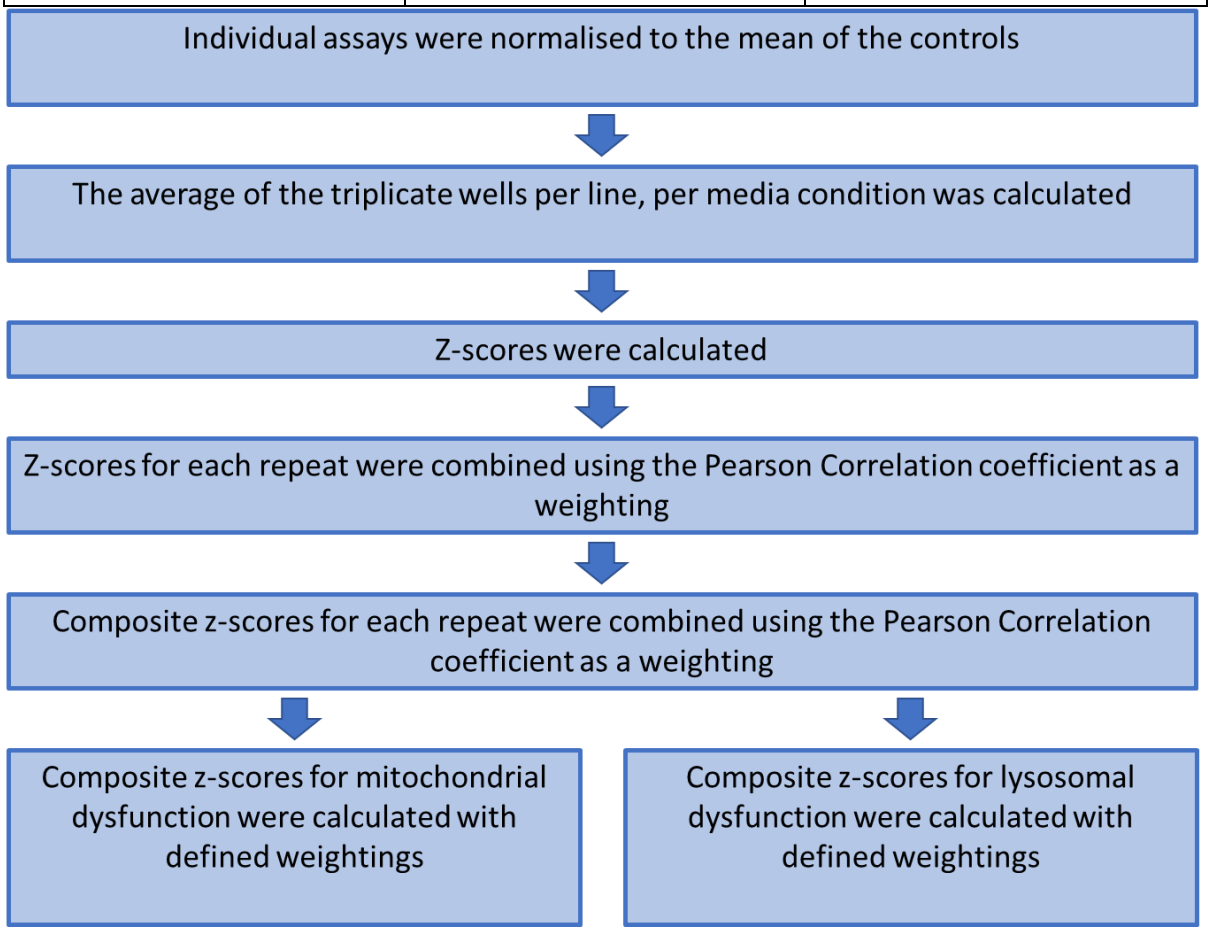

Figure 5: A flow chart demonstrating the method for scoring the cohort for mitochondrial and lysosomal function.

2.5 In-depth Assessment Methods

2.5.1 Mitochondrial Reassessment using Mitotracker Green

This assay enabled the measurement of mitochondria by TMRM in an MMP-dependent manner and by mitotracker green in an MMP-independent manner. This enabled the measurement of total mitochondria and functional mitochondria. Fibroblast lines were seeded into six wells of a black 96-well plate (Agilent; 204626-100) at a density of 1000 cells per well, as described above 2.3.2 Fibroblast

Maintenance). The next day, three wells were fed with EMEM media and three with galactose media and cultured for 72 hours. Cells were incubated for 1 hour with Phenol Free Minimum Essential Medium containing 80 nM TMRM, 1 µM mitotracker green (Thermofisher; M7514) and 20 µM Hoechst 33528. The media was changed to Phenol Free MEM only and the cells were imaged on the InCell Analyzer 2000 using the 60X magnification lens. Imaging exposures were optimised per plate for the Cy3 (Excitation 530-560/Emission 570-650), FITC (Excitation 460-490/Emission 500-550) and DAPI channels (Excitation 355-385/Excitation 430-500). Images were analysed using InCell Developer Toolbox, to segment TMRM or mitotracker green labelled mitochondria and nuclei. This enabled the quantification of MMP, mitochondria per cell, mitochondria form factor, percentage of perinuclear mitochondria and long vs small mitochondria ratio.

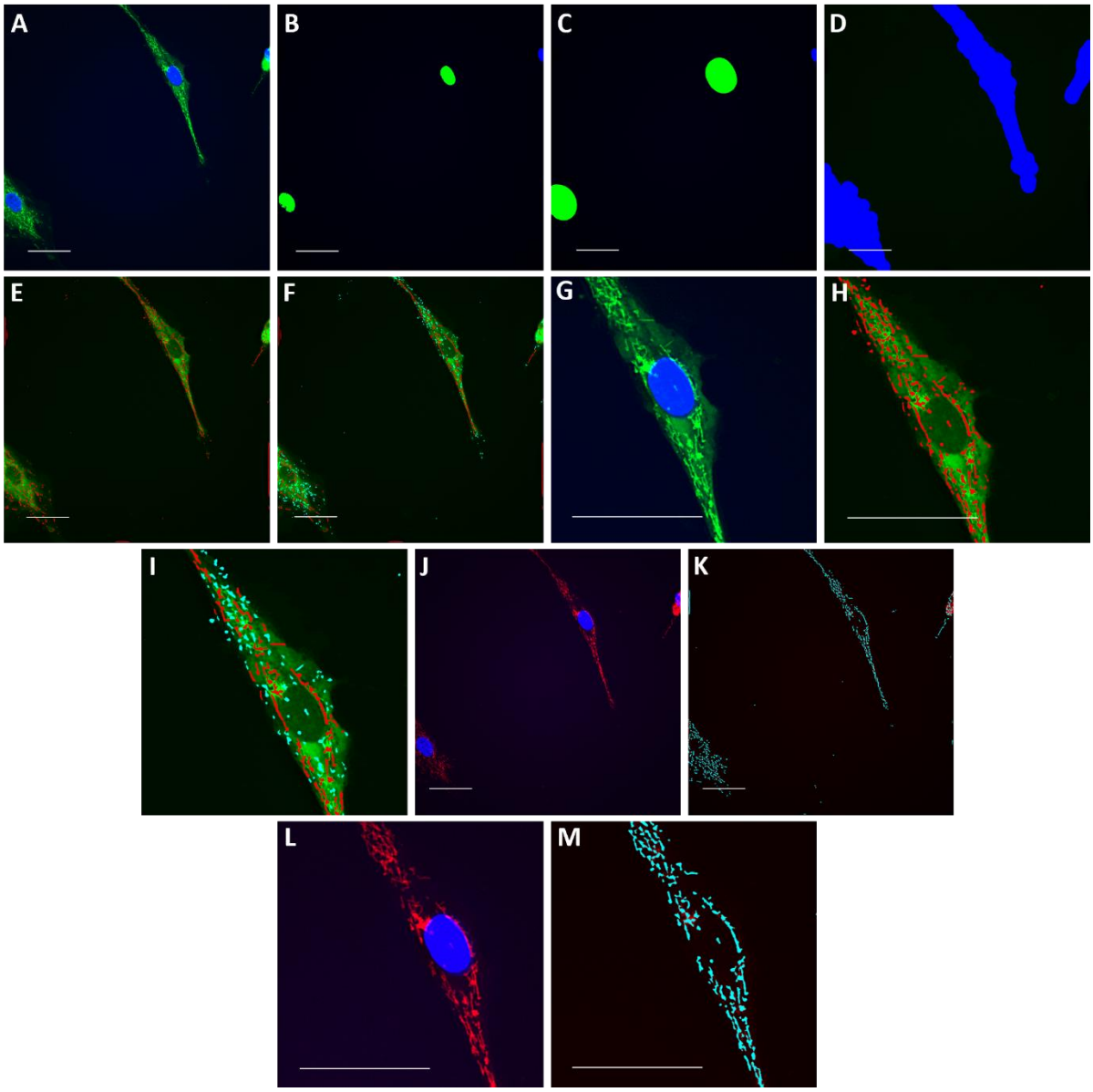

Figure 6: Representative images of the image analysis using the Incell Developer Toolbox for the mitochondrial reassessment using mitotracker green. A) Mitochondria and nuclei stained with mitotracker green (green) and hoechst (blue), **B)** Nuclei segmentation (green), **C)** Perinuclear region segmentation (green), **D)** Cell region segmentation (blue), **E)** Segmentation of mitochondria (red) using mitotracker green (green), **F)** Segmentation of long (red) and small mitochondria (light blue) using mitotracker green (green), **G)** A magnified image of mitochondria stained using mitotracker green (green) and nuclei stained using hoechst (blue), **H)** A magnified image of the segmentation of mitochondria (red) using mitotracker green (green), **I)** A magnified image of the segmentation of long (red) and small mitochondria (light blue) using mitotracker green (green), **J)** Mitochondria and nuclei stained with TMRM (red) and Hoechst (blue), **K)** Segmentation of the mitochondria (light blue) using TMRM (red), **L)** A magnified image of mitochondria stained using TMRM (red) and nuclei stained using

hoechst (blue), **M)** A magnified image of the segmentation of mitochondria (light blue) using TMRM (red). Scale bar = 40 µm.

2.5.2 Mitochondrial and Lysosomal Reassessment using Mitotracker Green

Fibroblast lines were seeded into three wells of a black 96-well plate (Agilent; 204626-100) at a density of 1000 cells per well, as described above (2.3.2 Fibroblast Maintenance). The next day, the wells were fed with EMEM media (.

Table 6) cultured for 72 hours. Cells were incubated for 1 hour with Phenol Free Minimum Essential Medium containing 80 nM TMRM, 1 µM mitotracker green, 50 nM lysotracker red (Thermofisher; L12492) and 20 µM Hoechst 33528. The media was changed to Phenol Free MEM only immediately before imaging.

Imaging was completed using the 40X water objective on the Opera Phenix at 37 °C and 5 % CO_2. The AlexaFluor 488 (Excitation 488/Emission 500-550), AlexaFluor 568 (Excitation 530-560/Emission 570-650), AlexaFluor 647 (Excitation 615-645/Emission 655-760) and DAPI channel (Excitation 355-385/Emission 430-500) were utilised to image the four dyes. Eight fields were imaged per well, with three z-stacks spaced 0.5 µm apart. Analysis was carried out using the Harmony analysis software. Firstly, the z-stacks were merged to produce a maximum projection and a basic flatfield correction was applied. Nuclei were then segmented, followed by the cellular region. The mitochondrial region of the mitotracker green dye was next to be segmented, followed by the TMRM mitochondria region and finally the lysotracker far red lysosome region (Figure 7). This enabled us to quantify MMP, mitochondria per cell, lysosomes per cell and average lysosome area.

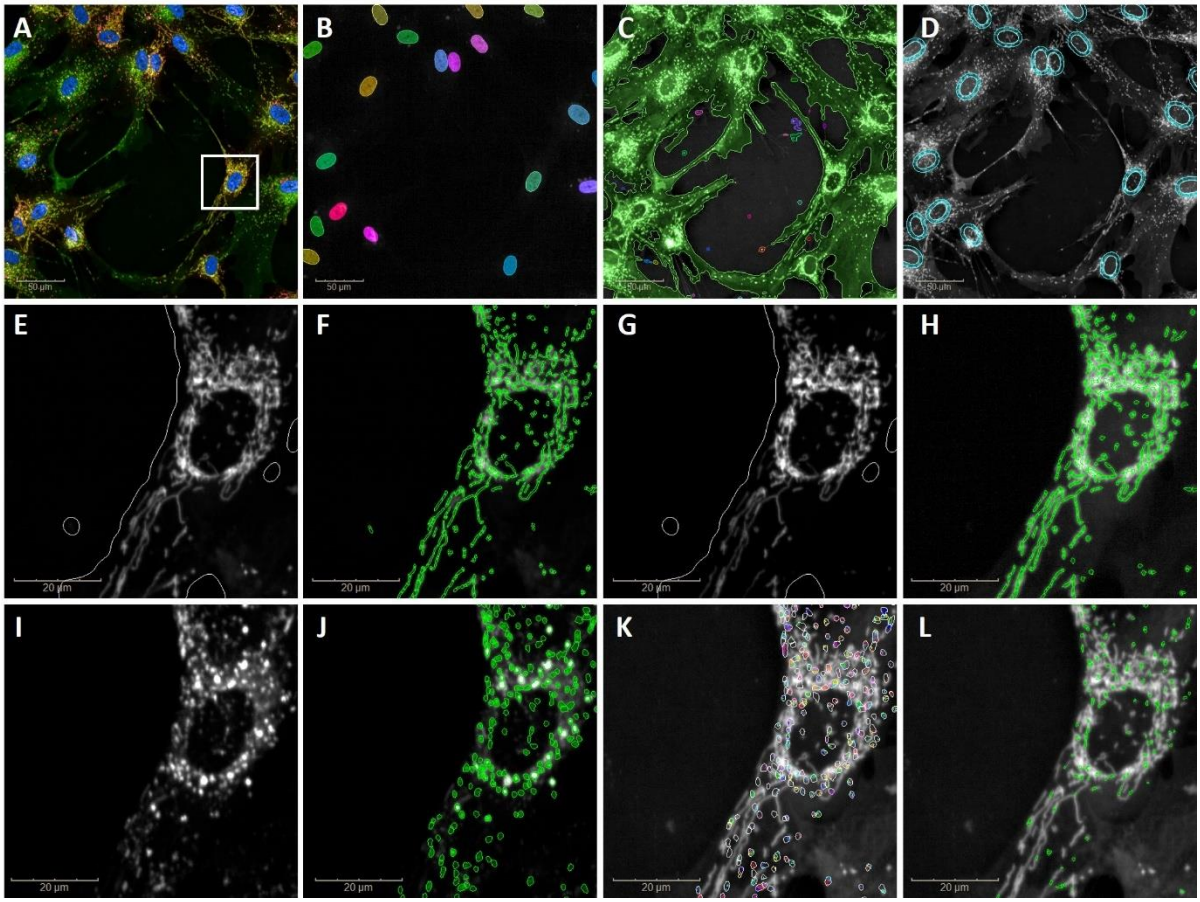

Figure 7: Representative images of the image analysis of the mitochondrial and lysosomal assessment using TMRM, mitotracker green and lysotracker red. A) Merged image of mitochondria stained with TMRM (orange) and mitotracker green (green), lysosomes stained with lysotracker red (red) and nuclei stained with Hoechst (blue), **B)** nuclei segmentation using Hoechst (coloured), **C)** Cell region segmentation using the four channels (coloured), **D)** Perinuclear region segmentation (blue), **E)** A magnified image of mitochondria stained with mitotracker green (white), **F)** A magnified image of mitochondria segmented (green) using mitotracker green (white), **G)** A magnified image of mitochondria stained with TMRM (white), **H)** A magnified image of mitochondria segmented (green) using TMRM (white), **I)** A magnified image of lysosomes stained with lysotracker red (white), **J)** A magnified image of lysosomes segmented (green) using lysotracker red (white), **K)** A magnified image of the mitochondria segmented (coloured) within the lysosomes (white rings) using mitotracker green (white), **L)** A magnified image of the final selection of mitochondria segmented (green) within the lysosomes using mitotracker green (white). The white box in **A** shows the location of the images used for **E/F/G/H/I/J/K/L**. Scale bar = 20 or 50 µm.

2.5.3 ATP with Inhibitors

Fibroblasts were plated at a density of 2000 cells per well in a white 384-well plate (Greiner Bio-One; 781983), as previously described (2.3.2 Fibroblast Maintenance). The following day the media was changed so that fifteen wells were cultured in EMEM media and fifteen in galactose media for 72 hours at 37 °C and 5 % CO_2. Prior to assaying the cells were incubated for 30 minutes at 37 °C with toxins that block various metabolic pathways (Table 8). Due to the size of the plate, the toxin position was changed for each repeat to ensure plate location and time of media changing did not alter results. The cells were immediately lysed using 50 µL PBS mixed with 12.5 µL ATPlite lysis buffer and agitated on an orbital shaker for 5 minutes at room temperature. Following lysis, 12.5 µL ATPlite substrate solution was added and again the plate was agitated for 5 minutes before being incubated at room temperature in the dark for 10 minutes. ATP levels were assessed by measuring luminescence. 12.5 µL cyquant solution, consisting of PBS with 20 % HBSS and 0.2 % cyquant dye, was added and incubated at 37 °C for 1 hour. Fluorescence was measured as described above.

Table 8: The composition of media used to inhibit various metabolic pathways in order to assess ATP production.

Condition	**Media Composition**
Basal	Phenol Free MEM
Oxidative Phosphorylation inhibition	Phenol Free MEM, containing 1 µM Oligomycin
Glycolysis inhibition	Phenol Free MEM, containing 50 mM 2 Deoxyglucose
Fatty Acid metabolism inhibition	Phenol Free MEM, containing 15 µM Etomoxir
Glutamine inhibition	Phenol Free MEM, containing 20 µM BPTES

2.5.4 Seahorse Assay

Fibroblasts were plated into an XF96 cell culture microplate (Agilent; 103793-100) at a density of 16,000 cells per well as described above (2.3.2 Fibroblast Maintenance). They were kept at 37 °C and 5 % CO_2 overnight. The following day the media was removed, and fresh EMEM media was added to each well. The XFe96 sensor cartridge was hydrated on day 2, 200 µL diH_2O was added to each well and placed in a 37 °C oven with atmospheric CO_2 levels overnight. On day 3 the water was removed from the calibrant plate and replaced with 200 µl pre-warmed Seahorse XF Calibrant Solution 1 hour prior to toxin loading, this solution was pre-warmed in a 37 °C oven with atmospheric CO_2 levels overnight. A minimum of six well technical repeats were used per condition.

2.5.4.1 MitoStress Assay

This assay enables the measurement of oxygen consumption and extracellular acidification under different conditions. Oligomycin blocks ATP synthase preventing ATP-linked oxidative phosphorylation, this enables the proportion of oxygen consumption being used for ATP production to be quantified. Carbonyl cyanide m-chlorophenyl hydrazone (CCCP) uncouples the mitochondrial ETC causing the ETC to work at its maximum rate, enabling the measurement of maximal respiration. Rotenone and antimycin inhibit complex I and III preventing oxidative phosphorylation completely.

Media in the cell plate was removed and replaced with 180 µL Seahorse XF base medium, supplemented with 10 mM glucose, 2 mM glutamine and 1 mM sodium pyruvate, and incubated at 37 °C and atmospheric CO_2 for 1 hour prior to the assay. The cartridge was then loaded with toxins diluted in seahorse XF base medium to 10X assay concentration, Port A: 15 µM oligomycin, Port B: 15 µM CCCP, Port C: 5 µM rotenone and 5 µM antimycin. Upon injection, this creates final concentrations: oligomycin 1.5 µM, CCCP 1.5 µM, rotenone 0.5 µM and antimycin 5 µM.

The calibrant plate was loaded into the Seahorse XFe96 Analyzer to calibrate the sensors. Following this, the cell plate was loaded. The machine measured basal O_2 and H^+ for 18 minutes, cycling between 3 minutes mixing and 3 minutes measuring. This was followed by each port being injected and measured for 18 minutes until all ports had been completed.

2.5.4.2 Fuel Flex Assay

The Fuel Flex assay enables the quantification of the dependency and capacity for mitochondria to use different fuel types for oxidative phosphorylation. Etomoxir inhibits carnitine palmitoyltransferase 1a (O'Connor, 2018) blocking the transport of fatty-CoA into the mitochondria preventing fatty acid oxidation. BPTES is a glutaminase inhibitor (Zhang *et al.*, 2023) and blocks the conversion of glutamine to glutamate preventing glutamine sourced ATP production. UK5099 inhibits the mitochondrial pyruvate carrier preventing pyruvate from being used by the citric acid cycle, thus blocking glucose use for oxidative phosphorylation.

Media in the cell plate was removed and replaced with 180 µL Seahorse XF base medium, supplemented with 10 mM glucose, 2 mM glutamine and 1 mM sodium pyruvate, and incubated at 37 °C and atmospheric CO_2 for 1 hour prior to the assay. The cartridge was then loaded with toxins diluted in seahorse XF base medium to 10X assay concentration, Port C: Toxin mix 1, Port D: Toxin mix 2, for combinations see Table 9.

The calibrant plate was loaded into the Seahorse XFe96 Analyzer to calibrate the sensors. Following this, the cell plate was loaded. The machine measured basal O_2 and H^+ levels for 54 minutes, then port

C was injected and measured for 36 minutes, followed by port D injection and levels were measured for a further 36 minutes with mixing and measurements alternating every 3 minutes.

Table 9: A table showing the final concentrations of each toxin for the fuel flex test.

Measurement	Port C: Toxin Mix 1	Port D: Toxin Mix 2
Glucose dependency	2 µM UK5099	20 µM BPTES , 15 µM Etomoxir
Glutamine dependency	20 µM BPTES	15 µM Etomoxir, 2 µM UK5099
Fatty acid dependency	15 µM Etomoxir	20 µM BPTES, 2 µM UK5099
Glucose Capacity	20 µM BPTES, 15 µM Etomoxir	2 µM UK5099
Glutamine Capacity	15 µM Etomoxir, 2 µM UK5099	20 µM BPTES
Fatty acid capacity	20 µM BPTES, 2 µM UK5099	15 µM Etomoxir

2.5.4.3 Normalisation

Following the assay, the cell plate was fixed. The cell media was removed and incubated with 50 µL 4% PFA at 37 °C for 15 minutes. The PFA was removed and the wells were washed with PBS and then stained with PBS and Hoechst 20 µM solution for 2 minutes. The dye solution was discarded and replaced with PBS. The plate was then imaged on the InCell Analyzer 2000. The images were analysed using the InCell Developer Toolbox. The nuclei were segmented and counted (Figure 8). The results were generated using the Seahorse Wave software. The raw results are normalised to the number of nuclei per well.

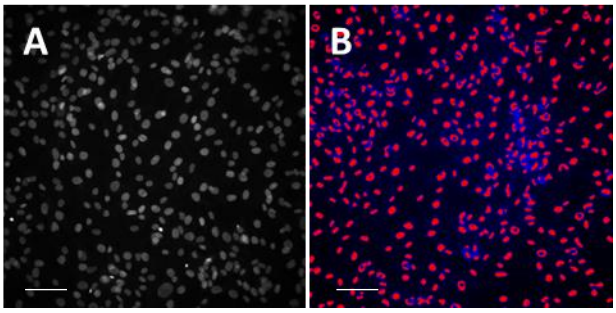

Figure 8: Representative images of the segmentation of nuclei for the normalisation of the Seahorse ZF Analyzer assays. A) Nuclei stained with Hoechst (white), **B)** Nuclei segmentation (red) using Hoechst (blue). Scale bar = 40 µm.

2.5.5 Complex Assays

2.5.5.1 Complex I Activity

This assay measures complex I activity using the Abcam Complex I Enzyme Activity Assay Kit (ab109721). The assay works by capturing complex I using specific antibodies. A solution containing NADH and a reducing dye is then added. When NADH is oxidised to NAD+, the dye is reduced and absorbs light at 450 nm. This enables the measurement of absorbance to quantify activity.

Cells were cultured as described above (2.3.2 Fibroblast Maintenance). Two T75 flasks were required per cell line. 72 hours prior to the assay one flask was switched into galactose media. The flask was pelleted as described previously (2.3.2 Fibroblast Maintenance). The cell pellet was lysed in 5 µL 10x detergent and 50 µl PBS for 30 minutes on ice. The lysate was centrifuged at 16,000 g and 4°C for 20 minutes. 50 µL of supernatant was transferred to a plate well and incubated at room temperature for 3 hours. The remaining supernatant was saved for a BCA assay. Following incubation, the wells are washed with 1X buffer. 200 µL of assay solution (1X buffer, 2 mM NADH, 1X dye) was added to each well immediately before measuring absorbance at 450 nm every 30 seconds for 2 hours using the Pherastar Plastreader (BMG labtech).

2.5.5.2 Complex II Activity

This assay measures complex II activity using the Abcam kit (ab109908). Complex II is immunocaptured within the well. Complex II receives electrons from $FADH_2$ and transfers them to ubiquinone to form ubiquinol. The reduction of ubiquinone is coupled to the reduction of the DCPIP dye decreasing its absorbance. Activity can be quantified from the change in absorbance over time.

Four T75 flasks of fibroblasts were used per cell line, two flasks cultured in galactose media for 72 hours and two in EMEM media. The cells were pelleted as previously described (2.3.2 Fibroblast Maintenance). The pellet was resuspended in 50 µl PBS and 5µl 10X detergent and lysed for 30 minutes on ice. The lysate was centrifuged at 16,000 g and 4 °C for 20 minutes. 50 µL of supernatant was loaded into a well of the complex II assay plate and incubated at room temperature for 2 hours. 5 µL of supernatant was saved for protein estimation by a BCA assay. Following incubation, the supernatant was removed and the well was washed with 1X buffer and 40 µL phospholipid mix was added and incubated for 30 minutes at room temperature. 200 µL of activity solution (Complex II Activity Buffer, 0.002 % ubiquinone, 0.02% succinate and 0.01% DCPIP) was added and the plate was immediately assayed on the Pherastar Platereader. Absorbance was measured at 600 nm and room temperature every 30 seconds for 2 hours.

2.5.5.3 Complex IV Activity

This assay measures complex IV by measuring cytochrome c oxidation using the Abcam kit (ab109909). The complex IV is immunocaptured and the oxidation of reduced cytochrome c is assessed by the shift in fluorescent wavelength. Activity is determined by the rate of change.

Four T75 flasks were used per cell line, two flasks remained in glucose media and two were cultured in galactose media for 72 hours. The cells were pelleted as previously described (2.3.2 Fibroblast Maintenance). The pellet was resuspended in 50 µL PBS and 5 µL 10X detergent and incubated on ice for 30 minutes. The suspension was centrifuged at 12,000 g and 4 °C for 20 minutes. 50 µL of supernatant was added to a well of the microplate and 5 µL used for a BCA assay. The plate was incubated at room temperature for 3 hours. Following incubation, the wells were washed twice with 300 µL solution 1 (diH_2O, 5 % tube 1 buffer) and 200 µL assay buffer (Solution 1, 5 % Reagent C) was added to each well. The plate was immediately assayed using the Pherastar Platereader to read absorbance at 550 nm and 30 °C every minute for 2 hours.

2.5.5.4 Complex V Activity

This assay measures Complex V activity by measuring NADH oxidation to NAD+ which is coupled to the hydrolysis of ATP to ADP using the Abcam kit (ab109714). The reduction of NADH results in a shift in absorbance enabling the rate of change to be measured. Three T75 flasks were used per line. The cells were pelleted as previously described (2.3.2 Fibroblast Maintenance) and resuspended in 50 µL PBS. The homogenate was frozen in liquid nitrogen and then immediately thawed in a water bath at 37 °C. The supernatant was aspirated and the pellet was resuspended in 50 µL Solution 1. 2 µL of the solution was removed and the protein was estimated using the BCA assay. The sample was then further diluted to 5.5 mg/mL. Detergent was added to dilute the sample to 5.0 mg/mL and the sample was incubated on ice for 30 minutes. The sample was then spun at 16,000 g for 20 minutes at 4 °C. 150 µg of sample was added to each well of the microplate and incubated at room temperature for 3 hours. Following incubation, the sample was removed and the well was washed twice with 300 µL of Solution 1. 40 µL Lipid mix was added and the plate was incubated for a further 45 minutes at room temperature. Immediately before measuring 200 µL Reagent mix was added and the absorbance was measured at 340 nm every minute for 2 hours using the Pherastar Platereader.

2.5.5.5 Complex Assay Result Analysis

The results produce a curved slope showing absorbance or fluorescence against time. The gradient of this line was calculated using the MARS software (BMG Labtech). This gradient was normalised to protein content which was calculated by a BCA assay and finally normalised to the mean activity of

the controls in EMEM media. Complex V was normalised to the rate of citrate synthase to ensure mitochondrial content did not bias results.

2.5.5.6 Citrate Synthase Assay

Citrate synthase is an enzyme in the citric acid cycle that is commonly used to measure mitochondria content. Citrate synthase catalyses the reaction of acetyl-CoA with oxaloacetate to form citrate, CoA and H^+. This reaction is coupled with CoA reacting with 5-5´-dithio-2-nitrobenzoic acid to form 5-thio-2-nitrobenzoate, a yellow substance whose absorbance can be measured.

A solution containing 50 µM Acetyl-CoA, 100 µM 5-5´-dithio-2-nitrobenzoic acid, 0.01 % Triton X-100, 150 µg cell lysate from the complex V assay and buffered with 100 mM Tris HCl (pH 8.0) was added to a 96-well plate. Immediately before measuring, oxaloacetic acid was added to each well at a final concentration of 500 µM. The absorbance of wavelength 412 nm was measured every 5 seconds for 5 minutes. The rate was calculated by assessing absorbance over time.

2.5.5.7 BCA

This assay was used to estimate protein concentration for a range of assays. The Pierce BCA protein assay kit (Thermofisher; 23227) was used. Protein samples and bovine serum albumin (BSA) standards were plated in triplicate in a clear 96-well plate (Corning; 3590). 5 µL BSA standard was added with concentrations ranging from 0 µg/mL to 1200 µg/mL. 1 µL protein sample was diluted 1:2 and plated in triplicate. Reagent A and B were mixed in a ratio of 50:1 to form the assay mix. 200 µL of assay mix was added to each well. The plate was incubated for 1 hour, then absorbance was measured at 562 nm using the Pherastar Platereader. Linear regression analysis was applied using the MARS software (BMG Labtech) taking into account protein sample dilution in order to calculate the concentration of protein in each sample.

2.5.6 Cathepsin D Activity Assay

The Cathepsin D activity assay kit (ab65302) was used to quantify CatD activity. The CatD substrate is tagged with a 7-Methoxycoumarin-4-acetic acid fluorophore, which fluoresces upon cleavage of the substrate. The assay requires three confluent T75 flasks of fibroblasts. The cells are cultured and pelleted as previously described (2.3.2 Fibroblast Maintenance). The cell pellet was resuspended in ice-cold PBS and pelleted again by centrifugation at 550 g for 4 minutes. The PBS was removed and the pellet was resuspended in 110 µL ATPlite lysis buffer (PerkinElmer). The suspension was immediately homogenised using a 25G needle (BD Microlance; 300600) and 1 mL syringe (Terumo; MDSS01SE) and placed on ice for 10 minutes. The suspension was homogenised again using the needle and syringe. The suspension was centrifuged at 17,000 g and 4 °C for 5 minutes. 35 µL of the sample

was added to 2 wells of a black 96-well plate (an assay well and a negative control well) and 5 µL of sample was saved for a BCA assay. 50 µL CD reaction buffer and 2 µL substrate were added to each assay well. 52 µL CD reaction buffer was added to each negative control well. The plate was incubated for 2 hours at 37 °C. Fluorescence was then measured using the Pherastar Platereader (Excitation 330 nm/ Emission 490 nm). The results for each sample well were adjusted to the average of the non-substrate wells and cell sample free negative controls. This activity value was then normalised to the protein content of each sample estimated by the BCA assay.

2.5.7 Mitophagy

Mitophagy is induced by damaging mitochondria with oligomycin and antimycin. These inhibit complex V, by blocking the proton pore, and complex III, by blocking ubiquinone binding. Assessing the difference between induced and basal mitophagy enables an understanding of mitophagy capabilities of the cells.

iDA neurons were plated in a black 96-well plate as previously described (2.3.5 Induced Dopaminergic Neuron Differentiation). At the end of differentiation, they were assayed. The media was aspirated and a dye solution containing Phenol Free MEM, 1 µM Mitotracker green, 80 nM TMRM, 50 nM lysotracker far red and 20 µM Hoechst was added for 1 hour. Immediately before imaging, media in the wells per cell line was replaced. Three wells per line were replaced with Phenol Free MEM containing 10 µM oligomycin and 4 µM antimycin to trigger mitophagy induction and three wells per line were replaced with Phenol Free MEM only.

Imaging was completed using the 40X water objective on the Opera Phenix at 37 °C and 5 % CO_2. The AlexaFluor 488 (Excitation 488/Emission 500-550), AlexaFluor 568 (Excitation 530-560/Emission 570-650), AlexaFluor 647 (Excitation 615-645/Emission 655-760) and DAPI channel (Excitation 355-385/Emission 430-500) were utilised to image the four dyes. Eight fields were imaged per well, with six z-stacks spaced 0.5 µM apart. Seven timepoints were measured, 35 minutes apart. Analysis was carried out using the Harmony analysis software. Firstly, the z-stacks were merged to produce a maximum projection and a basic flatfield correction was applied. Nuclei, mitochondria, lysosomes were segmented as described above 2.5.2 Mitochondrial and Lysosomal Reassessment using Mitotracker Green). Further segmentation enabled us to identify mitochondria with lysosomes and lysosomes within mitochondria (Figure 7). This enabled the quantification of basal levels of mitochondria per cell, mitochondrion average area, MMP, the ratio of functional mitochondria to mitochondria, lysosomes per cell, total lysosome area and average lysosome area from timepoint 1. Mitophagy was assessed by calculating the induced divided by basal mitophagy index. This enabled

the assessment of the percentage of mitochondria co-occurring with lysosomes, the number of functional mitochondria and the MMP across the seven timepoints.

2.5.8 Lysosome pH Assay

Low mixed group fibroblasts were cultured and 1000 cells were plated per well into six wells of a black 96-well plate as described previously (2.3.2 Fibroblast Maintenance). 4 hours before assaying three wells were converted to Phenol Free MEM containing 400 nM bafilomycin A1. 1 hour prior to imaging the plate's media was removed and replaced with Phenol Free MEM containing 1 µM lysosensor DND-189, 1 µM Hoechst with or without 400 nM bafilomycin A1. Immediately prior to imaging the dye solution was aspirated and replaced with Phenol Free MEM.

The lysosomal dysfunction subgroup fibroblasts were cultured following the protocol above (2.3.2 Fibroblast Maintenance). 3 hours before imaging half the wells per line were switched to Phenol Free MEM containing 10 µM chloroquine. 1 hour prior to imaging the media was removed from all wells and replaced with Phenol Free MEM containing 1 µM Lysosensor DND-189, 1 µM SYTO nucleic acid deep red with or without 10 µM chloroquine. Immediately prior to imaging the dye solutions are aspirated and Phenol Free MEM was added.

iDA neurons from the low mixed group and lysosomal dysfunction subgroup were differentiated as described (2.3.5 Induced Dopaminergic Neuron Differentiation). At the end of differentiation, half the wells were incubated with 10 µM chloroquine for 3 hours before imaging. 1 hour before imaging the media was replaced with Phenol Free MEM containing 1 µM Lysosensor DND-189, 1 µM SYTO nucleic acid deep red with or without 10 µM chloroquine. Immediately before imaging the media was removed and replaced with Phenol Free MEM.

Imaging for this assay utilised the 40X water objective on the OperaPhenix set at 37 °C and 5 % CO_2. The Sapphire (Excitation 355-385/Emission 500-550) and AlexaFluor 647 (Excitation 615-645/Emission 655-760) channels were used with exposures and powers adjusted to each plate. Fibroblasts were imaged with a minimum of nine fields per well and three Z-planes. iDA neurons were imaged with a minimum of nine fields and six Z-planes. The Harmony analysis software was used to segment nuclei and lysosomes (Figure 9). Firstly, the z-stacks were merged to produce a maximum projection and a basic flatfield correction was applied. Optimally acidic lysosomes per cell, total optimally acidic lysosome area, average area of optimally acidic lysosomes and acidification of the lysosomes (intensity) were quantified.

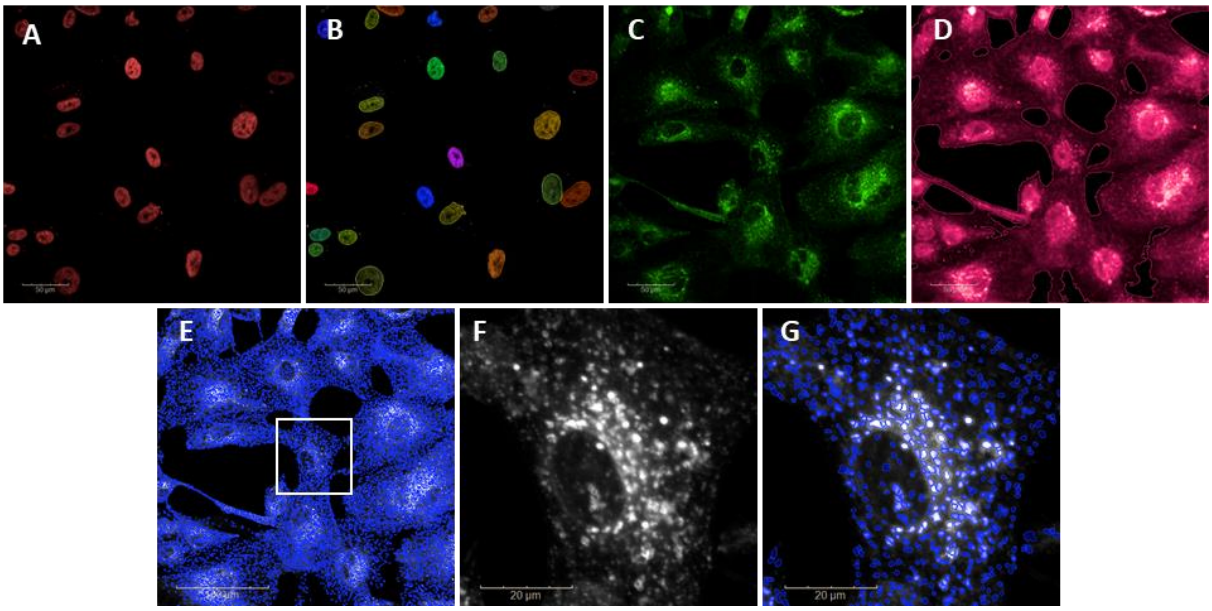

Figure 9: Representative images of the image analysis of the lysosenor assay. These images were taken from neurons but the segmentation was the same for fibroblasts. **A)** Nuclei stained with SYTO nucleic acid deep red (red), **B)** Nuclei segmentation (coloured), **C)** Lysosomes stained with lysosensor DND-189 (green), **D)** Cell region segmented from the combination of the nuclei and lysosome images (coloured), **E)** Segmentation of the lysosomes (blue) using lysosensor (white), **F)** A magnified image of lysosensor staining (white), **G)** A magnified image of the segmentation of the lysosomes (blue) using lysosensor (white). The white box in **E** shows the location of the images used for **F** and **G**. Scale bar = 20, 50 or 100 µm.

2.5.9 Cathepsin B Activity Assay

CatB activity was assessed using the Abcam's MagicRed kit (ab270772). MagicRed is a fluorescently tagged substrate of CatB that is endocytosed into the cell and degraded in the lysosome. The fluorophore is self-quenched when complete, but upon cleavage the fluorophore is released and fluoresces.

Fibroblasts from the low mixed group and lysosomal dysfunction subgroup were cultured and 1000 cells were plated per well in a black 96-well plate (Agilent) as described (2.3.2 Fibroblast Maintenance). On day 2, the media was switched, three wells were cultured in EMEM media and three in galactose media for 72 hours before assaying. This assay was also conducted in iDA neurons from both groups. The iDA neurons were differentiated as described above (2.3.5 Induced Dopaminergic Neuron Differentiation).

The MagicRed CatB substrate was reconstituted in 200 µL DMSO and aliquoted for long term storage at -20 °C. On the day of the assay, MagicRed was thawed and immediately diluted 1:10 in diH_2O. The

MagicRed mix was then diluted 1:25 in Phenol Free MEM. The media was aspirated from the wells and replaced with 100 µL dye solution for 1 hour at 37 °C and 5 % CO_2. The dye mix was removed and replaced with Phenol Free MEM containing 1 µg/mL Hoechst 33342 and incubated at 37 °C and 5 % CO_2 for 10 minutes. The second dye mix was then removed and replaced with Phenol Free MEM. Fibroblasts were imaged at 37 °C and 5 % CO_2 on the InCell Analyzer 2000 using the 60X objective. A minimum of ten fields were imaged. iDA neurons were imaged on the 40X water objective on the OperaPhenix, which was set to 37 °C and 5 % CO_2. A minimum of nine fields were imaged and six Z-planes. Imaging utilised the Cy3 (Excitation 530-560/Emission 570-650) and DAPI channels (Excitation 355-385/Excitation 430-500) on both microscopes. Analysis of the neuron images was completed using Harmony (Figure 11) and analysis of the fibroblasts was performed using the InCell Developer Toolbox (Figure 10). For the fibroblasts the lysosomes, nuclei and perinuclear region were segmented to measure the number of CatB active lysosomes, total CatB active lysosome area, average area of CatB active lysosomes and CatB activity in the lysosomes. These were measured in the whole cell and the perinuclear region separately (Figure 10). In neurons the same segmentation and quantifications were made only in the whole cell (Figure 11).

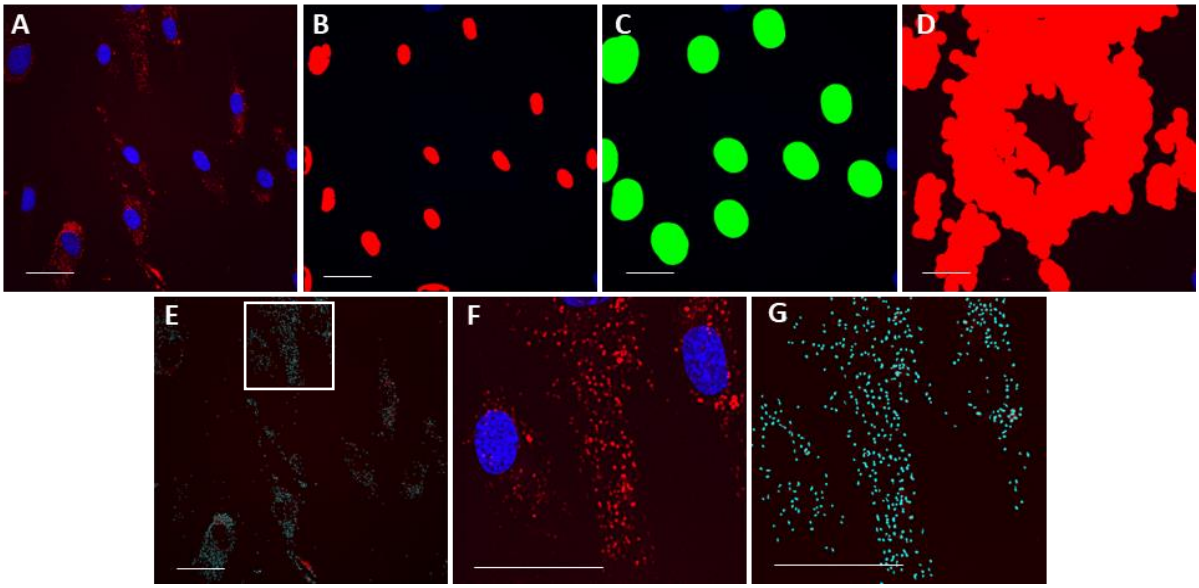

Figure 10: Representative images of the image analysis of the CatB assay in fibroblasts using the Incell Developer Toolbox. A) Nuclei stained with hoechst (blue), lysosome stained with MagicRed (red), **B)** Nuclei segmentation (red), **C)** Segmentation of the perinuclear region (green), **D)** Segmentation of the cell region (red), **E)** Segmentation of the lysosomes (light blue) using MagicRed (red), **F)** A magnified image of the nuclei stained with hoechst (blue) and lysosomes stained with MagicRed (red), **G)** Segmentation of the lysosomes (light blue) in the magnified image using MagicRed (red). The white box in **E** shows the location of the images used for **F** and **G**. Scale bar = 40 µm.

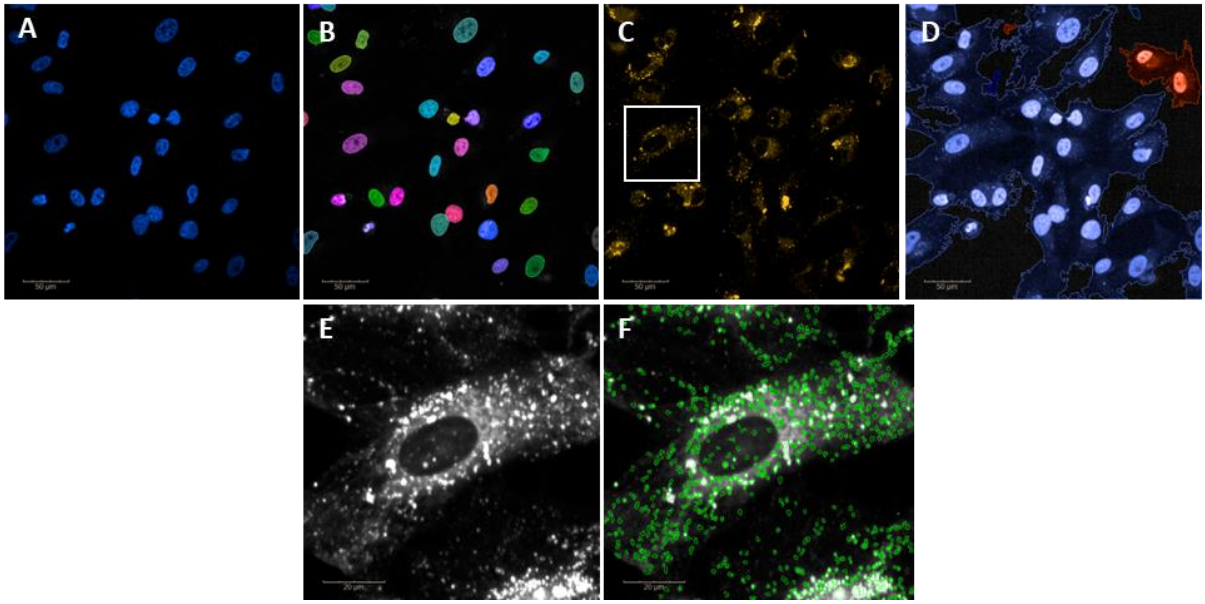

Figure 11: Representative images of the image analysis of the CatB assay in iDA neurons using the Harmony analysis software. **A)** Nuclei stained with Hoechst (blue), **B)** Nuclei segmentation (coloured), **C)** Lysosomes stained with MagicRed (orange), **D)** Cell region segmented from the combination of the nuclei and lysosome images (coloured), **E)** A magnified image of the lysosomes stained with MagicRed (white), **F)** Segmentation of the lysosomes (green) stained with MagicRed (white) in the magnified image. The white box in **C** shows the location of the images used for **F** and **G**. Scale bar = 20 or 50 µm.

2.5.10 Cathepsin Activity Assay

The cathepsin activity assay is a live staining assay that uses the fluorescent substrate DQ-BSA. This fluorophore is self-quenching, however, upon cathepsin-mediated cleavage fluoresces. The iDA neurons were cultured as described previously (2.3.5 Induced Dopaminergic Neuron Differentiation). On the day of assaying the culturing media was replaced with 70 µL Phenol Free MEM containing 25 µg/mL DQ-BSA red (Thermofisher; D-12051) and incubated at 37 °C and 5 % CO_2 for one and a half hours. The media was replaced with 70 µL of Phenol Free MEM containing 25 µg/mL DQ-BSA red with or without 1 mM L-leucyl-L-leucine methyl ester (Llome, sigma; L7393). After another three hours of incubation, the media was again replaced with another 70 µL of Phenol Free MEM with and without containing 25 µg/mL DQ-BSA red with or without 1 mM L-leucyl-L-leucine methyl ester (Llome) and incubated for a final hour. At the end of this incubation, the media was replaced with 90 µL Phenol Free MEM containing 1 µg/ mL Hoechst 33342 and incubated for 10 minutes. Immediately before imaging the media was replaced with Phenol Free MEM. The iDA neurons were imaged by the 40X water objective on the OperaPhenix, which was set to 37 °C and 5 % CO_2. A minimum of nine fields were imaged and six Z-planes. Analysis of the neuron images was completed using Harmony. Imaging utilised the Cy3 (Excitation 530-560/Emission 570-650) and DAPI channels (Excitation 355-385/Excitation 430-500).

Image analysis used the Harmony analysis software. Firstly, the z-stacks were merged to produce a maximum projection and a basic flatfield correction was applied. The lysosomes and nuclei were segmented (Figure 12) and the number of cathepsin active lysosomes per cell, total cathepsin active lysosome area per cell, average cathepsin active lysosome area and intensity of cy3 within the lysosomes was quantified to measure cathepsin activity.

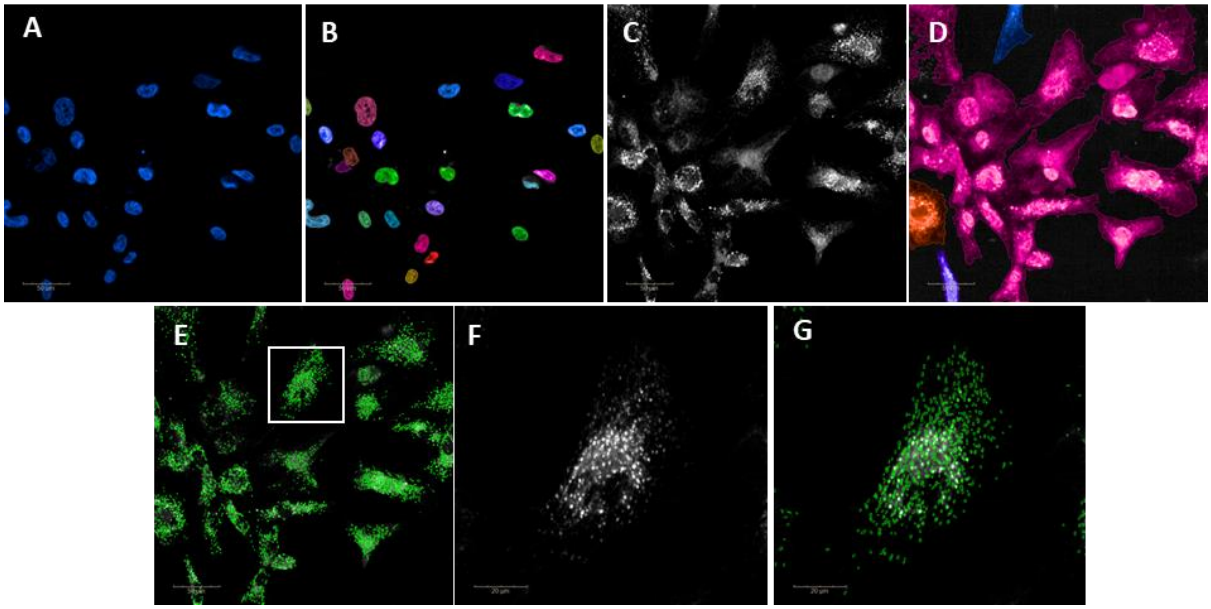

Figure 12: Representative images of the DQ-BSA assay image analysis measuring cathepsin activity in iDA neurons using the Harmony analysis software. A) Nuclei stained with Hoechst (blue), **B)** Nuclei segmentation (coloured), **C)** Lysosomes stained with DQ-BSA (white), **D)** Cell region segmented from the combination of the nuclei and lysosome images (coloured), **E)** Lysosomes segmented (green) using DQ-BSA (white), **F)** A magnified image of the lysosomes stained with DQ-BSA (white), **G)** Segmentation of the lysosomes (green) stained with DQ-BSA (white) in the magnified image. The white box in **E** shows the location of the images used for **F** and **G**. Scale bar = 20 or 50 µm.

2.5.11TMRM and Lysotracker Green

iDA neurons were cultured as previously described (2.3.5 Induced Dopaminergic Neuron Differentiation). Cells were incubated for 1 hour with Phenol Free Minimum Essential Medium containing 80 nM tetra-methylrhodamine methyl ester, 1 µM lysotracker green DND-26 and 20 µM Hoechst 33528. The media was changed to Phenol Free MEM only and the cells were imaged on the Opera Phoenix (PerkinElmer) using the 40X magnification water lens. Nine fields of view and six Z-planes were images for each well. Imaging exposures were optimised per plate for the Cy3 (Excitation 530-560/Emission 570-650), FITC (Excitation 460-490/Emission 500-550) and DAPI channels (Excitation 355-385/Excitation 430-500). Images were subsequently analysed using Harmony to segment nuclei, mitochondria and lysosomes. Firstly, the z-stacks were merged to produce a

maximum projection and a basic flatfield correction was applied. This enables the quantification of mitochondria per cell, MMP, average mitochondrion area, lysosomes per cell, total lysosome area and average lysosome area.

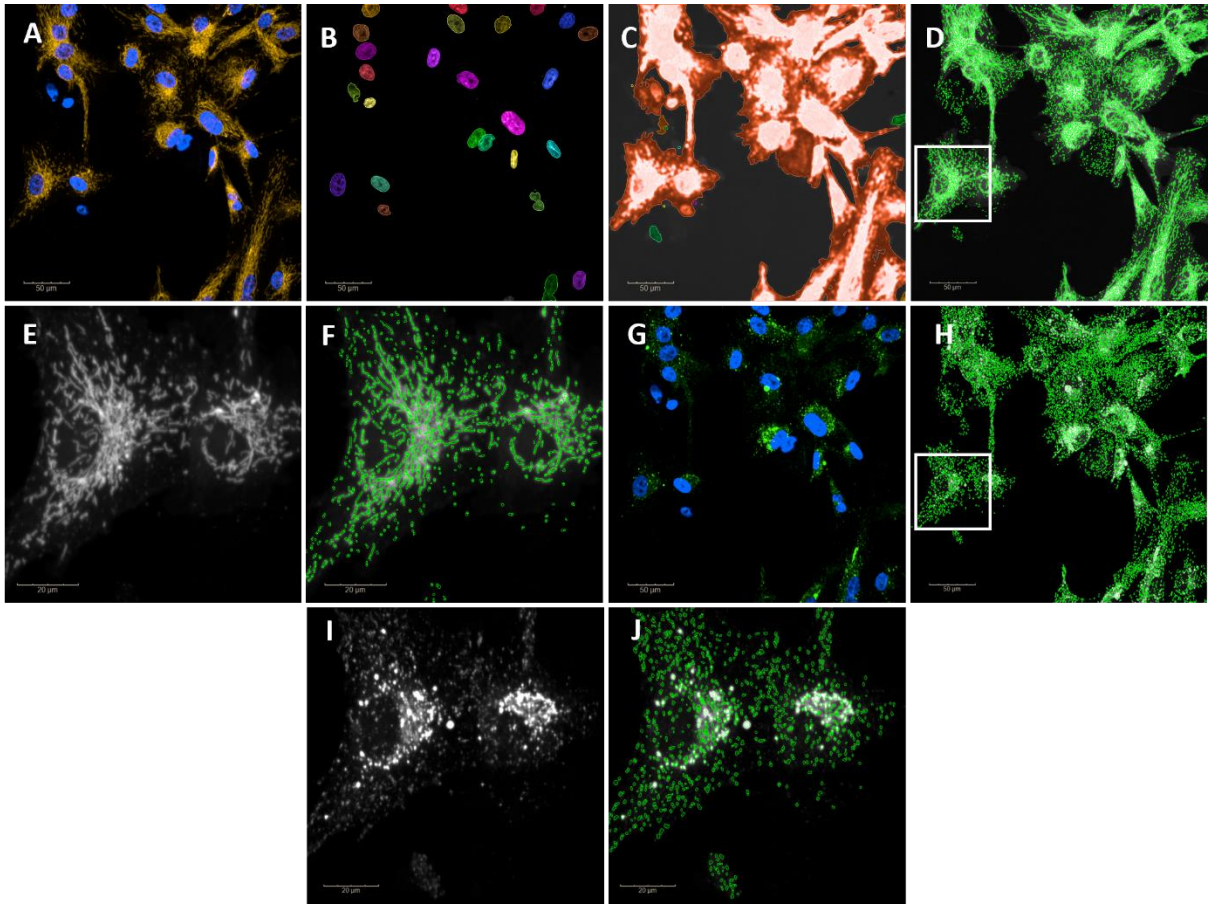

Figure 13: Representative images of the TMRM and lysotracker green assay image analysis in iDA neurons using the Harmony analysis software. **A)** Nuclei stained with Hoechst (blue) and mitochondria stained with TMRM (orange), **B)** Nuclei segmentation (coloured), **C)** Cell region segmented from the combination of the three channels (coloured), **D)** Mitochondria segmented (green) using TMRM (white), **E)** A magnified image of the mitochondria stained with TMRM (white), **F)** A magnified image of the segmentation of the mitochondria (green) using TMRM (white), **G)** Nuclei stained with Hoechst (blue) and lysosomes stained with lysotracker green (green), **H)** Segmentation of the lysosomes (green) using lysotracker green (white), **I)** A magnified image of the lysosomes stained with lysotracker green (white), **J)** A magnified image of the segmentation of the lysosomes (green) using lysotracker green (white). The white boxes in **D** and **H** show the location of the images used for **E/F** and **I/J**. Scale bar = 20 or 50 µm.

2.5.12 Neurite Outgrowth Assay

Neuron morphology was assessed using the Neurite Outgrowth kit from Thermofisher (A15001). This stains the membrane of the cells and viable cells. iDA neurons were plated and differentiated as described previously (2.3.5 Induced Dopaminergic Neuron Differentiation). At the end of the differentiation the media was replaced with Phenol Free MEM containing 0.004 % cell membrane stain 1000X, 0.002 % cell viability stain 1000X and 50 µM Hoechst for 30 minutes. Imaging was carried out using the OperaPhenix 20X air objective. The Cy3 (Excitation 530-560/Emission 570-650), FITC (Excitation 460-490/Emission 500-550) and DAPI channels (Excitation 355-385/Excitation 430-500) channels were used. Exposure times were optimised for each plate and a minimum of seven fields and six Z-planes were imaged. Image analysis was carried out using the Harmony analysis software. Firstly, the z-stacks were merged to produce a maximum projection and a basic flatfield correction was applied. The nuclei and neurons were segmented in order to measure the morphology and percentage of neuronal cells and viable cells was calculated (Figure 14).

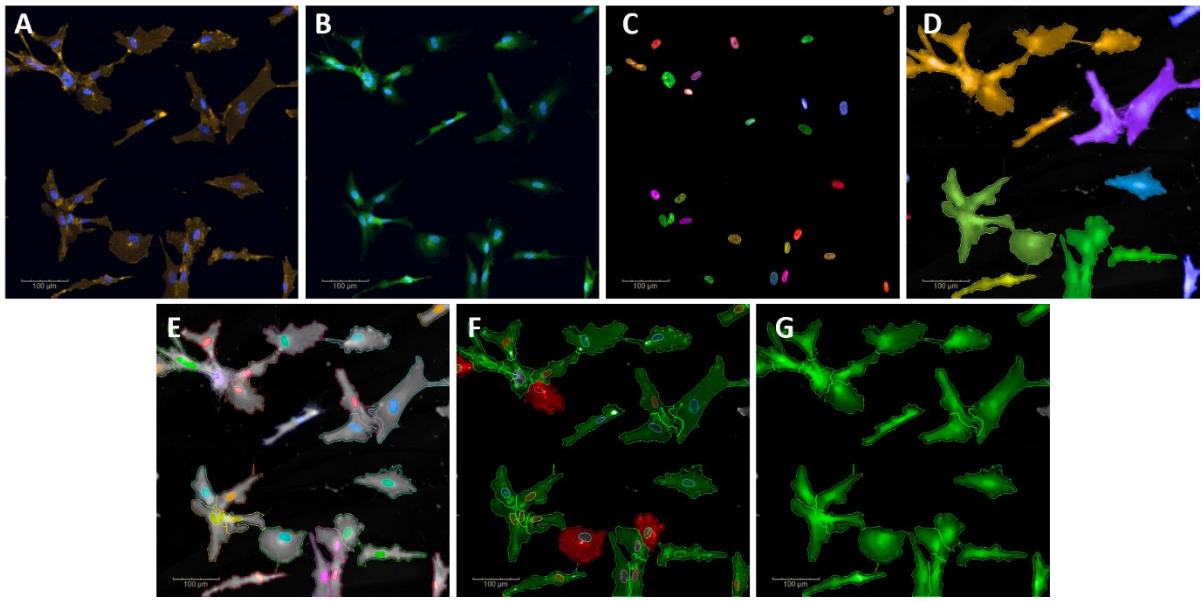

Figure 14: Representative images of the neurite outgrowth assay image analysis. A) iDA neurons stained with the membrane stain (orange) and Hoechst (blue), **B)** iDA neurons stained with the cell viability stain (green) and Hoechst (blue), **C)** Nuclei segmentation using Hoechst (coloured), **D)** Cell region segmentation using the membrane stain (coloured), **E)** Cell segmentation using the membrane stain (coloured), **F)** Neuronal cell selection using machine learning (green = neuronal, red = non-neuronal), **G)** Viable cell selection using threshold intensity (green = viable, red = not viable). Scale bar = 100 µm.

2.5.13 MitoROS Assay

MitoROS was assessed using the NpFr2 probe. This probe was kindly provided by Professor Elizabeth New, University of Sydney. The probe targets mitochondria using a triphenylphosphonium tag and fluoresces when oxidised by ROS.

iDA neurons were differentiated as described previously (2.3.5 Induced Dopaminergic Neuron Differentiation). The media was removed and replaced with PhenoL Free MEM containing 40 µM NpFr2 and 20 µM Hoechst 33528. The plate was incubated at 37 and 5 % CO for 30 minutes. The dye solution was replaced with Phenol Free MEM immediately prior to imaging. Imaging used the Opera Phoenix (PerkinElmer) 40X magnification water lens. Nine fields of view and six Z-planes were images for each well. Imaging exposures were optimised per plate for the FITC (Excitation 460-490/Emission 500-550) and DAPI channels (Excitation 355-385/Excitation 430-500). Images were subsequently analysed using Harmony to segment nuclei and mitoROS spots. Firstly, the z-stacks were merged to produce a maximum projection and a basic flatfield correction was applied. The segmentation enabled the quantification of the intensity of the mitoROS stain within the mitoROS spot region.

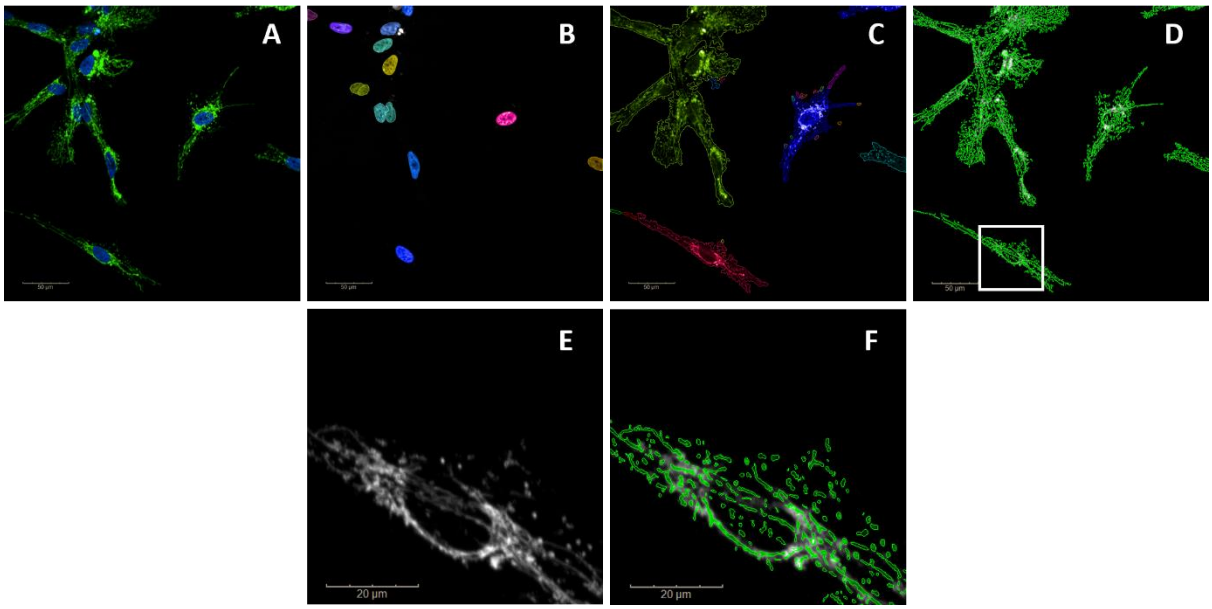

Figure 15: Representative images of the MitoROS assay image analysis. A) MitoROS stained with NpFr2 (green) and nuclei stained with Hoechst (blue), **B)** Nuclei segmentation (coloured), **C)** Cell segmentation (coloured), **D)** MitoROS segmentation (green) using NrFp2 (white), **E)** A magnified image of MitoROS using NpFr2 (white), **F)** A magnified image of the MitoROS segmentation (green) using NpFr2 (white). The white box in **D** shows the image region of **E** and **F**. Scale bar = 20 – 50 µm.

2.5.14 Immunocytochemistry

Cells were first fixed in 96-well black plates (Agilent). Fibroblasts were fixed by removing the media and adding 50 µL PFA solution (PBS containing 4 % formaldehyde) and were incubated for 15 minutes at 37 °C. The wells were then washed twice with 100 µL PBS and stored at 4 °C with 200 µL PBS. iDA neurons were fixed by adding 50 µL PFA solution to the media in each well and incubating the plate at 37 °C for 15 minutes. The solution was then aspirated and another 50 µL PFA solution was added for 15 minutes at 37 °C. The wells were then washed twice with 100 µL PBS and stored at 4 °C with 200 µL PBS.

The PBS was aspirated and cells were permeabilised with 50 µL PBS containing 10 % TWEEN 20 (PBST, Sigma; 11332465001) and 0.1 % Trition (Sigma; 93443) and incubated for 10 minutes. They were washed twice with PBST before blocking using PBST containing 5 % horse serum (Sigma; H0146) for 1 hour. The primary antibody (Table 10) solution was added and the plate was agitated on a rocker at 4 °C overnight. The cells were washed twice with PBST and incubated at room temperature in the dark with secondary antibodies (Table 10) for 1 hour. Cells were washed twice with PBST and incubated with PBS containing 10 µM Hoechst for 2 minutes before changing to 100 µL PBS for imaging.

Imaging was carried out using the OperaPhenix 20X air objective or 40X water objective. Exposure times were optimised for each plate and channel dictated by the secondary antibodies used. Fibroblasts were imaged using a minimum of nine fields and six Z-planes. iDA neurons were imaged using a minimum of seven fields and six Z-planes. Image analysis was carried out using the Harmony analysis software. Firstly, the z-stacks were merged to produce a maximum projection and a basic flatfield correction was applied. Image analysis of LAMP2 segemented the lysosomes and nuclei, to quantify lysosomes per cell, total lysosome area and average lysosome area (Figure 16). The nuclei and cells were segmented for the TH, DAT, β-III-Tubulin and MAP2 images, to quantify the number of positive cells (Figure 17).

Table 10: Antibodies used for immunocytochemistry. The table shows the antibody target, dilution, species and catalogue number for each antibody.

Antibody	Dilution	Species	Catalogue number
Dopamine Transporter (DAT)	1:1000	Mouse	ma5-24796
Tyrosine Hydroxylase (TH)	1:1000	Rabbit	ab112
β-III-Tubulin	1:1000	Chicken	ab9354
LAMP2a	1:1000	Mouse	sc-18822
Microtubule associated protein 2 (MAP2)	1:1000	Rabbit	ab32454
Pax6	1:1000	Rabbit	ab5790
Nestin	1:1000	Mouse	ab18102

Table 11: Secondary antibodies used for immunocytochemistry. The table shows the antibody name, dilution, target species and catalogue number for each antibody.

Antibody	Dilution	Species	Catalogue number
Donkey anti-Mouse IgG (H+L) Highly Cross-Adsorbed Secondary Antibody, Alexa Fluor 488	1:1000	Mouse	A21202
Goat anti-Rabbit IgG (H+L) Cross-Adsorbed Secondary Antibody, Alexa Fluor™ 488	1:1000	Rabbit	A11008
Donkey anti-Mouse IgG (H+L) Highly Cross-Adsorbed Secondary Antibody, Alexa Fluor™ 568	1:1000	Mouse	A10037
Donkey anti-Rabbit IgG (H+L) Highly Cross-Adsorbed Secondary Antibody, Alexa Fluor 568	1:1000	Rabbit	A10042
Donkey anti-Chicken IgY (H+L) Highly Cross Adsorbed Secondary Antibody, Alexa Fluor 647	1:1000	Chicken	A78952

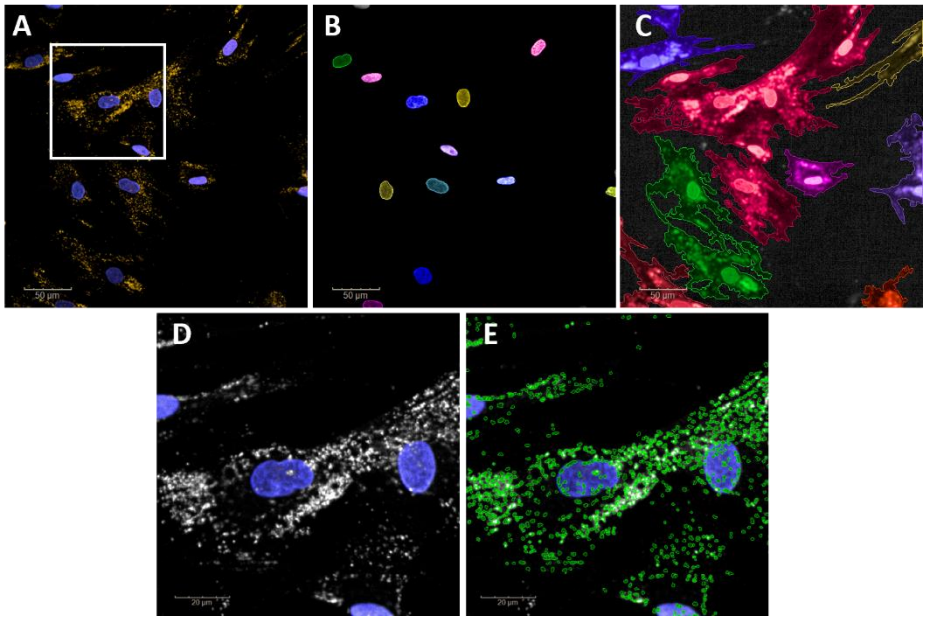

Figure 16: Representative images of the image analysis of the LAMP2a staining. A) Lysosomes stained with the LAMP2a antibody (orange) and nuclei stained with hoechst (blue), **B)** Nuclei segmentation using Hoechst (coloured), **C)** Cell region segmentation using both channels (coloured), **D)** A magnified image of the lysosomes stained with the LAMP2a antibody (white) and nuclei stained with hoechst (blue), **E)** A magnified image of the lysosome segmentation (green) using the LAMP2a antibody (white) and nuclei stained with hoechst (blue). The white box in **A** shows the image region used for images **D** and **E**. Scale bar = 20 and 50 µm.

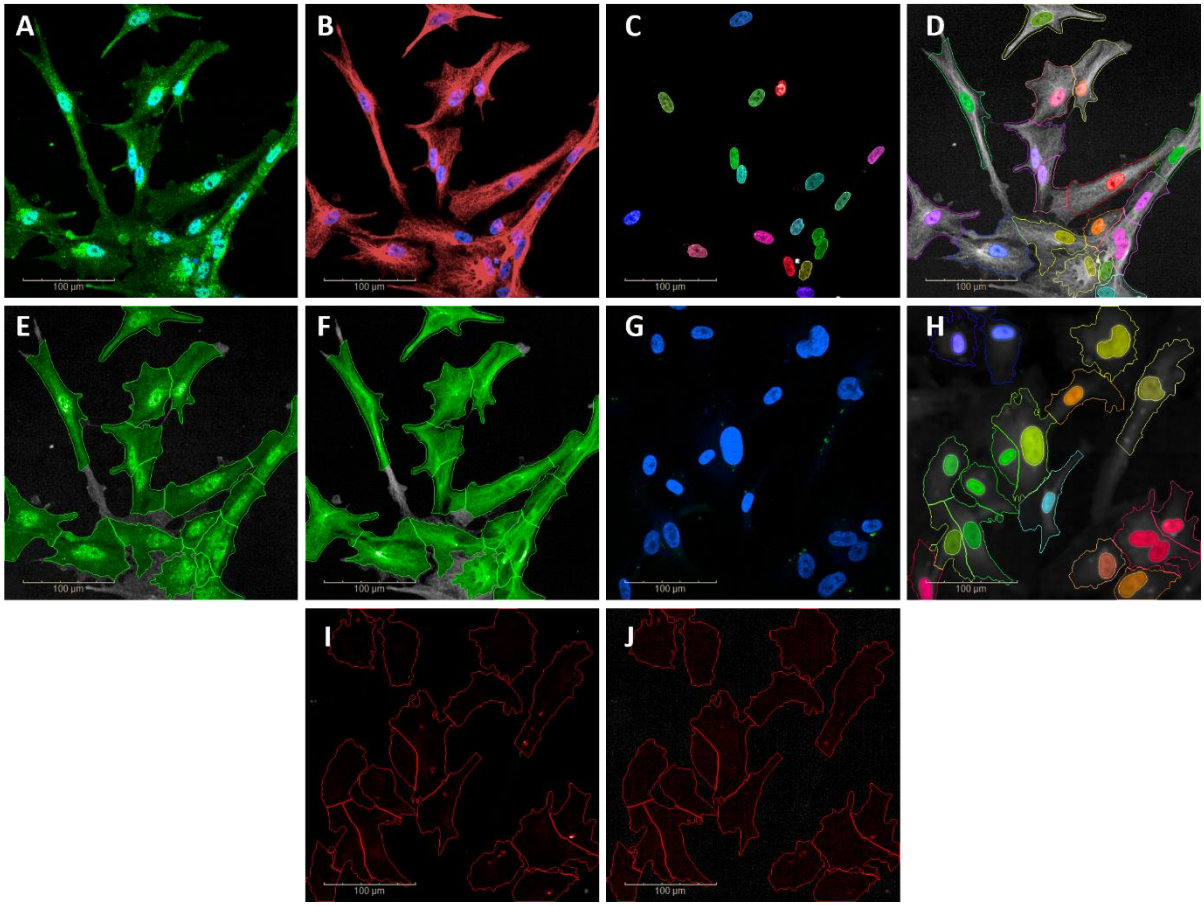

Figure 17: Representative images of the image analysis of the neuronal characterisation using TH and β-III-Tubulin. A) TH stained with antibody (green) and nuclei stained with Hoechst (blue), **B)** β-III-Tubulin stained with antibody (red) and nuclei stained with hoechst (blue), **C)** Nuclei segmentation using hoechst (coloured), **D)** Cell segmentation using the three channels (coloured), **E)** Selection of TH positive cells using a mean intensity threshold, **F)** Selection of β-III-Tubulin positive cells using a mean intensity threshold, **G)** Secondary only control; TH secondary antibody (green), β-III-Tubulin secondary antibody (red), and nuclei stained with Hoechst (blue), **H)** Secondary antibody only cell segmentation using the three channels (coloured), **I)** Selection of TH positive cells in the secondary antibody only image using a mean intensity threshold, **J)** Selection of β-III-Tubulin positive cells in the secondary antibody only image using a mean intensity threshold. Scale bar = 100 µm.

2.5.15 Optimisation of assays

Most assays were already optimised by Professor Heather Mortiboys and previous lab members before their use in this project. Optimisation involved the use of positive controls and negative controls. In most instances, particularly live imaging, these controls were generated using inhibitors and toxins. For example, CCCP was used to depolarise mitochondria (Scaduto and Grotyohann, 1999) and act as a negative control for TMRM. Llome produces a negative control for lysosome measurements because it damages the lysosome membrane causing deacidification and therefore

preventing enzyme activity (Eriksson, Wäster and Öllinger, 2020), thus acting as a negative control for DQ-BSA. Many other toxins were used for a variety of assays including oligomycin, antimycin, chloroquine, aloxistatin, pepstatin A and conduritol B epoxide. The use of toxins enabled the assessment of signal-to-noise ratios to determine whether the concentrations of dyes were enabling the measurement of biologically meaningful results rather than differences in background fluorescence or artificial factors relating to dye concentration. This is particularly important for TMRM as high concentrations can cause aggregation and thus an inaccurate measurement of MMP (Ward, 2010).

2.5.16 Statistical Analysis

Results from the in-depth assays were analysed in two ways. Individual cell line data shows the mean of three independent assays from independent passages. Imaging and ATP assays used three technical well repeats for each condition, from which a mean was calculated per assay. Oxygen consumption assays used six technical repeats from which a mean for the assay was calculated. Individual patients were then compared to their corresponding age- and sex-matched control by an unpaired T-test with Welch correction. Controls were compared to one another using the same method to determine natural variance. Grouped data used the mean of at least three individual cell lines, which were assessed in the three independent assays. An unpaired T-test with Welch correction compared the patient group to the control group. Due to the low n number, normality tests were not used and the T-test is underpowered meaning results should be interpreted cautiously because low-powered tests can over exaggerate the effect size. Low power was also the reason that multiple comparison corrections and tests were not included, further work using greater numbers of cell lines should use these tests.

All neuron assay repeats used independent differentiations from independent iNPC passages. Neuron parameters for some patients were not statistically assessed because time constraints prevented the assessment of three independent assays. Therefore, statistical analysis would be inappropriate due to a lack of power.

3 Chapter 3: Stratification of a New sPD Cohort

3.1 Introduction

3.1.1 Mitochondrial and Lysosomal Dysfunction in Patient-Derived Fibroblasts

PD has been characterised as one disorder since it was defined by James Parkinson in 1817 (Goetz, 2011). Currently, clinicians and researchers subgroup PD into fPD, determined by the presence of family history and subsequent genetic testing (Bandres-Ciga *et al.*, 2020) or sPD if there is no genetic history. Despite this classification, clinical trials continue to fail and many have proposed that further stratification is necessary (Espay *et al.*, 2017; Carling *et al.*, 2020; Giuliano *et al.*, 2023) .

Multiple teams have attempted to stratify PD using clinical scores, brain imaging and biomarkers. To date these methods have not enabled successful clinical trial selection and thus compound approval. Although, it is important to note that they were not all designed to enable this; each has its strengths and weaknesses. This project utilises patient-derived cell models to stratify a new cohort of sPD patients into small, homogeneous subgroups. This stratification method is based on the identification of common patterns of mitochondrial and lysosomal dysfunction in patient-derived fibroblasts.

Importantly, studies using fibroblasts describe similar dysfunction to that which is observed in post-mortem brain samples further evidencing fibroblasts' usefulness as a model (Bindoff *et al.*, 1989; Schapira *et al.*, 1990; Shoffner *et al.*, 1991; Winkler-Stuck *et al.*, 2004; Keeney *et al.*, 2006; Mortiboys *et al.*, 2008, 2010; Grünewald *et al.*, 2010, 2014; Papkovskaia *et al.*, 2012; McNeill *et al.*, 2014; Gegg *et al.*, 2015; Li *et al.*, 2019). Like post-mortem projects, studies of mitochondria in fibroblasts have produced conflicting results. One study identified altered complex I and IV activity (Winkler-Stuck *et al.*, 2004) while another found no defects in these complexes but a deficit in complex V activity (del Hoyo *et al.*, 2010). This conflict may be due to differing methods or the result of heterogeneity as these studies had small numbers of cell lines leading to insufficient sampling of the population to detect heterogeneity. Two studies have used large numbers of patient fibroblasts both demonstrating heterogeneity in mitochondrial function. Milanese et al., (2019) assessed respiration of forty-seven PD patients compared to twenty-one age- and sex-matched controls. Results for basal respiration and spare capacity, in both glucose and galactose-containing media, showed greater variability in the PD population than the control population, although no statistical test was done to assess significance. It is important to note that abnormalities in mitochondrial function were only unmasked in several patients when respiration was measured in galactose-containing media, highlighting further variability between patients. However, the PD patients' mitochondria appear to adapt by increasing

mitochondria respiration to a greater extent than controls when forced to use oxidative phosphorylation alone under galactose conditions. This is possibly due to a compensatory mechanism which cannot sustain demand long term. The other study, Carling et al., (2020), compared one hundred sPD patients to fifty age- and sex-matched healthy controls. ATP and MMP were measured to assess mitochondrial function, both showed no difference between the average for controls or patients. However, the variance in the patient population was significantly greater for both ATP and MMP with several patients having ATP or MMP levels that were more than two standard deviations from the mean of the controls. The combination of these two studies with the contradictory nature of smaller studies assessing sPD patient mitochondria demonstrate the heterogeneity in mitochondrial dysfunction and the need to stratify patients in order to produce targeted treatments.

In contrast, very little work has been conducted on lysosomes in sPD, particularly in fibroblasts. The majority of the work understandably centres around the main genetic variants in genes implicated in lysosomal functions, such as *LRRK2, GBA1, TMEM175* and *ATP13A2*. Mutations in these genes indicate possible mechanisms for dysfunction; however, they cannot explain the presence of lysosomal dysfunction in the vast majority of PD patients. Despite this, few studies have been conducted with the models and numbers of participants that are sufficiently powered to identify lysosomal dysfunction heterogeneity within the sPD population. A study by Thomas *et al.* (2021) utilised patient-derived fibroblasts to assess GCase activity and lysosomal dysfunction in sPD patients and GBA N370S mutation carriers. Thirty-one PD patients were assessed for GCase activity, GCase protein levels and LIMP2 protein levels. There was a significant difference between the means of the healthy controls and the PD patients, but the data also showed clear heterogeneity; many patients scored similarly to the control cohort and the variance between the patients appeared larger than the control or GBA N370S patient groups, however, this was not statistically measured by the authors (Thomas *et al.*, 2021). Another study utilising patient-derived fibroblasts found no difference in the number or localisation of lysosomes between healthy controls, sPD, LRRK2 G2019S and LRRK2 R1441C mutation carriers under basal conditions (Smith *et al.*, 2016). However, elevated levels of lysosomes are often reported in LRRK2 mutation carriers, even LRRK2 patient-derived fibroblasts, suggesting that these results should be interpreted with caution. Lysosomal dysfunction is likely linked to dysfunction in the earlier stages of autophagy. One study in sPD patients identified an increased number of autophagosomes and autolysosomes in three PD patients compared to age-matched controls (Teves *et al.*, 2018). However, due to the number of patients, it is not possible to comment on heterogeneity and lysosomes were not directly measured. Carling *et al.* (2020), assessed lysosome count and total lysosome area, which were elevated in sPD patients. There was significantly greater variation in the

patient population for both parameters showing the presence of heterogeneity when larger cohorts are assessed.

Carling *et al.* (2020) are the only group to take this assessment further and attempt to stratify the sPD cohort by pathological mechanisms observed in patient fibroblasts. Two distinct groups were identified, one defined by mitochondrial dysfunction and the other by lysosomal dysfunction. Further investigation validated these subgroups by assessing complex activity, lysosomal enzyme activity in fibroblasts and dysfunction in iNPC-derived iDA neurons. The study set a foundation for this PhD project, in which a new cohort of thirty-five sPD patients and twenty-five neurologically healthy, age- and sex-matched controls were biopsied and assessed for mitochondrial and lysosomal dysfunction using an expanded set of parameters for stratification. The aim was to validate the previous method and define a detailed method for use in future projects. The method proposed is not an exhaustive method and as expected did not stratify the entire cohort of patients.

3.1.2 Previous Work

Previous work within the lab, carried out by Dr Sarah Roscoe, Stephen Bradley, Dr Thomas Payne and the author began the assessment of mitochondrial and lysosomal dysfunction. The assessment of some of the cohort was delayed by the COVID-19 pandemic and completed by the author during the first year of the PhD. Dr Payne, with help from Dr Sarah Roscoe, established the biopsies and carried out clinical assessments for all participants.

3.1.3 Aims and Objectives

The aim of this chapter is to investigate the heterogeneity of mitochondrial and lysosomal dysfunction in patient-derived fibroblasts from a new cohort of sPD patients and healthy controls and establish a method for stratification.

Hypothesis:

We hypothesise that mitochondrial and lysosomal dysfunction in a new sPD patient cohort would be more heterogeneous than the control group but population means would not differ significantly. We hypothesise that this would enable the stratification of the patients into smaller, more homogenous subgroups defined by distinct patterns of dysfunction.

Objectives:

-To measure mitochondrial and lysosomal dysfunction in the cohort and assess heterogeneity.

-To identify and define distinct subgroups within the cohort.

-To assess mitochondrial and lysosomal dysfunction within fPD patients to compare the sPD subgroups with genetically stratified groups.

Genetic variability within the cohort of sPD patients was assessed prior to the author joining the project. Most of the results from this chapter were published in Payne *et al.* (2023) and will not be individually referenced.

Payne T, Burgess T, Bradley S, Roscoe S, Sassani M, Dunning MJ, Hernandez D, Scholz S, McNeill A, Taylor R, Su L, Wilkinson I, Jenkins T, Mortiboys H, Bandmann O. Multimodal assessment of mitochondrial function in Parkinson's disease. Brain. 2024 Jan 4;147(1):267-280. doi: 10.1093/brain/awad364. PMID: 38059801; PMCID: PMC10766247.

3.2 Results

3.2.1 The Cohort

A new cohort of thirty-five sPD patients and twenty-five neurologically healthy controls was selected for this study. Unfortunately, three participants had to be withdrawn due to biopsy issues. One patient was withdrawn due to the biopsy not establishing before the first COVID-19 lockdown, one control was lost due to recurrent bacterial infections preventing assessment and one control was removed due to extremely aberrant results and growth. The final cohort consisted of thirty-four patients and twenty-three controls, which showed no significant differences in age, sex or familial history of PD (Table 12). There were two cases of fPD identified using the Neurochip platform, a 28-year-old female with a heterozygous *SNCA* G51D and a 50-year-old female with a homozygous *PRKN (c.337-376del)* mutation (Payne, *et al.*, 2023). No PD-related gene mutations or GBA risk variants were identified in the control population.

Table 12: Demographics of the cohort. No significant differences exist between the control and PD population for age, sex or familial history. **a** Chi-squared test, **b** Unpaired T-test with Welch's correction.

Demographics

	Control (n=23)	Parkinson's (n = 34)	
Sex			**p-value**
Male (n, %)	11 (48)	18 (53)	*0.0.6664*[a]
Female (n, %)	12 (52)	16 (47)	
Age			
Minimum	28	28	*0.9373*[b]
Maximum	81	82	
Mean ± SD	60.00 ± 11.14	60.24 ± 10.85	
Family history of PD in a first-degree relative			
Yes (n, %)	6 (26)	3 (9)	*0.139*[a]
No (n, %)	17 (74)	31 (91)	

Table 13: Clinical features of the cohort. Predictive risk score uses a prognostic model to predict the risk of postural instability or dementia after 5 years (Velseboer *et al.,* 2016).

Clinical Features		
	Control (n=23)	**Parkinson's (n = 34)**
Disease Duration (months)		
Minimum	*NA*	2
Maximum	*NA*	32
Mean ± SD	*NA*	13.76 ± 7.60
Modified Hoehn & Yahr		
Minimum	*NA*	1
Maximum	*NA*	3
Mean ± SD	*NA*	2.01 ± 0.40
MDS-UPDRS Part III scores		
Minimum	*NA*	14
Maximum	*NA*	54
Mean ± SD	*NA*	32.60 ± 10.03
Non-Motor Symptom Scale		

Minimum	*NA*	3
Maximum	*NA*	119
Mean ± SD	*NA*	38.71 ± 31.39
Total Levodopa Equivalent Daily Dosage (mg)		
Minimum	*NA*	0
Maximum	*NA*	1000
Mean ± SD	*NA*	368.38 ± 221.38
Predictive Risk Score		
Minimum	*NA*	0.03
Maximum	*NA*	0.91
Mean ± SD	*NA*	0.40 ± 0.26

3.2.2 Heterogeneity in Mitochondria

Previous work demonstrated that mitochondrial parameters are heterogeneous in PD patients (Ambrosi *et al.*, 2014; Dölle *et al.*, 2016; Milanese *et al.*, 2019; Carling *et al.*, 2020; Barnhoorn *et al.*, 2024). We measured 10 mitochondrial parameters to determine mitochondrial health (Table 7, Figure 18**,** Figure 19). A comparison of the population means found no significant difference between patients and controls for any parameters under galactose conditions (Figure 19).

Significant differences in population means were observed in glucose media for mitochondrial form factor (patients: 101.1 % ± 2.4, controls: 100 % ± 1.4, p = 0.012, Figure 18D), long mitochondrial form factor (patients: 100.7 % ± 1.8, controls: 100 % ± 1.0, p = 0.020, Figure 18H) and long vs small mitochondria ratio (patients: 103.3 % ± 7.9, controls: 100 % ± 5.1, p = 0.022, Figure 18J).

As expected, the patient population displayed significantly more variation in all mitochondrial health parameters in glucose than the control population (Figure 18). Fibroblasts cultured in galactose media showed a similar trend (Figure 19). This variation, combined with the similar population means, is consistent with previously published findings (Milanese *et al.*, 2019; Carling *et al.*, 2020) and confirms the heterogeneity of the mitochondrial phenotypes in this cohort. Similar to the results from Carling *et al.* (2020), there were several patients with extremely high or low scores in each parameter,

highlighting the variation seen and the requirement for studies to use as many patients as possible when assessing mitochondria in sPD.

In order to stratify the patient population, we calculated z-scores, as described in the methods chapter (2.4.4 Statistical Analysis). The combination of glucose and galactose z-scores to produce a single composite z-score per parameter per line per group did not alter the trend of these results. Mitochondrial form factor (patients: 0.73 ± 1.43, controls: 0 ± 0.95, p = 0.014, Appendix 2: Figure 122D), long mitochondrial form factor (patients: 0.66 ± 1.41, controls: 0 ± 0.91, p = 0.024, Appendix 2: Figure 122H) and long vs small mitochondria ratio (patients: 0.62 ± 1.29, controls: 0 ± 0.91, p = 0.026, Appendix 2: Figure 122J) were significantly different when comparing the population means. All parameters except small mitochondrial form factor (p = 0.065, Appendix 2: Figure 122F) and long vs small mitochondria ratio (p = 0.089, Appendix 2: Figure 122G) were significantly more variable in the patient population.

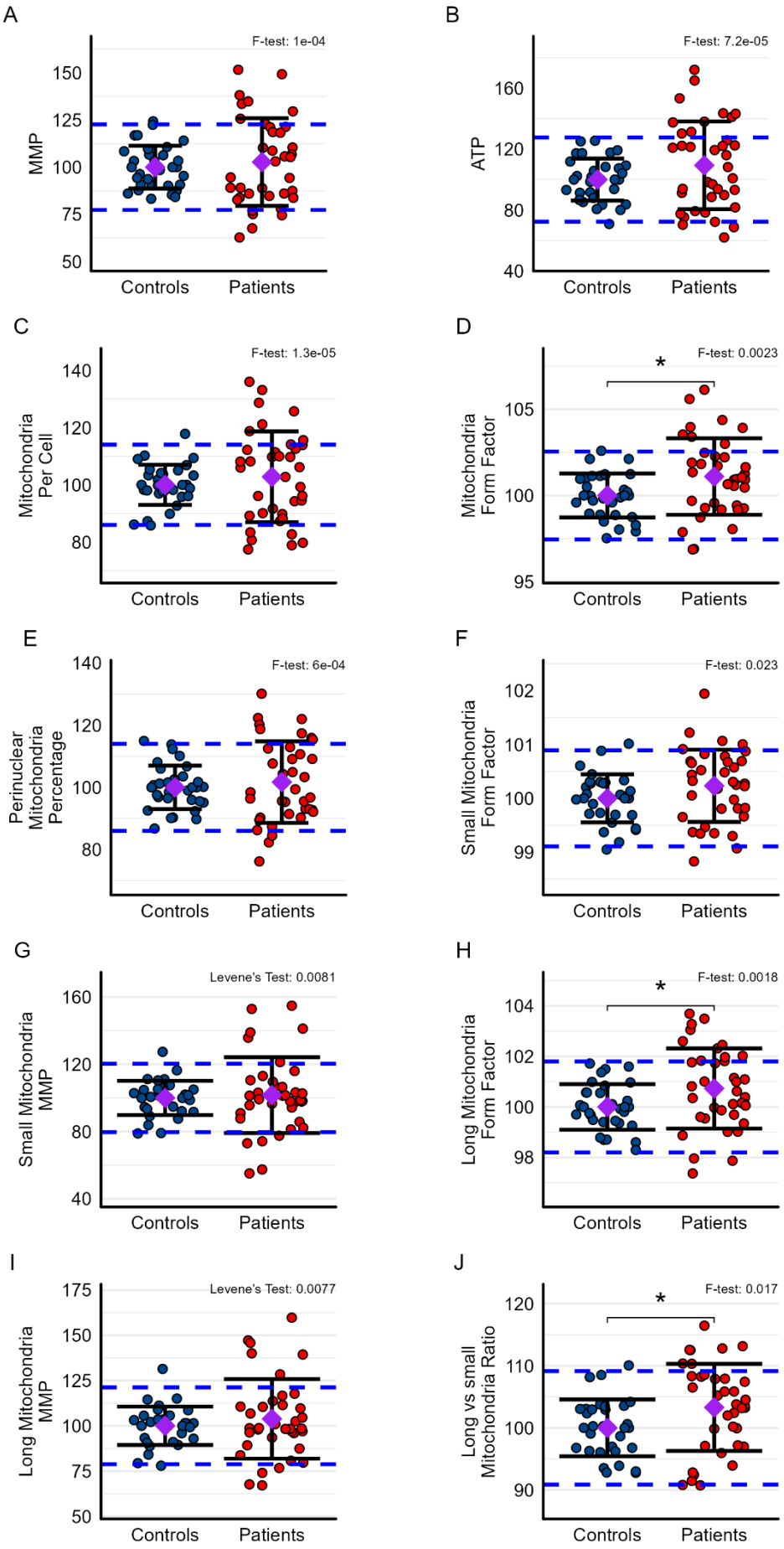
A
F-test: 1e-04
MMP
150
125
100
75
50
Controls
Patients
B
F-test: 7.2e-05
ATP
160
120
80
40
Controls
Patients
C
F-test: 1.3e-05
Mitochondria Per Cell
140
120
100
80
Controls
Patients
D
*
F-test: 0.0023
Mitochondria Form Factor
105
100
95
Controls
Patients
E
F-test: 6e-04
Perinuclear Mitochondria Percentage
140
120
100
80
Controls
Patients
F
F-test: 0.023
Small Mitochondria Form Factor
102
101
100
99
Controls
Patients
G
Levene's Test: 0.0081
Small Mitochondria MMP
160
120
80
40
Controls
Patients
H
*
F-test: 0.0018
Long Mitochondria Form Factor
104
102
100
98
Controls
Patients
I
Levene's Test: 0.0077
Long Mitochondria MMP
175
150
125
100
75
50
Controls
Patients
J
*
F-test: 0.017
Long vs small Mitochondria Ratio
120
110
100
90
Controls
Patients

Figure 18: A comparison of the mitochondrial phenotypes in the patient and control populations in glucose media. A) MMP, **B)** ATP, **C)** Number of mitochondria per cell, **D)** Mitochondrial form factor, **E)** The percentage of mitochondria in the perinuclear region, **F)** Form factor for the small mitochondria population, **G)** MMP for the small mitochondria population, **H)** Form factor for the long mitochondria population, **I)** MMP for the long mitochondria population, **J)** Long vs small mitochondria ratio. Each point represents the mean of three biological repeats for each cell line which have been normalised to the average of the age- and sex-matched controls on the plate. The normality of the control population (blue) and patient population (red) were assessed using the Shapiro-Wilks normality test. The means of each population (purple diamond) were compared using an unpaired T-test with Welch's correction if normally distributed or by a Mann-Whitney U test if non-normally distributed, significance is depicted by significance symbols (* $p < 0.05$). The difference in variance within each population was assessed using an F-test for normally distributed parameters or a Levene's test for non-normally distributed data ($p < 0.05$). The blue dotted line depicts two standard deviations from the mean for the control population.

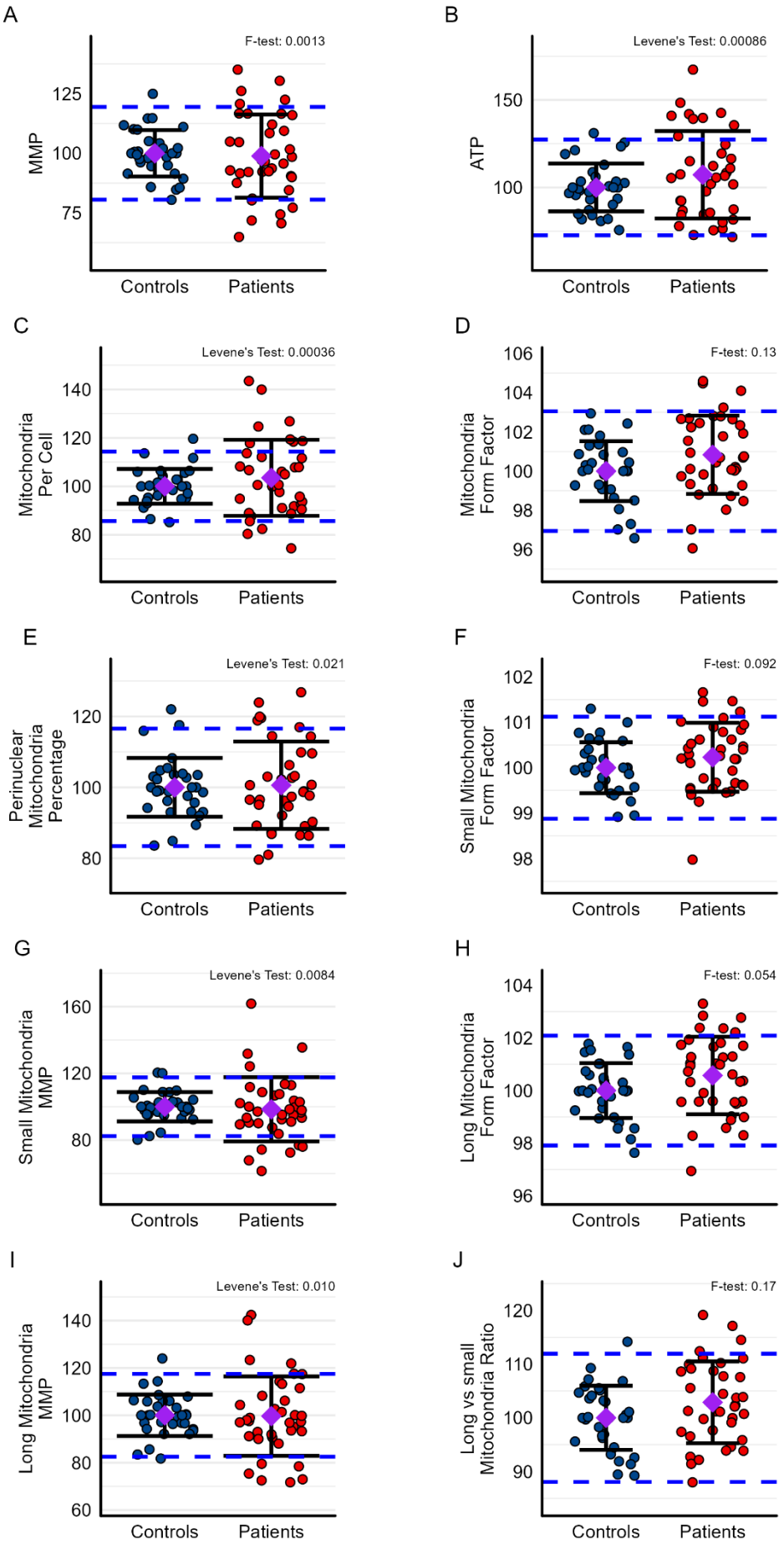
A
F-test: 0.0013
MMP
125
100
75
Controls
Patients
B
Levene's Test: 0.00086
ATP
150
100
Controls
Patients
C
Levene's Test: 0.00036
Mitochondria Per Cell
140
120
100
80
Controls
Patients
D
F-test: 0.13
Mitochondria Form Factor
106
104
102
100
98
96
Controls
Patients
E
Levene's Test: 0.021
Perinuclear Mitochondria Percentage
120
100
80
Controls
Patients
F
F-test: 0.092
Small Mitochondria Form Factor
102
101
100
99
98
Controls
Patients
G
Levene's Test: 0.0084
Small Mitochondria MMP
160
120
80
Controls
Patients
H
F-test: 0.054
Long Mitochondria Form Factor
104
102
100
98
96
Controls
Patients
I
Levene's Test: 0.010
Long Mitochondria MMP
140
120
100
80
60
Controls
Patients
J
F-test: 0.17
Long vs small Mitochondria Ratio
120
110
100
90
Controls
Patients

Figure 19: A comparison of the mitochondrial phenotypes in the patient and control populations in galactose media. A) MMP, **B)** ATP, **C)** Number of mitochondria per cell, **D)** Mitochondrial form factor, **E)** The percentage of mitochondria in the perinuclear region, **F)** Form factor for the small mitochondria population, **G)** MMP for the small mitochondria population, **H)** Form factor for the long mitochondria population, **I)** MMP for the long mitochondria population, **J)** Long vs small mitochondria ratio. Each point represents the mean of three biological repeats for each cell line which have been normalised to the average of the age- and sex-matched controls on the plate. The normality of the control population (blue) and patient population (red) were assessed using the Shapiro-Wilks normality test. The means of each population (purple diamond) were compared using an unpaired T-test with Welch's correction if normally distributed or by a Mann-Whitney U test if non-normally distributed, significance is depicted by significance symbols (* $p < 0.05$). The difference in variance within each population was assessed using an F-test for normally distributed parameters or a Levene's test for non-normally distributed data ($p < 0.05$). The blue dotted line depicts two standard deviations from the mean for the control population.

3.2.3 Heterogeneity in Lysosomes

Similar to mitochondrial health, lysosome function and morphology are heterogeneous in PD (Carling *et al.*, 2020; Thomas *et al.*, 2021). Lysosomes per cell, average lysosome area and lysosome form factor were assessed to determine dysfunction. There were no significant differences between the population means for any of the parameters in both glucose and galactose (Figure 20**,** Figure 21). However, there was significantly more variation in the number of lysosomes per cell (glucose: p = 0.003, galactose: p = 0.006) and lysosome form factor (glucose: p = 0.03, galactose: p = 0.03) in the PD population than the control population (Figure 20A and C, Figure 21A and C). The average area of the lysosomes was significantly more variable in patients under glucose conditions (p = 0.006, Figure 20B) but not galactose (p = 0.1, Figure 21B). This demonstrates that lysosomal morphology in the PD population is significantly more heterogeneous than in the control population. Several patients were observed to have very high or low scores in each parameter, again suggesting a difference in dysfunction between patients.

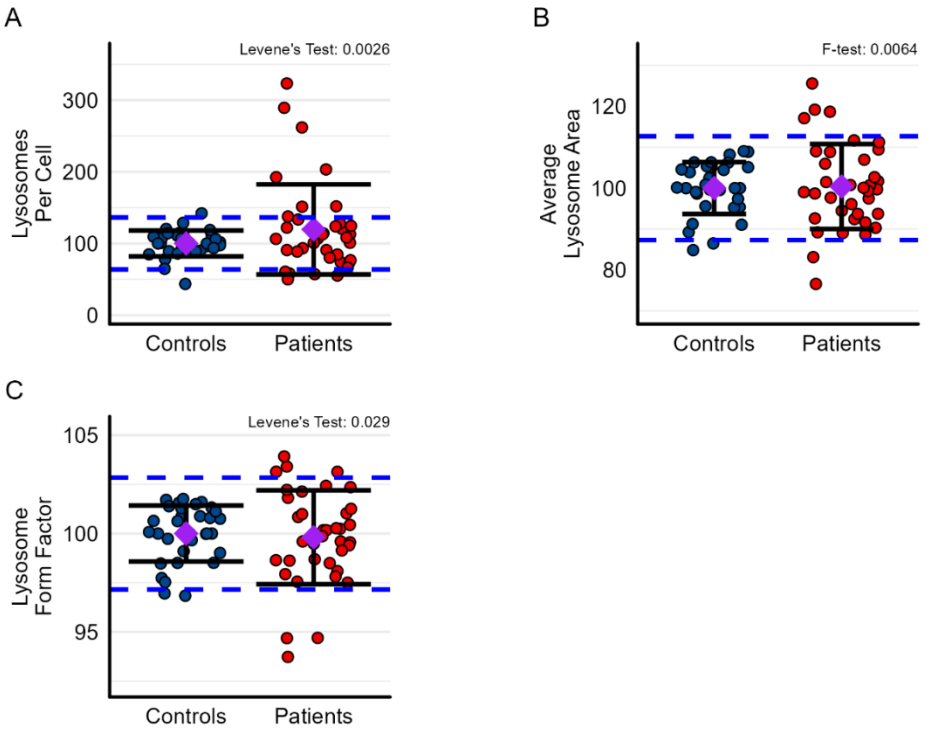

Figure 20: A comparison of the lysosomal phenotypes in the patient and control populations in <u>glucose</u> media. A) Number of lysosomes per cell, **B)** Average lysosome area, **C)** Lysosomal form factor. Each point represents the mean of three biological repeats for each cell line which have been normalised to the average of the age- and sex-matched controls on the plate. The normality of the control population (blue) and patient population (red) were assessed using the Shapiro-Wilks normality test. The means of each population (purple diamond) were compared using an unpaired T-test with Welch's correction if normally distributed or by a Mann-Whitney U test if non-normally distributed, significance is depicted by significance symbols (* p < 0.05). The difference in variance

within each population was assessed using an F-test for normally distributed parameters or a Levene's test for non-normally distributed data ($p < 0.05$). The blue dotted line depicts two standard deviations from the mean for the control population.

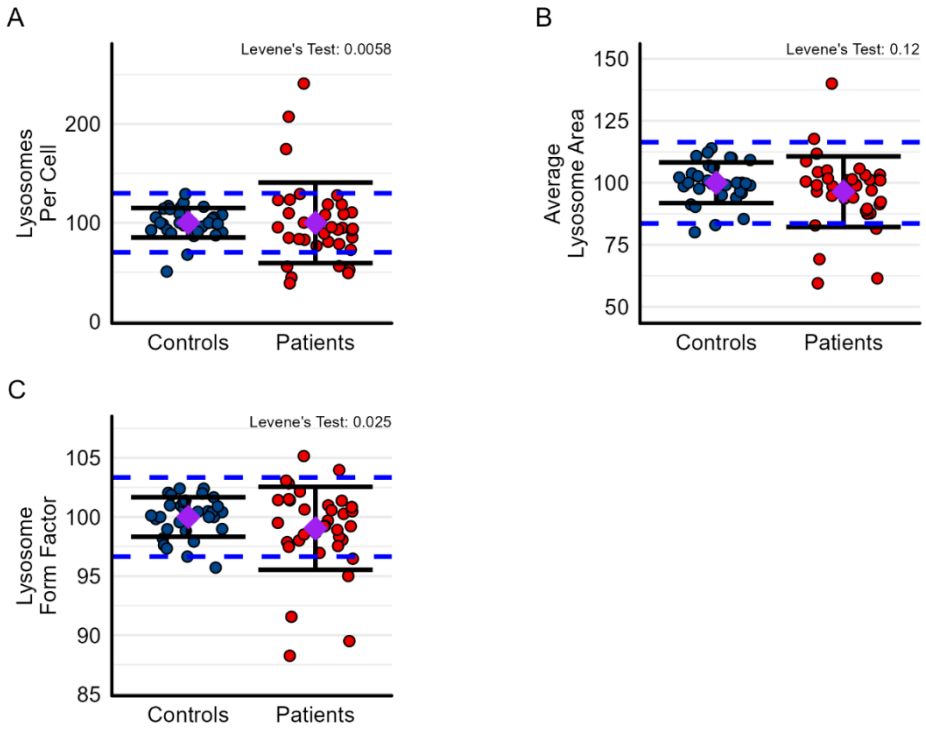

Figure 21: A comparison of the lysosomal phenotypes in the patient and control populations in <u>galactose</u> media. A) Number of lysosomes per cell, **B)** Average lysosome area, **C)** Lysosomal form factor. Each point represents the mean of three biological repeats for each cell line which have been normalised to the average of the age- and sex-matched controls on the plate. The normality of the control population (blue) and patient population (red) were assessed using the Shapiro-Wilks normality test. The means of each population (purple diamond) were compared using an unpaired T-test with Welch's correction if normally distributed or by a Mann-Whitney U test if non-normally distributed, significance is depicted by significance symbols (* $p < 0.05$). The difference in variance within each population was assessed using an F-test for normally distributed parameters or a Levene's test for non-normally distributed data ($p < 0.05$). The blue dotted line depicts two standard deviations from the mean for the control population.

Calculating z-scores and combining them to produce a single composite z-score accounting for all three technical repeats, three biological repeats and both media conditions did not change the heterogeneity of the cohort. The number of lysosomes, average size and form factor showed no

significant difference in population means but significantly more variation in patient population than the controls (p = 0.0024, p = 0.030, p = 0.023 respectively, Appendix 2: Figure 123).

3.2.4 Organelle Dysfunction Scores

To determine whether mitochondrial dysfunction and lysosomal abnormalities are more prevalent in the PD population a unique method for scoring mitochondrial and lysosomal health was developed.

To calculate a single mitochondrial dysfunction score, the composite z-score for each parameter was combined using a weighted equation, where functional and morphological parameters accounted for 45 % each and localisation accounted for 10 %, see (Table 7) for the full weightings. Combining the scores produced a single mitochondrial health score per patient. There was significantly more dysfunction in the PD population than in the controls (patients: 1.47 ± 0.73, controls: 0.70 ± 0.34, p = 0.0000008) and significantly more variation (p = 0.00022) (Figure 22). The score indicates the degree of difference between the patients' mitochondrial network and the control populations, enabling the identification of patients with the most dysfunction across the most parameters. It cannot inform on the type of dysfunction; for this, the composite z-scores for each parameter were used.

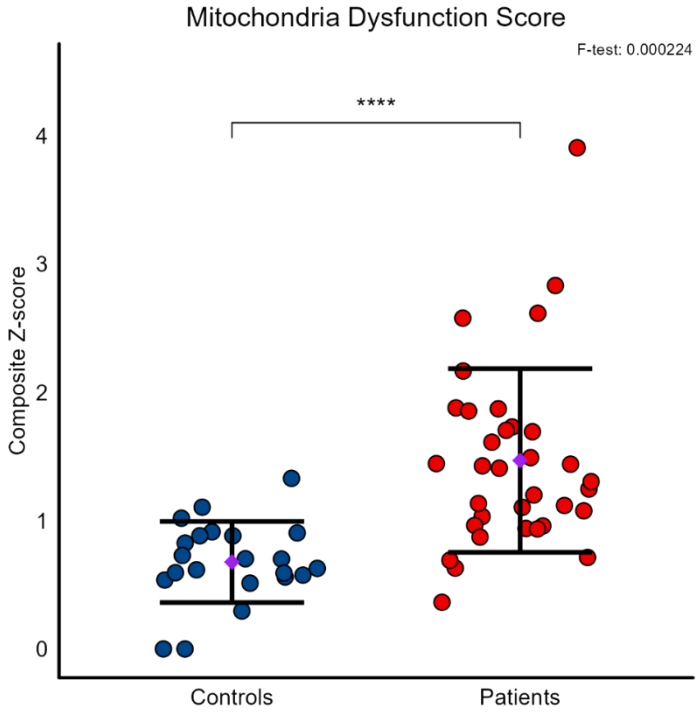

Figure 22: A comparison of the mitochondrial dysfunction composite z-scores for the patient and control populations. This shows a significant increase in dysfunction in the patient population. Each point represents an individual's composite z-score for mitochondrial dysfunction. The means of each population (purple diamond) were compared using an unpaired T-test with Welch's correction, significance is depicted by significance symbols (**** p < 0.0001). The difference in variance within each population was assessed using an F-test (p < 0.05). Error bars show standard deviation.

A lysosomal dysfunction score was generated by equally weighting the three morphology parameters. There was significantly more lysosomal dysfunction in the patient population (patients: 1.40 ± 1.28, controls: 0.69 ± 0.53, p = 0.0097) and significantly more variation between patients (p = 0.00013) (Figure 23).

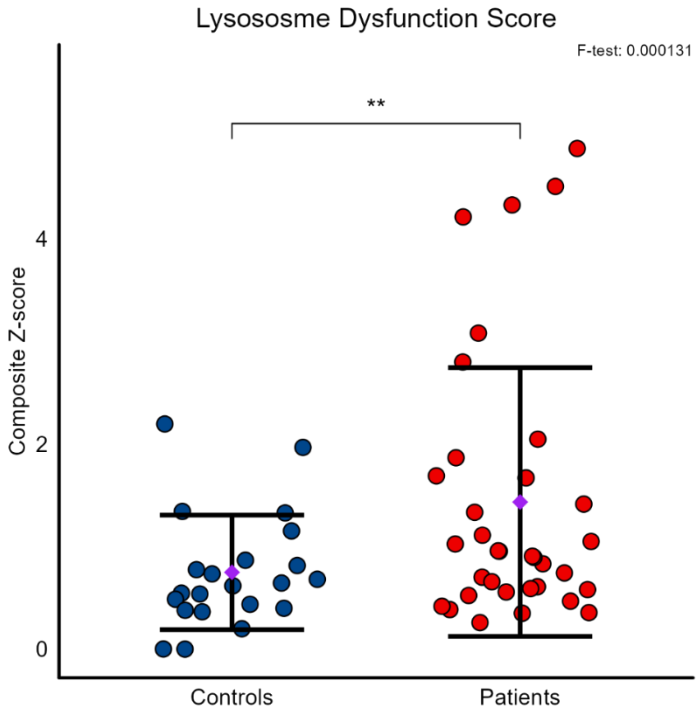

Figure 23: A comparison of the lysosomal dysfunction composite z-scores for the patient and control populations. This shows a significant increase in dysfunction in the patient population. Each point represents an cell lines composite z-score for lysosomal dysfunction. The means of each population (purple diamond) were compared using an unpaired T-test with Welch's correction, significance is depicted by significance symbols (** $p < 0.01$). The difference in variance within each population was assessed using an F-test ($p < 0.05$). Error bars show standard deviation.

3.2.5 Stratification of the Parkinson's Disease Population

Once heterogeneity was confirmed, the PD population was stratified to identify unique, more homogeneous subgroups. Patients in each group were selected by identifying common patterns of dysfunction across all thirteen parameters. Four distinct groups were identified using this method, and further interrogation of each individual media condition, repeat and well result enabled a confident selection. The four groups were a lysosomal dysfunction subgroup, a mitochondrial dysfunction subgroup, a subgroup with both mitochondrial and lysosomal dysfunction defined by an increased number of both organelles (named high mixed group) and a mitochondrial and lysosomal

subgroup defined by a reduced number of both organelles (named low mixed group). These groups are highlighted in the mitochondrial and lysosomal dysfunction composite z-score results in Appendix 3 (Figure 124, Figure 125). The patterns of dysfunction can be clearly identified within the tables showing every cell line's composite z-score per parameter, the organelle dysfunction score and their dysfunction ranking in Appendix 3 (Table 32, Table 33).

3.2.5.1 The Lysosomal Dysfunction Subgroup

This group was defined by a reduced number of lysosomes (< -1 z-score), a reduced lysosome area (< -0.9 z-score) and in two patients a low lysosomal form factor (< -0.7 z-score, Table 15). However, these patients displayed no or limited mitochondrial abnormalities with mitochondrial health z-scores of less than 1.5 (

Table 14). The only consistent mitochondrial abnormality was an increase in mitochondrial branching and mitochondrial length, highlighted by a > 1 z-score for mitochondrial FF z-score and long vs small mitochondrial ratio (

Table 14).

Table 14: Lysosomal Dysfunction Subgroup - A table showing composite z-scores for each mitochondrial parameter for each cell line. Z-scores greater than 1 (green), less than -1 (red) and values between 1 and -1 (white).

ID	ATP027	ATP037	ATP043
Group	12	12	10
MMP	0.16	0.37	-1.02
ATP	-1.42	0.38	2.02
Mitochondria Per Cell	-0.69	-0.37	1.02
Mitochondria FF	1.85	2.95	1.20
Perinuclear Mitochondria Percentage	-0.06	-0.44	-1.38
Small Mitochondria FF	0.94	1.90	1.81
Small Mitochondria MMP	-0.27	0.09	-1.98
Long Mitochondria FF	1.71	2.40	0.24
Long Mitochondria MMP	0.07	1.06	-1.84
Long vs small Mitochondria Ratio	1.64	2.70	1.00
z-score Mitochondrial Dysfunction	0.96	1.13	1.43

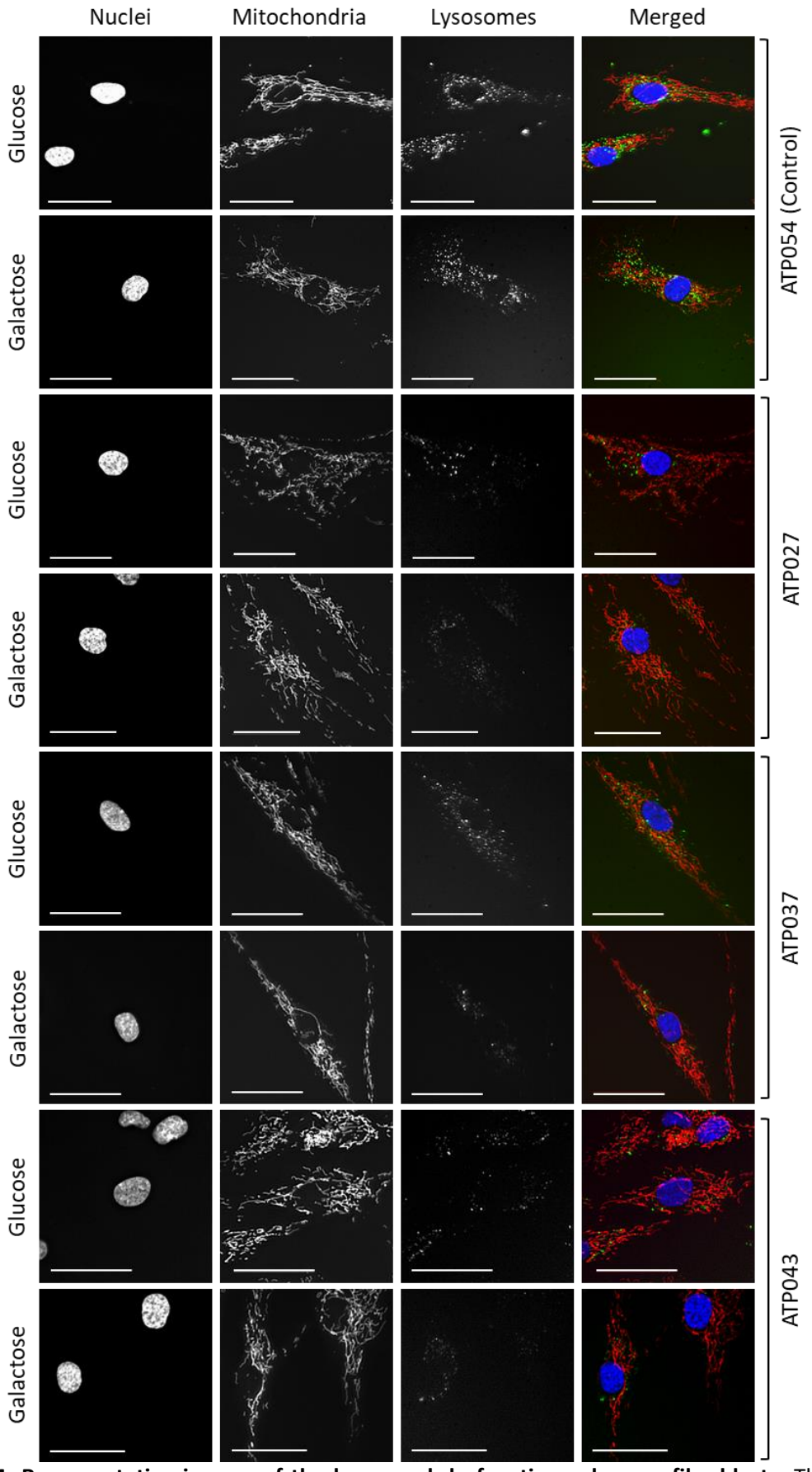

Figure 24: Representative images of the lysosomal dysfunction subgroup fibroblasts. The nuclei, mitochondria and lysosome staining shown individually and merged (blue, red and green respectively) in glucose and galactose media. Scale bar = 40 µm.

Table 15: Lysosomal Dysfunction Subgroup - A table showing composite z-scores for each lysosomal parameter for each cell line. Z-scores less than -1 (red) and values between 1 and -1 (white).

ID	ATP027	ATP037	ATP043
Group	12	12	10
Lysosomes Per Cell	-1.95	-2.40	-1.22
Individual Lysosome Area	-1.32	-3.11	-0.95
Lysosome FF	-0.73	-3.74	-1.16
z-score Lysosomal Dysfunction	1.33	3.08	1.11

3.2.5.2 The Mitochondrial Dysfunction Subgroup

Mitochondrial dysfunction was apparent within this subgroup (> 1.5 z-score, Table 16), with an absence of lysosomal dysfunction (< 1 z-score, Table 17). MMP and the percentage of perinuclear mitochondria were reduced (< -1 z-score), while ATP and the number of mitochondria per cell were increased in all patients (> 1 z-score, Table 16). Two patients showed consistent dysfunction in mitochondrial morphology, shown by increased mitochondrial branching and an increased percentage of elongated mitochondria (Table 16). Lysosomal dysfunction did not reach the threshold for selection within this group. The patients all scored < 1 z-score for lysosomal health; however, all patients had a small increase in the number of lysosomes (< 1 z-score, Table 17). The average lysosomal area and lysosome form factor were normal (Table 17).

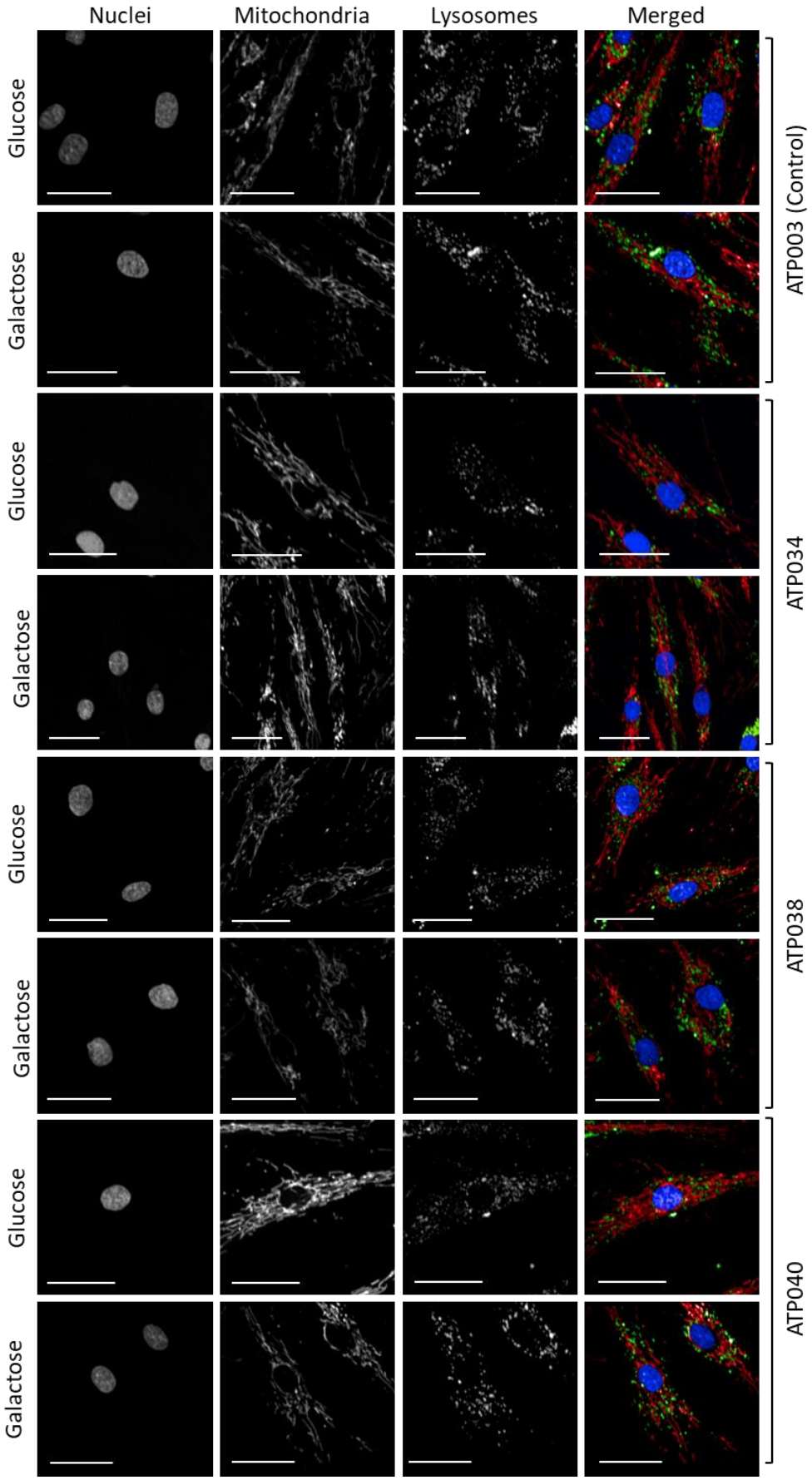

Figure 25: Representative images of the mitochondrial dysfunction subgroup fibroblasts. The nuclei, mitochondria and lysosome staining shown individually and merged (blue, red and green respectively) in glucose and galactose media. Scale bar = 40 µm.

Table 16: Mitochondrial Dysfunction Subgroup - A table showing composite z-scores for each mitochondrial parameter for each cell line. Z-scores greater than 1 (green), less than -1 (red) and values between 1 and -1 (white).

ID	ATP034	ATP038	ATP040
Group	6	7	7
MMP	-1.10	-2.40	-2.12
ATP	1.78	2.16	3.77
Mitochondria Per Cell	4.12	2.50	2.50
Mitochondria FF	1.54	0.31	2.52
Perinuclear Mitochondria Percentage	-2.51	-1.59	-1.99
Small Mitochondria FF	1.09	0.94	2.15
Small Mitochondria MMP	-0.59	-2.44	-2.68
Long Mitochondria FF	2.11	-0.40	1.90
Long Mitochondria MMP	-0.64	-2.55	-2.46
Long vs small Mitochondria Ratio	2.00	-0.06	2.64
z-score Mitochondrial Dysfunction	1.87	1.61	2.66

Table 17: Mitochondrial Dysfunction Subgroup - A table showing composite z-scores for each lysosomal parameter for each cell line. Z-scores greater than 1 (green) and values between 1 and -1 (white).

ID	ATP034	ATP038	ATP040
Group	6	7	7
Lysosomes Per Cell	1.80	1.04	1.42
Individual Lysosome Area	0.20	-0.19	0.42
Lysosome FF	0.87	-0.74	-0.14
z-score Lysosomal Dysfunction	0.96	0.66	0.66

3.2.5.3 High Mixed Group: The Mitochondrial and Lysosomal Dysfunction Subgroup with a Greater Number of Organelles

The previous stratification identified two subgroups defined by dysfunction in one organelle only (Carling *et al.*, 2020). This method identified two additional subgroups defined by dysfunction in both

organelles. Although both structures were dysfunctional, the types of abnormalities defining the two groups were very different, highlighting the heterogeneous nature of PD.

The high mixed group was defined by mitochondrial health scores greater than 2 (Table 18). MMP and the percentage of perinuclear mitochondria were reduced (< -1.4 z-scores) and ATP and the number of mitochondria per cell were increased across all patients (> 2.2 z-scores, Table 18). All patients displayed an increase in mitochondria form factor and long mitochondrial form factor (< 1.4 z-scores, Table 18). Small mitochondrial form factor and long vs small mitochondria ratio were increased in two patients (< 1.4 z-scores, Table 18). This demonstrates altered morphology and function of the mitochondrial network.

Lysosomes were dysfunctional in this group showing extreme lysosomal health scores greater than 4 (Table 19). This was due to astonishingly high numbers of lysosomes per cell (> 7 z-scores) and increased lysosome area and form factor (> 2 z-scores, Table 19).

Table 18: High mixed group: A table showing composite z-scores for each mitochondrial parameter in each cell line. Z-scores greater than 1 (green), less than -1 (red) and values between 1 and -1 (white).

ID	ATP017	ATP019	ATP035
Group	2	2	2
MMP	-2.92	-3.49	-1.48
ATP	5.35	3.15	3.33
Mitochondria Per Cell	5.47	6.04	2.23
Mitochondria FF	3.97	1.38	2.83
Perinuclear Mitochondria Percentage	-1.75	-2.92	-1.66
Small Mitochondria FF	3.59	0.28	1.79
Small Mitochondria MMP	-4.23	-3.97	-1.88
Long Mitochondria FF	3.44	2.30	2.33
Long Mitochondria MMP	-3.14	-2.95	-0.80
Long vs small Mitochondria Ratio	2.78	0.65	1.48
z-score Mitochondrial Dysfunction	3.90	2.83	2.16

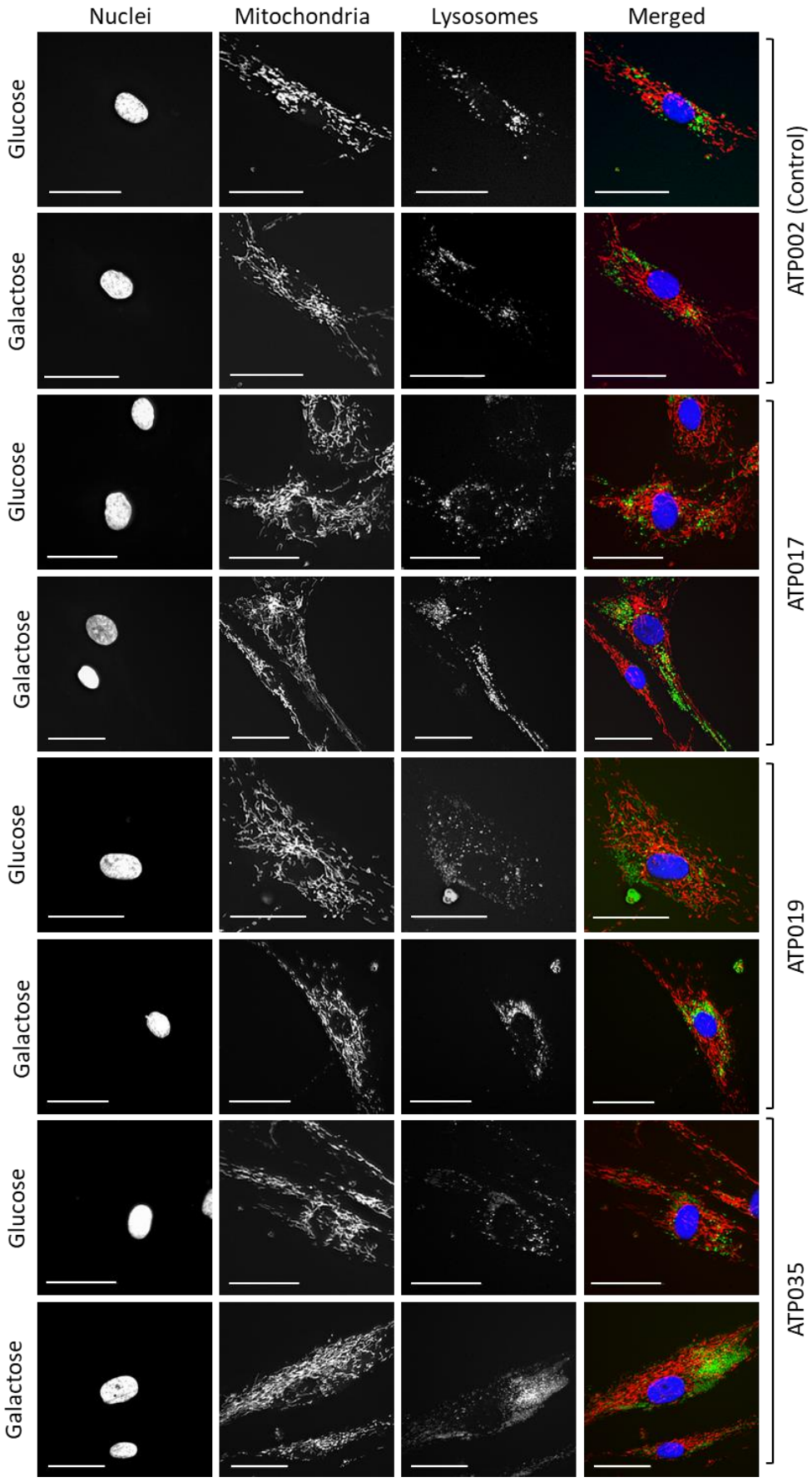

Figure 26: Representative images of the high mixed group fibroblasts. The nuclei, mitochondria and lysosome staining shown individually and merged (blue, red and green respectively) in glucose and galactose media. Scale bar = 40 µm.

Table 19: High mixed group: A table showing composite z-scores for each lysosomal parameter for each cell line. Z-scores greater than 1 (green) and values between 1 and -1 (white).

ID	ATP017	ATP019	ATP035
Group	2	2	2
Lysosomes Per Cell	8.57	9.26	7.34
Individual Lysosome Area	3.90	2.25	3.12
Lysosome FF	2.16	2.02	2.18
z-score Lysosomal Dysfunction	4.88	4.51	4.21

3.2.5.4 Low Mixed Group: The Mitochondrial and Lysosomal Dysfunction Subgroup with a Lower Number of Organelles

Similar to the other mixed group, this subgroup has mitochondrial and lysosomal health scores greater than 1.5 (Table 20, Table 21). However, the pattern of dysfunction is very different. Patients had an increased MMP and percentage of perinuclear mitochondria (> 1.7 z-scores, Table 20). A reduced number of mitochondria was observed in each patient (> -2.2 z-scores) and decreased ATP levels were identified in three patients (< -1.3 z-scores), the fourth patient showed trends towards reduced ATP levels but only had a z-score of -0.54 (Table 20). No consistent pattern was identified when assessing mitochondria form factor or the long vs small mitochondria ratio, although, three patients had extreme scores for each parameter (Table 20). The pattern of lysosomal dysfunction was different from the high mixed group. Patients had a reduced number of lysosomes (< -2 z-scores), lysosomal area (< - 1.7 z-scores) and lysosome form factor (< -1.2 z-scores, Table 21).

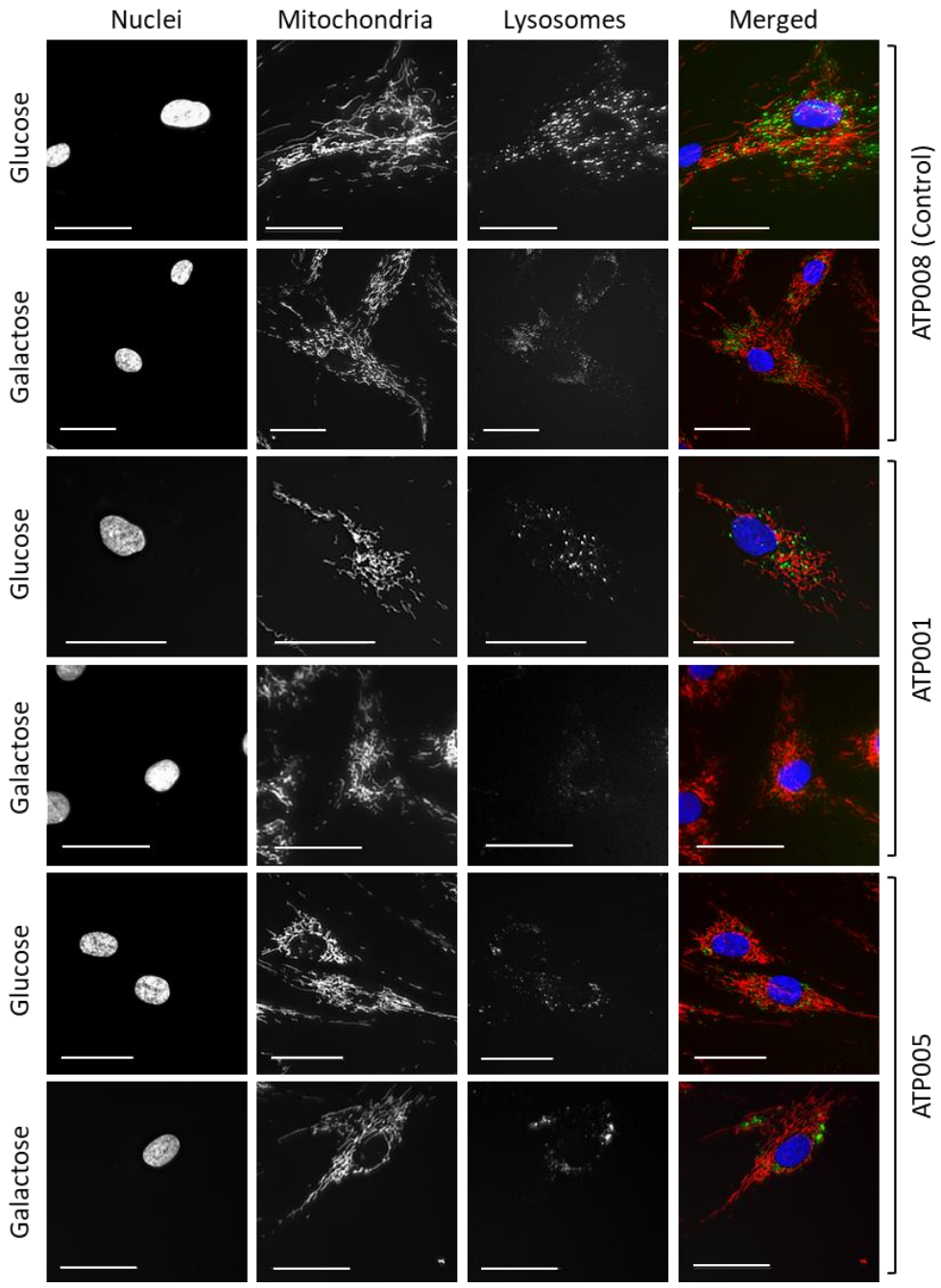

Figure 27: Representative images of two of the patients in the low mixed group. The nuclei, mitochondria and lysosome staining shown individually and merged (blue, red and green respectively) in glucose and galactose media. Scale bar = 40 µm.

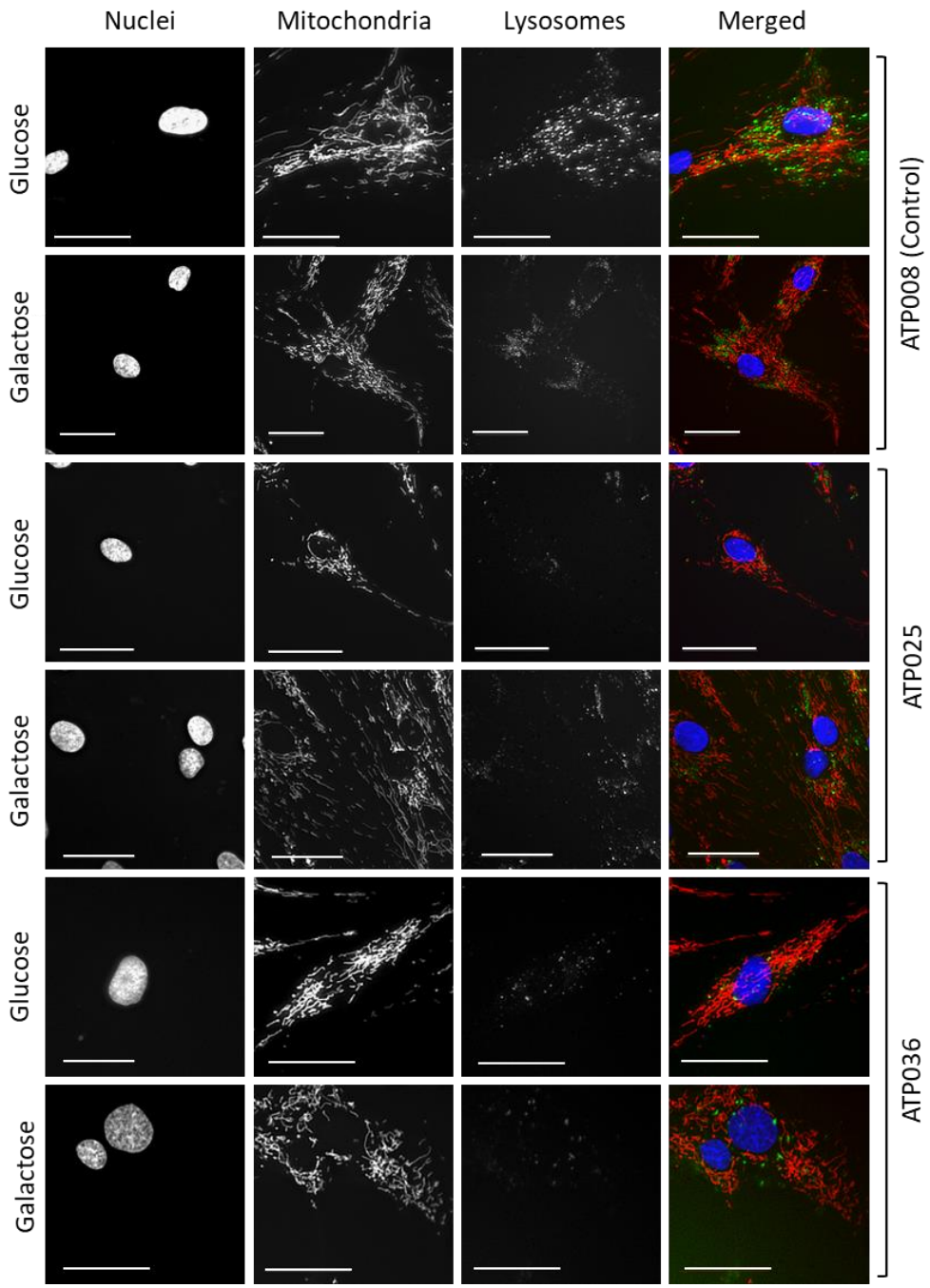

Figure 28: Representative images of the other two patients in the low mixed group. The nuclei, mitochondria and lysosome staining shown individually and merged (blue, red and green respectively) in glucose and galactose media. Scale bar = 40 µm.

Table 20: Low mixed group - A table showing composite z-scores for each mitochondrial parameter for each cell line. Z-scores greater than 1 (green), less than -1 (red) and values between 1 and -1 (white).

ID	ATP001	ATP005	ATP025	ATP036
Group	13	1	1	11
MMP	2.74	4.12	3.01	2.35
ATP	-1.30	-1.62	-2.16	-0.54
Mitochondria Per Cell	-2.22	-3.26	-2.54	-2.37
Mitochondria FF	-2.54	2.51	0.44	1.35
Perinuclear Mitochondria Percentage	3.07	2.64	1.78	2.71
Small Mitochondria FF	-2.95	1.06	-0.06	0.93
Small Mitochondria MMP	5.87	3.47	3.40	3.14
Long Mitochondria FF	-1.94	2.52	0.91	0.77
Long Mitochondria MMP	4.17	4.57	4.14	3.49
Long vs small Mitochondria Ratio	-1.88	2.24	0.26	1.49
z-score Mitochondrial Dysfunction	2.58	2.61	1.88	1.73

Table 21: Low mixed group - A table showing composite z-scores for each lysosomal parameter for each cell line. Z-scores less than -1 (red) and values between 1 and -1 (white).

ID	ATP001	ATP005	ATP025	ATP036
Group	13	1	1	11
Lysosomes Per Cell	-2.91	-2.44	-2.64	-3.18
Individual Lysosome Area	-2.66	-2.39	-1.69	-4.35
Lysosome FF	-2.82	-1.30	-1.26	-5.45
z-score Lysosomal Dysfunction	2.80	2.04	1.86	4.33

3.2.6 Familial Parkinson's Disease Assessment

Following stratification of the sporadic cohort, we assessed several familial patients with the aim of identifying mutant genotypes that had similar phenotypes to the sporadic subgroups. Previous reports have shown distinctly different patterns of dysfunction between different mutations in patient-derived models of PD (Mortiboys *et al.*, 2008, 2010; Grünewald *et al.*, 2010, 2014; Heeman *et al.*, 2011; Papkovskaia *et al.*, 2012; Chung *et al.*, 2016; Thomas *et al.*, 2021; Labrador-Garrido *et al.*, 2023). There is still some heterogeneity within genotypes, likely due to lifestyle factors (Marras, Canning and Goldman, 2019; Gabbert *et al.*, 2023) and exact genetic mutation. We used a new group of fPD patients who were biopsied and established by Dr Dereck Narendra's lab at the Inherited Movement Disorders Unit. The familial cohort was age- and sex-matched, ensuring no difference between the familial and control populations. The lines were screened in the same way as the sPD cohort, however, due to the patient biopsies being established in high glucose media, the assays were also conducted in high glucose media (DMEM media) and galactose media. Each patient was statistically compared to an age- and sex-matched control and all the controls were compared to ensure that phenotypes were consistent between the controls set up from multiple sites (Appendix 40: Figure 126, Figure 127, Figure 128, Figure 129).

3.2.6.1 Familial Parkinson's Disease: LRRK2

Three patients with LRRK2 mutations were assessed. These patients varied in age and sex, two had heterozygous LRRK2 G2019S mutations and one had heterozygous LRRK2 digenic G2019S and R1441G mutations (Table 22).

Table 22: LRRK2 patient and control sex, age at onset and age at biopsy.

Patient	Mutation	Sex	Age at Onset (years)	Age at Biopsy (years)
LRRK2 1	LRRK2 G2019S, R1441G compound het	Female	56	68
LRRK2 2	LRRK2 G2019S het	Male	46	66
LRRK2 3	LRRK2 G2019S het	Male	55	70
Control 1	-	Female	-	54
Control 2	-	Male	-	75

Previous reports in LRRK2 patient-derived fibroblasts noted reduced MMP and ATP (Mortiboys *et al.*, 2010; Papkovskaia *et al.*, 2012; Grünewald *et al.*, 2014), but differing morphology (Mortiboys *et al.*, 2010; Grünewald *et al.*, 2014). In high glucose media, two LRRK2 patients had a small reduction in

MMP, but not significant (LRRK2 1: 17 % ± 15, LRRK2 3: 11 % ± 12, Figure 30A). However, no difference in MMP was observed in galactose media (Figure 31A). No differences were observed when the small and long mitochondria population MMPs were assessed separately (Figure 26F and H, Figure 30F and H). A reduction in form factor demonstrates decreased interconnectivity, this was observed in all two lines in high glucose media (LRRK2 1: 4.5 % ± 4.8, LRRK2 2: 5 % ± 1.5, Figure 30D) and in galactose (LRRK2 1: 5.7 % ± 3.9, LRRK2 2: 6.2 % ± 2.2, Figure 31D) with LRRK2 2 reaching significance in both media conditions (high glucose: p = 0.029, Figure 30D, galactose: p = 0.040, Figure 31D). LRRK2 3 had significantly increased interconnectivity in the long mitochondria population in galactose (1.6 % ± 0.4, p = 0.016, Figure 31G), matching previous reports. ATP levels did not differ from the controls (Figure 30B, Figure 31B). LRRK2 1 and 2 had a reduced long vs small mitochondrial ratio in galactose (LRRK2 1: 24 % ± 11, LRRK2 2: 20 % ± 5, Figure 31I) and high glucose media (LRRK2 1: 20 % ± 17, LRRK2 2: 14 % ± 7, Figure 30I), neither were significant.

Lysosomal phenotyping replicated the literature (MacLeod *et al.*, 2006, 2013; Bravo-San Pedro *et al.*, 2013; Hockey *et al.*, 2015; Schapansky *et al.*, 2018), with patients having elevated lysosomal number, average lysosomal area and lysosomal form factor. The LRRK2 compound het mutant had a significantly elevated number of lysosomes in both media (high glucose: 64 % ± 15, p = 0.046, Figure 33A, galactose: 42 % ± 16, p = 0.017, Figure 33A), while one of the LRRK2 G2019S patients had significantly larger lysosomes in galactose media (LRRK2 2: 16.4 % ± 9.5 p = 0.032, Figure 33B).

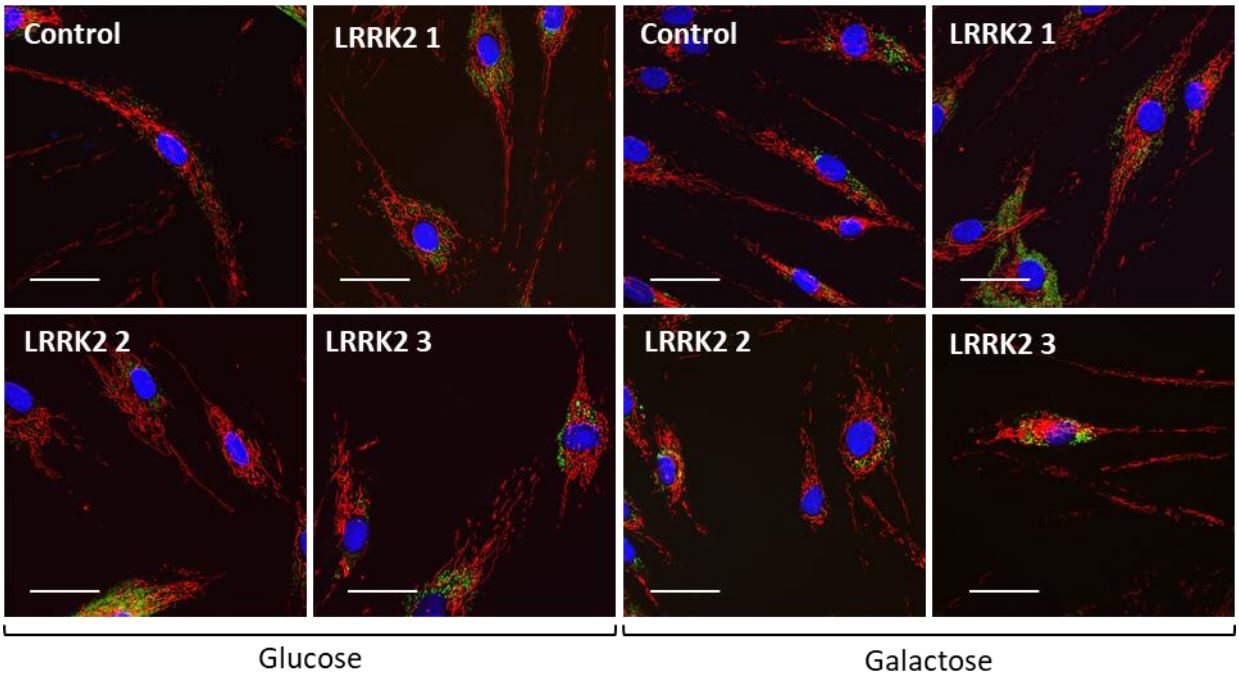

Figure 29: Representative images of the LRRK2 PD patient-derived fibroblasts. The nuclei, mitochondria and lysosome staining shown individually and merged (blue, red and green respectively) in glucose and galactose media. Scale bar = 40 µm.

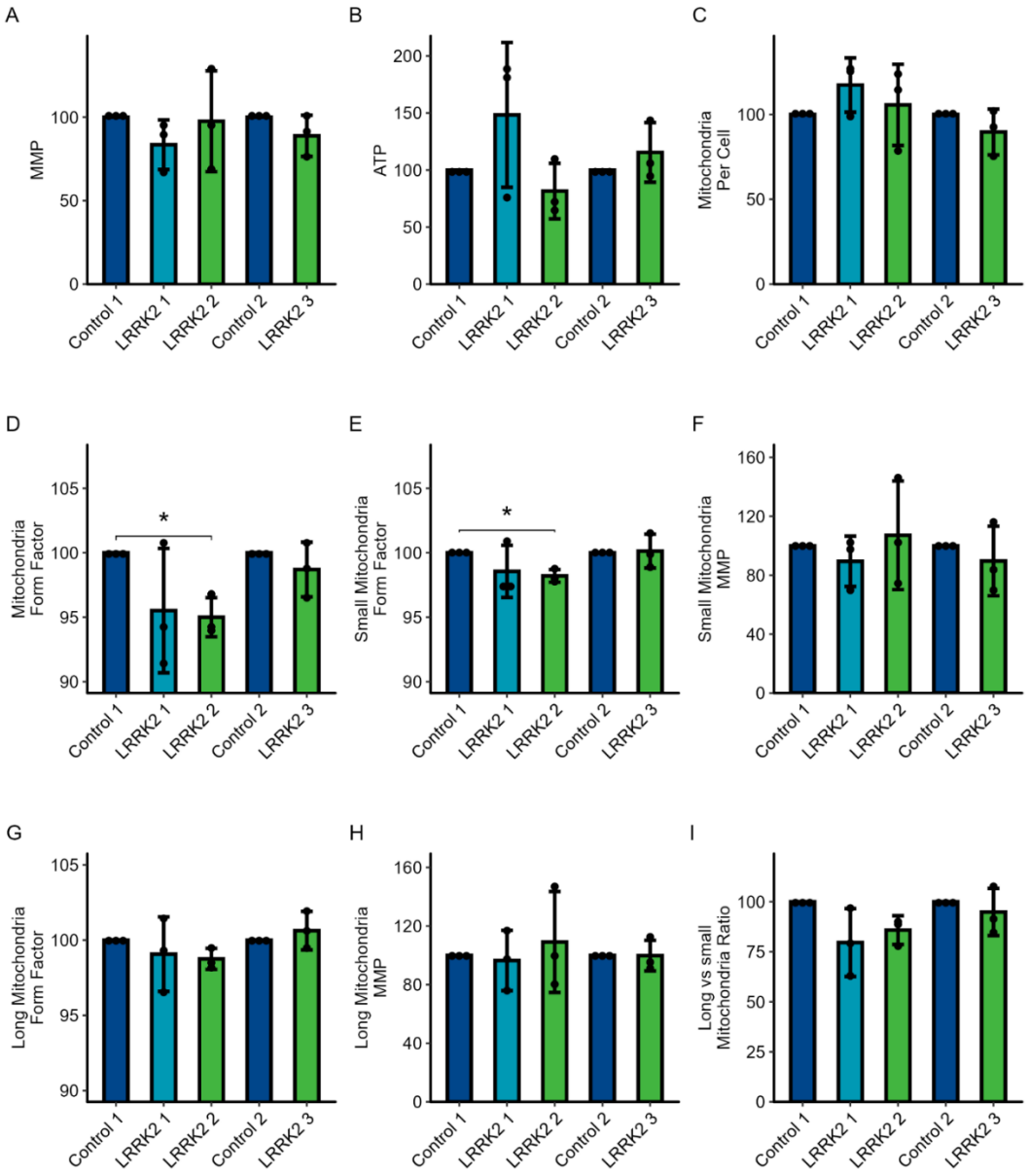

Figure 30: A comparison of the mitochondrial phenotypes between patients carrying a heterozygous LRRK2 mutation and age- and sex-matched controls in <u>high glucose</u> media. A) MMP, **B)** ATP, **C)** Number of mitochondria per cell, **D)** Mitochondrial form factor, **E)** The percentage of mitochondria in the perinuclear region, **F)** Form factor for the small mitochondria population, **G)** MMP for the small mitochondria population, **H)** Form factor for the long mitochondria population, **I)** MMP for the long mitochondria population, **J)** Long vs small mitochondria ratio. Controls (dark blue), LRRK2 G2019S and R1441G mutant patient (light blue) and LRRK2 G2019S patients (green). Data was normalised to the average of the age- and sex-matched control per repeat and error bars show standard deviation (n = 3). The means of each patient were compared to the corresponding age- and sex-matched control by an unpaired T-test with Welch's correction (* $p < 0.05$).

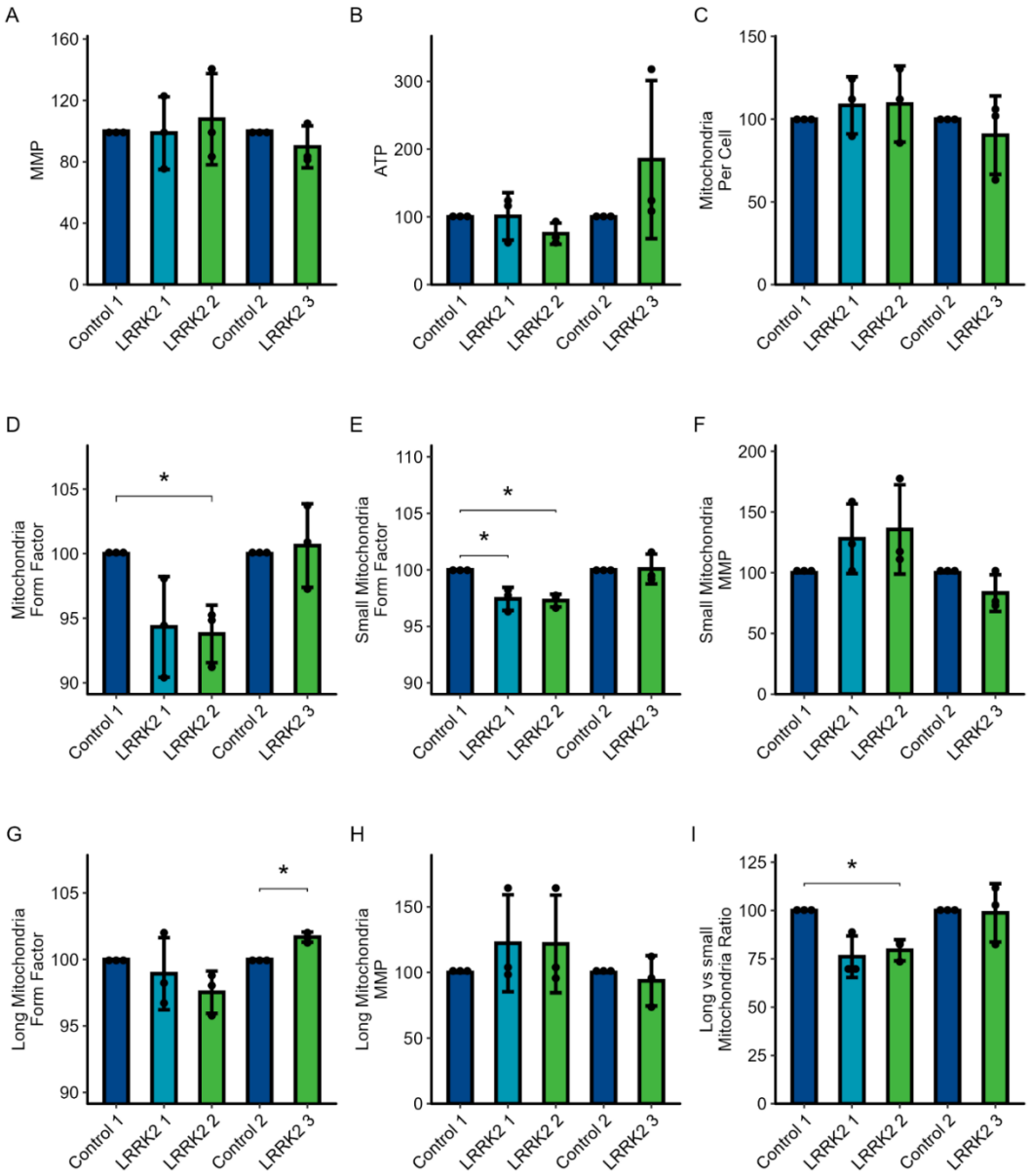

Figure 31: A comparison of the mitochondrial phenotypes between patients carrying a heterozygous LRRK2 mutation and age- and sex-matched controls in <u>galactose</u> media. A) MMP, **B)** ATP, **C)** Number of mitochondria per cell, **D)** Mitochondrial form factor, **E)** The percentage of mitochondria in the perinuclear region, **F)** Form factor for the small mitochondria population, **G)** MMP for the small mitochondria population, **H)** Form factor for the long mitochondria population, **I)** MMP for the long mitochondria population, **J)** Long vs small mitochondria ratio. Controls (dark blue), LRRK2 G2019S and R1441G mutant patient (light blue) and LRRK2 G2019S patients (green). Data was normalised to the average of the age- and sex-matched control per repeat and error bars show standard deviation (n = 3). The means of each patient were compared to the corresponding age- and sex-matched control by an unpaired T-test with Welch's correction (* $p < 0.05$).

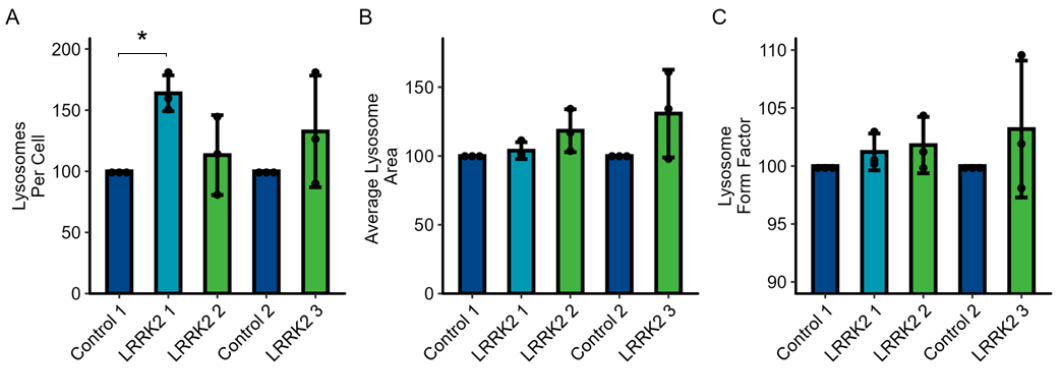

Figure 32: A comparison of the lysosomal phenotypes between patients carrying a heterozygous LRRK2 mutation and age- and sex-matched controls in high glucose media. A) Number of lysosomes per cell, **B)** Average lysosome area, **C)** Lysosomal form factor. Controls (dark blue), LRRK2 G2019S and R1441G mutant patient (light blue) and LRRK2 G2019S patients (green). Data was normalised to the average of the age- and sex-matched control per repeat and error bars show standard deviation (n = 3). The means of each patient were compared to the corresponding age- and sex-matched control by an unpaired T-test with Welch's correction (* $p < 0.05$).

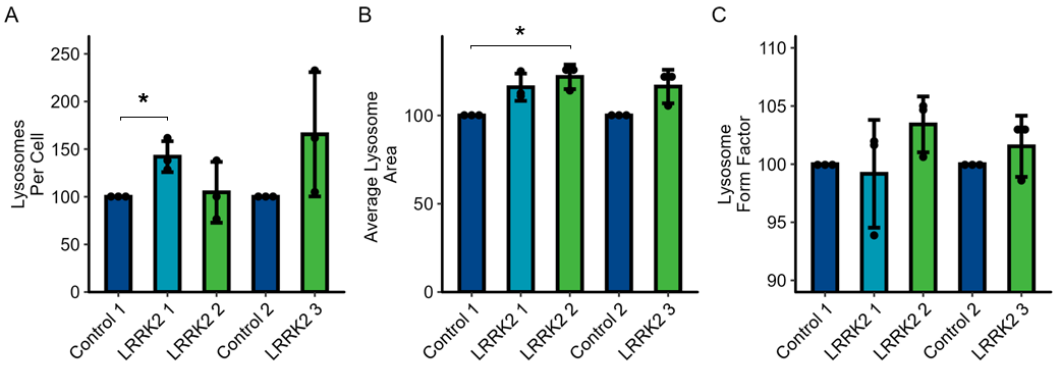

Figure 33: A comparison of the lysosomal phenotypes between patients carrying a heterozygous LRRK2 mutation and age- and sex-matched controls in galactose media. A) Number of lysosomes per cell, **B)** Average lysosome area, **C)** Lysosomal form factor. Controls (dark blue), LRRK2 G2019S and R1441G mutant patient (light blue) and LRRK2 G2019S patients (green). Data was normalised to the average of the age- and sex-matched control per repeat and error bars show standard deviation (n = 3). The means of each patient were compared to the corresponding age- and sex-matched control by an unpaired T-test with Welch's correction (* $p < 0.05$).

3.2.6.2 Familial Parkinson's Disease: GBA

GBA mutations have been implicated in mitochondrial (Baden *et al.*, 2023) and lysosomal dysfunction (Gegg *et al.*, 2012; García-Sanz *et al.*, 2017; Collins *et al.*, 2018; Smith *et al.*, 2023), however, the contribution to PD manifestation is still unclear. This is likely due to the variation in mutations and the result of them being a risk that elevates susceptibility, rather than being a cause of PD (Riboldi and Di Fonzo, 2019). The GBA patients had GBA N370S mutations, this is the most common, but least severe, *GBA1* point mutation associated with PD. Included in the group was a patient with GBA N370S and LRRK2 G2019S mutations.

Table 23: GBA patient and control sex, age at onset and age at biopsy.

Patient	Mutation	Sex	Age at Onset (years)	Age at Biopsy (years)
GBA 1	GBA N370S het	Female	47	51
GBA 2	GBA N370S het	Female	52	66
GBA & LRRK2	GBA N370S het and LRRK2 G2019S het	Female	59	68
Control 1	-	Female	-	54
Control 2		Female	-	66
Control 3	-	Female	-	64

GBA 1's phenotype matched the sporadic low mixed group. The line had elevated MMP in both media conditions (high glucose: 33 % ± 27, Figure 35A, galactose: 13 % ± 19, Figure 36A) but decreased ATP (29 % ± 18, Figure 35B) and number of mitochondria per cell (19 % ± 21, Figure 35C) in high glucose. These alterations were not significant when compared to the matched control. In contrast, GBA 2 matched the sporadic high mixed group. MMP was significantly reduced (high glucose: 49 % ± 5, p = 0.0002/0.0001, Figure 35A, galactose: 63 % ± 5, p = 0.001/0.002, Figure 36A). ATP (high glucose: 68 % ± 15, p = 0.008/0.003, Figure 35B, galactose: 76 % ± 21, p = 0.013/0.015, Figure 36B) and the number of mitochondria (high glucose: 89 % ± 20, p = 0.014/0.017, Figure 35C, galactose: 94 % ± 24, p = 0.014/0.015, Figure 36C) were significantly increased compared to both controls in high glucose and galactose conditions. Interestingly, GBA 1 had a significant reduction in form factor (8.3 % ± 3.0, p = 0.037, Figure 36D) and long vs small mitochondria ratio (28 % ± 5, p = 0.010, Figure 36I), in galactose, but GBA 2 showed no morphological difference to the controls (Figure 36).

Combinations of GBA and LRRK2 mutations in the same patient have been reported to be protective (Yahalom *et al.*, 2019; Omer *et al.*, 2020; Ortega *et al.*, 2021). In keeping with these reports, neither MMP (Figure 35A, Figure 36A), ATP (Figure 35B, Figure 36B) or mitochondria per cell (Figure 35C,

Figure 36C) were altered in the GBA & LRRK2 patients' cells. Morphologically however the mitochondria are different. In high glucose media, the small mitochondria had a reduction in form factor (1.7 % ± 0.08, p = 0.027, Figure 35E) and thus interconnectivity compared to Control 2. While in galactose a reduction can be seen in the ratio of long to small mitochondria (13 % ± 3, p = 0.036, Figure 36I) and the whole population form factor (3.9 % ± 1.2, p = 0.030, Figure 36D) as well as the small mitochondria population form factor (2.0 % ± 0.9, p = 0.046, Figure 36E) compared to Control 2. An increase in MMP in the long mitochondria population (45 % ± 18, p = 0.018, Figure 35H) was also observed. No significant differences were observed compared to Control 3 (Figure 36, Figure 37).

Assessment of lysosomal phenotype showed that the GBA patients matched the same sporadic subgroups identified by mitochondrial phenotypes. GBA 1 had a significant decrease in the number of lysosomes (16 % ± 6, p = 0.048, Figure 37A) and their size (13 % 5, p = 0.044, Figure 37B) in high glucose, although no difference was observed in galactose media(Figure 38A, Figure 38B). GBA 2 had a greater number of lysosomes, which was significant in galactose media (high glucose: 80 % ± 45, Figure 37A, galactose: 208 % ± 25, p = 0.005/0.005, Figure 38A), and significantly larger lysosomes (high glucose: 27 % ± 7, p = 0.009/0.008, Figure 37B, galactose: 18 % ± 5, p = 0.021/0.008, Figure 38B). The GBA & LRRK2 patient showed no difference to the controls in high glucose media (Figure 37), but a significantly increased lysosomal size (8.6 % ± 5.3, p = 0.013, Figure 38B) in galactose media.

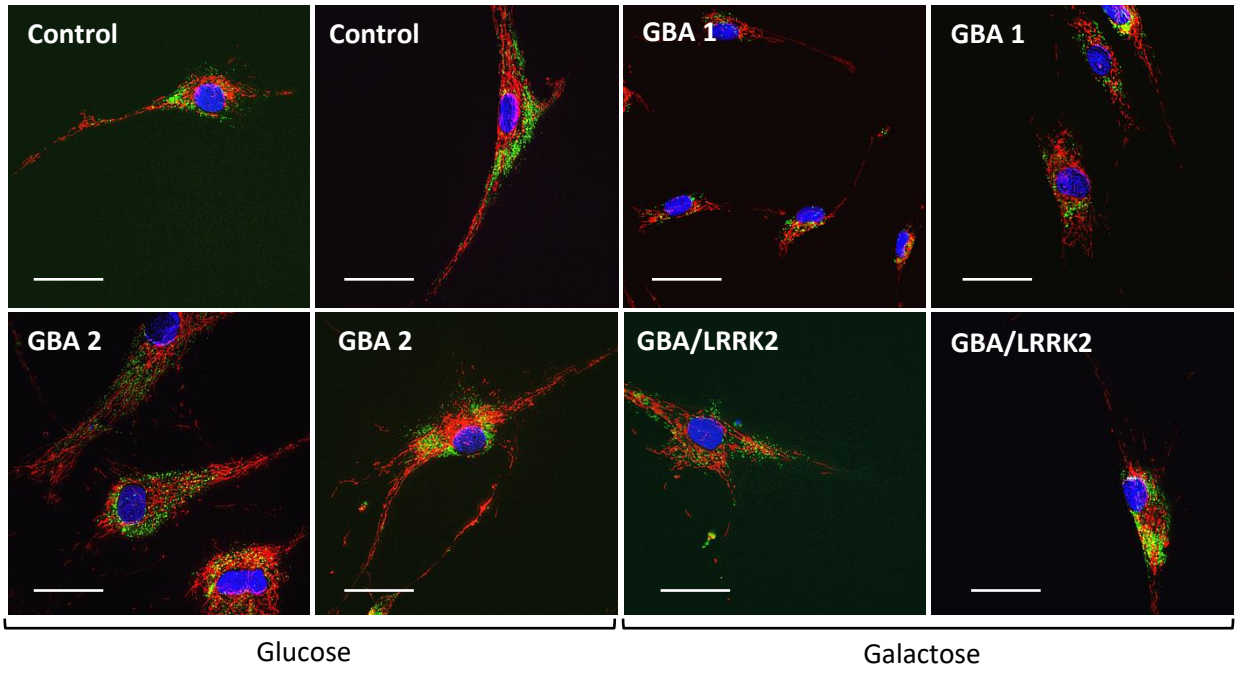

Figure 34: Representative images of the GBA PD patient-derived fibroblasts. The nuclei, mitochondria and lysosome staining shown individually and merged (blue, red and green respectively) in glucose and galactose media. Scale bar = 40 µm.

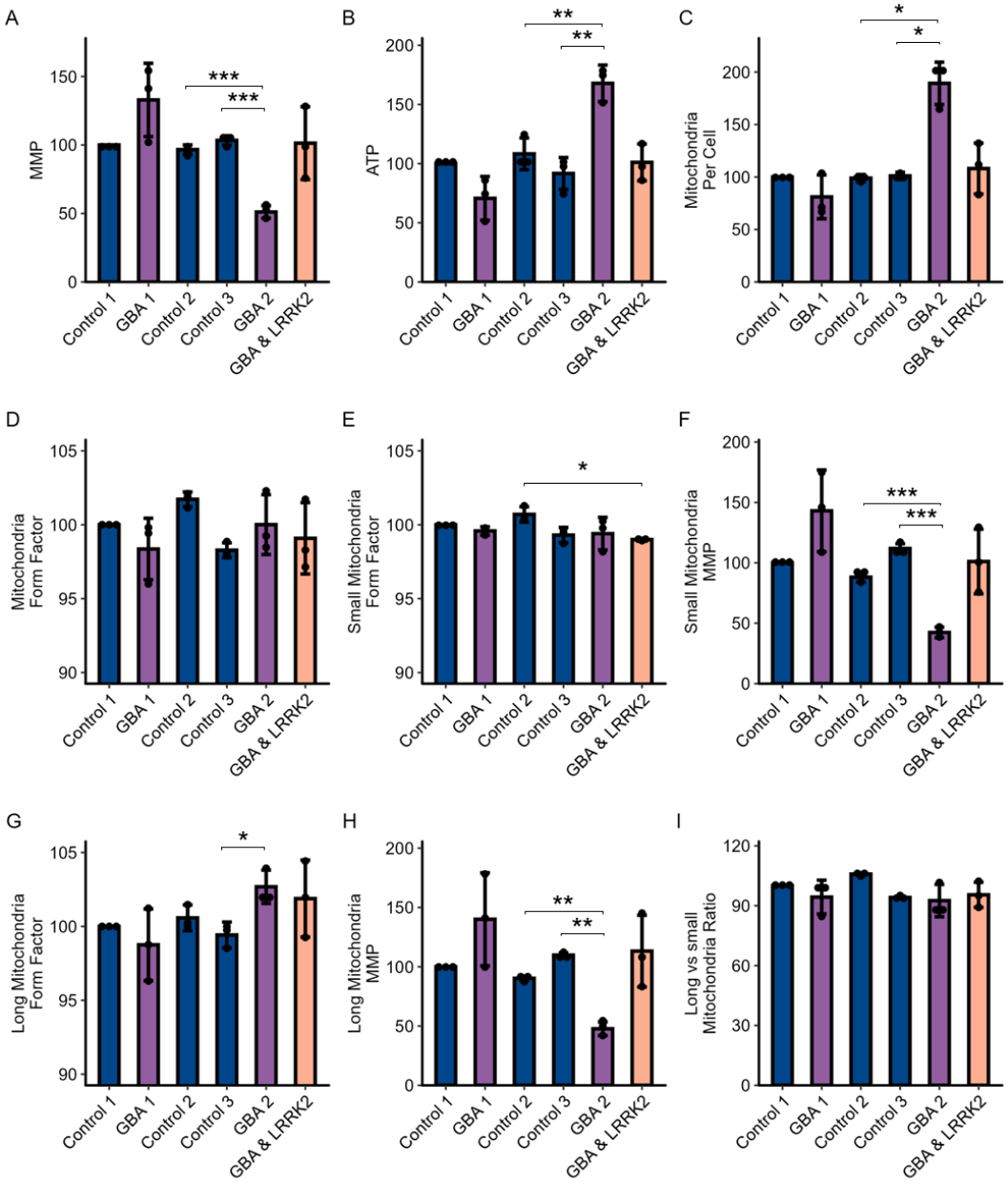

Figure 35: A comparison of the mitochondrial phenotypes between patients carrying a heterozygous GBA N370S mutation or digenic LRRK2 G2019S and GBA N370S mutations with age- and sex-matched controls in <u>high glucose</u> media. **A)** MMP, **B)** ATP, **C)** Number of mitochondria per cell, **D)** Mitochondrial form factor, **E)** The percentage of mitochondria in the perinuclear region, **F)** Form factor for the small mitochondria population, **G)** MMP for the small mitochondria population, **H)** Form factor for the long mitochondria population, **I)** MMP for the long mitochondria population, **J)** Long vs small mitochondria ratio. Controls (dark blue), GBA N370S mutant patient (purple) and GBA N370S and LRRK2 G2019S patients (pink). Data was normalised to the average of the age- and sex-matched control per repeat and error bars show standard deviation (n = 3). The means of each patient were compared to the corresponding age- and sex-matched control by an unpaired T-test with Welch's correction (* $p < 0.05$, ** $p < 0.01$, *** $p < 0.001$).

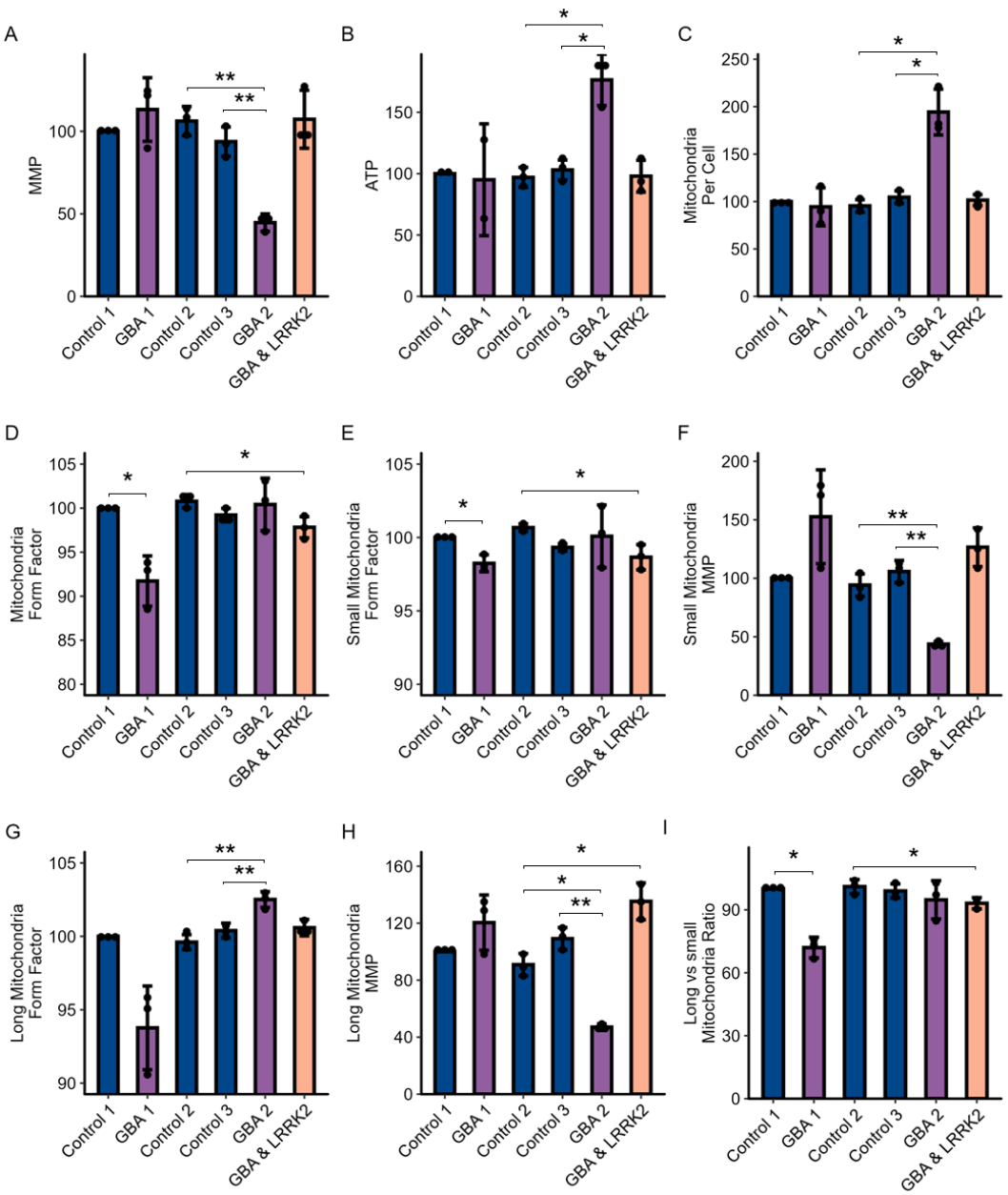

Figure 36: A comparison of the mitochondrial phenotypes between patients carrying a heterozygous GBA N370S mutation or digenic LRRK2 G2019S and GBA N370S mutations with age- and sex-matched controls in <u>galactose</u> media. A) MMP, **B)** ATP, **C)** Number of mitochondria per cell, **D)** Mitochondrial form factor, **E)** The percentage of mitochondria in the perinuclear region, **F)** Form factor for the small mitochondria population, **G)** MMP for the small mitochondria population, **H)** Form factor for the long mitochondria population, **I)** MMP for the long mitochondria population, **J)** Long vs small mitochondria ratio. Controls (dark blue), GBA N370S mutant patient (purple) and GBA N370S and LRRK2 G2019S patients (pink). Data was normalised to the average of the age- and sex-matched control per repeat and error bars show standard deviation (n = 3). The means of each patient were compared to the corresponding age- and sex-matched control by an unpaired T-test with Welch's correction (* $p < 0.05$, ** $p < 0.01$).

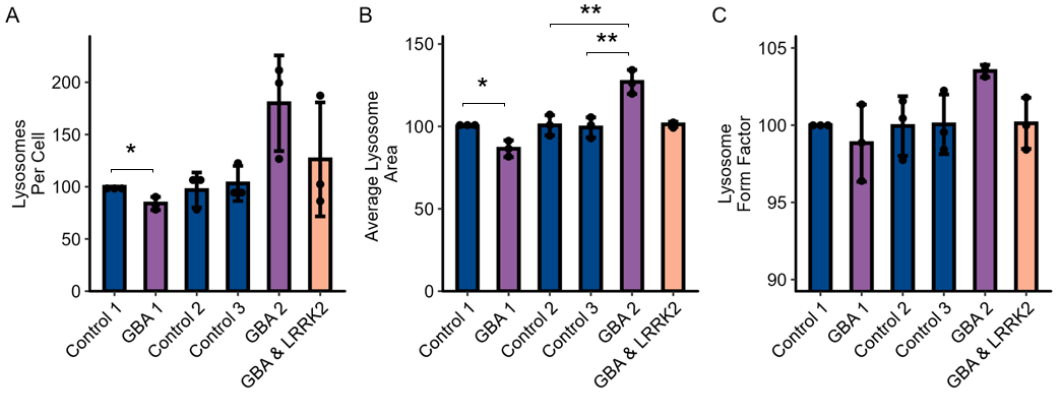

Figure 37: A comparison of the lysosomal phenotypes between patients carrying a heterozygous GBA N370S mutation or digenic LRRK2 G2019S and GBA N370S mutations with age- and sex-matched controls in high glucose media. A) Number of lysosomes per cell, **B)** Average lysosome area, **C)** Lysosomal form factor. Controls (dark blue), GBA N370S mutant patient (purple) and GBA N370S and LRRK2 G2019S patients (pink). Data was normalised to the average of the age- and sex-matched control per repeat and error bars show standard deviation (n = 3). The means of each patient were compared to the corresponding age- and sex-matched control by an unpaired T-test with Welch's correction (* $p < 0.05$, ** $p < 0.01$).

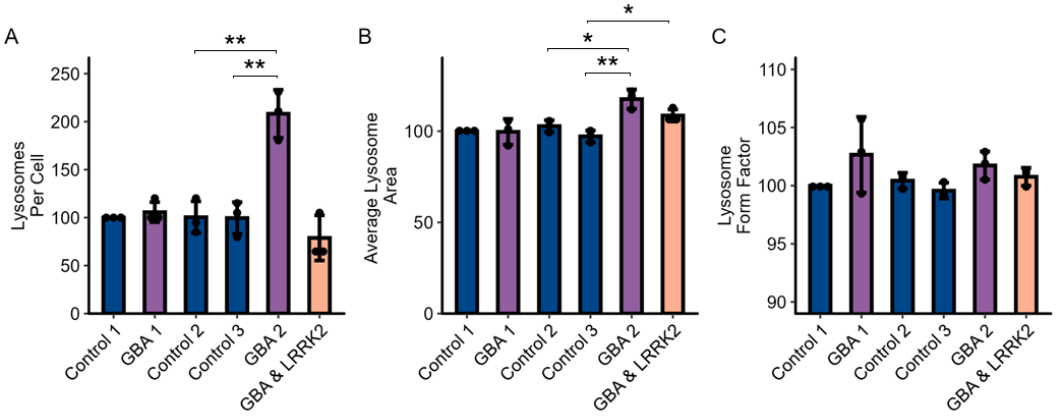

Figure 38: A comparison of the lysosomal phenotypes between patients carrying a heterozygous GBA N370S mutation or digenic LRRK2 G2019S and GBA N370S mutations with age- and sex-matched controls in galactose media. A) Number of lysosomes per cell, **B)** Average lysosome area, **C)** Lysosomal form factor. Controls (dark blue), GBA N370S mutant patient (purple) and GBA N370S and LRRK2 G2019S patients (pink). Data was normalised to the average of the age- and sex-matched control per repeat and error bars show standard deviation (n = 3). The means of each patient were compared to the corresponding age- and sex-matched control by an unpaired T-test with Welch's correction (* $p < 0.05$, ** $p < 0.01$).

3.2.6.3 Familial Parkinson's Disease: Parkin

Two sisters with Parkin mutations were assessed in this study. Both carry the same heterozygous point and deletion mutations and were assessed against the same age- and sex-matched control (Table 24).

Table 24: Parkin patient sex, age at onset and age at biopsy.

Patient	Mutation	Sex	Age at Onset (years)	Age at Biopsy (years)
Parkin 1	PARK2 V56E, and partial gene deletion including exon 7	Female	35	50
Parkin 2	PARK2 V56E, and partial gene deletion including exon 7	Female	32	39
Control 1	-	Female	-	54

Both Parkin patients showed no difference in ATP levels in either media condition (Figure 40B, Figure 41B). MMP was significantly decreased in Parkin 2 (27 % ± 4, p = 0.007, Figure 40A), along with a significant increase in the number of mitochondria per cell (29 % ± 5, p = 0.012, Figure 40A) in high glucose. This trend was observed in galactose but did not reach significance (MMP: 16 % ± 12, Figure 41A, mitochondria per cell: 15 % ± 20, Figure 41B). Both Parkin patients' mitochondria had reduced branching (form factor) in both media conditions (high glucose: Parkin 1: 3.0 % ± 1.6, Parkin 2: 1.4 % ± 2.7, Figure 40D, galactose: Parkin 1: 5.2 % ± 2.8, Parkin 2: 3.2 % ± 1.7, p = 0.040, Figure 41D) with Parkin 2 reaching significance in galactose media. Reduced form factor was also observed in the small mitochondria population in both patients (high glucose: Parkin 1: 1.2 % ± 1.1, Parkin 2: 0.9 % ± 0.7, Figure 40E, galactose: Parkin 1: 1.8 % ± 1.3, Parkin 2: 1.2 % ± 0.6, p = 0.034, Figure 41E). Parkin 1 showed no difference in branching in the long mitochondria population in high glucose media (Figure 40G) but a significant reduction in galactose (2.9 % ± 0.6, p = 0.016, Figure 41G). On the other hand, Parkin 2 showed increased interconnectivity in high glucose media (1.5 % ± 2.7, Figure 40G) and no difference in galactose media (Figure 41G). The sisters both had a reduction in the number of long mitochondria compared to small mitochondria in high glucose (Parkin 1: 13 % ± 7, Parkin 2: 8 % ± 10, Figure 40I) and galactose; Parkin 2 reached significance in galactose (Parkin 1: 14 % ± 8, Parkin 2: 12 % ± 5, p = 0.017, Figure 41I).

Lysosome content has not been reported in Parkin patient-derived fibroblasts before. Both patients had an elevated number of lysosomes in high glucose media (Parkin 1: 25 % ± 32, Parkin 2: 49 % ± 28, Figure 42A). This difference was not observed in galactose media (Figure 43A). The lysosomes were

larger in both patients under high glucose culturing conditions (Parkin 1: 16 % ± 6, Parkin 2: 16 % ± 8, p = 0.049, Figure 42B). No difference in lysosome form factor was observed (Figure 42C, Figure 43C).

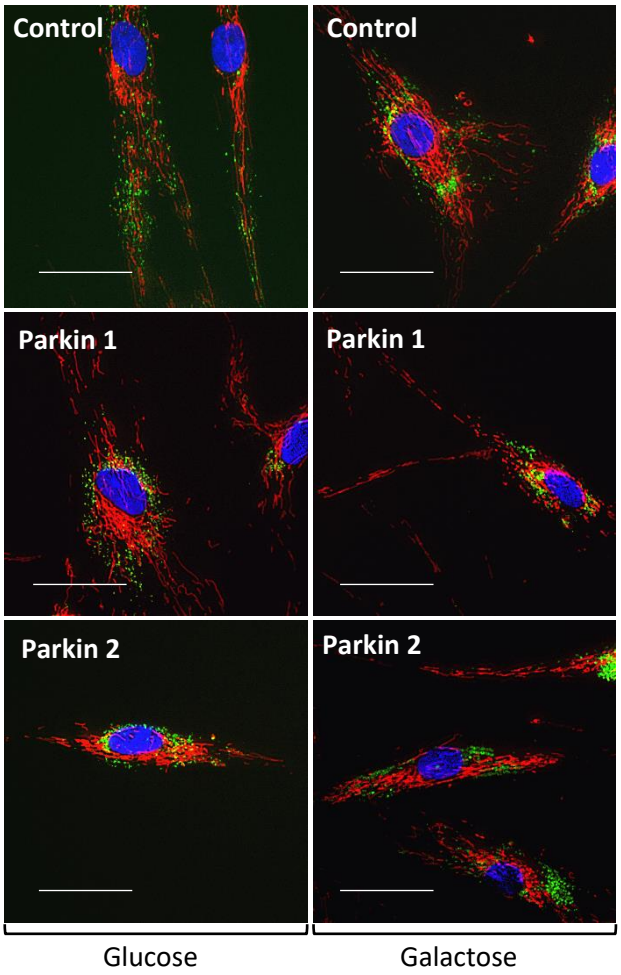

Figure 39: Representative images of the Parkin PD patient-derived fibroblasts. The nuclei, mitochondria and lysosome staining shown individually and merged (blue, red and green respectively) in glucose and galactose media. Scale bar = 40 µm.

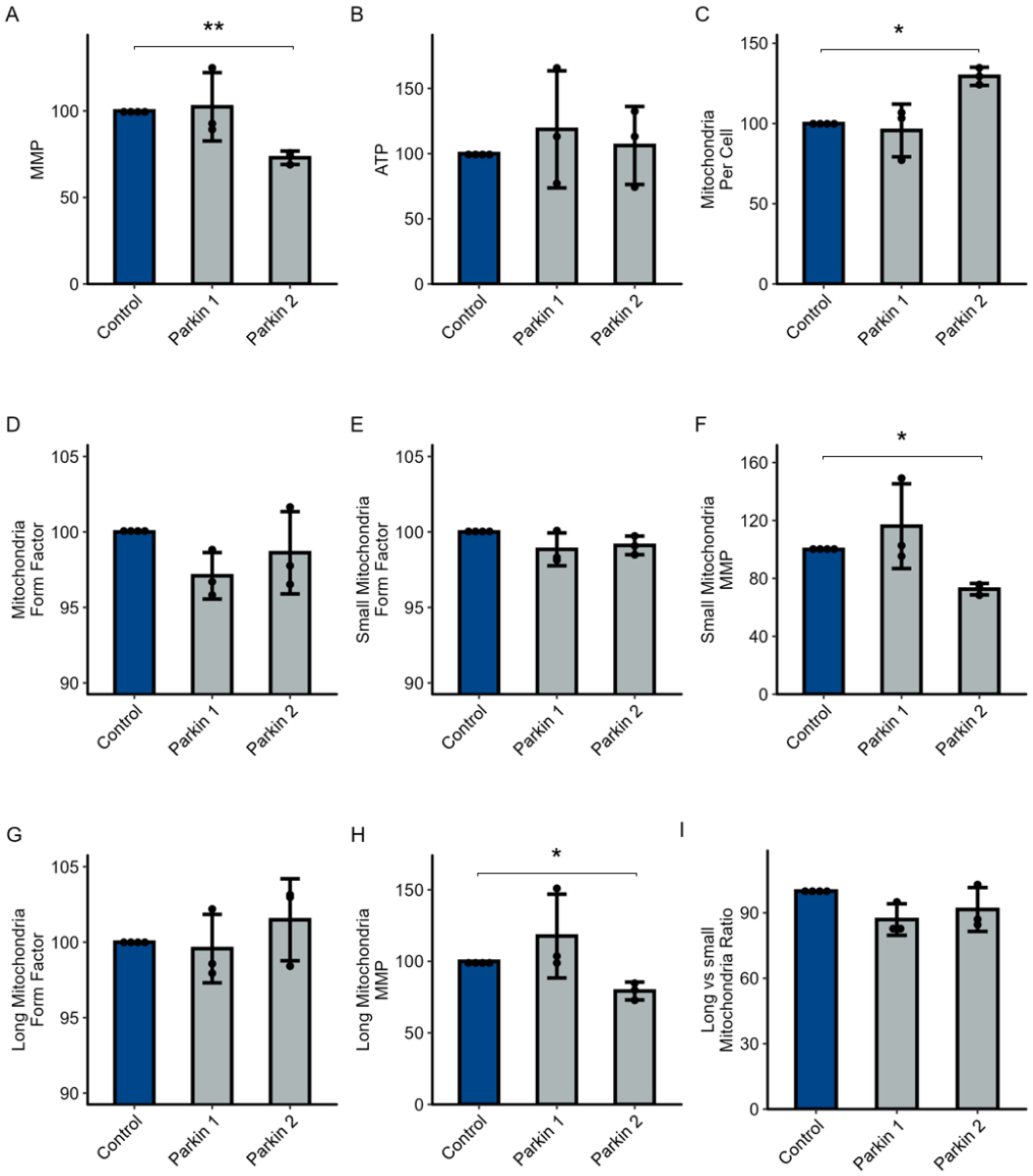

Figure 40: A comparison of the mitochondrial phenotypes of two related patients carrying heterozygous Parkin mutations with age- and sex-matched controls in high glucose media. A) MMP, **B)** ATP, **C)** Number of mitochondria per cell, **D)** Mitochondrial form factor, **E)** The percentage of mitochondria in the perinuclear region, **F)** Form factor for the small mitochondria population, **G)** MMP for the small mitochondria population, **H)** Form factor for the long mitochondria population, **I)** MMP for the long mitochondria population, **J)** Long vs small mitochondria ratio. Controls (blue), Parkin patients (grey). Data was normalised to the average of the age- and sex-matched control per repeat and error bars show standard deviation (n = 3). The means of each patient were compared to the corresponding age- and sex-matched control by an unpaired T-test with Welch's correction (* $p < 0.05$, ** $p < 0.01$).

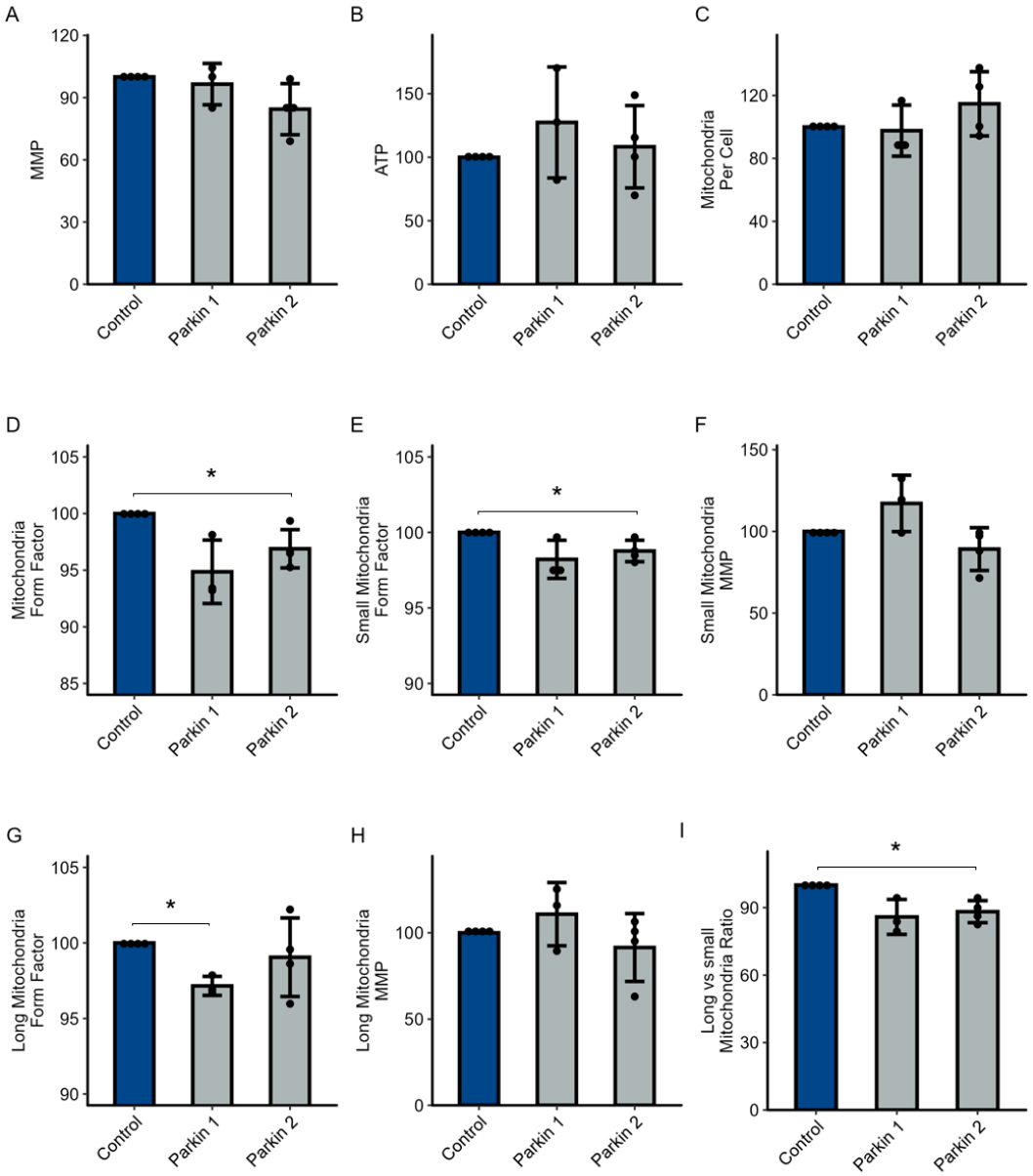

Figure 41: A comparison of the mitochondrial phenotypes of two related patients carrying heterozygous Parkin mutations with age- and sex-matched controls in galactose media. A) MMP, **B)** ATP, **C)** Number of mitochondria per cell, **D)** Mitochondrial form factor, **E)** The percentage of mitochondria in the perinuclear region, **F)** Form factor for the small mitochondria population, **G)** MMP for the small mitochondria population, **H)** Form factor for the long mitochondria population, **I)** MMP for the long mitochondria population, **J)** Long vs small mitochondria ratio. Controls (blue), Parkin patients (grey). Data was normalised to the average of the age- and sex-matched control per repeat and error bars show standard deviation (n = 3/4). The means of each patient were compared to the corresponding age- and sex-matched control by an unpaired T-test with Welch's correction (* $p < 0.05$).

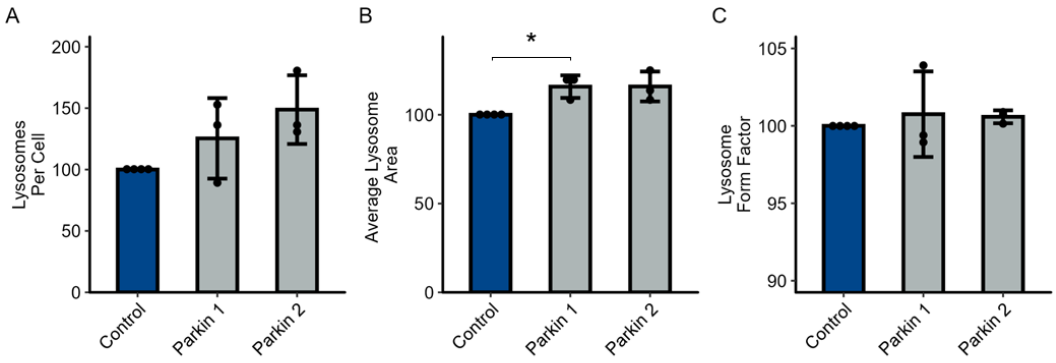

Figure 42: A comparison of the mitochondrial phenotypes of two related patients carrying heterozygous Parkin mutations with age- and sex-matched controls in high glucose media. A) Number of lysosomes per cell, **B)** Average lysosome area, **C)** Lysosomal form factor. Data was normalised to the average of the age- and sex-matched control per repeat and error bars show standard deviation (n = 3). The means of each patient were compared to the corresponding age- and sex-matched control by an unpaired T-test with Welch's correction (* $p < 0.05$).

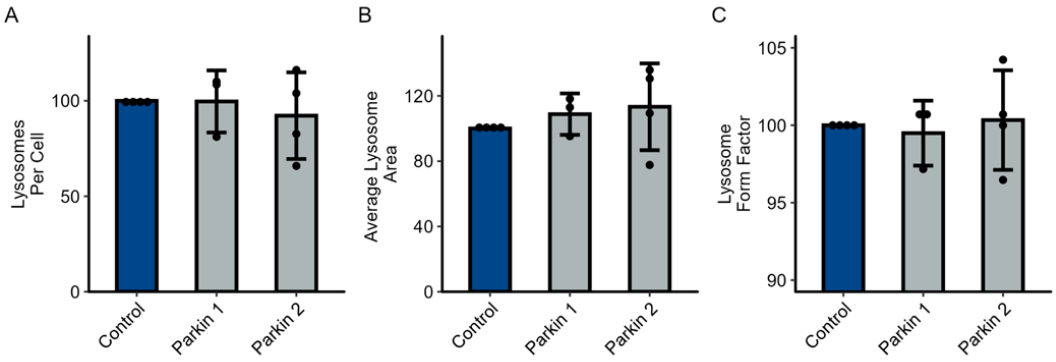

Figure 43: A comparison of the mitochondrial phenotypes of two related patients carrying heterozygous Parkin mutations with age- and sex-matched controls in galactose media. A) Number of lysosomes per cell, **B)** Average lysosome area, **C)** Lysosomal form factor. Data was normalised to the average of the age- and sex-matched control per repeat and error bars show standard deviation (n = 3/4). The means of each patient were compared to the corresponding age- and sex-matched control by an unpaired T-test with Welch's correction (* $p < 0.05$).

3.3 Discussion

This chapter has focused on the initial screening of mitochondrial and lysosomal dysfunction in a new cohort of sPD patients, biopsied at the University of Sheffield. The aim was to assess heterogeneity and stratify the cohort based on phenotypic patterns of dysfunction to produce unique subgroups that are mechanistically more homogeneous. Overall, the cohort demonstrated significantly more heterogeneity than the control group across both mitochondrial and lysosomal parameters and thirteen patients were stratified into four distinct subgroups.

3.3.1 Clinical Trial Drawbacks

Despite the funding and effort of researchers globally, failure during clinical trials means there are no disease-modifying therapies available to treat PD. There are several theorised reasons for clinical trial failure such as a lack of biomarkers, durations of trials and the heterogeneity of the PD population. There are no proven biomarkers for PD that can indicate disease modification by a therapeutic agent. The recent success in establishing the α-syn seed amplification assay may enable the diagnosis of PD before symptoms and provide a valuable window for initiating treatments before disease onset, once they are available (Concha-Marambio *et al.*, 2023; Iftikhar *et al.*, 2024). However, it cannot distinguish between different types of parkinsonism, the severity, stage of disease or types of cellular dysfunction (Concha-Marambio *et al.*, 2023). Extensive work is being conducted to develop blood-based biomarkers (Giuliano *et al.*, 2023), including mtDNA markers (Gonzalez-Hunt *et al.*, 2020; Qi *et al.*, 2023). These would provide a minimally invasive method of determining efficacy, but a one-size-fits-all marker still eludes researchers. Brain imaging could provide valuable insight into therapeutic effects. Phosphorus magnetic resonance spectroscopy imaging has been utilised by multiple clinical trials to date (Sathe *et al.*, 2020; Schultz *et al.*, 2022; Payne *et al.*, 2023), but a single methodology that can stratify patients has not been established.

Instead of biomarkers, quantitative clinical measures may improve clinical trial assessment. Medical technology continues to advance at a rapid rate, leading to the development of many devices that may help indicate compound efficacy. Clinicians rely on the MDS-UPDRS scale to determine PD symptom severity. This is subjective and regardless of experience, clinicians will score the same movements differently on different days (Siderowf *et al.*, 2002). Furthermore, patients' symptom severity fluctuates throughout the day and over longer periods of time (Carpi *et al.*, 2023). The short examination by a clinician during a clinical trial cannot effectively mitigate this. Medical devices such as watches, chest straps (Channa, Popescu and Ciobanu, 2020) and smartphone applications (Tripathi *et al.*, 2022) may improve trials by continually evaluating symptoms for the duration of the trial, generating a broader understanding of compound efficacy and mitigating human bias to some extent.

Devices can also be used during clinical examination to quantitatively measure symptom severity without human bias, as utilised by the UP study (Payne *et al.*, 2020; Payne *et al.*, 2023).

The second issue with PD clinical trials is trial duration. Understandably there is a balance between cost, speed and effectiveness of clinical trials. However, PD progression is heterogeneous among patients. Many patients progress slowly and can survive for years after diagnosis; thus, short trial duration cannot identify differences between placebo and therapeutics due to a lack of progression in the controls. Many Phase II trials are 52 weeks or fewer (Chan, 2011; Klein, 2022; Surmeier *et al.*, 2022; Payne *et al.*, 2023). This may hinder successful therapeutics from progressing to Phase III due to trial design or funding restrictions.

Heterogeneity in PD is a growing area of interest. Ideally, clinical trials would consist of a cohort of patients whose disease is driven by a mechanism of dysfunction that the prospective therapeutic targets. The cohort would also display a symptom or biomarker that can determine the effectiveness of the compound and target engagement. It is common knowledge that PD is clinically heterogeneous, leading to a lack of a homogenous symptom to measure. Heterogeneity of a mechanism level adds further complexity as a proportion of the patient cohorts' disease may not be driven by the targeted dysfunctional mechanism and therefore the therapeutic will be ineffective. For example, a therapeutic targeting mitochondria is unlikely to be effective in a patient whose disease is driven by a lysosomal deficit.

Multi-arm multi-stage trials (MAMS) assessing multiple disease-modifying compounds alongside one another attempt to mitigate heterogeneity and reduce the slow design of clinical trials. These have been used in cancer (Carthon and Antonarakis, 2016) and two are being conducted in PD. The first is the Australian Parkinson's Mission Clinical Trial 1 (ACTRN12620000560998), which is assessing three compounds (Alogliptin, Albuterol and Nivadipine) with one placebo group but has no additional stages (Lewis, 2021). The second is the Edmond J Safra Accelerating Clinical Trials in Parkinson's Disease trial (EJS-ACT-PD) that will start by assessing the effectiveness of three compound arms compared to one placebo arm (Foltynie *et al.*, 2024). Participants showing a lack of response to medication will be able to change treatment after a designated period of time to target a different dysfunctional pathway and thus, hopefully, their PD (Gonzalez-Robles *et al.*, 2023). The EJS-ACT-PD trial is expected to expand to six compounds in the future (Foltynie *et al.*, 2024), which could drastically improve the likelihood of finding a successful compound. However, studies of this magnitude are expensive and time-consuming. If stratification before treatment was possible it would greatly increase the likelihood of success for each patient and minimise costs due to extended timelines required to allow patients to switch treatment arms.

3.3.2 Mechanistic Heterogeneity

As mentioned previously, heterogeneity is present in the PD population both mechanistically and clinically. The first aim of this study was to further our understanding of mitochondrial and lysosomal heterogeneity in PD. Disease models such as toxin or genetic models have provided a good foundation for our understanding of PD mechanisms, specifically since the identification of genetic mutations that drive PD. However, they cannot provide an understanding of heterogeneity in sporadic disease. Studies using patient samples are therefore crucial to understand the heterogeneous complexities of PD.

Our study found no significant differences between the patient population and controls across thirteen mitochondrial and lysosomal parameters in galactose. Mitochondrial form factor, small mitochondrial form factor and long vs small mitochondria ratio were significantly increased in the patient population when cultured in glucose. Significantly more variability was observed in the PD population compared to the controls in all parameters in glucose and nine parameters in galactose. This is in keeping with results from Carling *et al.* (2020), who found no difference in ATP levels or MMP between the PD and control populations. However, the patient population was significantly more variable than the controls. Likewise, Milanese *et al.* (2019), assessed basal respiration in glucose and galactose conditions finding no difference between patients and controls when pooled, but variation in the patients is greater than in the controls (not statistically measured). Heterogeneity in the fibroblast lines ATP/ADP ratio was also observed. Both studies align with our results showing that mitochondrial function in PD patient fibroblasts is heterogeneous. Glucose and galactose conditions were utilised to unmask mitochondrial abnormalities in the patient-derived fibroblasts. Fibroblasts rely on glycolysis as the main source of ATP production (Bernard *et al.*, 2007). Culturing in galactose for 72 hrs causes the cell to rely on oxidative phosphorylation as glycolysis of galactose does not yield ATP (Galant *et al.*, 2024). It is possible that patients with high-functioning mitochondria in glucose become metabolically exhausted in galactose due to higher energy demands and that patients with lower-functioning mitochondria in glucose increase mitochondrial function in galactose to compensate. This would result in less variation under galactose conditions.

Mitochondrial form factor and long vs small mitochondria ratio were significantly increased in the PD population in glucose media. The long mitochondria population also had an increased form factor in the PD population. This shows an elongation and interconnectivity of the mitochondria, particularly in longer mitochondria. There are two theories for this phenotype. Firstly, mitochondria may increase fusion to share mitochondrial metabolites and mtDNA. Increased fusion is observed in response to glucose starvation and it is theorised that the sharing of metabolites enhances the networks' function

(Mishra and Chan, 2016). Cells cultured in galactose increase their mitochondrial length (Rossignol *et al.*, 2004; Galant *et al.*, 2024). The increased interconnectivity in PD patients in glucose but not in galactose suggests that their mitochondria are already elongated in PD and that culturing in galactose causes an increased elongation in the controls. Fusion and fission are required to maintain a functional network and cell. It is possible that further fusion cannot occur in the patients in galactose media as it may result in network decline and cell death. In theory, a lack of metabolic flexibility in the patients would have greater implications on neurons than other cell types, explaining their vulnerability in PD. On the other hand, mitochondria length may be due to dysfunctional mitochondrial fission, which occurs in cells with Parkin mutations or deficiencies (Kamienieva, Duszyński and Szczepanowska, 2021). Fission is the first step in mitophagy, which is dysfunctional in PD (Malpartida *et al.*, 2021) and could result in a more fused and dysfunctional network.

Studies in large cohorts of PD patients have not assessed lysosomes generally. Carling *et al.* (2020) is the only study of note. We identified significantly more variation in the number of lysosomes per cell and lysosome form factor between control and patient groups but no difference in population means. The average area of the lysosomes was significantly more variable in glucose but not galactose conditions. The previous study found greater variation in lysosome number per cell and total lysosome area in the patient population, although, a significant increase in both parameters compared to the controls was observed. The difference in PD population means for the number of lysosomes per cell may be due to population sampling differences. Although a study size of thirty-four patients is a vastly improved number on most studies, the Carling study assessed one hundred patients. Due to the difference in size, the percentage of patients affected by lysosome dysfunction specifically the increased number may be different between the groups. Another explanation is that difference in glucose concentration during biopsy establishment and maintenance may alter lysosome acidification and content to different extents in patients and controls. Carling *et al.* (2020) used high glucose DMEM to establish skin biopsies and culture the fibroblasts whereas low glucose EMEM was used for this study. Glucose depletion results in the assembly of v-ATPase pumps in the lysosome membrane that drive acidification (Parra and Hayek, 2018). Further investigation of the lysosome response to glucose is required in both patient and control fibroblasts.

3.3.3 Stratification

3.3.3.1 Sporadic Parkinson's Disease

Multiple studies have attempted to stratify sPD, but none have been successfully utilised in clinical trials. Several methods have been developed including clinical, genetic, biomarker and phenotypic. Each method has advantages and disadvantages and should be used based on the purpose of

stratification. It is well-documented that cellular dysfunction does not correlate with clinical features (Carling *et al.*, 2020; Payne *et al.*, 2023; Arena *et al.*, 2024). Thus, to improve clinical trials, methods assessing biomarkers, disease phenotypes and genetics should be used. These attempt to form uniform groups whose disease is driven by a defining biological feature. With advancements in the genetic understanding of PD and reduction in genotyping costs, using genetics is a very viable method for stratification. Despite variation being present within genotypes the groups are far more homogenous than unstratified PD. However, genetic mutations in PD, particularly in certain ethnic populations, are rare (Singleton, Farrer and Bonifati, 2013; Lill, 2016; Bandres-Ciga *et al.*, 2020). Not only this but the therapeutic agent has to target that specific genetic cause. This makes it difficult to use genetic classification for large studies, such as Phase III trials.

Selecting patients based on genetic risk variants, which are identified by GWAS studies, and polygenic risk scores could enable the selection of larger populations. Polygenic risk scores combine the risk associated with variants into one individual score per person. To do this risk variants are assigned a weighting based on the level of risk they cause. Many polygenic risk score studies are still in the early stages, attempting to differentiate between healthy individuals and PD patients (Dehestani, Liu and Gasser, 2021). A mitochondrial polygenic risk score has been developed for sPD that stratifies patients based on oxidative phosphorylation gene variants and initial results show differential effectiveness of UDCA treatment on patients within the two groups (Arena *et al.*, 2024).

To date, only one study has attempted to stratify patients based on the dysfunction observed in individual patient cells. In theory, stratification via this method should produce groups based on the primary mechanism of disease enabling a targeted therapeutic approach. Carling *et al.* (2020) subtyped sPD patients and found two groups. One defined by mitochondrial dysfunction and one defined by lysosomal dysfunction. Initial stratification was based on ATP levels and lysosomes per cell. This study provided a foundation for the methodology used in this PhD project. The number of parameters assessed were expanded to ten mitochondrial parameters and three lysosomal parameters. The mitochondrial parameters spanned functional, morphological and distribution measures to completely assess mitochondrial health. Lysosomal parameters enabled a better understanding of the lysosome's morphology and not just the quantity of the lysosomes. In this new approach we used composite z-scoring to combine parameters enabling the calculation of scores for mitochondrial and lysosomal dysfunction. The aim was to produce a score that enabled the rapid identification of patients whose PD was driven by mitochondrial abnormalities or lysosomal dysfunction, followed by further interrogation of the data to form subgroups. z-scoring is a method commonly utilised by psychologists to combine results from tests with unequal scoring (PsychAssessment.com.au). This was important as subtle changes in one parameter may be masked

by large changes in another. For instance, mitochondrial form factor, which had a standard deviation of less than 1.4 %, would have very little effect on a mitochondrial dysfunction score if combined with ATP levels, which had a standard deviation of over 17.9 %. This would unequally weight the scores; however, z-scoring provides a uniform scale that can be combined equally (Wiesen, 2006).

z-scores not only provided a method for scoring organelle dysfunction, but their use enabled the easy identification of degrees of dysfunction within individual parameters. The z-score for each parameter for each patient shows how different the cell line is from the average of the controls. Combination using the coefficient of covariance prevents repeats or media conditions with greater variation from introducing bias (PsychAssessment.com.au). Thus, enabling the identification of patterns of abnormalities and the degree of abnormality across parameters per patient. This methodology has never been attempted before to stratify PD patients.

Stratification this way is hypothesis-based and has advantages and disadvantages. The scoring method and stratification use biologically meaningful results, which can allude to possible dysfunctional mechanisms and define the group by characteristics that can be targeted therapeutically. However, it relies upon human bias. Parameters were selected based on our expertise and previous literature, which limits the breadth of information that is used to stratify groups and may incorrectly stratify individuals who are defined by a parameter that was excluded. Further human bias could be introduced when identifying patterns of dysfunction manually. These all introduce a level of error that cannot be avoided in hypothesis-based approaches.

A prediction classifier, based on machine learning, could have been used to identify groups using an unbiased approach for stratification (D'Sa *et al.*, 2023). This method is advantageous because it does not limit classification to human-selected parameters and therefore, does not bias classification to specific parameters, but it is still limited to the parameters that are measured. This method also removes human error in the identification of patterns of dysfunction, because it uses computers to process vast quantities of data including complex image texture and morphological profiles that the human brain cannot. However, this approach is not truly unbiased. The classifier is trained using example images, which bias the classification towards specific cellular profiles. One example study is D'Sa et al. (2023), who used patients with genetic mutations and toxin models to train the prediction classifier. This method would be highly effective if these models accurately replicated subgroups, but this is unknown and arguably unlikely. Eventually, the development of an artificial intelligence method of stratification that can use biologically meaningful parameters and image analysis parameters to identify groups without prior subgroup training. This method would require training using a diverse control population. However, this technique was not available for this PhD project. Therefore, the

hypothesis-based method was selected because, despite its drawbacks, we believe it identifies the most biologically meaningful subgroups that could be targeted therapeutically effectively.

Four distinct subgroups were identified using this new methodology. A mitochondrial dysfunction subgroup, a lysosomal dysfunction subgroup and two groups defined by mitochondrial and lysosomal dysfunction (high mixed group and low mixed group). The mitochondrial dysfunction subgroup was defined by a reduced MMP and perinuclear mitochondria percentage but elevated ATP levels and mitochondria per cell. No differences in lysosome size or form factor were observed in any of the patients. Compared to the mean of the control population, a small increase in lysosome count was observed. This difference was minimal, however, compared to the difference observed in other patients. It is important to note that these patients do not share the same phenotype as the mitochondrial dysfunction subgroup in the previous study as those patients were defined by reduced ATP levels (Carling *et al.*, 2020). Reduced MMP is commonly associated with PD, this phenotype is observed after treatment with MPTP, but is also seen in Parkin, LRRK2 and sporadic patient fibroblasts. However, Parkin and LRRK2 patient-derived fibroblasts usually have reduced ATP levels (Mortiboys *et al.*, 2008, 2010; Grünewald *et al.*, 2010, 2014; Papkovskaia *et al.*, 2012; Haylett *et al.*, 2016). This subgroup will be further explored in Chapter 5.

The lysosomal dysfunction subgroup patients had fewer lysosomes and smaller lysosomes than the controls. These patients also had an increased mitochondrial form factor and ratio of long to small mitochondria suggesting an elongation of the network. However, no functional mitochondrial parameters were similar or extreme. Diseases with a reduced number of lysosomes are relatively rare. Lysosomal storage disorders are arguably the most researched diseases involving lysosome dysfunction. No lysosomal storage disorder is associated with a reduced number of lysosomes, the majority involve an increased number due to substrate accumulation with the vacuolar organelle (Platt, 2018). Deficits in autophagy may lead to reduced numbers of lysosomes due to a lack of fusion between autophagosomes and lysosomes, as seen with bafilomycin A1 treatment (Yoshimori *et al.*, 1991). Although, the majority of studies report an increase in lysosome number in PD, several studies have identified patients with depletions. Treatment of mice and BE-M17 neuroblastoma cells with MPTP caused depletion of lysosomes (Dehay *et al.*, 2010) and dopaminergic neurons in patients' SN have depleted LAMP1/LAMP2 levels suggesting a reduction in lysosome number (Alvarez-Erviti *et al.*, 2010; Dehay *et al.*, 2010). This group will be further explored in Chapter 4.

The mixed groups both display extreme mitochondrial and lysosomal dysfunction. However, the patterns of dysfunction are completely different. Patients in the high mixed group display elevated mitochondria and lysosome numbers per cell but reduced MMP and perinuclear mitochondria

percentage. Three of the patients have elevated ATP levels. In contrast, the low mixed group has a reduced number of lysosomes and mitochondria and reduced ATP levels, but elevated MMP levels and percentage of mitochondria within the perinuclear region. No uniform mitochondrial morphology abnormalities were observed in the low mixed group, but the long mitochondria form factor was increased in all patients in the high mixed group suggesting an increase in branching and possible elongation, a phenotype that has been observed in some LRRK2 and Parkin patient fibroblasts (Mortiboys *et al.*, 2008, 2010). Similarities between the mitochondrial dysfunction subgroup and high mixed groups can be observed. Likewise, lysosome phenotypes in the low mixed group and lysosomal dysfunction subgroup are similar. It could be argued that, instead of identifying four groups, this study has identified two groups with patients at different stages of disease. It is possible that the groups with single organelle dysfunction represent the early stages of the disease, unveiling the triggering mechanism of the disease and the mixed groups represent patients in later stages of the disease. The cells of the mixed group patients may have altered organelle function and morphology in an attempt to compensate for damage or the organelles may have become dysfunctional due to a build-up of damage from the driving mechanism. All patients for this study were biopsied within 3 years of diagnosis to capture the earliest stages of the disease and measure the driving mechanisms of the disease without secondary dysfunction where possible. Patients also reported symptom onset, with an average of three and a half years prior to biopsy and a maximum time of eleven years. However, the patients that were classified into the mixed groups were all biopsied within two years of diagnosis and three years of symptom onset, except for ATP001 whose symptoms manifested nine years prior to biopsy. This suggests that there are four distinct groups rather than two. Of course, disease progresses differently in different patients and differences in grouping will be explored in a longitudinal study by Rhiannon Brown which is currently underway.

Thirty-eight percent of the cohort were stratified into subgroups based on mitochondrial and lysosomal dysfunction. The remaining patients were unstratified for a variety of reasons. Firstly, the patients showed similar patterns of dysfunction to a subgroup, but with less extreme phenotypes, such as ATP023 (Appendix 3: Table 32). However, to enable validation and further investigation we limited groups to the three/four patients with the most extreme dysfunction. Limiting group size enabled the maximum investigation with the time and funding available. Expansion of the subgroups could be conducted upon success of initial validation. Secondly, several patients displayed unique patterns of dysfunction. ATP046 for instance has higher ATP, MMP and mitochondria per cell (Appendix 3: Table 32), which is inconsistent with any of the subgroups but highlights clear mitochondrial dysfunction. Our cohort consisted of thirty-four patients, thus, provides an assessment of a small sample of the sPD population. The patients with unique patterns of dysfunction may

represent rare subgroups that would require larger sample sizes to detect or a subgroup that was insufficiently sampled by chance. Finally, several patients showed no mitochondrial or lysosomal dysfunction, such as ATP007 (Appendix 3: Table 32). Multiple mechanisms, beside mitochondrial and lysosomal dysfunction, have been shown to drive PD including α-syn toxicity, inflammation and oxidative stress. Thus, it was hypothesised that PD in patients lacking mitochondrial and lysosomal dysfunction is driven by an alternative mechanism of disease. As discussed previously, fibroblasts are poor models for studying these mechanisms and therefore, we were unable to investigate this theory. Further studies reprogramming the patient fibroblasts into stem cells or assessing other bio-samples could uncover subgroups caused by these mechanisms. This theory is further supported by the expected results in patient ATP049, whose PD is driven by an SNCA G51D mutation. This patient had the lowest score for mitochondrial dysfunction indicating no mitochondrial abnormalities and was in the bottom 15 % for lysosomal dysfunction, again indicating normal lysosomes. Although, studies of SNCA mutations have reported mitochondrial (Tanaka *et al.*, 2001; Nakamura *et al.*, 2011; Arias-Fuenzalida *et al.*, 2017) and lysosomal dysfunction (Cuervo *et al.*, 2004; Xilouri *et al.*, 2009), fibroblasts express extremely low levels of α-syn (Hoepken *et al.*, 2008). Therefore, the issues resulting from α-syn driven PD are unlikely to be observed in fibroblasts.

3.3.3.2 LRRK2

Several studies have reported reduced MMP and/or ATP in LRRK2 G2019S patient-derived fibroblasts (Mortiboys *et al.*, 2010, 2015; Papkovskaia *et al.*, 2012; Su and Qi, 2013; Grünewald *et al.*, 2014). One study reported no difference in MMP or ATP in galactose media, but elevated MMP and reduced ATP in high glucose (Juárez-Flores *et al.*, 2018). However, assessments of respiration have produced more conflicting results. Papkovskaia *et al.* (2012) showed elevated oxygen consumption during basal and maximal respiration, Grünewald *et al.* (2014) found no difference in either state and Mortiboys *et al.* (2015) observed reduced basal and maximal respiration. This change in respiratory capacity may be due to the culturing conditions; Papkovskaia et al. and Grünewald et al. used high glucose media, while Mortiboys et al. used low glucose and galactose media. Reports of mitochondrial form factor also differed significantly (Mortiboys *et al.*, 2010; Grünewald *et al.*, 2014; Juárez-Flores *et al.*, 2018). No differences in ATP or MMP were observed in any of the LRRK2 lines in galactose media in this study and only a small reduction in MMP was observed in high glucose media for two of the LRRK2 lines. The galactose results are consistent with one previous study (Juárez-Flores *et al.*, 2018) but differ from the majority of reports (Mortiboys *et al.*, 2010, 2015; Papkovskaia *et al.*, 2012; Grünewald *et al.*, 2014). Interestingly, complex I activity is upregulated in non-manifesting LRRK2 G2019S carriers but reports of ATP levels were again conflicting (Mortiboys *et al.*, 2015; Juárez-Flores *et al.*, 2018). It is possible that mitochondrial function is upregulated in non-manifesting LRRK2 mutation carriers as a

compensatory mechanism, which results in exhaustion and subsequent failure to maintain the elevated function required (Juárez-Flores *et al.*, 2018). This may account for the differences observed between the results of this study and previous work.

Mitochondria morphology, however, did differ in this PhD project. All three lines showed decreases in mitochondrial form factor in high glucose media and two lines in galactose conditions, which was due to a reduced form factor in the small mitochondrial population. The reduced branching corresponded with a reduction in the ratio of long to small mitochondria demonstrating a fragmentation of the network in LRRK2 1 and 2. This is consistent with Grünewald *et al.* (2014) and Juárez-Flores *et al.* (2018). LRRK2 3 showed the opposite with an increased form factor in the long mitochondria population in galactose suggesting increased branching, consistent with observations by Mortiboys *et al.* (2010). Results from the four studies suggest that mitochondrial morphology can differ between LRRK2 patients and that growth in galactose conditions can exacerbate abnormalities. Similar to function, LRRK2 G2019S non-manifesting carriers had a different phenotype to manifesting carriers. The mitochondria were elongated in the non-manifesting and smaller in the manifesting patients (Juárez-Flores *et al.*, 2018). It is possible that elongation occurs to maintain a compensatory high-functioning network, which results in network failure and fragmentation through the course of the disease. Therefore, assessing patients at different stages of disease may uncover a reason for this heterogeneity.

LRRK2 is implicated in autophagy regulation and many studies in patient-derived cells and transfected cell models have reported alterations in lysosomes, specifically an increase in lysosome count/content and enlargement (MacLeod *et al.*, 2006, 2013; Bravo-San Pedro *et al.*, 2013; Hockey *et al.*, 2015; Schapansky *et al.*, 2018). Consistent with these reports all three lines had an increased number of lysosomes in high glucose and LRRK2 1 and 3 remained high in galactose. LRRK2 2 and 3's lysosomes were swollen in both conditions and LRRK2 1's were enlarged in galactose. This suggests a blockage in lysosome degradation leading to cargo full lysosomes remaining in the cell. This phenotype matched the lysosomes seen in the high mixed group. LRRK2 is involved in endosome mannose-6-phosphate receptor trafficking to the lysosome (MacLeod *et al.*, 2013). Mannose-6-phosphate receptors package hydrolases and chaperone them to the lysosome, suggesting a reduction in degradation capabilities (MacLeod *et al.*, 2013). Other studies have supported this theory showing reduced degradation in the lysosome (Orenstein *et al.*, 2013; Henry *et al.*, 2015). In neurons, the lack of degrading ability appears to result in α-syn build-up in the lysosomes (Orenstein *et al.*, 2013). Due to low α-syn expression levels in fibroblasts this should be investigated in iPSC or iNPC-derived neurons by future studies.

3.3.3.3 GBA

Most of the research into *GBA1* mutations has focused on the lysosomal activity of the GCase enzyme, transport to the lysosome and its effect on α-syn. Very little has investigated mitochondrial function. Various models of disease, including patient-derived GBA N370S iPSC-derived neurons have demonstrated that GCase mutations or reduced activity via knockdown or inhibition results in reduced mitochondrial function (Cleeter *et al.*, 2013; Osellame *et al.*, 2013; S. Kim *et al.*, 2021). However, morphology differed between models. *Gba1* heterozygous knockout mouse neurons show a non-significant increase in elongated mitochondrial networks (Osellame *et al.*, 2013). In contrast, inhibition or knockdown of GCase in SH-SY5Y cells was associated with significant fragmentation of the network (Cleeter *et al.*, 2013). The patient-derived GBA N370S iPSC-derived iDA neuron model showed reduced mitochondria density (S. Kim *et al.*, 2021). Recent findings have shown that GCase contains a mitochondrial targeting sequence and is imported into the mitochondria where it regulates complex I assembly. Heterozygous mutations (L444P and E328K) in GBA cause reduced complex I activity due to defects in assembly (Baden *et al.*, 2023). In this project, the two GBA patients showed opposing mitochondrial phenotypes. One showed elevated ATP and mitochondria per cell but reduced MMP. An increase in long mitochondria branching was observed as well. In contrast, the other showed smaller changes with reduced ATP and a slight increase in MMP. This line also showed significant fragmentation of the network. GBA mutations are only risk factors for disease and N370S is the mildest type associated with PD (Smith and Schapira, 2022). It is possible that mitochondrial problems in these lines are a result of environmental and lifestyle damage (Marras, Canning and Goldman, 2019) rather than direct results of the mutations. Many nutrients restore mitochondria function (Capriglia *et al.*, 2023) and several environmental toxins have been linked with mitochondrial dysfunction (Park, Davis and Sue, 2018). Increased mitochondrial form factor and long vs small mitochondria ratio have been reported in L444P mutant mice hippocampal neurons and L444P patient-derived fibroblasts (Li *et al.*, 2019). This mutation is far more severe than N370S (Smith and Schapira, 2022) but could suggest an impact of GBA on mitochondria morphology as seen in one of the patients in our study. Interestingly, the N370S mutations impact on complex I activity was not reported by Baden *et al.* (2023). This mutation may not impact complex I function or mitochondrial function. Larger cohorts of patient-derived fibroblasts with GBA mutants would be required to understand mitochondrial dysfunction in the GBA PD population.

Two studies of GBA heterozygous PD patients, one of GBA E326K and the other of GBA N370S, found no difference in LAMP1 content suggesting no change in lysosome levels (McNeill *et al.*, 2014; Thomas *et al.*, 2021). An assessment of the data in Thomas *et al.* (2021), showed that despite no change in population means, the GBA patients had variable lysosome content, one patient had very high LAMP1

levels and several had low LAMP1 levels compared to the majority of the controls. Another study of GBA N370S fibroblasts showed elevated lysosome content and lysosome clustering (García-Sanz *et al.*, 2017), which aligns with the elevated levels seen in postmortem GBA patient cingulate cortex (Li *et al.*, 2019). Mixed results have been seen in iDA neurons with one study showing no difference (Yang *et al.*, 2020) and another observing increased lysosome numbers and size (Schöndorf *et al.*, 2014). Evaluation of the GBA patients in this project identified one patient (GBA 1) with a reduced number of lysosomes and smaller lysosomes; this was only observed under high glucose conditions. The other patient (GBA 2) had enlarged lysosomes and an increased number of lysosomes in both media conditions. The difference in lysosome phenotype between GBA 1 in high glucose and galactose may be due to glucose depletion. The mammalian v-ATPase assembles upon glucose depletion driving acidification of the lysosomes (Parra and Hayek, 2018). If the GBA patients are under heightened stress, they may have a greater response to glucose depletion resulting in the acidification of more lysosomes, enabling their detection by lysotracker. Other studies would not have observed this, except García-Sanz *et al.* (2017), as previous studies measured lysosome content by the presence of LAMP1 and not acidic lysosomes. García-Sanz *et al.* (2017) only assessed fibroblasts in high glucose media so sensitivity to glucose depletion would not have been detected. GBA 2 resembles the phenotype observed in many lysosome storage disorders and aligns with the observed phenotype in some studies (Schöndorf *et al.*, 2014; García-Sanz *et al.*, 2017; Li *et al.*, 2019). Swollen lysosomes suggest an increase in undegraded cargo. Multiple studies have identified reduced glycosidase and protease activity in GBA patients (García-Sanz *et al.*, 2017; Collins *et al.*, 2018; Yang *et al.*, 2020; Smith *et al.*, 2023) suggesting a disruption in recycling that could result in lysosome swelling. Results from this study suggest that GBA patients can have varying dysfunctional pathways. This is expected as GBA mutations are risk factors and only 9.1 % of carriers develop PD (Riboldi and Di Fonzo, 2019). Other factors such as lifestyle (Marras, Canning and Goldman, 2019), exposure to environmental toxins (De Miranda *et al.*, 2022) and genetic variants are likely required to cause PD manifestation, much like sPD. Therefore, aside from activity deficits, variable phenotypes would be expected. Larger studies of GBA patients at early stages of manifestation would be required to investigate this hypothesis.

3.3.3.4 LRRK2 and GBA

It is still unclear what role LRRK2 plays in GCase regulation. A study of GCase activity in LRRK2 G2019S iPSC-derived iNeurons reported reduced GCase activity (Ysselstein *et al.*, 2021), while a recent study identified variable activity, one patient had increased activity, two patients were normal and one had reduced activity (Labrador-Garrido *et al.*, 2023). Similar activity variability was also reported in the sPD patients in this study (Labrador-Garrido *et al.*, 2023). Assessment of GCase activity in the blood of LRRK2 patients showed elevated GCase activity (Alcalay *et al.*, 2015; Sosero and Gan-Or, 2023).

However, due to the different tissues and methods of GCase activity assessment, it is unclear how LRRK2 affects GCase. Alterations may be cell type dependent as a study noted elevated GCase activity in LRRK2 G2019S fibroblasts, no differences in iPSC-derived iNeurons and increased activity in the PBMCs (Kedariti *et al.*, 2022). Patients carrying LRRK2 and GBA mutations have a slower cognitive decline, lower rates of depression and less severe MDS-UPDRS scores than patients with GBA mutations, suggesting a protective effect of LRRK2 mutations (Yahalom *et al.*, 2019; Omer *et al.*, 2020; Ortega *et al.*, 2021). This theory aligns with the results observed in the LRRK2 G2019S, GBA N370S patient. No difference in mitochondrial function was observed suggesting they are protected. The reduction in form factor and long vs small mitochondria ratio observed in galactose may highlight elevated fission resulting in increased mitophagy to maintain the network. Combined with an increase in long mitochondrial MMP suggests that the network is high functioning and trimming dysfunctional segments efficiently. This patient still developed PD. Neurons have a higher mitochondrial demand than fibroblasts. Therefore, the protection may become insufficient in neurons earlier than in the fibroblasts, which would explain the observed lack of dysfunction but the manifestation of disease.

Swelling of the lysosomes is observed in both GBA and LRRK2 patients (MacLeod *et al.*, 2013; Henry *et al.*, 2015; Hockey *et al.*, 2015). The LRRK2/GBA patient displayed enlarged lysosomes suggesting dysfunction in lysosome degradation. Both LRRK2 and GCase interact directly with the mitochondria (Singh, Zhi and Zhang, 2019; Baden *et al.*, 2023). It is possible that elevated LRRK2 kinase activity combined with GBA mutations prevent mitochondrial dysfunction, but their functions in lysosomes are independent so dysfunction occurs. This may lead to lysosomal dysfunction-driven PD without mitochondrial dysfunction, possibly leading to less severe and later manifestation of the disease. However, it should be noted that cells from very few patients with dual mutations have ever been assessed and this theory comes from results in one patient. Studies with a greater number of individuals would be required to investigate the association further.

3.3.3.5 Parkin

Parkin mutations are heterogeneous with over 140 pathogenic variants identified. Age of onset can vary between seven and seventy-one years old (Menon *et al.*, 2024). Three patients carrying pathogenic Parkin mutations were assessed during this PhD. One was identified in the initial screen, via genetic assessment, carrying a homozygous (c.337-376del) in exon 3 resulting in a frameshift. Her age at the onset of symptoms was forty-two years old. Two sisters were obtained from Dr Narendra's lab, these carried V56E point mutations and partial gene deletions including exon 7. Their age at onset was thirty-five and thirty-two years old.

Previous studies have identified varied mitochondrial dysfunction phenotypes in Parkin patient-derived fibroblasts (Mortiboys *et al.*, 2008; Grünewald *et al.*, 2010; Zanellati *et al.*, 2015; Haylett *et al.*, 2016; Kamienieva *et al.*, 2023). ATP levels were reduced in Parkin patient-derived fibroblasts but to varying degrees (Mortiboys *et al.*, 2008; Grünewald *et al.*, 2010; Zanellati *et al.*, 2015). Some studies reported decreased MMP (Mortiboys *et al.*, 2008; Haylett *et al.*, 2016) and some reported no difference (Grünewald, Kumar and Sue, 2019; Kamienieva *et al.*, 2023). This suggests MMP can vary depending on the patient and mutation but could also be due to different methods of assessment. Mitochondrial mass varied showing an increase (Grünewald *et al.*, 2010) or no change in mass (Mortiboys *et al.*, 2008; Kamienieva *et al.*, 2023). Similarly, form factor varied, either increased (Mortiboys *et al.*, 2008), decreased (Haylett *et al.*, 2016) or no change (Grünewald *et al.*, 2010; Kamienieva *et al.*, 2023). It is important to note that assays, culturing conditions and mutations varied amongst these studies and it is unclear what accounts for the variation. The Parkin patient in the initial screen had reduced MMP, mildly reduced ATP (10-15 %) and reduced perinuclear mitochondria percentage under both media conditions. The reduced MMP is consistent with the varied MMP observed in the previous studies (Mortiboys *et al.*, 2008; Haylett *et al.*, 2016), however, ATP reductions were far milder (Mortiboys *et al.*, 2008; Grünewald *et al.*, 2014; Zanellati *et al.*, 2015). No difference in mitochondria count or form factor were observed in our Parkin patient again replicating some of the previous studies (Mortiboys *et al.*, 2008; Grünewald *et al.*, 2014; Kamienieva *et al.*, 2023). Mortiboys *et al.* (2008), was the only study to assess fibroblasts in low glucose and galactose conditions. These patients had a far more extreme phenotype, however, all these patients carried exon 2 deletions, which could account for the different degrees of dysfunction.

The two sisters carrying Parkin mutations showed varied results. Both had similar ages of onset; however, they were biopsied after different disease duration (Parkin 1 = 15 years, Parkin 2 = 7 years). Parkin 1 showed no difference in MMP, ATP or mitochondria per cell. In contrast, Parkin 2 showed reduced MMP in high glucose and increased mitochondria per cell in galactose. Both sisters had reduced long vs small mitochondria ratios and reductions in form factor suggesting fragmentation of the network, like Haylett *et al.* (2016) observed. Only one patient assessed in the previous literature carried an exon 7 deletion. The difference in deletion may account for different mitochondrial phenotypes to previous reports. The sisters, however, have the same mutation and different degrees of mitochondrial dysfunction, a similar difference was seen in the sisters assessed by Haylett *et al.* (2016). Disease duration does not account for the worsened dysfunction in either study. Other factors such as lifestyle (Marras, Canning and Goldman, 2019; Gabbert *et al.*, 2023), environmental factors (De Miranda *et al.*, 2022) and age at biopsy may be the cause of these differences.

Lysosome dysfunction has not been researched in Parkin-mediated PD. Research has focused on the role of Parkin in mitophagy initiation, mitochondrial derived vesicle formation and mitochondrial and lysosomal contact sites. Lysosome count and size were increased in both patients in glucose media, but no difference was observed in galactose media. The increase in lysosomes may be a response to increased mitochondrial dysfunction in an attempt to clear damaged mitochondria (Malik *et al.*, 2023). This heightened response may not be able to compensate further when subjected to glucose depletion (Parra and Hayek, 2018), resulting in no difference between controls and patients in galactose media.

3.3.4 Conclusions

In this chapter, the mitochondrial and lysosomal dysfunction in a new cohort of sPD patients was assessed. The PD population exhibited greater variability than the controls in the majority of parameters in both glucose and galactose conditions. Mitochondrial morphology parameters were the only parameters to differ between the populations showing an increase in mitochondrial interconnectivity. In depth investigation into patterns of mitochondrial and lysosomal dysfunction enabled the identification of four distinct subgroups. Interestingly, no consistent phenotype was observed in the LRRK2 or GBA mutation carriers and the Parkin patients showed limited mitochondrial dysfunction. Thus, none of the genotypes showed similar patterns of dysfunction to the sPD subgroups. The stratification of the cohort established a foundation for further work to validate the subgroups and investigate mechanisms of disease, which will be discussed in the following chapters. Ultimately, stratification of PD by disease mechanism could improve participant selection for clinical trials, increasing the chance of success. Further work and expansion could enable a personalised treatment approach that would provide the best care outcomes for patients once treatments become widely available. Stratification of patients based on mitochondrial and lysosomal dysfunction is not the entire answer. Its use as part of a detailed stratification method alongside assessments of polygenic risk scores, genetic variants, inflammation and the microbiome could provide the platform for treatment that the Parkinson's community is searching for.

4 Chapter 4: Validation and Investigation of the Lysosomal Dysfunction Subgroup

4.1 Introduction

Dysfunction in the clearance of proteins has long been described in PD, however, much of this work has focused on α-syn and its aggregation. Lysosomes play an integral role in the recycling of cellular and extracellular components. They are small membranous compartments that contain degrading enzymes, called hydrolases, and undergo acidification (Cooper and Hausman, 2007). This process of transport and degradation is exceptionally important in neurons due to their morphology and age. Lysosomes are mainly gathered in the soma of neurons and due to the greater proportion of cytoplasm in axons and dendrites, efficiency is crucial and results in neurons being easily overwhelmed (Colacurcio and Nixon, 2016). This results in neurons being exquisitely sensitive to lysosomal changes and is possibly the cause of CNS degradation in many lysosomal storage disorders and neurodegenerative diseases. Lysosomal dysfunction has been linked to multiple genetic variants that are associated with fPD (Funayama *et al.*, 2002; Ramirez *et al.*, 2006; Zimprich *et al.*, 2011; Lesage *et al.*, 2016; Milanowski *et al.*, 2022) as well as being identified in some sPD patients (Carling *et al.*, 2020; Thomas *et al.*, 2021).

Several genetic variants identified occur within hydrolases. Hydrolases enable lysosomes to degrade lipids, proteins and carbohydrates. Each hydrolase is structurally unique and targets specific substrate sites to cleave large molecules. Lysosomes compartmentalise these enzymes to ensure the safety of healthy cellular components and regulate the lumen microenvironment to control enzyme activity. Lysosomes acidify and mature upon fusion of an autophagosome or endosome. This process relies on v-ATPase, which is a proton pump in the lysosomal membrane. v-ATPases are structurally similar to the ATP synthase complex in mitochondria and are formed of 14 protein subunits arranged into two domains, a membrane-bound domain and a cytosolic domain. v-ATPases function by hydrolysing ATP to provide the energy required to transport H^+ ions into the lysosome lumen at a pH-dependent rate. The efflux and influx of other ions, such as Ca^{2+} and Cl^- ameliorate the electrogenic gradient produced. Acidification is essential to hydrolase activation. Many hydrolases operate optimally between pH 4.2-5.3, although, each enzyme has a different active range. For example, CatD, a non-specific aspartyl protease, functions optimally at pH 4.0 (as reviewed by Colacurcio and Nixon, 2016), and can only undergo autoactivation below pH 4.5 (Richo and Conner, 1994). In contrast, CatB, a cysteine protease, functions optimally at pH 6.0 but has been reported to function in the cytosol and extracellular matrix in diseases such as cancer, suggesting it is able to function at a neutral pH (Colacurcio and Nixon, 2016;

Yoon *et al.*, 2023). It is proposed that this gradual acidification enables a sequence of hydrolase activation to enable the breakdown of extremely complex cellular components such as mitochondria (Colacurcio and Nixon, 2016).

CatB, CatD and GCase are hydrolases that have been implicated in PD pathology (reviewed in 1.1.3.2 GBA and 1.3.2 Lysosomes in Parkinson's Disease). CatD activity is reduced in GBA mutation carriers, which is rescued when GCase activity is rescued by ambroxol (Yang *et al.*, 2020). A possible rescue mechanism is an increase in ceramide, a known activator of CatD (Heinrich *et al.*, 2000) and the product of GCase catalysis. CatD and CatB are involved in the clearance of α-syn by cleaving the monomers (Qiao *et al.*, 2008; Sevlever, Jiang and Yen, 2008; Cullen *et al.*, 2009; Crabtree *et al.*, 2014; R. McGlinchey and Lee, 2015; McGlinchey *et al.*, 2019). CatB cleaves α-syn into the truncated forms that have a higher propensity for aggregation (Baba *et al.*, 1998; Murray *et al.*, 2003; Levitan *et al.*, 2011; Ma *et al.*, 2018) and are the main forms identified in Lewy Bodies (R. McGlinchey and Lee, 2015; McGlinchey *et al.*, 2019). CatD cleave alternate sites on α-syn (McGlinchey *et al.*, 2019) and dysfunction may result in the generation of truncated forms of α-syn by CatB.

These findings all demonstrate that hydrolases and acidification play an important role in PD pathology and proteolysis deficits. Therefore, the investigation of lysosomes within our lysosomal subgroup was conducted by assessing lysosome morphology and pH, as well as CatB activity and CatD activity in the patient-derived fibroblasts and iDA neurons. Unfortunately, optimisation of the GCase activity assay was limited by time constraints.

4.2 Aims and Objectives

Hypothesis:

We hypothesise that the function of lysosomes within the lysosome dysfunction subgroup would be significantly reduced compared to controls and investigation would identify specific deleterious mechanisms that result in the disease.

This chapter aims to outline the investigation of lysosome function in the lysosomal dysfunction subgroup.

Objectives:

- To validate initial screening results.

- To investigate lysosome pH, hydrolase activity and morphology in the fibroblasts from patients in the subgroup.

- To investigate lysosome pH, hydrolase activity and morphology in iDA neurons from patients in the subgroup.

-To screen some lysosomal modulators and assess the effect on lysosomal morphology, pH and hydrolase activity.

4.3 Results

4.3.1 Assessment of Lysosomal Dysfunction in Patient-Derived Fibroblast.

The patients assessed were grouped into the lysosomal dysfunction subgroup. There was no trend in sex or age (Table 25). They were compared to three age- and sex-matched controls. Individual comparisons were statistically measured between each patient and the corresponding control and between the three controls and between each group when combined.

This subgroup was defined by a reduced number of lysosomes, which were also smaller than the controls lysosomes in the initial screening. These results were measured using the lysotracker green dye which localises to acidic compartments.

Table 25: A summary of the fibroblast cell lines that were assessed in the lysosomal dysfunction subgroup.

Cell line	Age at biopsy (years)	Sex
Patient 1	61	Male
Patient 2	66	Male
Patient 3	53	Female
Control 1	58	Male

Control 2	62	Male
Control 3	53	Female

4.3.1.1 Lysosome Number, Area and Size by LAMP2a Staining.

To validate initial screening LAMP2a staining was assessed. LAMP2a is localised to the lysosomal membrane enabling the measurement of lysosomal number, size and total lysosomal area (Figure 44). It is important to note that LAMP2a is present in all lysosomes regardless of their pH and enzyme activity. The assessment showed no difference in total lysosome area (Figure 45D) or number (Figure 45B) when comparing the patient and control groups. Individually the controls were very consistent. However, the patients were more variable. Patient 3 had significantly less lysosomes (25 % ± 5, p= 0.003, Figure 45A) and lower total lysosome area than Control 3 (24 % ± 4, p = 0.005, Figure 45C) in glucose conditions. Whereas, Patient 1 had an increased number (32 % ± 18, Figure 45) and total area (27 % ± 16, Figure 45C) in galactose. When assessing size, no significant difference was observed between the pooled groups (Figure 45F). Patient 1 had significantly smaller lysosomes compared to Control 1 in both conditions (glucose 4.5 % ± 1.7, p = 0.02, galactose 4.2 % ± 1.7, p =0.03, Figure 45E).

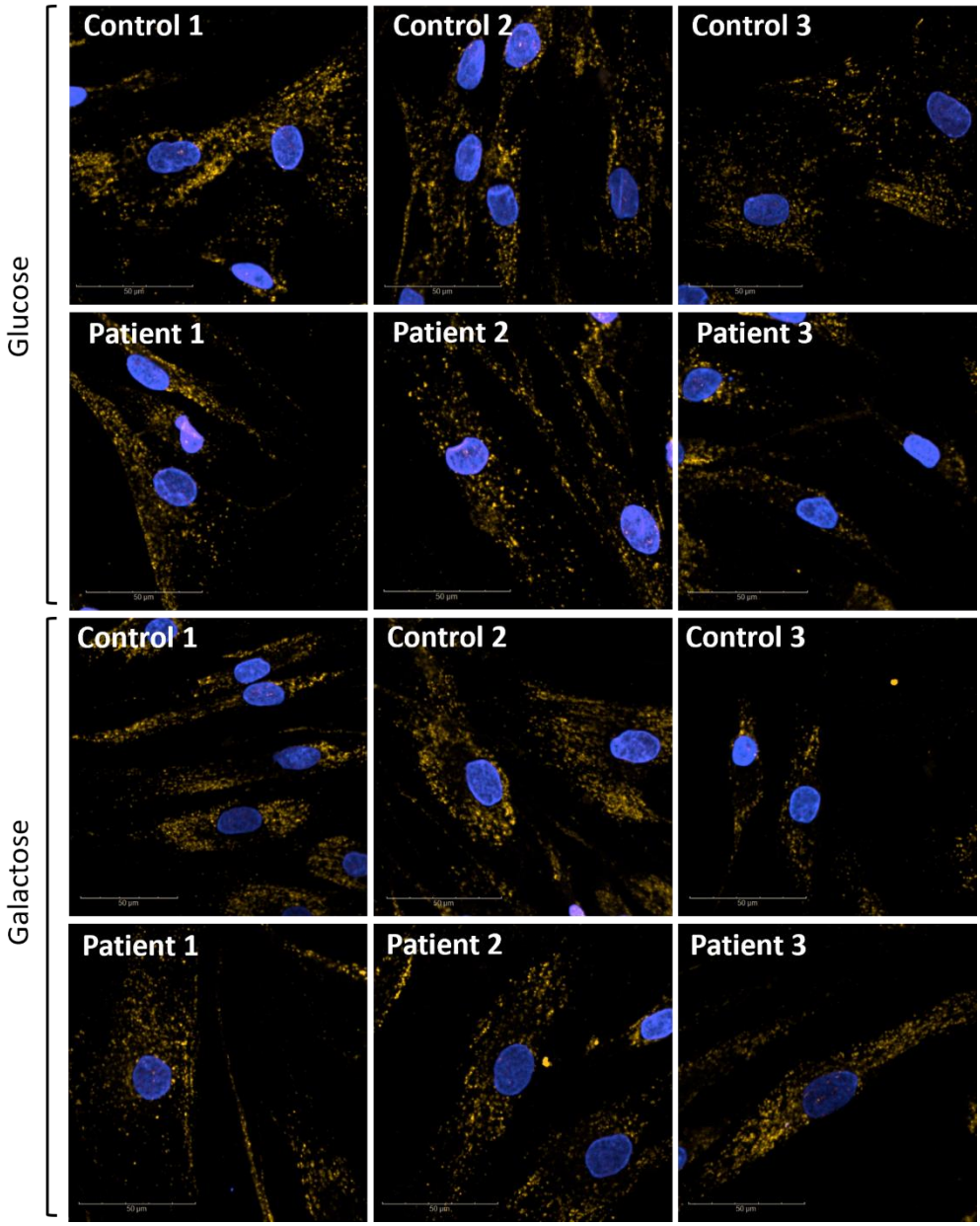

Figure 44: Representative images of LAMP2a stained lysosomes in patient-derived fibroblasts from the lysosomal dysfunction subgroup. Nuclei (blue) and lysosomes (orange). These lysosomes are stained regardless of functioning capability. Scale bar = 50 µm.

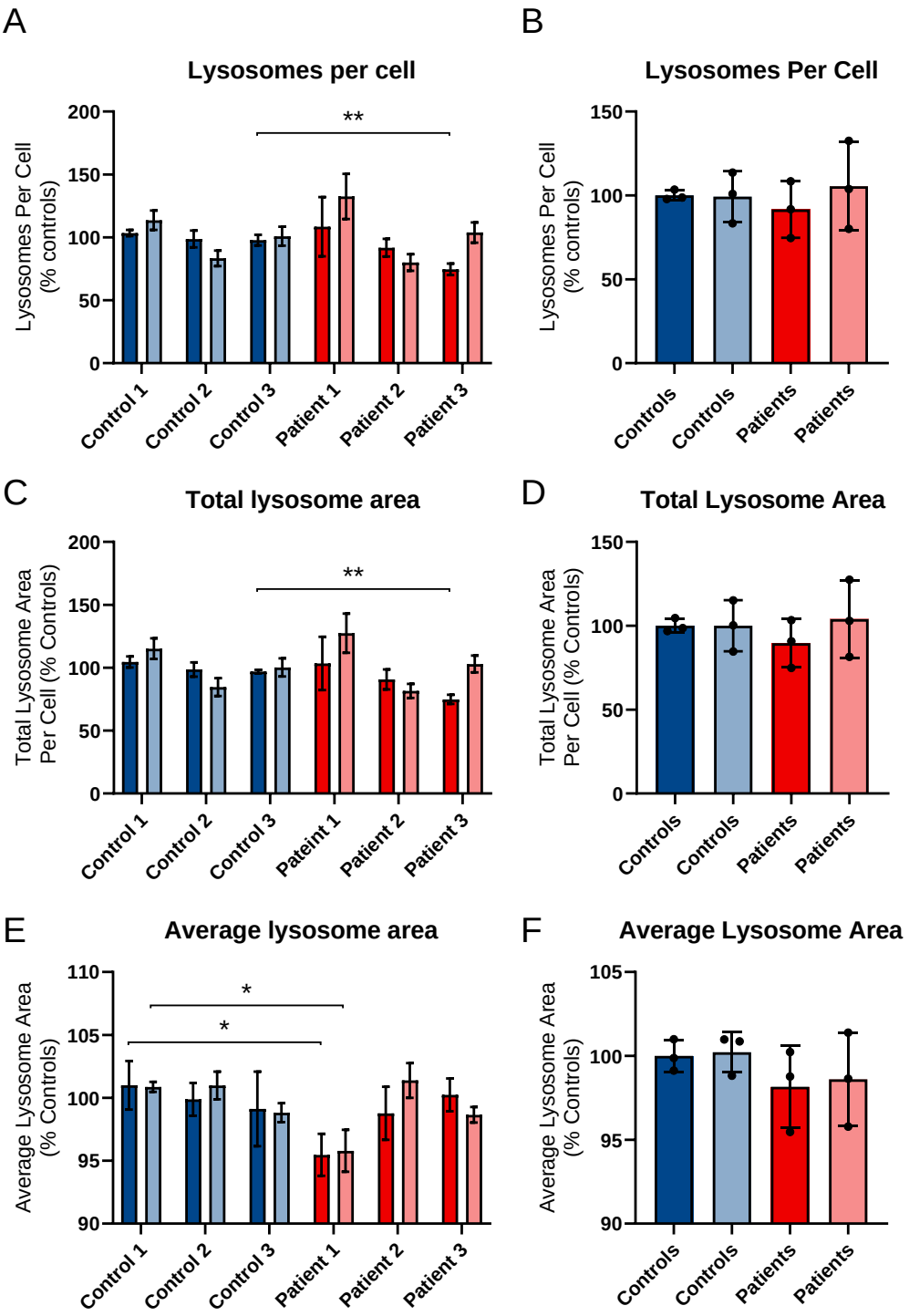

Figure 45: Lysosome phenotype determined by LAMP2a immunocytochemistry. A/B) Lysosomes per cell, **C/D)** Total lysosome area, **E/F)** Average lysosome area. **A/C/E)** Each patient (red) and control (blue) presented separately, dark bars represent glucose conditions and light bars represent galactoses. Results for each condition were normalised to the average of the controls in each repeat. Patients were compared to the corresponding control per condition by an unpaired T-test with Welch correction (* $p < 0.05$, ** $p < 0.01$). **B/D/F)** Combined patient and control groups per media condition. The glucose and galactose groups were compared separately by unpaired T-test with Welch correction (* $p < 0.05$) (n = 3).

4.3.1.2 Lysosome pH

Lysosomal pH plays an important role in lysosomal degradation and particularly in activating hydrolases. Lysosensor green DND-189 was used as its fluorescence is pH dependent, thus demonstrating acidification within lysosomes. Lysotracker green which was used to stratify the subgroups localised to acidic compartments within the cell, but its fluorescence is independent of pH. It is important to note that lysosensor green enables the measurement of lysosomes with an optimal pH (Figure 47), between pH 4 and 5. Lysotracker localises to acidic compartments and thus pH can vary between pH 3 and 6.

Interestingly, results between patients were consistent with Control 1 and Control 2, which age- and sex-match Patient 1 and Patient 2 (Figure 46). However, Control 3 showed a significantly lower number of lysosomes at the optimal pH (20 % ± 8, p = 0.01/0.04, Figure 46A) and total optimally acidic lysosomal area compared to Control 1 and Control 2 (17 % ± 11, p = 0.008/0.03, Figure 46B). Acidification in the controls was more variable as well (Figure 46D). The greater the intensity the more acidic the lysosome. Patient 1 and Control 3 had significantly reduced acidification (more neutral pH) than Control 1 (Patient 1: 28 % ± 18, p = 0.02, Control 3: 26 % ± 20, p = 0.03, Figure 46D). The patients generally had similar acidification to Control 2 and Control 3 (Figure 46D).

When assessed as groups there was no difference between patients and controls when measuring the optimally acidic lysosome number (Figure 48A), total area (Figure 48B) or average area (Figure 48C). A small reduction in acidification is observed (8 % ± 6, Figure 48D), but more controls would be required to assess the variation of pH in the control population. The results indicate that grouping using lysotracker selected for lysosomes with a more varied pH, suggesting that the patients have a less variable pH range compared to controls (Figure 48).

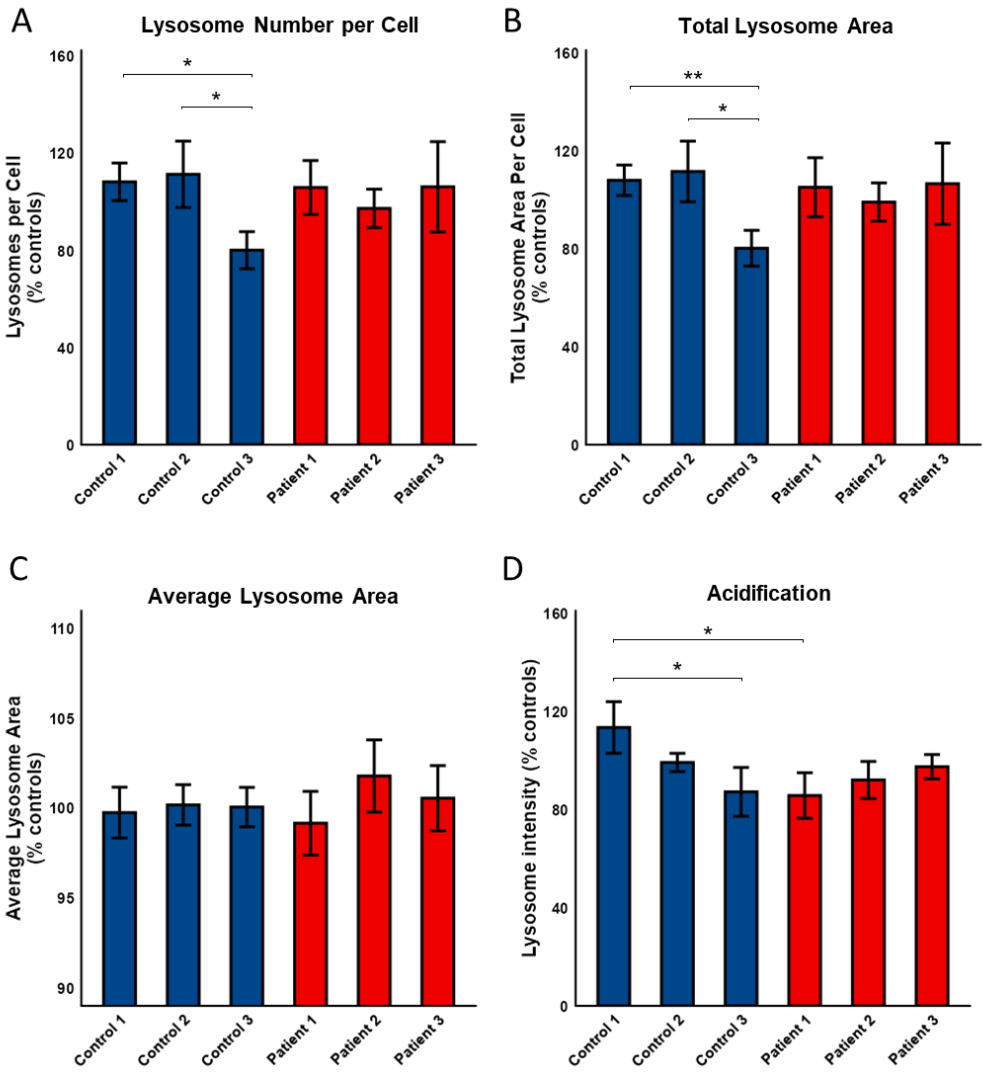

Figure 46: Lysosome pH and lysosomal phenotype in patient-derived fibroblasts were assessed using lysosensor. A) The number of optimally acidic lysosomes per cell, **B)** The total optimally acidic lysosome area per cell, **C)** The average area of optimally acidic lysosomes, **D)** Lysosome Acidification. Patients (red) were compared to the corresponding Control (blue) by unpaired T-tests with Welch correction (* $p < 0.05$, ** $p < 0.01$). Differences between controls were also determined this way. Error bars depict standard deviation (n = 3).

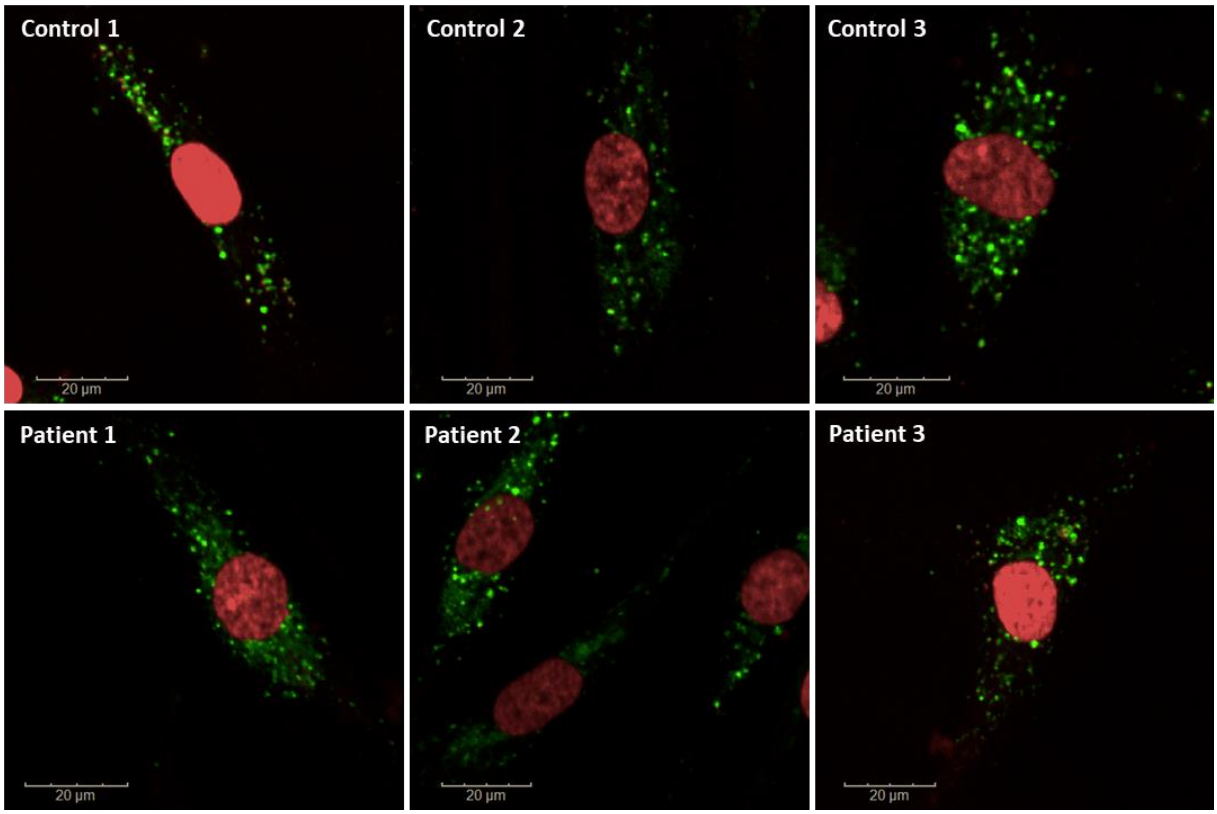

Figure 47: Representative images of optimally acidic lysosomes in patient-derived fibroblasts from the lysosomal dysfunction subgroup. Nuclei (red) and optimally acidic lysosomes (green). Scale bar = 20 µm.

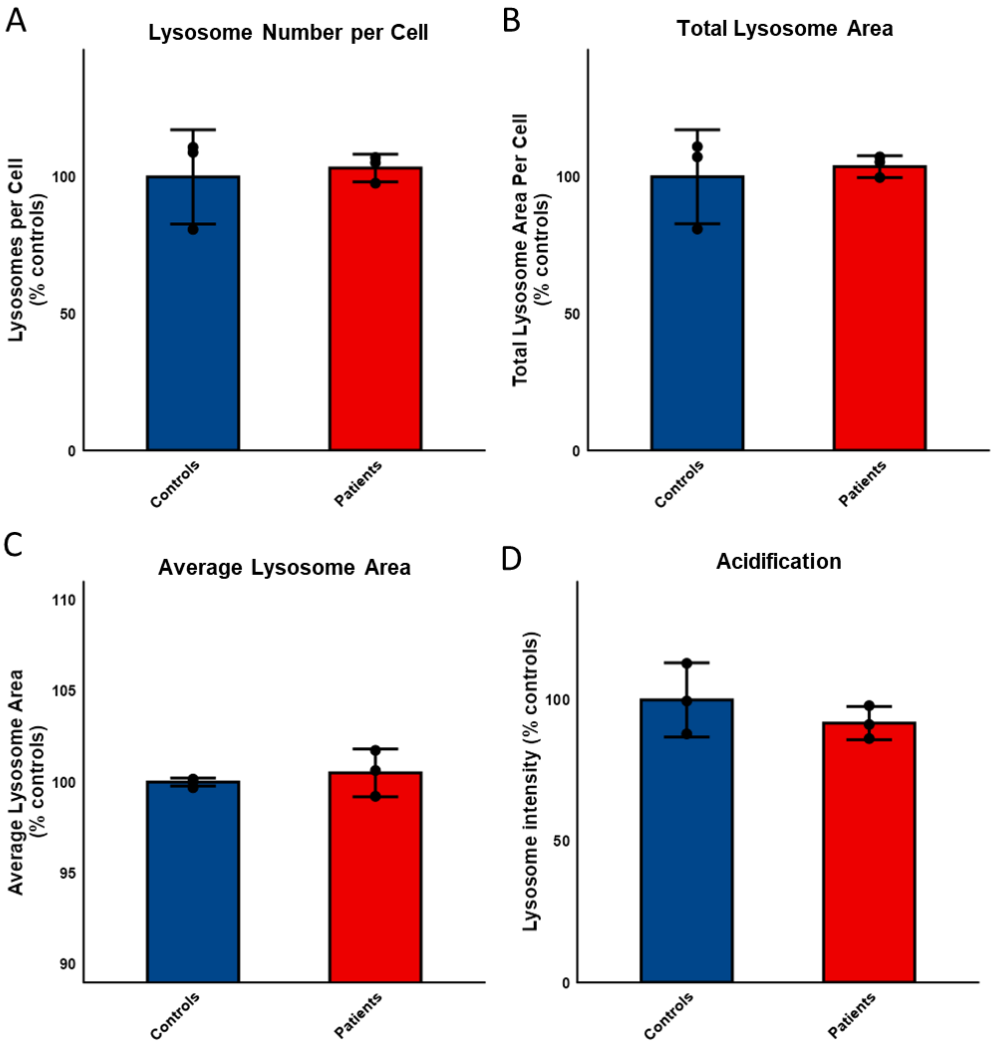

Figure 48: Lysosome pH and lysosomal phenotype assessed using Lysosensor. A) The number of optimally acidic lysosomes per cell, **B)** The total optimally acidic lysosome area per cell, **C)** The average area of optimally acidic lysosomes, **D)** Acidification. The patient group (red) was compared to the control group (blue) by an unpaired T-test with Welch correction (* $p < 0.05$). Error bars depict standard deviation (n = 3).

4.3.1.3 Cathepsin B Activity

Alterations in CatB activity are reported in various models of PD with conflicting results (Henry *et al.*, 2015; Yadavalli and Ferguson, 2023; Jones-Tabah *et al.*, 2024; Lu *et al.*, 2024). Therefore, CatB activity was measured in the lysosomal dysfunction subgroup. This was done using MagicRed a fluorescent tagged substrate for CatB, upon cleavage it releases the cresyl violet fluorophore enabling detection of activity (Figure 49).

Overall measures of CatB active lysosomes were consistent across the controls (Figure 50). However, Control 1 showed a significant increase in the number of CatB active lysosomes compared to Control 2 and Control 3 in glucose (Control 2: 25 ± 13, p = 0.02, Control 3: 22 % ± 17, p = 0.05 Figure 50A). This trend continued when assessing the perinuclear region; Control 1 had a significantly greater number of CatB active lysosomes (20 % ± 4, p = 0.02, Figure 50E) and total perinuclear CatB active lysosome area than Control 2 (34 % ± 7, p = 0.04, Figure 50F).

Patients were compared to their corresponding controls. Patient 1 showed a significantly reduced number of CatB active lysosomes in glucose conditions (44 % ± 17, p = 0.03, Figure 50A). A trend that was magnified in the perinuclear region where Patient 1 had a significantly reduced number of CatB active lysosomes in glucose (68 % ± 17, p = 0.004, Figure 50E) and non-significantly in galactose (43 % ± 6, Figure 50E). Patient 1 displayed a reduction in the total area of the CatB active lysosomes per cell in glucose (56 % ± 16, p = 0.008, Figure 50B). Like CatB active lysosomes per cell, this reduction was observed in the perinuclear region; total CatB active lysosome area in glucose was significant (88 % ± 14, p = 0.0002, Figure 50F) and non-significant in galactose (47 % ± 11, Figure 50F). Patient 3 had an increase in total CatB active lysosome area in the whole cell (glucose: 89 % ± 82, galactose: 128 % ± 131, Figure 50B) and perinuclear region (glucose: 83 % ± 80, galactose: 88 % ± 61, Figure 50F), however, this was not significant and fairly variable. Patient 2 had significantly reduced total lysosome area compared to Control 2 in galactose (50 % ± 35, p = 0.04, Figure 50B). The average area of the CatB active lysosomes was increased in Patient 3 (15 % ± 16, Figure 50C) but not significantly, whereas Patient 1's CatB active lysosomes were significantly smaller in glucose (17 % ± 5, p = 0.02, Figure 50C). In both media conditions Patient 1 demonstrated significantly smaller perinuclear CatB active lysosomes than Control 1 (glucose: 33 % ± 6, p = 0.008, galactose: 12 % ± 10, p = 0.04, Figure 50C), and Patient 3 showed significantly larger CatB active lysosomes in the perinuclear region in glucose (20 % ± 16, p = 0.03). Cathepsin B activity was significantly reduced in Patient 1 (37 % ± 7, p = 0.003, Figure 50D), whereas Patient 3 has significantly higher CatB activity in its CatB active lysosomes (54 % ± 18, p = 0.006, Figure 50D).

Comparing the patient group to the controls showed no difference between the groups for any parameters. However, the variability among the patients was much higher than the controls (Figure 51).

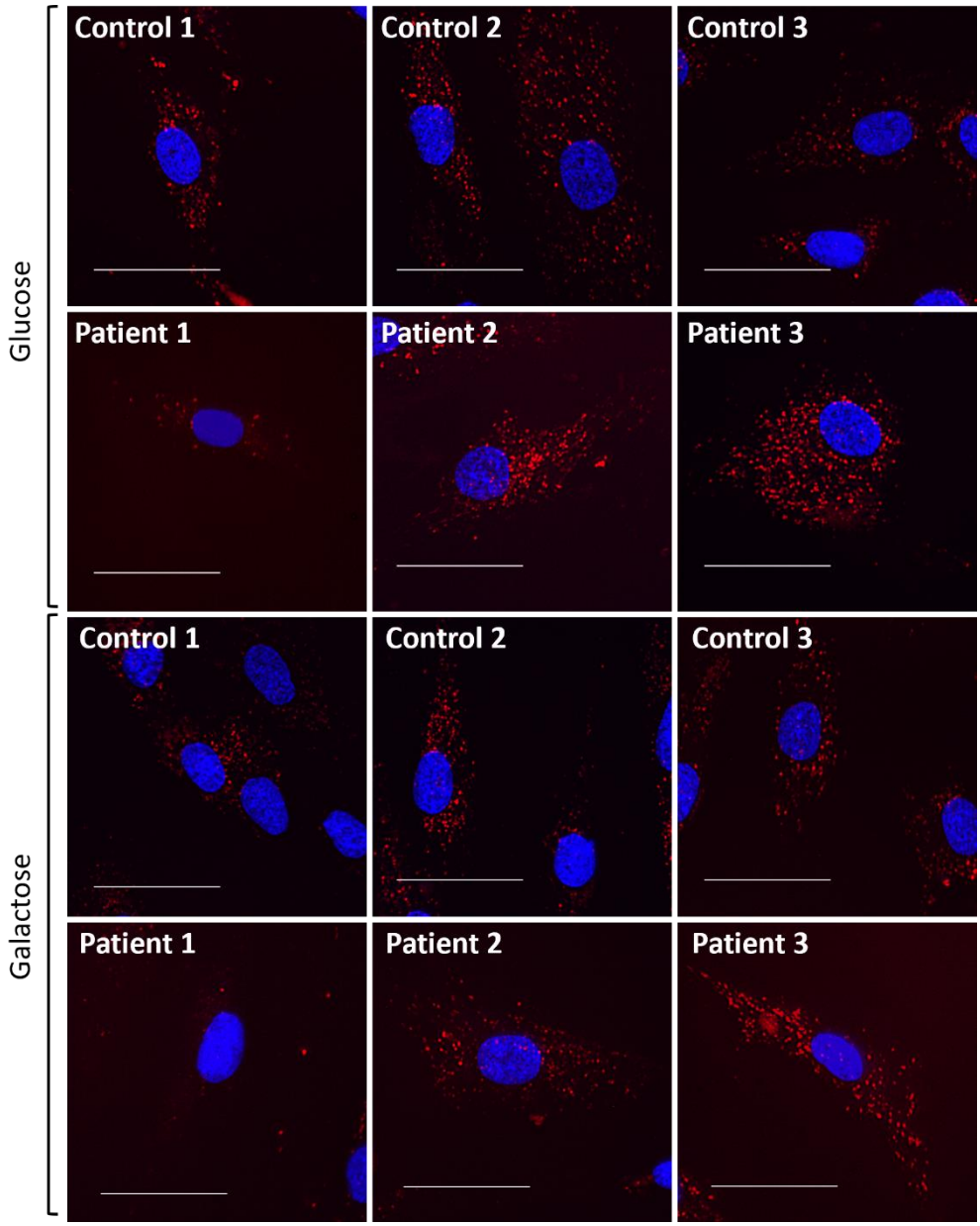

Figure 49: Representative images of CatB active lysosomes in patient-derived fibroblasts from the lysosomal dysfunction subgroup. Nuclei (blue) and CatB active lysosomes (red). Scale bar = 40 µm.

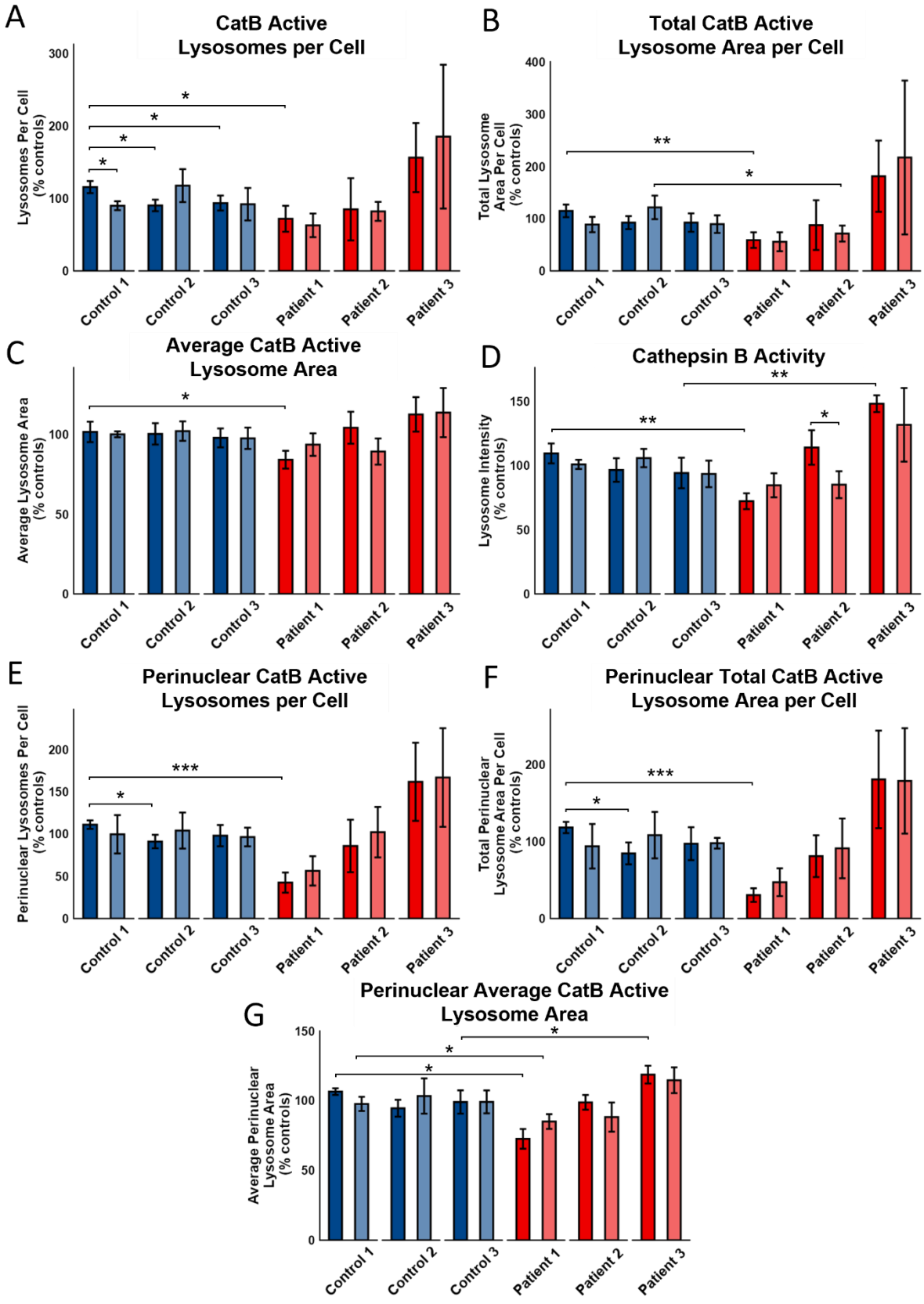

Figure 50: Cathepsin B active lysosomes in patient-derived fibroblasts from the lysosome dysfunction subgroup. A) The number of CatB active lysosomes per cell, **B)** The total CatB active lysosome area per cell, **C)** The average area of CatB active lysosomes, **D)** Cathepsin B activity, **E)** Perinuclear CatB active lysosomes per cell, **F)** Total area of perinuclear CatB active lysosomes, **G)** Average area of perinuclear CatB active lysosomes. Patients (red) were compared to the

corresponding control (blue) by unpaired T-tests with Welch correction (* $p < 0.05$, ** $p < 0.01$). Differences between controls were also determined this way. Results from the glucose (dark) and galactose (Light) culture conditions were normalised to the average of the controls per repeat for each condition. Error bars depict standard deviation (n = 3).

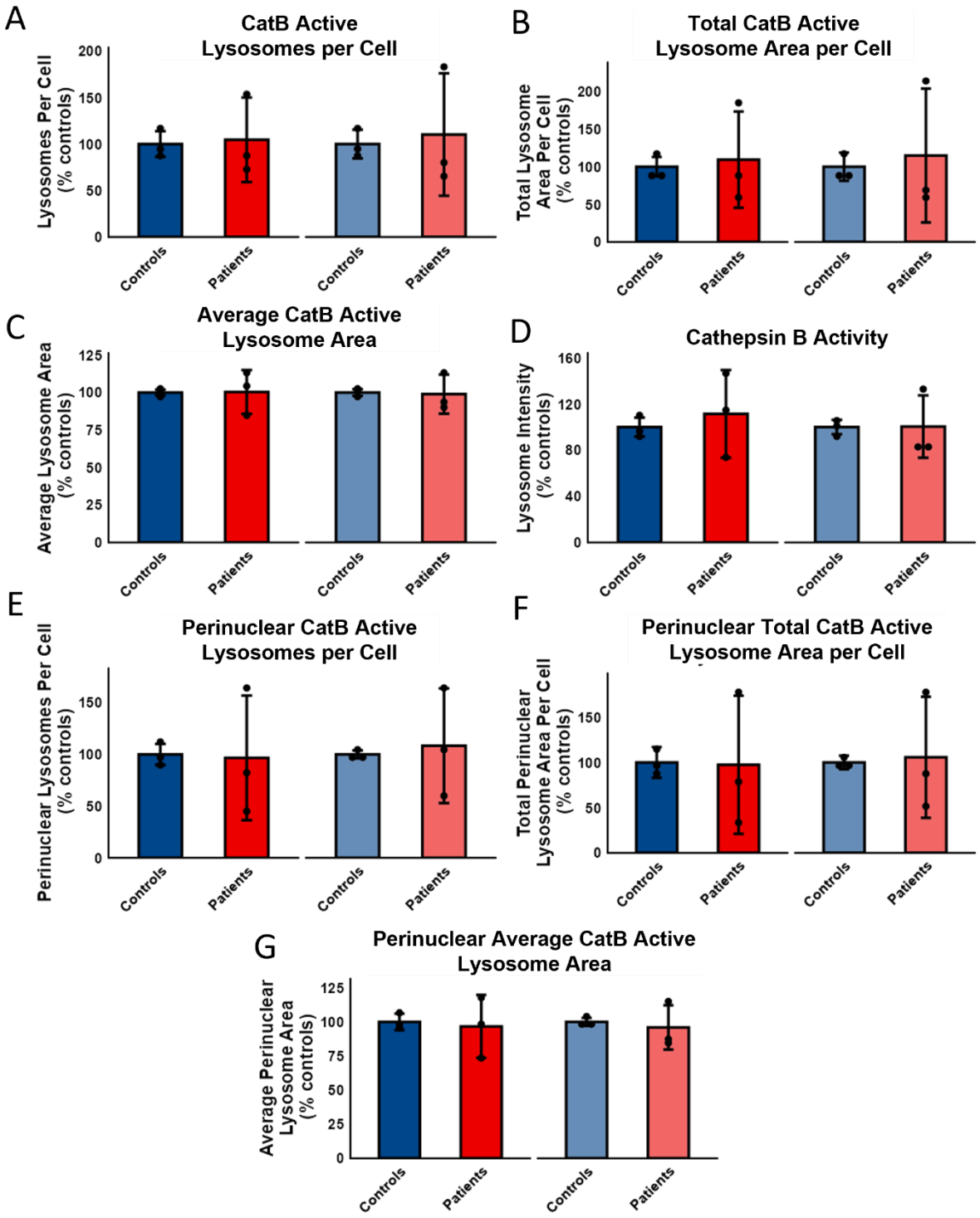

Figure 51: Cathepsin B active lysosomes in patient-derived fibroblasts. A) The number of CatB active lysosomes per cell, **B)** The total CatB active lysosome area per cell, **C)** The average area of CatB active

lysosomes, **D)** Cathepsin B activity, **E)** Perinuclear CatB active lysosomes per cell, **F)** Total area of perinuclear CatB active lysosomes, **G)** Average area of perinuclear CatB active lysosomes. The patient group (red) was compared to the control group (blue) by unpaired T-tests with Welch correction per culture condition (* $p < 0.05$). Results from the glucose (dark) and galactose (Light) culture conditions were normalised to the average of the controls per repeat for each condition. Error bars depict standard deviation (n = 3).

4.3.1.4 Cathepsin D Activity

Due to the reported reduction of CatD activity in various PD phenotypes, including the lysosomal subgroup identified by Carling *et al.* (2020), the activity was assessed in the fibroblasts. Activity was measured by a fluorometric kit (Abcam), that uses a CatD specific protein sequence (GKPILFFRLK(Dnp)-D-R-NH2) labelled with 7-methoxycoumarin-4-acetic acid. CatD cleaves the substrate sequence releasing the fluorophore. Total fluorescence was measured and normalised to total protein content. The subgrouped patients show a significant 23 % ± 8 reduction in CatD activity compared to the controls when grouped (Figure 52B).

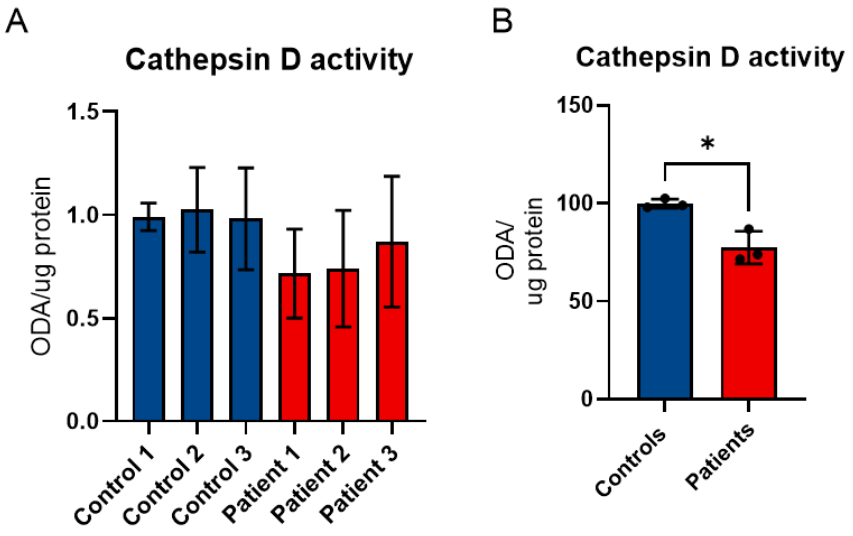

Figure 52: CatD activity in patient-derived fibroblasts from the lysosomal dysfunction subgroup. A) CatD activity in each cell line, **B)** CatD activity between the patient and control group. Patients (red) were compared to the corresponding control (blue) by unpaired T-tests with Welch correction (* $p < 0.05$). Differences between controls were tested in addition. The patient group was compared to the control group by an unpaired T-test with Welch correction (* $p < 0.05$). Error bars depict standard deviation (n = 3).

4.3.1.5 GCase Activity Optimisation

GCase activity is frequently assessed in PD models and has been reported to be decreased in patient-derived cells from GBA mutants and sPD patients (Schöndorf *et al.*, 2014; Rocha *et al.*, 2015; Huebecker *et al.*, 2019; Thomas *et al.*, 2021). Methods for assessing GCase activity were reviewed by Ysselstein *et al.* (2021), who outlined the advantages and disadvantages of the various methods. The most commonly used method for detecting GCase activity was the use of cell lysate combined with a fluorescent substrate, however, this involved removing GCase from the lysosomal microenvironment and conducting the assay at a defined pH. As a result, and to reduce the number of cells required, the use of GCase substrate 5-(Pentafluorobenzoylamino) Fluorescein Di-β-D-Glucopyranoside (PFB-FDglu) was opted for. This method involves measuring the cleavage of the substrate in lysosomes in live cells over time. Due to difficulties with the optimisation, only one repeat is shown here. The pursuit of this assay was stopped due to a lack of efficacy seen across SH-SY5Y cells, iDA neurons and fibroblasts. However, a new methodology published by Labrador-Garrido *et al.* (2023) promoted the reanalysis of one of the optimisation assays. Results from the reanalysis suggest that the new methodology may yield reliable results (Figure 53), however, due to time constraints further optimisation was not possible.

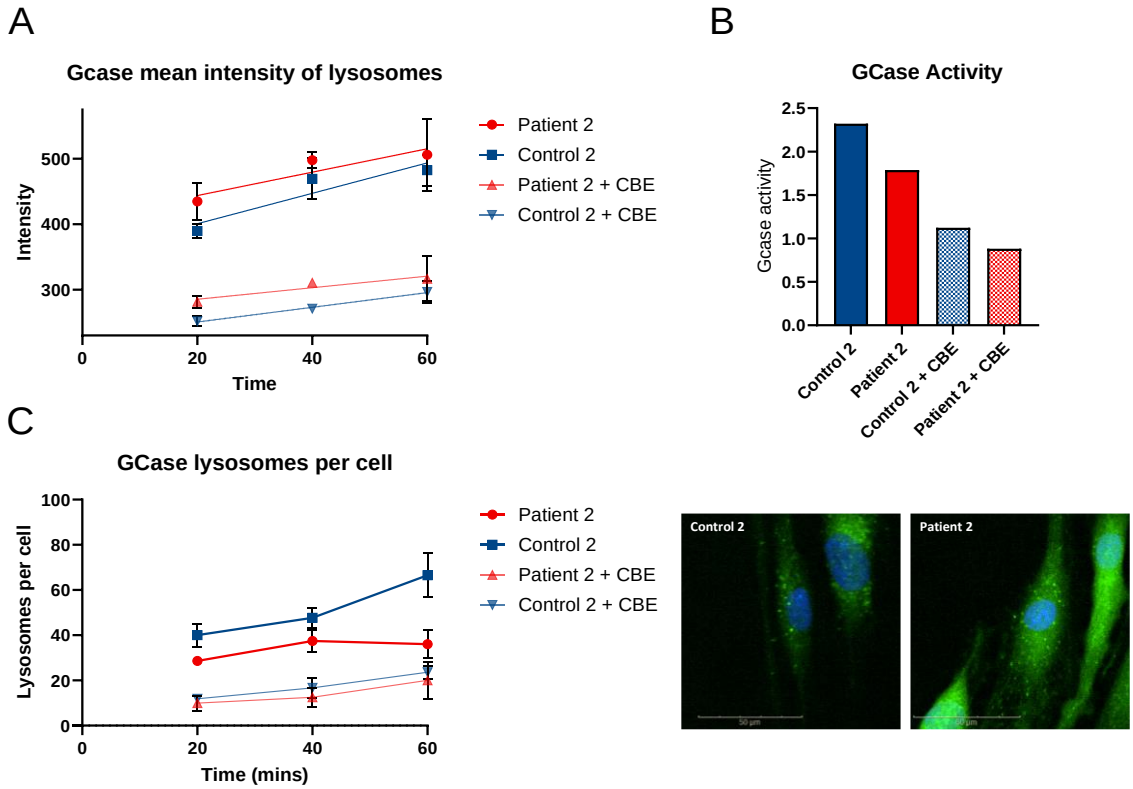

Figure 53: GCase activity optimisation results from one repeat. A) Average lysosomal intensity after incubation with PFB-FDglu for 20, 40 and 60 minutes, **B)** Quantification of the gradient to assess GCase activity, **C)** The number of GCase active lysosomes measured per cell after incubation with PFB-FDglu

for 20, 40 and 60 minutes. Controls (blue), patients (red), CBE was used at 100uM (checked pattern). Error bars depict standard deviation. No statistics were conducted on this data due to only one biological repeat being presented. Error bars depict standard deviation between three technical well triplicates. Representative images of Control 2 and Patient 2 at 60 minutes incubation, scale bar = 50 µm.

4.3.2 Assessment of Lysosomal Dysfunction in iDopaminergic Neurons

Successful reprogramming and differentiation was achieved for Patient 2, Patient 3 and Control 2. To ensure age- and sex-matching another control was added, Control 4. Two familial mutants, the GBA/LRRK2 patient and one of the GBA N370S patients, were also added to compare trends between sporadic and familial subgroups. Due to slow growth of the GBA mutant, only one repeat was possible in the phenotyping assays; therefore, it has not been included in statistical comparisons. Due to the number of patients no group comparisons were conducted.

Table 26: A summary of the iDA neuron lines that were assessed.

Cell line	Age at biopsy (years)	Sex
Patient 2	66	Male
Patient 3	53	Female
GBA	51	Female
GBA/LRRK2	68	Female
Control 2	62	Male
Control 4	55	Female

4.3.2.1 Lysosome Dysfunction Subgroup iDopaminergic Neuron Generation and Characterisation

Generation of iNPCs is similar to the generation of iPSCs; the Yamanaka factors, Oct4, Klf4, c-Myc and Sox2, were transduced into to the patient-derived fibroblasts by a retrovirus vector. The cells were incubated for 24 hours before the virus was removed. Two days later, the cells were cultured in pre-iNPC media to drive neuronal progenitor cell generation. Morphological changes happened within two weeks; the fibroblasts, which were flat and long, began to shorten and thicken forming small stem cell-like cells. At twelve days the cells were cultured in iNPC media to enhance growth and enable the removal of untransduced fibroblasts. Culturing was continued to produce stocks and generate a homogenous cell line. Due to the mixed population method, rather than clonal expansion, this relies on several splits and continued growth of all the colonies. The process was slow and labour-intensive, with some lines taking up to 4 months to generate a stable and usable iNPC line. Several attempts were made to produce iNPC lines for all three patients and their corresponding controls, however, Patient 1 did not reprogramme after two attempts. The control for Patient 3 did not reprogramme

either so an alternative age- and sex-matched control, that was generated for previous studies, was used. Reprogramming of the familial lines was more successful with one GBA carrier and the GBA/LRRK2 carrier producing stable cell lines. Growth and generation of the GBA line was slow so only one repeat was performed due to time constraints. Future work will complete the phenotyping and assessment of this line. Once a stable iNPC line was generated the cells were stained for Pax6 and Nestin (Figure 54). Pax6 is a transcription factor that is expressed in the nucleus where it regulates neurogenesis and maintains multipotency (Sansom *et al.*, 2009). Nestin is a type VI intermediate

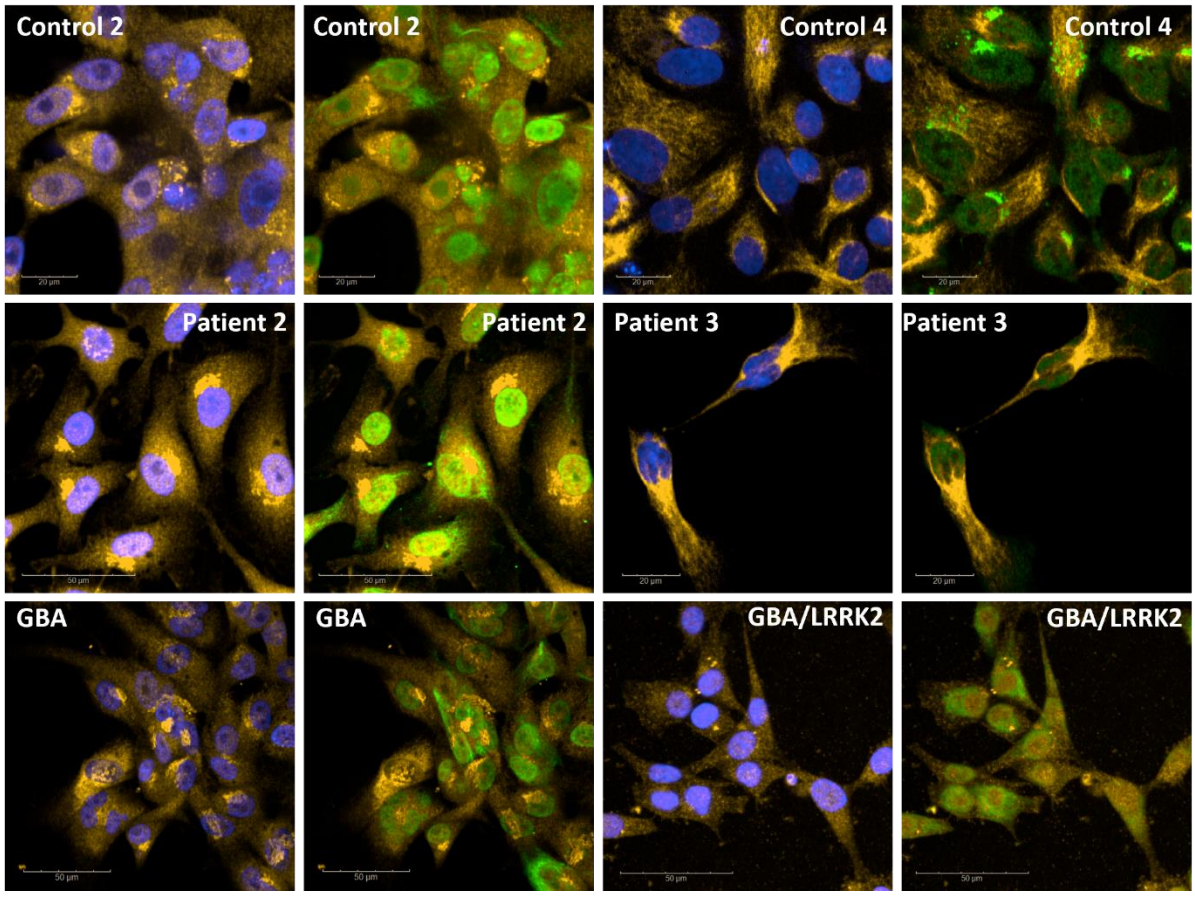

filament and an important part of neural cells' cytoskeleton (Bernal and Arranz, 2018).

Figure 54: Representative images of Pax6 and Nestin staining in iNPCs from each cell line. Nuclei (blue), Pax6 (green) and Nestin (orange). Scale bar = 20 µm or 50 µm.

Differentiation of the neurons followed the protocol outlined in Schwartzentruber *et al.* (2020). Cells were cultured for twenty-seven days to produce iDA neuron-like cells, which will be referred to as iDA neurons throughout. To ensure the cells were like neurons, the morphology and protein expression were assessed. B-III-Tubulin, a component of the neuron's cytoskeleton (Guo, Walss-Bass and Ludueña, 2010), and MAP2, a regulator of the neuron's cytoskeleton (DeGiosio *et al.*, 2022), were assessed and the percentage of positive cells were calculated (Figure 55, Figure 56). The controls, sporadic patients and GBA/LRRK2 line expressed β-III-Tubulin in the vast majority of cells (96 % ± 8, Figure 57A), however,

the GBA line only expressed it in 56 % of cells (Figure 57A). This may be due to the growth nature of the GBA line which formed clusters of cells with projections leading to higher expression in the projecting neurons but lower expression in the centre. Interestingly, 98 % of the GBA cells expressed MAP2 (Figure 57B). Subsequent repeats and differentiation will be important to understand the GBA lines expression and growth patterns. Overall, the six lines had high expression of MAP2 (94 % ± 5, Figure 57B). TH and DAT were used as dopaminergic markers (Figure 55, Figure 56). TH catalyses the production of dopamine from tyrosine (Daubner, Le and Wang, 2011) and DAT removes dopamine from the extracellular space to control neurotransmission (Nepal *et al.*, 2023). Expression of DAT was consistent across the cell lines with a high number of positively stained cells (90 % ± 7, Figure 57D). Similar, to β-III-Tubulin, TH was highly expressed in the controls, sporadic patients and GBA/LRRK2 line (96 % ± 6, Figure 57C), but the GBA line only expressed TH in 56% of cells (Figure 57C). The GBA line forms some clusters of cells with long projections. TH and β-III-Tubulin antibodies did not stain the centre of these clusters, which may account for the reduced percentage of positive cells. Only one repeat was conducted so further work is required to optimise antibody permeablisation.

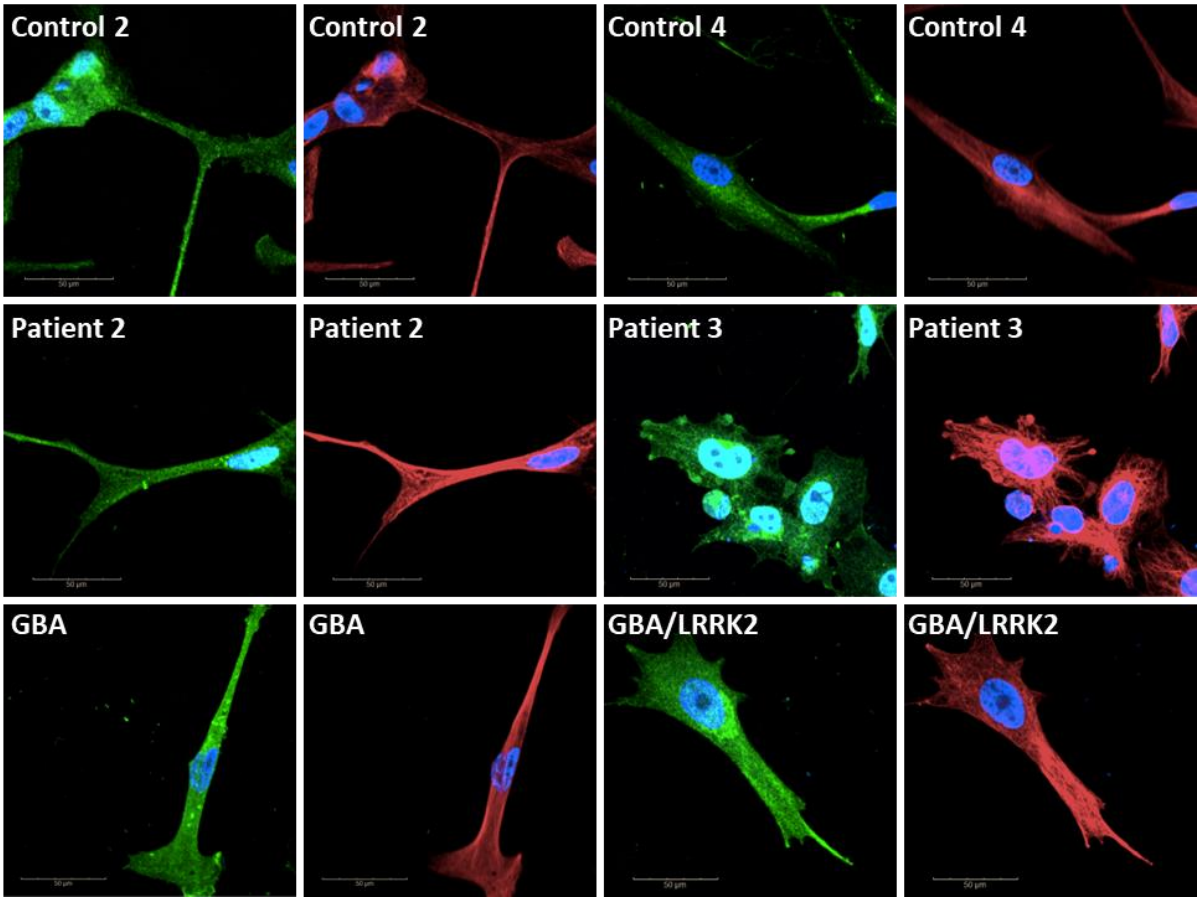

Figure 55: Representative images of TH and β-III-Tubulin staining in iDA neurons from each cell line. Nuclei (blue), TH (green) and β-III-Tubulin (red). Scale bar = 50 µm.

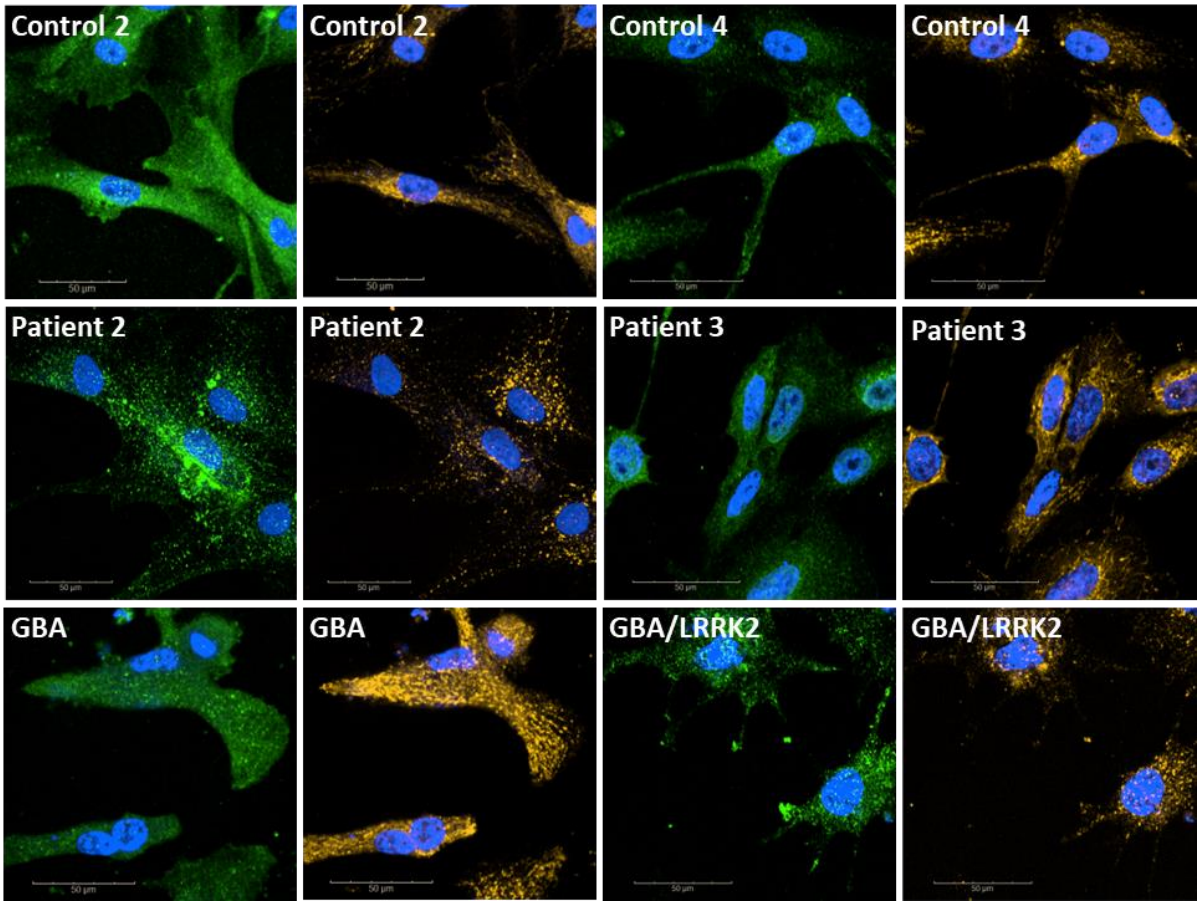

Figure 56: Representative images of DAT and MAP2 staining in iDA neurons from each cell line.

Nuclei (blue), DAT (green) and MAP2 (orange). Scale bar = 50 µm.

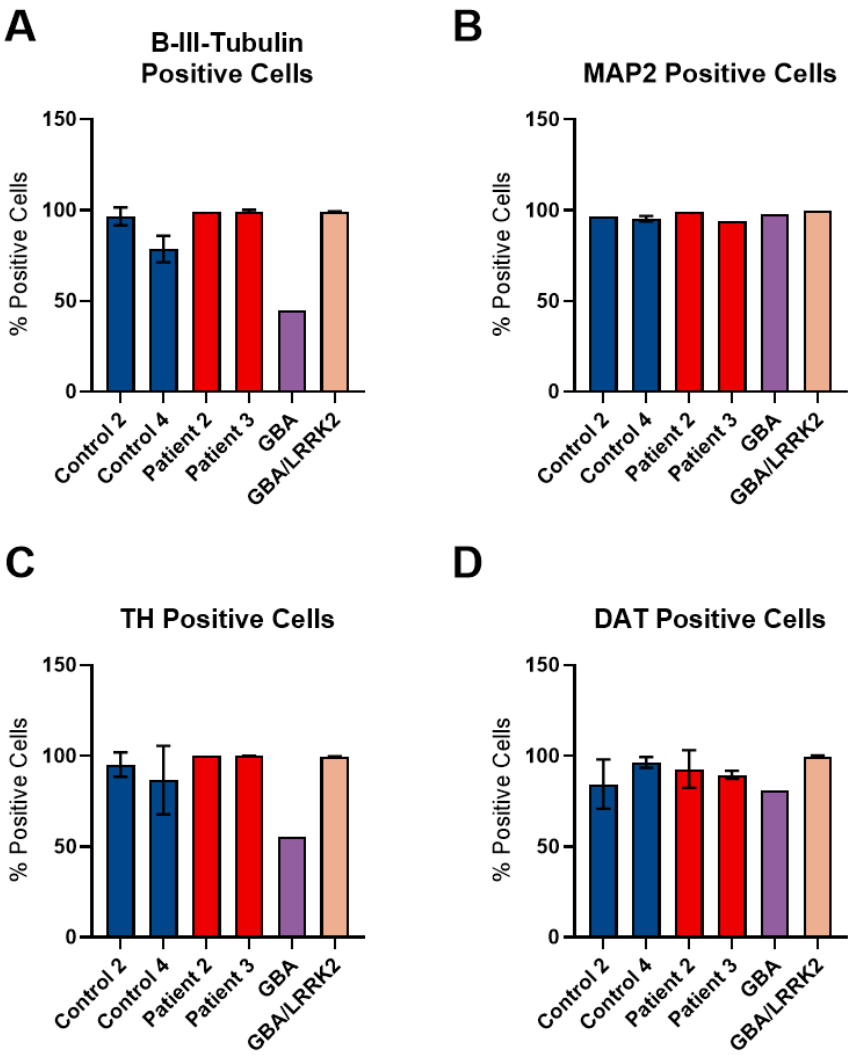

Figure 57: Neuronal marker expression in the iDA neurons from the lysosomal subgroup and familial mutation carriers. A) Percentage of cells expressing β-III-Tubulin, **B)** Percentage of cells expressing MAP2, **C)** Percentage of cells expressing TH, **D)** Percentage of cells expressing DAT. Controls (blue, n = 2), sporadic patients (red, n = 2), the GBA/LRRK2 patient (pink, n = 2) and the GBA patient (purple, n = 1). Error bars depict standard deviation.

Neuronal morphology and viability were assessed using the neurite outgrowth kit from Thermofisher (Figure 58). Staining of the membrane enables the segmentation of individual cells and the assessment of their morphology. A machine learning approach utilising fifteen morphology parameters, spanning width, length, roundness and cellular profiles identified neuron-like cells. This enables the calculation of the percentage of cells with neuronal morphology after machine training. An average of 63 % of cells we classified as neuronal in the controls (Control 1: 58 % ± 11, Control 2: 68 % ± 11, Figure 59A). Assessment of classified neuronal cell roundness (Control 2: 100 % ± 1, Control 4: 101 % ± 1, Figure 59C) and width to length (Control 2: 100 % ± 1, Control 4: 100 % ± 1, Figure 59D) showed no difference between the lines. Patient 2 and the GBA/LRRK2 had a similar distribution of morphology to the

controls (Patient 2: 72 % ± 11, GBA/LRRK2: 58 % ± 13, Figure 59A). Patient 2's cells showed no difference from the controls in width to length ratio (Figure 59D). But was significantly less round (93 % ± 1, p = 0.006, Figure 59C), which is likely due to small projections on the cells. The GBA/LRRK2 cells showed a higher width to length ratio (106 % ± 6, Figure 59D) but a lower cell roundness (89 % ± 3, p = 0.002, Figure 59C), these cells were less elongated but had many sharp projections. In contrast, Patient 3 and the GBA patient were less neuronal (Patient 3: 39 % ± 6, GBA: 29 %, Figure 59A). The cells that were neuron-like in Patient 3 were more rounded (93 % ± 3, Figure 59C) and less elongated (106 % ± 4, Figure 59D) than the controls. In contrast, the neuron-like cells in the GBA patient had lower width to length ratio (96 % Figure 59D), showing they produce long thin projections off the cell clusters. Cell viability did not differ between the six lines (Figure 59B).

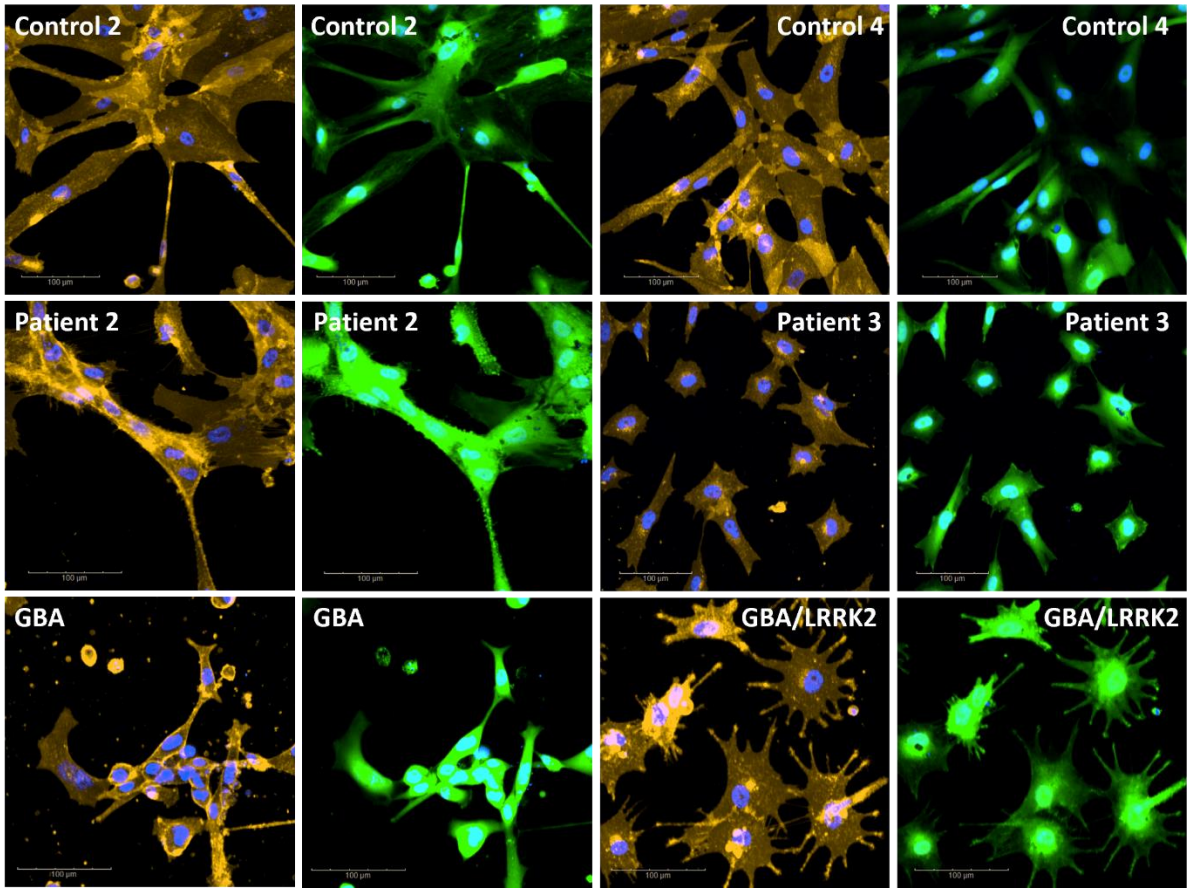

Figure 58: Representative images of the neuronal outgrowth staining in iDA neurons from each cell line. Nuclei (blue), cell viability stain (green) and membrane stain (orange). Scale bar = 100 µm.

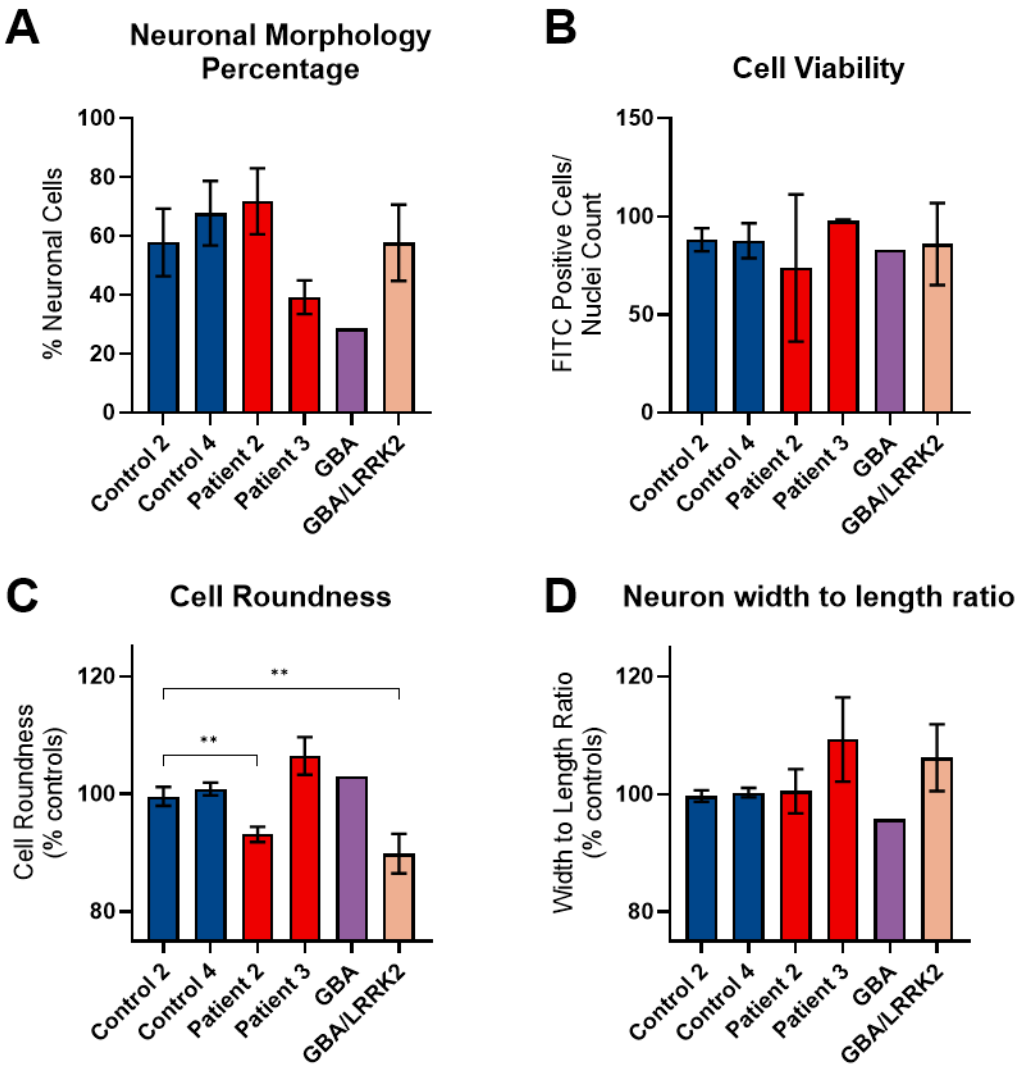

Figure 59: Neuronal marker expression in the iDA neurons from the lysosomal subgroup and familial mutation carriers. A) Percentage of cells expressing β-III-Tubulin, **B)** Percentage of cells expressing MAP2, **C)** Percentage of cells expressing TH, **D)** Percentage of cells expressing DAT. Patient 2 (red, n = 3) and the GBA/LRRK2 patient (pink, n = 3) were compared to the corresponding control (blue, n = 3) by unpaired T-tests with Welch correction (** $p < 0.01$). The GBA line (purple, n = 1) and Patient 3 (red, n = 2) were not statistically tested. Error bars depict standard deviation.

4.3.2.2 Assessment of Lysosome Number, Area and Size.

Lysosome assessment was first conducted using the lysotracker green fluorophore to determine if the lysosome phenotype observed in the initial screen in fibroblasts was consistent in the neurons (Figure 60). Although not significant the opposite trend was observed. Patient 2 and 3 had more lysosomes (Patient 2: 24 % ± 54, Patient 3: 43 % ± 45, Figure 61A) and a corresponding greater total lysosomal area (Patient 2: 47 % ± 63, Patient 3: 57 % ± 52, Figure 61B). The average size of their lysosomes was greater, significantly in Patient 2 compared to its corresponding control (20 % ± 2, p = 0.000008, Figure 61C). Patient 3's lysosomes were also larger but not significantly (8 % ± 3, Figure 61C). Despite variable data, the GBA/LRRK2 patient had a non-significant increase in lysosome number (42 % ± 92, Figure 61A) and total area (50 % ± 104). In contrast, the GBA N370S patient had a reduced lysosome number (47 %, Figure 61A) and total area (46 %, Figure 61B) for one repeat. This does replicate the results seen in glucose conditions in the GBA N370S initial assessment.

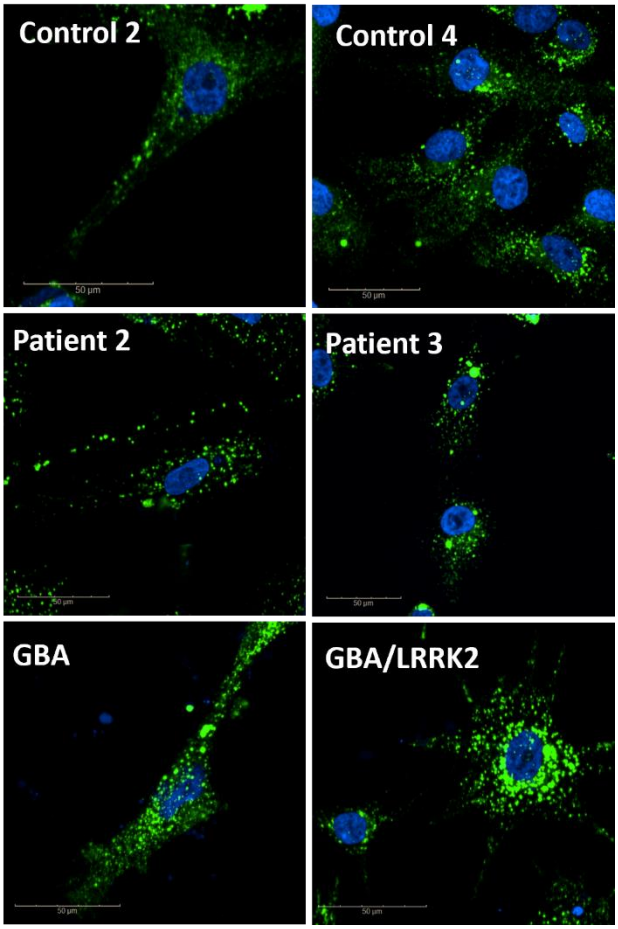

Figure 60: Representative images of the lysosome staining with lysotracker green in iDA neurons from each cell line. Nuclei (blue) and lysosomes (green). Scale bar = 50 µm.

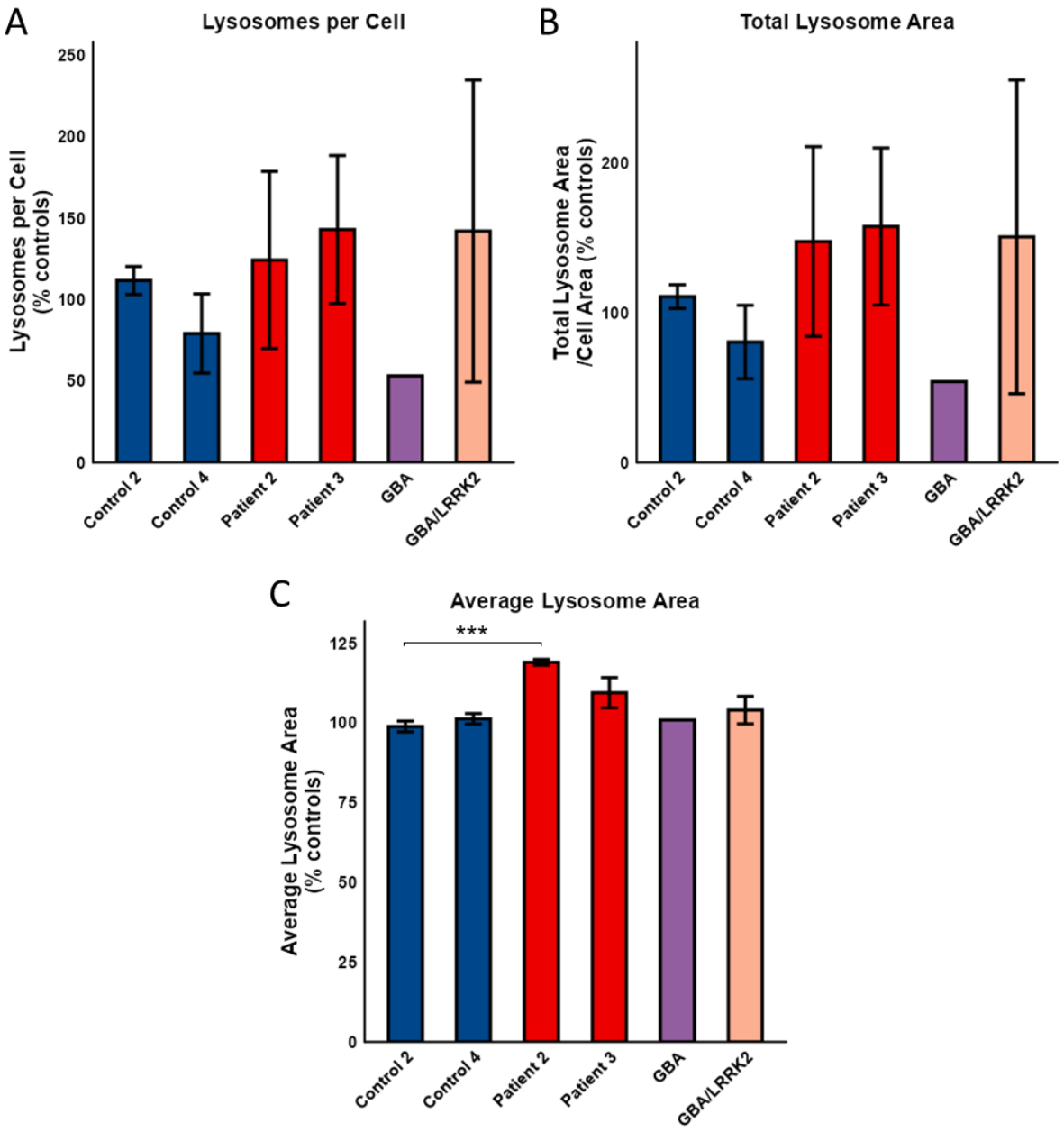

Figure 61: Lysosome phenotype stained by lysotracker green in induced dopaminergic neurons. A) Lysosomes per cell, **B)** Total lysosome area adjusted by cell area, **C)** Average lysosome area. Sporadic patients (red, n = 3/4) and the GBA/LRRK2 patient (pink, n = 4) were compared to the corresponding control (blue, n = 3/4) by unpaired T-tests with Welch correction (*** $p < 0.001$). The GBA patient (purple, n = 1) was not statistically tested. Error bars depict standard deviation.

4.3.2.3 Assessment of Lysosome pH.

Lysosomal pH is integral to optimal lysosome degradation. Assessment using lysosensor enables the measurement of lysosomes with an optimal pH, between pH 4 and 5 (Figure 62). Nevertheless, the assessment showed similar results to lysotracker green, which localises in lysosomes with a broader pH range. Patient 2 had a significant increase in the number of optimally acidic lysosomes compared

to Control 2 (56 % ± 41, p = 0.03 Figure 63A). Optimally acidic lysosomes per cell (Patient 3: 127 % ± 79, GBA/LRRK2: 112 % ± 138, Figure 63A) and total optimal lysosome area (Patient 3: 24 % ± 31, GBA/LRRK2: 28 % ± 35, Figure 63B) were non-significantly elevated in Patient 3 and GBA/LRRK2. The average optimally acidic lysosome size was significantly increased in Patient 2 compared to Control 2 (9 % ± 4, p = 0.02, Figure 63C) and non-significantly in Patient 3 (7 % ± 7, Figure 63C). Acidification was more variable between controls (14 % ± 5, p = 0.01, Figure 63D), but Patient 2 was significantly less acidic than Control 2 (12 % ± 9, p = 0.03, Figure 63D). Unexpectedly the GBA patient had a lower total optimal lysosome area (39 %, Figure 63B) but more acidic lysosomes (30 %, Figure 63D); it will be interesting if this trend continues in subsequent repeats. Likewise, the GBA/LRRK2 patient's acidification was elevated (24 % ± 16, Figure 63D).

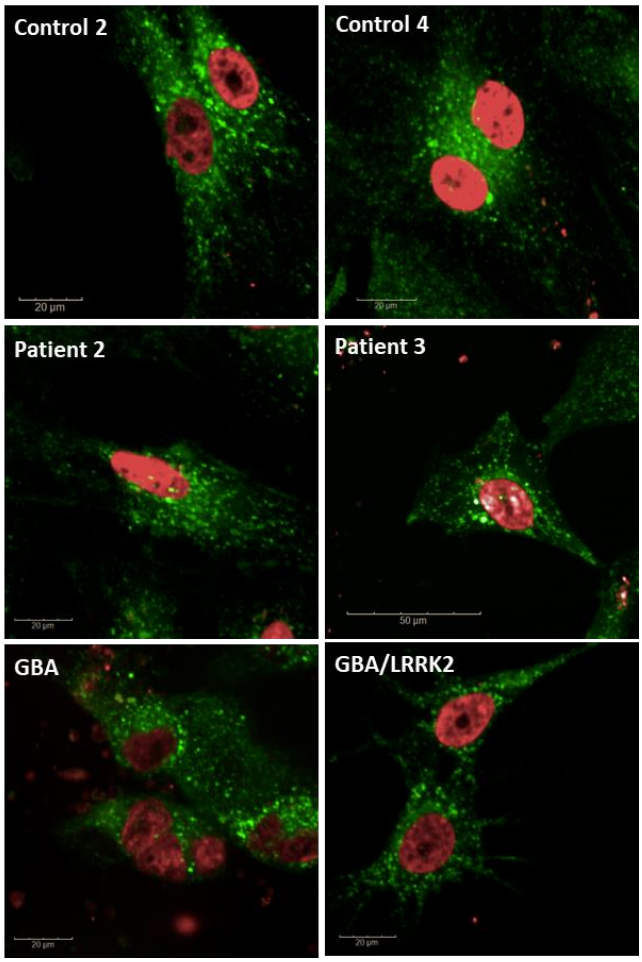

Figure 62: Representative images of lysosensor staining in iDA neurons from each cell line. Nuclei (red) and optimally acidic lysosomes (green). Scale bar = 20 µm.

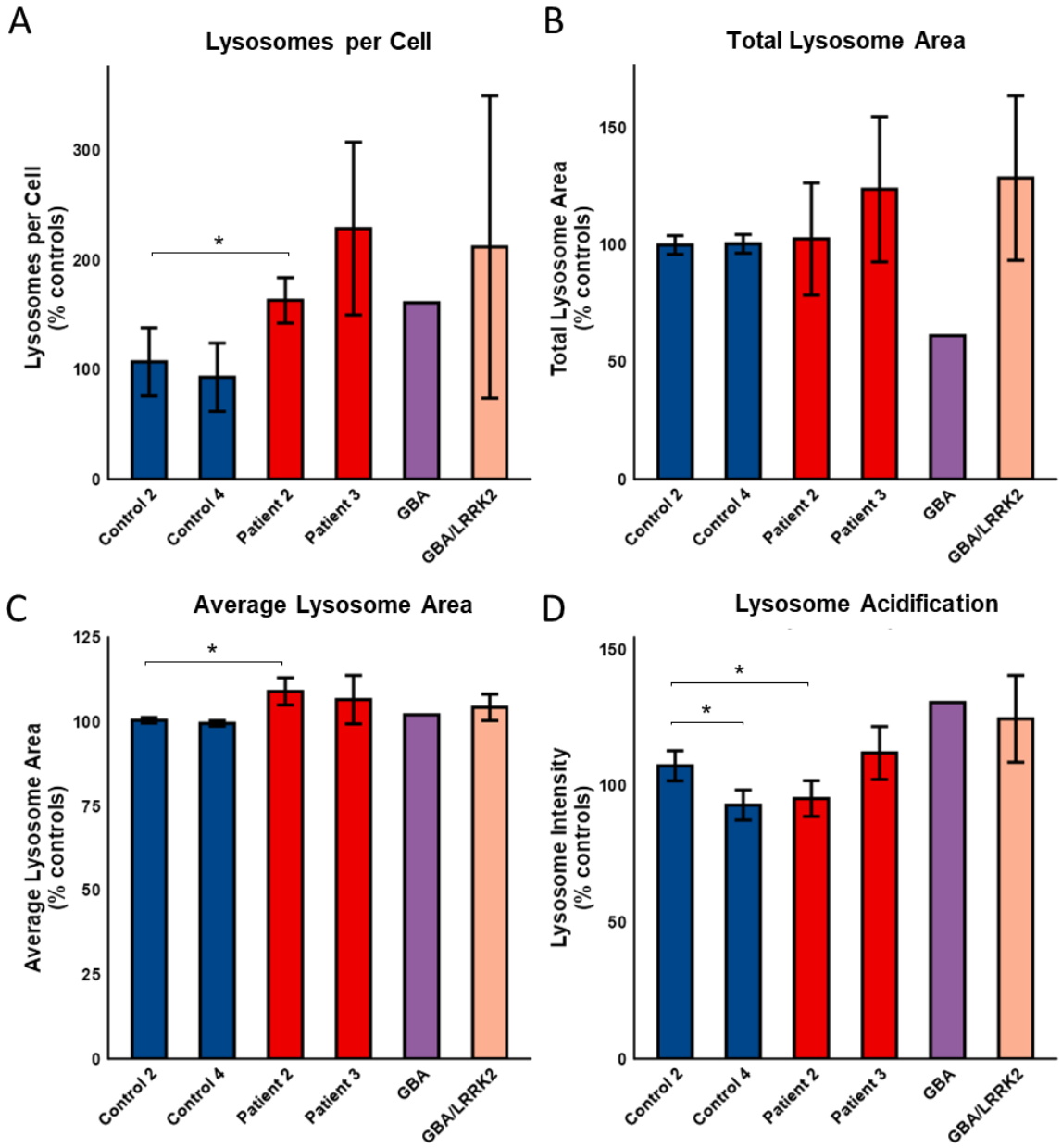

Figure 63: Lysosome pH and phenotype in the iDA neurons assessed by lysosensor. A) Optimally acidic lysosomes per cell, **B)** Total optimally acidic lysosome area adjusted by cell area, **C)** Average optimally acidic lysosome area, **D)** Lysosome Acidification. Sporadic patients (red, n = 3/4) and the GBA/LRRK2 patient (pink, n = 4) were compared to the corresponding control (blue, n = 3/4) by unpaired T-tests with Welch correction (* $p < 0.05$). The GBA patient (purple, n = 1) was not statistically tested. Error bars depict standard deviation.

4.3.2.4 Cathepsin Activity.

Cathepsin activity is important in lysosomes; many of the enzymes have similar targets and can compensate for one another. Importantly, as seen with α-syn, multiple cathepsins are utilised to cleave the same molecule for complete degradation. Unfortunately, many of the cathepsins do not have substrate fluorophores that are established for live *in vitro* measurement of cathepsin activity within lysosomes. The DQ-BSA substrate fluorophore is a general cathepsin target that releases its fluorophore upon cleavage (Figure 64). This fluorescence is not altered by pH and thus, regardless of the lysosome microenvironment, only changes in cathepsin activity are assessed.

Like CatB activity in the fibroblasts, cathepsin active lysosome phenotypes were varied. Patient 2 had a non-significant reduction in the number of cathepsin active lysosomes (25 % ± 35, Figure 65A) and a significant reduction in total cathepsin active lysosome area (47 % ± 14, p = 0.002, Figure 65B) compared to Control 2. Patient 3 and the GBA/LRRK2 neurons had a non-significant increase in cathepsin active lysosome number (Patient 3: 62 % ± 39, GBA/LRRK2: 108 % ± 154, Figure 65A) and the GBA/LRRK2 patient showed elevated total cathepsin active lysosome area compared to Control 2 (65 % ± 19, p = 0.002, Figure 65B). The GBA patient had increased cathepsin active lysosome number (85 %) and total area (26 %). The trend of increased lysosome area continued with Patient 2 and the GBA/LRRK2 patient having significantly larger cathepsin active lysosomes (Patient 2: 13 % ± 1, p = 0.000005, GBA/LRRK2: 12 % ± 5, p = 0.01, Figure 65C) and Patient 3 showing non-significant increases (11 % ± 6, Figure 65C). Likewise, all three had significantly larger cathepsin active lysosomes in the perinuclear regions (Patient 2: 11 % ± 2, p = 0.00009, Patient 3: 12 % ± 1, p = 0.001, GBA/LRRK2: 12 % ± 5, p =0.02, Figure 65E). Despite this consistency, activity varied between patients. Patient 2 had significantly reduced cathepsin activity within the cathepsin active lysosomes compared to Control 2 (13 % ± 4, p = 0.006 Figure 65D), Patient 3 appeared unaltered and the GBA/LRRK2 patient was significantly increased (22 % ± 11, p = 0.03, Figure 65D). Likewise, the GBA patient had elevated activity (36 %, Figure 65D). These trends in cathepsin activity continued when assessing the perinuclear cathepsin active lysosomes (Patient 2: 17 % ± 7, p = 0.01, GBA/LRRK2: 33 % ± 16, p = 0.02, Figure 65F).

Interestingly, when treated with Llome, all four patients demonstrated greater cell death (Patient 2: 58 % ± 7, p = 0.02, Patient 3: 69 % ± 8, p = 0.02, GBA: 60 %, GBA/LRRK2: 59 % ± 10, p = 0.02, Figure 66) than the controls suggesting an increase in sensitivity compared to the controls (Figure 66).

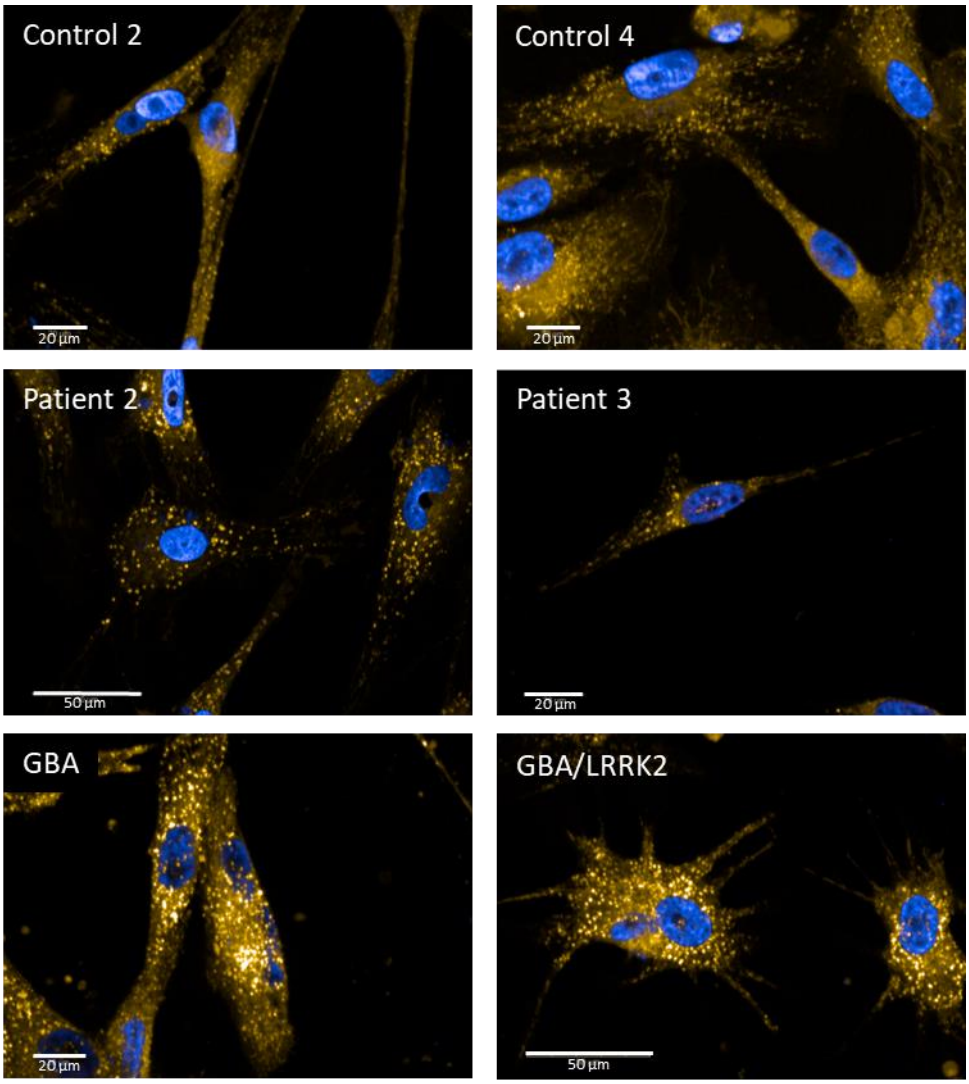

Figure 64: Representative images of DQ-BSA staining in the iDA neurons from each cell line showing cathepsin activity. Nuclei (blue) and cathepsin active lysosomes (orange). Scale bar = 20 µm or 50 µm.

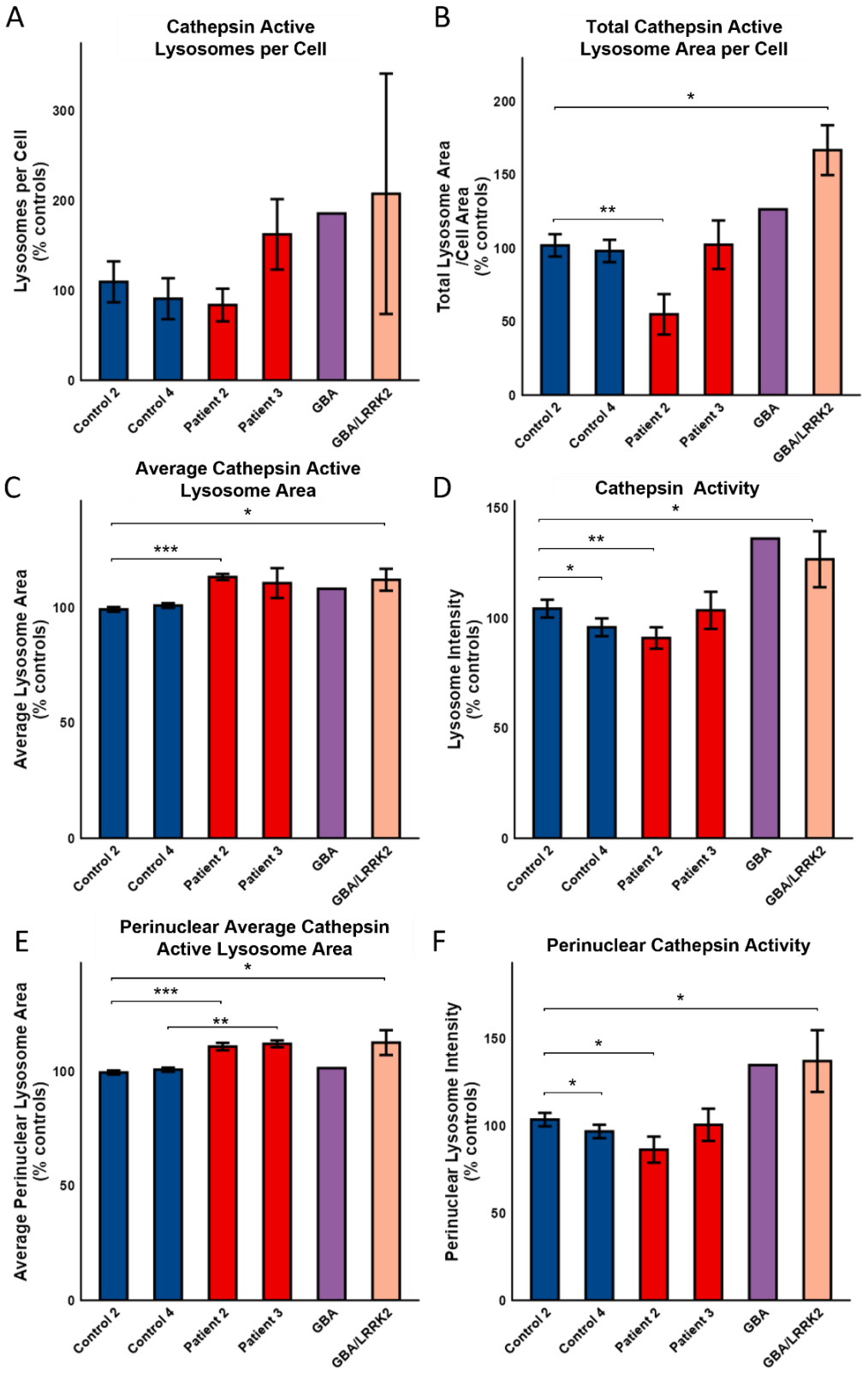

Figure 65: Cathepsin active lysosome phenotype in the iDA neurons. A) Cathepsin active lysosomes per cell, **B)** Total cathepsin active lysosome area adjusted by cell area, **C)** Average cathepsin active lysosome area, **D)** Cathepsin Activity, **E)** Average area of perinuclear cathepsin active lysosomes, **F)** Cathepsin activity in perinuclear lysosomes. Sporadic patients (red, n = 3/4) and the GBA/LRRK2 patient (pink, n = 4) were compared to the corresponding control (blue, n = 3/4) by unpaired T-tests with Welch correction (* $p < 0.05$, ** $p < 0.01$, *** $p < 0.001$). The GBA patient (purple, n = 1) was not statistically tested. Error bars depict standard deviation.

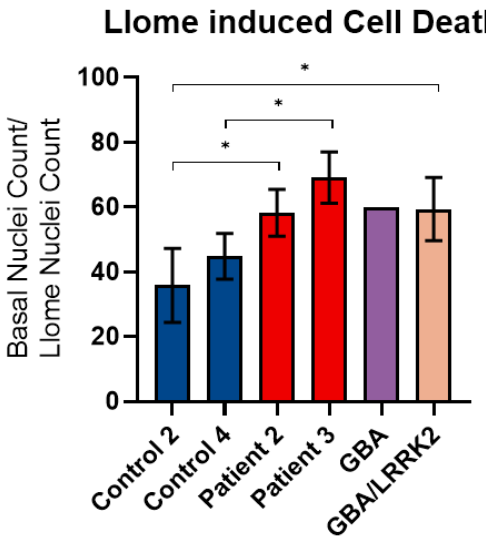

Figure 66: Cell death due to sensitivity to Llome. Sporadic patients (red, n = 3/4) and the GBA/LRRK2 patient (pink, n = 4) were compared to the corresponding control (blue, n = 3/4) by unpaired T-tests with Welch correction (* $p < 0.05$). The GBA patient (purple, n = 1) was not statistically tested. Each treatment was normalised to the basal condition per repeat. Error bars depict standard deviation.

4.3.2.5 Cathepsin B Activity

The trend in CatB activity observed in the fibroblasts continued in the iDA neurons. Significant differences were observed between Control 2 and Control 4 for CatB active lysosomes per cell (36 % ± 20, p = 0.04, Figure 68A), average CatB active lysosome area (7 % ± 3, p = 0.03, Figure 68C) and CatB activity within CatB active lysosomes (22 % ± 10, p = 0.02, Figure 68D).

CatB active lysosomes per cell (Patient 3: 135 % ± 125, GBA/LRRK2: 96 % ± 106, Figure 68A) and total CatB active lysosome area (Patient 3: 32 % ± 41, GBA/LRRK2: 28 % ± 25, Figure 68B) were elevated in Patient 3 and the GBA/LRRK2 patient, although, repeats were variable. Both sporadic patients had increased CatB active lysosomal size (Patient 2: 11 % ± 6, p = 0.01, Patient 3: 15 % ± 5, p = 0.03, Figure 68C). The GBA patient had larger CatB active lysosomes as well (15 %, Figure 68C). Patient 3 had significantly greater CatB activity within CatB active lysosomes (25 % ± 10, p = 0.03, Figure 68D) compared to Control 4 but this could be due to Control 4 having lower activity. The GBA patient had elevated CatB activity within CatB active lysosomes (64 %, Figure 68D).

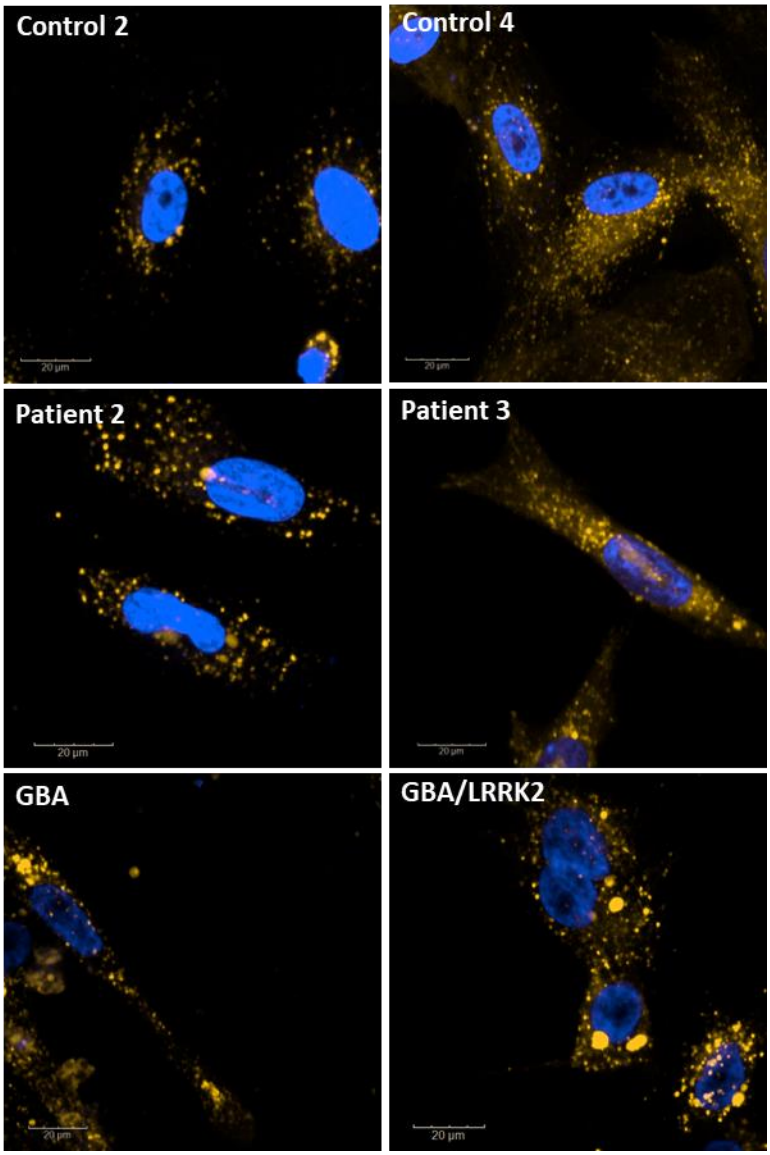

Figure 67: Representative images of MagicRed staining in the iDA neurons from each cell line showing CatB activity. Nuclei (blue) and CatB active lysosomes (orange). Scale bar = 20 µm.

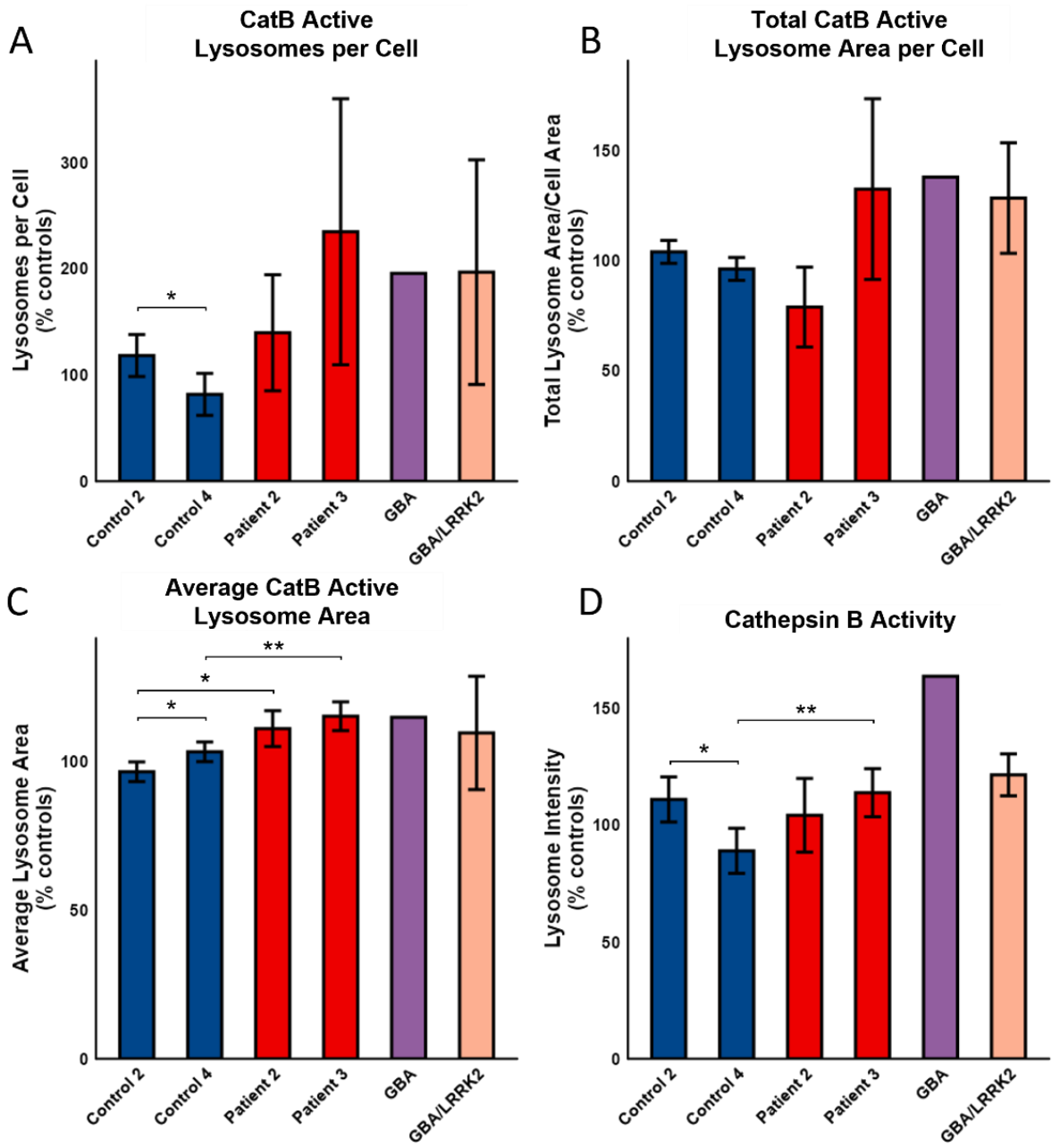

Figure 68: Cathepsin B active lysosome phenotype in the iDA neurons. A) CatB active lysosomes per cell, **B)** Total CatB active lysosome area adjusted by cell area, **C)** Average CatB active lysosome area, **D)** Cathepsin B Activity. Sporadic patients (red, n = 3/4) and the GBA/LRRK2 patient (pink, n = 5) were compared to the corresponding control (blue, n = 3/4) by unpaired T-tests with Welch correction (* $p < 0.05$, ** $p < 0.01$). The GBA patient (purple, n = 1) was not statistically tested. Error bars depict standard deviation.

4.3.2.6 Mitochondria Assessment

Neuronal phenotypes are often more severe than the phenotype observed in fibroblasts. Due to this the mitochondrial phenotype was assessed. This was done using TMRM to be consistent with the initial screen. The percentage of mitochondria undergoing mitophagy was also assessed to determine

if mitochondrial or lysosomal phenotypes were related to aberrations in mitophagy. However, this assessment was limited.

The number of functional mitochondria (Patient 2: 84 % ± 69, Patient 3: 104 % ± 43, p = 0.02, Figure 70A) and total area of functional mitochondria (Patient 2: 94 % ± 72, Patient 3: 92 % ± 36, p = 0.02, Figure 70B) was increased in both sporadic patients, significantly in Patient 3. These were highly variable in the GBA/LRRK2 patient, but the average functional mitochondria size was reduced (3 % ± 1, p = 0.04, Figure 70C). To assess mitochondrial function MMP was calculated. Patient 2 had reduced MMP but not significantly (19 % ± 18, Figure 70F).

The percentage of mitochondria co-occurring with lysosomes (measured by lysotracker green) was used to determine mitophagy. Mitophagy was significantly reduced in Patient 2 (27 % ± 10, p = 0.007, Figure 70D) but not Patient 3. Interestingly, mitochondria co-occurring with lysosomes were significantly larger in both sporadic patients than mitochondria in the control lysosomes (Patient 2: 2.5 % ± 1.1, p = 0.008, Patient 3: 3.4 % ± 0.9, p = 0.007, Figure 70E) and non-significantly in the GBA/LRRK2 patient (2.4 % ± 2.9, Figure 70E). The GBA neurons also had larger mitochondria within lysosomes (3 %, Figure 70E) and elevated mitophagy (22 %, Figure 70D).

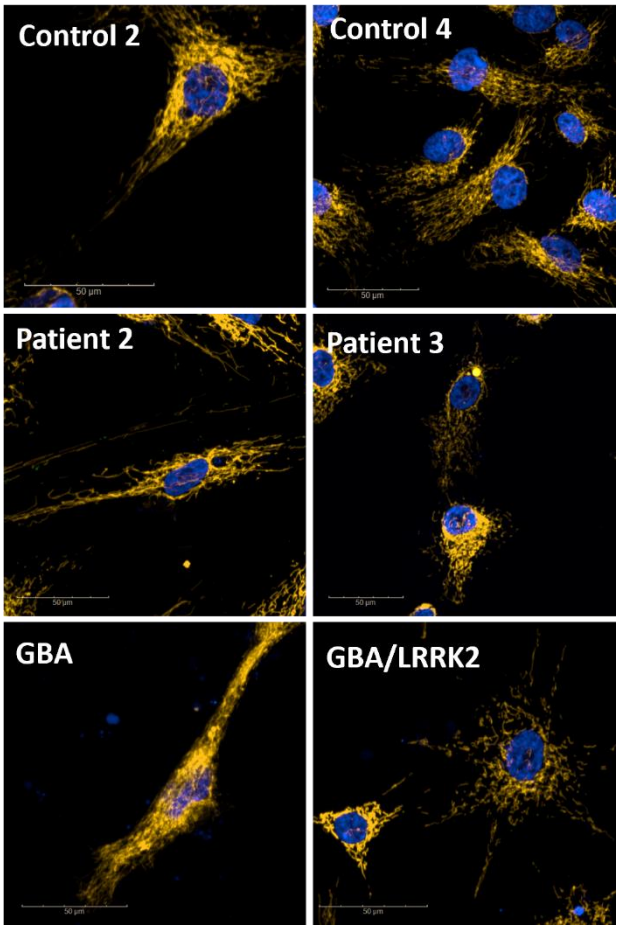

Figure 69: Representative images of functional mitochondria stained with TMRM in the iDA neurons from each cell line. Nuclei (blue) and functional mitochondria (orange). Scale bar = 50 µm.

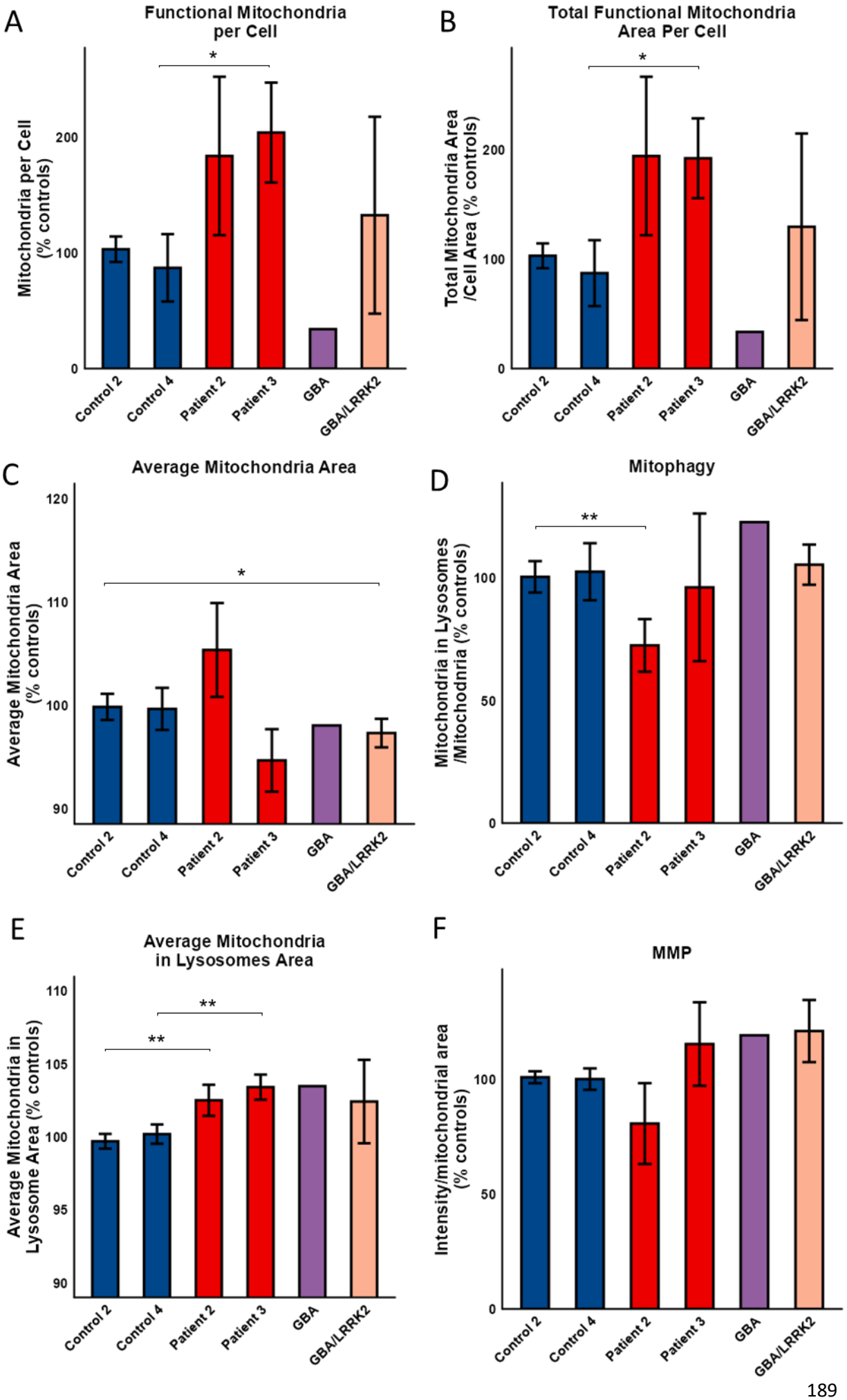
A
Functional Mitochondria per Cell
Mitochondria per Cell (% controls)
0
100
200
*
Control 2
Control 4
Patient 2
Patient 3
GBA
GBA/LRRK2
B
Total Functional Mitochondria Area Per Cell
Total Mitochondria Area /Cell Area (% controls)
0
100
200
*
Control 2
Control 4
Patient 2
Patient 3
GBA
GBA/LRRK2
C
Average Mitochondria Area
Average Mitochondria Area (% controls)
90
100
110
120
*
Control 2
Control 4
Patient 2
Patient 3
GBA
GBA/LRRK2
D
Mitophagy
Mitochondria in Lysosomes /Mitochodnria (% controls)
0
50
100
**
Control 2
Control 4
Patient 2
Patient 3
GBA
GBA/LRRK2
E
Average Mitochondria in Lysosomes Area
Average Mitochondria in Lysosome Area (% controls)
90
95
100
105
110
**
**
Control 2
Control 4
Patient 2
Patient 3
GBA
GBA/LRRK2
F
MMP
Intensity/mitochondrial area (% controls)
0
50
100
Control 2
Control 4
Patient 2
Patient 3
GBA
GBA/LRRK2

Figure 70: Mitochondrial phenotype in the iDA neurons from the lysosomal dysfunction subgroup and familial patients. A) Functional mitochondria per cell, **B)** Total functional mitochondria area adjusted by cell area, **C)** Average functional mitochondria area, **D)** Mitophagy, **E)** Average area of mitochondria undergoing mitophagy. Sporadic patients (red, n = 3/4) and the GBA/LRRK2 patient (pink n = 4) were compared to the corresponding control (blue n = 3/4) by unpaired T-tests with Welch correction (* $p < 0.05$, ** $p < 0.01$). The GBA patient (purple n = 1) was not statistically tested. Error bars depict standard deviation.

4.3.3 Therapeutic Screen in the Lysosomal Dysfunction Subgroup.

The purpose of subgrouping is to enable targeted therapeutic approaches with group specific treatments. As proof of concept, a small-scale screen with three chosen modulators to determine the effectiveness of stratification was begun. These were Ambroxol, Venglustat and Cardiolipin. This was conducted in iDA neurons as they are the predominant cell type affected in PD. The modulators were chosen based on results from the fibroblasts as neuron phenotyping was ongoing. Ambroxol, a repurposed cough medicine that is currently in Phase III clinical trial, is a chaperone that transports GCase from the endoplasmic reticulum to the lysosome (Mullin *et al.*, 2020). Venglustat is a glucosylceramide synthase inhibitor that failed in Phase III clinical trial. Inhibition of glucosylceramide synthase prevents the accumulation of the GCase substrate, glucosylceramide. Reduced CatD activity proved harder to target due to CatB and CatD's involvement in metastasis and cancer progression (Tan *et al.*, 2013). Very few activators of cathepsins have been reported, however, Cardiolipin elevates CatD activity (Watabe and Yago, 1983). Therefore, Cardiolipin was included as a proof of concept with the understanding that small molecule activators would need to be generated for a viable therapeutic strategy.

Due to time constraints, only one or two biological repeats were completed per assay. For this reason, no statistics have been calculated and work will be completed by the subsequent PhD student, Rhiannon Brown.

4.3.3.1 Lysosome Acidification

Results showed similar trends in Patient 2 and the GBA patient. Ambroxol did not change the total optimally acidic lysosome area and increased the average optimally acidic lysosome size in a dose-dependent fashion (Patient 2: 7-57 %, GBA: 2-25 %, Figure 71B). Reduced total optimally acidic lysosome area was observed in the GBA/LRRK2 patient (19-43 %, Figure 71A). All cell lines showed dose-dependent increases in acidification of the lysosomes, particularly at 30 µM, but this increase was extreme in Control 4, Patient 3, GBA and GBA/LRRK2 (Control 2: 30 %, Control 4: 130 % ± 82, Patient 2: 298 %, Patient 3: 25 %, GBA: 117 %, GBA/LRRK: 214 %, Figure 71C).

Venglustat increased average optimally acidic lysosome size in five of the lines, but no difference between patients was observed (Control 4: 1-44 %, Patient 2: 4-36 %, Patient 3: 4-37 %, GBA: 3-41 %, GBA/LRRK2: 100 µM 22 %, Figure 72B). At 100 µM total optimally acidic lysosome area was reduced extensively in the GBA patient (53 %, Figure 72A). Interestingly, Patient 3 showed elevated total area at 100 µM (26 %, Figure 72A). Five cell lines showed increased acidification at 100 µM but only the GBA patient showed an elevation at 10 µM (Control 4: 176 %, Patient 2: 82 %, Patient 3: 105 %, GBA: 10 µM = 61 %, 100 µM = 177 %, GBA/LRRK2: 107 %, Figure 72C). No difference in acidification response was observed between patients and Control 4 (Figure 72C).

Cardiolipin did not alter the average size (Figure 73B) or total area (Figure 73A) of optimally acidic lysosomes, except in the GBA/LRRK2 patient that had a reduced lysosome size (15 % Figure 73B). Cardiolipin reduced acidification slightly in the sporadic patients and Control 2 but increased it in the fPD patients (Control 2: 9 %, Patient 2: 8 %, Patient 3: 6 %, GBA: 7 %, GBA/LRRK: 14 %, Figure 73C).

Total optimally acidic lysosome area for Pateint 3 (Figure 71A, Figure 72A, (Figure 73A) was lower in the therapeutic screen than the controls but higher in initial assays. This may be due to differences between rounds of differentiation or a response to the vehicle chemicals. More repeats are required to understand this observation and will be conducted by Rhiannon Brown.

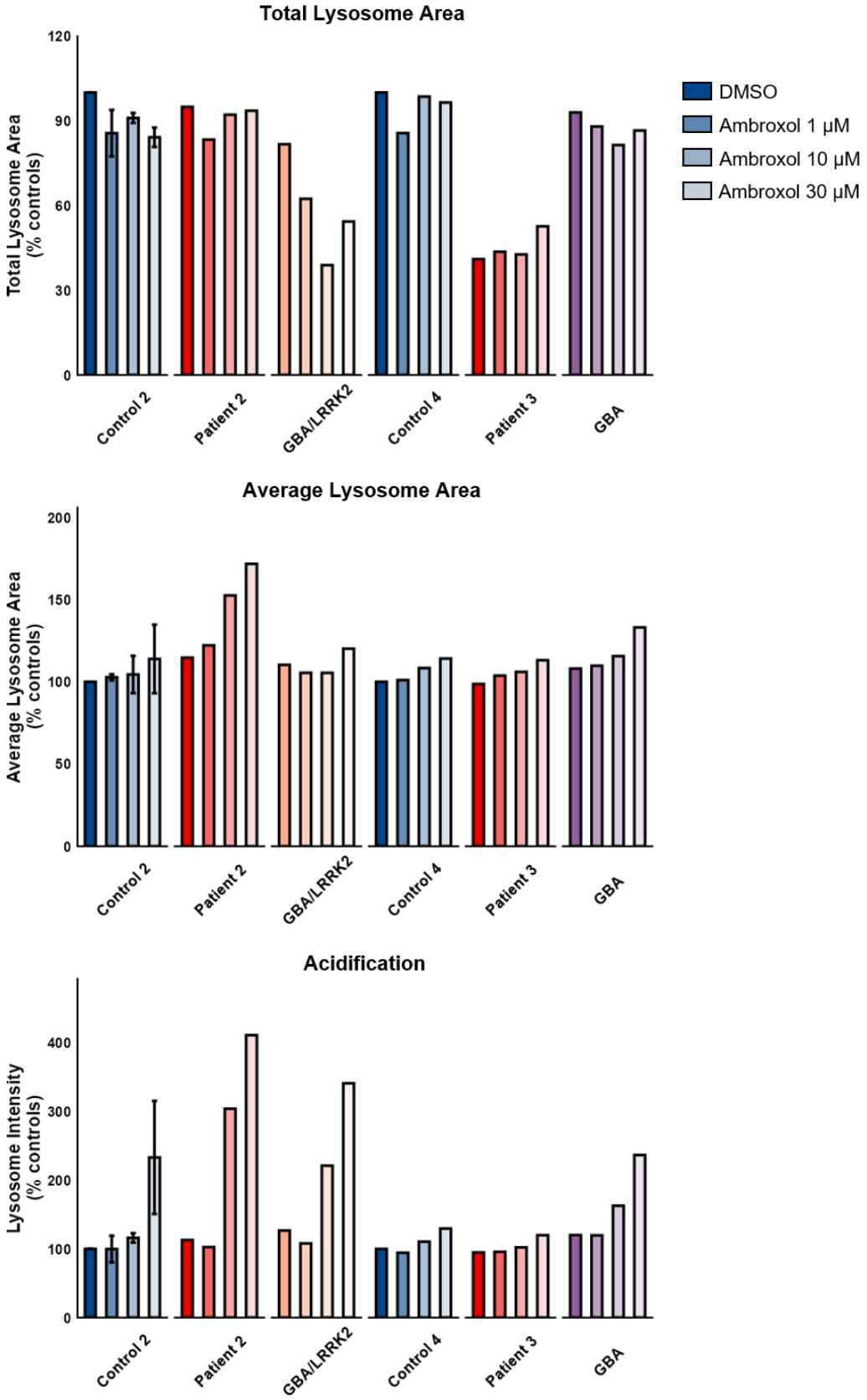

Figure 71: The effect of Ambroxol treatment on acidic lysosomes in the iDA neurons from the sporadic PD, GBA and GBA/LRRK2 patients. A) Total lysosome area adjusted by cell area, **B)** Average lysosome area, **C)** Lysosome pH (acidification). Patient 2 (red, n = 1) and the GBA/LRRK2 (pink, n = 1) were normalised to Control 2 (blue, n = 2) and Patient 3 (red, n = 1) and the GBA patient (purple, n = 1) were normalised to Control 4 (blue, n = 1). Ambroxol was assessed at 1, 10 and 30 µM.

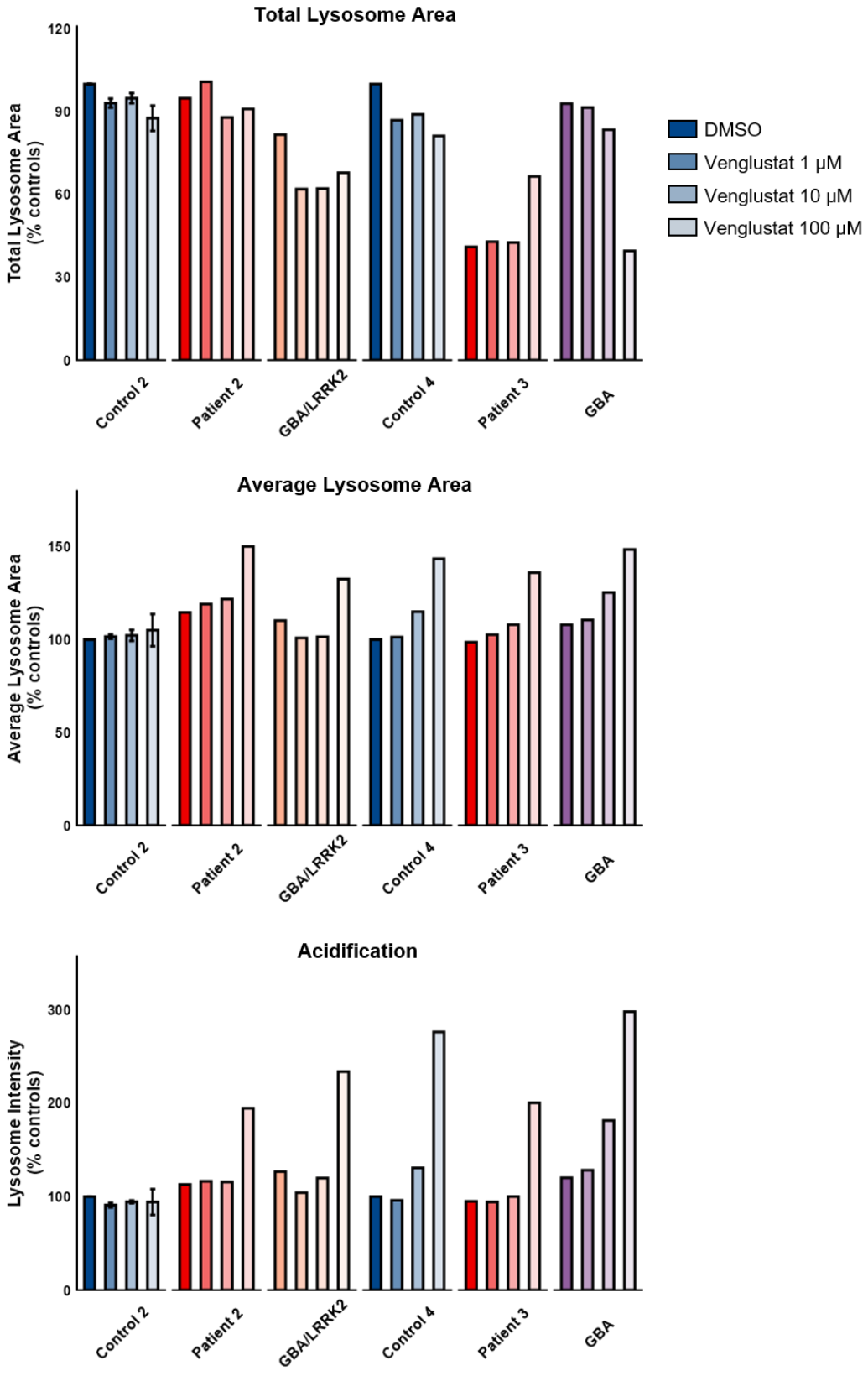

Figure 72: The effect of Venglustat treatment on acidic lysosomes in the iDA neurons from the sporadic PD, GBA and GBA/LRRK2 patients. A) Total lysosome area adjusted by cell area, **B)** Average lysosome area, **C**) Lysosome pH (acidification). Patient 2 (red, n = 1) and the GBA/LRRK2 (pink, n = 1) were normalised to Control 2 (blue, n = 2) and Patient 3 (red, n = 1) and the GBA patient (purple, n = 1) were normalised to Control 4 (blue, n = 1). Venglustat was assessed at 1, 10 and 100 µM.

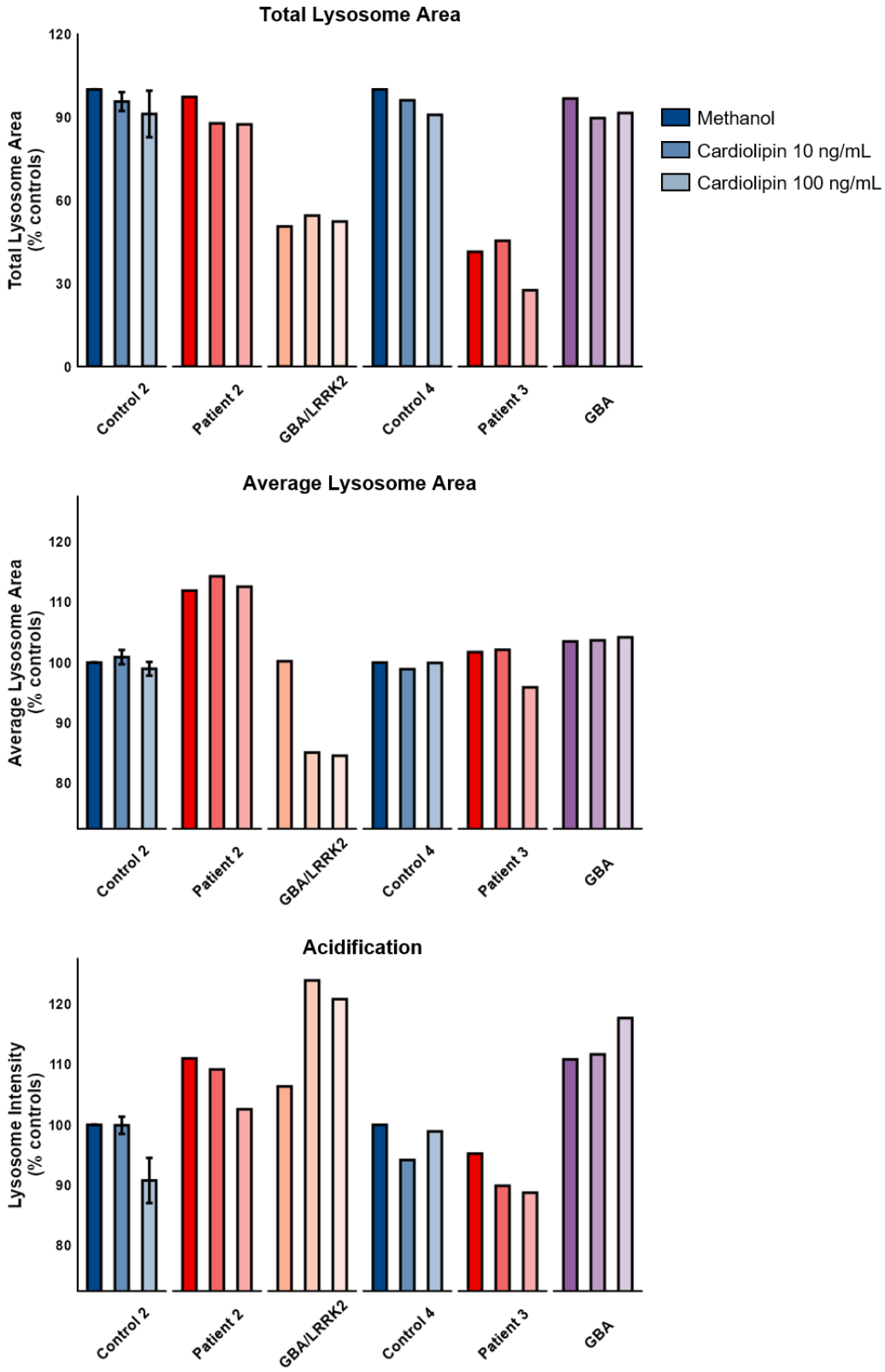

Figure 73: The effect of Cardiolipin treatment on acidic lysosomes in the iDA neurons from the sporadic PD, GBA and GBA/LRRK2 patients. A) Total lysosome area adjusted by cell area, **B)** Average lysosome area, **C)** Lysosome pH (acidification). Patient 2 (red, n = 1) and the GBA/LRRK2 (pink, n = 1) were normalised to Control 2 (blue, n = 2) and Patient 3 (red, n = 1) and the GBA patient (purple, n = 1) were normalised to Control 4 (blue, n = 1). Cardiolipin was assessed at 10 and 100 ng/mL.

4.3.3.2 Cathepsin Activity

Despite no change in acidic lysosome total area, Ambroxol at 10 µM and 30 µM elevated the total area of cathepsin active lysosomes in the sporadic patients and controls, the increase was greater in the patients (Control 2: 30-34 %, Control 4: 11-40 %, Patient 2: 61-65 %, Patient 3: 47-52 %, Figure 74A), except the GBA patient. The average cathepsin active lysosome area was increased in Patient 2 (5-16 %, Figure 74C) and the GBA patient (7-10 %, Figure 74C). Cathepsin activity within the cathepsin active lysosomes was raised in five of the lines but to a greater extent in all four patients (Control 4: 14-30 %, Patient 2: 48-65 %, Patient 3: 20-50 %, GBA: 35-57 %, GBA/LRRK2 67-75 %, Figure 74C).

Venglustat, did not change the cathepsin active lysosome total area (Figure 75A), average area (Figure 75B) or cathepsin activity (Figure 75C) in any of the cell lines at 1 µM and 10 µM. 100 µM increased cathepsin activity in Control 4 (15 %), Patient 3 (41 %) and the GBA patient (28 %) to a similar extent (Figure 75C).

In contrast, 100 ng/ml Cardiolipin reduced the total cathepsin active lysosome area (35 %, Figure 65A) and dramatically reduced average cathepsin active lysosome area (11 %) in Patient 2 but did not change area in the controls or the familial patients. This reduction in average area partially restored the patient's cathepsin active lysosome size to within the control range. Unexpectedly, cardiolipin did not elevate cathepsin activity. No change was observed in any of the cell lines, except Patient 2, which showed reductions in activity (14 %, Figure 76).

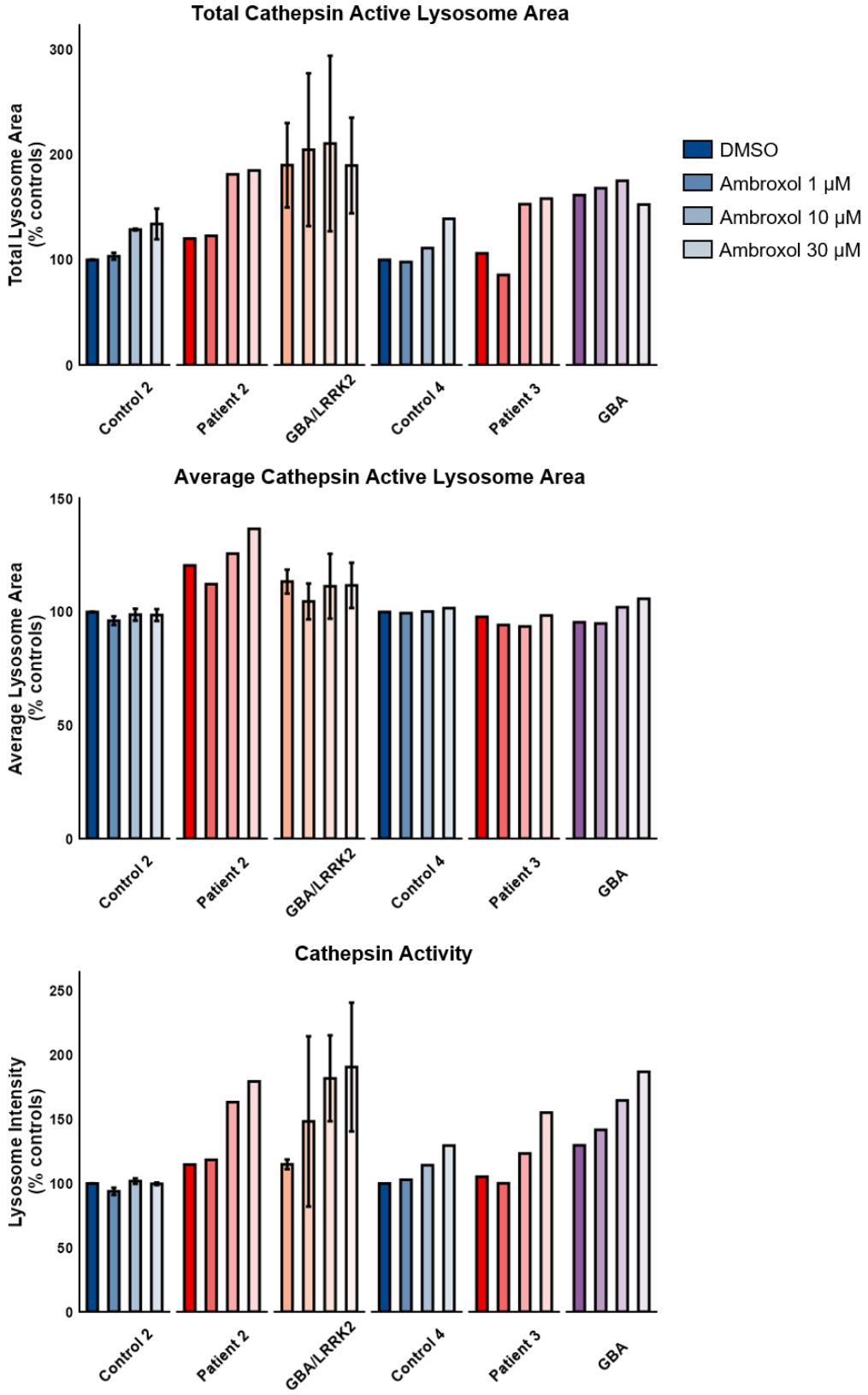

Figure 74: The effect of Ambroxol treatment on cathepsin activity in the iDA neurons from the sporadic PD, GBA and GBA/LRRK2 patients. A) Total cathepsin active lysosome area adjusted by cell area, **B)** Average cathepsin active lysosome area, **C)** Cathepsin activity. Patient 2 (red, n = 1) and the GBA/LRRK2 (pink, n = 2) were normalised to Control 2 (blue, n = 2) and Patient 3 (red, n = 1) and the GBA patient (purple, n = 1) were normalised to Control 4 (blue, n = 1). Ambroxol was assessed at 1, 10 and 30 µM.

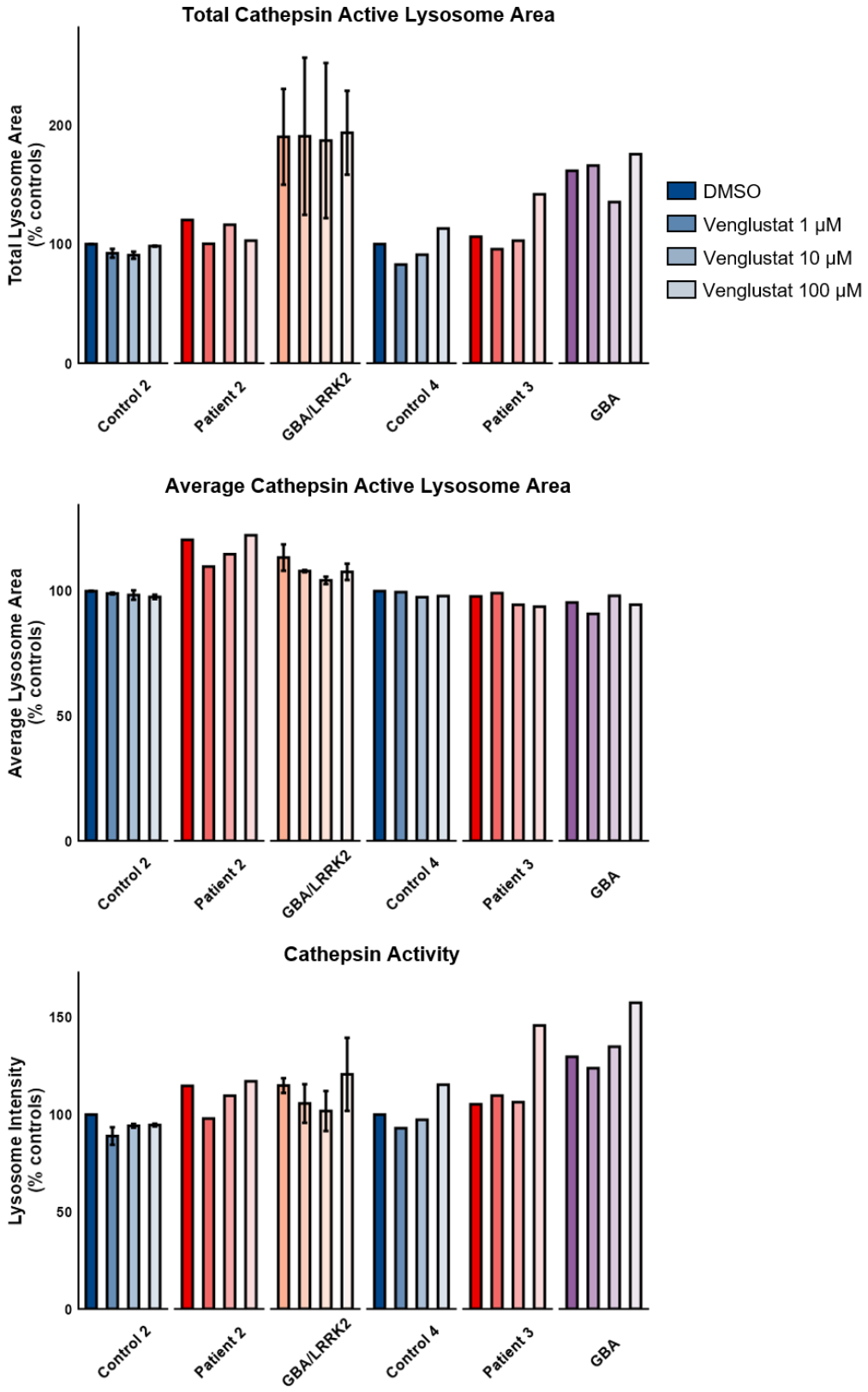

Figure 75: The effect of Venglustat treatment on cathepsin activity in the iDA neurons from the sporadic PD, GBA and GBA/LRRK2 patients. A) Total cathepsin active lysosome area adjusted by cell area, **B)** Average cathepsin active lysosome area, **C)** Cathepsin activity. Patient 2 (red, n = 1) and the GBA/LRRK2 (pink, n = 2) were normalised to Control 2 (blue, n = 2) and Patient 3 (red, n = 1) and the GBA patient (purple, n = 1) were normalised to Control 4 (blue, n = 1). Venglustat was assessed at 1, 10 and 100 µM.

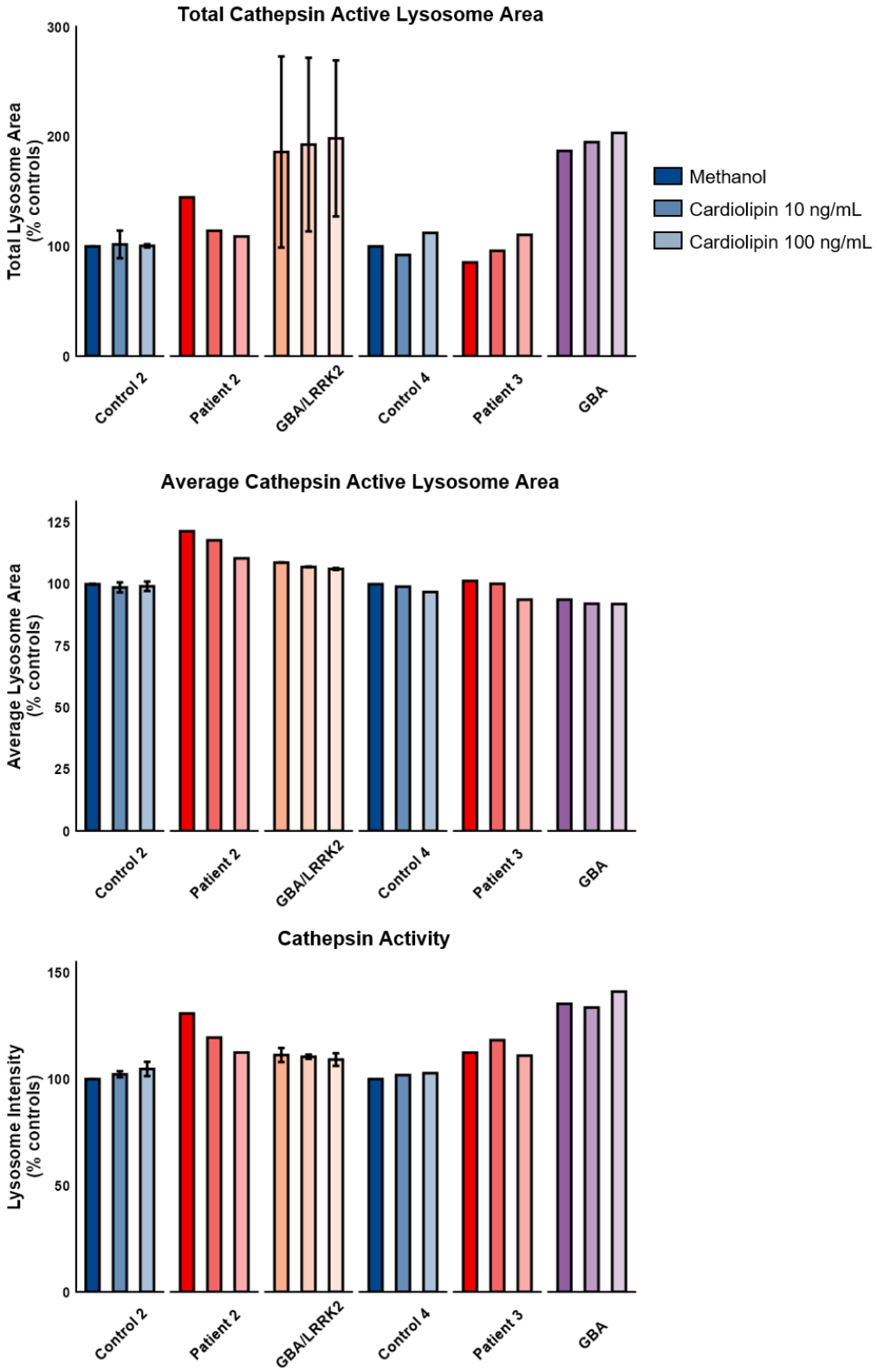

Figure 76: The effect of Cardiolipin on cathepsin activity in the iDA neurons from the sporadic PD, GBA and GBA/LRRK2 patients. A) Total cathepsin active lysosome area adjusted by cell area, **B)** Average cathepsin active lysosome area, **C)** Cathepsin activity. Patient 2 (red, n = 1) and the GBA/LRRK2 (pink, n = 2) were normalised to Control 2 (blue, n = 2) and Patient 3 (red, n = 1) and the GBA patient (purple, n = 1) were normalised to Control 4 (blue, n = 1). Ambroxol was assessed at 10 and 100 ng/mL.

4.4 Discussion

This chapter has investigated the lysosomal dysfunction subgroup in detail to assess disease driving mechanisms and explores a targeted therapeutic approach in iDA neurons. The aim was to validate the classification of the subgroup and identify mechanisms of dysfunction that can be targeted therapeutically. The three patient fibroblast lines were defined by a reduced number of lysosomes and smaller lysosomes but no abnormalities in mitochondrial function.

4.4.1 Fibroblast Phenotype.

4.4.1.1 LAMP2a Staining of Lysosomes

Assessment of lysosome content regularly relies upon LAMP protein immunocytochemistry. When pooled as a group the patients showed no difference in the number of lysosomes, total area of lysosomes or average area. However, one patient did display low numbers of lysosomes and very small lysosomes when compared to its corresponding control. LAMP2a is a crucial lysosome membrane protein that is present in immature and mature lysosomes (Qiao *et al.*, 2023), thus, lysosomes are stained regardless of their functionality. This implies that there is no difference between patients and controls in their ability to form lysosome structures. Whether these lysosomes are active, loaded with hydrolases and fusing with vesicles cannot be determined. Very few studies have assessed lysosomes in sPD cells. One study noted no difference in LAMP staining between pooled sPD patients and controls (Thomas *et al.*, 2021),. Several studies assessing patients with *GBA1* mutations observed no differences as well (McNeill *et al.*, 2014; Thomas *et al.*, 2021).

4.4.1.2 Acidification

During lysosome maturation, acidification of the lumen occurs to activate enzymes and enhance degradation. Defective acidification has been observed in patients with ATP13A1 mutations (Dehay *et al.*, 2012). Surprisingly, assessment of the subgroup using lysosensor green DND-189 revealed no differences between the patients and the controls. These patients showed a reduced number of lysosomes in the initial screen when assessed with lysotracker green. Lysotracker localises to acidic compartments regardless of pH, whereas lysosenor diffuses ubiquitously and only fluoresces upon protonation (*LysoTracker ® and LysoSensor ™ Probes*). The difference in localisation and fluorescence mechanism may influence results. Lysosensor is optimal at pH 4-5 leading to bright fluorescence and thus enables the measurement of optimally acidic lysosomes. In contrast, lysotracker has a broader pH range, sequestering in acidic compartments between pH 3-6. Thus, patients and controls have similar numbers of optimally acidic lysosomes however, the controls may have more lysosomes with a broader range of acidic pHs. The group was assessed in glucose conditions to determine basal lysosome levels. A reassessment of the initial screen results showed that two patients displayed worse

lysosome reductions in galactose media than glucose. Glucose depletion drives acidification of the lysosomes (Parra and Hayek, 2018), which may account for the lack of differences observed in glucose alone. This would suggest that the patients are unable to upregulate acidification upon glucose depletion. The brain is incredibly sensitive to glucose accounting for 20 % of the body's glucose usage (Howarth, Gleeson and Attwell, 2012). Neurons are the greatest users of glucose in the brain (Howarth, Gleeson and Attwell, 2012). When glucose levels are low cells rely on other metabolic pathways. A lack of adaptability of lysosomes may drive metabolic dysfunction in neurons, however, this is not observed in fibroblasts due to their reliance on glycolysis and other fuel types (Wang, Liang and Dai, 2022).

4.4.1.3 Cathepsin B

CatB is a cysteine protease that has been associated with PD. This association varies depending on the study. One study suggested that elevated CatB levels are protective (Lu *et al.*, 2024), while others suggest that CatB variants elevate the risk (Chang *et al.*, 2017; Nalls *et al.*, 2019; Blauwendraat *et al.*, 2020) and CatB is involved in the formation of truncated α-syn (McGlinchey *et al.*, 2019). Assessment in fibroblasts showed that when pooled there was no significant difference between patients and controls. However, when assessed separately two patients displayed reduced CatB active lysosome count and total CatB active lysosome area. One of the patients showed even greater reductions when the CatB active lysosomes in the perinuclear region were compared, suggesting a broader distribution of lysosomes in this patient. The third patient had an increased CatB active lysosome count and total area. CatB activity within the lysosomes was also more heterogeneous in the patients. No difference between culturing in glucose and galactose was observed suggesting that glucose depletion does not affect CatB activation in the controls compared to the patients despite having a possible impact on acidification (Parra and Hayek, 2018). This may be because CatB can be active at a neutral pH (Werle *et al.*, 1997) and thus differences in acidification may be irrelevant. Interestingly despite the patients having very similar acidification of lysosomes, CatB activity varies suggesting that pH is not the determining factor. Different protein levels of CatB have been observed in different disease models of PD (Qiao *et al.*, 2008; Hu *et al.*, 2022; Yadavalli and Ferguson, 2023). Protein levels may determine activity in the fibroblasts, this variation may be natural across healthy individuals as several studies have reported certain genetic variants of *CTSB* enable different protein expression levels and have correlated this to the risk of PD. Elevated CatB levels are associated with reduced risk (Lu *et al.*, 2024; Yusufujiang, Zeng and Li, 2024). Thus, the patient with elevated CatB active lysosomes and activity may be compensating for the dysfunction of CatD. Further investigation into the loading of CatB into lysosomes and total CatB protein levels would be interesting. Subgrouping via lysosome morphology using lysotracker does not produce a homogenous CatB phenotype in the patient's fibroblasts.

4.4.1.4 Cathepsin D

Studies identified deficits in CatD activity in patient-derived fibroblasts and neurons derived from PD patient neural crest stem cells (Carling *et al.*, 2020; Yang *et al.*, 2020). Using the same method of assessment, we identified a significant reduction in CatD activity in the pooled patient group compared to the controls. CatD is involved in α-syn cleavage (Qiao *et al.*, 2008; Cullen *et al.*, 2009; Crabtree *et al.*, 2014; R. P. McGlinchey and Lee, 2015; McGlinchey *et al.*, 2019) and is the most abundant aspartyl protease in the brain (Yadati *et al.*, 2020). It was reported that CatB cleaves α-syn to form truncated α-syn (McGlinchey *et al.*, 2019). Reduced CatD activity may result in a reduced ability to degrade the truncated variant further because it cleaves alternative sites to CatB. Evaluation of α-syn forms in SNCA A53T mice found the most common truncated form to be 1-90 amino acids, this variant can only be produced by CatB (McGlinchey *et al.*, 2019). Truncated variants of α-syn aggregate more readily (Serpell *et al.*, 2000; Murray *et al.*, 2003; Levitan *et al.*, 2011; Iyer *et al.*, 2017; Ma *et al.*, 2018), especially within acidic environments such as the lysosome lumen (Uversky, Li and Fink, 2001). Thus, reduced activity of CatD may drive or exacerbate α-syn aggregations contributing to PD pathology. The exact cause of the reduced activity is unknown, however, ambroxol, the GCase chaperone, rescues CatD activity (Yang *et al.*, 2020) and a study showed that ceramide the product of GCase catalysis can activate CatD (Heinrich *et al.*, 2000). It is therefore possible that GCase activity is having a knock on effect on CatD. Due to difficulties with optimisation and ultimately time constraints, assessment of GCase activity within these cells was not possible. However, future work will investigate this theory.

4.4.2 Neurons

The use of induced cell types is becoming more common in neurodegenerative diseases. Neurons are lifelong cells that do not proliferate and their architecture is critical to memory, movement and other vital processes. Therefore, biopsying these cells is not possible. Postmortem tissue provides a valuable source of disease-relevant cell types, however, there are many drawbacks. Firstly, there is a limited supply of tissue per person. Secondly, most donations come from patients succumbing to the disease, meaning that late stages of the disease can be investigated but early stages cannot (Hartmann, 2004). Finally, postmortem cells cannot be used for drug screens.

Other patient-derived samples provide disease-relevant information but cannot reveal the vulnerability of the affected cell type, in PD's case, Dopaminergic neurons. iPSC and iNPC induced neurons and glia are valuable models of disease that maintain the dysfunction phenotypes and polygenic risk of the patient. iPSCs are the most common model; produced from hair follicles, fibroblasts or blood cells, they have the capability of differentiating into any cell type (Cerneckis, Cai

and Shi, 2024). iNPCs are produced from skin fibroblasts using the same Yamanaka factors as iPSCs, however, the cells are forced down the neuronal progenitor cell route early in reprogramming (Meyer *et al.*, 2014). This is possible due to the fibroblasts and neuronal cells shared ectodermal origin. Prevention from reaching pluripotency maintains the cells' ageing phenotype and cumulative lifestyle damage (Gatto *et al.*, 2021). Another advantage is that they are not clonal, unlike iPSCs, which prevents clonal bias (Willmann *et al.*, 2013). One disadvantage of iNPCs is that they can only differentiate into central nervous system neurons (Schwartzentruber *et al.*, 2020), astrocytes (Meyer *et al.*, 2014) and oligodendrocytes (Ferraiuolo *et al.*, 2016). For these reasons, iNPCs were the chosen model for this project. iNPC differentiation is a shorter protocol for iDA neurons compared to iPSCs (Schwartzentruber *et al.*, 2020), which greatly improved throughput and reduced cost. Differentiation of the neurons followed the protocol described by Schwartzentruber *et al.* (2020), which established TH-positive neuron cultures (89 %). Differentiation of the six cell lines successfully produced neurons expressing β-III-Tubulin, MAP2, DAT and TH. Further investigation showed neuronal morphology in the controls (Schwartzentruber *et al.*, 2020), Patient 2 and the GBA/LRRK2 patient. PRKN patient cells showed increased roundness and reduced elongation similar to that observed in Patient 3 and the GBA patient. One aspect that should be explored is the expression of non-neuronal markers to assess contamination of the differentiation but due to time constraints, this was not possible. Some expression markers that could be assessed are glial fibrillary acidic protein and vimentin for astrocytes (Meyer *et al.*, 2014) or myelin basic protein and neural/glial antigen 2 for oligodendrocytes (Ferraiuolo *et al.*, 2016). In theory, due to lineage, microglia cannot be differentiated using iNPCs, but ionized calcium-binding adapter molecule 1 could be used to confirm this (Jurga, Paleczna and Kuter, 2020).

Neurons derived from iNPCs express α-syn as expected and patients even form Lewy Body-like aggregates (Hughes, 2023). Thus, mechanisms that would not influence phenotypes in fibroblasts contribute to pathology, such as α-syn toxicity and oxidative stress. Previous studies have shown that the mitochondrial and lysosomal dysfunction phenotypes are consistent between fibroblasts and iDA neurons (Mortiboys *et al.*, 2008; Carling *et al.*, 2020; Schwartzentruber *et al.*, 2020). Parkin patient iDA neurons showed reduced MMP and ATP levels but to a greater extent than the fibroblasts (Schwartzentruber *et al.*, 2020). Likewise, sPD patients iDA neurons from the mitochondrial dysfunction subgroup showed reduced MMP and ATP levels and patients from the lysosomal dysfunction subgroup showed an increase in the number of lysosomes per cell (Carling *et al.*, 2020). The generation of iNPCs and the subsequent differentiation was a time-consuming and labour-intensive task, which limited their exploration.

4.4.2.1 Lysosome Morphology and Acidification

Lysotracker green was used in a similar fashion to the initial screen to assess lysosome morphology in two sPD patients from the lysosomal dysfunction subgroup, the GBA N370S patient (GBA 1) and the LRRK2 G2019S, GBA N370S digenic patient. In contrast to the fibroblasts, both sporadic patients showed an increase in total lysosome area, although the results in the patients were variable. Interestingly, assessment with lysosensor showed an increase in the number of optimally acidic lysosomes per cell in both sporadic patients, but no difference in total lysosome area. Lysosensor showed no difference in the lysosomes pH between the patients and controls so it is unclear why lysotracker and lysosensor produced differing results. The assays were completed on neurons from the same differentiation, albeit different plates. Lysotracker accumulates in acidic compartments and fluoresces in a pH-independent fashion. Accumulation can occur in acidic pHs and no defined optimal pH is reported, but it is suggested to accumulate between pH 3-6 (*LysoTracker ® and LysoSensor ™ Probes*). Lysosensor on the other hand fluoresces optimally between pH 4-5. The intensity tails off quickly as the pH shifts towards pH 6 (Lin *et al.*, 2001). It could be argued that lysotracker accumulates in lysosomes with a lower acidity than lysosensor causing a difference in lysosome sampling. Segmentation relies upon the intensity of the lysosomes so if lower pH lysosomes do not fluoresce enough with lysosensor they would be excluded. Despite the differences both assays suggest an increase in the lysosome content per cell, which is consistent with Carling *et al.* (2020), although, the patients were grouped by different defining features.

4.4.2.2 Cathepsin Activity

The CatD assay utilised in the fibroblasts requires large amounts of protein, thus using the iDA neurons was not feasible. No fluorescent substrates enabling the specific measurement of live *in vitro* CatD activity are currently available, so DQ-BSA was utilised to measure total cathepsin activity. The number of cathepsin active lysosomes showed no difference in the sporadic patients, but the total area of cathepsin active lysosomes was reduced in Patient 2. No difference in activity within lysosomes was observed.

CatB activity was assessed to determine its contribution to protein degradation in the neurons. No significant differences were observed in the number of CatB active lysosomes or their total area in the patients. Increases in these parameters were variable in Patient 3. This suggests that CatB is not responsible for the reduced cathepsin active lysosome content observed in Patient 2 in the DQ-BSA assay. CatB activity within the lysosomes did not differ between Control 2, Patient 2 and Patient 3, but was lower in Control 4. Suggesting that further investigation of variation between controls should be conducted.

The LRRK2/GBA patient showed a very different phenotype. Its cathepsin active lysosome total area and cathepsin activity within those lysosomes were significantly increased. The LRRK2/GBA patient also showed an elevated total CatB active lysosome area, however, CatB activity was not increased in these lysosomes, demonstrating that more lysosomes in LRRK2/GBA patient are carrying out increased protein degradation, but CatB is not responsible for the increased degradation.

Enlarged cathepsin active lysosomes were observed in the sporadic patients. This increase in size was observed in CatB active lysosomes as well. Suggesting that despite enlargement, the lysosomes remain functional.

4.4.2.3 Enlarged Lysosomes

In the acidic lysosome assays and enzyme activity assays, enlarged lysosomes were observed in the sporadic patients. This phenomenon was observed in LRRK2 G2019S transgenic mouse astrocytes and GBA N370S patient-derived fibroblasts (Henry *et al.*, 2015; García-Sanz *et al.*, 2017). Enlarged lysosomes are commonly seen in lysosomal storage disorders (Platt, 2018; de Araujo *et al.*, 2020). Enlarged lysosomes would suggest the accumulation of a substrate, as seen in lysosomal storage disorders. This could be caused by two mechanisms, reduced degradation or reduced release of lysosomal contents. An accumulating substance has yet to be identified but proposed candidates are α-syn, glucosylceramide or glucosylsphingosine. Reduced GCase activity results in significant but modest increases in glucosylceramide and glucosylsphingosine in sPD brains (Rocha *et al.*, 2015; Huebecker *et al.*, 2019), but is not associated with Lewy Bodies (Clark *et al.*, 2006; Kurzawa-Akanbi *et al.*, 2021), suggesting possible sequestration within lysosomes. Not all studies found an increase (Gegg *et al.*, 2015), which may be due to heterogeneity in sPD patients GCase activity (Thomas *et al.*, 2021; Labrador-Garrido *et al.*, 2023). Lysosomes are a possible origin for α-syn aggregates and inhibition of CatB caused α-syn aggregation to initiate in LAMP1 lysosomes (Tsujimura *et al.*, 2015). Our results and others have suggested that CatD activity deficits are observed in PD (Carling *et al.*, 2020; Yang *et al.*, 2020). Knockout of *CTSD* in SH-SY5Y cells resulted in the enlargement of a proportion of lysosomes, although no significant difference was observed in the total population (Gallwitz *et al.*, 2024). Studies of lysosomes tend to focus on one enzyme and its substrates, however, cathepsins have a broad range of substrates and dysfunction may impact other hydrolases. Thus, enlargement may not be specific to a single substrate but a broad accumulation of substrates resulting in cargo full lysosomes.

Cargo full lysosomes could also be caused by problems with releasing contents once degraded. LRRK2 has been implicated in the retrograde transport of lysosome contents to the golgi. Dysfunction caused by LRRK2 mutations resulted in lysosome swelling (MacLeod *et al.*, 2013; Pang *et al.*, 2022), therefore, it is plausible to suggest that dysregulation in this pathway may contribute to sPD. Enlarged lysosomes

in Niemann-Pick disease Type C are caused by the defective transport of cholesterol out of the lysosomes (Kosicek *et al.*, 2018). Dysfunction of lysosome transporters could contribute to PD, although this has not been investigated.

Evidence suggests that enlargement could result from dysfunction in lysosome fission. Lysosomes undergo fusion to engulf content, this leads to an enlargement of the lysosome. Lysosomes undergo fission to reduce their size and produce vesicles that can be transported to other parts of the cell. Dysfunction in lysosome fission is linked to enlarged lysosomes in hereditary spastic paraplegia. Other evidence shows that inhibiting PIKfyve, a fission regulator, leads to enlargement of the lysosomes. One study theorised that GCase deficiency increased cholesterol leading to dysfunctional fission in PD (de Araujo *et al.*, 2020). Lysosomal fission is still not understood and aside from the study mentioned has not been investigated in PD.

Overall, our results suggest that lysosome dysfunction is greater in the four patients than the controls. Treatment with Llome causes lysosome membrane permeabilisation and enzyme release into the cytosol. It is commonly used as a negative control. Interestingly, all four patients showed increased cell death compared to the controls. This suggests an increase in sensitivity and an inability to adapt to stress. It is unclear whether the cell death is due to an inability to compensate for reduced lysosome function or that protease-activated caspase apoptosis is triggered more easily.

4.4.2.4 Treatment with Lysosome Targeting Compounds

Targeting lysosome mechanisms with small molecules has been investigated as a possible treatment. This is an early proof of concept screen, and no target engagement assays were conducted. Thus, the lack of efficacy may be due to incorrect dosing or target engagement. Three compounds were chosen, Ambroxol, Venglustat and Cardiolipin. Ambroxol is a GCase chaperone that is about to be assessed in a Phase III clinical trial. Ambroxol was included because it has been shown to rescue CatD activity (Yang *et al.*, 2020). Venglustat inhibits glucosylceramide synthase, which produces glucosylceramide, the substrate of GCase. Venglustat failed in a Phase III clinical trial so assessment could highlight whether failure was due to a general lack of effect on lysosomes or possibly due to other factors such as mechanism heterogeneity in the trial. The final substance, cardiolipin, was added as a known CatD activator (Watabe and Yago, 1983). This was included instead of small molecules because few cathepsin activators have been reported or investigated as increased CatB and CatD activity is associated with metastasis in cancer (Tan *et al.*, 2013). Due to time constraints, only one or two repeats per assay were conducted, thus results should be interpreted with caution.

Ambroxol was the only treatment to have an effect at multiple doses. It caused a dose dependent increase in lysosome size, which was unexpected considering that patients already have an increased

lysosome area. Lysosome acidification also increased in both patients and controls when treated with 10 µM and 30 µM Ambroxol. This increase in acidification would suggest that the lysosomes are attempting to increase their degrading activity. Ambroxol did not alter the total optimally acidic lysosome area. However, it showed a dose dependent increase in total cathepsin active lysosome area in the sporadic patients and their controls and increased cathepsin activity in both patients to a greater extent than the controls. It is unclear how Ambroxol elevates cathepsin activity, however, the product of GCase catalysis, ceramide, is an activator of CatD (Heinrich *et al.*, 2000).

Venglustat showed good target engagement in the preclinical animal studies reducing glucosylceramide dramatically (Viel *et al.*, 2021). However, assessment of Venglustat in this screen showed minimal impacts on lysosomes unless treated at 100 µM. Concentrations of 100 µM are exceptionally high for a compound *in vitro* study and suggest very high concentrations would be required in the clinic. At 100 µM Venglustat dramatically increased the average lysosome area and pH of the six cell lines. Venglustat did not alter the total cathepsin active lysosome area or cathepsin active lysosome size. Failure of Venglustat at trial and a lack of alterations in this screen could suggest that the accumulation of glucosylceramide does not drive PD. GCases' other substrate glucosylsphingosine may have a detrimental role in PD. It is important to note that the lack of response in this screen may be due to a lack of target engagement. Further research with different dosing regimes may result in different activity.

4.4.2.5 Mitochondrial Dysfunction

The fibroblasts of these patients showed very little mitochondrial dysfunction. Assessment of the mitochondria in the sporadic patients showed an increase in functional mitochondria per cell and increased total mitochondria area. Mitophagy was assessed to determine whether deficits were driving an increase in mitochondria. Significant reductions were identified in Patient 2 but not in any of the other patients, however, the average size of the mitochondrial undergoing mitophagy was increased. Increased mitochondrial content has been observed in several genotypes of PD and sporadic patients. However, MMP is not affected in these patients, so it is unclear why the network is increased.

4.4.2.6 Conclusion

This chapter has outlined the investigation of the lysosomal dysfunction subgroup. Investigation of lysosomal function in the fibroblasts highlighted a reduction in CatD activity similar to other studies (Carling *et al.*, 2020; Yang *et al.*, 2020). Lysosome function and morphology were then investigated in iDA neurons and demonstrated an enlargement of the lysosomes in the sporadic patients. Enlargement may be due to reduced degradation, product release or fission, however, these are

processes which are still unclear in PD. Although, lysosomes were enlarged no deficit in acidification or cathepsin activity was observed, however, CatD was not assessed. Finally, our limited therapeutic assays showed that Ambroxol elevated cathepsin activity, in keeping with previous research. Further work to understand Ambroxol's full effect will be conducted in the future.

5 Chapter 5: Assessment and Validation of the Mitochondrial Dysfunction Subgroup and Low Mixed Subgroup

5.1 Introduction

Mitochondrial dysfunction has been associated with PD since the 1980s when MPTP was associated with Parkinsonian symptoms. Multiple mitochondrial toxins have since been identified as environmental risks for PD, such as rotenone (Sherer *et al.*, 2003) and paraquat (Mollace *et al.*, 2003). Today mitochondrial dysfunction is widely recognised as a hallmark of PD. No specific cause of mitochondrial dysfunction has been identified in sPD, although several genetic mutations in mitochondrial-associated genes result in early-onset fPD (Kitada *et al.*, 1998; Valente *et al.*, 2001; Bonifati *et al.*, 2003).

Mitochondrial dysfunction in sPD is heterogeneous, which may account for the varied results published to date. One commonly identified deficit is a reduction in complex I activity, which has been observed in postmortem SN, platelets and patient-derived fibroblasts (Bindoff *et al.*, 1989; Schapira *et al.*, 1990; Benecke, Strümper and Weiss, 1993; Keeney *et al.*, 2006; Carling *et al.*, 2020). MPTP, rotenone and paraquat are all complex I inhibitors further associating complex I activity deficiency with PD (Langston *et al.*, 1984; Mollace *et al.*, 2003; Sherer *et al.*, 2003). However, reduced complex I activity has not been observed in all studies (Winkler-Stuck *et al.*, 2004; del Hoyo *et al.*, 2010; Subrahmanian and LaVoie, 2021). A recent study identified a complex I deficient subgroup of sPD, by quantifying the levels of complex I in the brain (Flønes *et al.*, 2024), suggesting that conflicts are due to heterogeneity. However, different methodologies may also account for the differences. Another study quantified complex I levels in iPSC-derived iDA neurons finding high variation in the patients (Schmidt *et al.*, 2023). Complex I is the first respiratory complex in the ETC and pumps protons across the IMM to the intermembrane space maintaining MMP.

Abnormal MMP and respiratory chain activity have also been identified in sPD, however, these are again variable. Some studies on patient-derived fibroblasts have identified elevated MMP (Antony *et al.*, 2020; Deus *et al.*, 2020), others identified no difference (Carling *et al.*, 2020; Arena *et al.*, 2024) and some have shown a deficit (Carling *et al.*, 2020). Similarly, reports of mitochondrial oxidative phosphorylation function vary. A report by Ambrosi *et al.* (2014), identified a small deficit in basal respiration and a significant reduction in maximal respiration. This was linked with a reduction in proton leakage. However, the same research group identified elevated maximal respiration in multiple

sPD patients from a new cohort. In this instance, the methodology is unlikely to account for the variability and thus, the results likely reflect the heterogeneity of respiratory chain activity in sPD. Reduced maximal respiration and elevated maximal respiration have been identified independently as well (Teves *et al.*, 2018; Corenblum *et al.*, 2023). Altered vulnerability to respiratory chain dysfunction may be related to genetic risk factors in PD or lifestyle of patients. Arena *et al.* (2024) outlined a polygenic risk score that classified patients based on oxidative phosphorylation-related gene risk. Fibroblasts with a high oxidative phosphorylation risk score showed significantly higher basal respiration compared to those with a low risk. This was also associated with increased ATP-linked respiration and increased proton leakage, which has been previously shown in sPD (Teves *et al.*, 2018). This variation is shown in other models of sPD, iPSC-derived iDA neurons showed no significant difference in maximal respiration when cultured in glucose-containing media, however, the variation in the patients was greater with several patients showing exceptionally low or high maximal respiration (Corenblum *et al.*, 2023; Schmidt *et al.*, 2023). When the culturing conditions were altered to culture with pyruvate instead of glucose the iDA neurons showed significantly lower basal and maximal respiration, suggesting an inability to compensate (Schmidt *et al.*, 2023).

It is well-established that respiratory complexes and mitochondria are the main source of damaging ROS (Murphy, 2009). However, it is unclear whether ROS damage to the ETC drives the reduced activity and dysfunctional respiration or if other mechanisms result in dysfunction which generates harmful levels of ROS resulting in further damage. Keeney *et al.* (2006) assessed complex I from the PFC of patients and found elevated oxidative damage, particularly in catalytic subunits. Levels of damage inversely correlated with the rate of NADH electron transfer suggesting that oxidative damage is related to dysfunction (Keeney *et al.*, 2006). Despite these results, it is still unclear which occurs first, although, increased ROS is associated with healthy ageing (Brand *et al.*, 2004) suggesting that ROS levels may be the catalyst. Whereas, rotenone and MPTP inhibit complex I causing elevated ROS, suggesting that dysfunction occurs first (Wu *et al.*, 2003; de Siqueira *et al.*, 2023).

Mitophagy is required to maintain a healthy mitochondrial network that is able to adapt to the metabolic demands of the cell. Dysregulation of mitochondrial quality control is proposed to result in increased levels of damaged mitochondria and elevated ROS in PD. PINK1 and Parkin mutations cause the dysregulation of mitophagy (as reviewed by Pickrell & Youle, 2015) resulting in mitochondrial dysfunction (Mortiboys *et al.*, 2008; Grünewald *et al.*, 2010). Understandably much of the research into mitophagy has been conducted on familial mutant models of PD. However, elevated levels of phosphorylated ubiquitin have been observed in some sPD patients' postmortem brain tissue (Shiba-Fukushima *et al.*, 2017; Hou *et al.*, 2018). Furthermore, dysfunction in PINK1/Parkin-mediated mitophagy in fibroblasts and iPSC-derived neurons from sPD patients results in the accumulation of

Miro1, which is similar to familial mutation carriers (Hsieh *et al.*, 2016; Shaltouki *et al.*, 2018). Elevated Miro1 levels have been identified in PD postmortem brain tissue as well (Shaltouki *et al.*, 2018). Many companies are targeting mitophagy with small molecules to develop disease-modifying treatments for PD. For example, ubiquitin specific peptidase 30 (USP30) inhibitors prevent the removal of ubiquitin chains on mitochondria, thus, result in heightened degradation (Tsefou *et al.*, 2021). USP30 inhibitors partially rescued MMP in iNPC-derived iDA neurons carrying PRKN mutations by increasing mitophagy (Rusilowicz-Jones *et al.*, 2022). This method of treatment could be translated to sPD.

These findings all demonstrate the role of mitochondrial dysfunction in sPD and its heterogeneous nature. Findings from the initial screen identified mitochondrial dysfunction in the mitochondrial dysfunction subgroup and low mixed group. The low mixed group was also defined by lysosome dysfunction, which was reviewed in Chapter 4. Mitochondrial function and morphology were assessed in the fibroblasts of both groups in a variety of assays. Additionally, limited investigation of mitochondrial ROS production, mitophagy and mitochondrial function was conducted in iDA neurons from the patients in each group. Lysosome dysfunction, specifically acidification and cathepsin activity, was assessed in the low mixed group.

5.1.1 Aims and Objectives

Hypothesis:

We hypothesise that investigation of organelle dysfunction within the two groups would identify unique mechanisms of dysfunction and demonstrate homogeneity within the groups.

This chapter aims to outline the mitochondrial and lysosomal dysfunction identified in the mitochondrial dysfunction subgroup and low mixed group.

Mitochondrial dysfunction subgroup objectives:

- To validate the mitochondrial phenotype observed in the initial screen with new controls.
- To assess respiration and ATP production in the patient-derived fibroblasts.
- To assess mitophagy, mitochondrial function, morphology and ROS production in the iDA neurons.

Low mixed group objectives:

- To validate the mitochondrial and lysosomal phenotype observed in the initial screen.
- To assess mechanisms of mitochondrial and lysosomal dysfunction in detail in the patient-derived fibroblasts.
- To assess mitochondrial and lysosomal function in iDA neurons.

5.2 Results

5.2.1 Assessment of the Mitochondrial Dysfunction Group Patient-Derived Fibroblasts

The patients assessed in this group were defined by mitochondrial dysfunction but no lysosome dysfunction. Specifically, these patients had an increased number of mitochondria and elevated ATP levels but reduced MMP and percentage of perinuclear mitochondria. Interestingly, no defining alterations in mitochondrial morphology were observed across the three patients, with only Patient 1 and Patient 3 showing increased form factor. The three patients were compared to three age- and sex-matched controls (Table 27). Statistical comparisons were made between each patient and their corresponding control and the three controls and between the patient and control groups.

Table 27: A summary of the patient and control cell lines that were assessed.

Cell line	Age at biopsy (years)	Sex
Patient 1	63	Female
Patient 2	59	Male
Patient 3	51	Male
Control 1	64	Female
Control 2	62	Male
Control 3	53	Male

5.2.1.1 Validation

Following the initial screen the subgroup was assessed using mitotracker green and TMRM to determine if the phenotype remained consistent with the new controls. Mitotracker green was used to stain all mitochondria. Two of the patients had reduced MMP as seen in the original screen. Patient 1's MMP was normal in glucose, but lower in galactose (20 % ± 6, p = 0.04, Figure 78A). Patient 3's MMP was lower in both conditions (glucose: 21 % ± 7, p = 0.04, galactose: 31 % ± 5, p = 0.002, Figure 78A). When separated into the long and small populations Patient 1 (long: glucose: 18 % ± 5, galactose: 32 % ± 11, p = 0.02, Figure 78E, short: galactose: 18 % ± 2, p = 0.02, Figure 78F) and Patient 3 (long: glucose: 12 ± 24, galactose: 33 % ± 6, p = 0.007, Figure 78E, short: glucose: 18 % ± 17, galactose: 25 % ± 3, p = 0.007, Figure 78F) showed a reduced MMP, which reached significance in galactose media. The short mitochondria in Patient 1 showed no difference in MMP in glucose but the long mitochondria population MMP was reduced, suggesting a dysfunction of the main network that cannot be compensated when cultured in galactose.

Mitochondrial morphology parameters were assessed in the mitotracker green stained mitochondria. Only Patient 3 had an elevated number of mitochondria (glucose: 102 % ± 20, p = 0.001, galactose:

119 % ± 21, p = 0.006, Figure 78B). No difference in the percentage of perinuclear mitochondria (Figure 78C) or form factor (Figure 78D) was observed in any of the patients. The long vs small mitochondrial ratio did not differ from the controls in any of the patients (Figure 78G). Differing results may be due to the use of mitotracker which stains all mitochondria, regardless of function or the use of different controls.

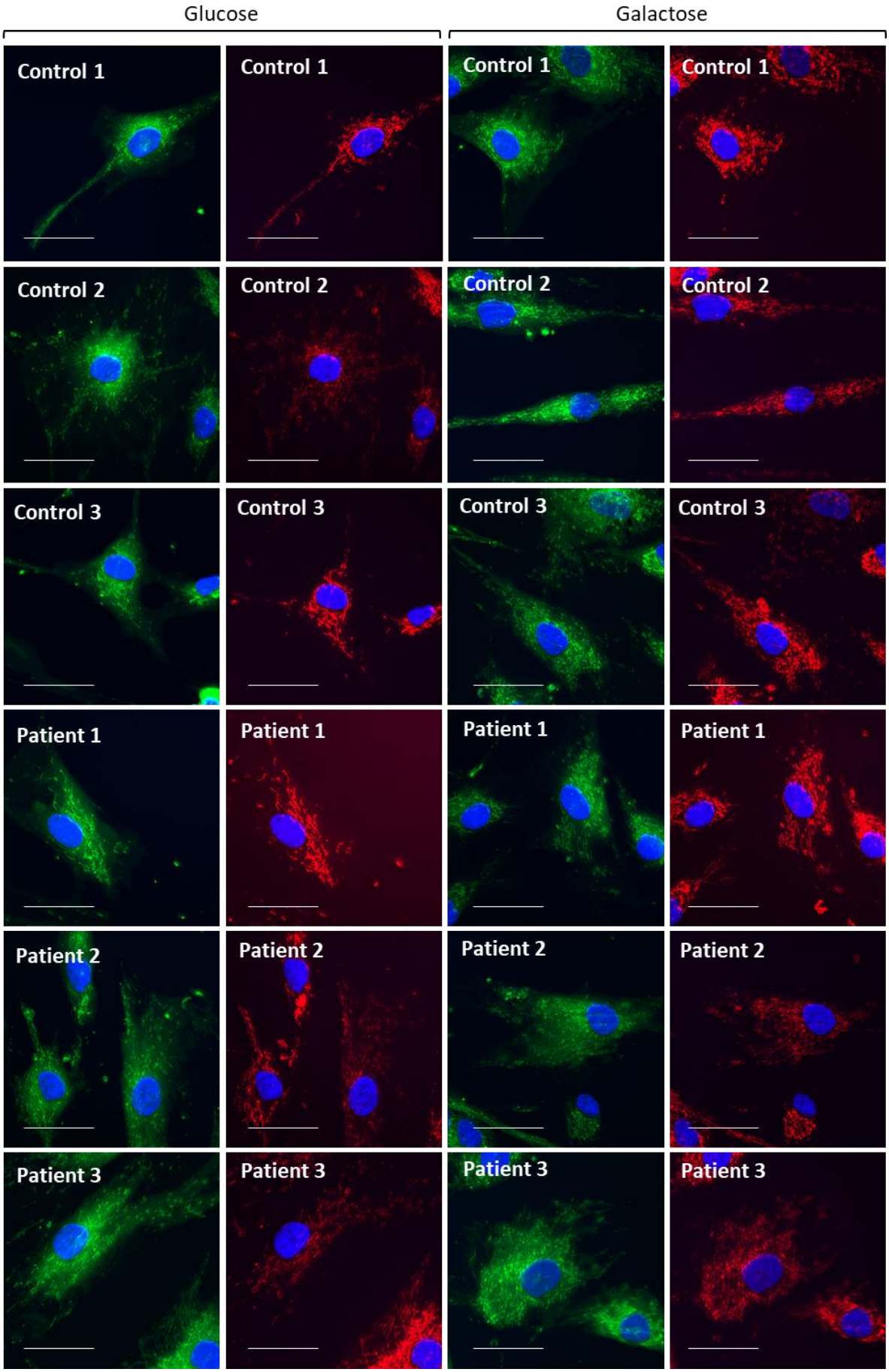

Figure 77: Representative images of mitotracker green and TMRM staining of mitochondria in the mitochondrial dysfunction subgroup. Nuclei (blue), mitotracker green (green) and TMRM (red). Scale bar = 40 µm.

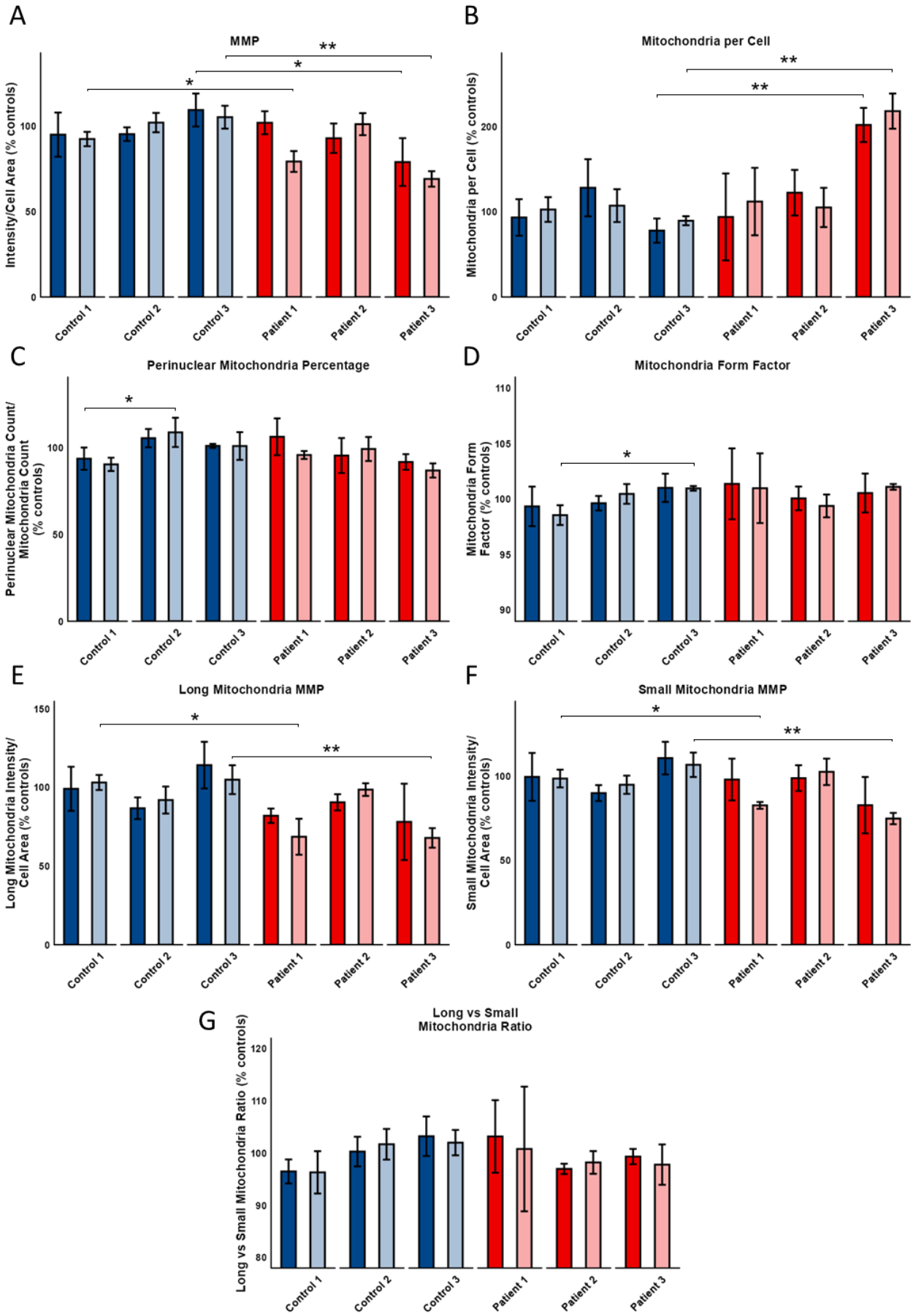
A
MMP
Intensity/Cell Area (% controls)
0
50
100
*
*
**
Control 1
Control 2
Control 3
Patient 1
Patient 2
Patient 3
B
Mitochondria per Cell
Mitochondria per Cell (% controls)
0
100
200
**
**
C
Perinuclear Mitochondria Percentage
Perinuclear Mitochondria Count/ Mitochondria Count (% controls)
0
50
100
*
D
Mitochondria Form Factor
Mitochondria Form Factor (% controls)
90
95
100
105
110
*
E
Long Mitochondria MMP
Long Mitochondria Intensity/ Cell Area (% controls)
0
50
100
150
*
**
F
Small Mitochondria MMP
Small Mitochodnria Intensity/ Cell Area (% controls)
0
50
100
*
**
G
Long vs Small Mitochondria Ratio
Long vs Small Mitochondria Ratio (% controls)
80
90
100
110
120

Figure 78: Mitochondrial dysfunction phenotype validation with new controls. A) MMP, **B)** Mitochondria per cell, **C)** Perinuclear mitochondria percentage, **D)** Mitochondria Form Factor, **E)** Long mitochondria MMP, **F)** Short mitochondria MMP, **G)** Long vs small mitochondria ratio. The controls (blue) and patients (red) were assessed in glucose (dark bars) and galactose media (light bars). Results for each cell line were normalised to the average of the controls per culture condition for each repeat. The patients were compared to the corresponding control by unpaired T-tests with Welch correction (* $p < 0.05$, ** $p < 0.01$), and differences between control lines were assessed using the same method. Error bars depict standard deviation (n = 3).

5.2.1.2 ATP levels

ATP production was increased in the patients in the mitochondrial dysfunction subgroup. Therefore, to assess the contribution of different ATP-producing pathways the group was cultured in glucose and galactose media like the initial screen. Thirty minutes before lysis, the cells were treated with either DMSO (vehicle), oligomycin, 2-deoxyglucose, etomoxir or BPTES. Oligomycin inhibits Complex V of the ETC preventing ATP production by oxidative phosphorylation. 2-deoxyglucose inhibits phosphoglucose isomerase preventing ATP production by glycolysis but allowing glucose to be processed through the pentose phosphate pathway (Singh *et al.*, 2023). Etomoxir inhibits carnitine palmitoyltransferase 1a (O'Connor, 2018) blocking the transport of fatty-CoA into the mitochondria preventing fatty acid oxidation. BPTES is a glutaminase inhibitor (Zhang *et al.*, 2023) and blocks the conversion of glutamine to glutamate preventing glutamine sourced ATP production.

All conditions were normalised to the mean of the controls in glucose conditions. Normal variation between the controls can be observed in both glucose and galactose media (vehicle), specifically Control 1 had lower ATP levels in glucose (21 % ± 13, Figure 79A), which remained lower when cultured in galactose media (19 % ± 32, Figure 79B). Whereas, Control 2 had higher ATP levels in glucose (20% ± 19, Figure 79A), which remained higher under galactose conditions (18% ± 18, Figure 79B). These differences are highlighted by the significant difference between Control 1 and 2 in glucose media ($p = 0.05$, Figure 79A). Inhibiting oxidative phosphorylation with oligomycin caused an average reduction of 15 % ± 9 in the controls in glucose conditions (Figure 79A), whereas in galactose only Control 3's ATP levels were reduced (14 % ± 27, Figure 79B); this links with Control 1 and 2 not increasing ATP levels in galactose media suggesting they have not converted to oxidative phosphorylation. Inhibiting glycolysis had the greatest effect on ATP levels in all the controls causing reductions of 71 % ± 4 in glucose and galactose conditions ($p = 0.02/0.02$, Figure 80). Inhibiting fatty acid oxidation and glutamine oxidation did not affect ATP levels in the controls on a group level (Figure 80).

The vehicle ATP levels in the patients were assessed to determine consistency with the initial screen. Two of the patients showed the same phenotype observed in the initial screen. Patient 1 had normal ATP levels in glucose (Figure 79A), but increased ATP levels in galactose conditions (29 % ±73, Figure 79B) and Patient 3 had increased ATP levels in both culturing conditions (glucose: 36 %± 40, galactose: 42 % ± 39, Figure 79). ATP levels in Patient 2 were in line with the average of the controls (Figure 79), which was inconsistent with the initial screen, however, it should be noted that different controls were used to assess Patient 2 in the initial screen. Inhibiting oxidative phosphorylation in the patients caused a reduction in ATP by 15 % in glucose (Figure 80A) (Patient 1: 14 % ± 37, Patient 2: 7 % ± 4, Patient 3: 22 % ± 22, Figure 79A) but no change in galactose (Figure 80B). Similar to the controls, inhibiting glycolysis caused a significant reduction of 68 % ± 6 and 69 % ± 7 in glucose and galactose conditions, respectively ($p = 0.01/0.03$, Figure 80). Inhibiting glutamine or fatty acid oxidation did not alter ATP levels in the patients when assessing them as a group (Figure 80).

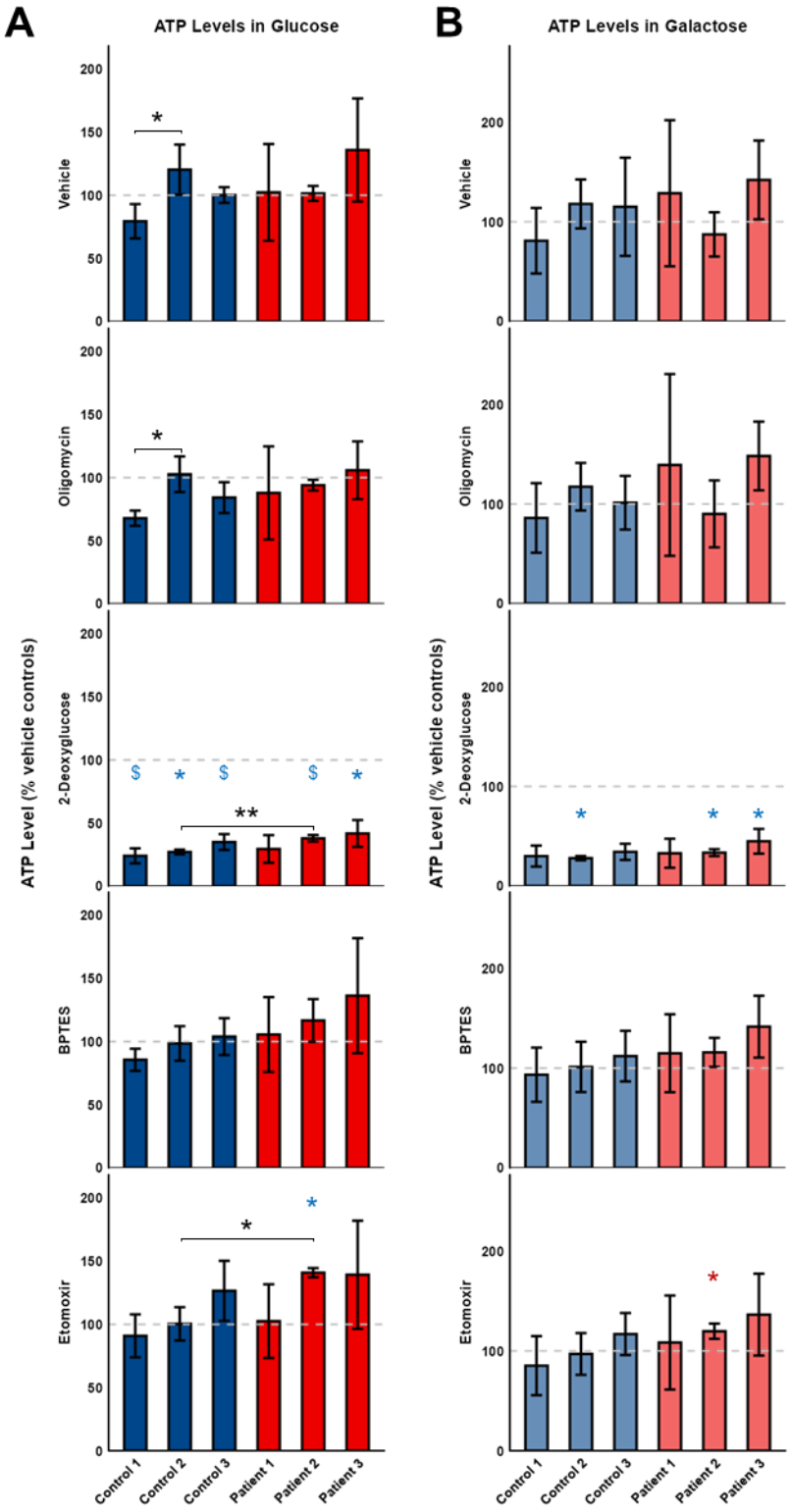

Figure 79: ATP levels and ATP production pathways in each cell line. A/B) ATP levels measured after 30 minutes of inhibition with oligomycin, 2-deoxyglucose, etomoxir or BPTES to block various ATP production mechanisms. This was assessed in glucose **(A)** and galactose **(B)**. Results for each patient (red) and control (blue) are presented separately, dark bars represent glucose conditions and light bars represent galactoses (n = 3). Results for each cell line were normalised to the average of the controls in glucose media for each repeat. Patients were compared to the corresponding control per condition by an unpaired T-test with Welch correction (black significance symbols, * $p < 0.05$, ** $p <$

0.01). Differences between the vehicle and inhibitors were assessed by unpaired T-tests with Welch correction (blue significance symbols, * p < 0.05, $ p < 0.01). Differences between glucose and galactose culturing conditions per toxin were assessed by unpaired T-tests with Welch correction (red significance symbol, * p < 0.05). The average of the vehicle treated controls in glucose is depicted by the grey dashed line. Error bars depict standard deviation (n = 3).

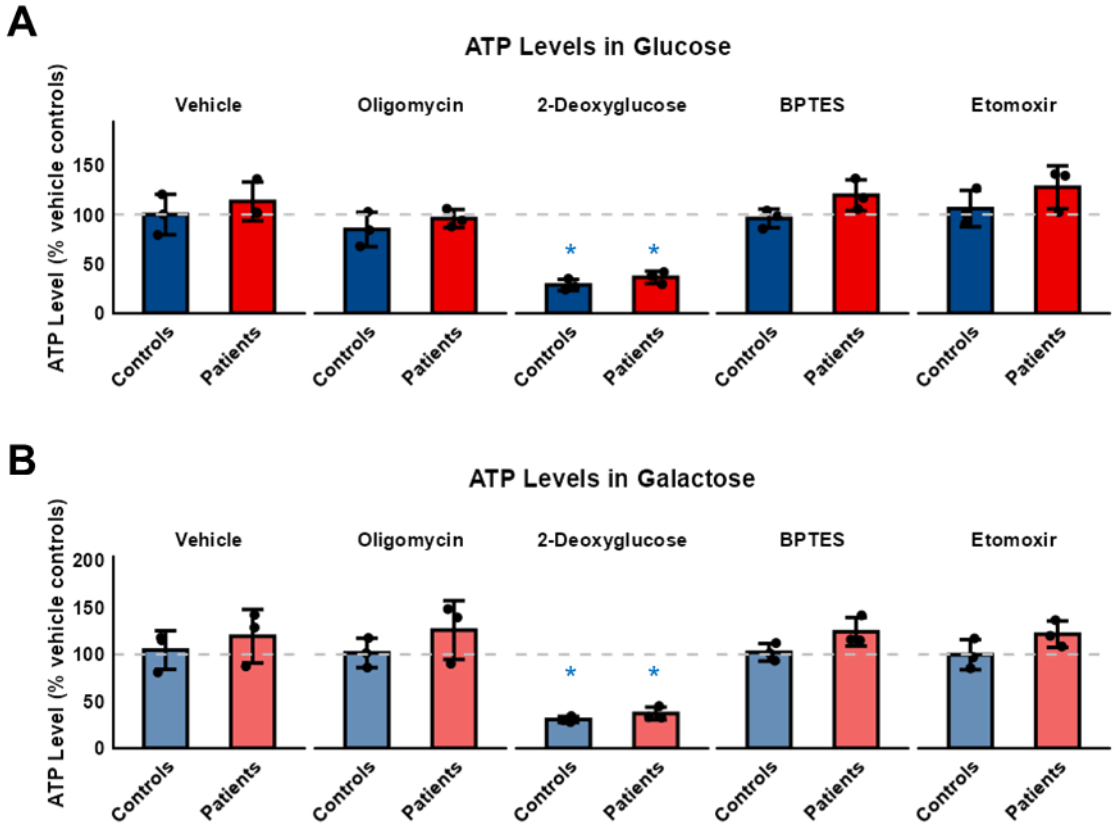

Figure 80: ATP levels and ATP production pathways in the patient and control groups. A/B) ATP levels measured after 30 minutes of inhibition with oligomycin, 2-deoxyglucose, etomoxir or BPTES to block various ATP production mechanisms. The patient (red) and control (blue) groups were assessed in glucose (**A,** dark bars) and galactose (**B**, light bars). Results for each cell line were normalised to the average of the controls in glucose media for each repeat. The patient group was compared to the control group per condition by unpaired T-tests with Welch correction (black significance symbols, * p < 0.05). Differences between the vehicle and inhibitors were assessed by unpaired T-tests with Welch correction (blue significance symbols, * p < 0.05). Differences between glucose and galactose culturing per toxin were assessed by unpaired T-tests with Welch correction (red significance symbol, * p < 0.05). The average of the vehicle-treated controls in glucose is depicted by the grey dashed line. Error bars depict standard deviation (n = 3).

5.2.1.3 Respiratory Complex Activity

The respiratory complexes form the ETC. Three complexes (I, III and IV) are proton pumps that generate the MMP. Altered complex activity has been reported in a variety of PD models and genotypes (Parker, Boyson and Parks, 1989; Mann *et al.*, 1992; Yoshino *et al.*, 1992; Benecke, Strümper and Weiss, 1993; Cardellach *et al.*, 1993; Mortiboys *et al.*, 2008, 2010; del Hoyo *et al.*, 2010; Carling *et al.*, 2020). The Abcam Complex activity kits were used to measure the Vmax of the complexes and all results were normalised to the average activity in the control group cultured in glucose.

No difference in complex I activity was observed in the patients under glucose conditions (Figure 81A). When cultured in galactose media, complex I activity increased by 24% ± 7 in the control group and 53 % ± 20 in the patient group (Figure 81A). The increase in the patient group was driven by increased activity in Patient 1 (81 % ± 25) and Patient 3 (63 % ± 62, Figure 81B).

Variability was observed in the control group in glucose media when assessing complex II activity. Control 2 had very high complex II activity, 32 % + 20 above the average (Figure 81D). Control 1 and 3 both had lower activity than the average by 12 % ± 10 and 30 % ± 21 (Figure 81D). When compared as groups, the patients showed a 31 % ± 25 increase in complex II activity in glucose compared to controls (Figure 81C). The increased activity in glucose was due to increased activity in Patient 1 (40 % ± 28) and Patient 3 (52 % ± 39, Figure 81D), when compared to the average of the controls. When compared to their corresponding controls, Patient 1's complex II was 52 % ± 69 more active (Figure 81D). Patient 3's activity was 82 % ± 23 greater than Control 3 ($p = 0.04$, Figure 81D). Patient 2's complex II activity was 29 % ± 64 lower than Control 2 (Figure 81D). In galactose media, the patient and control group did not differ (Figure 81C). Culturing in galactose media reduced complex activity in Patient 1 and 3 by 8 % ± 46 and 25 % ± 26 respectively, whereas Patient 2's activity increased by 16 % ± 30 (Figure 81D).

Complex IV activity in the controls was similar to complex II activity. Control 1 and Control 3 had similar levels of activity, but Control 2 had higher levels by 40 % ± 24 on average in glucose and 39% + 24 in galactose (Figure 81F). Despite Control 2 having high levels of activity, the patients had greater complex IV activity in both culturing conditions (glucose; 22 % ± 13, galactose: 14 % ± 15, Figure 81E). When cultured in galactose complex IV activity did not differ to the glucose conditions in either controls or patients (Figure 81E). Similar to complex I and II, Patient 1 and Patient 3 had the highest levels of activity in glucose media (23 % ± 27, and 36 % ± 39, Figure 81F).

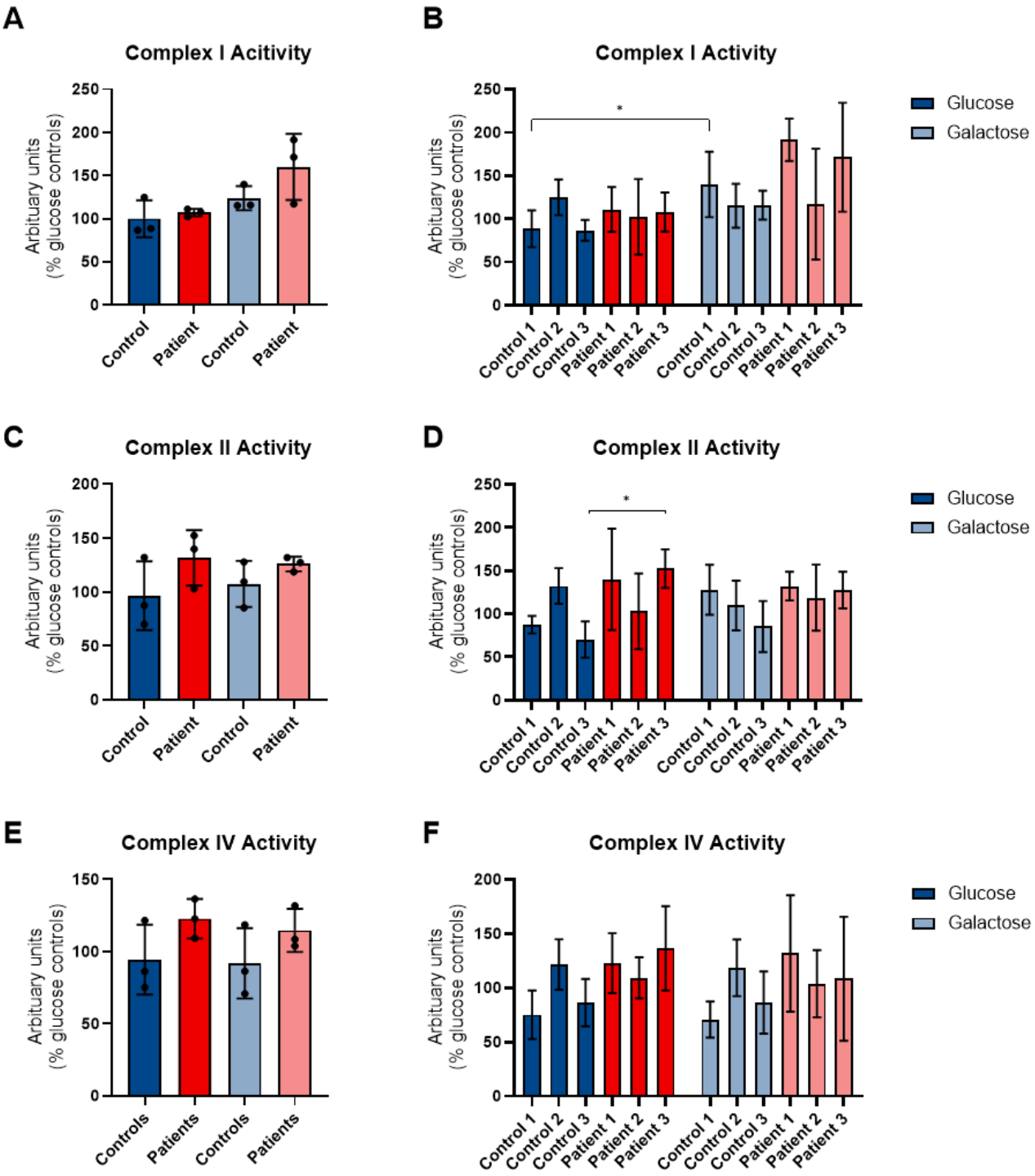

Figure 81: Complex I, II and IV activity in the mitochondrial dysfunction subgroup. A/B) Complex I activity, **C/D)** Complex II activity, **E/F)** Complex IV activity. **A/C/E)** show the results per group, **B/D/F)** show the results per cell line. The controls (blue) and patients (red) were assessed in glucose (dark bars) and galactose media (light bars). Results for each cell line were normalised to the average of the controls in glucose media for each repeat. **A/C/E)** The patient group was compared to the control group per media condition by unpaired T-tests with Welch correction (* $p < 0.05$). Differences in activity between the glucose and galactose conditions were assessed by unpaired T-tests with Welch

correction (* $p < 0.05$). **B/D/F)** The patients were compared to the corresponding control by unpaired T-tests with Welch correction (* $p < 0.05$), and differences between control lines were assessed using the same method. Differences in activity between the glucose and galactose conditions were evaluated by unpaired T-tests with Welch correction (* $p < 0.05$). Error bars depict standard deviation ($n = 3$).

5.2.1.4 Mitochondrial Respiration

Reduced MMP can indicate reduced oxidative phosphorylation. Several studies have assessed oxidative phosphorylation using the Seahorse XF Analyzer, with conflicting results reporting increased oxygen consumption (Milanese *et al.*, 2019) or decreased oxygen consumption (Ambrosi *et al.*, 2014; Milanese *et al.*, 2019).

Results for the controls were more variable than the patient's suggesting stratification identified a homogeneous phenotype (not statistically assessed). The patients showed a small reduction in basal respiration (9% ± 3, Figure 82A). Treatment with CCCP uncouples the mitochondria, leading to maximal respiration, mimicking the highest functioning capacity of the ETC. The patients' maximal respiration was 20 % ± 2 lower than the controls ($p = 0.0008$, Figure 82B). This corresponds with a significantly lower spare capacity (20 % ± 5, $p = 0.007$, Figure 82E), which reflects the ability of mitochondria to adapt to high energy demands. ATP production (11 % ± 5, Figure 82I) and proton leakage (25 % ± 15, Figure 82F) were decreased.

Measures of glycolysis can be interpreted from the MitoStress test extracellular acidification (ECAR) results. These should be considered indicators of possible glycolytic changes as two pathways can alter ECAR. The first is glycolysis, by producing lactate, however, the production of CO_2 by the citric acid cycle can also result in increased acidification. The ratio of oxygen consumption rate (OCR) to ECAR can also imply the energetic status of the cell line. Basal ECAR was variable between patients (Figure 83A). Compared to their corresponding controls, Patient 1 had elevated ECAR (41 % ± 39) and Patient 3 showed a small reduction in ECAR (10 % ± 23, Figure 83C). The ratio of OCR:ECAR under basal conditions showed a reduced Basal OCR:ECAR in Patient 1 (20 % ± 14) and an increase in Patient 3 (27 % ± 17, Figure 83D). When the mitochondria were uncoupled with CCCP the maximal ECAR was measured to assess glycolytic rate vs oxidative phosphorylation when mitochondria are functioning at their maximum capacity. Maximal ECAR did not differ between Patient 1 or Patient 2 and their control (Figure 83G). Patient 3 had a small reduction in maximal ECAR (11 % ± 17, Figure 83G). The maximal OCR:ECAR ratio was calculated and showed a reduction of 15 % ± 8 in the patient group (Figure 83H). This suggests a greater reliance on aerobic respiration in the patients.

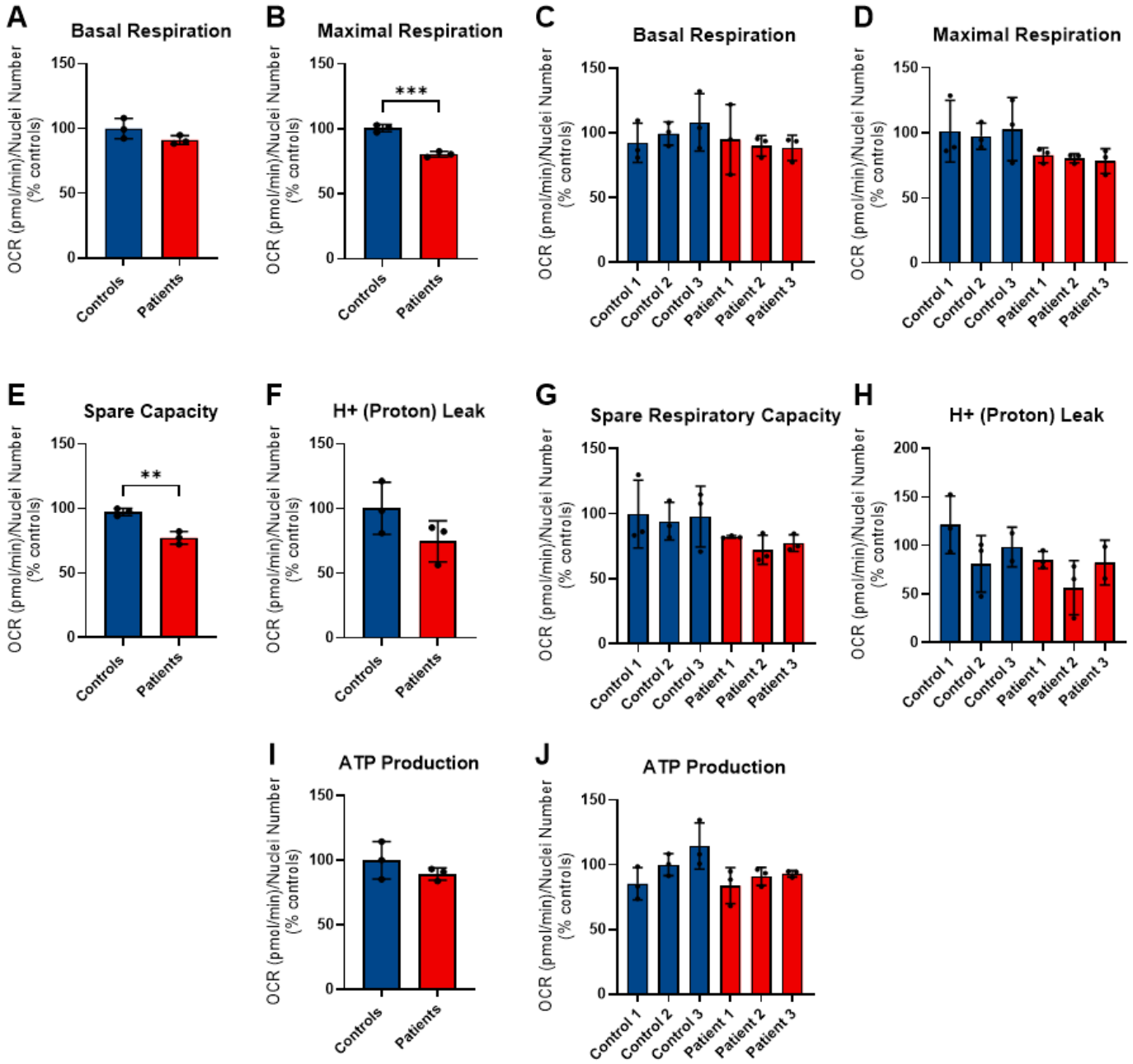

Figure 82: Measures of mitochondrial respiration in the mitochondrial dysfunction subgroup. A/C) Basal respiration, **B/D)** Maximal respiration, **E/G)** Spare capacity, **F/H)** H^+ (proton) leakage, **I/J)** ATP production by mitochondria. **A/B/E/F/I)** show the patient and controls grouped (n = 3), where the patients (red) were compared to the controls (blue) by an unpaired T-test with Welch correction (** $p < 0.01$, *** $p < 0.001$). **C/D/G/H/J)** show each cell line separately (n = 3), where each patient was compared to the corresponding control by unpaired T-tests with Welch correction (* $p < 0.05$) and differences between control lines were assessed by the same method. Error bars depict standard deviation.

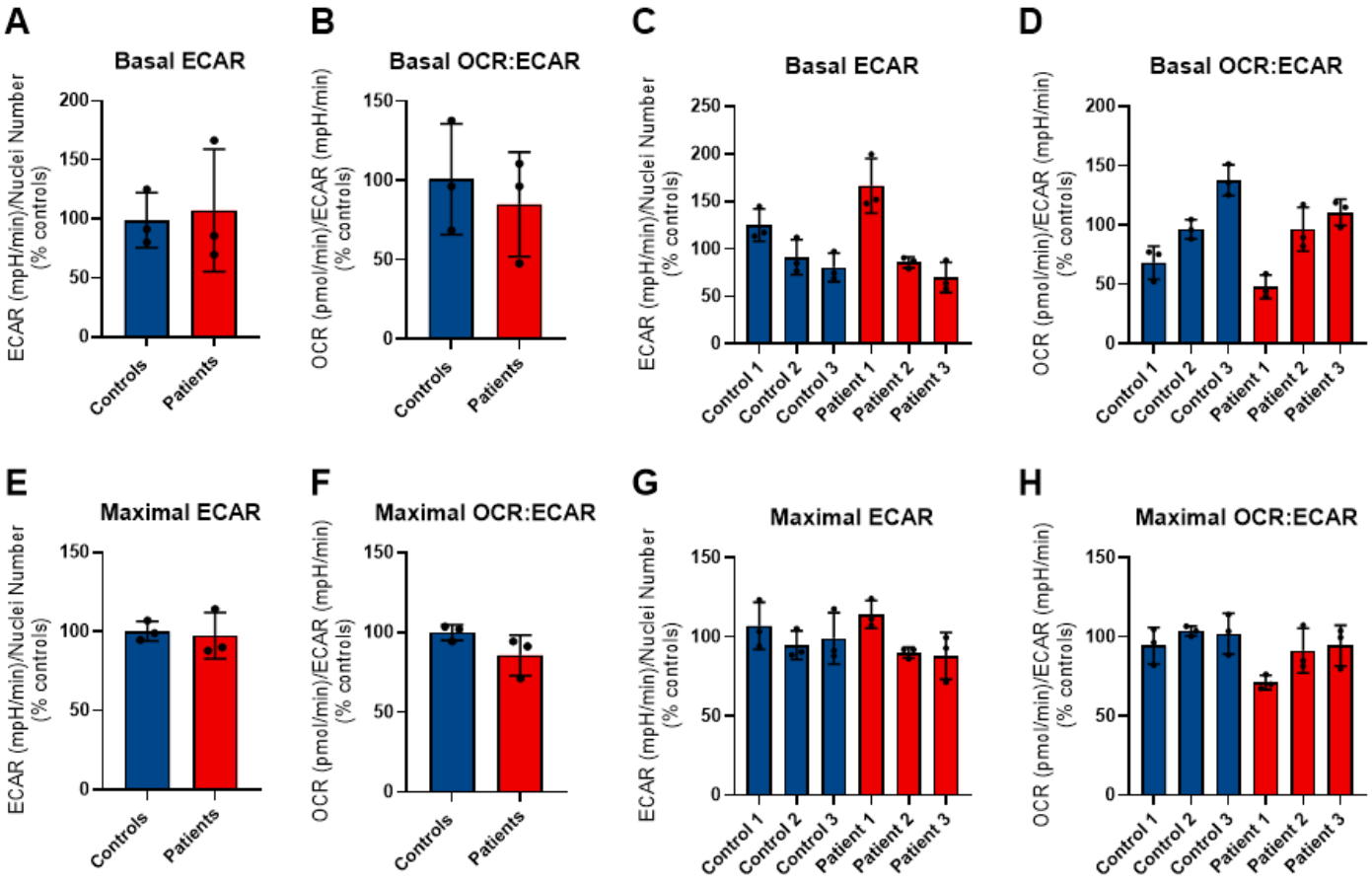

Figure 83: Measures of glycolysis in the mitochondrial dysfunction subgroup. A/C) Basal ECAR, **B/D)** Basal OCR:ECAR, **E/G)** Maximal ECAR, **F/H)** Maximal OCR:ECAR. **A/B/E/F)** show the patient and controls grouped (n = 3), where the patients (red) were compared to the controls (blue) by an unpaired T-test with Welch correction (** $p < 0.01$, *** $p < 0.001$). **C/D/G/H)** show each cell line separately (n = 3), where each patient was compared to the corresponding control by unpaired T-tests with Welch correction (* $p < 0.05$) and differences between control lines were assessed by the same method. Error bars depict standard deviation.

5.2.2 Generation and Assessment of the Mitochondrial Dysfunction Subgroup iDopaminergic Neurons.

5.2.2.1 Generation and Characterisation

Table 28: A summary of the patient and control induced dopaminergic neuron lines that were assessed.

Cell line	Age at biopsy (years)	Sex
Patient 3	51	Male
Control 4	52	Male

To enable assessment of the mitochondria and lysosomes in a disease-relevant cell type the fibroblasts were reprogrammed into iNPCs. The protocol is outlined in the previous chapters. Attempts to reprogramme all three patients and their controls were made. Unfortunately, only Patient 3 was successfully reprogrammed despite three attempts at reprogramming the other patients. Control 3 also did not reprogramme so Patient 3 was age- and sex-matched with an alternative control, which was reprogrammed with the low mixed subgroup. Successful reprogramming was confirmed by Pax6 and Nestin staining (Figure 84).

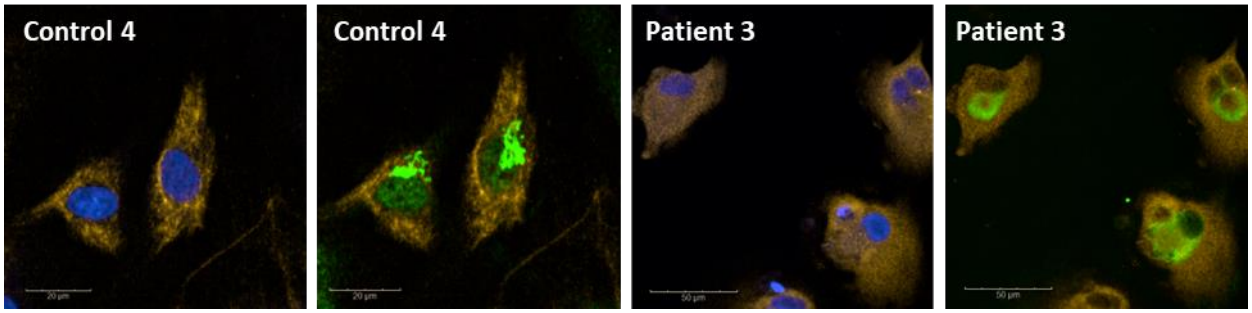

Figure 84: Representative images of the iNPCs from the mitochondrial dysfunction subgroup stained for Pax6 and Nestin. Nuclei (blue), Pax6 (green) and Nestin (orange). Scale bar = 20 µm.

Neuronal differentiation followed the same protocol described in the Schwartzentruber *et al.* (2020) study, producing stable iDA neuron-like cells. The iDA neurons from both lines expressed high levels of B-III-Tubulin (92 % ± 8, Figure 87A) and MAP2 (99 % ± 1, Figure 87B), which are neuron markers (Figure 85, Figure 86). High levels of TH (97 % ± 4, Figure 87C) and DAT (84 % ± 14.7, Figure 87D) were expressed showing dopaminergic expression (Figure 85, Figure 86).

Neuronal morphology was also assessed. The neurite outgrowth kit was used to stain the cell membrane and machine learning selected cells with a neuronal morphology (Figure 88). 55 % ± 17 of control cells and 64 % ± 13 of patient cells were classified as neuronal (Figure 89A). The lower

percentage in the control is likely due to cells clustering and producing long projections from the cell ball. The neuronal cells in the patient showed no difference in roundness (Figure 89C) or width to length ratio (Figure 89D) to the control. No difference in cell viability was observed either (Figure 89B).

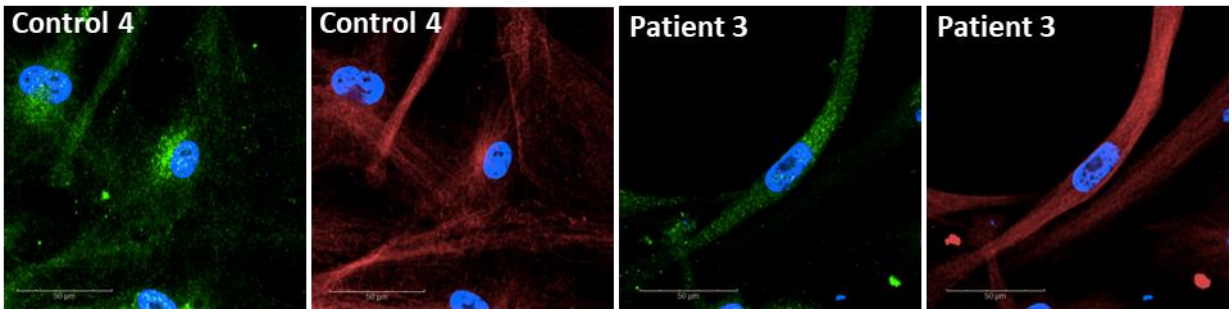

Figure 85: Representative images of the iDA neurons from the mitochondrial dysfunction subgroup stained for β-III-Tubulin and TH. Nuclei (blue), TH (green) and B-III-Tubulin (red). Scale bar = 50 µm.

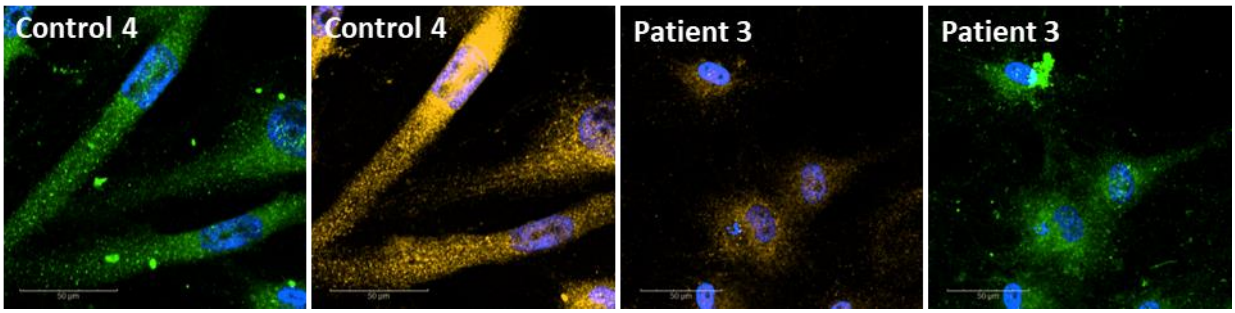

Figure 86: Representative images of the iDA neurons from the mitochondrial dysfunction subgroup stained for MAP2 and DAT. Nuclei (blue), DAT (green) and MAP2 (orange). Scale bar = 50 µm.

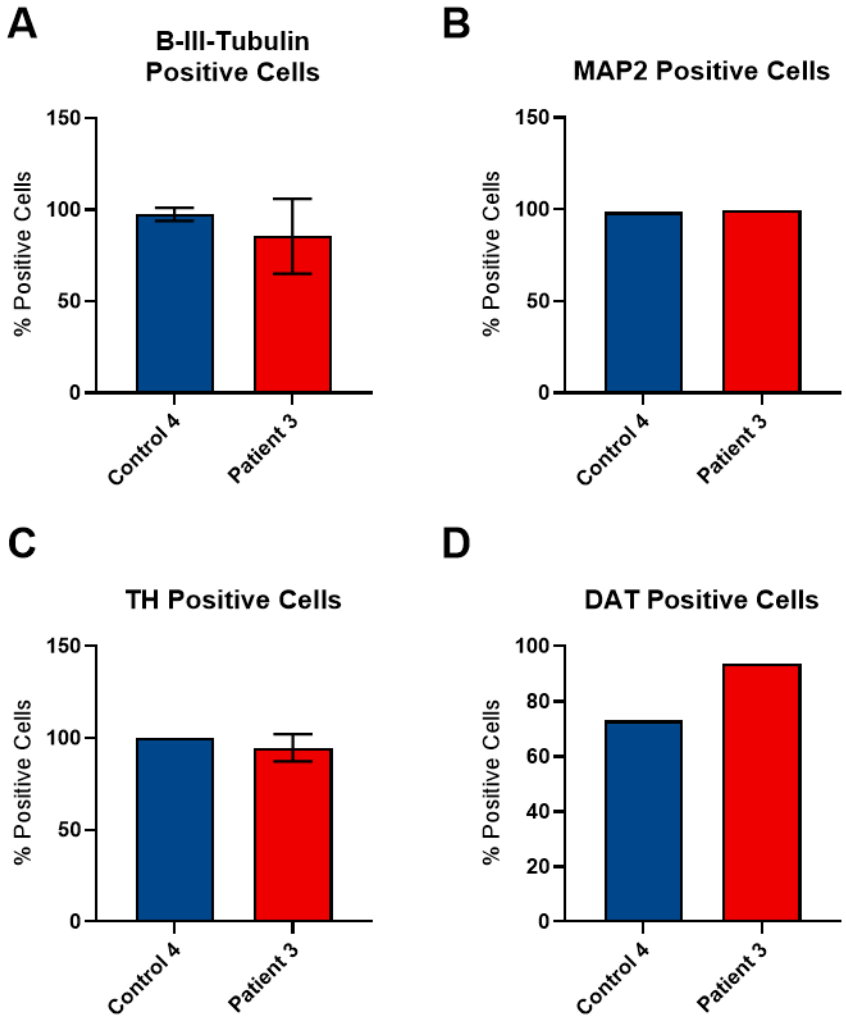

Figure 87: Characterisation of the dopaminergic neurons using TH, DAT, β-III-Tubulin and MAP2. A) Percentage of cells positively stained for β-III-Tubulin, **B)** Percentage of cells positively stained for MAP2, **C)** Percentage of cells positively stained for TH, **D)** Percentage of cells positively stained for DAT. No statistical assessment was conducted due to a reduced number of independent assay repeats (n = 1/2). Error bars depict standard deviation.

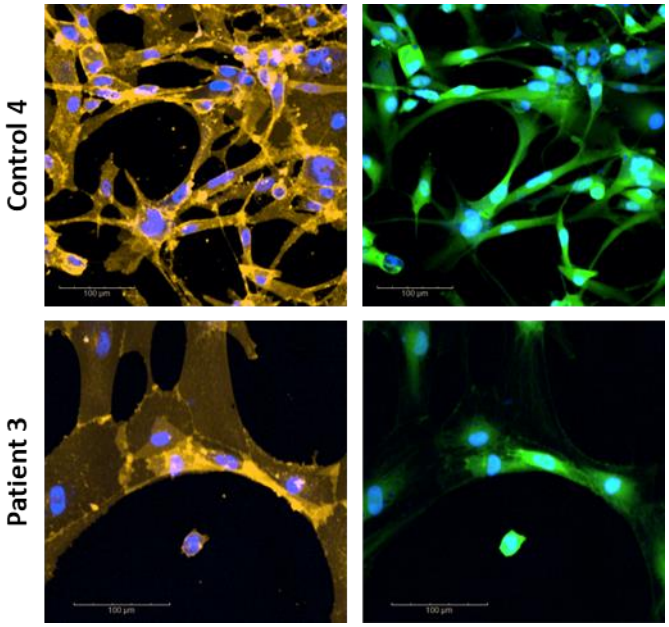

Figure 88: Representative images of the iDA neurons from the mitochondrial dysfunction subgroup stained to assess morphology and cell viability. Nuclei (blue), membrane (orange) and cell viability (green). Scale bar = 100 µm.

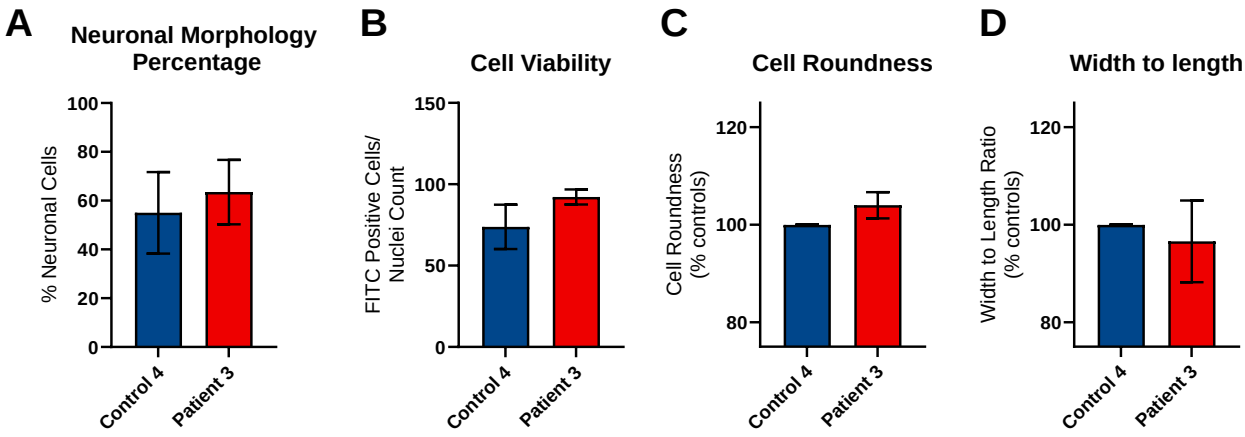

Figure 89: Characterisation of the dopaminergic neuron morphology. A) Percentage of cells with neuronal morphology, **B)** Cell viability, **C)** Neuronal cell roundness, **D)** Neuronal cell width to length ratio. The patient was compared to the control by an unpaired T-test with Welch correction (* $p < 0.05$). Error bars depict standard deviation (n = 3).

5.2.2.2 Mitochondria Assessment and Mitophagy

Similar to the validation in the fibroblasts, the neurons were assessed with mitotracker green and TMRM. Unexpectedly, the MMP of Patient 3 was significantly higher than Control 5 (38 % ± 14, $p = 0.04$, Figure 91B). But a small reduction in the number of mitochondria was observed (25 % ± 8, Figure 91B). This is the opposite of the results in the fibroblasts. Interestingly, the ratio of functional mitochondria to mitochondria, measured by the ratio of TMRM mitochondria to mitotracker green

mitochondria, was reduced in the patient (18% ± 12, Figure 91C). The average area of the mitochondria did not differ (Figure 91D).

Mitophagy deficits are reported in PD (Malpartida *et al.*, 2021). Due to the dysfunction observed in the fibroblasts, we assessed mitophagy in the neurons. Assessment of mitophagy was conducted by adding oligomycin and antimycin immediately before imaging. The toxins inhibit oxidative phosphorylation, thus, triggering mitophagy and the clearance of damaged mitochondria. The mitophagy index was calculated by the ratio of induced to basal results. The percentage of mitochondria undergoing mitophagy rapidly increased after induction and remained constant. No difference in mitophagy was observed between the patient and control (Figure 92A). The recovery of MMP was measured between timepoint 2 and 7, and no difference was observed between the lines (Figure 92B). However, the patient maintained a higher number of functional mitochondria after induction with the toxins (Control 4: 0.06 ± 0.04, Patient 3: 0.22 ± 0.04, Figure 92C). There was no difference in recovery of functional mitochondria in either cell line (Figure 92C).

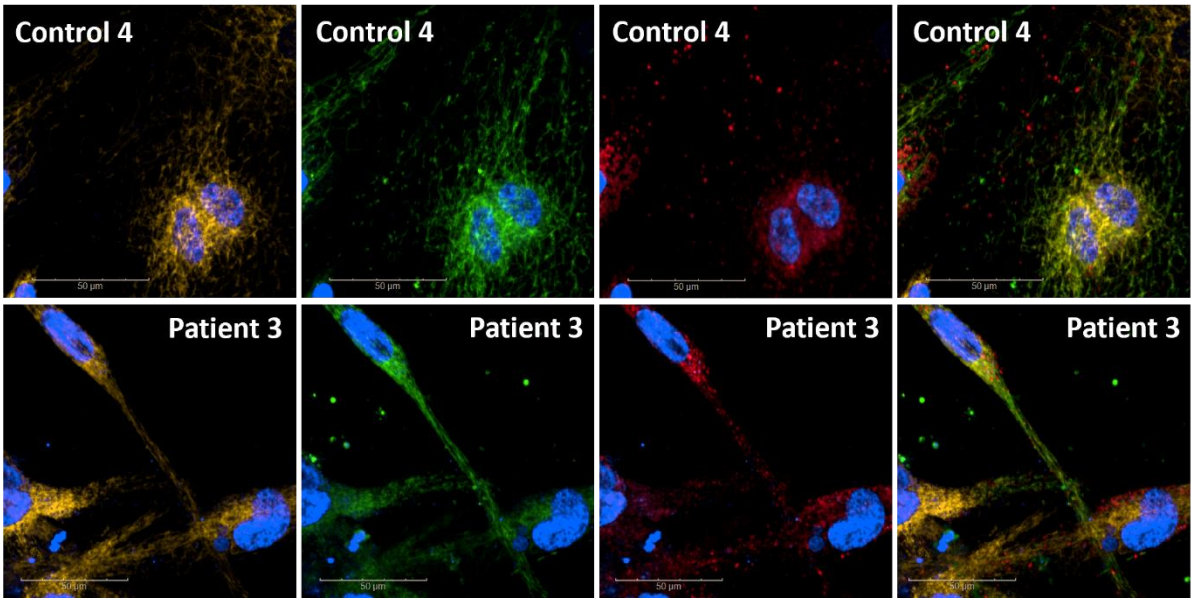

Figure 90: Representative images of the iDA neurons from the mitochondrial dysfunction subgroup stained with TMRM, mitotracker green and lysotracker red to assess mitophagy. Nuclei (blue), TMRM (orange), mitotracker green (green) and lysotracker red (red). Images on the right show all four channels merged. Scale bar = 50 µm.

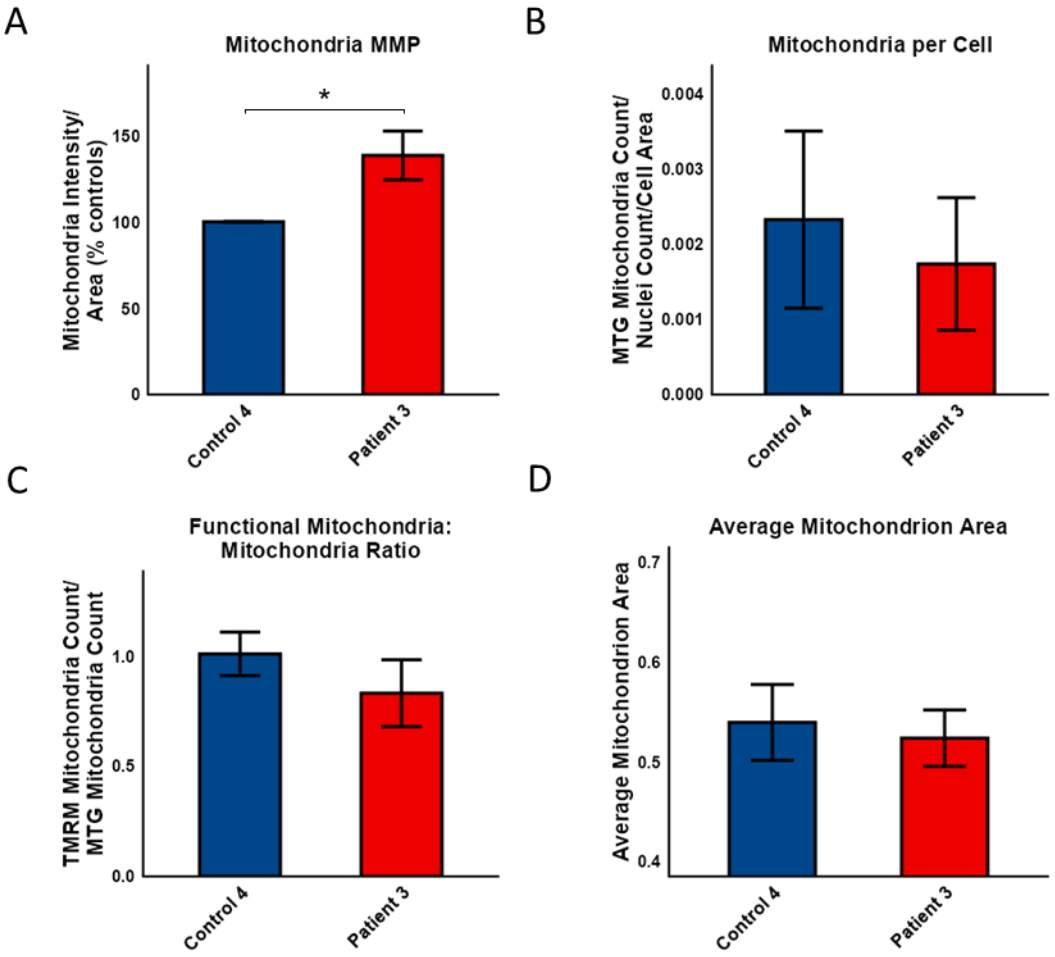

Figure 91: Assessment of mitochondrial function in the mitochondrial dysfunction subgroup iDA neurons. A) Mitochondria MMP, **B)** Mitochondria per cell, **C)** Functional mitochondria: Mitochondria ratio, **D)** Average mitochondrion size. The patient was compared to the corresponding control by an unpaired T-test with Welch correction (* $p < 0.05$). Error bars depict standard deviation (n = 3).

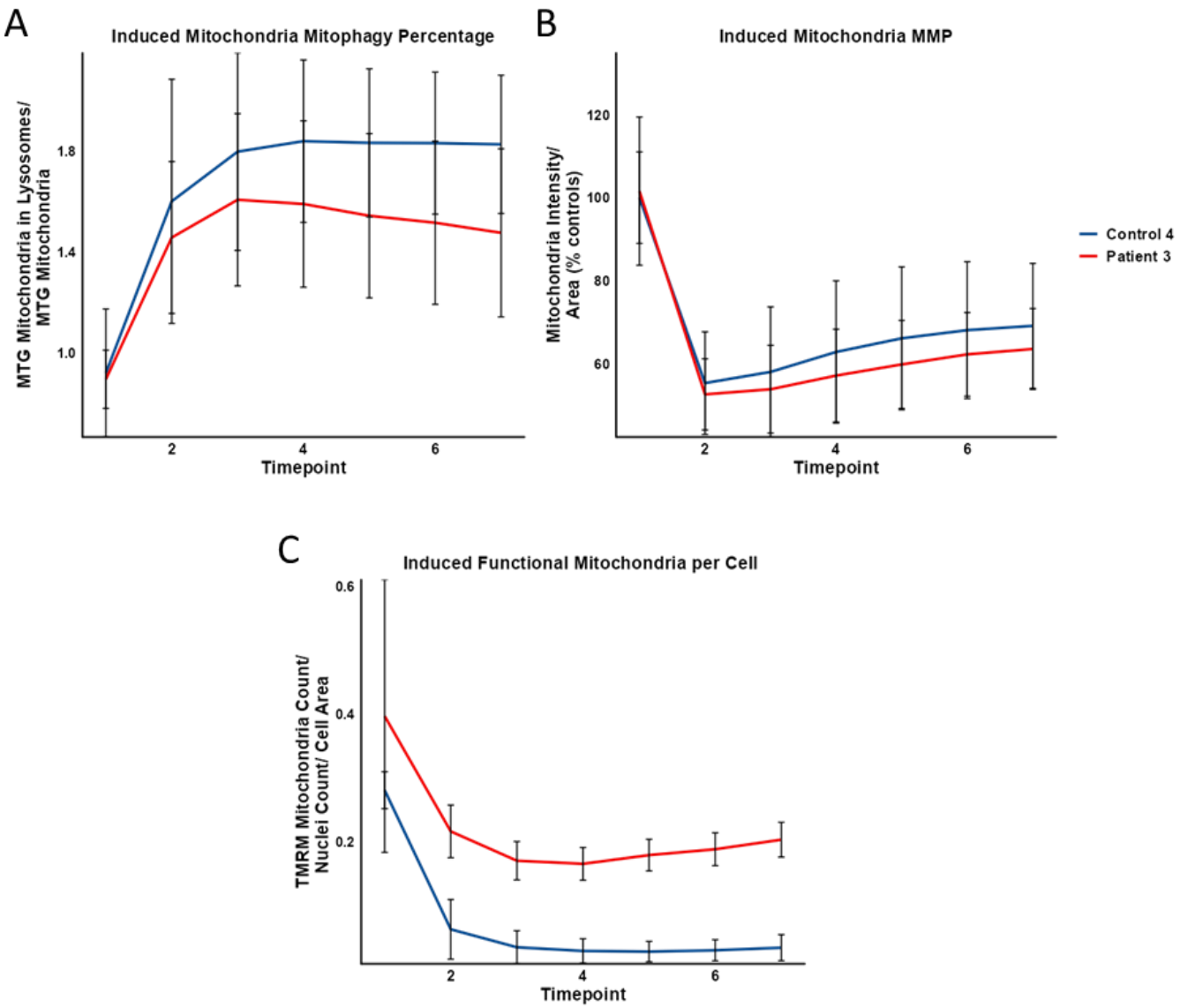

Figure 92: Assessment of mitophagy and mitochondria recovery in the mitochondrial dysfunction subgroup iDA neurons. A) Induced mitochondria mitophagy percentage, **B)** Induced mitochondria MMP, **C)** Induced functional mitochondria per cell. The patient was compared to the corresponding control at timepoint 2 by an unpaired T-test with Welch correction (* $p < 0.05$). The rate of mitophagy and recovery between timepoints 1-2 and 2-7 were statistically assessed by unpaired T-tests with Welch correction (* $p < 0.05$). Error bars depict standard deviation (n = 3).

5.2.2.3 MitoROS

ROS are vital signalling molecules in the cell; however, in PD ROS can increase to harmful levels, leading to oxidative stress and damage. The leakage of electrons from the ETC is the main source of ROS in the cell. This was not investigated in the fibroblasts, due to the low levels of oxidative phosphorylation and consequently low ROS levels. The NpFr2 probe uses a triphenylphosphonium tag to localise to the mitochondria and the flavin moiety increases fluorescence by 115-fold when oxidised. Thus, enabling the measurement of mitochondrial ROS (MitoROS). A small elevation in MitoROS levels was observed in Patient 3 (7 % ± 6, Figure 93).

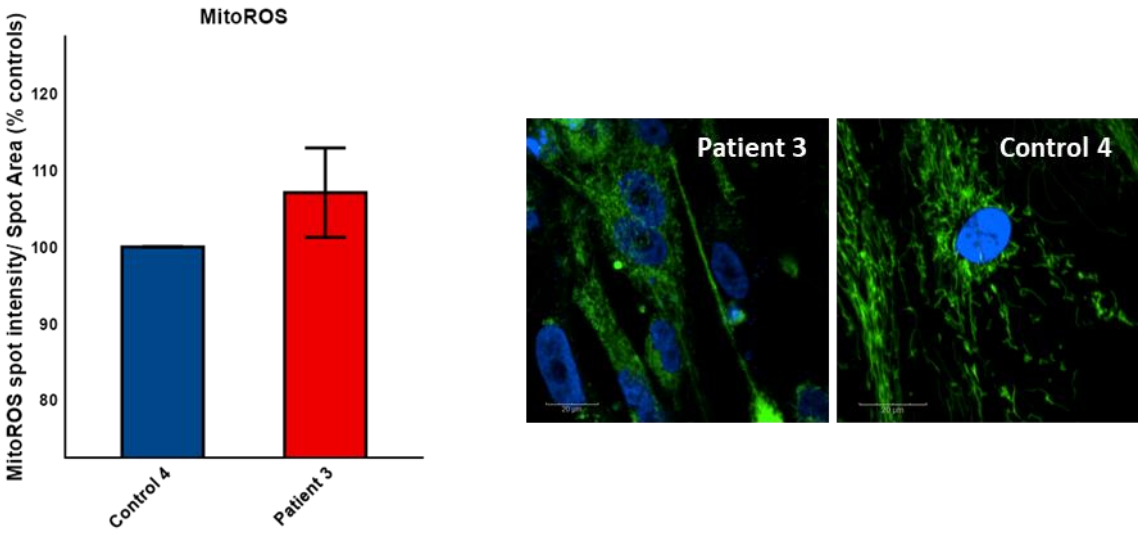

Figure 93: MitoROS levels in iDopaminergic neurons from the mitochondrial dysfunction subgroup. The graph shows Patient 3 (red) compared to Control 4 (blue) (n = 3), where the patient was compared to the control by an unpaired T-test with Welch correction (* $p < 0.05$). Error bars depict standard deviation. Representative images show the NpFr2 staining (green) in the patient and control, nuclei (blue), scale bar = 20 µm.

5.2.3 Assessment of the Low Mixed Group Patient-Derived Fibroblasts.

Four patients were stratified into the low mixed group. These were defined by both mitochondrial and lysosomal abnormalities. All four patients had lower numbers of mitochondria and lysosomes. Their mitochondria had a higher MMP and there was an increase in the percentage that were within the perinuclear region. Like the mitochondrial dysfunction group, no trend in mitochondrial morphology was observed. Patients had smaller lysosomes than the control population.

The four patients were paired with four age- and sex-matched controls (Table 29). Due to difficulty thawing Control 4, Patient 4 was paired with Control 5 for some assays. Statistical comparisons were made between each patient and their corresponding control, between the four controls, and between the patient and control groups.

Table 29: A summary of the patient and control fibroblasts that were assessed in the low mixed group.

Cell line	Age at biopsy (years)	Sex
Patient 1	53	Male
Patient 2	69	Female
Patient 3	54	Female
Patient 4	68	Female
Control 1	52	Male
Control 2	66	Female
Control 3	56	Female
Control 4	67	Female
Control 5	71	Female

5.2.3.1 Mitochondria and Lysosome Phenotype Validation

Once stratified the low mixed group were assessed using mitotracker green, TMRM and lysotracker green to determine mitochondrial and lysosomal phenotypes compared to the different collection of controls. No significant differences in MMP or mitochondria per cell were observed when comparing patients and their corresponding controls. When assessed as a group there was no statistical differences in either parameter, however, a small increase in MMP (21 % ± 7, Figure 94A) and a small decrease in mitochondria per cell (10 % ± 6, Figure 94B) were observed. No differences in lysosomes per cell (Figure 94E) or average lysosome area (Figure 94F) were observed either. This is not unexpected as the assay was conducted in glucose, but reassessment of the mitochondrial and lysosomal dysfunction phenotypes from the original screen found more pronounced abnormalities in galactose conditions than glucose. The control group showed far greater natural variation, demonstrating that classification made the patients more homogenous.

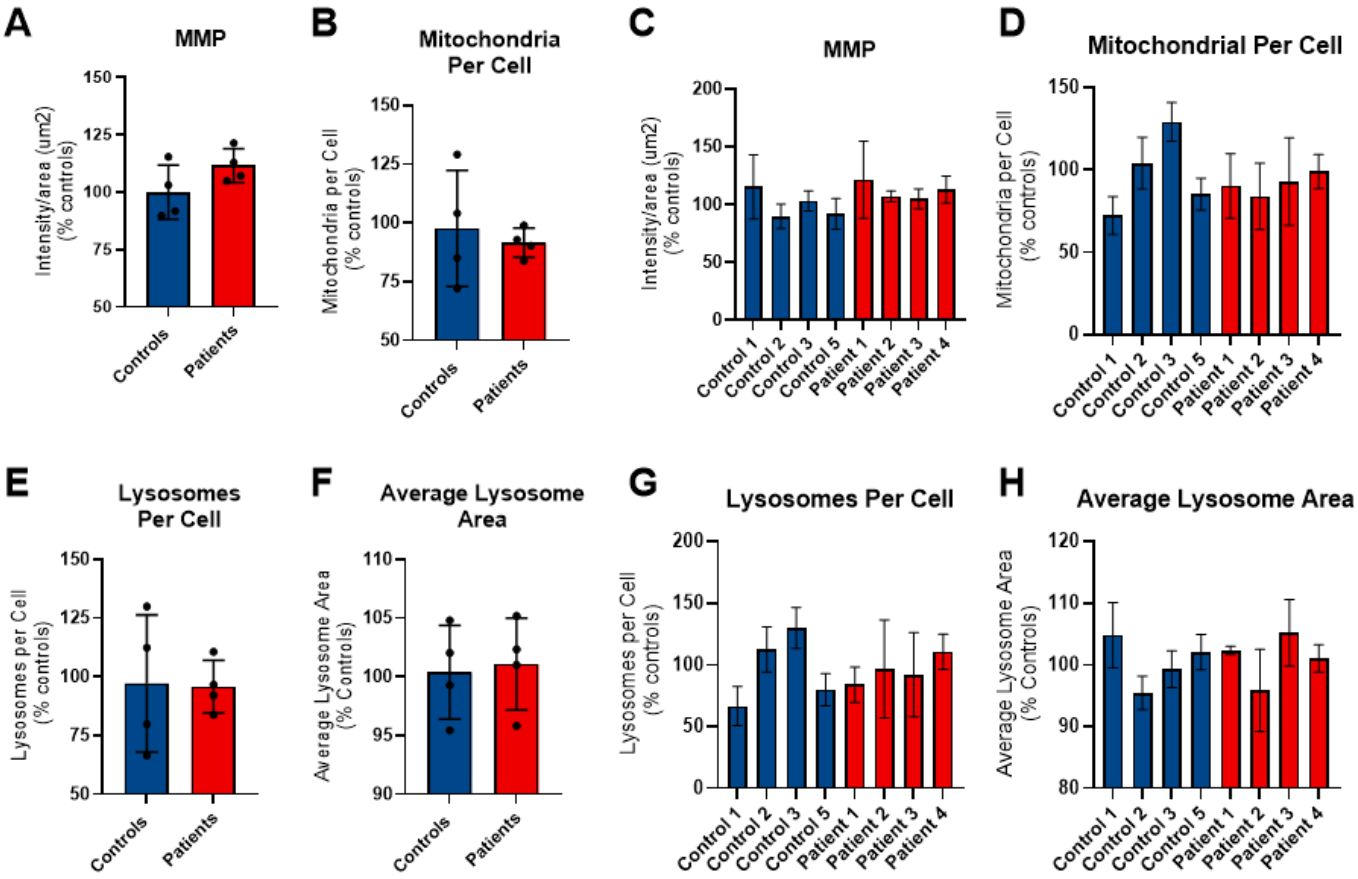

Figure 94: Mitochondrial and lysosomal dysfunction validation for the low mixed group with new controls. A/C) MMP, **B/D)** Mitochondria per cell, **E/F)** Lysosomes per cell, **G/H)** Average lysosome area. **A/B/E/F)** show the results per group, **C/D/G/H)** show the results per cell line. The patient's (red) results were normalised to the average of the controls (blue) per repeat. The patients were compared to the corresponding controls by unpaired T-tests with Welch correction (* $p < 0.05$), and differences between control lines were assessed using the same method. The pooled patient group was compared to the control group by an unpaired T-test with Welch correction (* $p < 0.05$). Error bars depict standard deviation (n = 3).

5.2.3.2 Complex V Activity

This subgroup had reduced ATP levels but elevated MMP. MMP is an electron gradient across the IMM that is maintained by complexes I-IV, thus, high MMP suggests that these complexes are working efficiently. However, the mitochondria are not generating enough ATP. It was hypothesised that complex V may be dysfunctional in this subgroup as reported by del Hoyo et al. (2010). This assay uses the Complex V ELISA kit by Abcam, which enables the isolation and assessment of Complex V Vmax activity. Unexpectedly, all patients had elevated Complex V activity compared to their corresponding controls, although results were variable (Figure 95A). Complex V activity was significantly higher in the patient subgroup compared to the control population, with an average increase of 19% ± 6 (Figure 95B).

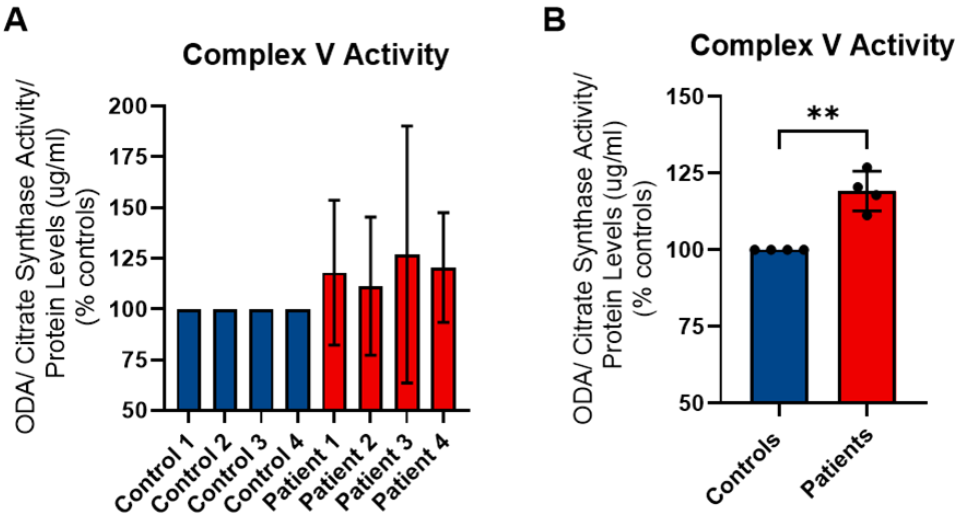

Figure 95: Complex V Vmax activity in the low mixed group. A) Complex V activity showing each patient and control (n = 2-4), **B)** Complex V activity showing combined patients and controls (n = 4). Results for each patient were normalised to the control for each repeat. Patients were compared to the corresponding control by an unpaired T-test with Welch correction (* $p < 0.05$). Combined patient and control groups were compared by an unpaired T-test with Welch correction (* $p < 0.05$, ** $p < 0.01$). Error bars depict standard deviation.

5.2.3.3 Mitochondrial Respiration

This subgroup showed an elevated MMP in the initial screen and increased complex V activity, suggesting that the mitochondria are working harder than in the controls. Two assessments of respiration were conducted using the Seahorse XF Analyzer.

A fuel flexibility test, which measures the dependency of the mitochondria on a particular fuel type by inhibiting oxidation. This also measures the capacity of the mitochondria to use a fuel type when all other fuels are depleted. No differences were observed between the patients and controls in their dependency on glucose, glutamine or fatty acids as the primary source of energy (Figure 96G). The capacity for different fibroblasts lines to use different fuel sources was more variable than dependency on the fuel types. No differences in capacity were observed between the patients and controls when grouped (Figure 96H). When assessed individually Patient 3 showed a greater capacity to utilise glucose than the corresponding control (17 ± 5, $p = 0.007$, Figure 96B).

The standard MitoStress test was used to assess the mitochondria oxidative phosphorylation ability. No differences were observed in basal respiration (Figure 97A), maximal respiration (Figure 97B) or spare capacity (Figure 97E) when the groups were pooled. Control 3 and Patient 1 showed elevated maximal respiration (Figure 97D) and spare capacity (Figure 97G). However, this did not significantly differ from the other controls and can be considered natural variation. Similarly, no difference in ATP production was observed (Figure 97I). Coupling efficiency and H^+ leakage determine whether protons can pass from the intermembrane space into the matrix without passing through complex V. As expected, no difference in leakage (Figure 97F) or coupling efficiency (Figure 97J) were observed. Assessment of the ratio of oxidative phosphorylation to glycolysis shown by the OCR:ECAR ratios showed no differences between the patients and controls (Figure 97M, Figure 97N).

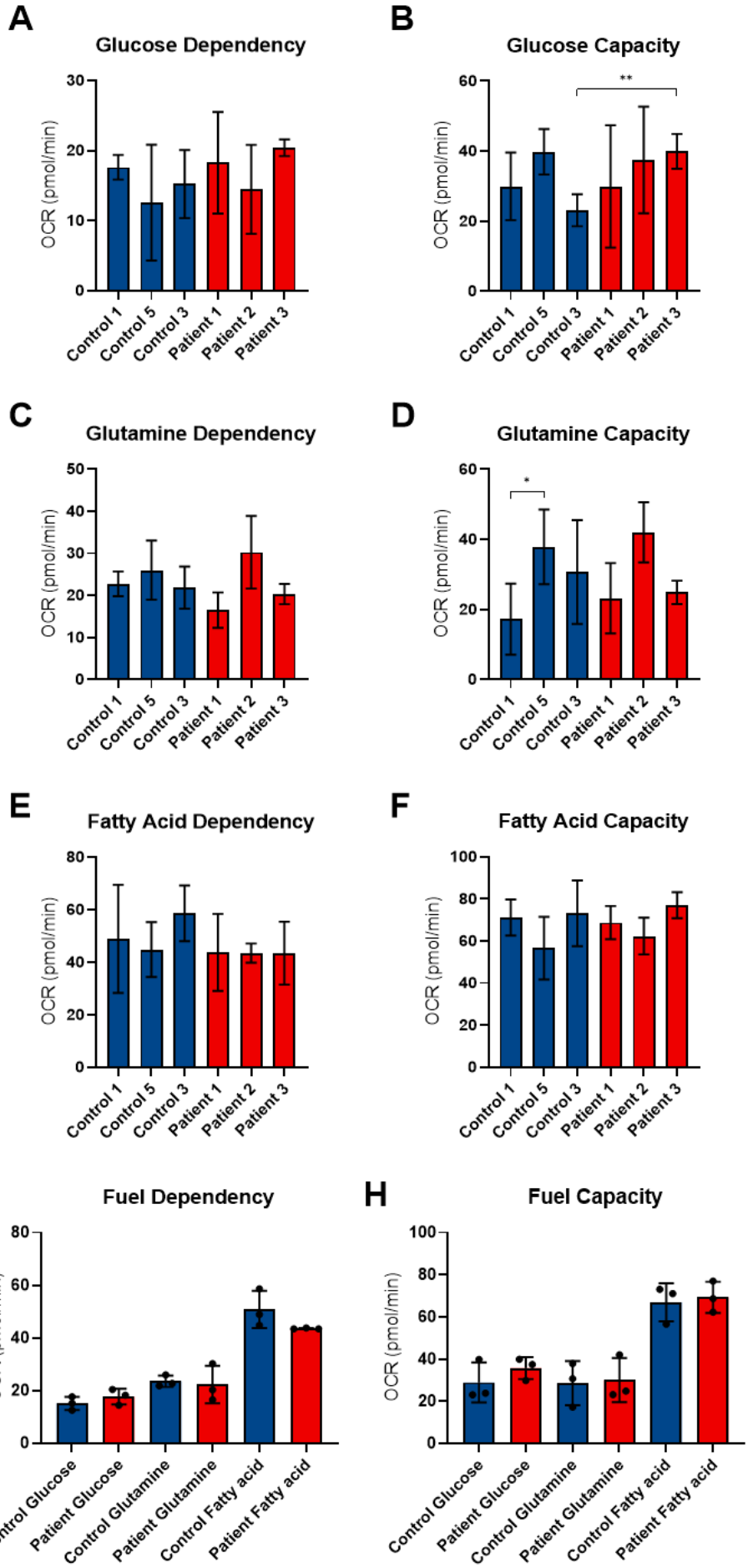
A
Glucose Dependency
OCR (pmol/min)
Control 1
Control 5
Control 3
Patient 1
Patient 2
Patient 3
B
Glucose Capacity
**
C
Glutamine Dependency
D
Glutamine Capacity
*
E
Fatty Acid Dependency
F
Fatty Acid Capacity
G
Fuel Dependency
Control Glucose
Patient Glucose
Control Glutamine
Patient Glutamine
Control Fatty acid
Patient Fatty acid
H
Fuel Capacity

Figure 96: Assessment of the dependency and capacity to use different fuel types for oxidative phosphorylation in the low mixed group fibroblasts. A) Glucose dependency, **B)** Glucose capacity, **C)** Glutamine dependency, **D)** Glutamine capacity, **E)** Fatty acid dependency, **F)** Fatty acid capacity, **G)** Grouped data for fuel dependency, **H)** Grouped data for fuel capacity. **A/B/C/D/E/F)** show the results per cell line. The patients (red) were compared to the corresponding controls (blue) by unpaired T-tests with Welch correction (* $p < 0.05$), and differences between control lines were assessed using the same method. The pooled patient group was compared to the control group by an unpaired T-test with Welch correction (* $p < 0.05$). Error bars depict standard deviation (n = 3/4).

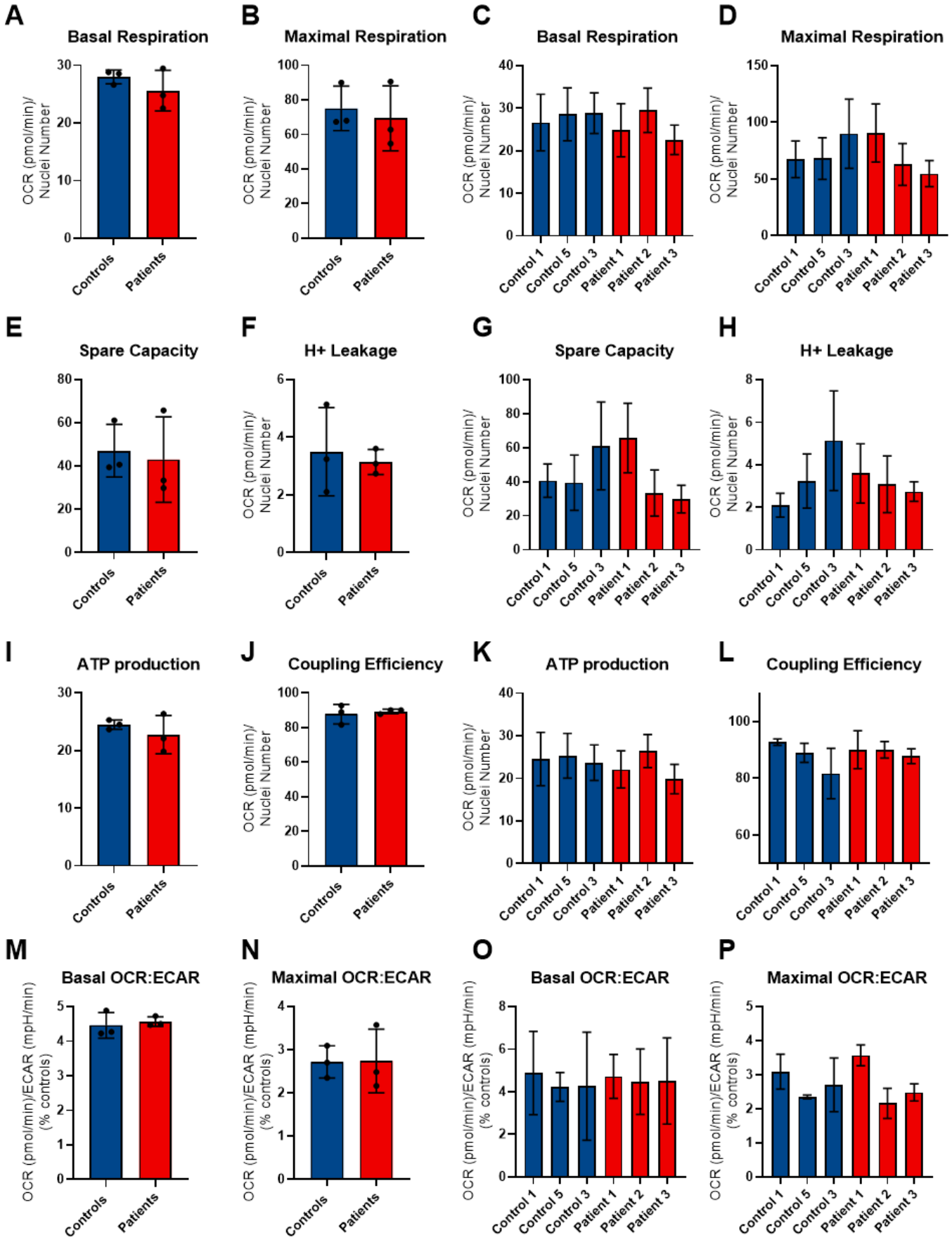
A
Basal Respiration
OCR (pmol/min)/ Nuclei Number
Controls
Patients
B
Maximal Respiration
C
Basal Respiration
Control 1
Control 5
Control 3
Patient 1
Patient 2
Patient 3
D
Maximal Respiration
E
Spare Capacity
F
H+ Leakage
G
Spare Capacity
H
H+ Leakage
I
ATP production
J
Coupling Efficiency
K
ATP production
L
Coupling Efficiency
M
Basal OCR:ECAR
OCR (pmol/min)/ECAR (mpH/min) (% controls)
N
Maximal OCR:ECAR
O
Basal OCR:ECAR
P
Maximal OCR:ECAR

Figure 97: Assessment of mitochondrial oxidative phosphorylation in low mixed group fibroblasts. A/C) Basal Respiration, **B/ D)** Maximal respiration, **E/G)** Spare capacity, **F/H)** H^+ Leakage, **I/K)** ATP production, **J/L)** Coupling efficiency, **M/O)** Basal OCR:ECAR, **N/P)** Maximal OCR:ECAR. **A/B/E/F/I/J/M/N)** show the results per group, **C/D/G/H/K/L/O/P)** show the results per cell line. The patient's (red) results were compared to the corresponding controls by unpaired T-tests with Welch correction (* $p < 0.05$), and differences between control lines were assessed using the same method. The pooled patient group was compared to the control group by an unpaired T-test with Welch correction (* $p < 0.05$). Error bars depict standard deviation (n = 3/4).

5.2.3.4 Cathepsin B

Alterations in lysosome morphology are associated with alterations in lysosome function, specifically hydrolase activity. GWAS studies have linked CatB to PD (Chang *et al.*, 2017; Nalls *et al.*, 2019; Blauwendraat *et al.*, 2020), therefore CatB activity was assessed using Abcam's MagicRed probe, a fluorescent substrate of CatB. Significant variation in the number and total area of CatB active lysosomes was observed between the controls in glucose conditions (Number of CatB active lysosomes: 90 – 109 %, Figure 99B and Total CatB active lysosome area: 81-122 %, Figure 99B and D). A similar trend was observed in galactose conditions, but significance was not reached (Figure 99B and D). Control 2 had significantly smaller CatB active lysosomes compared to the other controls (7-12 %, Figure 99F). The Cathepsin B activity within the controls' lysosomes was also varied in glucose (90-113 %, Figure 99H).

The patients showed similar variation to the controls in both media conditions. Assessment of the patients to their corresponding age- and sex-matched controls found no notable differences in total CatB active lysosome area (Figure 99D), average CatB active lysosome area (Figure 99F) or Cathepsin B activity within the lysosomes (Figure 99H). Several patients were significantly different to their corresponding control for total CatB active lysosome area (Patient 3: 33 % ± 11, $p = 0.004$, Patient 4: 35 % ± 9, $p = 0.05$,Figure 99D), however, the results were within the normal range of the control variation. Patient 2 had a decreased number of CatB active lysosomes by 31 % ± 21 in glucose ($p = 0.05$, Figure 99B).

Assessment of the patient and control groups showed no population differences in galactose media (Figure 99A, C, E and G). In glucose, the patients had 14 % ± 18 fewer CatB active lysosomes (Figure 99A). This corresponded with the 17 % ± 21 lower total CatB active lysosome area (Figure 99C). The CatB active lysosomes were similar in size (Figure 99E) and Cathepsin B activity in the lysosomes did not differ (Figure 99G).

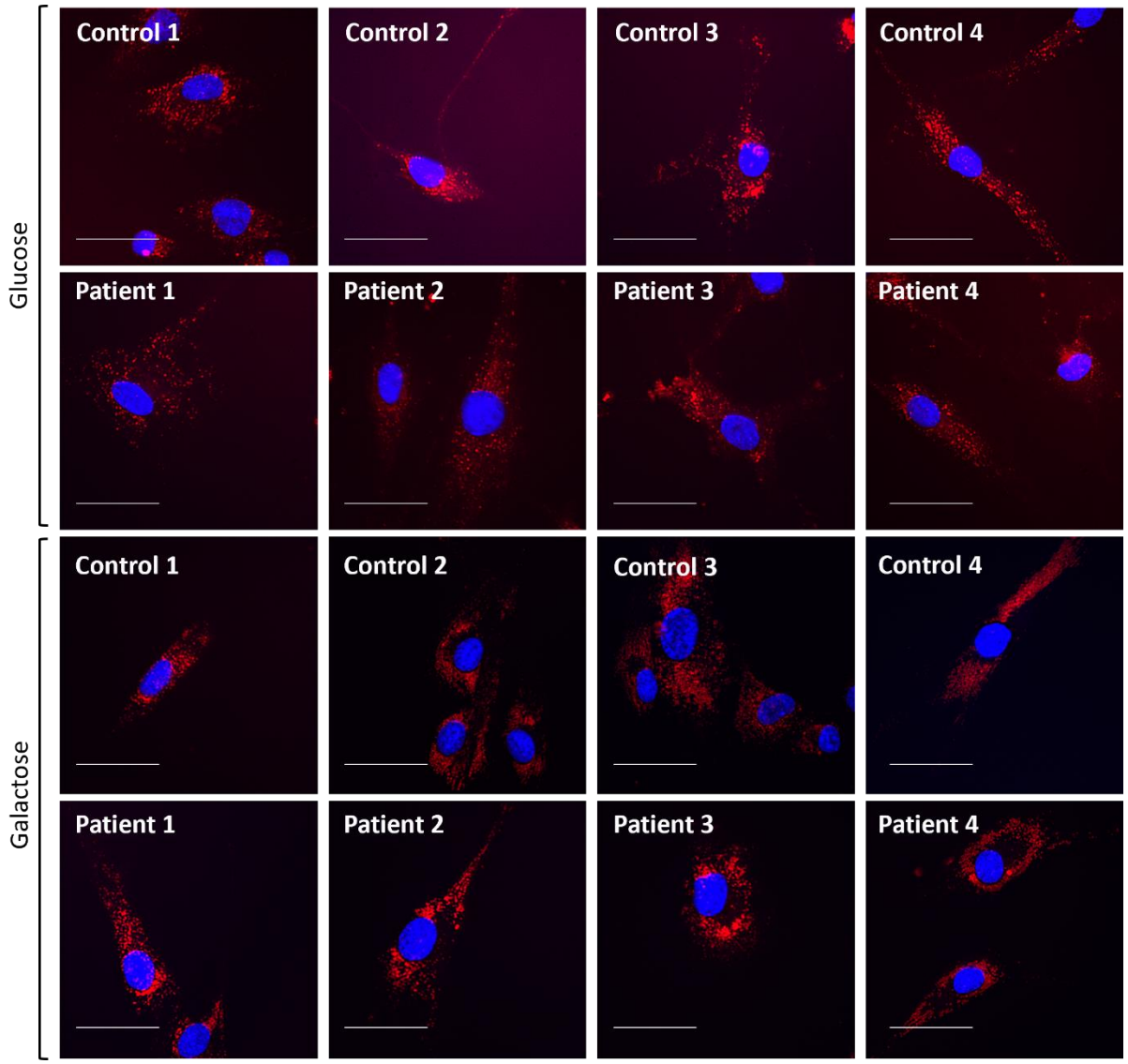

Figure 98: Representative images of CatB MagicRed staining in fibroblasts from the low mixed group. Nuclei (blue) and CatB active lysosomes (red). Scale bar = 40 µm.

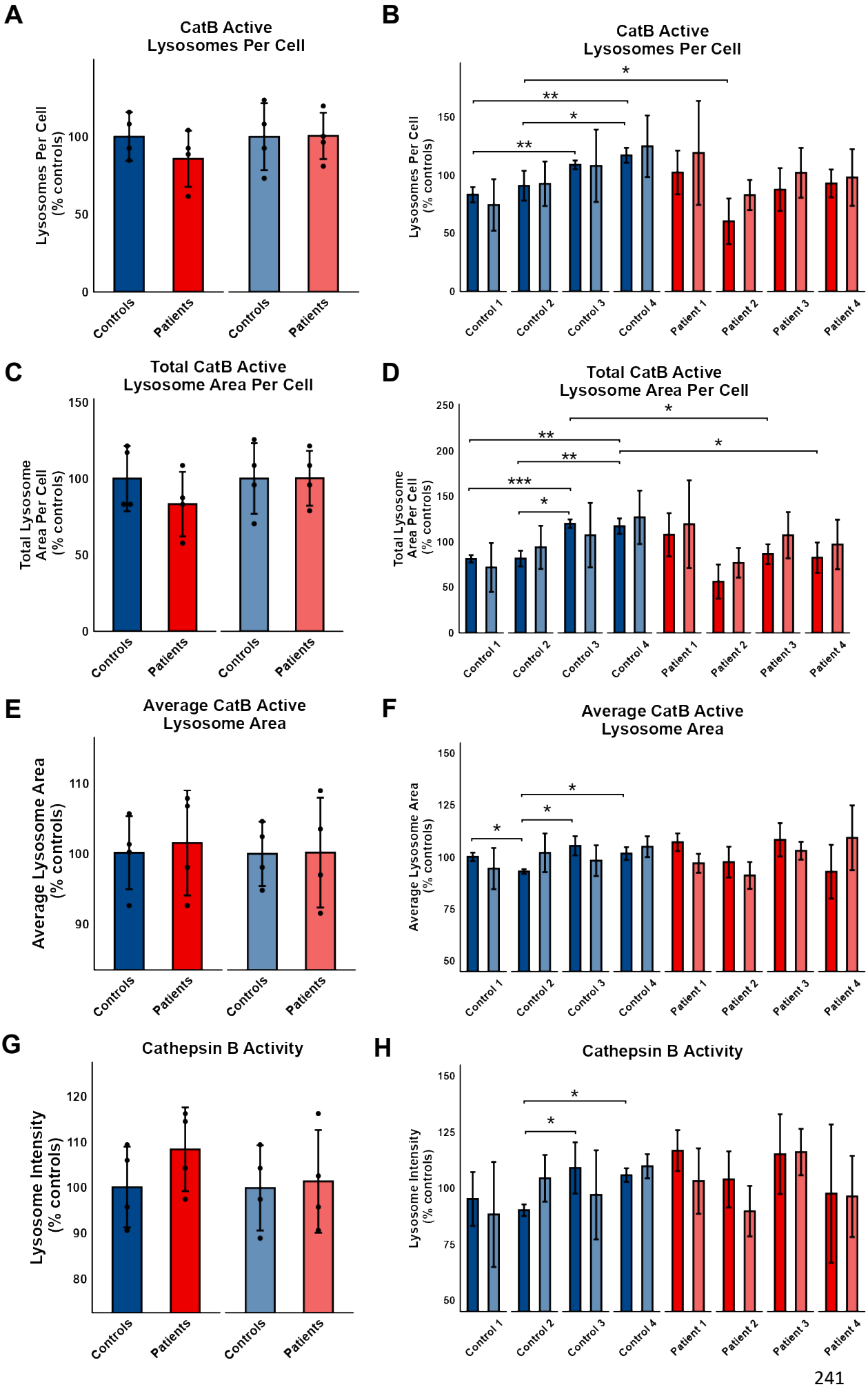
A
CatB Active
Lysosomes Per Cell
Lysosomes Per Cell
(% controls)
Controls
Patients
Controls
Patients
B
CatB Active
Lysosomes Per Cell
Lysosomes Per Cell
(% controls)
Control 1
Control 2
Control 3
Control 4
Patient 1
Patient 2
Patient 3
Patient 4
C
Total CatB Active
Lysosome Area Per Cell
Total Lysosome
Area Per Cell
(% controls)
D
Total CatB Active
Lysosome Area Per Cell
E
Average CatB Active
Lysosome Area
Average Lysosome Area
(% controls)
F
Average CatB Active
Lysosome Area
G
Cathepsin B Activity
Lysosome Intensity
(% controls)
H
Cathepsin B Activity

Figure 99: Cathepsin B active lysosomes in patient-derived fibroblasts from the low mixed group. A/B) The number of CatB active lysosomes per cell, **C/D)** The total CatB active lysosome area per cell, **E/F)** The average area of CatB active lysosomes, **G/H)** Cathepsin B activity. **A/C/E/G)** The pooled data for the patient and control groups (n = 4), where the patients (red) were compared to the controls (blue) by an unpaired T-test with Welch correction (* $p < 0.05$). **B/D/F/H)** show the cell lines individually, where the patients were compared to the corresponding control by unpaired T-tests with Welch correction (* $p < 0.05$, ** $p < 0.01$) (n = 3). Differences between controls and differences between glucose and galactose conditions were determined the same manner. Results from the glucose (dark) and galactose (light) culture conditions were normalised to the average of the controls per repeat for each condition. Error bars depict standard deviation.

5.2.3.5 Lysosomal pH

Lysosomal pH is vital to hydrolase activation. pH can be assessed using the Lysosensor DND-189. The probe fluoresces in acidic environments in a pH-dependent fashion. Results for each parameter were normalised to the average of the controls. Control 5 was used in this assay instead of Control 4 due to difficulties recovering Control 4 from thawing.

Control 1 and Control 5 showed no difference in number of optimally acidic lysosomes (Figure 101B), total optimally acidic lysosome area (Figure 101D) or lysosome acidity (Figure 101H). Control 3 and Control 2 were the most variable across parameters differing in the numbers of optimally acidic lysosomes (16 %, Figure 101B) and total optimally acidic lysosome area (18 %, Figure 101D).

The patient group was more homogenous. The number of optimally acidic lysosomes and total lysosome area for Patient 1, 2 and 3 fell within a 15 % range and did not differ from the average of the controls (Figure 101B and D). Patient 4 displayed 19 % ± 15 more optimally acidic lysosomes (Figure 101B) and 18 % ± 13 greater total optimally acidic lysosome area (Figure 101D). The average size and acidity of the optimally acidic lysosomes did not differ between patients and controls (Figure 101F, Figure 101H). No statistical differences were observed between the control and patient groups for any parameters. However, the controls were more variable than the patient.

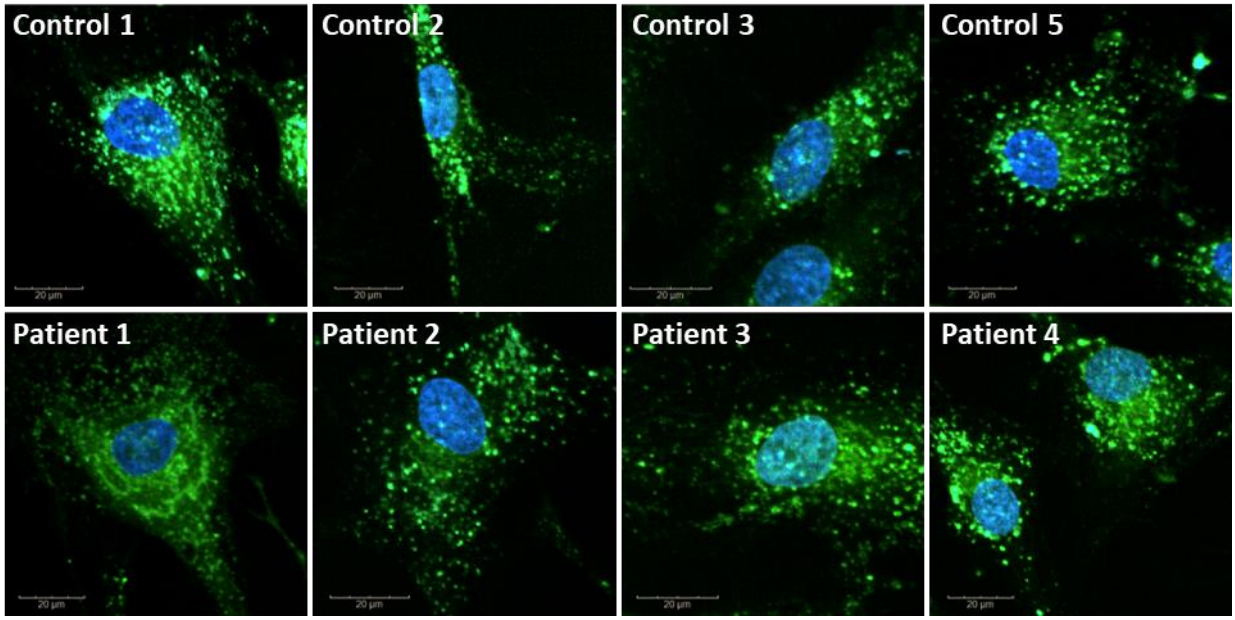

Figure 100: Representative images of optimally acidic lysosomes in the fibroblasts from the low mixed group stained with lysosensor. Nuclei (blue) and lysosensor (green). Scale bar = 50 µm.

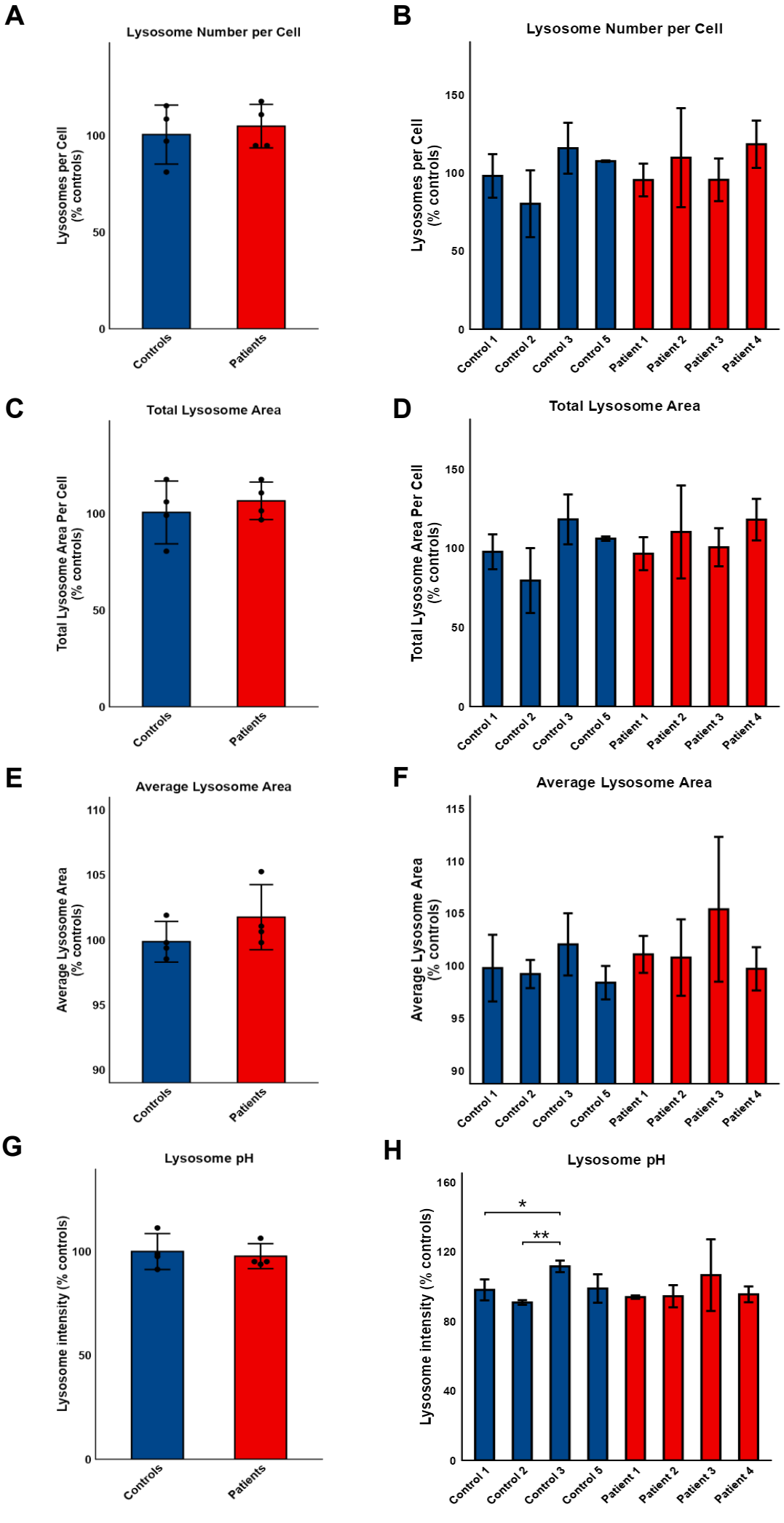
A
Lysosome Number per Cell
Lysosomes per Cell (% controls)
0
50
100
Controls
Patients
B
Lysosome Number per Cell
Lysosomes per Cell (% controls)
0
50
100
150
Control 1
Control 2
Control 3
Control 5
Patient 1
Patient 2
Patient 3
Patient 4
C
Total Lysosome Area
Total Lysosome Area Per Cell (% controls)
0
50
100
Controls
Patients
D
Total Lysosome Area
Total Lysosome Area Per Cell (% controls)
0
50
100
150
Control 1
Control 2
Control 3
Control 5
Patient 1
Patient 2
Patient 3
Patient 4
E
Average Lysosome Area
Average Lysosome Area (% controls)
90
95
100
105
110
Controls
Patients
F
Average Lysosome Area
Average Lysosome Area (% controls)
90
95
100
105
110
115
Control 1
Control 2
Control 3
Control 5
Patient 1
Patient 2
Patient 3
Patient 4
G
Lysosome pH
Lysosome intensity (% controls)
0
50
100
Controls
Patients
H
Lysosome pH
Lysosome intensity (% controls)
0
40
80
120
160
*
**
Control 1
Control 2
Control 3
Control 5
Patient 1
Patient 2
Patient 3
Patient 4

Figure 101: Acidic lysosomes in the patient-derived fibroblasts from the low mixed group. A/B) The number of optimally acidic lysosomes per cell, **C/D)** The total optimally acidic lysosome area per cell, **E/F)** The average area of optimally acidic lysosomes, **G/H)** Lysosomal acidification. **A/C/E/G)** Patients and controls were grouped (n = 4), where the patients (red) were compared to the controls (blue) by an unpaired T-test with Welch correction (* $p < 0.05$). **B/D/F/H)** Patients were compared to the corresponding Control by unpaired T-tests with Welch correction (* $p < 0.05$, ** $p < 0.01$) (n = 3, except control 5 where n = 2). Differences between controls were also determined this way. Error bars depict standard deviation.

5.2.4 Generation and Assessment of the Low Mixed Group Induced Dopaminergic Neurons

Patient 2, Patient 3 and Control 5 were successfully reprogrammed into iNPCs. Control 6 was paired with Patient 3 to ensure age- and sex-matching (Table 30). The patient and control pairs were assayed separately due to a shortened differentiation protocol for Patient 3. Each patient was normalised to the control, however, due to time constraints there is an insufficient number of repeats to assess statistically.

Table 30: A summary of the patient and control induced dopaminergic neurons that were assessed for the low mixed group.

Cell line	Age at biopsy (years)	Sex
Patient 2	69	Female
Patient 3	54	Female
Control 5	71	Female
Control 6	55	Female

5.2.4.1 Low Mixed Group iDopaminergic Neuron Generation and Characterisation

iNPCs were generated as stated previously. Three patients were successfully reprogrammed, however, Patient 4 was not assessed due to time constraints. Patient 2 was paired with Control 5 from the fibroblast assays and Patient 3 was paired with an age- and sex-matched control from a previous study. Pax6 and Nestin staining confirmed that iNPCs were generated (Figure 102).

Differentiation of Patient 2 and Control 5 followed the standard protocol. Patient 3 did not survive the twenty-seven day protocol, therefore, it was cultured on a shortened protocol. Despite the reduced differentiation length, all lines produced iDA neurons successfully, which was demonstrated by protein expression (β-III-Tubulin: 89 % ± 15, MAP2: 99 % ± 1, TH: 96 % ± 6, DAT: 99 % ± 3, Figure 103, Figure 104, Figure 105). Characterisation of the iDA neuron morphology found that an average

of 63 % ± 4 of control cells were neuronal (Figure 109, Figure 110A). The patients had a slightly lower percentage of cells with neuronal morphology (Patient 2: 48 % ± 11, Patient 3: 57 % ± 10, Figure 110A). No difference in cell viability was observed (Figure 110B). The neuronal cells from Patient 2 were rounder than the controls (Patient 2: 10 % ± 9, Figure 110C) and had a greater width to length ratio (10 % ± 10, Figure 110D). This shows that the cells do not elongate as much as the Control 5.

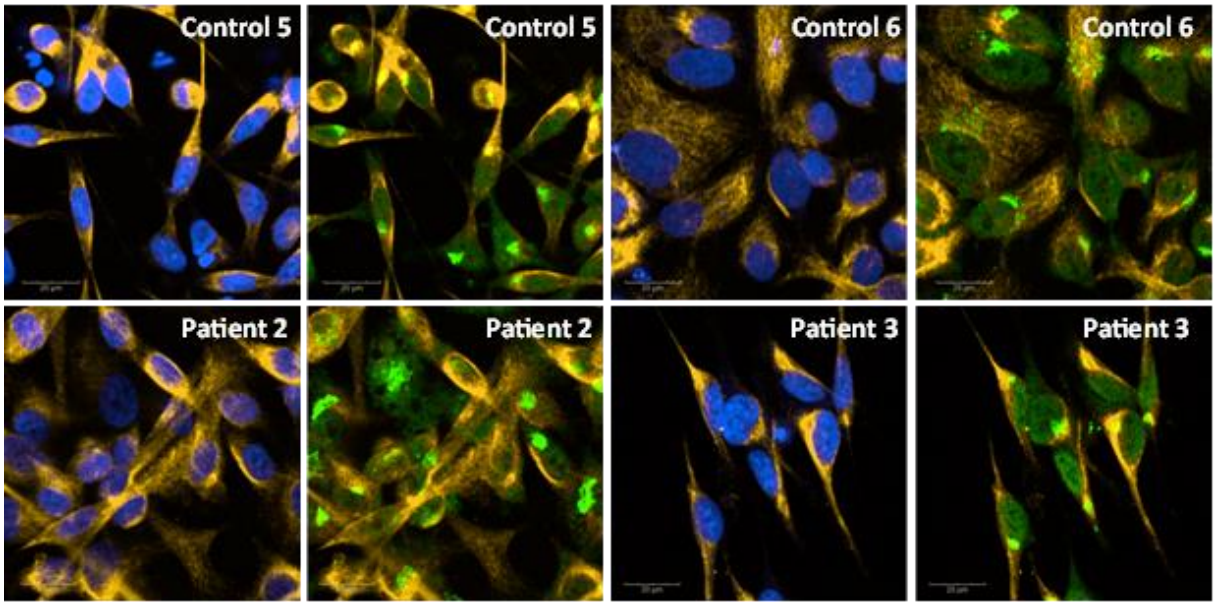

Figure 102: Representative images of the iNPCs from the low mixed group stained for Pax6 and Nestin. Nuclei (blue), Pax6 (green) and Nestin (orange). Scale bar = 20 µm.

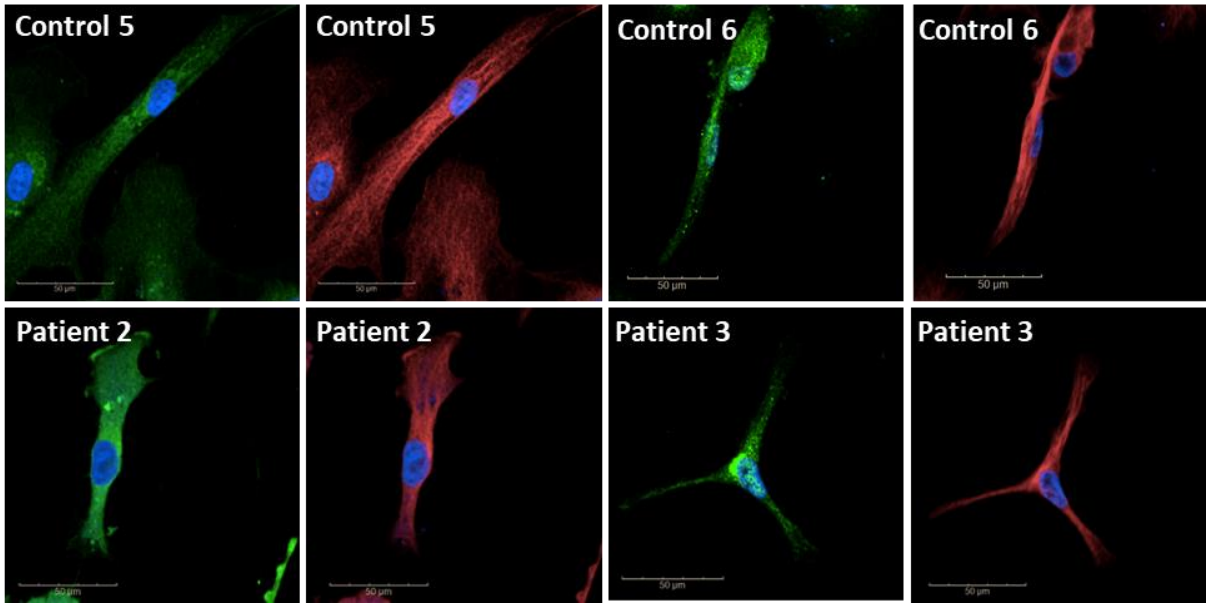

Figure 103: Representative images of the iDA neurons from the low mixed group stained for TH and β-III-Tubulin. Nuclei (blue), TH (green) and β-III-Tubulin (orange). Scale bar = 50 µm.

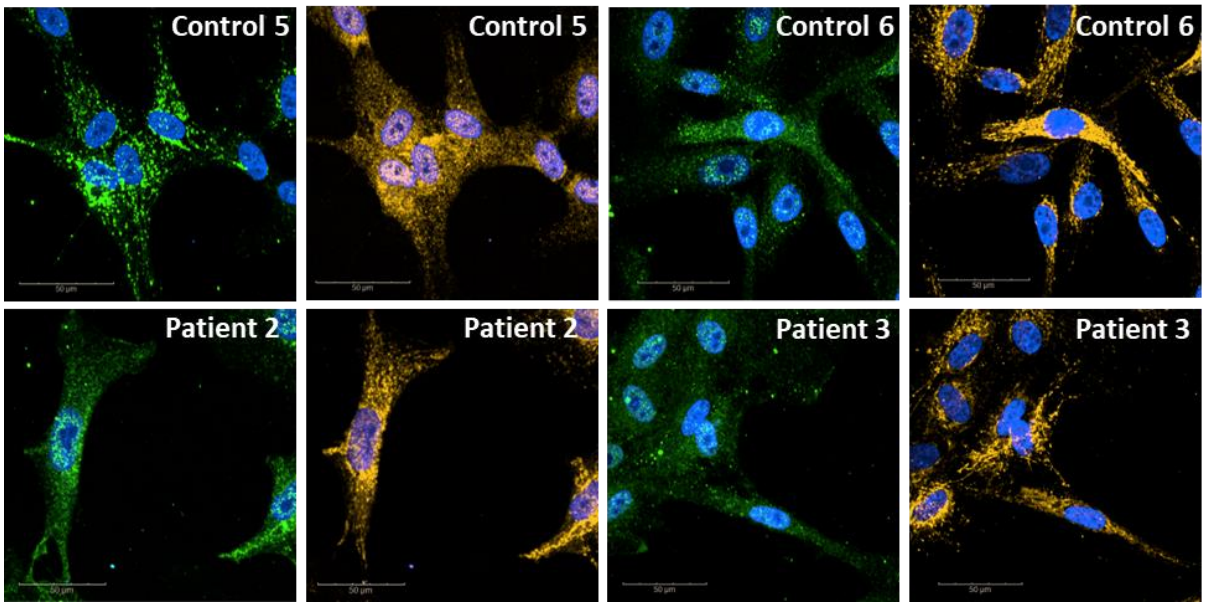

Figure 104: Representative images of the iDA neurons from the low mixed group stained for MAP2 and DAT. Nuclei (blue), DAT (green) and MAP2 (orange). Scale bar = 50 µm.

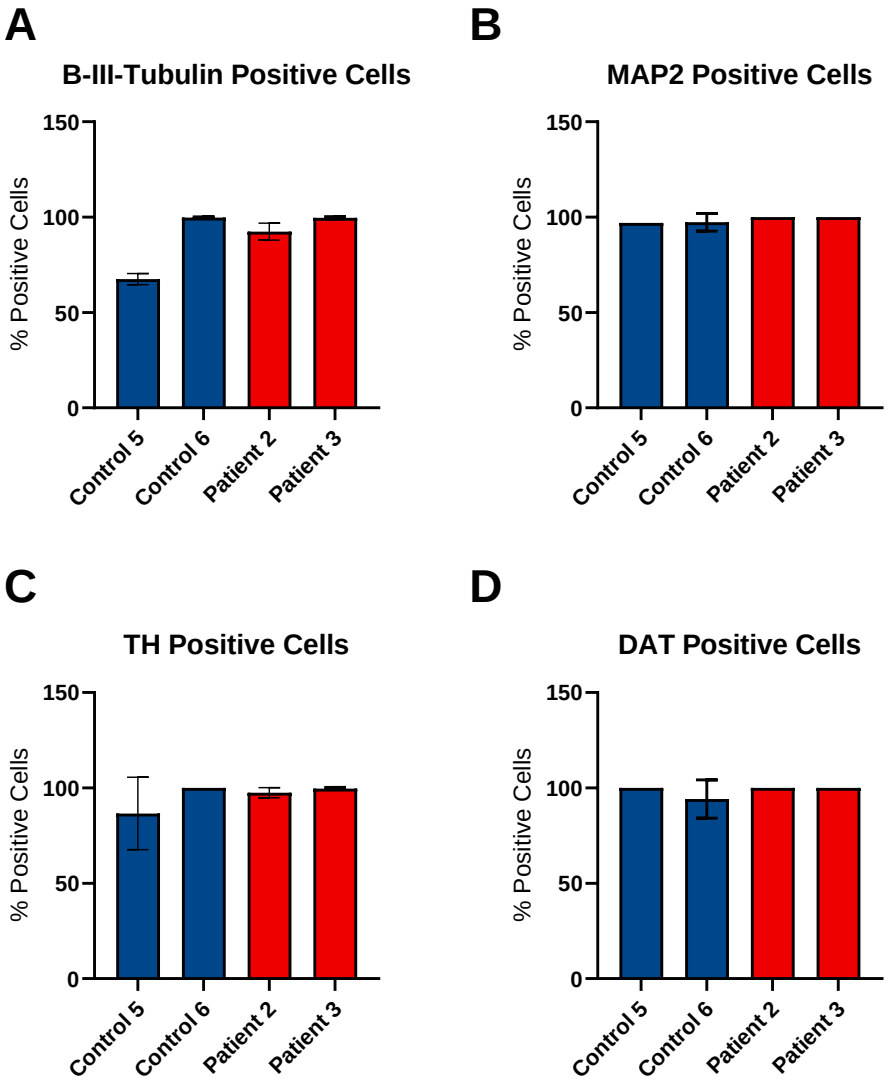

Figure 105: Characterisation of the dopaminergic neurons using TH, DAT, β-III-Tubulin and MAP2. A) Percentage of cells positively stained for β-III-Tubulin, **B)** Percentage of cells positively stained for MAP2, **C)** Percentage of cells positively stained for TH, **D)** Percentage of cells positively stained for DAT. No statistical assessment was conducted due to a reduced number of independent assay repeats (n = 2/3). Error bars depict standard deviation.

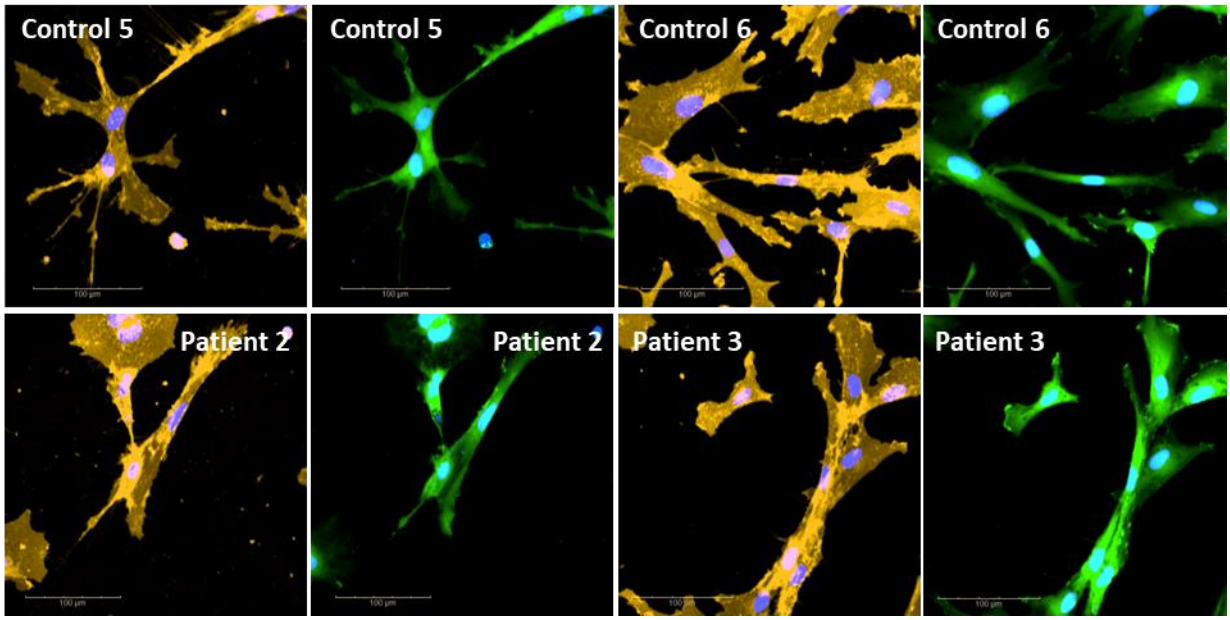

Figure 106: Representative images of the iDA neurons from the low mixed group stained to assess morphology and cell viability. Nuclei (blue), membrane (orange) and cell viability (green). Scale bar = 100 µm.

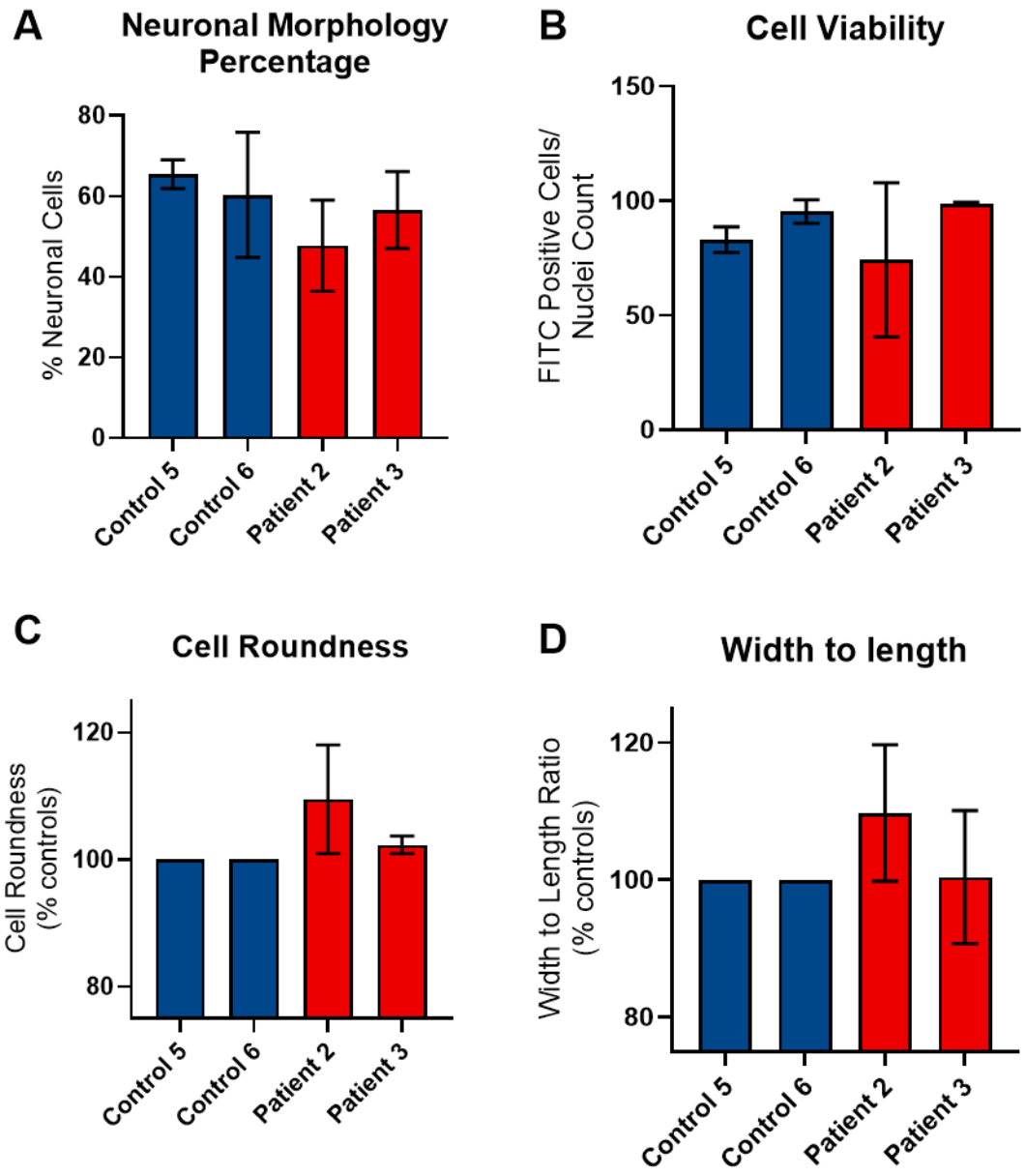

Figure 107: Characterisation of the dopaminergic neuron morphology. A) Percentage of cells with neuronal morphology, **B)** Cell viability, **C)** Neuronal cell roundness, **D)** Neuronal cell width to length ratio. Patient 2 was compared to the corresponding control by an unpaired T-test with Welch correction (* $p < 0.05$). Patient 3 was not statistically assessed because only two independent assays were completed in the time frame. Error bars depict standard deviation (n = 2/3).

5.2.4.2 Mitophagy

To understand the mitochondrial deficits in the neurons, the cells were assessed using TMRM and mitotracker green. Both patients had an elevated number of mitochondria per cell (Patient 2: 230 % ± 89, Patient 3: 75 % ± 55, Figure 109B). Similar to the initial screen both patients had an elevated MMP (Patient 2: 53 % ± 34, Patient 3: 18 % ± 26, Figure 109A). However, the ratio of functional mitochondria to mitochondria, assessed by calculating the ratio of TMRM-positive mitochondria to mitotracker green mitochondria, showed no difference between patients and controls (Figure 109C). This suggests that the number of mitochondria is increased but the proportion of the network that is functional does not differ. No difference in the average area of the mitochondria was observed (Figure 109D).

Induction of mitophagy drives a rapid rise in mitochondria co-occurring with lysosomes within 30 minutes in the controls (Figure 110A). The co-occurrence reduces rapidly in Patient 2 and Control 6 over the following 210 minutes (Control 6: -0.062 ± 0.008, Patient 2: -0.047 ± 0.045, Figure 110A). In contrast, Patient 3 does not initiate mitophagy to the same extent as the other three lines (Other lines: 0.22 ± 0.03, Patient 3: 0.09 ± 0.01) and the percentage of mitochondria co-occurring with lysosomes at timepoint 2 was significantly lower than Control 6 (Control 6: 0.35 ± 0.18, Patient 3: 0.30 ± 0.12, $p = 0.03$, Figure 110A). There were no significant differences in the rates of mitophagy between timepoint 2 and 7 for the patient and their corresponding controls (Figure 110A).

The recovery of MMP and the number of functional mitochondria were assessed to understand the flexibility of the cell lines. Induction caused a similar reduction in functional mitochondria in all cell lines (Figure 110C). There were no differences observed in MMP recovery (Figure 110B). Patient 2 and 3 produced functional mitochondria faster than the controls (Controls: 0.0078, Patient 2: 0.043, Patient 3: 0.022, Figure 110C).

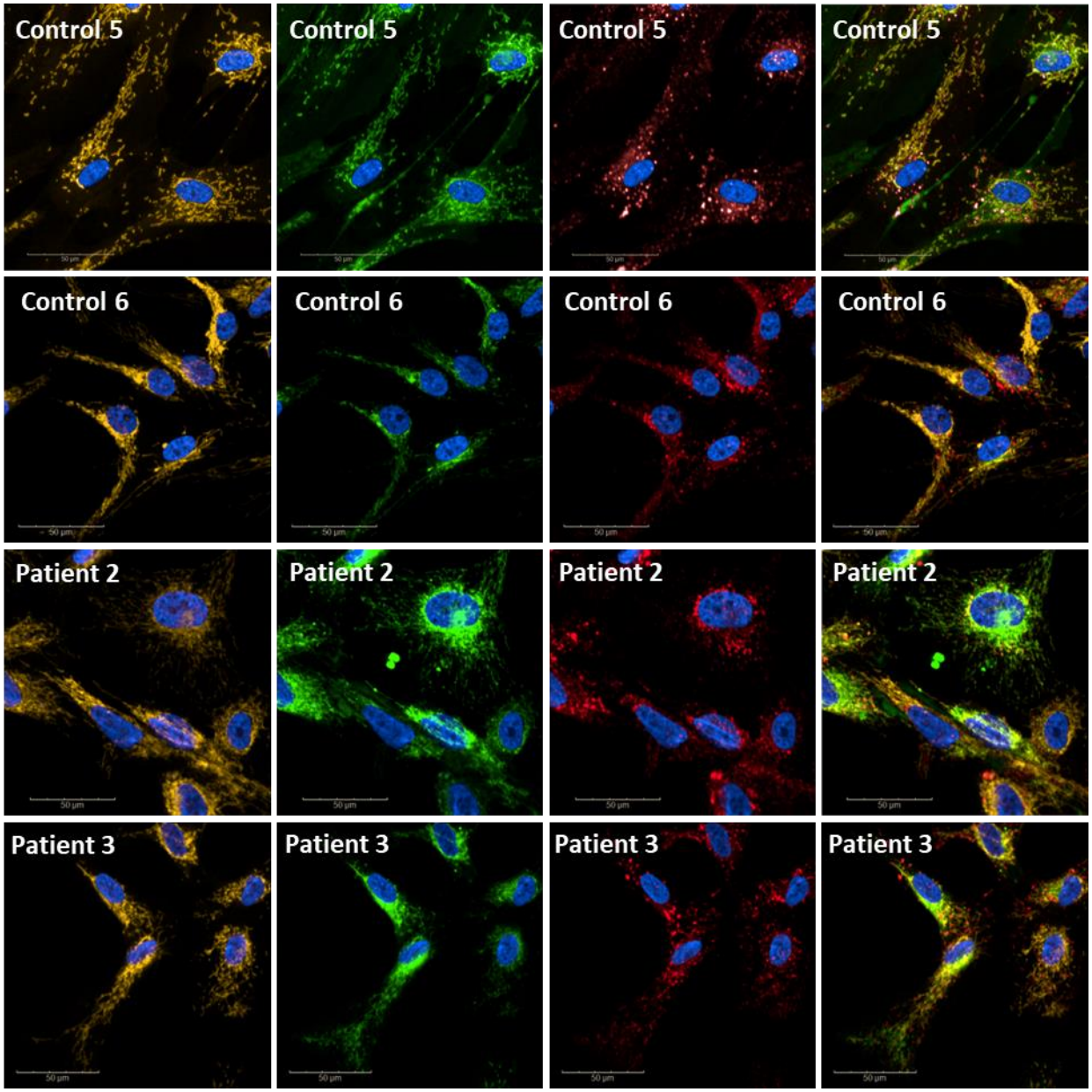

Figure 108: Representative images of the iDA neurons from the low mixed group stained with TMRM, mitotracker green and lysotracker red to assess mitophagy. Nuclei (blue), TMRM (orange), mitotracker green (green) and lysotracker red (red). Images on the right show all four channels merged. Scale bar = 50 µm.

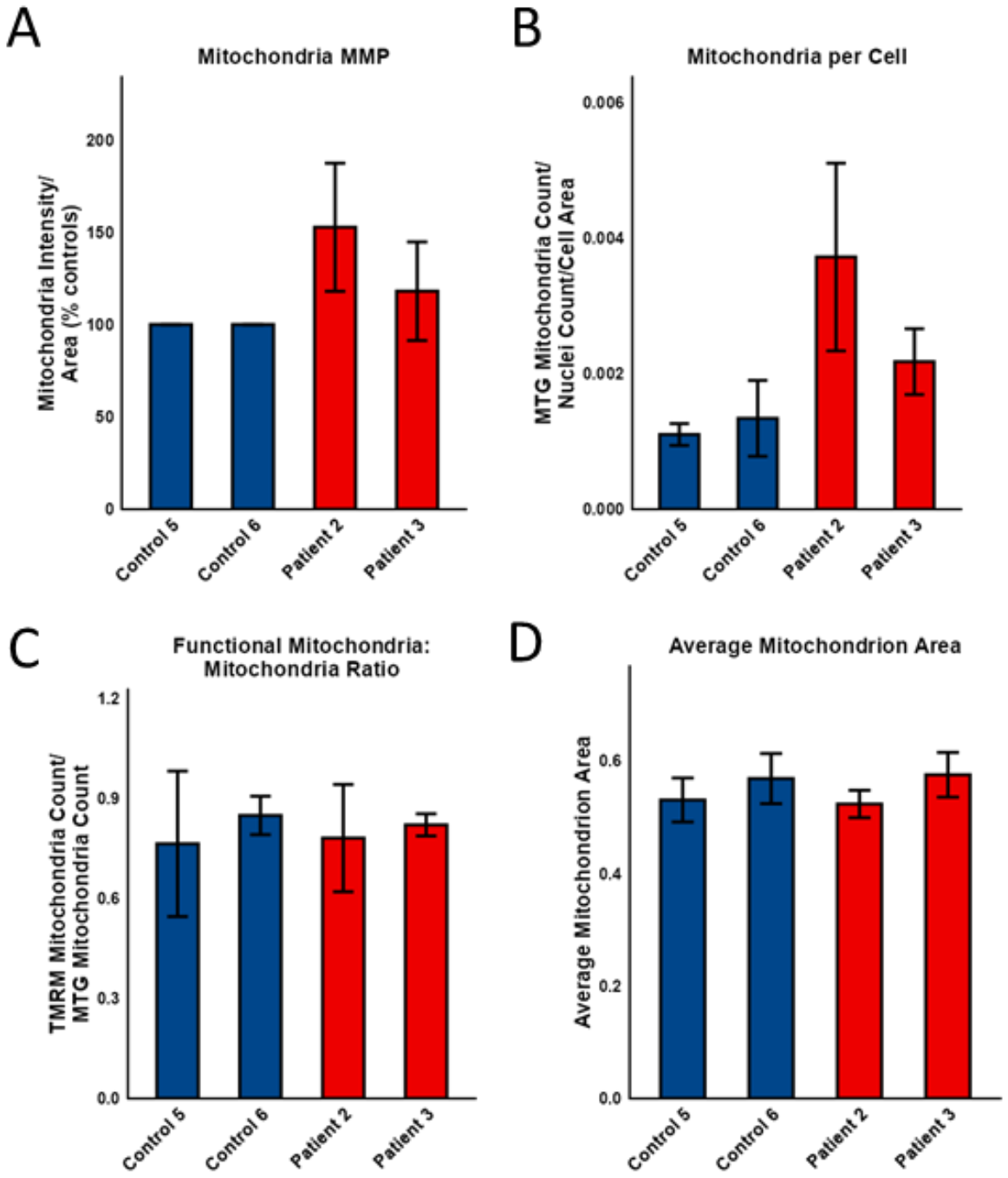

Figure 109: Assessment of mitochondrial function in the low mixed group iDA neurons. A) Mitochondria MMP, **B)** Mitochondria per cell, **C)** Functional mitochondria: Mitochondria ratio, **D)** Average mitochondrion size. Patient 3 was compared to the corresponding control by unpaired T-tests with Welch correction (* $p < 0.05$, $n = 3$). Patient 2 and Control 5 were not statistically tested because only two independent assays were completed in the time frame. Error bars depict standard deviation.

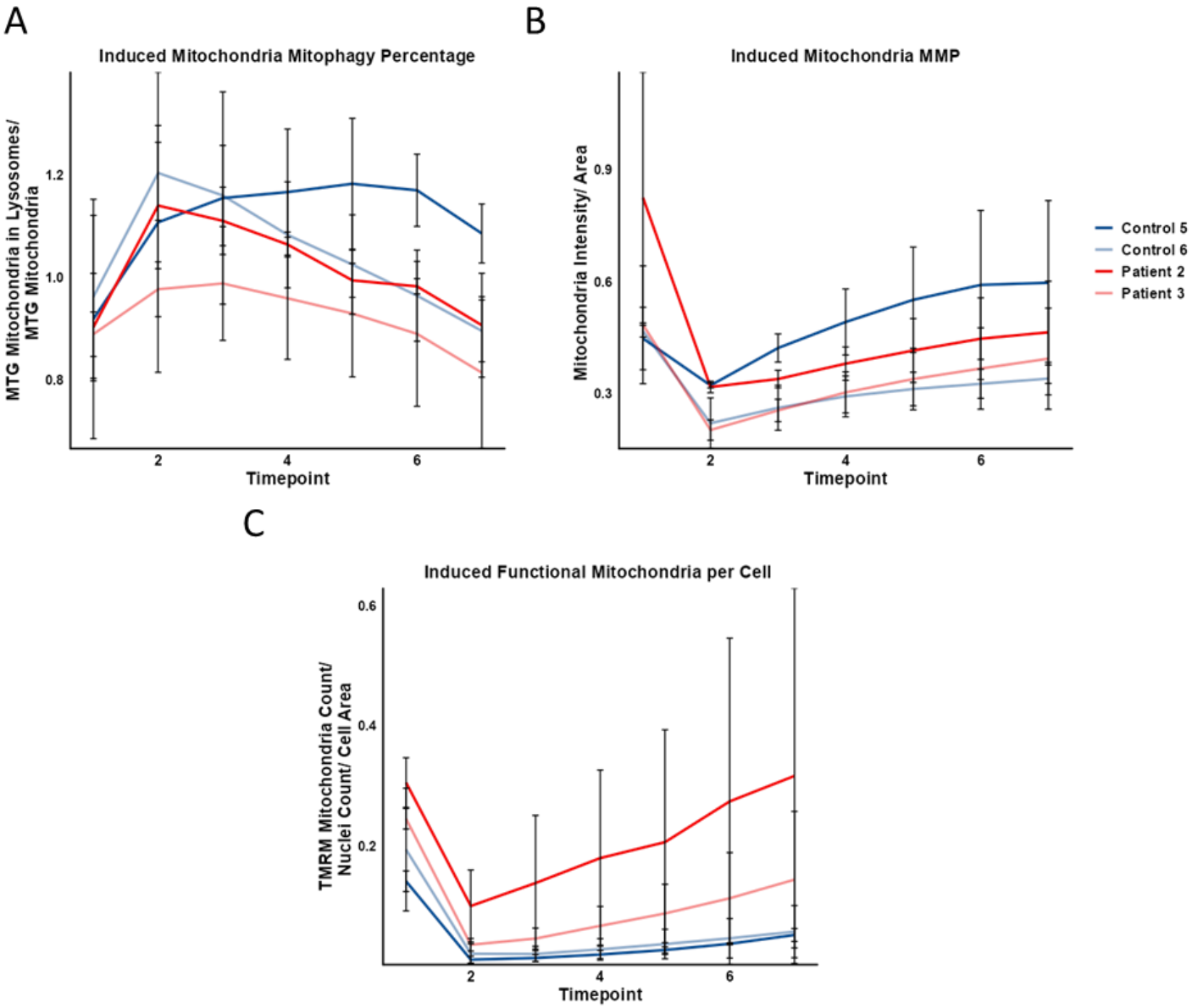

Figure 110: Assessment of mitophagy and mitochondria recovery in the low mixed group iDA neurons. A) Induced mitochondria mitophagy percentage, **B)** Induced mitochondria MMP, **C)** Induced functional mitochondria per cell. Patient 3 was compared to the corresponding control at timepoint 2 by an unpaired T-test with Welch correction (* $p < 0.05$). The rate of mitophagy and recovery between timepoints 1-2 and 2-7 were statistically assessed by unpaired T-tests with Welch correction (* $p < 0.05$, $n = 3$). Patient 2 and Control 5 were not statistically tested because only two independent assays were completed in the time frame. Error bars depict standard deviation.

5.2.4.3 MitoROS

As previously mentioned, ROS levels are higher in the cells from some PD patients than healthy individuals (Chang & Chen, 2020). Due to the mitochondrial abnormalities observed in this subgroup the level of ROS produced by the mitochondria was assessed in the same assay as the mitochondrial dysfunction subgroup neurons. A small elevation in mitoROS was observed in both patients (Patient 2: 12 % ± 11, Patient 3: 18 % 14, Figure 111).

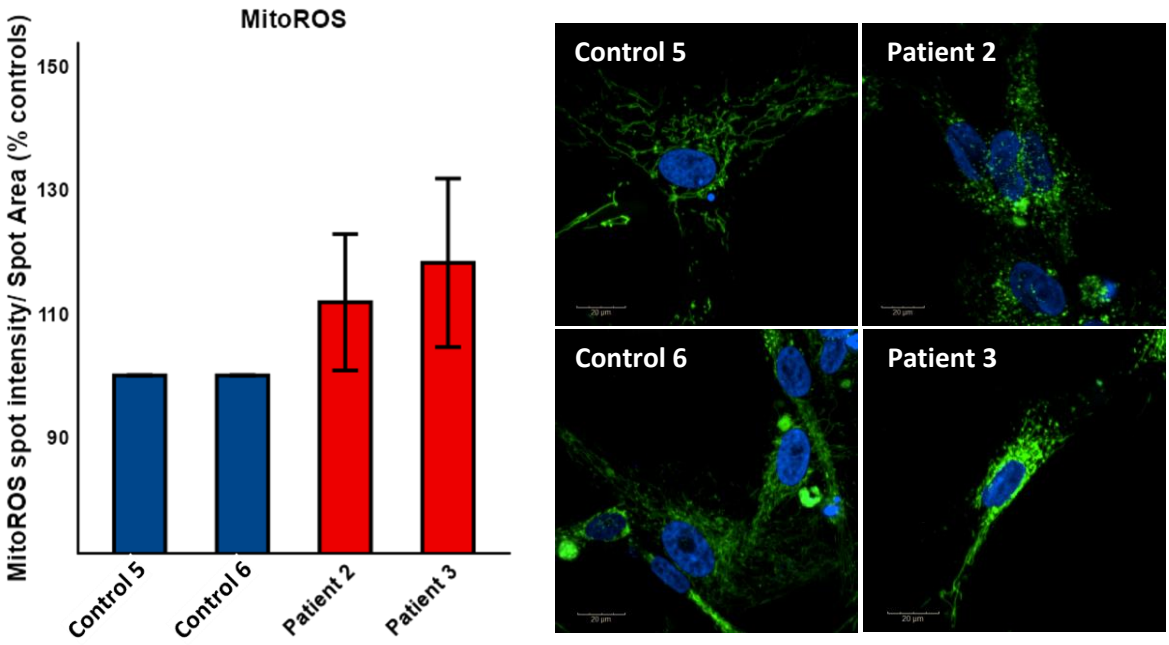

Figure 111: MitoROS levels in iDopaminergic neurons from the low mixed group. The graph shows Patient 2 and 3 (red) compared to Control 5 and 6 (blue) (n = 2). No statistical assessment was conducted because only two independent assay repeats were conducted within the time frame. Error bars depict standard deviation. Representative images show the NpFr2 staining (green) of the iDA neurons from the low mixed group, nuclei (blue) and scale bar = 20 µm.

5.2.4.4 Lysosome pH

To explore lysosome pH in the neurons, Lysosensor DND-189 was utilised. Despite no differences between the patient and control fibroblasts, this assay was still conducted because neurons are more sensitive to lysosomal abnormalities due to their extensive cytoplasm and lifespan (Colacurcio and Nixon, 2016). Both Patient 2 and Patient 3 had an elevated number of optimally acidic lysosomes per cell by 261 % ± 19 and 195 % ± 44 (Figure 113A), respectively. This corresponded with an increased total optimally acidic lysosome area; Patient 2 showed a 24 % ± 23 increase and Patient 3 showed a 49 % ± 54 increase (Figure 113B). Patient 2's lysosomes were the same size as Control 5, but Patient 3's lysosomes were 4 % ± 1 larger than Control 6's lysosomes (Figure 113C). The lysosomes in both patients were more acidic than the corresponding controls by 27 % ± 39 and 35 % ± 16 (Figure 113D).

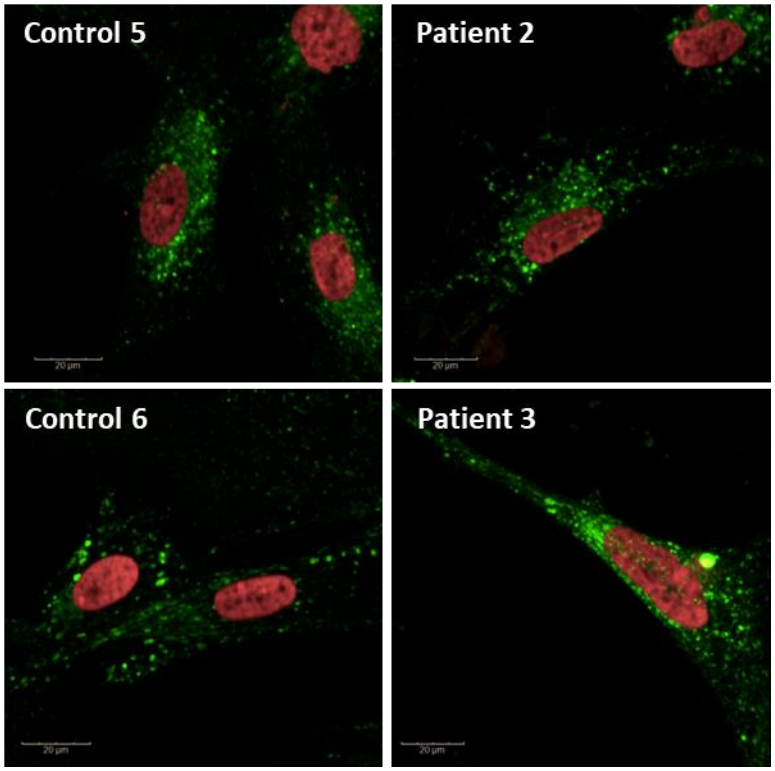

Figure 112: Representative images of the optimally acidic lysosomes in the low mixed group iDA neurons stained with lysosensor. Nuclei (red) and lysosensor (green). Scale bar = 20 µm.

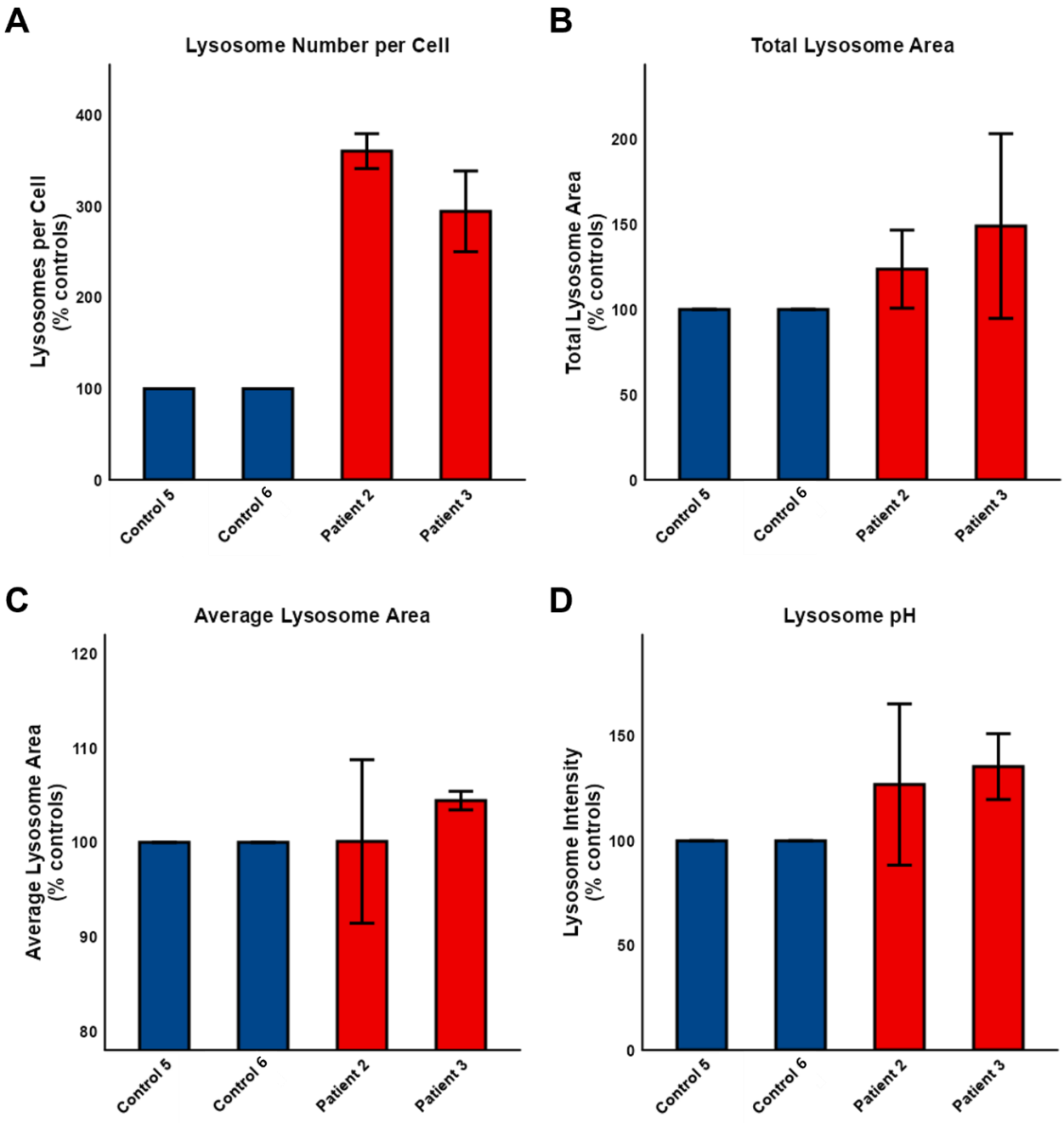

Figure 113: Acidic lysosomes in iDopaminergic neurons from low mixed group. A) The number of optimally acidic lysosomes per cell, **B)** The total optimally acidic lysosome area per cell, **C)** The average area of optimally acidic lysosomes, **D)** Lysosomal acidification. Patients (red) were normalised to the corresponding Control (blue) (n = 2). No statistical assessment was conducted because only two independent assay repeats were conducted within the time frame. Error bars depict standard deviation.

5.2.4.5 Cathepsin Activity

Due to the elevated pH, the activity of cathepsin enzymes was assessed to determine the lysosomes' functional capabilities. Both patients had an increased number of cathepsin active lysosomes per cell

by 550 % and 169 % ± 8 (Figure 114A). This corresponded with a 92 % increase in the total Cathepsin active lysosome area in Patient 2 and a 42 % ± 3 increase in Patient 3 (Figure 114B). Interestingly, Patient 2 had smaller lysosomes by 12 %, although only one repeat was conducted and should be interpreted with caution. Patient 3 had larger lysosomes by 8 % ± 1 (Figure 114C). Consistent with the

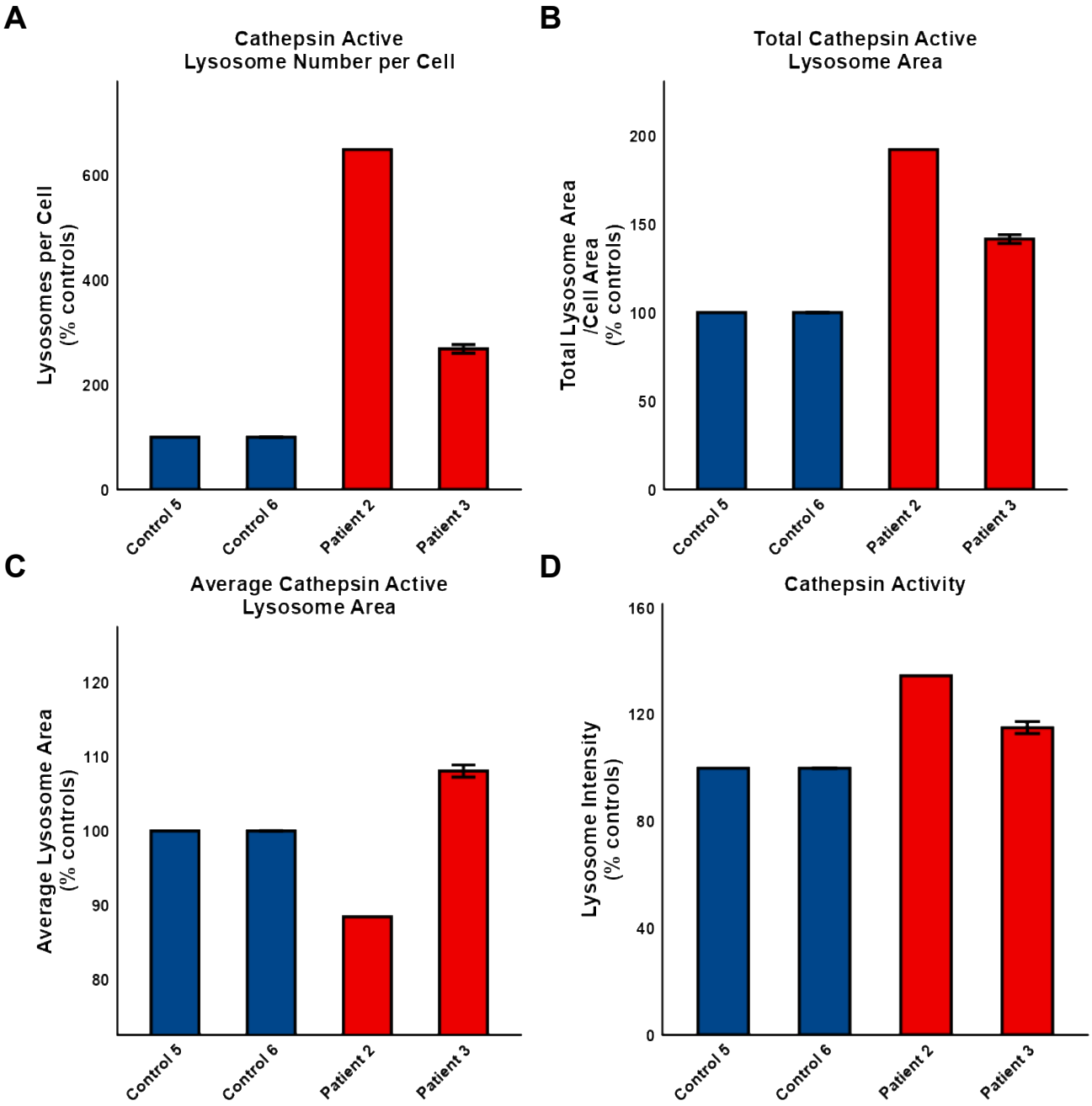

increased acidification, both patients had increased cathepsin activity, Patient 2 by 35 % and Patient 3 by 15 % ± 2 (Figure 114D).

Figure 114: Cathepsin active lysosomes in iDopaminergic neurons from low mixed group. A) The number of cathepsin active lysosomes per cell, **B)** The total cathepsin active lysosome area per cell, **C)** The average area of cathepsin active lysosomes, **D)** cathepsin activity. Patients (red) were normalised

to the corresponding control (blue) (n = 1-2). No statistical assessment was conducted because only two independent assay repeats were conducted within the time frame. Error bars depict standard deviation.

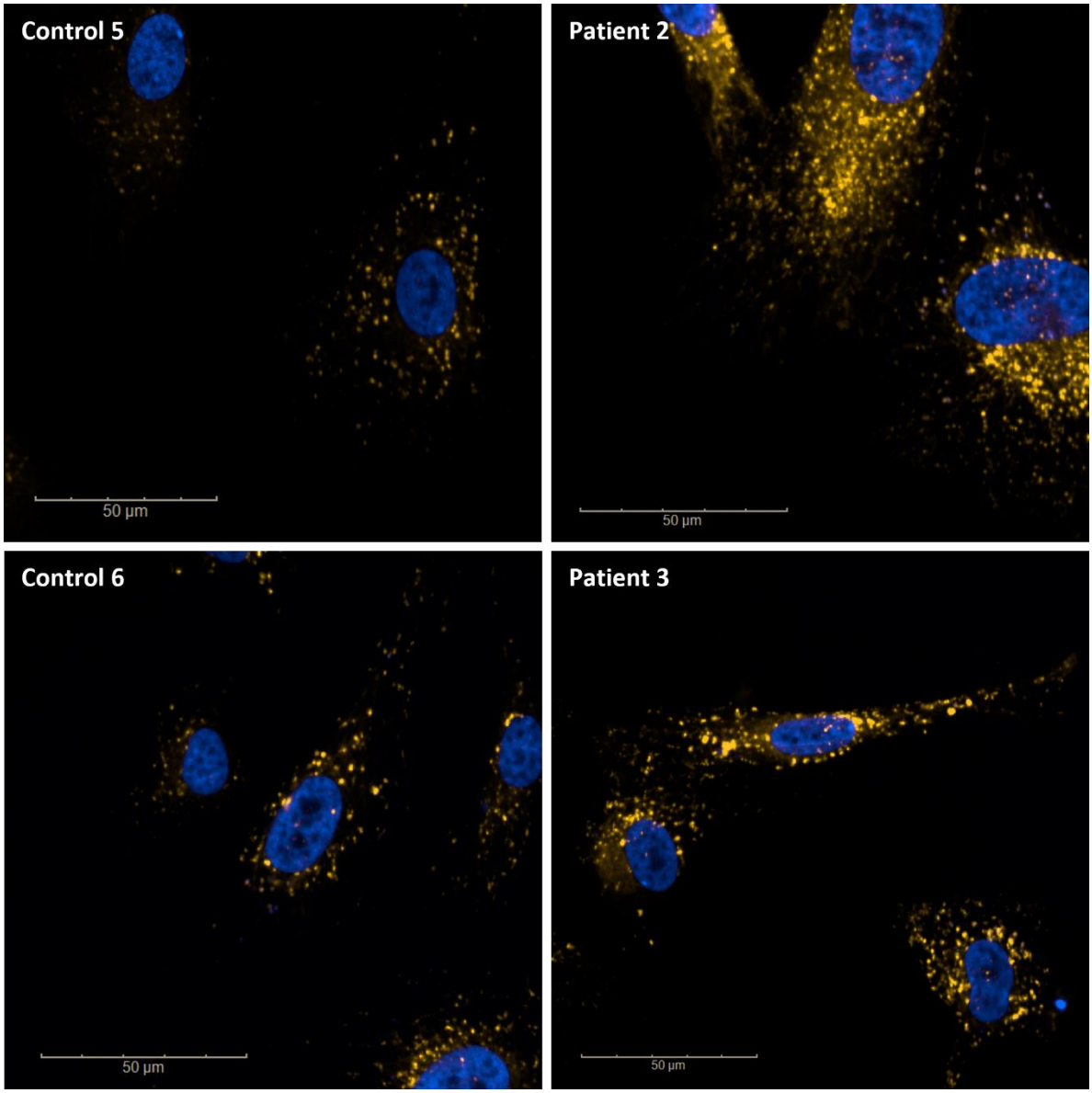

Figure 115: Representative images from the DQ-BSA assay showing cathepsin active lysosomes in the iDA neurons from the mixed low group. Nuclei (blue) and cathepsin active lysosomes (orange). Scale bar = 50 µm.

5.2.4.6 Cathepsin B Activity

The increased cathepsin activity in the neurons demonstrates general cathepsin activity. However, CatB has been linked to PD and specifically α-syn truncation formation (McGlinchey *et al.*, 2019). Thus, CatB activity was assessed revealing similar trends to the general cathepsin activity results. Patient 2 had an extremely high number of CatB active lysosomes, elevated by 1559% ± 153. Patient 3 also displayed a greater number of CatB active lysosomes by 71 % ± 88 (Figure 117A). Total CatB active lysosome area was increase in Patient 2 by 77 % ± 18 but did not differ in Patient 3 (Figure 117B). In keeping with the acidified lysosome results, Patient 2 had normal sized lysosomes, but Patient 3 had larger lysosomes by 6 % ± 1 (Figure 117C). CatB activity was elevated in both patients, by 13 % ± 8 in Patient 2 and 31 % ± 2 in Patient 3 (Figure 117D).

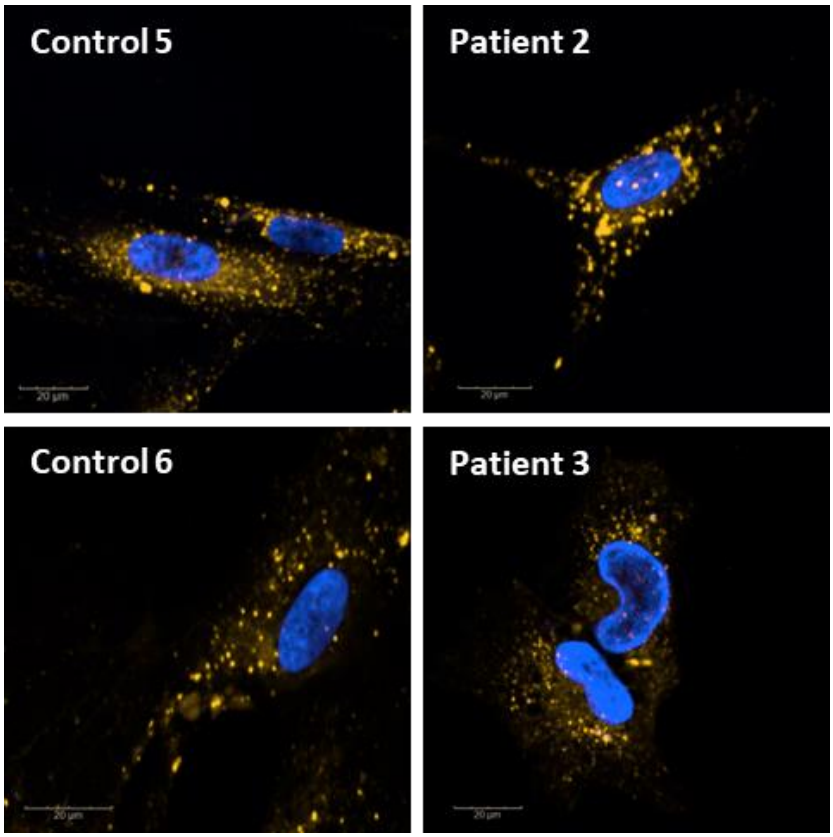

Figure 116: Representative images showing CatB active lysosomes in the iDA neurons from the low mixed group stained with MagicRed. Nuclei (blue) and CatB active lysosomes (orange). Scale bar = 50 μm.

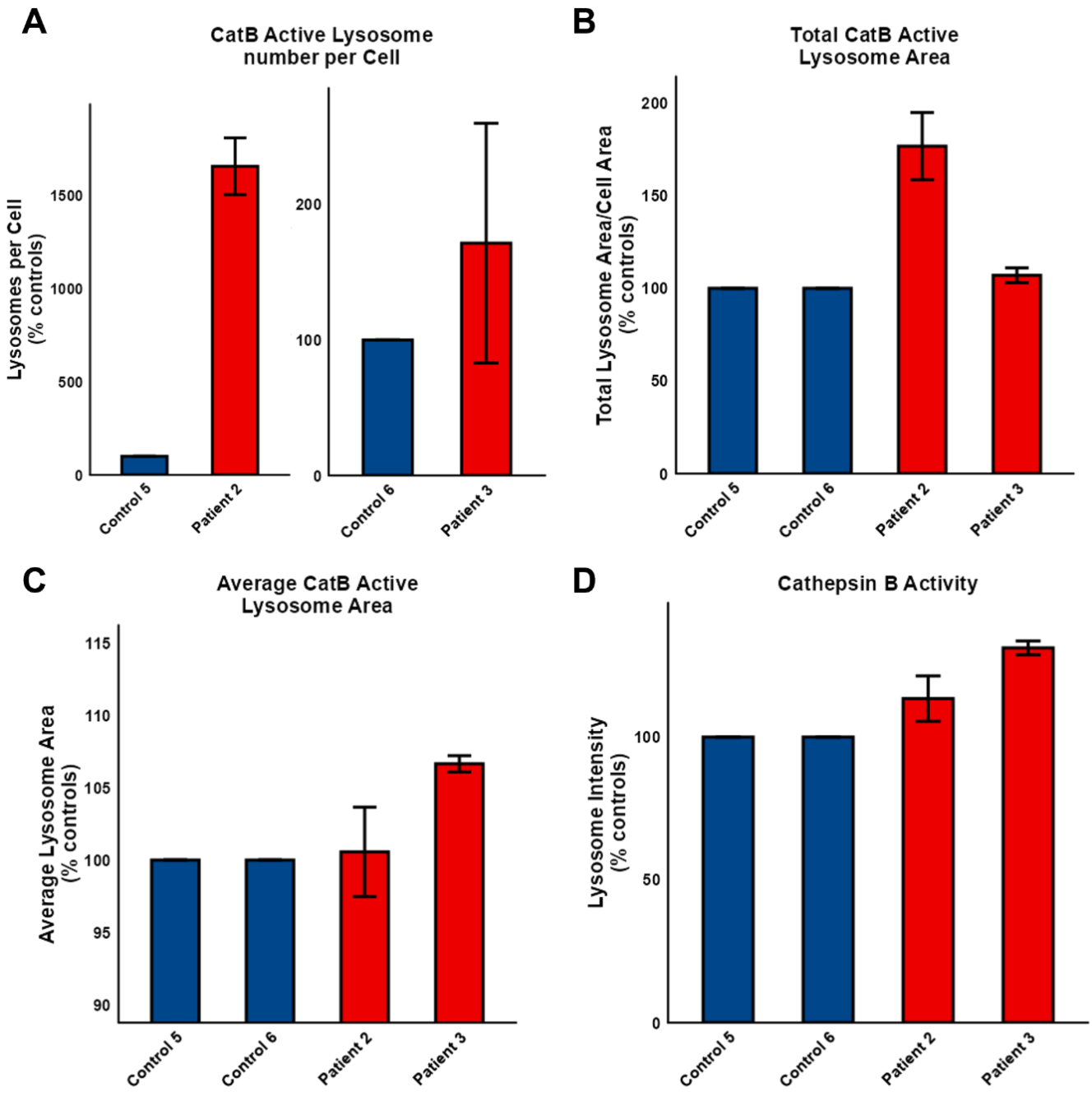

Figure 117: CatB active lysosomes in iDA neurons from the low mixed group. A) The number of CatB active lysosomes per cell, **B)** The total CatB active lysosome area per cell, **C)** The average area of CatB active lysosomes, **D)** Cathepsin B activity. Patients (red) were normalised to the corresponding Control (blue) (n = 2). No statistical assessment was conducted because only two independent assay repeats were conducted within the time frame. Error bars depict standard deviation.

5.3 Discussion

This chapter aims to outline the mitochondrial and lysosomal dysfunction in the mitochondrial dysfunction subgroup and low mixed group. Investigation of the patient's fibroblasts and subsequently iNPC-derived iDA neurons aimed to identify dysfunctional mechanisms that may define PD pathology in these groups.

5.3.1 Investigation of the Mitochondrial Dysfunction Subgroup Fibroblasts

The three patients in the mixed mitochondrial subgroup showed reductions in MMP and perinuclear mitochondria percentage in the initial screen. Elevated ATP levels and increased numbers of mitochondria were also observed but no lysosomal dysfunction.

5.3.1.1 Validation

To determine whether initial stratification was successful the three patients were reassessed. Control 2 was introduced to ensure age- and sex-matching. Initial validation showed consistent phenotypes for Patient 1 and Patient 3, namely increased MMP in galactose and an increase in mitochondria number for Patient 3. Both patients had elevated ATP levels in galactose, which was also consistent with the initial screen. Validation of mitochondria per cell and morphology was carried out using mitotracker green instead of TMRM, which was used for the initial screen. The aim was to validate findings using an independent method of assessment. Mitotracker green accumulates in the mitochondria independently of MMP, whereas TMRM accumulates in an MMP-dependent manner, enabling the quantification of MMP. The difference in the number of mitochondria may be due to a difference in the way dyes sequester within the mitochondria. Once inside mitochondria, mitotracker green forms an epoxy resin that prevents dissipation but can alter mitochondria function and inhibit MMP (Neikirk *et al.*, 2023), which could result in higher numbers of mitochondria, whether this would affect patients or healthy cells differently is unclear. Another possibility is that the natural variability between the controls that Patient 1 was initially assessed with may be different to the controls in validation. Natural variation between controls was observed in the initial screen and Carling *et al.* (2020). However, validation was deemed successful for Patient 1 and Patient 3.

Patient 2 showed no difference from the controls. As discussed, the corresponding control was not assessed with it in the initial screen. It is possible that natural variation in the controls led to the incorrect stratification of this patient. One of the limitations of this study is the inability to assess the entire cohort in the same assays, which will be discussed in the next chapter. Therefore, the lines were separated into groups to enable assessment. The results were normalised to the controls on the plate

enabling analysis of the entire cohort. Natural variation in the controls could result in a patient falsely appearing to be dysfunctional.

5.3.1.2 Mitochondrial Respiration and ATP Levels

ATP production within the cell is a flexible process that uses a variety of fuel types and pathways. Fibroblasts are heavily reliant on glycolysis, which was observed in both the patients and controls by similar reductions in ATP levels when glycolysis was inhibited. No difference in ATP levels were observed when inhibiting fatty acid oxidation, glutamine oxidation or oxidative phosphorylation, suggesting that the patients and controls do not rely on different mechanisms of ATP production.

Oxidative phosphorylation relies upon the function of the individual respiratory complexes. Reduced complex activity has been reported in patient-derived cells and tissue (Schapira *et al.*, 1990; Benecke, Strümper and Weiss, 1993; Winkler-Stuck *et al.*, 2004; Mortiboys *et al.*, 2008, 2015). We investigated the activity of complex I, II and IV because all three have been reported to be dysfunctional in various cell models. No difference in complex I activity was observed in glucose media, however, complex I activity was elevated in Patient 1 and Patient 3 in galactose. This corresponded with both patients showing elevated complex II and complex IV activity independent of culturing conditions. The patients display elevated ATP levels and reduced MMP, thus, the activity of the respirator complexes may be upregulated in the patients to maintain higher ATP production or in an attempt to restore MMP levels. Despite reduced complex I activity being heavily associated with PD, a recent review of the literature found that only one study has shown reduced complex I activity using an enzymatic ELISA assay (Subrahmanian and LaVoie, 2021). This was the Carling *et al.* (2020) study, who assessed levels in patients that had severely reduced ATP levels, the opposite of the phenotype observed in this subgroup. In contrast, del Hoyo *et al.* (2010) showed elevated complex I activity in unstratified PD patients. This study also found no difference in complex II or complex IV activity. Oxygen consumption can be utilised to measure complex I's contribution to oxidative phosphorylation. Similar to the enzymatic assay, only one study has observed reduced complex I activity in patient-derived fibroblasts (Subrahmanian and LaVoie, 2021). Using this method elevated complex I and IV activity were observed in fibroblasts from sPD patients (Wiedemann *et al.*, 1999; Winkler-Stuck *et al.*, 2004). Elevations in complex II activity are consistent with those observed in LRRK2 and Parkin patient-derived fibroblasts (Mortiboys *et al.*, 2008, 2015), however, these patients showed dysfunction in other complexes suggesting that upregulation may be compensatory. As mentioned in the introduction to this chapter, oxidative stress may play an important role in complex dysfunction. Oxidative stress is rarely studied in dermal fibroblasts (Thanan *et al.*, 2014; Bhat *et al.*, 2015) and we consider them poor models for measuring such stress. This is due to reduced reliance on oxidative phosphorylation and thus a lack of ROS production. This is also observed by the high coupling efficiency in the fibroblast seahorse assays.

Therefore, investigation of oxidative stress was not carried out in the fibroblasts. Investigation of this nature could be conducted in the iDA neurons in the future as iDA neurons naturally produce high levels of ROS (Meiser, Weindl and Hiller, 2013; Thanan *et al.*, 2014).

Despite elevated complex I, II and IV activity, MMP remains low. Therefore, we assessed the function of the entire respiratory chain using the Seahorse XF Analyzer. No significant difference in basal respiration was observed, consistent with previous studies (Ambrosi *et al.*, 2014; Milanese *et al.*, 2019). Maximal respiration and spare capacity were significantly reduced in the three patients. This suggests an inability to adapt to higher energy demands. Dopaminergic neurons rely on oxidative phosphorylation as their main source of ATP production and have higher bioenergetic needs than other cell types (Henrich *et al.*, 2023). Therefore, a reduced maximal function would have a greater effect on neuronal health. Reduced maximal respiration was observed in patient-derived fibroblasts in a previous study (Ambrosi *et al.*, 2014) and is associated with familial forms of PD (Mortiboys *et al.*, 2015). However, Milanese *et al.* (2019) showed elevated spare capacity in the patient population. It should be noted that several patients showed reduced maximal respiration, however. Due to stratification, it is plausible that these patients would show a similar phenotype to this subgroup. A small reduction in proton leakage and no difference in coupling efficiency suggests that MMP is not reduced due to an uncoupling of the mitochondrial membrane or proton leakage. The ratio of OCR to ECAR was calculated to determine shifts in the metabolic reliance of the cells. No difference was observed in basal conditions, however, the patients showed a reduced ratio during maximal respiration. This suggests that they are relying on glycolysis more than the controls to meet energy demands.

Overall results in the fibroblasts suggest that stratification selected two patient lines that showed distinctly similar patterns of mitochondrial dysfunction and that the third patient despite similarities in reduced oxidative phosphorylation was not representative of this subgroup. The two patients showed elevated complex activity and ATP production suggesting upregulated mitochondrial respiration that is unable to compensate further when pushed towards maximal energy demands.

5.3.2 Investigation of the Mitochondrial Dysfunction Subgroup iDopaminergic Neurons

The mitochondrial dysfunction subgroup proved difficult to reprogramme, but Patient 3 was successfully converted into a stable iNPC line. This patient showed the most extreme differences in the fibroblast assays. Results from the neurons should act as indicators of this group's phenotype but should be interpreted with caution due to the use of only one control and one patient. In contrast to the fibroblasts, a significant increase in MMP was observed in the patient corresponding with a

reduced number of mitochondria. The patient also had a lower percentage of functional mitochondria compared to the control. This would suggest that a proportion of the network is hyper-functional elevating MMP but that a proportion of the network is dysfunctional. This aligns with the theory that the mitochondria may be upregulating respiration to maintain ATP demand, as seen in the fibroblasts. Reduced MMP is regularly reported in neurons derived from iPSCs or iNPCs (Little *et al.*, 2018; Carling *et al.*, 2020; Schwartzentruber *et al.*, 2020). Schmidt *et al.* (2023) showed that a proportion of mitochondria in patient iPSCs-derived iDA neurons had extremely high MMP compared to controls, however, no population differences were observed. Barnhoorn *et al.* (2024) found similar metabolic alterations between peripheral cells and iPSC-derived iDA neurons. The study assessed respiration in erythroblasts finding a reduced basal and maximal respiration when cultured in glucose. However, iDA neurons showed no difference in basal respiration and certain patients showed elevated maximal respiration. Although MMP was not measured, it would suggest that peripheral cells from patients have lower oxidative phosphorylation, which may be caused by a reduced cell type-dependent reliance on oxidative phosphorylation. In contrast, neuronal cells that rely on oxidative phosphorylation increase oxidative phosphorylation to compensate. Interestingly, some of the PD patients also relied more heavily on complex I for oxidative phosphorylation (Barnhoorn *et al.*, 2024). Assessment of basal respiration in iPSC-derived PINK1 mutant neurons showed elevated basal respiration but did not increase oxygen consumption during maximal respiration (Cooper *et al.*, 2012), suggesting that the cells were already compensating to their greatest potential. Upregulated oxidative phosphorylation may protect the patient in the short term, but over a longer period of time upregulation is unlikely to be sustainable. It is possible that our sPD patient would show similar alterations in respiration which should be investigated in future studies.

Deficits in mitophagy were not observed when assessing the percentage of mitochondria that co-occur with lysosomes, indicating that dysregulation of mitophagy may not be responsible for the increased proportion of dysfunctional mitochondria. Upon mitophagy induction with oligomycin and antimycin, the patient retained a greater number of functional mitochondria compared to the control. Despite this retention, MMP still reduced to the same level as the control and did not recover faster. It is plausible that these mitochondria are unable to recover. Further investigation of mitophagy is required, however, time constraints prevented this.

5.3.3 Investigation of the Low Mixed Group Patient-Derived Fibroblasts

Four patients were stratified into the low mixed group. These patients showed distinct patterns of mitochondrial and lysosomal dysfunction. MMP was increased, but ATP and mitochondria per cell were reduced. The cells had a reduced number of lysosomes, which were also smaller. Assessment of

the fibroblasts with new controls using TMRM, mitotracker green and lysotracker green found a small increase in MMP but no difference in mitochondria per cell. Mitochondria per cell was quantified from the number of mitotracker green mitochondria. Mitotracker green stains mitochondria independently from membrane potential (Neikirk *et al.*, 2023). Therefore, it is possible that an assessment of the functional mitochondrial population would show a reduction in mitochondria. The use of mitotracker green is also shown to affect the function of the ETC and if the patients are more vulnerable to stress due to a lack of flexibility, may result in less extreme differences in MMP. However, it is more likely that natural control variation accounts for the lack of severity in the MMP difference and mitochondria per cell. Of the controls, only Control 2 was included in the controls grouped with these patients in the initial screen. Assessment of the patients compared to Control 2 shows that the patients had higher MMP and lower counts of mitochondria. The grouped nature of this screening is a limitation of the study and will be discussed in the next chapter. However, results for the patients were very similar showing that the stratification was successful in reducing the variance between patients. The lysosome phenotype showed similar difficulties. The number of lysosomes and size did not differ from the controls but the variance in the patients was much smaller. Similar to the lysosomal dysfunction group, reassessment of the initial screen showed that the lysosomal phenotype was greatly worsened in galactose culturing conditions. The validation assay was conducted under glucose conditions so we hypothesise that assessment in galactose may unmask the deficit again. Glucose deficiency triggers the acidification of lysosomes in a compensatory mechanism to provide metabolites for the cell to use to generate ATP (Parra and Hayek, 2018). Future work assessing lysosomes should be carried out in galactose conditions to determine if there is a dysfunctional response to reduced glucose. This was not assessed in our in-depth assays because, to our knowledge, altered culturing conditions have not been utilised in the investigation of lysosome dysfunction in PD. However, when compared to Control 2 the patients showed a reduced number of lysosomes.

Higher MMP would suggest that oxidative phosphorylation maintains the proton gradient. Leakage of protons or dysfunction in complex I, III or IV would lead to lower MMP. Investigation of oxidative phosphorylation using the seahorse Mitostress test assesses the function of the ETC up to complex IV but cannot allude to complex V activity. No difference was observed in basal or maximal respiration. This shows the heterogeneous nature of mitochondrial function in PD as the mitochondrial dysfunction group showed lower levels of maximal respiration. As expected, coupling efficiency and proton leakage did not differ from the controls. Further assessment to determine fuel type dependency and capacity showed no alterations between patients and controls either. Comparison of OCR:ECAR suggested no differences in the cell's dependency on glycolysis and oxidative

phosphorylation. The combination of these results would suggest that complex I-IV of the ETC are able to maintain proton pumping efficiently and indicate that glycolysis is functional as well.

However, despite oxidative phosphorylation, MMP and glycolysis appearing functional, ATP levels were reduced, possibly due to an inability to produce ATP. Complex V is downstream of oxygen consumption in oxidative phosphorylation and therefore not measured directly by the MitoStress test. Complex V is ATP synthase and uses protons passing through its pore to generate ATP. Measurement of complex V activity showed that activity was significantly elevated in the patients. This conflicts with a previous study that showed complex V activity was reduced by 20 % in sPD patients (del Hoyo *et al.*, 2010). Likewise, a mutation in CHCHD2 reduces the assembly of complex V and results in PD (Chen *et al.*, 2024). No other studies have reported complex V activity. The enzymatic assay used to assess complex V only measure the Vmax of the enzyme in an artificially perfect microenvironment in a plate. This suggests that levels of ATP synthase may be increased, that the complex V assembles efficiently and that under ideal conditions can function effectively. However, other factors such as cristae structure and formation may affect efficient assembly and function in vitro (De Los Rios Castillo *et al.*, 2011; Nath, 2022). If complex V activity is elevated, then reduced ATP levels may be caused by an increased consumption of ATP by energy-demanding processes in the cell. Fibroblasts are not metabolically active cells and therefore, the expected cause of elevated ATP consumption is difficult to predict.

The lysosomal phenotype of the mixed group was investigated further to determine if altered acidification or enzyme activity contributed to the patient's disease. The patients showed no difference in acidification to the controls. The cells were assessed in glucose culturing conditions again and thus assessment in galactose media may be required to unmask differences in acidification capabilities. Assessment of CatB activity was conducted in glucose and galactose culturing conditions. High variation was observed in the controls and the patients, but similar to the observed variation in the controls assessed with the lysosomal dysfunction subgroup. Culturing in galactose conditions did not result in any notable differences in the CatB active lysosome phenotype. However, CatB is activated at a more neutral pH (Colacurcio and Nixon, 2016) than the majority of cathepsins so altered acidification caused by glucose depletion (Parra and Hayek, 2018) may not affect the activity of CatB.

5.3.4 Investigation of the Low Mixed Group iDopaminergic Neurons

Three patients were successfully reprogrammed into iNPCs. Unfortunately, time constraints prevented the assessment of Patient 4. Patient 2 and Patient 3 were assessed against two age- and sex-matched controls, however, due to different differentiation protocols they were evaluated separately. Therefore, results should be interpreted cautiously as the assessment of control variation

is limited. Interestingly, both patients showed an elevated number of mitochondria per cell. No differences in the ratio of functional mitochondria to total mitochondria were observed, thus, the network appears to be highly functional in the patients. Higher MMP in Patient 2 was consistent with the fibroblast assays. Patients may have an increased number of mitochondria to maintain the energy demands of the cell. During cardio exercise, high energy demands alter the mitochondrial network and long-term training can cause permanent differences, specifically increasing the mitochondrial content of the cell (Huertas *et al.*, 2019). It is possible that continual demand has caused the increase mitochondria in this instance. Like the mitochondrial dysfunction subgroup iDA neuron line, it is unclear whether the patients can sustain increased activity over long periods of time and whether they are capable of adapting to further metabolic stressors. Barnhoorn et al., (2024) showed that specific groups of patients grown in glucose media had elevated basal respiration compared to controls, however, when they cultured the iDA neurons in galactose the patients did not increase respiration. This suggests that the mitochondria in some patients cannot adapt as easily to increased metabolic burden as the controls. Further assessment of respiration in these patient lines would answer these questions. Similar to the mitochondrial dysfunction subgroup patient, a small increase in mitoROS was observed. Whether this small elevation is due to increased mitochondrial content or dysfunction is unclear. The increase observed was marginal compared to those observed in Parkin patient iNPC-derived iDA neurons (Schwartzentruber *et al.*, 2020) so the physiological effect may not result in oxidative stress damage. However, ROS are critical signalling molecules in the cell (Thanan *et al.*, 2014). Small increases in ROS may result in altered signalling and downstream effects in the cell. This was not explored but should be considered for future investigations. It would be interesting to observe the effect of antioxidant agents on the levels of mitoROS in this group as several are being assessed in clinical trials (McFarthing *et al.*, 2024).

Lysosomal assessment of the patients was not statistically assessed as only two repeats were conducted. Assessment of acidic lysosomes showed a greater number of lysosomes in both patients. A greater number of cathepsin active and CatB active lysosomes were also observed in this group. A greater number of lysosomes has been reported in PD iPSC and iNPC neurons by other studies (Schöndorf *et al.*, 2014; Carling *et al.*, 2020; Kuo *et al.*, 2022). Acidity in the patients lysosomes is greater than in the controls and cathepsin activity is elevated. Elevated cathepsin activity is associated with elevated acidification and the hydrolases are activated at an acidic pH (Yadati *et al.*, 2020). Several studies have shown that reduced CatB activity is linked with PD (Tsujimura *et al.*, 2015; Yadavalli and Ferguson, 2023) and that higher CatB levels are associated with a reduced risk of PD (Lu *et al.*, 2024). However, elevated CatB levels are observed in early-onset Alzheimer's Disease (Wu *et al.*, 2023). Whether higher levels are a compensatory effect as suggested by Lu *et al.* (2024) or detrimental as

expected in early-onset Alzheimer's Disease is unclear. Further exploration of cystatin B, a cathepsin inhibitor, could uncover the driving cause of elevated activity (Wu *et al.*, 2023). Interestingly, Wu *et al.* (2023) observed reduced CatD activity in early-onset Alzheimer's Disease suggesting a possible inverse relationship between the two hydrolases. Assessment of cathepsin activity in the neurons cannot allude to CatD activity, however, further investigation should be conducted to understand the two hydrolases. Due to the lack of fluorescent substrates for CatD, assessment of protein levels may provide the best method. Besides lysosome degradation, cathepsins play an integral role in apoptosis and necroptosis by cleavage activation of apoptotic or necroptotic machinery (Yadati *et al.*, 2020). It is possible that elevated levels make the cells more sensitive to apoptotic triggers or that leakage initiates early cell death. Elevated cytosolic CatD levels have been observed in Alzheimer's Disease postmortem brain tissue (Yadati *et al.*, 2020) and CatB association with mitochondria disrupts mitochondrial function and results in cell death (Baici *et al.*, 2006), further alluding to dysfunctional mechanisms that could be increased in PD.

Results from both mitochondria and lysosomes suggest that the two organelles are highly functional in the neurons of the low mixed group. The elevated function may be compensatory to keep up with demand but predispose the patients to stress vulnerability. A lack of flexibility in sensitive cells, such as neurons, would result in cell death.

5.3.5 Conclusion

In summary, unique patterns of dysfunction were observed in both fibroblast subgroups. Alterations in mitochondrial function defined the two groups and investigation observed elevated MMP or mitochondria count in the limited patient iDA neurons. Despite different phenotypes, results would suggest that the mitochondrial networks of the patients are upregulating function, possibly in a compensatory manner, and a lack of further flexibility could leave the cells vulnerable to stress. Lysosomal dysfunction in the low mixed group was marked by an elevation in number, acidification and enzyme activity and further investigation to understand the implications of this are required.

6 Chapter 6: Discussion

6.1 A Summary of the Thesis Findings

PD is the second most common neurodegenerative disease, but no disease-modifying therapies are currently available. Given the increasing prevalence (Ray Dorsey *et al.*, 2018), devastating effect on patients and the socioeconomic burden on society (Findley *et al.*, 2011; Albarmawi *et al.*, 2022) there is an urgent need for therapeutic success. As discussed throughout this thesis, PD is a heterogeneous disease both mechanistically and clinically. This makes the development of treatments and biomarkers incredibly difficult. Therapeutics target specific mechanisms of dysfunction and, thus, can only rescue pathology in patients who are affected by the targeted mechanisms. It is proposed that heterogeneity is one of the reasons for continual trial failure (Espay *et al.*, 2017). Much of the research into PD mechanisms of disease is conducted in genotypes of PD to reduce heterogeneity, however, mutations are only present in roughly 15 % of the population (Bandres-Ciga *et al.*, 2020). Therefore, methods for stratifying sPD must be developed to improve therapeutic development and biomarker discovery.

The first aim of this study was to assess heterogeneity in the fibroblasts of a new cohort of sPD patients (Payne, Burgess, *et al.*, 2023) and stratify the patients based on patterns of mitochondrial and lysosomal dysfunction. No significant difference in mitochondrial function morphology or localisation was observed for the majority of parameters. However, variation in the patient population was significantly greater for 85 % of parameters, showing clear heterogeneity. Assessment of lysosome morphology showed no difference between the populations but significantly more variation in the patients for 83 % of parameters. The combination of the results using z-scoring enabled the identification of patients with excessively abnormal organelles and subsequent investigation of specific patterns of dysfunction enabled the identification of four distinct subgroups. Two defined by dysfunction in either mitochondria or lysosomes and two defined by distinctly different patterns of dysfunction in both organelles.

To validate these subgroups, the fibroblasts for each group were investigated in-depth to identify common dysfunctional mechanisms. Generation of iNPCs and differentiation into iDA neurons enabled the assessment of organelle function in a disease-relevant cell type that maintained the ageing characteristics of the patient. Investigation of sPD using patient-derived cells is limited in the literature and the use of iPSC or iNPC-derived iDA neurons is rare. The investigation of our lysosomal

subgroup found a reduction in CatD activity in the fibroblasts, an enzyme that is crucial to α-syn degradation. Further assessment of the neurons found that lysosomes in the sPD patients were enlarged.

Investigation of the mitochondrial dysfunction subgroup identified elevated complex I, II, and IV activity but a reduced ability to elevate respiration to meet demand in patient fibroblasts. Further work in the neurons showed that MMP was elevated but mitochondria count was reduced. The low mixed group showed an elevated MMP and complex V activity in the fibroblasts and an increased number of functioning mitochondria and lysosomes in iDA neurons. Both groups suggest an upregulation of organelle function to maintain cellular demands.

6.2 Importance of These Findings for Parkinson's Disease Research and Clinical Trials

Findings from this thesis and other studies are setting the foundation for a disease phenotyping approach to stratifying patients with PD. Two hallmarks of PD, mitochondrial and lysosomal dysfunction have been widely studied in fPD but results from the few sPD studies are conflicting. This is possibly due to methodology but most likely due to heterogeneity. Clear heterogeneity of mitochondrial dysfunction has been observed by us and multiple other studies (Milanese *et al.*, 2019; Carling *et al.*, 2020; Payne, Burgess, *et al.*, 2023; Barnhoorn *et al.*, 2024; Fløthings *et al.*, 2024). In contrast, lysosome dysfunction has not been studied on a large enough scale to date but showed clear heterogeneity in this thesis and the study by Carling *et al.* (2020). Multiple prospective therapeutics target these pathways and are entering clinical trials. To ensure success, stratification will be vital to participant selection.

Ambroxol, a chaperone of GCase, is currently being assessed in two Phase III clinical trials. GBA mutations are more prevalent than typical genetic causes of PD, enabling trial stratification. The ASPRO-PD trial is not selecting patients based on genetic stratification but requires that patients are genetic screened to identify their GBA status. This trial will likely use this information during result analysis. Whereas the GREAT trial is only recruiting patients with a known GBA mutation. Besides other GCase-targeting therapeutics, no lysosome-targeting compounds are currently being assessed in clinical trials, however, stratification methods could be important to the development of such compounds. Compounds targeting energy metabolism are far more common (McFarthing *et al.*, 2024). Compounds, such as UDCA and nicotinamide riboside, target mitochondrial dysfunction. Stratification selecting patients using patient-derived fibroblasts could improve the chances of trial success. The polygenic risk score developed by Arena *et al.* (2024) showed that different subgroups responded to UDCA to different degrees, demonstrating the need for stratification.

Currently, clinical trials assess compound efficacy by comparing patients using the MDS-UPDRS score. The use of a biomarker to either show compound efficacy or target engagement would also improve trial success. Biomarker studies have been unsuccessful so far and this may be due to heterogeneity. Stratification by cellular mechanisms, such as the method we have outlined, could enable the identification of biomarkers for specific subgroups. This would not only enable cheaper and faster trial selection but also wide-scale personalised medicine approaches in the clinic.

Despite stratification, patients within the groups still show some differences in lysosome enzyme function, mitochondrial function and organelle morphology. Stratification may produce groups that are homogenous enough to improve clinical trial success, but more specific personalised treatment approaches may be required for clinical use. For example, CatB activity is variable among patients in both the fibroblasts and iDA neurons. The implications of this are unclear but CatB activity is associated with PD risk (Nalls *et al.*, 2019; Lu *et al.*, 2024). Ultimately, certain factors may result in different combinations of therapeutics to target different mechanisms within individual patients.

6.2.1 Limitations of this Study

This study used the fibroblasts from fifty-seven individuals to assess heterogeneity. This is still a small number when comparing heterogeneity, however, the inclusion of more participants would have been unmanageable due to the time constraints and limited manpower. In addition, twenty-three controls are a limited number to assess the breadth of variability within healthy individuals. Participant recruitment was linked to a ^{31}Phosphorus magnetic resonance spectroscopy study, the largest of its kind (Payne, Burgess, *et al.*, 2023), which also limited numbers due to the expense of imaging. The cohort size was deemed acceptable for this preliminary proof of concept study. However, validation of the subgroups would be required in a larger cohort of patients and controls with a more diverse ethnic background.

Although the study size was limited it was still unmanageable to screen all the fibroblast cell lines at the same time. To screen the cells two assays were used and the lines were divided into thirteen groups with the patients having age- and sex-matched controls. One reason was to reduce the number of cell lines culturing and assaying at one time as it would be impossible for one person to maintain all the lines. The second reason was to enable screening to start while biopsies were procured and established. However, due to this grouping, results for the patients were normalised to the controls on the plate to enable comparison across repeats and groups. Variation of the controls was observed in the in-depth assays suggesting that natural variation could lead to the false positive stratification of patients. Future studies should consider assessing variability in the control population and selecting a set of controls that represent the variability or use a specific control across every group providing a

designated line that control variability can be compared to. The use of automated tissue culture is a plausible method for scaling up the number of lines that can be assessed at one time, however, current costs of such equipment limit their use in an academic setting. The initial costs are not the only limiting factor, upscaling culturing requires specific disposable items, such as pipette tips and plates, and cell culture media, both of which are incredibly expensive (Daniszewski *et al.*, 2018).

Although fibroblasts and iNPC's are excellent models of sPD, the use of other patient-derived samples would strengthen this stratification method. As previously mentioned, fibroblasts have several weaknesses, including low expression of α-syn. The use of a patient-derived cell that expressed α-syn to a greater extent could help further unravel the complexity of these subgroups. Other groups have used erythroblasts (Barnhoorn *et al.*, 2024), which have a moderate expression of α-syn (Expression Atlas, 2025). These cells and other blood cells are difficult to image, but mitochondrial and lysosomal dysfunction could be assessed by measuring a variety of parameters including oxygen consumption (Barnhoorn *et al.*, 2024), mtDNA damage (Gonzalez-Hunt *et al.*, 2020), RNA transcription, proteomics, metabolomics and lysosomal enzyme activity assays (Kedariti *et al.*, 2022). However, addition of these cell types would not have been possible due to labour time constraints. Furthermore, extensive optimisation of these assays would be required before they could be used for stratification. Another model that may further validate the findings of this study is the use of postmortem brain tissue. Use of the participant's brain tissue may elude to specific organelle dysfunction, in a similar fashion to Fløtnes et al. (2024). This would enable assessment of the vulnerable cell type in PD, dopaminergic neurons, and in cells that highly express α-syn. It could also enable the assessment of other mechanism that fibroblasts cannot model, such as inflammation and oxidative stress. However, the participants were selected at early stages of the disease and most were expected to survive for many more years. Likewise, waiting for control tissue samples could extend the study by decades. Future global collaborations or the use of pre-collected sample populations, such as the Parkinson's Progression Markers Initiative, could enable a stratification method using multiple cell types and tissues.

A further limitation of screening is the lack of functional assessment of lysosomes or autophagy pathways. The introduction of more functional markers could enable a more informed stratification of lysosome dysfunction. It is 5 years since the start of this study and methods for assessing lysosomes have progressed. The procurement of new microscopes, such as the Operetta CLS, enables a greater number of channels to be assessed, for example cell painting techniques which use five fluorescent markers. Additions of fluorescently labelled lysosome substrates, such as PFB-FDglu, which can measure GCase activity (Labrador-Garrido *et al.*, 2023), could further our understanding. Another dye,

cyto-ID labels autophagic vesicles (Guo *et al.*, 2015) which are reportedly increased in sPD (Alvarez-Erviti *et al.*, 2010; Dehay *et al.*, 2010; Schöndorf *et al.*, 2014).

6.2.2 Future Work and Conclusions.

In conclusion, the stratification of sPD is vital to the success of therapeutic development, biomarker discovery and the generation of personalised treatment plans. New methods for stratification are currently being explored in a variety of areas including polygenic risk scores, clinical stratification and phenotypic stratification. A combination of methods will most likely provide the most accurate stratification. This study outlines a new method for stratifying the sPD patient population by mitochondrial and lysosomal dysfunction phenotypes. The approach is feasible to use for clinical trials that are targeting mitochondria or lysosomes therapeutically. The earnings by companies and savings by healthcare providers from successful therapeutics will far outweigh the costs, time and labour to stratify trial participants. Further research should take three main approaches. Firstly, validation of the final subgroup and completion of the proof-of-concept therapeutic screens is required and is currently being conducted by Rhiannon Brown. This will enable further refinement of the initial screen, indicate which trials would benefit from this stratification approach and further our understanding of disease mechanisms in PD. Another aspect is further research of the iDA neurons, the reprogramming of more patients and subsequent phenotyping of the lines in both iDA neurons and astrocytes could enable a better understanding of targets for therapeutic development. It would also allow other factors of PD pathology, such as oxidative stress, inflammation and α-syn, to be explored in the subgroups.

Secondly, longitudinal follow-up studies on patients, particularly those who are stratified, should be conducted to validate findings and further our understanding of disease progression. Many stratification studies to date haven't utilised follow-up studies (Mestre *et al.*, 2021). A follow-up study of the tremor-dominant PIGD clinical subgroups found that many patients did not maintain their stratified status (Simuni *et al.*, 2016; Lee *et al.*, 2019). This follow-up study will help determine whether two or four distinctly different subgroups have been identified by our methodology and determine the validity of this method.

Finally, global attempts to combine methods should be conducted. We should assess our subgroups using the polygenic risk score developed by Arena *et al.* (2024) and if possible, eventually assess complex I levels postmortem using the same method as Flønes *et al.*, (2024). Combining methods could enable a highly detailed approach to patient stratification by assessment of mitochondrial and lysosomal phenotypes. Using multiple approaches could highlight unifying features across groups and provide greater target information for therapeutic development and clinical trial design. Ultimately,

expanding the stratification to encompass other techniques assessing inflammation, microbiome alterations and α-syn, to name a few, could produce an exhaustive phenotypic screening method of patients for clinical trials and treatment in the clinic.

References

Abbott, A. (2010) 'Levodopa: The story so far', *Nature*. Available at: https://doi.org/10.1038/466S6a.

Adebayo, M. *et al.* (2021) 'Mitochondrial fusion and fission: The fine-tune balance for cellular homeostasis', *FASEB Journal*. Available at: https://doi.org/10.1096/fj.202100067R.

Adeva-Andany, M.M. *et al.* (2019) 'Mitochondrial β-oxidation of saturated fatty acids in humans', *Mitochondrion*. Available at: https://doi.org/10.1016/j.mito.2018.02.009.

Albarmawi, H. *et al.* (2022) 'The economic burden of Parkinson disease among Medicare beneficiaries', *Journal of Managed Care and Specialty Pharmacy*, 28(4). Available at: https://doi.org/10.18553/JMCP.2022.28.4.405.

Alcalay, R.N. *et al.* (2014) 'Comparison of parkinson risk in ashkenazi jewish patients with gaucher disease and gba heterozygotes', *JAMA Neurology*, 71(6). Available at: https://doi.org/10.1001/jamaneurol.2014.313.

Alcalay, R.N. *et al.* (2015) 'Glucocerebrosidase activity in Parkinson's disease with and without GBA mutations', *Brain*, 138(Pt 9), pp. 2648–2658. Available at: https://doi.org/10.1093/brain/awv179.

Allen, S.P. *et al.* (2014) 'Superoxide dismutase 1 mutation in a cellular model of amyotrophic lateral sclerosis shifts energy generation from oxidative phosphorylation to glycolysis', *Neurobiology of Aging*, 35(6), pp. 1499–1509. Available at: https://doi.org/10.1016/j.neurobiolaging.2013.11.025.

Alvarez-Erviti, L. *et al.* (2010) 'Chaperone-mediated autophagy markers in Parkinson disease brains', *Arch Neurol*, 67(12), pp. 1464–1472. Available at: https://doi.org/10.1001/archneurol.2010.198.

Ambrosi, G. *et al.* (2014) 'Bioenergetic and proteolytic defects in fibroblasts from patients with sporadic Parkinson's disease', *Biochim Biophys Acta*, 1842(9), pp. 1385–1394. Available at: https://doi.org/10.1016/j.bbadis.2014.05.008.

Anheim, M. *et al.* (2012) 'Penetrance of Parkinson disease in glucocerebrosidase gene mutation carriers', *Neurology*, 78(6). Available at: https://doi.org/10.1212/WNL.0b013e318245f476.

Antonin, W. *et al.* (2002) 'Crystal structure of the endosomal snare complex reveals common structural principles of all snares', *Nature Structural Biology*, 9(2). Available at: https://doi.org/10.1038/nsb746.

Antony, P.M.A. *et al.* (2020) 'Fibroblast mitochondria in idiopathic Parkinson's disease display morphological changes and enhanced resistance to depolarization', *Scientific Reports*, 10(1). Available at: https://doi.org/10.1038/s41598-020-58505-6.

Appel-Cresswell, S. *et al.* (2013) 'Alpha-synuclein p.H50Q, a novel pathogenic mutation for Parkinson's disease', *Movement Disorders*, 28(6). Available at: https://doi.org/10.1002/mds.25421.

de Araujo, M.E.G. *et al.* (2020) 'Lysosomal size matters', *Traffic*. Available at: https://doi.org/10.1111/tra.12714.

Arena, G. *et al.* (2024) 'Polygenic Risk Scores Validated in Patient-Derived Cells Stratify for Mitochondrial Subtypes of Parkinson's Disease', *Annals of Neurology*, 96(1), pp. 133–149. Available at: https://doi.org/10.1002/ana.26949.

Arias-Fuenzalida, J. *et al.* (2017) 'FACS-Assisted CRISPR-Cas9 Genome Editing Facilitates Parkinson's Disease Modeling', *Stem Cell Reports*, 9(5). Available at: https://doi.org/10.1016/j.stemcr.2017.08.026.

Asano, T. *et al.* (2011) 'Distinct Mechanisms of Ferritin Delivery to Lysosomes in Iron-Depleted and Iron-Replete Cells', *Molecular and Cellular Biology*, 31(10). Available at: https://doi.org/10.1128/mcb.01437-10.

Ashtari, N. *et al.* (2016) 'Lysosomal Acid Phosphatase Biosynthesis and Dysfunction: A Mini Review Focused on Lysosomal Enzyme Dysfunction in Brain', *Current Molecular Medicine*, 16(5). Available at: https://doi.org/10.2174/1566524016666160429115834.

Auburger, G. *et al.* (2012) 'Primary skin fibroblasts as a model of Parkinson's disease', *Molecular Neurobiology*, 46(1). Available at: https://doi.org/10.1007/s12035-012-8245-1.

Baba, M. *et al.* (1998) 'Aggregation of α-synuclein in Lewy bodies of sporadic Parkinson's disease and dementia with Lewy bodies', *American Journal of Pathology*, 152(4).

Baden, P. *et al.* (2023) 'Glucocerebrosidase is imported into mitochondria and preserves complex I integrity and energy metabolism', *Nature Communications*, 14(1). Available at: https://doi.org/10.1038/s41467-023-37454-4.

Baici, A. *et al.* (2006) 'Regulation of human cathepsin B by alternative mRNA splicing: Homeostasis, fatal errors and cell death', *Biological Chemistry*. Available at: https://doi.org/10.1515/BC.2006.125.

Ballabio, A. and Bonifacino, J.S. (2020) 'Lysosomes as dynamic regulators of cell and organismal homeostasis', *Nature Reviews Molecular Cell Biology*, pp. 101–118. Available at: https://doi.org/10.1038/s41580-019-0185-4.

Ballard, P.A., Tetrud, J.W. and Langston, J.W. (1985) 'Permanent human parkinsonism due to 1-methyl-4-phenyl-1,2,3,6-tetrahydropyridine (MPTP): seven cases', *Neurology*, 35(7), pp. 949–956. Available at: https://doi.org/10.1212/wnl.35.7.949.

Bandres-Ciga, S. *et al.* (2020) 'Genetics of Parkinson's disease: An introspection of its journey towards precision medicine', *Neurobiol Dis*, 137, p. 104782. Available at: https://doi.org/10.1016/j.nbd.2020.104782.

Barnhoorn, S. *et al.* (2024) 'Orthogonal analysis of mitochondrial function in Parkinson's disease patients', *Cell Death and Disease*, 15(4). Available at: https://doi.org/10.1038/s41419-024-06617-6.

Bartels, A.L. *et al.* (2010) '[11C]-PK11195 PET: quantification of neuroinflammation and a monitor of anti-inflammatory treatment in Parkinson's disease?', *Parkinsonism Relat Disord*, 16(1), pp. 57–59. Available at: https://doi.org/10.1016/j.parkreldis.2009.05.005.

Bauernfeind, F. *et al.* (2011) 'Cutting edge: reactive oxygen species inhibitors block priming, but not activation, of the NLRP3 inflammasome', *J Immunol*, 187(2), pp. 613–617. Available at: https://doi.org/10.4049/jimmunol.1100613.

Bell, S.M. *et al.* (2024) 'Increasing hexokinase 1 expression improves mitochondrial and glycolytic functional deficits seen in sporadic Alzheimer's disease astrocytes', *Molecular Psychiatry* [Preprint]. Available at: https://doi.org/10.1038/s41380-024-02746-8.

Benecke, R., Strümper, P. and Weiss, H. (1993) 'Electron transfer complexes I and IV of platelets are abnormal in Parkinson's disease but normal in Parkinson-plus syndromes', *Brain*, 116 (Pt 6, pp. 1451–1463. Available at: https://doi.org/10.1093/brain/116.6.1451.

Berg, D. *et al.* (2014) 'Time to redefine PD? Introductory statement of the MDS Task Force on the definition of Parkinson's disease', *Movement Disorders*, 29(4). Available at: https://doi.org/10.1002/mds.25844.

Berg, D. *et al.* (2021) 'Prodromal Parkinson disease subtypes — key to understanding heterogeneity', *Nature Reviews Neurology*. Available at: https://doi.org/10.1038/s41582-021-00486-9.

Bernal, A. and Arranz, L. (2018) 'Nestin-expressing progenitor cells: function, identity and therapeutic implications', *Cellular and Molecular Life Sciences*. Available at: https://doi.org/10.1007/s00018-018-2794-z.

Bernard, G. *et al.* (2007) 'Mitochondrial bioenergetics and structural network organization', *Journal of Cell Science*, 120(5). Available at: https://doi.org/10.1242/jcs.03381.

Beylina, A. *et al.* (2021) 'Generation of fourteen isogenic cell lines for Parkinson's disease-associated leucine-rich repeat kinase (LRRK2)', *Stem Cell Research*, 53. Available at: https://doi.org/10.1016/j.scr.2021.102354.

Bhat, A.H. *et al.* (2015) 'Oxidative stress, mitochondrial dysfunction and neurodegenerative diseases; a mechanistic insight', *Biomed Pharmacother*, 74, pp. 101–110. Available at: https://doi.org/10.1016/j.biopha.2015.07.025.

Billingsley, K.J. *et al.* (2018) 'Genetic risk factors in Parkinson's disease', *Cell and Tissue Research*. Available at: https://doi.org/10.1007/s00441-018-2817-y.

Billingsley, K.J. *et al.* (2019) 'Mitochondria function associated genes contribute to Parkinson's Disease risk and later age at onset', *npj Parkinson's Disease*, 5(1). Available at: https://doi.org/10.1038/s41531-019-0080-x.

Bindoff, L.A. *et al.* (1989) 'Mitochondrial function in Parkinson's disease', *Lancet*, 2(8653), p. 49. Available at: https://doi.org/10.1016/s0140-6736(89)90291-2.

Blauwendraat, C. *et al.* (2017) 'NeuroChip, an updated version of the NeuroX genotyping platform to rapidly screen for variants associated with neurological diseases', *Neurobiology of Aging*, 57. Available at: https://doi.org/10.1016/j.neurobiolaging.2017.05.009.

Blauwendraat, C. *et al.* (2020) 'Genetic modifiers of risk and age at onset in GBA associated Parkinson's disease and Lewy body dementia', *Brain*, 143(1). Available at: https://doi.org/10.1093/brain/awz350.

Boengler, K., Heusch, G. and Schulz, R. (2011) 'Nuclear-encoded mitochondrial proteins and their role in cardioprotection', *Biochimica et Biophysica Acta - Molecular Cell Research*, pp. 1286–1294. Available at: https://doi.org/10.1016/j.bbamcr.2011.01.009.

Boman, A. *et al.* (2016) 'Distinct Lysosomal Network Protein Profiles in Parkinsonian Syndrome Cerebrospinal Fluid', *J Parkinsons Dis*, 6(2), pp. 307–315. Available at: https://doi.org/10.3233/JPD-150759.

Bonifacino, J.S. and Traub, L.M. (2003) 'Signals for sorting of transmembrane proteins to endosomes and lysosomes', *Annual Review of Biochemistry*. Available at: https://doi.org/10.1146/annurev.biochem.72.121801.161800.

Bonifati, V. *et al.* (2003) 'DJ-1 (PARK7), a novel gene for autosomal recessive, early onset parkinsonism', *Neurological Sciences*, 24(3). Available at: https://doi.org/10.1007/s10072-003-0108-0.

Bouhamdani, N., Comeau, D. and Turcotte, S. (2021) 'A Compendium of Information on the Lysosome', *Frontiers in Cell and Developmental Biology*. Available at: https://doi.org/10.3389/fcell.2021.798262.

Bourdenx, M., Bezard, E. and Dehay, B. (2014) 'Lysosomes and α-synuclein form a dangerous duet leading to neuronal cell death', *Front Neuroanat*, 8, p. 83. Available at: https://doi.org/10.3389/fnana.2014.00083.

Brand, M.D. *et al.* (2004) 'Mitochondrial superoxide: Production, biological effects, and activation of uncoupling proteins', *Free Radical Biology and Medicine*. Available at: https://doi.org/10.1016/j.freeradbiomed.2004.05.034.

Braulke, T. and Bonifacino, J.S. (2009) 'Sorting of lysosomal proteins', *Biochimica et Biophysica Acta - Molecular Cell Research*. Available at: https://doi.org/10.1016/j.bbamcr.2008.10.016.

Bravo-San Pedro, J.M. *et al.* (2013) 'The LRRK2 G2019S mutant exacerbates basal autophagy through activation of the MEK/ERK pathway', *Cellular and Molecular Life Sciences*, 70(1). Available at: https://doi.org/10.1007/s00018-012-1061-y.

Bright, N.A. *et al.* (1997) 'Dense core lysosomes can fuse with late endosomes and are re-formed from the resultant hybrid organelles', *Journal of Cell Science*, 110(17). Available at: https://doi.org/10.1242/jcs.110.17.2027.

Bright, N.A., Gratian, M.J. and Luzio, J.P. (2005) 'Endocytic delivery to lysosomes mediated by concurrent fusion and kissing events in living cells', *Current Biology*, 15(4). Available at: https://doi.org/10.1016/j.cub.2005.01.049.

Brotherus, J. and Renkonen, O. (1977) 'Subcellular distributions of lipids in cultured BHK cells: evidence for the enrichment of lysobisphosphatidic acid and neutral lipids in lysosomes', *Journal of Lipid Research*, 18(2). Available at: https://doi.org/10.1016/s0022-2275(20)41698-0.

Brüggemann, N. and Klein, C. (1993) *Parkin Type of Early-Onset Parkinson Disease*, *GeneReviews®*.

Bunk, J. *et al.* (2021) 'Cathepsin D Variants Associated With Neurodegenerative Diseases Show Dysregulated Functionality and Modified α-Synuclein Degradation Properties', *Frontiers in Cell and Developmental Biology*, 9. Available at: https://doi.org/10.3389/fcell.2021.581805.

Calo, L. *et al.* (2016) 'Synaptic failure and α-synuclein', *Movement Disorders*. Available at: https://doi.org/10.1002/mds.26479.

Campbell, M.C. *et al.* (2020) 'Parkinson disease clinical subtypes: key features & clinical milestones', *Annals of Clinical and Translational Neurology*, 7(8). Available at: https://doi.org/10.1002/acn3.51102.

Capriglia, F. *et al.* (2023) 'Clinical Trial Highlights: Modulators of Mitochondrial Function', *Journal of Parkinson's Disease*. Available at: https://doi.org/10.3233/JPD-239003.

Cardellach, F. *et al.* (1993) 'Mitochondria1 respiratory chain activity in skeletal muscle from patients with parkinson's disease', *Neurology*, 43(11). Available at: https://doi.org/10.1212/wnl.43.11.2258.

Carling, P.J. *et al.* (2020) 'Deep phenotyping of peripheral tissue facilitates mechanistic disease stratification in sporadic Parkinson's disease', *Progress in Neurobiology*, 187. Available at: https://doi.org/10.1016/j.pneurobio.2020.101772.

Carpi, M. *et al.* (2023) 'Both Motor and Non-Motor Fluctuations Matter in the Clinical Management of Patients with Parkinson's Disease: An Exploratory Study', *Journal of Personalized Medicine*, 13(2). Available at: https://doi.org/10.3390/jpm13020242.

Carthon, B.C. and Antonarakis, E.S. (2016) 'The STAMPEDE trial: Paradigm-changing data through innovative trial design', *Translational Cancer Research*, 5. Available at: https://doi.org/10.21037/tcr.2016.09.08.

Cecioni, S. *et al.* (2022) 'Quantifying lysosomal glycosidase activity within cells using bis-acetal substrates', *Nature Chemical Biology*, 18(3). Available at: https://doi.org/10.1038/s41589-021-00960-x.

Cerneckis, J., Cai, H. and Shi, Y. (2024) 'Induced pluripotent stem cells (iPSCs): molecular mechanisms of induction and applications', *Signal Transduction and Targeted Therapy*. Springer Nature. Available at: https://doi.org/10.1038/s41392-024-01809-0.

Chahine, L.M. *et al.* (2013) 'Clinical and biochemical differences in patients having parkinson disease with vs without GBA mutations', *JAMA Neurology*, 70(7), pp. 852–858. Available at: https://doi.org/10.1001/jamaneurol.2013.1274.

Chai, C. and Lim, K.L. (2013) 'Genetic insights into sporadic Parkinson's disease pathogenesis', *Curr Genomics*, 14(8), pp. 486–501. Available at: https://doi.org/10.2174/1389202914666131210195808.

Chan, P. *et al.* (1991) 'Rapid ATP Loss Caused by 1-Methyl-4-Phenyl-1,2,3,6-Tetrahydropyridine in Mouse Brain', *Journal of Neurochemistry*, 57(1). Available at: https://doi.org/10.1111/j.1471-4159.1991.tb02134.x.

Chan, P. (2011) *Efficacy and Safety of Lingzhi in Patients With Early Parkinson's Disease*, *clinicatrials.gov*. Available at: https://clinicaltrials.gov/study/NCT00224263 (Accessed: 9 August 2024).

Chang, D. *et al.* (2017) 'A meta-analysis of genome-wide association studies identifies 17 new Parkinson's disease risk loci', *Nature Genetics*, 49(10). Available at: https://doi.org/10.1038/ng.3955.

Chang, K.H. and Chen, C.M. (2020) 'The Role of Oxidative Stress in Parkinson's Disease', *Antioxidants (Basel)*, 9(7). Available at: https://doi.org/10.3390/antiox9070597.

Channa, A., Popescu, N. and Ciobanu, V. (2020) 'Wearable solutions for patients with parkinson's disease and neurocognitive disorder: A systematic review', *Sensors (Switzerland)*. Available at: https://doi.org/10.3390/s20092713.

Chaudhuri, K.R., Healy, D.G. and Schapira, A.H.V. (2006) 'Non-motor symptoms of Parkinson's disease: Diagnosis and management', *Lancet Neurology*. Available at: https://doi.org/10.1016/S1474-4422(06)70373-8.

Chen, X. *et al.* (2024) 'CHCHD2 Thr61Ile mutation impairs F1F0-ATPase assembly in in vitro and in vivo models of Parkinson's disease', *Neural Regeneration Research*, 19(1). Available at: https://doi.org/10.4103/1673-5374.378010.

Chia, S.J., Tan, E.K. and Chao, Y.X. (2020) 'Historical perspective: Models of Parkinson's disease', *International Journal of Molecular Sciences*. Available at: https://doi.org/10.3390/ijms21072464.

Chu, Y. *et al.* (2009) 'Alterations in lysosomal and proteasomal markers in Parkinson's disease: relationship to alpha-synuclein inclusions', *Neurobiol Dis*, 35(3), pp. 385–398. Available at: https://doi.org/10.1016/j.nbd.2009.05.023.

Chung, S.Y. *et al.* (2016) 'Parkin and PINK1 Patient iPSC-Derived Midbrain Dopamine Neurons Exhibit Mitochondrial Dysfunction and α-Synuclein Accumulation', *Stem Cell Reports*, 7(4). Available at: https://doi.org/10.1016/j.stemcr.2016.08.012.

Clark, I.E. *et al.* (2006) 'Drosophila pink1 is required for mitochondrial function and interacts genetically with parkin', *Nature*, 441(7097). Available at: https://doi.org/10.1038/nature04779.

Cleeter, M.W. *et al.* (2013) 'Glucocerebrosidase inhibition causes mitochondrial dysfunction and free radical damage', *Neurochem Int*, 62(1), pp. 1–7. Available at: https://doi.org/10.1016/j.neuint.2012.10.010.

Cockcroft, S. (2021) 'Mammalian lipids: Structure, synthesis and function', *Essays in Biochemistry*. Available at: https://doi.org/10.1042/EBC20200067.

Von Coelln, R. and Shulman, L.M. (2016) 'Clinical subtypes and genetic heterogeneity: Of lumping and splitting in Parkinson disease', *Current Opinion in Neurology*. Available at: https://doi.org/10.1097/WCO.0000000000000384.

Colacurcio, D.J. and Nixon, R.A. (2016) 'Disorders of lysosomal acidification—The emerging role of v-ATPase in aging and neurodegenerative disease', *Ageing Research Reviews*. Available at: https://doi.org/10.1016/j.arr.2016.05.004.

Collins, L.M. *et al.* (2018) 'Dermal fibroblasts from patients with Parkinson's disease have normal GCase activity and autophagy compared to patients with PD and GBA mutations', *F1000Research*, 6. Available at: https://doi.org/10.12688/f1000research.12090.2.

Concha-Marambio, L. *et al.* (2023) 'Seed amplification assay for the detection of pathologic alpha-synuclein aggregates in cerebrospinal fluid', *Nature Protocols*, 18(4). Available at: https://doi.org/10.1038/s41596-022-00787-3.

Cooper, G.M. and Hausman, R.E. (2007) *The Cell: A Molecular Approach 2nd Edition*, *Sinauer Associates*.

Cooper, O. *et al.* (2012) 'Familial Parkinson's disease iPSCs show cellular deficits in mitochondrial responses that can be pharmacologically rescued', *Sci Transl Med*, 4(141).

Corenblum, M.J. *et al.* (2023) 'Parallel neurodegenerative phenotypes in sporadic Parkinson's disease fibroblasts and midbrain dopamine neurons', *Progress in Neurobiology*, 229. Available at: https://doi.org/10.1016/j.pneurobio.2023.102501.

Crabtree, D. *et al.* (2014) 'Over-expression of an inactive mutant cathepsin D increases endogenous alpha-synuclein and cathepsin B activity in SH-SY5Y cells', *Journal of Neurochemistry*, 128(6), pp. 950–961. Available at: https://doi.org/10.1111/jnc.12497.

Cuervo, A.M. *et al.* (2004) 'Impaired degradation of mutant α-synuclein by chaperone-mediated autophagy', *Science*, 305(5688). Available at: https://doi.org/10.1126/science.1101738.

Cullen, V. *et al.* (2009) 'Cathepsin D expression level affects alpha-synuclein processing, aggregation, and toxicity in vivo', *Molecular Brain*, 2(1). Available at: https://doi.org/10.1186/1756-6606-2-5.

Cuppoletti, J., Aures-Fischer, D. and Sachs, G. (1987) 'The lysosomal H+ pump: 8-azido-ATP inhibition and the role of chloride in H+ transport', *BBA - Biomembranes*, 899(2). Available at: https://doi.org/10.1016/0005-2736(87)90409-3.

D'Sa, K. *et al.* (2023) 'Prediction of mechanistic subtypes of Parkinson's using patient-derived stem cell models', *Nature Machine Intelligence*, 5(8). Available at: https://doi.org/10.1038/s42256-023-00702-9.

Daniszewski, M. *et al.* (2018) 'Automated Cell Culture Systems and Their Applications to Human Pluripotent Stem Cell Studies', *SLAS Technology*. Available at: https://doi.org/10.1177/2472630317712220.

Daubner, S.C., Le, T. and Wang, S. (2011) 'Tyrosine hydroxylase and regulation of dopamine

synthesis', *Archives of Biochemistry and Biophysics*. Available at: https://doi.org/10.1016/j.abb.2010.12.017.

DeBerardinis, R.J. *et al.* (2007) 'Beyond aerobic glycolysis: Transformed cells can engage in glutamine metabolism that exceeds the requirement for protein and nucleotide synthesis', *Proceedings of the National Academy of Sciences of the United States of America*, 104(49). Available at: https://doi.org/10.1073/pnas.0709747104.

DeGiosio, R.A. *et al.* (2022) 'More than a marker: potential pathogenic functions of MAP2', *Frontiers in Molecular Neuroscience*, 15. Available at: https://doi.org/10.3389/fnmol.2022.974890.

Dehay, B. *et al.* (2010) 'Pathogenic lysosomal depletion in Parkinson's disease', *J Neurosci*, 30(37), pp. 12535–12544. Available at: https://doi.org/10.1523/JNEUROSCI.1920-10.2010.

Dehay, B. *et al.* (2012) 'Lysosomal dysfunction in Parkinson disease: ATP13A2 gets into the groove', *Autophagy*, 8(9), pp. 1389–1391. Available at: https://doi.org/10.4161/auto.21011.

Dehay, B. *et al.* (2013) 'Lysosomal impairment in Parkinson's disease', *Mov Disord*, 28(6), pp. 725–732. Available at: https://doi.org/10.1002/mds.25462.

Dehestani, M. *et al.* (2022) 'Mitochondrial and autophagy-lysosomal pathway polygenic risk scores predict Parkinson's disease', *Molecular and Cellular Neuroscience*, 121. Available at: https://doi.org/10.1016/j.mcn.2022.103751.

Dehestani, M., Liu, H. and Gasser, T. (2021) 'Polygenic risk scores contribute to personalized medicine of parkinson's disease', *Journal of Personalized Medicine*. Available at: https://doi.org/10.3390/jpm11101030.

Dell'Antone, P. (1979) 'Evidence for an ATP-driven "proton pump" in rat liver lysosomes by basic dyes uptake', *Biochemical and Biophysical Research Communications*, 86(1). Available at: https://doi.org/10.1016/0006-291X(79)90398-X.

Deng, H.X. *et al.* (2016) 'Identification of TMEM230 mutations in familial Parkinson's disease', *Nature Genetics*, 48(7). Available at: https://doi.org/10.1038/ng.3589.

Deus, C.M. *et al.* (2020) 'Mitochondrial Remodeling in Human Skin Fibroblasts From Sporadic Male Parkinson's Disease Patients Uncovers Metabolic and Mitochondrial Bioenergetic Defects', *Biochimica et biophysica acta. Molecular basis of disease*, 1866(3). Available at: https://doi.org/10.1016/j.bbadis.2019.165615.

Dickson, D.W. (2012) 'Parkinson's disease and parkinsonism: neuropathology', *Cold Spring Harb*

Perspect Med, 2(8). Available at: https://doi.org/10.1101/cshperspect.a009258.

Dölle, C. *et al.* (2016) 'Defective mitochondrial DNA homeostasis in the substantia nigra in Parkinson disease', *Nature Communications*, 7. Available at: https://doi.org/10.1038/ncomms13548.

Duffy, M.F. *et al.* (2018) 'Lewy body-like alpha-synuclein inclusions trigger reactive microgliosis prior to nigral degeneration', *Journal of Neuroinflammation*, 15(1). Available at: https://doi.org/10.1186/s12974-018-1171-z.

Duran, R. *et al.* (2013) 'The glucocerobrosidase E326K variant predisposes to Parkinson's disease, but does not cause Gaucher's disease', *Movement Disorders*, 28(2), pp. 232–236. Available at: https://doi.org/10.1002/mds.25248.

de Duve, C. *et al.* (1955) 'Tissue fractionation studies. 6. Intracellular distribution patterns of enzymes in rat-liver tissue.', *The Biochemical journal*, 60(4), pp. 604–617. Available at: https://doi.org/10.1042/bj0600604.

Van Dyke, R.W. (1993) 'Acidification of rat liver lysosomes: Quantitation and comparison with endosomes', *American Journal of Physiology - Cell Physiology*, 265(4 34-4). Available at: https://doi.org/10.1152/ajpcell.1993.265.4.c901.

Edvardson, S. *et al.* (2012) 'A deleterious mutation in DNAJC6 encoding the neuronal-specific clathrin-uncoating Co-chaperone auxilin, is associated with juvenile parkinsonism', *PLoS ONE*, 7(5), p. e36458. Available at: https://doi.org/10.1371/journal.pone.0036458.

Eliezer, D. *et al.* (2001) 'Conformational properties of α-synuclein in its free and lipid-associated states', *Journal of Molecular Biology*, 307(4). Available at: https://doi.org/10.1006/jmbi.2001.4538.

Eriksson, I., Wäster, P. and Öllinger, K. (2020) 'Restoration of lysosomal function after damage is accompanied by recycling of lysosomal membrane proteins', *Cell Death and Disease*, 11(5). Available at: https://doi.org/10.1038/s41419-020-2527-8.

Erkkinen, M., Kim, M. and Geschwind, M. (2018) 'Clinical Neurology and Epidemiology of the Major Neurodegenerative Diseases', *Cold Spring Harb Perspect Biol*, 10(4). Available at: https://doi.org/10.1101/cshperspect.a033118.

Eskelinen, E.L. (2006) 'Roles of LAMP-1 and LAMP-2 in lysosome biogenesis and autophagy', *Molecular Aspects of Medicine*. Available at: https://doi.org/10.1016/j.mam.2006.08.005.

Espay, A.J. *et al.* (2017) 'Biomarker-driven phenotyping in Parkinson's disease: A translational missing link in disease-modifying clinical trials', *Movement Disorders*. Available at:

https://doi.org/10.1002/mds.26913.

Evans, C.J. and Aguilera, R.J. (2003) 'DNase II: Genes, enzymes and function', *Gene*. Available at: https://doi.org/10.1016/j.gene.2003.08.022.

Fahn, S. (2008) 'The history of dopamine and levodopa in the treatment of Parkinson's disease', *Mov Disord*, 23 Suppl 3, pp. S497-508. Available at: https://doi.org/10.1002/mds.22028.

Fasching, C.L. (2018) 'Telomere length measurement as a clinical biomarker of aging and disease', *Critical Reviews in Clinical Laboratory Sciences*. Available at: https://doi.org/10.1080/10408363.2018.1504274.

Fearnley, J.M. and Lees, A.J. (1991) 'Ageing and Parkinson's disease: Substantia nigra regional selectivity', *Brain*, 114(5). Available at: https://doi.org/10.1093/brain/114.5.2283.

Feigin, V.L. *et al.* (2017) 'Global, regional, and national burden of neurological disorders during 1990–2015: a systematic analysis for the Global Burden of Disease Study 2015', *The Lancet Neurology*, 16(11), pp. 877–897. Available at: https://doi.org/10.1016/S1474-4422(17)30299-5.

Fellner, L. *et al.* (2013) 'Toll-like receptor 4 is required for α-synuclein dependent activation of microglia and astroglia', *GLIA*, 61(3). Available at: https://doi.org/10.1002/glia.22437.

Fereshtehnejad, S.M. *et al.* (2017) 'Clinical criteria for subtyping Parkinson's disease: Biomarkers and longitudinal progression', *Brain*, 140(7). Available at: https://doi.org/10.1093/brain/awx118.

Fernandes, H.J.R. *et al.* (2016) 'ER Stress and Autophagic Perturbations Lead to Elevated Extracellular α-Synuclein in GBA-N370S Parkinson's iPSC-Derived Dopamine Neurons', *Stem Cell Reports*, 6(3). Available at: https://doi.org/10.1016/j.stemcr.2016.01.013.

Ferraiuolo, L. *et al.* (2016) 'Oligodendrocytes contribute to motor neuron death in ALS via SOD1-dependent mechanism', *Proceedings of the National Academy of Sciences of the United States of America*, 113(42). Available at: https://doi.org/10.1073/pnas.1607496113.

Findley, L.J. *et al.* (2011) 'The economic burden of advanced Parkinson's disease: an analysis of a UK patient dataset.', *Journal of medical economics*, 14(1). Available at: https://doi.org/10.3111/13696998.2010.551164.

Flinn, L.J. *et al.* (2013) 'TigarB causes mitochondrial dysfunction and neuronal loss in PINK1 deficiency', *Annals of Neurology*, 74(6). Available at: https://doi.org/10.1002/ana.23999.

Fløtnes, I.H. *et al.* (2024) 'Mitochondrial complex I deficiency stratifies idiopathic Parkinson's disease', *Nature Communications*, 15(1). Available at: https://doi.org/10.1038/s41467-024-47867-4.

Foltynie, T. *et al.* (2024) *EJS-ACT-PD*, *https://ejsactpd.com/*. Available at: https://ejsactpd.com/ (Accessed: 30 August 2024).

Fonzo, A.D. *et al.* (2009) 'FBXO7 mutations cause autosomal recessive, early-onset parkinsonian-pyramidal syndrome', *Neurology*, 72(3). Available at: https://doi.org/10.1212/01.wnl.0000338144.10967.2b.

Friedman, J.R. and Nunnari, J. (2014) 'Mitochondrial form and function', *Nature*. Available at: https://doi.org/10.1038/nature12985.

Fujiwara, Y., Wada, K. and Kabuta, T. (2017) 'Lysosomal degradation of intracellular nucleic acids-multiple autophagic pathways', *Journal of Biochemistry*. Available at: https://doi.org/10.1093/jb/mvw085.

Funayama, M. *et al.* (2002) 'A new locus for Parkinson's Disease (PARK8) maps to chromosome 12p11.2-q13.1', *Annals of Neurology*, 51(3), pp. 296–301. Available at: https://doi.org/10.1002/ana.10113.

Funayama, M. *et al.* (2015) 'CHCHD2 mutations in autosomal dominant late-onset Parkinson's disease: A genome-wide linkage and sequencing study', *The Lancet Neurology*, 14(3). Available at: https://doi.org/10.1016/S1474-4422(14)70266-2.

Gabbert, C. *et al.* (2023) 'Lifestyle factors and clinical severity of Parkinson's disease', *Scientific Reports*, 13(1). Available at: https://doi.org/10.1038/s41598-023-31531-w.

Gagliardi, M. *et al.* (2018) 'DNAJC13 mutation screening in patients with Parkinson's disease from South Italy', *Parkinsonism and Related Disorders*, 55. Available at: https://doi.org/10.1016/j.parkreldis.2018.06.004.

Galant, L.S. *et al.* (2024) 'Culture of Bovine Aortic Endothelial Cells in Galactose Media Enhances Mitochondrial Plasticity and Changes Redox Sensing, Altering Nrf2 and FOXO3 Levels', *Antioxidants*, 13(7). Available at: https://doi.org/10.3390/antiox13070873.

Gallwitz, L. *et al.* (2024) 'Cellular depletion of major cathepsin proteases reveals their concerted activities for lysosomal proteolysis', *Cellular and Molecular Life Sciences*, 81(1). Available at: https://doi.org/10.1007/s00018-024-05274-4.

García-Sanz, P. *et al.* (2017) 'N370S-GBA1 mutation causes lysosomal cholesterol accumulation in Parkinson's disease', *Movement Disorders*, 32(10). Available at: https://doi.org/10.1002/mds.27119.

Gash, D.M. *et al.* (2008) 'Trichloroethylene: Parkinsonism and complex 1 mitochondrial

neurotoxicity', *Annals of Neurology*, 63(2). Available at: https://doi.org/10.1002/ana.21288.

Gatto, N. *et al.* (2021) 'Directly converted astrocytes retain the ageing features of the donor fibroblasts and elucidate the astrocytic contribution to human CNS health and disease', *Aging Cell*, 20(1). Available at: https://doi.org/10.1111/acel.13281.

Gegg, M.E. *et al.* (2012) 'Glucocerebrosidase deficiency in substantia nigra of parkinson disease brains', *Ann Neurol*, 72(3), pp. 455–463. Available at: https://doi.org/10.1002/ana.23614.

Gegg, M.E. *et al.* (2015) 'No evidence for substrate accumulation in Parkinson brains with GBA mutations', *Movement Disorders*, 30(8). Available at: https://doi.org/10.1002/mds.26278.

Geisler, S. *et al.* (2010) 'PINK1/Parkin-mediated mitophagy is dependent on VDAC1 and p62/SQSTM1', *Nat Cell Biol*, 12(2), pp. 119–131. Available at: https://doi.org/10.1038/ncb2012.

Giasson, B.I. *et al.* (2001) 'A Hydrophobic Stretch of 12 Amino Acid Residues in the Middle of α-Synuclein Is Essential for Filament Assembly', *Journal of Biological Chemistry*, 276(4). Available at: https://doi.org/10.1074/jbc.M008919200.

Giuliano, C. *et al.* (2023) 'Relevance of Biochemical Deep Phenotyping for a Personalised Approach to Parkinson's Disease', *Neuroscience*. Available at: https://doi.org/10.1016/j.neuroscience.2022.12.019.

Godin, L.M. *et al.* (2016) 'Decreased laminin expression by human lung epithelial cells and fibroblasts cultured in acellular lung scaffolds from aged mice', *PLoS ONE*, 11(3). Available at: https://doi.org/10.1371/journal.pone.0150966.

Goetz, C.G. (2011) 'The history of Parkinson's disease: Early clinical descriptions and neurological therapies', *Cold Spring Harbor Perspectives in Medicine*, 1(1). Available at: https://doi.org/10.1101/cshperspect.a008862.

Goker-Alpan, O. *et al.* (2004) 'Parkinsonism among Gaucher disease carriers', *Journal of Medical Genetics*, 41(12). Available at: https://doi.org/10.1136/jmg.2004.024455.

Gonzalez-Hunt, C.P. *et al.* (2020) 'Mitochondrial DNA damage as a potential biomarker of LRRK2 kinase activity in LRRK2 Parkinson's disease', *Scientific Reports*, 10(1). Available at: https://doi.org/10.1038/s41598-020-74195-6.

Gonzalez-Robles, C. *et al.* (2023) 'Outcome Measures for Disease-Modifying Trials in Parkinson's Disease: Consensus Paper by the EJS ACT-PD Multi-Arm Multi-Stage Trial Initiative', *Journal of Parkinson's Disease*, 13(6). Available at: https://doi.org/10.3233/JPD-230051.

Graves, A.R. *et al.* (2008) 'The Cl-/H+ antiporter ClC-7 is the primary chloride permeation pathway in lysosomes', *Nature*, 453(7196). Available at: https://doi.org/10.1038/nature06907.

Greene, J.C. *et al.* (2003) 'Mitochondrial pathology and apoptotic muscle degeneration in Drosophila parkin mutants', *Proc Natl Acad Sci U S A*, 100(7), pp. 4078–4083. Available at: https://doi.org/10.1073/pnas.0737556100.

Grünewald, A. *et al.* (2010) 'Mutant Parkin impairs mitochondrial function and morphology in human fibroblasts', *PLoS One*, 5(9), p. e12962. Available at: https://doi.org/10.1371/journal.pone.0012962.

Grünewald, A. *et al.* (2014) 'Does uncoupling protein 2 expression qualify as marker of disease status in LRRK2-associated Parkinson's disease?', *Antioxid Redox Signal*, 20(13), pp. 1955–1960. Available at: https://doi.org/10.1089/ars.2013.5737.

Grünewald, A., Kumar, K.R. and Sue, C.M. (2019) 'New insights into the complex role of mitochondria in Parkinson's disease', *Prog Neurobiol*, 177, pp. 73–93. Available at: https://doi.org/10.1016/j.pneurobio.2018.09.003.

Gu, G. *et al.* (2002) 'Mitochondrial DNA deletions/rearrangements in Parkinson disease and related neurodegenerative disorders', *Journal of Neuropathology and Experimental Neurology*, 61(7). Available at: https://doi.org/10.1093/jnen/61.7.634.

Guo, J., Walss-Bass, C. and Ludueña, R.F. (2010) 'The β isotypes of tubulin in neuronal differentiation', *Cytoskeleton*, 67(7). Available at: https://doi.org/10.1002/cm.20455.

Guo, S. *et al.* (2015) 'A rapid and high content assay that measures cyto-ID-stained autophagic compartments and estimates autophagy flux with potential clinical applications', *Autophagy*, 11(3). Available at: https://doi.org/10.1080/15548627.2015.1017181.

Haithcock, E. *et al.* (2005) 'Age-related changes of nuclear architecture in Caenorhabditis elegans', *Proceedings of the National Academy of Sciences of the United States of America*, 102(46). Available at: https://doi.org/10.1073/pnas.0506955102.

Hanson, S.R., Best, M.D. and Wong, C.H. (2004) 'Sulfatases: Structure, mechanism, biological activity, inhibition, and synthetic utility', *Angewandte Chemie - International Edition*. Available at: https://doi.org/10.1002/anie.200300632.

Hartmann, A. (2004) 'Postmortem studies in Parkinson's disease', *Dialogues in Clinical Neuroscience*, 6(3). Available at: https://doi.org/10.31887/dcns.2004.6.3/ahartmann.

Hasegawa, E. *et al.* (1990) '1-Methyl-4-phenylpyridinium (MPP+) induces NADH-dependent

superoxide formation and enhances NADH-dependent lipid peroxidation in bovine heart submitochondrial particles', *Biochemical and Biophysical Research Communications*, 170(3). Available at: https://doi.org/10.1016/0006-291X(90)90498-C.

Hasegawa, K. *et al.* (2009) 'Familial parkinsonism: Study of original Sagamihara PARK8 (I2020T) kindred with variable clinicopathologic outcomes', *Parkinsonism and Related Disorders*, 15(4). Available at: https://doi.org/10.1016/j.parkreldis.2008.07.010.

Hattori, N. and Sato, S. (2024) 'Mitochondrial dysfunction in Parkinson's disease', *Journal of Neural Transmission*, 131(12), pp. 1415–1428. Available at: https://doi.org/10.1007/s00702-024-02863-2.

Haylett, W. *et al.* (2016) 'Altered Mitochondrial Respiration and Other Features of Mitochondrial Function in Parkin-Mutant Fibroblasts from Parkinson's Disease Patients', *Parkinsons Dis*, 2016. Available at: https://doi.org/10.1155/2016/1819209.

He, J. *et al.* (2020) 'Oxidative Stress and Neuroinflammation Potentiate Each Other to Promote Progression of Dopamine Neurodegeneration', *Oxid Med Cell Longev*, 2020, p. 6137521. Available at: https://doi.org/10.1155/2020/6137521.

Healy, D.G. *et al.* (2008) 'Phenotype, genotype, and worldwide genetic penetrance of LRRK2-associated Parkinson's disease: a case-control study', *The Lancet Neurology*, 7(7). Available at: https://doi.org/10.1016/S1474-4422(08)70117-0.

Heckman, M.G. *et al.* (2014) 'The protective effect of LRRK2 p.R1398H on risk of Parkinson's disease is independent of MAPT and SNCA variants', *Neurobiology of Aging*, 35(1). Available at: https://doi.org/10.1016/j.neurobiolaging.2013.07.013.

van der Heeden, J.F. *et al.* (2016) 'Evaluation of severity of predominantly non-dopaminergic symptoms in Parkinson's disease: The SENS-PD scale', *Parkinsonism and Related Disorders*, 25. Available at: https://doi.org/10.1016/j.parkreldis.2016.02.016.

Heeman, B. *et al.* (2011) 'Depletion of PINK1 affects mitochondrial metabolism, calcium homeostasis and energy maintenance', *J Cell Sci*, 124(Pt 7), pp. 1115–1125. Available at: https://doi.org/10.1242/jcs.078303.

Heinrich, M. *et al.* (2000) 'Ceramide as an activator lipid of cathepsin D', *Advances in Experimental Medicine and Biology*, 477. Available at: https://doi.org/10.1007/0-306-46826-3_33.

Hendricks, R. and Khasawneh, M. (2021) 'Cluster analysis of categorical variables of parkinson's disease patients', *Brain Sciences*, 11(10). Available at: https://doi.org/10.3390/brainsci11101290.

Hendricks, R.M. and Khasawneh, M.T. (2021) 'A systematic review of Parkinson's disease cluster analysis research', *Aging and Disease*. Available at: https://doi.org/10.14336/AD.2021.0519.

Henrich, M.T. *et al.* (2023) 'Mitochondrial dysfunction in Parkinson's disease – a key disease hallmark with therapeutic potential', *Molecular Neurodegeneration*. Available at: https://doi.org/10.1186/s13024-023-00676-7.

Henry, A.G. *et al.* (2015) 'Pathogenic LRRK2 mutations, through increased kinase activity, produce enlarged lysosomes with reduced degradative capacity and increase ATP13A2 expression', *Human Molecular Genetics*, 24(21). Available at: https://doi.org/10.1093/hmg/ddv314.

von Herrmann, K.M. *et al.* (2018) 'NLRP3 expression in mesencephalic neurons and characterization of a rare NLRP3 polymorphism associated with decreased risk of Parkinson's disease', *npj Parkinson's Disease*, 4(1). Available at: https://doi.org/10.1038/s41531-018-0061-5.

Hirata, T. *et al.* (2003) 'Subunit rotation of vacuolar-type proton pumping ATPase. Relative rotation of the G and c subunits', *Journal of Biological Chemistry*, 278(26). Available at: https://doi.org/10.1074/jbc.M302756200.

Hockey, L.N. *et al.* (2015) 'Dysregulation of lysosomal morphology by pathogenic LRRK2 is corrected by TPC2 inhibition', *J Cell Sci*, 128(2), pp. 232–238. Available at: https://doi.org/10.1242/jcs.164152.

Hoepken, H.H. *et al.* (2008) 'Parkinson patient fibroblasts show increased alpha-synuclein expression', *Experimental Neurology*, 212(2). Available at: https://doi.org/10.1016/j.expneurol.2008.04.004.

Hofmann, K.W. *et al.* (2009) 'Interleukin-6 serum levels in patients with Parkinson's disease', *Neurochem Res*, 34(8), pp. 1401–1404. Available at: https://doi.org/10.1007/s11064-009-9921-z.

Hornung, V. *et al.* (2008) 'Silica crystals and aluminum salts activate the NALP3 inflammasome through phagosomal destabilization', *Nat Immunol*, 9(8), pp. 847–856. Available at: https://doi.org/10.1038/ni.1631.

Hou, X. *et al.* (2018) 'Age- and disease-dependent increase of the mitophagy marker phospho-ubiquitin in normal aging and Lewy body disease', *Autophagy*, 14(8). Available at: https://doi.org/10.1080/15548627.2018.1461294.

Howarth, C., Gleeson, P. and Attwell, D. (2012) 'Updated energy budgets for neural computation in the neocortex and cerebellum', *Journal of Cerebral Blood Flow and Metabolism*. Available at: https://doi.org/10.1038/jcbfm.2012.35.

del Hoyo, P. *et al.* (2010) 'Oxidative stress in skin fibroblasts cultures from patients with Parkinson's disease', *BMC Neurology*, 10. Available at: https://doi.org/10.1186/1471-2377-10-95.

Hsieh, C.H. *et al.* (2016) 'Functional Impairment in Miro Degradation and Mitophagy Is a Shared Feature in Familial and Sporadic Parkinson's Disease', *Cell Stem Cell*, 19(6). Available at: https://doi.org/10.1016/j.stem.2016.08.002.

Hu, M. *et al.* (2022) 'Parkinson's disease-risk protein TMEM175 is a proton-activated proton channel in lysosomes', *Cell*, 185(13). Available at: https://doi.org/10.1016/j.cell.2022.05.021.

Huebecker, M. *et al.* (2019) 'Reduced sphingolipid hydrolase activities, substrate accumulation and ganglioside decline in Parkinson's disease', *Molecular Neurodegeneration*, 14(1). Available at: https://doi.org/10.1186/s13024-019-0339-z.

Huertas, J.R. *et al.* (2019) 'Stay fit, stay young: Mitochondria in movement: The role of exercise in the new mitochondrial paradigm', *Oxidative Medicine and Cellular Longevity*. Available at: https://doi.org/10.1155/2019/7058350.

Hughes, R. (2023) *Uncovering the mechanism of action of a novel therapeutic compound for the treatment of Parkinson's disease*. University of Sheffield.

Iftikhar, I.H. *et al.* (2024) 'Alpha-synuclein pathology in isolated rapid eye movement sleep behaviour disorder: a meta-analysis', *Journal of Sleep Research* [Preprint]. John Wiley and Sons Inc. Available at: https://doi.org/10.1111/jsr.14204.

Ikeji, F. (2024) *Ambroxol to Slow Progression in Parkinson Disease (ASPro-PD)*, *ClinicalTrials.gov*. Available at: https://clinicaltrials.gov/study/NCT05778617?term=aspro-pd&rank=1 (Accessed: 30 August 2024).

Irizarry, M.C. *et al.* (1998) 'Nigral and cortical Lewy bodies and dystrophic nigral neurites in Parkinson's disease and cortical Lewy body disease contain α-synuclein immunoreactivity', *Journal of Neuropathology and Experimental Neurology*, 57(4). Available at: https://doi.org/10.1097/00005072-199804000-00005.

Itoh, K. *et al.* (2018) 'A brain-enriched drp1 isoform associates with lysosomes, late endosomes, and the plasma membrane', *Journal of Biological Chemistry*, 293(30). Available at: https://doi.org/10.1074/jbc.RA117.001253.

Iwai, A. *et al.* (1995) *The Precursor Protein of Non-Ap Component of Alzheimer's Disease Amyloid Is a Presynaptic Protein of the Central Nervous System*, *Neuron*.

Iyer, A. *et al.* (2017) 'C-Terminal Truncated α-Synuclein Fibrils Contain Strongly Twisted β-Sheets', *Journal of the American Chemical Society*, 139(43). Available at: https://doi.org/10.1021/jacs.7b07403.

Jaconi, M.E.E. *et al.* (1990) 'Cytosolic free calcium elevation mediates the phagosome-lysosome fusion during phagocytosis in human neutrophils', *Journal of Cell Biology*, 110(5). Available at: https://doi.org/10.1083/jcb.110.5.1555.

Jakes, R., Spillantini, M.G. and Goedert, M. (1994) 'Identification of two distinct synucleins from human brain', *FEBS Letters*, 345(1). Available at: https://doi.org/10.1016/0014-5793(94)00395-5.

Jankovic, J. (2008) 'Parkinson's disease: Clinical features and diagnosis', *Journal of Neurology, Neurosurgery and Psychiatry*, pp. 368–376. Available at: https://doi.org/10.1136/jnnp.2007.131045.

Janvier, K. and Bonifacino, J.S. (2005) 'Role of the endocytic machinery in the sorting of lysosome-associated membrane proteins', *Molecular Biology of the Cell*, 16(9). Available at: https://doi.org/10.1091/mbc.E05-03-0213.

Jonckheere, A.I., Smeitink, J.A.M. and Rodenburg, R.J.T. (2012) 'Mitochondrial ATP synthase: Architecture, function and pathology', *Journal of Inherited Metabolic Disease*, pp. 211–225. Available at: https://doi.org/10.1007/s10545-011-9382-9.

Jones-Tabah, J. *et al.* (2024) 'The Parkinson's disease risk gene cathepsin B promotes fibrillar alpha-synuclein clearance, lysosomal function and glucocerebrosidase activity in dopaminergic neurons', *Research Square*, 5(04–01).

Juárez-Flores, D.L. *et al.* (2018) 'Exhaustion of mitochondrial and autophagic reserve may contribute to the development of LRRK2 G2019S -Parkinson's disease', *Journal of Translational Medicine*, 16(1). Available at: https://doi.org/10.1186/s12967-018-1526-3.

Jurga, A.M., Paleczna, M. and Kuter, K.Z. (2020) 'Overview of General and Discriminating Markers of Differential Microglia Phenotypes', *Frontiers in Cellular Neuroscience*, 14. Available at: https://doi.org/10.3389/fncel.2020.00198.

Kahle, P.J. *et al.* (2000) 'Subcellular localization of wild-type and Parkinson's disease-associated mutant α-synuclein in human and transgenic mouse brain', *Journal of Neuroscience*, 20(17). Available at: https://doi.org/10.1523/jneurosci.20-17-06365.2000.

Kalia, L. V. *et al.* (2015) 'Clinical correlations with lewy body pathology in LRRK2-related Parkinson disease', *JAMA Neurology*, 72(1). Available at: https://doi.org/10.1001/jamaneurol.2014.2704.

Kamienieva, I. *et al.* (2023) 'In search for mitochondrial biomarkers of Parkinson's disease: Findings in parkin-mutant human fibroblasts', *Biochimica et Biophysica Acta - Molecular Basis of Disease*, 1869(7). Available at: https://doi.org/10.1016/j.bbadis.2023.166787.

Kamienieva, I., Duszyński, J. and Szczepanowska, J. (2021) 'Multitasking guardian of mitochondrial quality: Parkin function and Parkinson's disease', *Translational Neurodegeneration*. Available at: https://doi.org/10.1186/s40035-020-00229-8.

Ke, P.Y. (2024) 'Molecular Mechanism of Autophagosome–Lysosome Fusion in Mammalian Cells', *Cells*. Available at: https://doi.org/10.3390/cells13060500.

Kedariti, M. *et al.* (2022) 'LRRK2 kinase activity regulates GCase level and enzymatic activity differently depending on cell type in Parkinson's disease', *npj Parkinson's Disease*, 8(1). Available at: https://doi.org/10.1038/s41531-022-00354-3.

Keeney, P.M. *et al.* (2006) 'Parkinson's disease brain mitochondrial complex I has oxidatively damaged subunits and is functionally impaired and misassembled', *J Neurosci*, 26(19), pp. 5256–5264. Available at: https://doi.org/10.1523/JNEUROSCI.0984-06.2006.

Khani, M. *et al.* (2024) 'Towards a Global View of Parkinson's Disease Genetics', *Annals of Neurology*. John Wiley and Sons Inc, pp. 831–842. Available at: https://doi.org/10.1002/ana.26905.

Kim, C. *et al.* (2021) 'SUMOylation of mitofusins: A potential mechanism for perinuclear mitochondrial congression in cells treated with mitochondrial stressors', in *Biochimica et Biophysica Acta - Molecular Basis of Disease*. Available at: https://doi.org/10.1016/j.bbadis.2021.166104.

Kim, K.T. (2022) 'Lumbar puncture: considerations, procedure, and complications', *encephalitis*, 2(4). Available at: https://doi.org/10.47936/encephalitis.2022.00045.

Kim, S. *et al.* (2021) 'Dysregulation of mitochondria-lysosome contacts by GBA1 dysfunction in dopaminergic neuronal models of Parkinson's disease', *Nature Communications*, 12(1). Available at: https://doi.org/10.1038/s41467-021-22113-3.

Kitada, T. *et al.* (1998) 'Mutations in the parkin gene cause autosomal recessive juvenile parkinsonism', *Nature*, 392(6676). Available at: https://doi.org/10.1038/33416.

Klein, M. (2022) *Safety and Biomarker Study of PTC-589 in Participants With Parkinson's Disease*, *clinicatrials.gov*. Available at: https://clinicaltrials.gov/study/NCT02462603 (Accessed: 9 August 2024).

Koike, M. *et al.* (2000) 'Cathepsin D deficiency induces lysosomal storage with ceroid lipofuscin in

mouse CNS neurons', *Journal of Neuroscience*, 20(18). Available at: https://doi.org/10.1523/jneurosci.20-18-06898.2000.

Kornak, U. *et al.* (2001) 'Loss of the CIC-7 chloride channel leads to osteopetrosis in mice and man', *Cell*, 104(2). Available at: https://doi.org/10.1016/S0092-8674(01)00206-9.

Kosicek, M. *et al.* (2018) 'N-glycome of the lysosomal glycocalyx is altered in Niemann-Pick type C disease (NPC) model cells', *Molecular and Cellular Proteomics*, 17(4). Available at: https://doi.org/10.1074/mcp.RA117.000129.

Kraus, F. *et al.* (2021) 'Function and regulation of the divisome for mitochondrial fission', *Nature*. Available at: https://doi.org/10.1038/s41586-021-03214-x.

Krebs, C.E. *et al.* (2013) 'The sac1 domain of SYNJ1 identified mutated in a family with early-onset progressive parkinsonism with generalized seizures', *Human Mutation*, 34(9). Available at: https://doi.org/10.1002/humu.22372.

Krüger, R. *et al.* (1998) 'Ala30Pro mutation in the gene encoding α-synuclein in Parkinson's disease', *Nature Genetics*, 18(2). Available at: https://doi.org/10.1038/ng0298-106.

Kuo, S.H. *et al.* (2022) 'Mutant glucocerebrosidase impairs α-synuclein degradation by blockade of chaperone-mediated autophagy', *Science Advances*, 8(6). Available at: https://doi.org/10.1126/sciadv.abm6393.

Kurzawa-Akanbi, M. *et al.* (2021) 'Altered ceramide metabolism is a feature in the extracellular vesicle-mediated spread of alpha-synuclein in Lewy body disorders', *Acta Neuropathologica*, 142(6). Available at: https://doi.org/10.1007/s00401-021-02367-3.

Kustrimovic, N. *et al.* (2018) 'Parkinson's disease patients have a complex phenotypic and functional Th1 bias: cross-sectional studies of CD4+ Th1/Th2/T17 and Treg in drug-naïve and drug-treated patients', *J Neuroinflammation*, 15(1), p. 205. Available at: https://doi.org/10.1186/s12974-018-1248-8.

Labrador-Garrido, A. *et al.* (2023) 'Live cell in situ lysosomal GCase activity correlates to alpha-synuclein levels in human differentiated neurons with LRRK2 and GBA1 mutations', *Frontiers in Cellular Neuroscience*, 17. Available at: https://doi.org/10.3389/fncel.2023.1229213.

Laffita-Mesa, J.M., Paucar, M. and Svenningsson, P. (2021) 'Ataxin-2 gene: A powerful modulator of neurological disorders', *Current Opinion in Neurology*. Available at: https://doi.org/10.1097/WCO.0000000000000959.

Lang, A.E. and Espay, A.J. (2018) 'Disease Modification in Parkinson's Disease: Current Approaches, Challenges, and Future Considerations', *Mov Disord*, 33(5), pp. 660–677. Available at: https://doi.org/10.1002/mds.27360.

Langston, J.W. *et al.* (1984) '1-Methyl-4-phenylpyridinium ion (MPP+): Identification of a metabolite of MPTP, a toxin selective to the substantia nigra', *Neuroscience Letters*, 48(1). Available at: https://doi.org/10.1016/0304-3940(84)90293-3.

Lee, A.J. *et al.* (2017) 'Penetrance estimate of LRRK2 p.G2019S mutation in individuals of non-Ashkenazi Jewish ancestry', *Movement Disorders*, 32(10). Available at: https://doi.org/10.1002/mds.27059.

Lee, H.J., Patel, S. and Lee, S.J. (2005) 'Intravesicular localization and exocytosis of alpha-synuclein and its aggregates', *J Neurosci*, 25(25), pp. 6016–6024. Available at: https://doi.org/10.1523/JNEUROSCI.0692-05.2005.

Lee, J.W. *et al.* (2019) 'Alteration of tremor dominant and postural instability gait difficulty subtypes during the progression of Parkinson's disease: Analysis of the PPMI cohort', *Frontiers in Neurology*, 10(MAY). Available at: https://doi.org/10.3389/fneur.2019.00471.

Lee, P. (2024) *Study to Evaluate the Safety and Efficacy of ESC-derived Dopamine Progenitor Cell Therapy in PD Patients*, *clinicatrials.gov*. Available at: https://clinicaltrials.gov/study/NCT05887466?intr=embryonic&cond=Parkinsons Disease&rank=2#collaborators-and-investigators (Accessed: 3 January 2025).

Leisten, E.D., Woods, A.C. and Wong, Y.C. (2023) 'Super-resolution microscopy: Insights into mitochondria–lysosome crosstalk in health and disease', *Journal of Cell Biology*, 222(12). Available at: https://doi.org/10.1083/jcb.202305032.

Lesage, S. *et al.* (2013) 'G51D α-synuclein mutation causes a novel Parkinsonian-pyramidal syndrome', *Annals of Neurology*, 73(4). Available at: https://doi.org/10.1002/ana.23894.

Lesage, S. *et al.* (2016) 'Loss of VPS13C Function in Autosomal-Recessive Parkinsonism Causes Mitochondrial Dysfunction and Increases PINK1/Parkin-Dependent Mitophagy', *American Journal of Human Genetics*, 98(3), pp. 500–513. Available at: https://doi.org/10.1016/j.ajhg.2016.01.014.

Levitan, K. *et al.* (2011) 'Conserved C-terminal charge exerts a profound influence on the aggregation rate of α-synuclein', *Journal of Molecular Biology*, 411(2). Available at: https://doi.org/10.1016/j.jmb.2011.05.046.

Lewis, S. (2021) *A Randomised, Double-Blind, Parallel-Group, Placebo-Controlled, 60-Week, Phase II*

Clinical Trial on the effect of Three Re-Purposed Medications on Moderate Severity Parkinson's Disease, *www.anzctr.org.au/*. Available at: https://www.anzctr.org.au/Trial/Registration/TrialReview.aspx?id=375958 (Accessed: 30 August 2024).

Li, H. *et al.* (2019) 'Mitochondrial dysfunction and mitophagy defect triggered by heterozygous GBA mutations', *Autophagy*, 15(1), pp. 113–130. Available at: https://doi.org/10.1080/15548627.2018.1509818.

Li, J.Q., Tan, L. and Yu, J.T. (2014) 'The role of the LRRK2 gene in Parkinsonism', *Molecular neurodegeneration*. Available at: https://doi.org/10.1186/1750-1326-9-47.

Li, X., Sundquist, J. and Sundquist, K. (2012) 'Subsequent risks of Parkinson disease in patients with autoimmune and related disorders: A nationwide epidemiological study from Sweden', *Neurodegenerative Diseases*, 10(1–4). Available at: https://doi.org/10.1159/000333222.

Li, Y. *et al.* (2022) 'BNIP3L/NIX-mediated mitophagy: molecular mechanisms and implications for human disease', *Cell Death and Disease*. Available at: https://doi.org/10.1038/s41419-021-04469-y.

Lill, C.M. (2016) 'Genetics of Parkinson's disease', *Molecular and Cellular Probes*. Academic Press, pp. 386–396. Available at: https://doi.org/10.1016/j.mcp.2016.11.001.

Lin, H.J. *et al.* (2001) 'Fluorescence lifetime characterization of novel low-pH probes', *Analytical Biochemistry*, 294(2). Available at: https://doi.org/10.1006/abio.2001.5155.

Little, D. *et al.* (2018) 'A single cell high content assay detects mitochondrial dysfunction in iPSC-derived neurons with mutations in SNCA', *Scientific Reports*, 8(1). Available at: https://doi.org/10.1038/s41598-018-27058-0.

Liu, C. *et al.* (2021) 'The Membrane Interaction of Alpha-Synuclein', *Frontiers in Cellular Neuroscience*. Available at: https://doi.org/10.3389/fncel.2021.633727.

De Los Rios Castillo, D. *et al.* (2011) 'Atypical cristae morphology of human syncytiotrophoblast mitochondria: Role for complex V', *Journal of Biological Chemistry*, 286(27). Available at: https://doi.org/10.1074/jbc.M111.252056.

Lu, A. (2022) 'Endolysosomal cholesterol export: More than just NPC1', *BioEssays*, 44(10). Available at: https://doi.org/10.1002/bies.202200111.

Lu, C. *et al.* (2024) 'Exploring the Association between Cathepsin B and Parkinson's Disease', *Brain Sciences*, 14(5). Available at: https://doi.org/10.3390/brainsci14050482.

Lübke, T., Lobel, P. and Sleat, D.E. (2009) 'Proteomics of the lysosome', *Biochimica et Biophysica Acta - Molecular Cell Research*. Available at: https://doi.org/10.1016/j.bbamcr.2008.09.018.

LysoTracker ® and LysoSensor ™ Probes | 2 (no date).

Ma, L. *et al.* (2018) 'C-terminal truncation exacerbates the aggregation and cytotoxicity of α-Synuclein: A vicious cycle in Parkinson's disease', *Biochimica et Biophysica Acta - Molecular Basis of Disease*, 1864(12). Available at: https://doi.org/10.1016/j.bbadis.2018.10.003.

Ma, Y. *et al.* (2021) 'Fatty acid metabolism and acyl-CoA synthetases in the liver-gut axis', *World Journal of Hepatology*, 13(11). Available at: https://doi.org/10.4254/wjh.v13.i11.1512.

Macdonald, R. *et al.* (2018) 'Mitochondrial abnormalities in Parkinson's disease and Alzheimer's disease: can mitochondria be targeted therapeutically?', *Biochem Soc Trans*, 46(4), pp. 891–909. Available at: https://doi.org/10.1042/BST20170501.

MacLeod, D. *et al.* (2006) 'The Familial Parkinsonism Gene LRRK2 Regulates Neurite Process Morphology', *Neuron*, 52(4). Available at: https://doi.org/10.1016/j.neuron.2006.10.008.

MacLeod, D.A. *et al.* (2013) 'RAB7L1 Interacts with LRRK2 to Modify Intraneuronal Protein Sorting and Parkinson's Disease Risk', *Neuron*, 77(3). Available at: https://doi.org/10.1016/j.neuron.2012.11.033.

Magrinelli, F. *et al.* (2022) 'Dissecting the Phenotype and Genotype of PLA2G6-Related Parkinsonism', *Movement Disorders*, 37(1). Available at: https://doi.org/10.1002/mds.28807.

Majumdar, A. *et al.* (2011) 'Degradation of Alzheimer's amyloid fibrils by microglia requires delivery of CIC-7 to lysosomes', *Molecular Biology of the Cell*, 22(10). Available at: https://doi.org/10.1091/mbc.E10-09-0745.

Maleszewska, M., Mawer, J.S.P. and Tessarz, P. (2016) 'Histone Modifications in Ageing and Lifespan Regulation', *Current Molecular Biology Reports*, 2(1). Available at: https://doi.org/10.1007/s40610-016-0031-9.

Malik, N. *et al.* (2023) 'Induction of lysosomal and mitochondrial biogenesis by AMPK phosphorylation of FNIP1', *Science*, 380(6642). Available at: https://doi.org/10.1126/science.abj5559.

Malpartida, A.B. *et al.* (2021) 'Mitochondrial Dysfunction and Mitophagy in Parkinson's Disease: From Mechanism to Therapy', *Trends in Biochemical Sciences*. Available at: https://doi.org/10.1016/j.tibs.2020.11.007.

Mann, V.M. *et al.* (1992) 'Brain, skeletal muscle and platelet homogenate mitochondrial function in parkinson's disease', *Brain*, 115(2). Available at: https://doi.org/10.1093/brain/115.2.333.

Manzoni, C. *et al.* (2013) 'Pathogenic Parkinson's disease mutations across the functional domains of LRRK2 alter the autophagic/lysosomal response to starvation', *Biochem Biophys Res Commun*, 441(4), pp. 862–866. Available at: https://doi.org/10.1016/j.bbrc.2013.10.159.

Marder, K. *et al.* (2015) 'Age-specific penetrance of LRRK2 G2019S in the Michael J. Fox Ashkenazi Jewish LRRK2 Consortium', *Neurology*, 85(1). Available at: https://doi.org/10.1212/WNL.0000000000001708.

Marras, C., Canning, C.G. and Goldman, S.M. (2019) 'Environment, lifestyle, and Parkinson's disease: Implications for prevention in the next decade', *Movement Disorders*. Available at: https://doi.org/10.1002/mds.27720.

Marras, C. and Lang, A. (2013) 'Parkinson's disease subtypes: lost in translation?', *J Neurol Neurosurg Psychiatry*, 84(4), pp. 409–415. Available at: https://doi.org/10.1136/jnnp-2012-303455.

Martin, W.E. *et al.* (1973) 'Parkinson's disease: Clinical analysis of 100 patients', *Neurology*, 23(8). Available at: https://doi.org/10.1212/wnl.23.8.783.

Martin, W.F. (2010) 'The origin of mitochondria. Nature education', *Nature Education*, 3, p. 58.

Matsumine, H. *et al.* (1997) 'Localization of a gene for an autosomal recessive form of juvenile parkinsonism to chromosome 6q25.2-27', *American Journal of Human Genetics*, 60(3).

Matthews, G.D. *et al.* (2010) 'Weak mitochondrial targeting sequence determines tissue-specific subcellular localization of glutamine synthetase in liver and brain cells', *Journal of Cell Science*, 123(3). Available at: https://doi.org/10.1242/jcs.060749.

McFarthing, K. *et al.* (2023) 'Parkinson's Disease Drug Therapies in the Clinical Trial Pipeline: 2023 Update', *Journal of Parkinson's disease*, 13(4). Available at: https://doi.org/10.3233/JPD-239901.

McFarthing, K. *et al.* (2024) 'Parkinson's Disease Drug Therapies in the Clinical Trial Pipeline: 2024 Update', *Journal of Parkinson's Disease*, 14(5), pp. 899–912. Available at: https://doi.org/10.3233/JPD-240272.

McGeer, P.L. *et al.* (1988) 'Reactive microglia are positive for HLA-DR in the substantia nigra of Parkinson's and Alzheimer's disease brains', *Neurology*, 38(8), pp. 1285–1291. Available at: https://doi.org/10.1212/wnl.38.8.1285.

McGeer, P.L. and McGeer, E.G. (2004) 'Inflammation and neurodegeneration in Parkinson's disease',

Parkinsonism Relat Disord, 10 Suppl 1, pp. S3-7. Available at: https://doi.org/10.1016/j.parkreldis.2004.01.005.

McGlinchey, R. and Lee, J. (2015) 'Cysteine Cathepsins Are Essential in Lysosomal Degradation of α-Synuclein', *The FASEB Journal*, 29(S1). Available at: https://doi.org/10.1096/fasebj.29.1_supplement.564.8.

McGlinchey, R.P. *et al.* (2019) 'C-terminal α-synuclein truncations are linked to cysteine cathepsin activity in Parkinson's disease', *Journal of Biological Chemistry*, 294(25). Available at: https://doi.org/10.1074/jbc.RA119.008930.

McGlinchey, R.P. and Lee, J.C. (2015) 'Cysteine cathepsins are essential in lysosomal degradation of α-synuclein', *Proceedings of the National Academy of Sciences of the United States of America*, 112(30). Available at: https://doi.org/10.1073/pnas.1500937112.

McNeill, A. *et al.* (2014) 'Ambroxol improves lysosomal biochemistry in glucocerebrosidase mutation-linked Parkinson disease cells', *Brain*, 137(5). Available at: https://doi.org/10.1093/brain/awu020.

Meiser, J., Weindl, D. and Hiller, K. (2013) 'Complexity of dopamine metabolism', *Cell Commun Signal*, 11(1), p. 34. Available at: https://doi.org/10.1186/1478-811X-11-34.

Menon, P.J. *et al.* (2024) 'Genotype–phenotype correlation in PRKN-associated Parkinson's disease', *npj Parkinson's Disease*, 10(1). Available at: https://doi.org/10.1038/s41531-024-00677-3.

Mertens, J. *et al.* (2015) 'Directly Reprogrammed Human Neurons Retain Aging-Associated Transcriptomic Signatures and Reveal Age-Related Nucleocytoplasmic Defects', *Cell Stem Cell*, 17(6). Available at: https://doi.org/10.1016/j.stem.2015.09.001.

Mertens, J. *et al.* (2018) 'Aging in a dish: IPSC-derived and directly induced neurons for studying brain aging and age-related neurodegenerative diseases', *Annual Review of Genetics*. Available at: https://doi.org/10.1146/annurev-genet-120417-031534.

van der Merwe, C. *et al.* (2014) 'Mitochondrial impairment observed in fibroblasts from South African Parkinson's disease patients with parkin mutations', *Biochem Biophys Res Commun*, 447(2), pp. 334–340. Available at: https://doi.org/10.1016/j.bbrc.2014.03.151.

Mestre, T.A. *et al.* (2021) 'Parkinson's Disease Subtypes: Critical Appraisal and Recommendations', *Journal of Parkinson's Disease*. Available at: https://doi.org/10.3233/JPD-202472.

Meyer, K. *et al.* (2014) 'Direct conversion of patient fibroblasts demonstrates non-cell autonomous

toxicity of astrocytes to motor neurons in familial and sporadic ALS', *Proc Natl Acad Sci U S A*, 111(2), pp. 829–832. Available at: https://doi.org/10.1073/pnas.1314085111.

Migdalska-Richards, A. and Schapira, A.H.V. (2016) 'The relationship between glucocerebrosidase mutations and Parkinson disease', *Journal of Neurochemistry* [Preprint]. Available at: https://doi.org/10.1111/jnc.13385.

Miklossy, J. *et al.* (2006) 'LRRK2 expression in normal and pathologic human brain and in human cell lines', *Journal of Neuropathology and Experimental Neurology*, 65(10). Available at: https://doi.org/10.1097/01.jnen.0000235121.98052.54.

Milanese, C. *et al.* (2019) 'Peripheral mitochondrial function correlates with clinical severity in idiopathic Parkinson's disease', *Movement Disorders*, 34(8). Available at: https://doi.org/10.1002/mds.27723.

Milanowski, L.M. *et al.* (2022) 'Cathepsin B p.Gly284Val Variant in Parkinson's Disease Pathogenesis', *International Journal of Molecular Sciences*, 23(13), pp. 419–424. Available at: https://doi.org/10.3390/ijms23137086.

Mindell, J.A. (2012) 'Lysosomal acidification mechanisms', *Annual Review of Physiology*, 74. Available at: https://doi.org/10.1146/annurev-physiol-012110-142317.

De Miranda, B.R. *et al.* (2022) 'Preventing Parkinson's Disease: An Environmental Agenda', *Journal of Parkinson's Disease*. Available at: https://doi.org/10.3233/JPD-212922.

Mishra, P. and Chan, D.C. (2016) 'Metabolic regulation of mitochondrial dynamics', *Journal of Cell Biology*, 212(4). Available at: https://doi.org/10.1083/jcb.201511036.

Möbius, W. *et al.* (2003) 'Recycling compartments and the internal vesicles of multivesicular bodies harbor most of the cholesterol found in the endocytic pathway', *Traffic*, 4(4). Available at: https://doi.org/10.1034/j.1600-0854.2003.00072.x.

Mogi, M. *et al.* (1996) 'Interleukin (IL)-1β, IL-2, IL-4, IL-6 and transforming growth factor-α levels are elevated in ventricular cerebrospinal fluid in juvenile parkinsonism and Parkinson's disease', *Neuroscience Letters*, 211(1). Available at: https://doi.org/10.1016/0304-3940(96)12706-3.

Mollace, V. *et al.* (2003) 'The role of oxidative stress in paraquat-induced neurotoxicity in rats: Protection by non peptidyl superoxide dismutase mimetic', *Neuroscience Letters*, 335(3). Available at: https://doi.org/10.1016/S0304-3940(02)01168-0.

Mortiboys, H. *et al.* (2008) 'Mitochondrial function and morphology are impaired in parkin-mutant

fibroblasts', *Annals of Neurology*, 64(5). Available at: https://doi.org/10.1002/ana.21492.

Mortiboys, H. *et al.* (2010) 'Mitochondrial impairment in patients with Parkinson disease with the G2019S mutation in LRRK2', *Neurology*, 75(22). Available at: https://doi.org/10.1212/WNL.0b013e3181ff9685.

Mortiboys, H. *et al.* (2015) 'UDCA exerts beneficial effect on mitochondrial dysfunction in LRRK2G2019S carriers and in vivo', in *Neurology*, pp. 846–852. Available at: https://doi.org/10.1212/wnl.0000000000001905.

Mu, J. *et al.* (2017) 'Parkinson's disease subtypes identified from cluster analysis of motor and non-motor symptoms', *Frontiers in Aging Neuroscience*, 9(SEP). Available at: https://doi.org/10.3389/fnagi.2017.00301.

Müller, T. *et al.* (1998) 'Interleukin-6 levels in cerebrospinal fluid inversely correlate to severity of Parkinson's disease', *Acta Neurol Scand*, 98(2), pp. 142–144. Available at: https://doi.org/10.1111/j.1600-0404.1998.tb01736.x.

Mullin, S. *et al.* (2020) 'Ambroxol for the Treatment of Patients with Parkinson Disease with and Without Glucocerebrosidase Gene Mutations: A Nonrandomized, Noncontrolled Trial', *JAMA Neurology*, 77(4). Available at: https://doi.org/10.1001/jamaneurol.2019.4611.

Mullock, B.M. *et al.* (1998) 'Fusion of lysosomes with late endosomes produces a hybrid organelle of intermediate density and Is NSF dependent', *Journal of Cell Biology*, 140(3). Available at: https://doi.org/10.1083/jcb.140.3.591.

Murphy, E. *et al.* (2016) 'AHA Position Paper on Mitochondrial Function, Biology and Role in Disease.', *Circulation research*, 118(12).

Murphy, M.P. (2009) 'How mitochondria produce reactive oxygen species', *Biochemical Journal*. Available at: https://doi.org/10.1042/BJ20081386.

Murray, I.V.J. *et al.* (2003) 'Role of α-synuclein carboxy-terminus on fibril formation in vitro', *Biochemistry*, 42(28). Available at: https://doi.org/10.1021/bi027363r.

Muthukottiappan, P. and Winter, D. (2021) 'A proteomic view on lysosomes', *Molecular Omics*, pp. 842–859. Available at: https://doi.org/10.1039/d1mo00205h.

Mytilineou, C. *et al.* (1994) 'Impaired oxidative decarboxylation of pyruvate in fibroblasts from patients with Parkinson's disease', *Journal of Neural Transmission - Parkinson's Disease and Dementia Section*, 8(3). Available at: https://doi.org/10.1007/BF02260943.

Nakahira, K. *et al.* (2011) 'Autophagy proteins regulate innate immune responses by inhibiting the release of mitochondrial DNA mediated by the NALP3 inflammasome', *Nat Immunol*, 12(3), pp. 222–230. Available at: https://doi.org/10.1038/ni.1980.

Nakamura, K. *et al.* (2011) 'Direct membrane association drives mitochondrial fission by the Parkinson disease-associated protein α-synuclein', *Journal of Biological Chemistry*, 286(23). Available at: https://doi.org/10.1074/jbc.M110.213538.

Nalls, M.A. *et al.* (2019) 'Identification of novel risk loci, causal insights, and heritable risk for Parkinson's disease: a meta-analysis of genome-wide association studies', *The Lancet Neurology*, 18(12). Available at: https://doi.org/10.1016/S1474-4422(19)30320-5.

Nandhagopal, R. *et al.* (2011) 'Longitudinal evolution of compensatory changes in striatal dopamine processing in Parkinson's disease', *Brain*, 134(11). Available at: https://doi.org/10.1093/brain/awr233.

Narendra, D. *et al.* (2008) 'Parkin is recruited selectively to impaired mitochondria and promotes their autophagy', *J Cell Biol*, 183(5), pp. 795–803. Available at: https://doi.org/10.1083/jcb.200809125.

Narendra, D.P. *et al.* (2010) 'PINK1 is selectively stabilized on impaired mitochondria to activate Parkin', *PLoS Biol*, 8(1), p. e1000298. Available at: https://doi.org/10.1371/journal.pbio.1000298.

Nath, S. (2022) 'Supercomplex supercomplexes: Raison d'etre and functional significance of supramolecular organization in oxidative phosphorylation', *Biomolecular Concepts*, 13(1). Available at: https://doi.org/10.1515/bmc-2022-0021.

Nazareth, E.J.P. *et al.* (2013) 'High-throughput fingerprinting of human pluripotent stem cell fate responses and lineage bias', *Nature Methods*, 10(12), pp. 1225–1231. Available at: https://doi.org/10.1038/nmeth.2684.

Neethling, A. *et al.* (2019) 'Wild-type and mutant (G2019S) leucine-rich repeat kinase 2 (LRRK2) associate with subunits of the translocase of outer mitochondrial membrane (TOM) complex', *Experimental Cell Research*, 375(2). Available at: https://doi.org/10.1016/j.yexcr.2018.12.022.

Neikirk, K. *et al.* (2023) 'MitoTracker: A useful tool in need of better alternatives', *European Journal of Cell Biology*, 102(4). Available at: https://doi.org/10.1016/j.ejcb.2023.151371.

Nelson, N. (1992) 'Evolution of organellar proton-ATPases', *BBA - Bioenergetics*. Available at: https://doi.org/10.1016/0005-2728(92)90072-A.

Nepal, B. *et al.* (2023) 'Overview of the structure and function of the dopamine transporter and its protein interactions', *Frontiers in Physiology*. Available at: https://doi.org/10.3389/fphys.2023.1150355.

Neupane, P. *et al.* (2019) 'ATP Synthase: Structure, Function and Inhibition', *Biomolecular Concepts*, 10(1). Available at: https://doi.org/10.1515/bmc-2019-0001.

Nguyen, B.Y. *et al.* (2019) 'Mitochondrial function in the heart: the insight into mechanisms and therapeutic potentials', *British Journal of Pharmacology*. Available at: https://doi.org/10.1111/bph.14431.

Nguyen, H.N. *et al.* (2011) 'LRRK2 mutant iPSC-derived da neurons demonstrate increased susceptibility to oxidative stress', *Cell Stem Cell*, 8(3). Available at: https://doi.org/10.1016/j.stem.2011.01.013.

Nguyen, L.T.N. *et al.* (2022) 'Role of NLRP3 Inflammasome in Parkinson's Disease and Therapeutic Considerations', *Journal of Parkinson's Disease*. Available at: https://doi.org/10.3233/JPD-223290.

Nishioka, K. *et al.* (2022) 'Clinical Manifestations and Molecular Backgrounds of Parkinson's Disease Regarding Genes Identified From Familial and Population Studies', *Frontiers in Neurology*. Available at: https://doi.org/10.3389/fneur.2022.764917.

Nissinen, E. and Männistö, P.T. (2010) 'Biochemistry and pharmacology of catechol-O-methyltransferase inhibitors', in *International Review of Neurobiology*. Available at: https://doi.org/10.1016/B978-0-12-381326-8.00005-3.

Niu, J. *et al.* (2012) 'Leucine-rich repeat kinase 2 disturbs mitochondrial dynamics via dynamin-like protein', *Journal of Neurochemistry*, 122(3). Available at: https://doi.org/10.1111/j.1471-4159.2012.07809.x.

Nolfi-Donegan, D., Braganza, A. and Shiva, S. (2020) 'Mitochondrial electron transport chain: Oxidative phosphorylation, oxidant production, and methods of measurement', *Redox Biology*. Available at: https://doi.org/10.1016/j.redox.2020.101674.

O'Connor, K. (2018) 'How patents play a role in drug pricing'. The Pharmaletter. Available at: https://www.thepharmaletter.com/article/how-patents-play-a-role-in-drug-pricing.

Ohkuma, S., Moriyama, Y. and Takano, T. (1982) 'Identification and characterization of a proton pump on lysosomes by fluorescein isothiocyanate-dextran fluorescence', *Proceedings of the National Academy of Sciences of the United States of America*, 79(9 I). Available at: https://doi.org/10.1073/pnas.79.9.2758.

Olesen, M.A., Villavicencio-Tejo, F. and Quintanilla, R.A. (2022) 'The use of fibroblasts as a valuable strategy for studying mitochondrial impairment in neurological disorders', *Translational Neurodegeneration*. Available at: https://doi.org/10.1186/s40035-022-00308-y.

Omer, N. *et al.* (2020) 'A Possible Modifying Effect of the G2019S Mutation in the LRRK2 Gene on GBA Parkinson's Disease', *Movement Disorders*, 35(7), pp. 1249–1253. Available at: https://doi.org/10.1002/mds.28066.

Onishi, M. *et al.* (2021) 'Molecular mechanisms and physiological functions of mitophagy', *The EMBO Journal*, 40(3). Available at: https://doi.org/10.15252/embj.2020104705.

Orenstein, S.J. *et al.* (2013) 'Interplay of LRRK2 with chaperone-mediated autophagy', *Nat Neurosci*, 16(4), pp. 394–406. Available at: https://doi.org/10.1038/nn.3350.

Ortega, R.A. *et al.* (2021) 'Association of Dual LRRK2 G2019S and GBA Variations with Parkinson Disease Progression', *JAMA Network Open*, 4(4). Available at: https://doi.org/10.1001/jamanetworkopen.2021.5845.

Osellame, L.D. *et al.* (2013) 'Mitochondria and quality control defects in a mouse model of Gaucher disease--links to Parkinson's disease', *Cell Metab*, 17(6), pp. 941–953. Available at: https://doi.org/10.1016/j.cmet.2013.04.014.

Osellame, L.D., Blacker, T.S. and Duchen, M.R. (2012) 'Cellular and molecular mechanisms of mitochondrial function', *Best Practice and Research: Clinical Endocrinology and Metabolism*. Available at: https://doi.org/10.1016/j.beem.2012.05.003.

Ou, Z. *et al.* (2021) 'Global Trends in the Incidence, Prevalence, and Years Lived With Disability of Parkinson's Disease in 204 Countries/Territories From 1990 to 2019', *Frontiers in Public Health*, 9. Available at: https://doi.org/10.3389/fpubh.2021.776847.

De Pablo-Fernández, E. *et al.* (2019) 'Prognosis and Neuropathologic Correlation of Clinical Subtypes of Parkinson Disease', *JAMA Neurology*, 76(4), pp. 470–479. Available at: https://doi.org/10.1001/jamaneurol.2018.4377.

Paisán-Ruíz, C. *et al.* (2004) 'Cloning of the gene containing mutations that cause PARK8-linked Parkinson's disease', *Neuron*, 44(4). Available at: https://doi.org/10.1016/j.neuron.2004.10.023.

Palikaras, K., Lionaki, E. and Tavernarakis, N. (2018) 'Mechanisms of mitophagy in cellular homeostasis, physiology and pathology', *Nature Cell Biology*. Available at: https://doi.org/10.1038/s41556-018-0176-2.

Pang, S.Y.Y. *et al.* (2022) 'LRRK2, GBA and their interaction in the regulation of autophagy: implications on therapeutics in Parkinson's disease', *Translational Neurodegeneration*. Available at: https://doi.org/10.1186/s40035-022-00281-6.

Papkovskaia, T.D. *et al.* (2012) 'G2019s leucine-rich repeat kinase 2 causes uncoupling protein-mediated mitochondrial depolarization', *Human Molecular Genetics*, 21(19). Available at: https://doi.org/10.1093/hmg/dds244.

Park, J.S., Davis, R.L. and Sue, C.M. (2018) 'Mitochondrial Dysfunction in Parkinson's Disease: New Mechanistic Insights and Therapeutic Perspectives', *Current Neurology and Neuroscience Reports*. Available at: https://doi.org/10.1007/s11910-018-0829-3.

Parker, W.D., Boyson, S.J. and Parks, J.K. (1989) 'Abnormalities of the electron transport chain in idiopathic parkinson's disease', *Annals of Neurology*, 26(6). Available at: https://doi.org/10.1002/ana.410260606.

Parkinson's UK (2025) *MDS Unified Parkinson's Disease Rating Scale (MDS-UPDRS) - Parkinson's UK*, *Parkinson's UK*. Available at: https://www.parkinsons.org.uk/professionals/resources/mds-unified-parkinsons-disease-rating-scale-mds-updrs (Accessed: 3 January 2025).

Parkinson, J. (1817) *An essay on shaking palsy*, *Sherwood, Neely and Jones*.

Parnetti, L. *et al.* (2014) 'Cerebrospinal fluid lysosomal enzymes and alpha-synuclein in Parkinson's disease', *Movement Disorders*, 29(8). Available at: https://doi.org/10.1002/mds.25772.

Parnetti, L. *et al.* (2017) 'Cerebrospinal fluid β-glucocerebrosidase activity is reduced in parkinson's disease patients', *Movement Disorders*, 32(10). Available at: https://doi.org/10.1002/mds.27136.

Parra, K.J. and Hayek, S.R. (2018) 'A lysosomal proton pump turns on when glucose runs out', *Journal of Biological Chemistry*. Available at: https://doi.org/10.1074/jbc.H118.002950.

Payne, T. *et al.* (2020) 'Ursodeoxycholic acid as a novel disease-modifying treatment for Parkinson's disease: Protocol for a two-centre, randomised, double-blind, placebo-controlled trial, the "UP" study', *BMJ Open*, 10(8). Available at: https://doi.org/10.1136/bmjopen-2020-038911.

Payne, T., Appleby, M., *et al.* (2023) 'A Double-Blind, Randomized, Placebo-Controlled Trial of Ursodeoxycholic Acid (UDCA) in Parkinson's Disease.', *Movement disorders : official journal of the Movement Disorder Society* [Preprint]. Available at: https://doi.org/10.1002/mds.29450.

Payne, T., Burgess, T., *et al.* (2023) 'Multimodal assessment of mitochondrial function in Parkinson's disease.', *Brain : a journal of neurology* [Preprint]. Available at:

https://doi.org/10.1093/brain/awad364.

Peng, W. *et al.* (2023) 'Parkin regulates amino acid homeostasis at mitochondria-lysosome (M/L) contact sites in Parkinson's disease', *Science Advances*, 9(29). Available at: https://doi.org/10.1126/sciadv.adh3347.

Peng, W., Wong, Y.C. and Krainc, D. (2020) 'Mitochondria-lysosome contacts regulate mitochondrial Ca2+ dynamics via lysosomal TRPML1', *Proceedings of the National Academy of Sciences of the United States of America*, 117(32). Available at: https://doi.org/10.1073/pnas.2003236117.

Pickrell, A.M. and Youle, R.J. (2015) 'The roles of PINK1, parkin, and mitochondrial fidelity in Parkinson's disease', *Neuron*, 85(2), pp. 257–273. Available at: https://doi.org/10.1016/j.neuron.2014.12.007.

Pienta, K.J., Getzenberg, R.H. and Coffey, D.S. (1992) 'Characterization of nuclear morphology and nuclear matrices in ageing human fibroblasts', *Mechanisms of Ageing and Development*, 62(1). Available at: https://doi.org/10.1016/0047-6374(92)90140-9.

Pisoni, R.L. and Thoene, J.G. (1991) 'The transport systems of mammalian lysosomes', *BBA - Reviews on Biomembranes*. Available at: https://doi.org/10.1016/0304-4157(91)90002-E.

Plaitakis, A. *et al.* (2017) 'The glutamate dehydrogenase pathway and its roles in cell and tissue biology in health and disease', *Biology*. Available at: https://doi.org/10.3390/biology6010011.

Platt, F.M. (2018) 'Emptying the stores: Lysosomal diseases and therapeutic strategies', *Nature Reviews Drug Discovery*. Available at: https://doi.org/10.1038/nrd.2017.214.

Polymeropoulos, M.H. *et al.* (1997) 'Mutation in the α-synuclein gene identified in families with Parkinson's disease', *Science*, 276(5321). Available at: https://doi.org/10.1126/science.276.5321.2045.

Pryor, P.R. *et al.* (2000) 'The role of intraorganellar Ca2+ in late endosome-lysosome heterotypic fusion and in the reformation of lysosomes from hybrid organelles', *Journal of Cell Biology*, 149(5). Available at: https://doi.org/10.1083/jcb.149.5.1053.

Pryor, P.R. *et al.* (2004) 'Combinatorial SNARE complexes with VAMP7 or VAMP8 define different late endocytic fusion events', *EMBO Reports*, 5(6). Available at: https://doi.org/10.1038/sj.embor.7400150.

Puigròs, M. *et al.* (2024) 'Mitochondrial DNA deletions in the cerebrospinal fluid of patients with idiopathic REM sleep behaviour disorder', *eBioMedicine*, 102, p. 105065. Available at:

https://doi.org/10.1016/j.ebiom.2024.105065.

Pyle, A. *et al.* (2015) 'Reduced mitochondrial DNA copy number is a biomarker of Parkinson's disease', *Neurobiology of Aging*, 38. Available at: https://doi.org/10.1016/j.neurobiolaging.2015.10.033.

Qi, R. *et al.* (2023) 'A blood-based marker of mitochondrial DNA damage in Parkinson's disease', *Science Translational Medicine*, 15(711). Available at: https://doi.org/10.1126/SCITRANSLMED.ABO1557.

Qiao, L. *et al.* (2008) 'Lysosomal enzyme cathepsin D protects against alpha-synuclein aggregation and toxicity.', *Molecular brain*, 1. Available at: https://doi.org/10.1186/1756-6606-1-17.

Qiao, L. *et al.* (2023) 'LAMP2A, LAMP2B and LAMP2C: similar structures, divergent roles', *Autophagy*. Available at: https://doi.org/10.1080/15548627.2023.2235196.

Qin, X.Y. *et al.* (2016) 'Aberrations in Peripheral Inflammatory Cytokine Levels in Parkinson Disease: A Systematic Review and Meta-analysis', *JAMA Neurol*, 73(11), pp. 1316–1324. Available at: https://doi.org/10.1001/jamaneurol.2016.2742.

Qin, Z. *et al.* (2007) 'Role of different regions of α-synuclein in the assembly of fibrils', *Biochemistry*, 46(46). Available at: https://doi.org/10.1021/bi7014053.

Quadri, M. *et al.* (2013) 'Mutation in the SYNJ1 gene associated with autosomal recessive, early-onset parkinsonism', *Human Mutation*, 34(9), pp. 1208–1215. Available at: https://doi.org/10.1002/humu.22373.

Racette, B.A. *et al.* (2018) 'Immunosuppressants and risk of Parkinson disease', *Annals of Clinical and Translational Neurology*, 5(7). Available at: https://doi.org/10.1002/acn3.580.

Rajamäki, K. *et al.* (2010) 'Cholesterol crystals activate the NLRP3 inflammasome in human macrophages: a novel link between cholesterol metabolism and inflammation', *PLoS One*, 5(7), p. e11765. Available at: https://doi.org/10.1371/journal.pone.0011765.

Ramirez, A. *et al.* (2006) 'Hereditary parkinsonism with dementia is caused by mutations in ATP13A2, encoding a lysosomal type 5 P-type ATPase', *Nature Genetics*, 38(10), pp. 1184–1191. Available at: https://doi.org/10.1038/ng1884.

Ramsay, R.R., Salach, J.I. and Singer, T.P. (1986) 'Uptake of the neurotoxin 1-methyl-4-phenylpyridine (MPP+) by mitochondria and its relation to the inhibition of the mitochondrial oxidation of NAD+-linked substrates by MPP+', *Biochemical and Biophysical Research*

Communications, 134(2). Available at: https://doi.org/10.1016/S0006-291X(86)80483-1.

Ray Dorsey, E. *et al.* (2018) 'Global, regional, and national burden of Parkinson's disease, 1990–2016: a systematic analysis for the Global Burden of Disease Study 2016', *The Lancet Neurology*, 17(11), pp. 939–953. Available at: https://doi.org/10.1016/S1474-4422(18)30295-3.

Riboldi, G.M. and Di Fonzo, A.B. (2019) 'GBA, Gaucher disease, and parkinson's disease: From genetic to clinic to new therapeutic approaches', *Cells*. Available at: https://doi.org/10.3390/cells8040364.

Richo, G.R. and Conner, G.E. (1994) 'Structural requirements of procathepsin D activation and maturation', *Journal of Biological Chemistry*, 269(20). Available at: https://doi.org/10.1016/s0021-9258(17)36696-6.

Robak, L.A. *et al.* (2017) 'Excessive burden of lysosomal storage disorder gene variants in Parkinson's disease', *Brain*, 140(12). Available at: https://doi.org/10.1093/brain/awx285.

Rocha, E.M. *et al.* (2015) 'Progressive decline of glucocerebrosidase in aging and Parkinson's disease', *Annals of Clinical and Translational Neurology*, 2(4). Available at: https://doi.org/10.1002/ACN3.177.

Van Rooden, S.M. *et al.* (2010) 'The identification of Parkinson's disease subtypes using cluster analysis: A systematic review', *Movement Disorders*, pp. 969–978. Available at: https://doi.org/10.1002/mds.23116.

Rosenberg, J.B. *et al.* (2019) 'Advances in the treatment of neuronal ceroid lipofuscinosis', *Expert Opinion on Orphan Drugs*. Available at: https://doi.org/10.1080/21678707.2019.1684258.

Ross, O.A. *et al.* (2011) 'Association of LRRK2 exonic variants with susceptibility to Parkinson's disease: A case-control study', *The Lancet Neurology*, 10(10). Available at: https://doi.org/10.1016/S1474-4422(11)70175-2.

Rossignol, R. *et al.* (2004) 'Energy Substrate Modulates Mitochondrial Structure and Oxidative Capacity in Cancer Cells', *Cancer Research*, 64(3). Available at: https://doi.org/10.1158/0008-5472.CAN-03-1101.

Rudnik, S. and Damme, M. (2021) 'The lysosomal membrane—export of metabolites and beyond', *FEBS Journal*. Available at: https://doi.org/10.1111/febs.15602.

Rui, Q. *et al.* (2018) 'The Role of LRRK2 in Neurodegeneration of Parkinson Disease', *Current Neuropharmacology*, 16(9). Available at: https://doi.org/10.2174/1570159x16666180222165418.

Rusilowicz-Jones, E. V. *et al.* (2022) 'Benchmarking a highly selective USP30 inhibitor for enhancement of mitophagy and pexophagy', *Life Science Alliance*, 5(2). Available at: https://doi.org/10.26508/lsa.202101287.

Sagné, C. and Gasnier, B. (2008) 'Molecular physiology and pathophysiology of lysosomal membrane transporters', in *Journal of Inherited Metabolic Disease*. Available at: https://doi.org/10.1007/s10545-008-0879-9.

Salminen, A. *et al.* (2012) 'Mitochondrial dysfunction and oxidative stress activate inflammasomes: impact on the aging process and age-related diseases', *Cell Mol Life Sci*, 69(18), pp. 2999–3013. Available at: https://doi.org/10.1007/s00018-012-0962-0.

Sánchez-Danés, A. *et al.* (2012) 'Disease-specific phenotypes in dopamine neurons from human iPS-based models of genetic and sporadic Parkinson's disease', *EMBO Mol Med*, 4(5), pp. 380–395. Available at: https://doi.org/10.1002/emmm.201200215.

Sansom, S.N. *et al.* (2009) 'The level of the transcription factor Pax6 is essential for controlling the balance between neural stem cell self-renewal and neurogenesis', *PLoS Genetics*, 5(6). Available at: https://doi.org/10.1371/journal.pgen.1000511.

Sathe, A.G. *et al.* (2020) 'Pharmacokinetics, Safety, and Tolerability of Orally Administered Ursodeoxycholic Acid in Patients With Parkinson's Disease—A Pilot Study', *Journal of Clinical Pharmacology*, 60(6). Available at: https://doi.org/10.1002/jcph.1575.

Scaduto, R.C. and Grotyohann, L.W. (1999) 'Measurement of mitochondrial membrane potential using fluorescent rhodamine derivatives', *Biophysical Journal*, 76(1 I). Available at: https://doi.org/10.1016/S0006-3495(99)77214-0.

Scaffidi, P., Gordon, L. and Misteli, T. (2005) 'The Cell Nucleus and Aging: Tantalizing Clues and Hopeful Promises', *PLoS Biology*, 3(11). Available at: https://doi.org/10.1371/journal.pbio.0030395.

Schapansky, J. *et al.* (2018) 'Familial knockin mutation of LRRK2 causes lysosomal dysfunction and accumulation of endogenous insoluble α-synuclein in neurons', *Neurobiology of Disease*, 111. Available at: https://doi.org/10.1016/j.nbd.2017.12.005.

Schapira, A.H.V. *et al.* (1990) 'Mitochondrial Complex I Deficiency in Parkinson's Disease', *Journal of Neurochemistry*, 54(3). Available at: https://doi.org/10.1111/j.1471-4159.1990.tb02325.x.

Schapira, A.H.V., Chaudhuri, K.R. and Jenner, P. (2017) 'Non-motor features of Parkinson disease', *Nature Reviews Neuroscience*, pp. 435–450. Available at: https://doi.org/10.1038/nrn.2017.62.

Schmidt, S. *et al.* (2023) 'A reversible state of hypometabolism in a human cellular model of sporadic Parkinson's disease', *Nature Communications*, 14(1). Available at: https://doi.org/10.1038/s41467-023-42862-7.

Schöndorf, D.C. *et al.* (2014) 'IPSC-derived neurons from GBA1-associated Parkinson's disease patients show autophagic defects and impaired calcium homeostasis', *Nature Communications*, 5. Available at: https://doi.org/10.1038/ncomms5028.

Schultz, J.L. *et al.* (2022) 'A pilot to assess target engagement of terazosin in Parkinson's disease', *Parkinsonism and Related Disorders*, 94. Available at: https://doi.org/10.1016/j.parkreldis.2021.11.022.

Schulz-Schaeffer, W.J. (2010) 'The synaptic pathology of α-synuclein aggregation in dementia with Lewy bodies, Parkinson's disease and Parkinson's disease dementia', *Acta Neuropathologica*. Available at: https://doi.org/10.1007/s00401-010-0711-0.

Schulze, H., Kolter, T. and Sandhoff, K. (2009) 'Principles of lysosomal membrane degradation. Cellular topology and biochemistry of lysosomal lipid degradation', *Biochimica et Biophysica Acta - Molecular Cell Research*. Available at: https://doi.org/10.1016/j.bbamcr.2008.09.020.

Schwartzentruber, A. *et al.* (2020) 'Oxidative switch drives mitophagy defects in dopaminergic parkin mutant patient neurons', *Sci Rep*, 10(1), p. 15485. Available at: https://doi.org/10.1038/s41598-020-72345-4.

Selikhova, M. V *et al.* (2002) 'Impaired production of plasma interleukin-6 in patients with Parkinson's disease', *Bull Exp Biol Med*, 133(1), pp. 81–83. Available at: https://doi.org/10.1023/a:1015120930920.

Serpell, L.C. *et al.* (2000) 'Fiber diffraction of synthetic α-synuclein filaments shows amyloid-like cross-β conformation', *Proceedings of the National Academy of Sciences of the United States of America*, 97(9). Available at: https://doi.org/10.1073/pnas.97.9.4897.

Sevlever, D., Jiang, P. and Yen, S.H.C. (2008) 'Cathepsin D is the main lysosomal enzyme involved in the degradation of α-synuclein and generation of its carboxy-terminally truncated species', *Biochemistry*, 47(36). Available at: https://doi.org/10.1021/bi800699v.

Shaltouki, A. *et al.* (2018) 'Alpha-synuclein delays mitophagy and targeting Miro rescues neuron loss in Parkinson's models', *Acta Neuropathologica*, 136(4). Available at: https://doi.org/10.1007/s00401-018-1873-4.

Sherer, T.B. *et al.* (2003) 'Mechanism of Toxicity in Rotenone Models of Parkinson's Disease', *Journal*

of Neuroscience, 23(34). Available at: https://doi.org/10.1523/jneurosci.23-34-10756.2003.

Shiba-Fukushima, K. *et al.* (2017) 'Evidence that phosphorylated ubiquitin signaling is involved in the etiology of Parkinson's disease', *Human Molecular Genetics*, 26(16). Available at: https://doi.org/10.1093/hmg/ddx201.

Shimada, K. *et al.* (2012) 'Oxidized mitochondrial DNA activates the NLRP3 inflammasome during apoptosis', *Immunity*, 36(3), pp. 401–414. Available at: https://doi.org/10.1016/j.immuni.2012.01.009.

Shoffner, J.M. *et al.* (1991) 'Mitochondrial oxidative phosphorylation defects in Parkinson's disease', *Ann Neurol*, 30(3), pp. 332–339. Available at: https://doi.org/10.1002/ana.410300304.

Siderowf, A. *et al.* (2002) 'Test-retest reliability of the unified Parkinson's disease rating scale in patients with early Parkinson's disease: Results from a multicenter clinical trial', *Movement Disorders*, 17(4). Available at: https://doi.org/10.1002/mds.10011.

Siderowf, A. *et al.* (2023) 'Assessment of heterogeneity among participants in the Parkinson's Progression Markers Initiative cohort using α-synuclein seed amplification: a cross-sectional study', *The Lancet Neurology*, 22(5), pp. 407–417. Available at: https://doi.org/10.1016/S1474-4422(23)00109-6.

Sidransky, E. *et al.* (2009) 'Multicenter analysis of glucocerebrosidase mutations in Parkinson's disease', *N Engl J Med*, 361(17), pp. 1651–1661. Available at: https://doi.org/10.1056/NEJMoa0901281.

Sidransky, E. and Lopez, G. (2012) 'The link between the GBA gene and parkinsonism', *Lancet Neurol*, 11(11), pp. 986–998. Available at: https://doi.org/10.1016/S1474-4422(12)70190-4.

Siemeling, O. (2023) *GRoningen Early-PD Ambroxol Treatment (GREAT)*, *ClinicalTrials.gov*. Available at: https://clinicaltrials.gov/study/NCT05830396?cond=gba&term=GREAT &rank=1 (Accessed: 30 August 2024).

Siintola, E. *et al.* (2006) 'Cathepsin D deficiency underlies congenital human neuronal ceroid-lipofuscinosis', *Brain*, 129(6). Available at: https://doi.org/10.1093/brain/awl107.

Simuni, T. *et al.* (2016) 'How stable are Parkinson's disease subtypes in de novo patients: Analysis of the PPMI cohort?', *Parkinsonism and Related Disorders*, 28. Available at: https://doi.org/10.1016/j.parkreldis.2016.04.027.

Singh, A., Zhi, L. and Zhang, H. (2019) 'LRRK2 and mitochondria: Recent advances and current views',

Brain Res, 1702, pp. 96–104. Available at: https://doi.org/10.1016/j.brainres.2018.06.010.

Singh, R. *et al.* (2009) 'Autophagy regulates lipid metabolism', *Nature*, 458(7242). Available at: https://doi.org/10.1038/nature07976.

Singh, R. *et al.* (2023) '2-Deoxy-D-Glucose: A Novel Pharmacological Agent for Killing Hypoxic Tumor Cells, Oxygen Dependence-Lowering in Covid-19, and Other Pharmacological Activities', *Advances in Pharmacological and Pharmaceutical Sciences*. Available at: https://doi.org/10.1155/2023/9993386.

Singleton, A.B., Farrer, M.J. and Bonifati, V. (2013) 'The genetics of Parkinson's disease: progress and therapeutic implications', *Mov Disord*, 28(1), pp. 14–23. Available at: https://doi.org/10.1002/mds.25249.

de Siqueira, E.A. *et al.* (2023) 'Vitamin D3 actions on astrocyte cells: A target for therapeutic strategy in Parkinson's disease?', *Neuroscience Letters*, 793. Available at: https://doi.org/10.1016/j.neulet.2022.136997.

Sliter, D.A. *et al.* (2018) 'Parkin and PINK1 mitigate STING-induced inflammation', *Nature*, 561(7722), pp. 258–262. Available at: https://doi.org/10.1038/s41586-018-0448-9.

Smith, G.A. *et al.* (2016) 'Fibroblast Biomarkers of Sporadic Parkinson's Disease and LRRK2 Kinase Inhibition', *Molecular Neurobiology*, 53(8). Available at: https://doi.org/10.1007/s12035-015-9435-4.

Smith, L. and Schapira, A.H.V. (2022) 'GBA Variants and Parkinson Disease: Mechanisms and Treatments', *Cells*. Available at: https://doi.org/10.3390/cells11081261.

Smith, L.J. *et al.* (2023) 'The GBA variant E326K is associated with alpha-synuclein aggregation and lipid droplet accumulation in human cell lines', *Human Molecular Genetics*, 32(5). Available at: https://doi.org/10.1093/hmg/ddac233.

Sosero, Y.L. *et al.* (2021) 'LRRK2 p.M1646T is associated with glucocerebrosidase activity and with Parkinson's disease', *Neurobiology of Aging*, 103. Available at: https://doi.org/10.1016/j.neurobiolaging.2021.02.018.

Sosero, Y.L. and Gan-Or, Z. (2023) 'LRRK2 and Parkinson's disease: from genetics to targeted therapy', *Annals of Clinical and Translational Neurology*. Available at: https://doi.org/10.1002/acn3.51776.

Spinelli, J.B. and Haigis, M.C. (2018) 'The multifaceted contributions of mitochondria to cellular metabolism', *Nature Cell Biology*. Available at: https://doi.org/10.1038/s41556-018-0124-1.

St Louis, E.K. and Boeve, B.F. (2017) 'REM Sleep Behavior Disorder: Diagnosis, Clinical Implications,

and Future Directions', *Mayo Clinic Proceedings*. Available at: https://doi.org/10.1016/j.mayocp.2017.09.007.

Standards for Human Stem Cell Use in (no date). Available at: https://www.isscr.org/basic-research-standards

Stauch, K.L. *et al.* (2016) 'Loss of Pink1 modulates synaptic mitochondrial bioenergetics in the rat striatum prior to motor symptoms: concomitant complex I respiratory defects and increased complex II-mediated respiration', *Proteomics - Clinical Applications*, 10(12). Available at: https://doi.org/10.1002/prca.201600005.

Steinberg, B.E. *et al.* (2010) 'A cation counterflux supports lysosomal acidification', *Journal of Cell Biology*, 189(7). Available at: https://doi.org/10.1083/jcb.200911083.

Stige, K.E. *et al.* (2024) 'The STRAT-PARK cohort: A personalized initiative to stratify Parkinson's disease', *Progress in Neurobiology*. Elsevier Ltd. Available at: https://doi.org/10.1016/j.pneurobio.2024.102603.

Su, Y.C. and Qi, X. (2013) 'Inhibition of excessive mitochondrial fission reduced aberrant autophagy and neuronal damage caused by LRRK2 G2019S mutation', *Human Molecular Genetics*, 22(22). Available at: https://doi.org/10.1093/hmg/ddt301.

Subrahmanian, N. and LaVoie, M.J. (2021) 'Is there a special relationship between complex I activity and nigral neuronal loss in Parkinson's disease? A critical reappraisal', *Brain Research*, 1767. Available at: https://doi.org/10.1016/j.brainres.2021.147434.

Suresh Babu, S. *et al.* (2023) 'Characterization of human induced pluripotent stems cells: Current approaches, challenges, and future solutions', *Biotechnology Reports*. Available at: https://doi.org/10.1016/j.btre.2023.e00784.

Surmeier, D.J. *et al.* (2022) 'Re-Analysis of the STEADY-PD II Trial—Evidence for Slowing the Progression of Parkinson's Disease', *Movement Disorders*, 37(2). Available at: https://doi.org/10.1002/mds.28850.

Takahashi, K. and Yamanaka, S. (2006) 'Induction of Pluripotent Stem Cells from Mouse Embryonic and Adult Fibroblast Cultures by Defined Factors', *Cell*, 126(4). Available at: https://doi.org/10.1016/j.cell.2006.07.024.

Talley, J.T. and Mohiuddin, S.S. (2020) *Biochemistry, Fatty Acid Oxidation*, *StatPearls*.

Tan, E.K. *et al.* (2010) 'Multiple LRRK2 variants modulate risk of Parkinson disease: A Chinese

multicenter study', *Human Mutation*, 31(5). Available at: https://doi.org/10.1002/humu.21225.

Tan, G.-J. *et al.* (2013) 'Cathepsins mediate tumor metastasis', *World Journal of Biological Chemistry*, 4(4). Available at: https://doi.org/10.4331/wjbc.v4.i4.91.

Tan, Y.Y., Jenner, P. and Chen, S. Di (2022) 'Monoamine Oxidase-B Inhibitors for the Treatment of Parkinson's Disease: Past, Present, and Future', *Journal of Parkinson's Disease*. Available at: https://doi.org/10.3233/JPD-212976.

Tanaka, Y. *et al.* (2001) 'Inducible expression of mutant α-synuclein decreases proteasome activity and increases sensitivity to mitochondria-dependent apoptosis', *Human Molecular Genetics*, 10(9). Available at: https://doi.org/10.1093/hmg/10.9.919.

Tansey, M.G. and Romero-Ramos, M. (2019) 'Immune system responses in Parkinson's disease: Early and dynamic', *Eur J Neurosci*, 49(3), pp. 364–383. Available at: https://doi.org/10.1111/ejn.14290.

Telser, A. (2002) 'Molecular Biology of the Cell, 4th Edition', *Shock*, 18(3). Available at: https://doi.org/10.1097/00024382-200209000-00015.

Teves, J.M.Y. *et al.* (2018) 'Parkinson's disease skin fibroblasts display signature alterations in growth, redox homeostasis, mitochondrial function, and autophagy', *Frontiers in Neuroscience*, 11(JAN). Available at: https://doi.org/10.3389/fnins.2017.00737.

Thanan, R. *et al.* (2014) 'Oxidative stress and its significant roles in neurodegenerative diseases and cancer', *Int J Mol Sci*, 16(1), pp. 193–217. Available at: https://doi.org/10.3390/ijms16010193.

The Michael J Fox Foundation (2024) *Medications for Motor Symptoms*. Available at: https://www.michaeljfox.org/news/medications-motor-symptoms (Accessed: 21 August 2024).

Thomas, R. *et al.* (2021) 'Fibroblasts from idiopathic Parkinson's disease exhibit deficiency of lysosomal glucocerebrosidase activity associated with reduced levels of the trafficking receptor LIMP2', *Mol Brain*, 14(1), p. 16. Available at: https://doi.org/10.1186/s13041-020-00712-3.

Tolosa, E. *et al.* (2021) 'Challenges in the diagnosis of Parkinson's disease', *The Lancet Neurology*, pp. 385–397. Available at: https://doi.org/10.1016/S1474-4422(21)00030-2.

Tripathi, S. *et al.* (2022) 'Clinical Review of Smartphone Applications in Parkinson's Disease', *Neurologist*. Available at: https://doi.org/10.1097/NRL.0000000000000413.

Trivedi, P.C., Bartlett, J.J. and Pulinilkunnil, T. (2020) 'Lysosomal Biology and Function: Modern View of Cellular Debris Bin', *Cells*. Available at: https://doi.org/10.3390/cells9051131.

Trushina, E. (2019) 'Alzheimer's disease mechanisms in peripheral cells: Promises and challenges', *Alzheimer's and Dementia: Translational Research and Clinical Interventions*, 5. Available at: https://doi.org/10.1016/j.trci.2019.06.008.

Tsefou, E. *et al.* (2021) 'Investigation of USP30 inhibition to enhance Parkin-mediated mitophagy: tools and approaches', *Biochemical Journal*, 478(23). Available at: https://doi.org/10.1042/BCJ20210508.

Tsujimura, A. *et al.* (2015) 'Lysosomal enzyme cathepsin B enhances the aggregate forming activity of exogenous α-synuclein fibrils', *Neurobiology of Disease*, 73. Available at: https://doi.org/10.1016/j.nbd.2014.10.011.

Tsunemi, T. and Krainc, D. (2014) 'Zn2+ dyshomeostasis caused by loss of ATP13A2/PARK9 leads to lysosomal dysfunction and alpha-synuclein accumulation', *Human Molecular Genetics*, 23(11). Available at: https://doi.org/10.1093/hmg/ddt572.

Unknown (2025) *Expression Atlas*, *Expression Atlas*. Available at: https://www.ebi.ac.uk/gxa/genes/ensg00000145335?bs=%7B%22homo sapiens%22%3A%5B%22ORGANISM_PART%22%5D%7D&ds=%7B%22kingdom%22%3A%5B%22animals%22%5D%7D#baseline (Accessed: 12 January 2025).

Unknown (no date) *COMBINING SCORES FROM DIFFERENT TESTS 1: COMPOSITES*.

Uversky, V.N., Li, J. and Fink, A.L. (2001) 'Evidence for a Partially Folded Intermediate in α-Synuclein Fibril Formation', *Journal of Biological Chemistry*, 276(14). Available at: https://doi.org/10.1074/jbc.M010907200.

Valente, E.M. *et al.* (2001) 'Localization of a novel locus for autosomal recessive early-onset parkinsonism, PARK6, on human chromosome 1p35-p36', *American Journal of Human Genetics*, 68(4). Available at: https://doi.org/10.1086/319522.

van Veen, S. *et al.* (2020) 'ATP13A2 deficiency disrupts lysosomal polyamine export', *Nature*, 578(7795), pp. 419–424. Available at: https://doi.org/10.1038/s41586-020-1968-7.

Velseboer, D.C. *et al.* (2016) 'Development and external validation of a prognostic model in newly diagnosed Parkinson disease', *Neurology*, 86(11). Available at: https://doi.org/10.1212/WNL.0000000000002437.

Viel, C. *et al.* (2021) 'Preclinical pharmacology of glucosylceramide synthase inhibitor venglustat in a GBA-related synucleinopathy model', *Scientific Reports*, 11(1). Available at: https://doi.org/10.1038/s41598-021-00404-5.

Wang, S., Liang, Y. and Dai, C. (2022) 'Metabolic Regulation of Fibroblast Activation and Proliferation during Organ Fibrosis', *Kidney Diseases*. Available at: https://doi.org/10.1159/000522417.

Wang, X. *et al.* (2012) 'LRRK2 regulates mitochondrial dynamics and function through direct interaction with DLP1', *Human Molecular Genetics*, 21(9). Available at: https://doi.org/10.1093/hmg/dds003.

Wang, Y. and McLean, A.S. (2022) 'The Role of Mitochondria in the Immune Response in Critical Illness', *Critical Care*. Available at: https://doi.org/10.1186/s13054-022-03908-2.

Ward, M.W. (2010) 'Quantitative analysis of membrane potentials.', *Methods in molecular biology (Clifton, N.J.)*, 591. Available at: https://doi.org/10.1007/978-1-60761-404-3_20.

Watabe, S. and Yago, N. (1983) 'Phospholipids activate cathepsin D', *Biochemical and Biophysical Research Communications*, 110(3). Available at: https://doi.org/10.1016/0006-291X(83)91052-5.

Werle, B. *et al.* (1997) 'Cathepsin B fraction active at physiological pH of 7.5 is of prognostic significance in squamous cell carcinoma of human lung', *British Journal of Cancer*, 75(8). Available at: https://doi.org/10.1038/bjc.1997.196.

Westenberger, A. *et al.* (2024) 'Relevance of genetic testing in the gene-targeted trial era: the Rostock Parkinson's disease study', *Brain*, 147, p. 131. Available at: https://doi.org/10.1093/brain/awae188.

Wiedemann, F.R. *et al.* (1999) 'Detection of respiratory chain defects in cultivated skin fibroblasts and skeletal muscle of patients with Parkinson's disease', in *Annals of the New York Academy of Sciences*. Available at: https://doi.org/10.1111/j.1749-6632.1999.tb07870.x.

Wiesen, J. (2006) *Benefits, Drawbacks, and Pitfalls of z-Score Weighting*. Available at: http://annex.ipacweb.org/library/conf/06/wiesen.pdf (Accessed: 11 January 2025).

Wijeyekoon, R.S. *et al.* (2020) 'Cerebrospinal Fluid Cytokines and Neurodegeneration-Associated Proteins in Parkinson's Disease', *Movement Disorders*, 35(6). Available at: https://doi.org/10.1002/mds.28015.

Williams-Gray, C.H. *et al.* (2016) 'Serum immune markers and disease progression in an incident Parkinson's disease cohort (ICICLE-PD)', *Movement Disorders*, 31(7). Available at: https://doi.org/10.1002/mds.26563.

Willmann, C.A. *et al.* (2013) 'To Clone or Not to Clone? Induced Pluripotent Stem Cells Can Be Generated in Bulk Culture', *PLoS ONE*, 8(5). Available at:

https://doi.org/10.1371/journal.pone.0065324.

Wilson, G.R. *et al.* (2014) 'Mutations in RAB39B cause X-linked intellectual disability and early-onset parkinson disease with α-synuclein pathology', *American Journal of Human Genetics*, 95(6), pp. 729–735. Available at: https://doi.org/10.1016/j.ajhg.2014.10.015.

Winkler-Stuck, K. *et al.* (2004) 'Effect of coenzyme Q10 on the mitochondrial function of skin fibroblasts from Parkinson patients', *J Neurol Sci*, 220(1–2), pp. 41–48. Available at: https://doi.org/10.1016/j.jns.2004.02.003.

Wong, Y.C. *et al.* (2019) 'Regulation and Function of Mitochondria–Lysosome Membrane Contact Sites in Cellular Homeostasis', *Trends in Cell Biology*. Available at: https://doi.org/10.1016/j.tcb.2019.02.004.

Wong, Y.C., Ysselstein, D. and Krainc, D. (2018) 'Mitochondria-lysosome contacts regulate mitochondrial fission via RAB7 GTP hydrolysis', *Nature*, 554(7692). Available at: https://doi.org/10.1038/nature25486.

Wu, D.C. *et al.* (2003) 'NADPH oxidase mediates oxidative stress in the 1-methyl-4-phenyl-1,2,3,6-tetrahydropyridine model of Parkinson's disease', *Proc Natl Acad Sci U S A*, 100(10), pp. 6145–6150. Available at: https://doi.org/10.1073/pnas.0937239100.

Wu, K.P. *et al.* (2009) 'Structural reorganization of alpha-synuclein at low pH observed by NMR and REMD simulations', *J Mol Biol*, 391(4), pp. 784–796. Available at: https://doi.org/10.1016/j.jmb.2009.06.063.

Wu, Y. *et al.* (2023) 'Cathepsin B abundance, activity and microglial localisation in Alzheimer's disease-Down syndrome and early onset Alzheimer's disease; the role of elevated cystatin B', *Acta Neuropathologica Communications*, 11(1). Available at: https://doi.org/10.1186/s40478-023-01632-8.

Xilouri, M. *et al.* (2009) 'Abberant α-synuclein confers toxicity to neurons in part through inhibition of chaperone-mediated autophagy', *PLoS ONE*, 4(5). Available at: https://doi.org/10.1371/journal.pone.0005515.

Xu, H. and Ren, D. (2015) 'Lysosomal physiology', *Annual Review of Physiology*, 77. Available at: https://doi.org/10.1146/annurev-physiol-021014-071649.

Xu, M. *et al.* (2014) 'Abstract 537: Rgulation of ALG-2 in NAADP-induced Ca2+ Release via TRP-ML1 Channel in Mouse Coronary Arterial Myocytes', *Hypertension*, 64(suppl_1). Available at: https://doi.org/10.1161/hyp.64.suppl_1.537.

Yadati, T. *et al.* (2020) 'The Ins and Outs of Cathepsins: Physiological Function and Role in Disease Management', *Cells*. Available at: https://doi.org/10.3390/cells9071679.

Yadavalli, N. and Ferguson, S.M. (2023) 'LRRK2 suppresses lysosome degradative activity in macrophages and microglia through MiT-TFE transcription factor inhibition', *Proceedings of the National Academy of Sciences of the United States of America*, 120(31). Available at: https://doi.org/10.1073/pnas.2303789120.

Yahalom, G. *et al.* (2019) 'Carriers of both GBA and LRRK2 mutations, compared to carriers of either, in Parkinson's disease: Risk estimates and genotype-phenotype correlations', *Parkinsonism and Related Disorders*, 62. Available at: https://doi.org/10.1016/j.parkreldis.2018.12.014.

Yamashiro, D.J. and Maxfield, F.R. (1984) 'Acidification of endocytic compartments and the intracellular pathways of ligands and receptors', *Journal of Cellular Biochemistry*. Available at: https://doi.org/10.1002/jcb.240260404.

Yang, C. *et al.* (2014) 'Glutamine oxidation maintains the TCA cycle and cell survival during impaired mitochondrial pyruvate transport', *Molecular Cell*, 56(3). Available at: https://doi.org/10.1016/j.molcel.2014.09.025.

Yang, C. and Wang, X. (2021) 'Lysosome biogenesis: Regulation and functions', *Journal of Cell Biology*. Available at: https://doi.org/10.1083/jcb.202102001.

Yang, S. yu *et al.* (2020) 'Glucocerebrosidase activity, cathepsin D and monomeric α-synuclein interactions in a stem cell derived neuronal model of a PD associated GBA1 mutation', *Neurobiology of Disease*, 134. Available at: https://doi.org/10.1016/j.nbd.2019.104620.

Yokoyama, K. *et al.* (2003) 'Rotation of the Proteolipid Ring in the V-ATPase', *Journal of Biological Chemistry*, 278(27). Available at: https://doi.org/10.1074/jbc.M303104200.

Yoon, M.C. *et al.* (2023) 'Distinct Cleavage Properties of Cathepsin B Compared to Cysteine Cathepsins Enable the Design and Validation of a Specific Substrate for Cathepsin B over a Broad pH Range', *Biochemistry*, 62(15). Available at: https://doi.org/10.1021/acs.biochem.3c00139.

Yoshimori, T. *et al.* (1991) 'Bafilomycin A1, a specific inhibitor of vacuolar-type H+-ATPase, inhibits acidification and protein degradation in lysosomes of cultured cells', *Journal of Biological Chemistry*, 266(26), pp. 17707–17712. Available at: https://doi.org/10.1016/s0021-9258(19)47429-2.

Yoshino, H. *et al.* (1992) 'Mitochondrial complex I and II activities of lymphocytes and platelets in Parkinson's disease', *Journal of Neural Transmission - Parkinson's Disease and Dementia Section*, 4(1). Available at: https://doi.org/10.1007/BF02257619.

Ysselstein, D. *et al.* (2021) 'Evaluation of Strategies for Measuring Lysosomal Glucocerebrosidase Activity', *Movement Disorders*. Available at: https://doi.org/10.1002/mds.28815.

Yusufujiang, A., Zeng, S. and Li, H. (2024) 'Cathepsins and Parkinson's disease: insights from Mendelian randomization analyses', *Frontiers in Aging Neuroscience*, 16. Available at: https://doi.org/10.3389/fnagi.2024.1380483.

Zanellati, M.C. *et al.* (2015) 'Mitochondrial dysfunction in Parkinson disease: evidence in mutant PARK2 fibroblasts', *Front Genet*, 6, p. 78. Available at: https://doi.org/10.3389/fgene.2015.00078.

Zarranz, J.J. *et al.* (2004) 'The New Mutation, E46K, of α-Synuclein Causes Parkinson and Lewy Body Dementia', *Annals of Neurology*, 55(2). Available at: https://doi.org/10.1002/ana.10795.

Zhang, P. *et al.* (2016) 'Cdk5-Dependent Activation of Neuronal Inflammasomes in Parkinson's Disease', *Movement Disorders*, 31(3). Available at: https://doi.org/10.1002/mds.26488.

Zhang, Y. *et al.* (2023) 'The Glutaminase-1 Inhibitor [11C-carbony]BPTES: Synthesis and Positron Emission Tomography Study in Mice', *Pharmaceuticals*, 16(7). Available at: https://doi.org/10.3390/ph16070963.

Zhang, Z.W. *et al.* (2011) 'Red blood cell extrudes nucleus and mitochondria against oxidative stress', *IUBMB Life*, 63(7), pp. 560–565. Available at: https://doi.org/10.1002/iub.490.

Zhao, R.Z. *et al.* (2019) 'Mitochondrial electron transport chain, ROS generation and uncoupling (Review)', *International Journal of Molecular Medicine*, pp. 3–15. Available at: https://doi.org/10.3892/ijmm.2019.4188.

Zhou, R. *et al.* (2011) 'A role for mitochondria in NLRP3 inflammasome activation', *Nature*, 469(7329), pp. 221–225. Available at: https://doi.org/10.1038/nature09663.

Zimprich, A. *et al.* (2004) 'Mutations in LRRK2 cause autosomal-dominant parkinsonism with pleomorphic pathology', *Neuron*, 44(4). Available at: https://doi.org/10.1016/j.neuron.2004.11.005.

Zimprich, A. *et al.* (2011) 'A mutation in VPS35, encoding a subunit of the retromer complex, causes late-onset parkinson disease', *American Journal of Human Genetics*, 89(1), pp. 168–175. Available at: https://doi.org/10.1016/j.ajhg.2011.06.008.

Appendix

Appendix 1

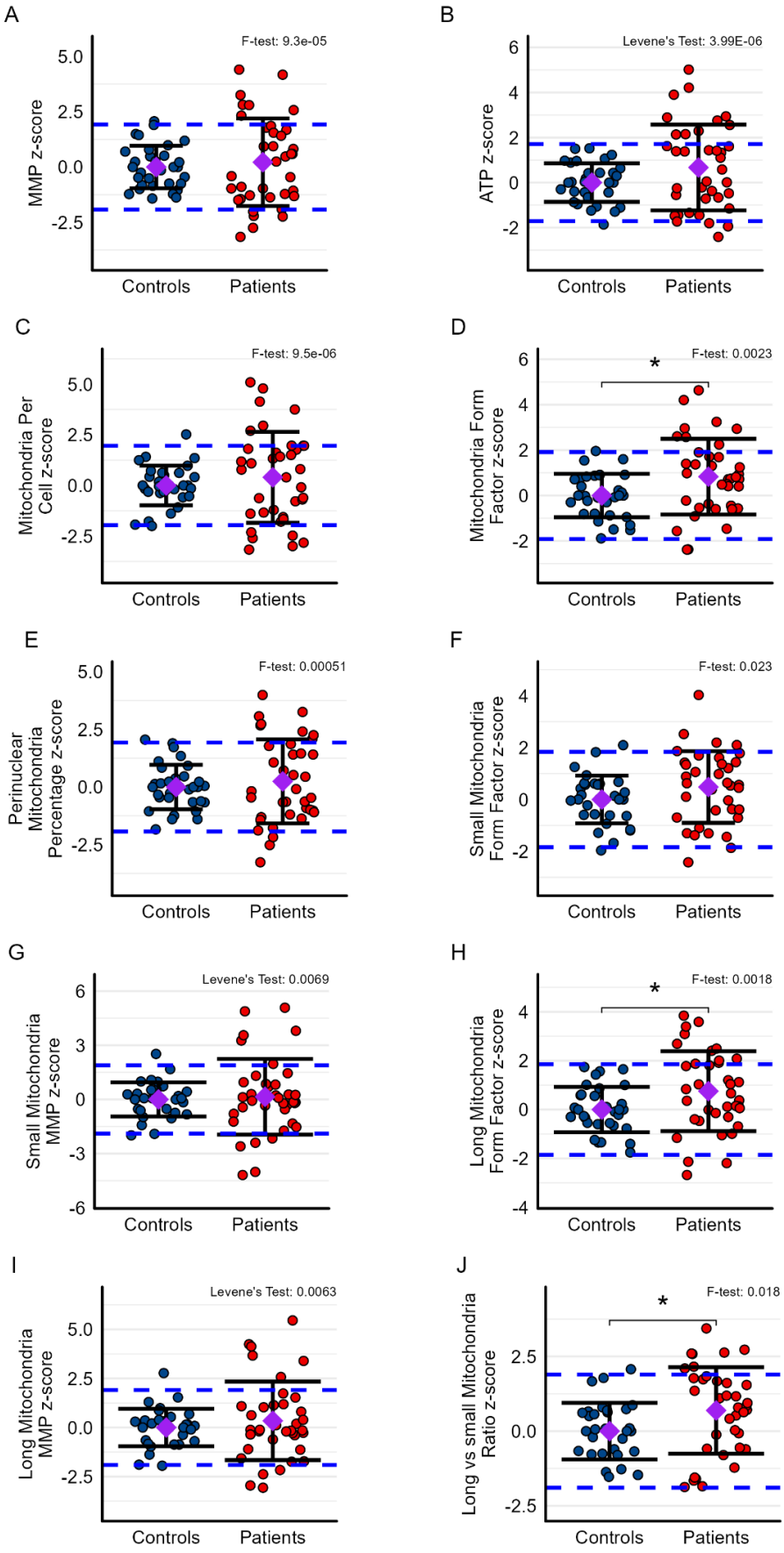

Figure 118: A comparison of the patient and control populations mitochondrial phenotype composite z-scores calculated by combining the composite z-scores three biological repeats in glucose media. A) MMP, **B)** ATP, **C)** Number of mitochondria per cell, **D)** Mitochondrial form factor, **E)** The percentage of mitochondria in the perinuclear region, **F)** Form factor for the small mitochondria population, **G)** MMP for the small mitochondria population, **H)** Form factor for the long mitochondria population, **I)** MMP for the long mitochondria population, **J)** Long vs small mitochondria ratio. Each point represents the mean z-score of three biological repeats for each cell line, these were calculated from the normalised data corrected for variation between repeats and using the whole control population. The normality of the control population (blue) and patient population (red) were assessed using the Shapiro-Wilks normality test. The means of each population (purple diamond) were compared using an unpaired T-test with Welch's correction if normally distributed or by a Mann-Whitney U test if non-normally distributed, significance is depicted by significance symbols (* $p < 0.05$). The difference in variance within each population was assessed using an F-test for normally distributed parameters or a Levene's test for non-normally distributed data ($p < 0.05$). The blue dotted line depicts two standard deviations from the mean for the control population.

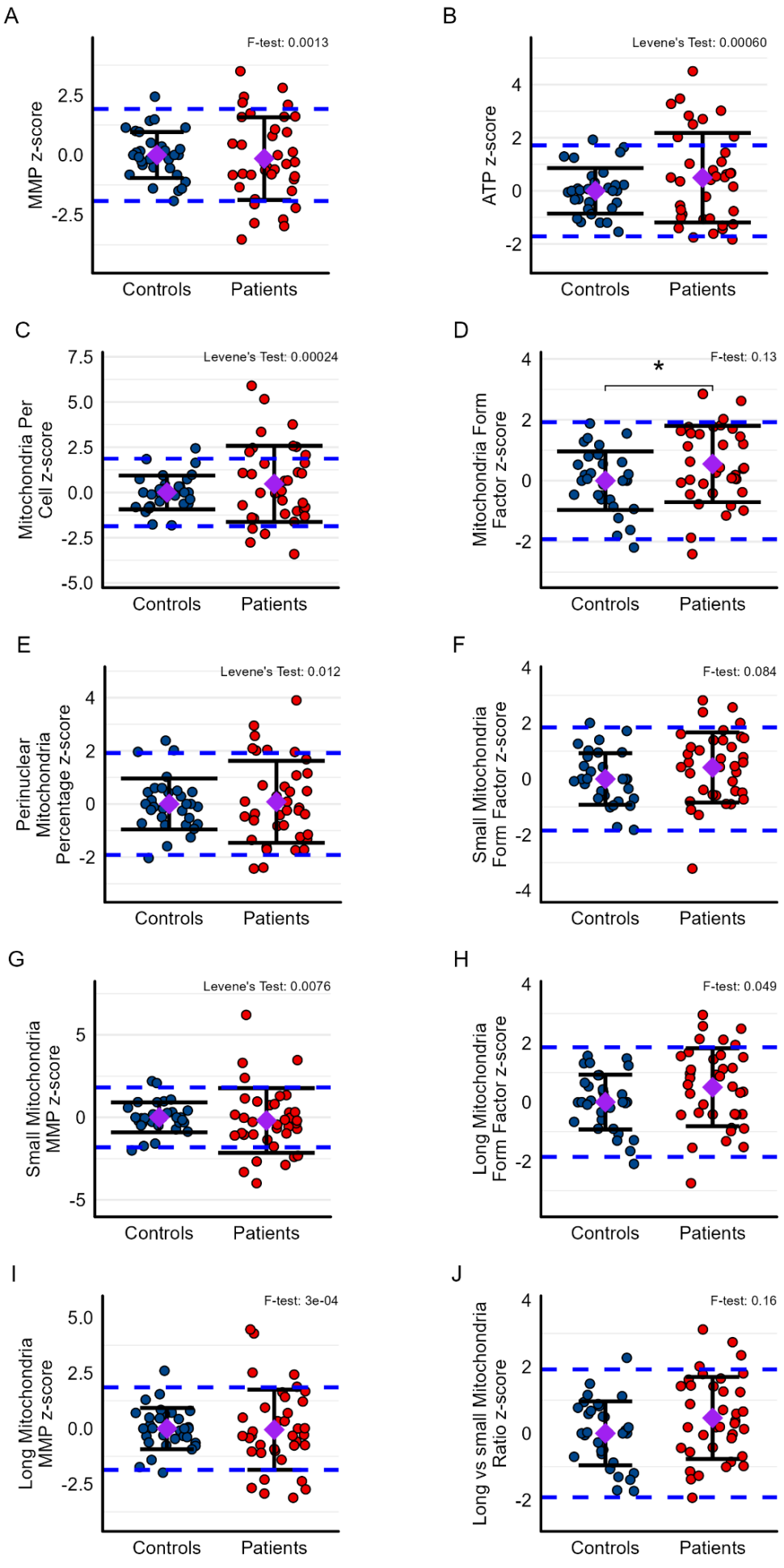
A
F-test: 0.0013
MMP z-score
2.5
0.0
-2.5
Controls
Patients
B
Levene's Test: 0.00060
ATP z-score
4
2
0
-2
Controls
Patients
C
Levene's Test: 0.00024
Mitochondria Per Cell z-score
7.5
5.0
2.5
0.0
-2.5
-5.0
Controls
Patients
D
F-test: 0.13
*
Mitochondria Form Factor z-score
4
2
0
-2
Controls
Patients
E
Levene's Test: 0.012
Perinuclear Mitochondria Percentage z-score
4
2
0
-2
Controls
Patients
F
F-test: 0.084
Small Mitochondria Form Factor z-score
4
2
0
-2
-4
Controls
Patients
G
Levene's Test: 0.0076
Small Mitochondria MMP z-score
5
0
-5
Controls
Patients
H
F-test: 0.049
Long Mitochondria Form Factor z-score
4
2
0
-2
Controls
Patients
I
F-test: 3e-04
Long Mitochondria MMP z-score
5.0
2.5
0.0
-2.5
Controls
Patients
J
F-test: 0.16
Long vs small Mitochondria Ratio z-score
4
2
0
-2
Controls
Patients

Figure 119: A comparison of the patient and control populations mitochondrial phenotype composite z-scores calculated by combining the composite z-scores three biological repeats in galactose media. A) MMP, **B)** ATP, **C)** Number of mitochondria per cell, **D)** Mitochondrial form factor, **E)** The percentage of mitochondria in the perinuclear region, **F)** Form factor for the small mitochondria population, **G)** MMP for the small mitochondria population, **H)** Form factor for the long mitochondria population, **I)** MMP for the long mitochondria population, **J)** Long vs small mitochondria ratio. Each point represents the mean z-score of three biological repeats for each cell line, these were calculated from the normalised data corrected for variation between repeats and using the whole control population. The normality of the control population (blue) and patient population (red) were assessed using the Shapiro-Wilks normality test. The means of each population (purple diamond) were compared using an unpaired T-test with Welch's correction if normally distributed or by a Mann-Whitney U test if non-normally distributed, significance is depicted by significance symbols (* $p < 0.05$). The difference in variance within each population was assessed using an F-test for normally distributed parameters or a Levene's test for non-normally distributed data ($p < 0.05$). The blue dotted line depicts two standard deviations from the mean for the control population.

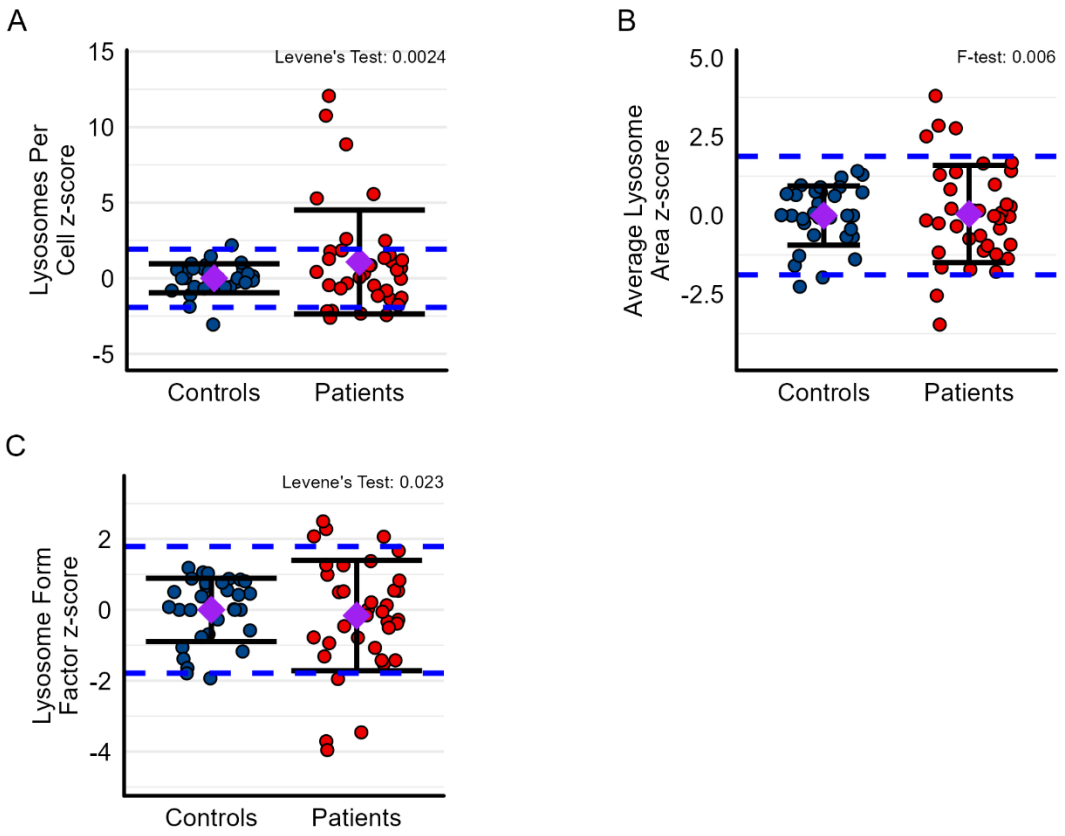

Figure 120: A comparison of the patient and control populations lysosomal phenotype composite z-scores calculated by combining the composite z-scores three biological repeats in glucose media. A) Number of lysosomes per cell, **B)** Average lysosome area, **C)** Lysosomal form factor. Each point represents the mean z-score of three biological repeats for each cell line, these were calculated from the normalised data corrected for variation between repeats and using the whole control population. The normality of the control population (blue) and patient population (red) were assessed using the Shapiro-Wilks normality test. The means of each population (purple diamond) were compared using an unpaired T-test with Welch's correction if normally distributed or by a Mann-Whitney U test if non-normally distributed, significance is depicted by significance symbols (* $p < 0.05$). The difference in variance within each population was assessed using an F-test for normally distributed parameters or a Levene's test for non-normally distributed data ($p < 0.05$). The blue dotted line depicts two standard deviations from the mean for the control population.

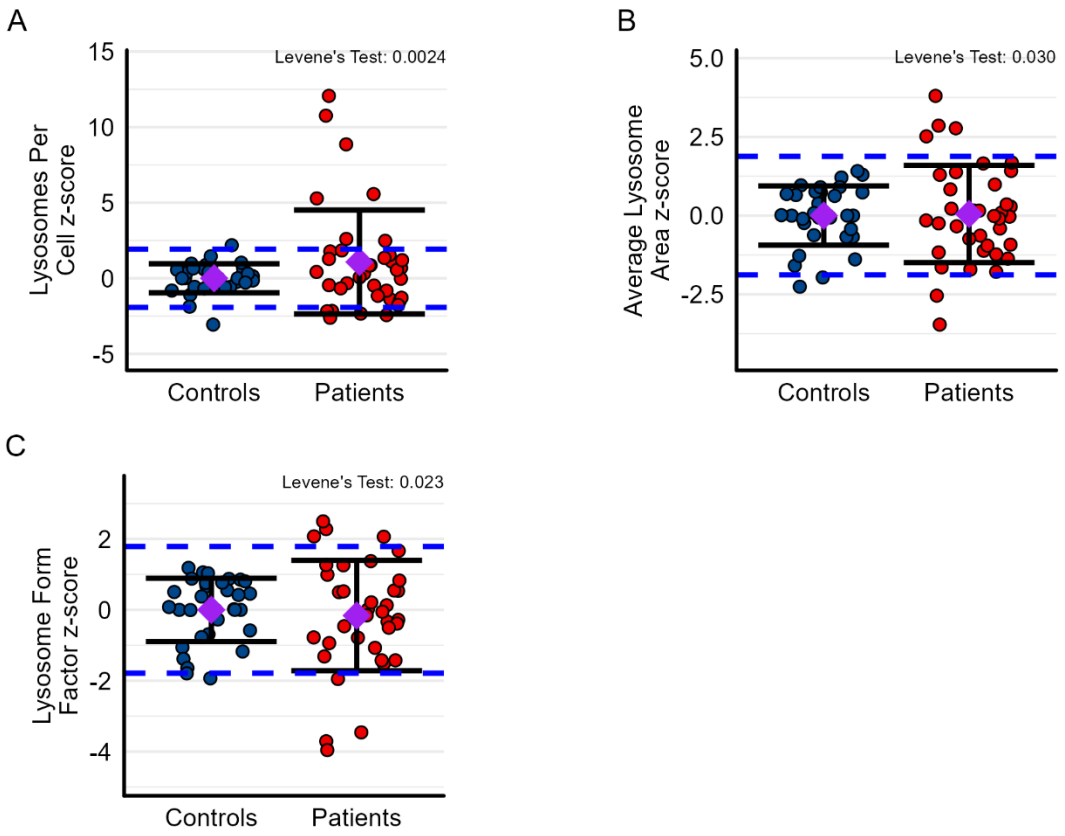

Figure 121: A comparison of the patient and control populations lysosomal phenotype composite z-scores calculated by combining the composite z-scores for glucose and galactose. A) Number of lysosomes per cell, **B)** Average lysosome area, **C)** Lysosomal form factor. Each point represents the mean z-score of three biological repeats for each cell line, these were calculated from the normalised data corrected for variation between repeats and using the whole control population. The normality of the control population (blue) and patient population (red) were assessed using the Shapiro-Wilks normality test. The means of each population (purple diamond) were compared using an unpaired T-test with Welch's correction if normally distributed or by a Mann-Whitney U test if non-normally distributed, significance is depicted by significance symbols (* $p < 0.05$). The difference in variance within each population was assessed using an F-test for normally distributed parameters or a Levene's test for non-normally distributed data ($p < 0.05$). The blue dotted line depicts two standard deviations from the mean for the control population.

Appendix 2

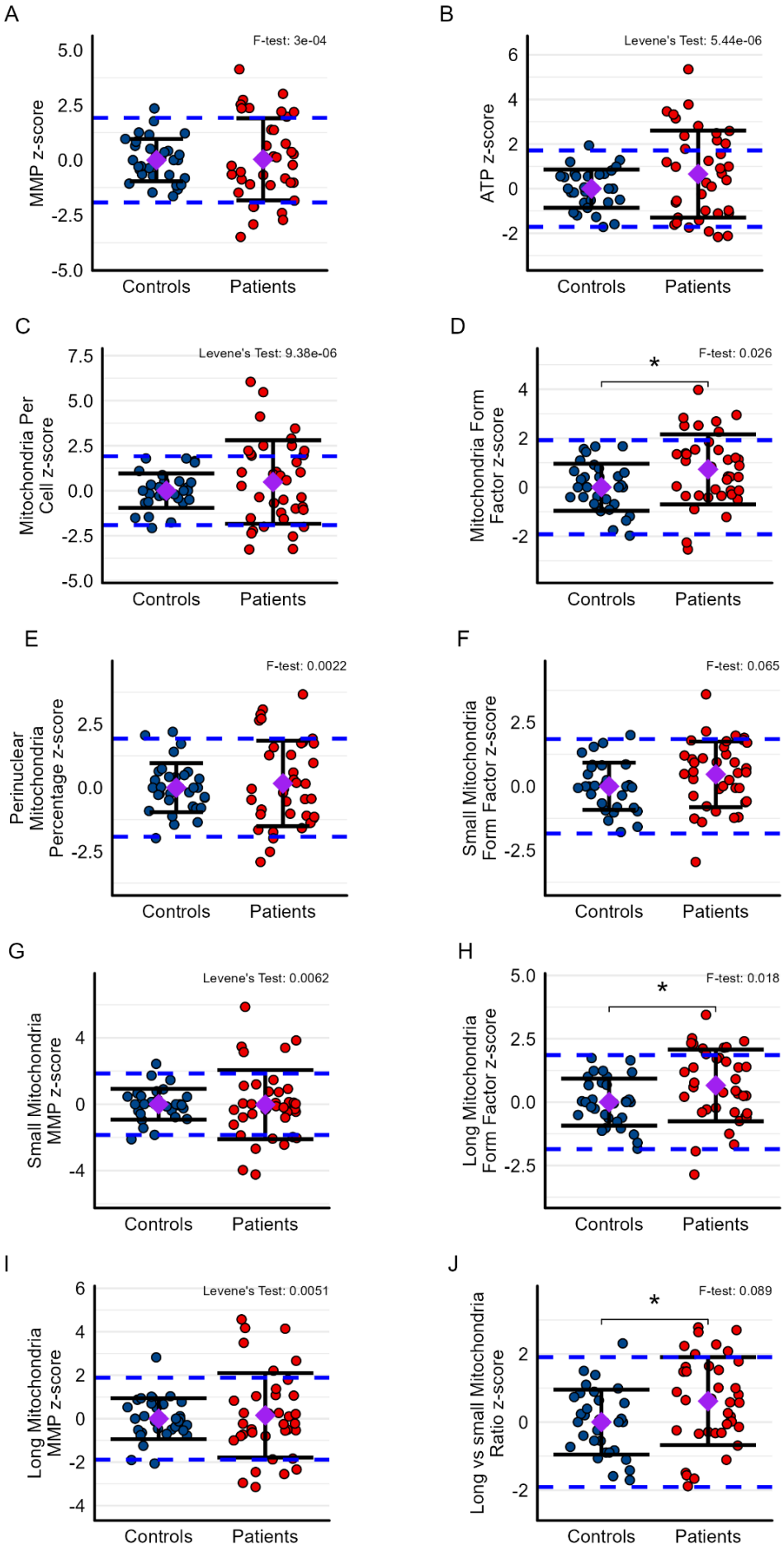
A
F-test: 3e-04
MMP z-score
5.0
2.5
0.0
-2.5
-5.0
Controls
Patients
B
Levene's Test: 5.44e-06
ATP z-score
6
4
2
0
-2
Controls
Patients
C
Levene's Test: 9.38e-06
Mitochondria Per Cell z-score
7.5
5.0
2.5
0.0
-2.5
-5.0
Controls
Patients
D
*
F-test: 0.026
Mitochondria Form Factor z-score
4
2
0
-2
Controls
Patients
E
F-test: 0.0022
Perinuclear Mitochondria Percentage z-score
2.5
0.0
-2.5
Controls
Patients
F
F-test: 0.065
Small Mitochondria Form Factor z-score
2.5
0.0
-2.5
Controls
Patients
G
Levene's Test: 0.0062
Small Mitochondria MMP z-score
4
0
-4
Controls
Patients
H
*
F-test: 0.018
Long Mitochondria Form Factor z-score
5.0
2.5
0.0
-2.5
Controls
Patients
I
Levene's Test: 0.0051
Long Mitochondria MMP z-score
6
4
2
0
-2
-4
Controls
Patients
J
*
F-test: 0.089
Long vs small Mitochondria Ratio z-score
2
0
-2
Controls
Patients

Figure 122: A comparison of the patient and control populations mitochondrial phenotype composite z-scores calculated by combining the composite z-scores for glucose and galactose. A) MMP, **B)** ATP, **C)** Number of mitochondria per cell, **D)** Mitochondrial form factor, **E)** The percentage of mitochondria in the perinuclear region, **F)** Form factor for the small mitochondria population, **G)** MMP for the small mitochondria population, **H)** Form factor for the long mitochondria population, I) MMP for the long mitochondria population, **J)** Long vs small mitochondria ratio. Each point represents the composite z-score for each cell line, these were calculated by combining the composite z-scores for glucose and galactose, correcting for variation between media conditions and using the whole control population. The normality of the control population (blue) and patient population (red) were assessed using the Shapiro-Wilks normality test. The means of each population (purple diamond) were compared using an unpaired T-test with Welch's correction if normally distributed or by a Mann-Whitney U test if non-normally distributed, significance is depicted by significance symbols (* $p < 0.05$). The difference in variance within each population was assessed using an F-test for normally distributed parameters or a Levene's test for non-normally distributed data ($p < 0.05$). The blue dotted line depicts two standard deviations from the mean for the control population.

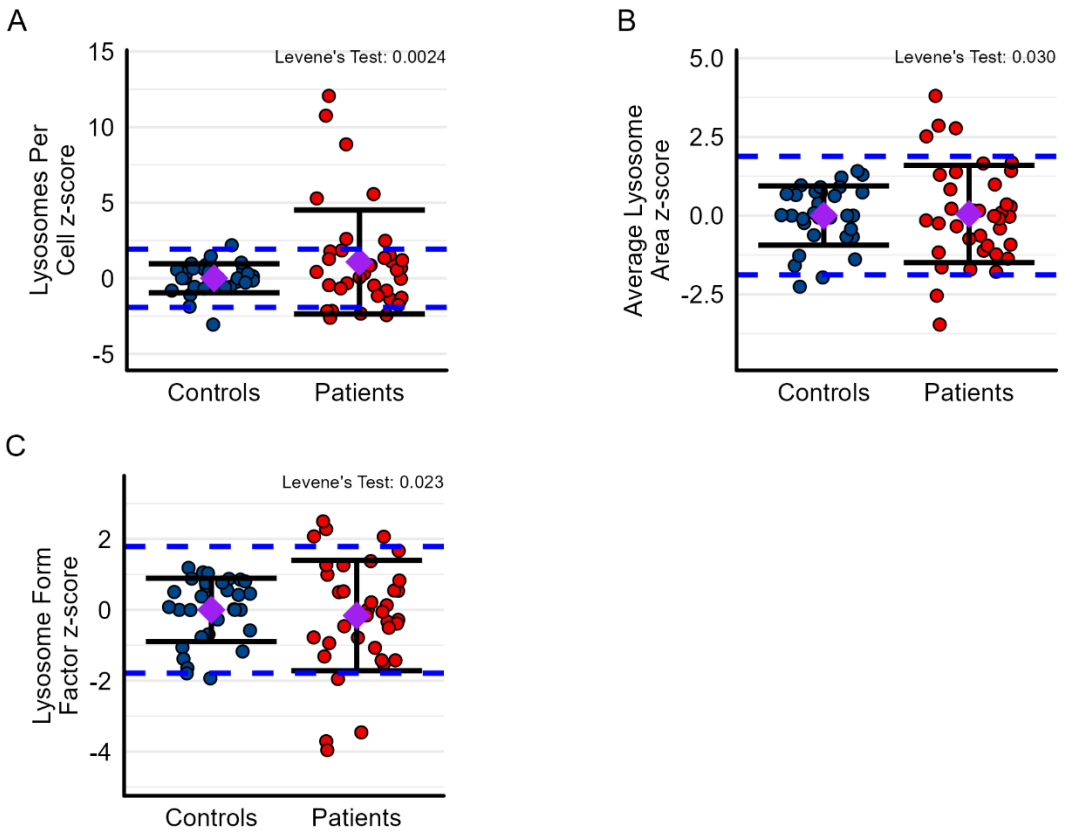

Figure 123: A comparison of the patient and control populations lysosomal phenotype composite z-scores calculated by combining the composite z-scores three biological repeats in glucose media. A) Number of lysosomes per cell, **B)** Average lysosome area, **C)** Lysosomal form factor. Each point represents the mean z-score of three biological repeats for each cell line, these were calculated from the normalised data corrected for variation between repeats and using the whole control population. The normality of the control population (blue) and patient population (red) were assessed using the Shapiro-Wilks normality test. The means of each population (purple diamond) were compared using an unpaired T-test with Welch's correction if normally distributed or by a Mann-Whitney U test if non-normally distributed, significance is depicted by significance symbols (* $p < 0.05$). The difference in variance within each population was assessed using an F-test for normally distributed parameters or a Levene's test for non-normally distributed data ($p < 0.05$). The blue dotted line depicts two standard deviations from the mean for the control population.

Appendix 3

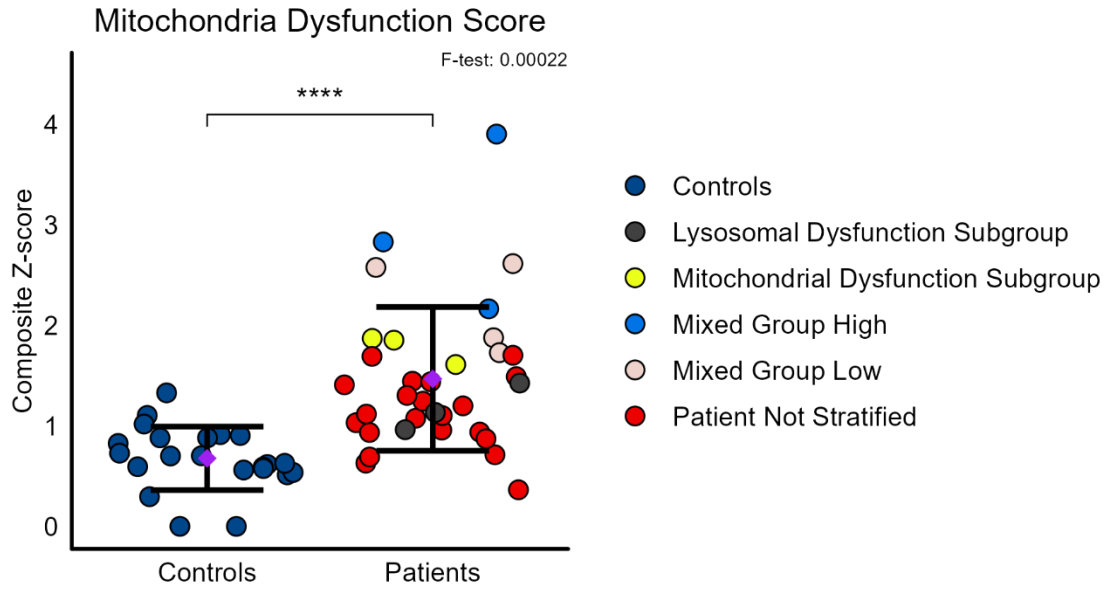

Figure 124: A comparison of the mitochondrial dysfunction composite z-scores for the patient and control populations. Each point represents the composite z-score for mitochondrial dysfunction, showing the stratified groups. The means of each population (purple diamond) were compared using an unpaired T-test with Welch's correction, significance is depicted by significance symbols (**** $p < 0.0001$). The difference in variance within each population was assessed using an F-test ($p < 0.05$). Error bars show standard deviation.

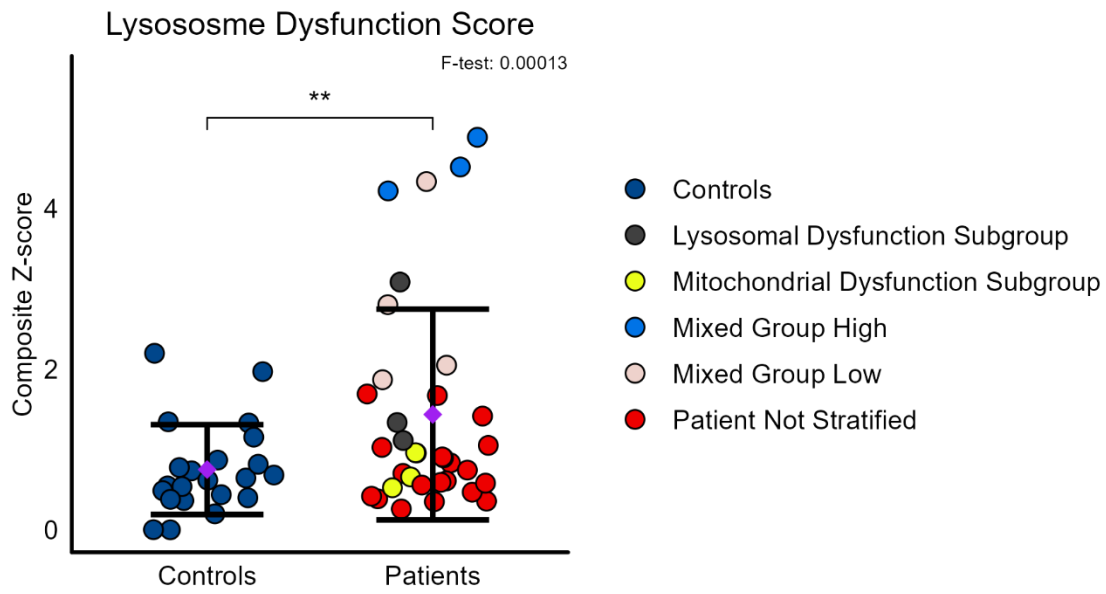

Figure 125: A comparison of the lysosomal dysfunction composite z-scores for the patient and control populations, showing the stratified groups. Each point represents the composite z-score for lysosomal dysfunction. The means of each population (purple diamond) were compared using an unpaired T-test with Welch's correction, significance is depicted by significance symbols (** $p < 0.01$). The difference in variance within each population was assessed using an F-test ($p < 0.05$). Error bars show standard deviation.

Table 31: Composite z-scores for mitochondrial and lysosomal parameters for patient cell lines. z-scores greater than 1 (green), less than -1 (red). Mitochondrial dysfunction scores greater than 1.5 (blue) and lysosomal dysfunction scores greater than 1 (blue). The last two columns show the ranking for mitochondrial or lysosomal dysfunction, the greater the score the worse the dysfunction (worst red, green best).

Subgroup	ID	Status	Group	MMP	ATP	Mitochondria Per Cell	Mitochondria Form Factor	Perinuclear Mitochondria Percentage	Small Mitochondria Form Factor	Small Mitochondria MMP	Long Mitochondria Form Factor	Long Mitochondria MMP	Long vs small Mitochondria Ratio	Composite z-score Mitochondria Dysfunction	Lysosomes Per Cell	Average Lysosome Area	Lysosomes Form Factor Per Cell	Composite z-score Lysososomes Dysfunction	Mitochondrial Dysfunction Ranking	Lysosomal Dysfunction Ranking
Mixed Group Low	ATP001	Patient	13	2.74	-1.30	-2.22	-2.54	3.07	-2.95	5.87	-1.94	4.17	-1.88	2.58	-2.91	-2.66	-2.82	2.80	65	64
	ATP005	Patient	1	4.12	-1.62	-3.26	2.51	2.64	1.06	3.47	2.52	4.57	2.24	2.61	-2.44	-2.39	-1.30	2.04	66	61
	ATP025	Patient	1	3.01	-2.16	-2.54	0.44	1.78	-0.06	3.40	0.91	4.14	0.26	1.88	-2.64	-1.69	-1.26	1.86	63	59
	ATP036	Patient	11	2.35	-0.54	-2.37	1.35	2.71	0.93	3.14	0.77	3.49	1.49	1.73	-3.18	-4.35	-5.45	4.33	60	67
Mixed Group High	ATP017	Patient	2	-2.92	5.35	5.47	3.97	-1.75	3.59	-4.23	3.44	-3.14	2.78	3.90	8.57	3.90	2.16	4.88	69	69
	ATP019	Patient	2	-3.49	3.15	6.04	1.38	-2.92	0.28	-3.97	2.30	-2.95	0.65	2.83	9.26	2.25	2.02	4.51	68	68
	ATP035	Patient	2	-1.48	3.33	2.23	2.83	-1.66	1.79	-1.88	2.33	-0.80	1.48	2.16	7.34	3.12	2.18	4.21	64	66
Lysosomal Dysfunction Subgroup	ATP027	Patient	12	0.16	-1.42	-0.69	1.85	-0.06	0.94	-0.27	1.71	0.07	1.64	0.96	-1.95	-1.32	-0.73	1.33	37	54
	ATP037	Patient	12	0.37	0.38	-0.37	2.95	-0.44	1.90	0.09	2.40	1.06	2.70	1.13	-2.40	-3.11	-3.74	3.08	45	65
	ATP043	Patient	10	-1.02	2.02	1.02	1.20	-1.38	1.81	-1.98	0.24	-1.84	1.00	1.43	-1.22	-0.95	-1.16	1.11	53	49
Mitochondrial Dysfunction Subgroup	ATP034	Patient	6	-1.10	1.78	4.12	1.54	-2.51	1.09	-0.59	2.11	-0.64	2.00	1.87	1.80	0.20	0.87	0.96	62	45
	ATP038	Patient	7	-2.40	2.16	2.50	0.31	-1.59	0.94	-2.44	-0.40	-2.55	-0.06	1.61	1.04	-0.19	-0.74	0.66	57	31
	ATP040	Patient	7	-2.12	3.77	2.50	2.52	-1.99	2.15	-2.68	1.90	-2.46	2.64	2.66	1.42	0.42	-0.14	0.66	67	32
	ATP040	Patient	12	-0.68	2.81	0.92	-0.41	-0.19	-0.98	-0.32	-0.22	-0.80	-0.29	1.04	-0.03	-0.63	-0.50	0.39	40	16
Patient Not Stratified	ATP007	Patient	6	0.65	-0.25	1.04	0.83	-0.54	-0.11	0.76	1.75	0.24	0.68	0.63	0.20	0.20	-2.67	1.02	16	46
	ATP010	Patient	12	0.75	1.55	-1.00	-0.14	0.16	-1.21	0.92	1.37	1.79	0.16	0.96	-0.82	-0.95	-0.72	0.83	36	39
	ATP012	Patient	6	0.27	0.99	1.97	1.14	-1.20	0.70	-0.46	1.39	-0.53	1.78	1.10	0.62	0.35	0.07	0.35	43	12
	ATP014	Patient	2	0.17	1.25	-0.50	1.52	0.60	1.24	0.08	1.60	1.09	1.01	0.94	3.53	0.85	0.62	1.67	33	58
	ATP016	Patient	3	2.52	-0.62	-1.53	-0.36	2.88	-0.37	0.05	0.59	-0.23	-1.49	1.08	-0.71	-0.84	-2.69	1.41	42	56
	ATP020	Patient	3	-2.12	-1.74	-2.00	-0.34	1.59	-0.78	1.20	-0.29	1.04	-0.34	1.25	-0.70	-0.28	-0.09	0.36	48	13
	ATP021	Patient	5	-0.22	-2.12	-0.90	-0.50	1.93	-0.63	-0.29	-0.58	-0.22	-0.69	1.03	-1.61	0.06	-0.43	0.70	39	35
	ATP023	Patient	11	-0.87	-1.54	1.95	-2.26	-0.86	-1.26	1.11	-2.86	0.26	-1.56	1.47	1.64	1.02	0.93	1.20	55	51
	ATP023	Patient	2	-0.65	3.46	1.02	1.35	-0.05	1.20	-0.34	1.19	0.83	0.89	1.42	3.13	1.90	1.51	2.18	52	62
	ATP026	Patient	4	1.97	0.67	1.58	-0.29	-1.10	-0.07	0.13	-0.75	0.10	0.02	0.69	0.84	-0.13	-0.19	0.38	18	15
	ATP028	Patient	1	1.38	0.26	-1.22	2.69	1.29	1.53	1.47	2.15	2.21	2.28	1.44	0.57	-0.62	-0.21	0.47	54	21
	ATP029	Patient	3	-0.83	0.91	3.45	0.43	-0.45	0.52	-0.46	0.33	-0.51	0.58	0.93	1.32	0.03	0.48	0.61	32	28
	ATP030	Patient	4	2.37	2.37	-0.36	-0.90	1.27	-1.40	0.01	-0.40	-0.49	-1.66	1.30	-0.84	0.67	-1.65	1.05	49	47
	ATP031	Patient	1	1.37	-1.92	-1.57	2.27	0.31	1.76	-0.12	2.17	1.37	1.53	1.49	-0.75	-0.61	0.41	0.59	56	26
	ATP032	Patient	6	-0.53	0.98	2.04	1.08	-1.05	0.57	-0.79	1.37	-0.73	1.62	1.12	0.91	-0.22	1.09	0.74	44	36
	ATP033	Patient	11	2.18	-1.07	-2.00	-0.13	1.74	-0.59	3.85	-0.60	2.66	-0.14	1.41	-1.07	0.82	0.98	0.95	51	44
	ATP039	Patient	4	-1.02	-0.98	-1.06	0.42	0.97	0.55	0.03	0.25	0.21	0.81	0.71	-0.20	-0.99	0.54	0.58	22	25
	ATP041	Patient	10	-0.26	1.19	0.26	0.04	-0.47	0.48	-1.23	0.21	-1.00	-0.24	0.61	0.14	-0.01	-0.60	0.25	14	5
	ATP041	Patient	3	-2.72	-1.11	-3.24	1.12	3.66	1.98	-0.80	0.45	-0.55	2.08	1.79	-1.08	-1.28	2.24	1.54	61	57
	ATP046	Patient	8	2.20	2.49	2.89	-1.21	1.75	-1.23	-0.19	-1.67	-0.25	-1.11	1.69	1.48	0.19	-1.05	0.90	58	43
	ATP047	Patient	7	-1.84	2.58	2.22	0.88	-1.15	1.70	-2.04	-0.44	-2.34	0.57	1.70	0.67	0.45	-0.54	0.56	59	24
	ATP048	Parkin (c.337-376del) Patient	10	-1.14	-0.99	0.83	-0.09	-1.02	0.01	-2.08	0.39	-1.87	-0.32	0.87	0.19	0.20	-0.38	0.26	28	6
	ATP049	SNCA G51D Patient	9	0.13	0.09	0.58	-0.35	0.19	0.25	0.73	-1.25	0.26	-0.32	0.36	-0.73	-0.17	-0.35	0.42	5	19

Table 32: Composite z-scores for mitochondrial and lysosomal parameters for control cell lines. z-scores greater than 1 (green), less than -1 (red). Mitochondrial dysfunction scores greater than 1.5 (blue) and lysosomal dysfunction scores greater than 1 (blue). The last two columns show the ranking for mitochondrial or lysosomal dysfunction, the greater the score the worse the dysfunction (worst red, green best).

Subgroup	ID	Status	Group	MMP	ATP	Mitochondria Per Cell	Mitochondria Form Factor	Perinuclear Mitochondria Percentage	Small Mitochondria Form Factor	Small Mitochondria MMP	Long Mitochondria Form Factor	Long Mitochondria MMP	Long vs small Mitochondria Ratio	Composite z-score Mitochondria Dysfunction	Lysosomes Per Cell	Average Lysosome Area	Lysosomes Form Factor Per Cell	Composite z-score Lysososomes Dysfunction	Mitochondrial Dysfunction Ranking	Lysosomal Dysfunction Ranking
Control	ATP002	Control	2	-0.67	0.66	0.52	-0.69	-0.18	-0.35	-0.39	-0.61	-0.50	-0.83	0.56	1.59	1.24	1.15	1.33	8	53
	ATP003	Control	3	0.11	-1.27	-1.76	-0.49	1.72	-1.02	0.90	-0.05	0.66	-0.89	1.00	-0.69	-0.34	-0.77	0.60	38	27
	ATP003	Control	7	0.65	1.20	-0.68	1.09	0.29	0.47	0.66	1.00	0.87	0.85	0.83	0.09	-1.42	-1.09	0.87	27	41
	ATP004	Control	1	-0.82	-0.49	1.64	-1.97	-0.39	-1.58	0.45	-1.84	-0.29	-1.71	1.05	-0.19	0.65	-0.04	0.29	41	8
	ATP004	Control	3	1.22	1.28	1.57	-1.18	-0.36	-0.98	-0.90	-1.60	-0.77	-1.42	1.16	0.19	0.94	-0.17	0.43	46	20
	ATP006	Control	3	-1.33	-0.01	0.19	1.67	-1.36	2.00	-0.01	1.65	0.12	2.31	0.93	0.50	-0.61	0.94	0.68	31	34
	ATP006	Control	4	2.35	0.07	0.51	0.42	-1.45	0.08	0.77	1.00	0.50	0.07	0.61	0.43	0.75	-0.71	0.63	13	29
	ATP006	Control	8	0.00	0.00	0.00	0.00	0.00	0.00	0.00	0.00	0.00	0.00	0.00	0.00	0.00	0.00	0.00	2.5	2.5
	ATP008	Control	1	-0.43	0.67	-0.18	0.41	-0.25	0.83	-0.94	0.10	-0.65	0.20	0.47	1.01	1.11	1.20	1.11	6	48
	ATP008	Control	4	-1.64	-0.61	-0.67	0.44	-0.74	0.86	-0.77	0.02	-0.37	0.99	0.71	-0.14	-0.69	0.16	0.33	21	11
	ATP008	Control	6	0.83	-0.17	1.79	0.32	-1.98	0.00	-0.40	0.67	-0.52	0.24	0.67	0.64	0.64	-1.39	0.89	17	42
	ATP009	Control	2	0.52	-0.14	-0.25	1.66	-0.23	1.69	0.13	1.24	0.96	1.38	0.70	0.88	0.87	0.85	0.87	20	40
	ATP013	Control	1	1.26	-0.18	-1.46	1.56	0.64	0.75	0.50	1.74	0.94	1.50	0.94	-0.82	-1.76	-1.16	1.25	34	52
	ATP013	Control	4	-0.71	0.55	0.16	-0.86	2.19	-0.94	0.00	-1.02	-0.12	-1.06	0.75	-0.29	-0.05	0.55	0.30	24	9
	ATP013	Control	7	-1.07	0.52	1.09	0.66	-0.91	1.32	-2.11	0.03	-1.90	0.74	0.95	0.37	0.29	0.26	0.31	35	10
	ATP015	Control	11	-0.36	-0.63	0.20	0.92	-0.49	0.82	0.14	0.77	0.70	0.89	0.59	0.46	-0.24	-0.50	0.40	11	18
	ATP015	Control	13	0.00	0.00	0.00	0.00	0.00	0.00	0.00	0.00	0.00	0.00	0.00	0.00	0.00	0.00	0.00	2.5	2.5
	ATP018	Control	2	0.16	-0.52	-0.27	-0.97	0.41	-1.34	0.26	-0.62	-0.46	-0.55	0.54	-2.47	-2.11	-2.00	2.19	7	63
	ATP022	Control	5	0.00	0.00	0.00	0.00	0.00	0.00	0.00	0.00	0.00	0.00	0.00	0.00	0.00	0.00	0.00	2.5	2.5
	ATP042	Control	6	0.96	0.56	-1.51	-0.40	2.06	-0.06	0.46	-0.51	0.53	-0.73	0.80	-0.63	0.14	0.07	0.28	25	7
	ATP042	Control	7	0.42	-1.72	-0.41	-1.75	0.62	-1.79	1.46	-1.04	1.03	-1.59	1.23	-0.46	1.13	0.83	0.81	47	37
	ATP044	Control	6	-0.64	-1.20	-2.07	0.00	0.74	0.02	0.01	-0.26	0.12	0.39	0.70	-0.65	-0.30	0.98	0.64	19	30
	ATP045	Control	6	-1.15	0.81	1.79	0.08	-0.81	0.04	-0.07	0.10	-0.12	0.10	0.59	0.64	-0.48	0.33	0.49	12	22
	ATP050	Control	9	0.00	0.00	0.00	0.00	0.00	0.00	0.00	0.00	0.00	0.00	0.00	0.00	0.00	0.00	0.00	2.5	2.5
	ATP051	Control	12	-1.12	0.99	0.46	-1.36	-0.79	-0.84	-0.24	-1.28	-0.54	-1.10	0.88	0.14	0.78	0.69	0.54	29	23
	ATP052	Control	11	0.36	0.63	-0.20	-0.92	0.49	-0.82	-0.14	-0.77	-0.70	-0.89	0.59	-0.46	0.24	0.50	0.40	10	17
	ATP053	Control	12	-0.27	0.55	0.34	1.44	0.02	1.54	-1.44	1.23	-1.25	1.10	0.83	0.78	0.09	0.27	0.38	26	14
	ATP054	Control	12	0.24	-1.59	-0.50	0.60	0.35	-0.04	-0.05	1.18	0.77	0.56	0.73	-0.54	-1.66	-1.82	1.34	23	55
	ATP055	Control	10	-1.47	-0.86	0.87	-0.37	-1.12	0.07	-1.85	-0.49	-2.06	-0.24	0.90	0.66	1.03	0.75	0.82	30	38
	ATP056	Control	12	1.16	0.06	-0.29	-0.68	0.43	-0.66	1.73	-1.13	1.02	-0.55	0.63	-0.38	0.79	0.87	0.68	15	33
	ATP057	Control	10	1.77	1.94	-0.24	0.77	1.41	0.24	2.43	0.68	2.82	0.64	1.33	1.71	0.80	0.94	1.15	50	50
	ATP058	Control	10	-0.30	-1.07	-0.62	-0.40	-0.28	-0.31	-0.58	-0.19	-0.76	-0.40	0.58	-2.37	-1.83	-1.70	1.97	9	60

Appendix 4

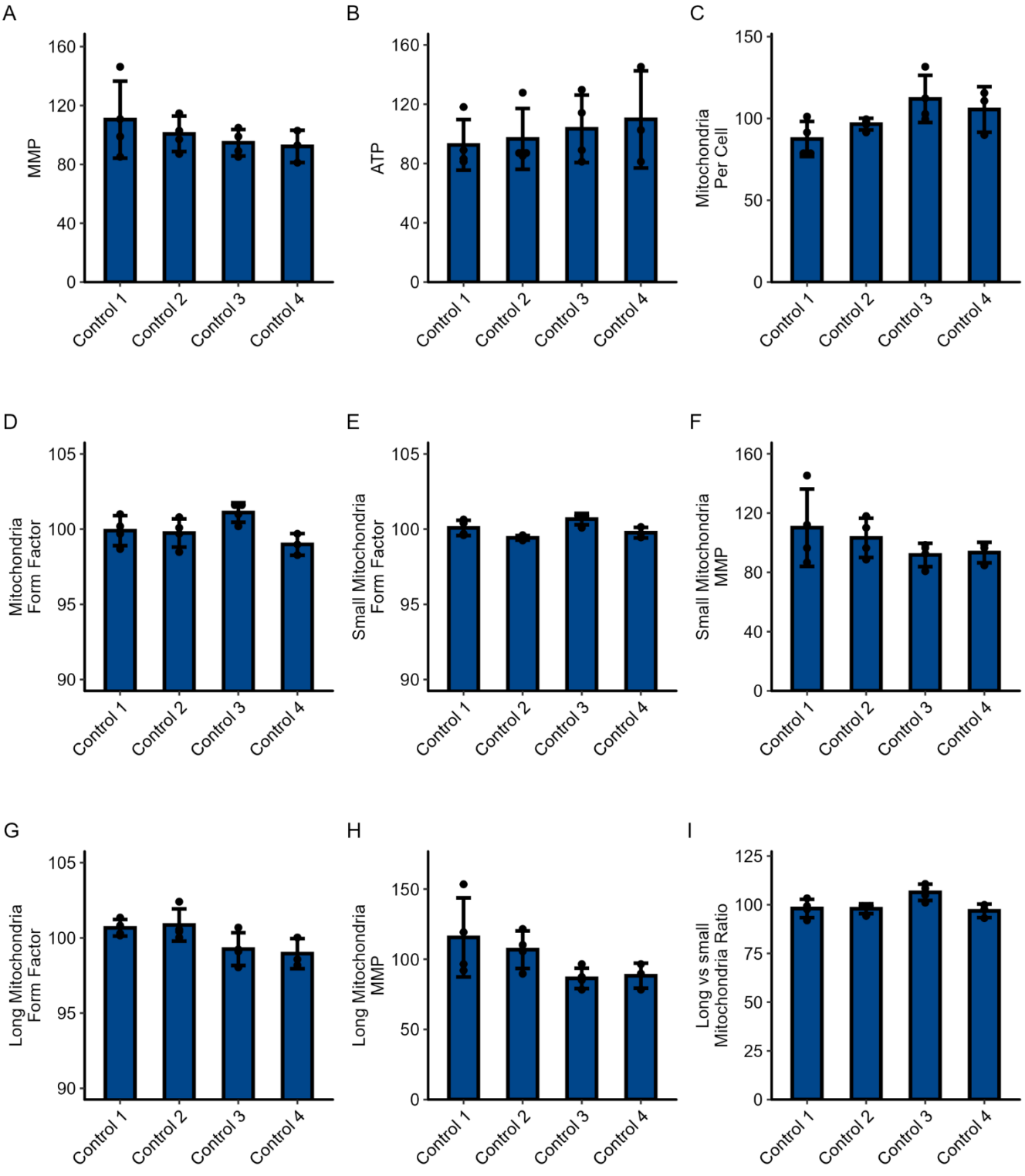
A
MMP
160
120
80
40
0
Control 1
Control 2
Control 3
Control 4
B
ATP
160
120
80
40
0
Control 1
Control 2
Control 3
Control 4
C
Mitochondria Per Cell
150
100
50
0
Control 1
Control 2
Control 3
Control 4
D
Mitochondria Form Factor
105
100
95
90
Control 1
Control 2
Control 3
Control 4
E
Small Mitochondria Form Factor
105
100
95
90
Control 1
Control 2
Control 3
Control 4
F
Small Mitochondria MMP
160
120
80
40
0
Control 1
Control 2
Control 3
Control 4
G
Long Mitochondria Form Factor
105
100
95
90
Control 1
Control 2
Control 3
Control 4
H
Long Mitochondria MMP
150
100
50
0
Control 1
Control 2
Control 3
Control 4
I
Long vs small Mitochondria Ratio
125
100
75
50
25
0
Control 1
Control 2
Control 3
Control 4

Figure 126: A comparison of the mitochondrial phenotypes of the four controls used to assess the familial PD patients in high glucose media. A) MMP, **B)** ATP, **C)** Number of mitochondria per cell, **D)** Mitochondrial form factor, **E)** Form factor for the small mitochondria population, **F)** MMP for the small mitochondria population, **G)** Form factor for the long mitochondria population, **H)** MMP for the long mitochondria population, **I)** Long vs small mitochondria ratio. Controls (blue), Parkin patients (grey). Data was normalised to the average of the age- and sex-matched control per repeat and error bars show standard deviation (n = 3/4). The means of each patient were compared to the corresponding age- and sex-matched control by a one-way ANOVA (* $p < 0.05$).

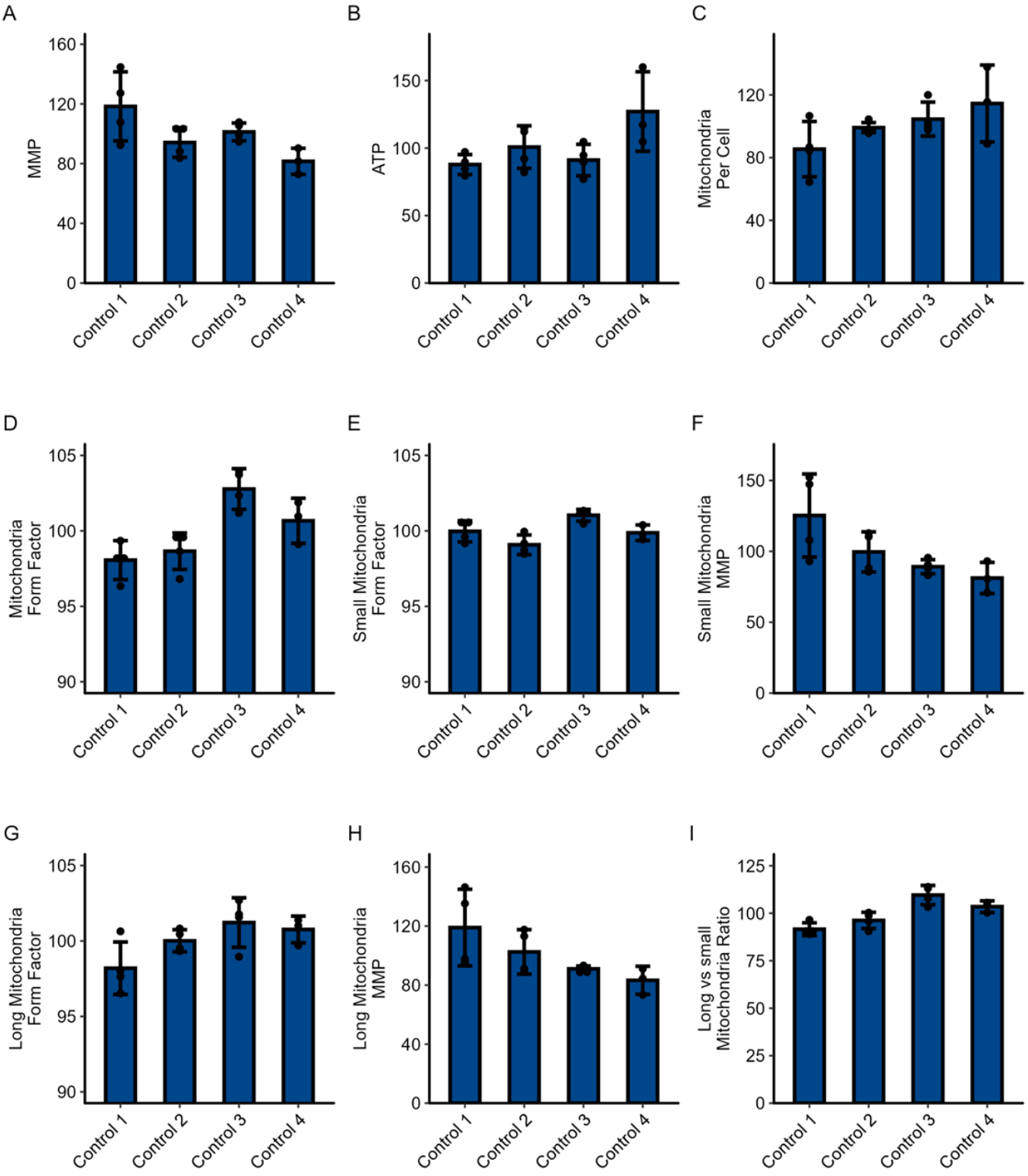
A
MMP
160
120
80
40
0
Control 1
Control 2
Control 3
Control 4
B
ATP
150
100
50
0
C
Mitochondria Per Cell
120
80
40
0
D
Mitochondria Form Factor
105
100
95
90
E
Small Mitochondria Form Factor
F
Small Mitochondria MMP
150
50
G
Long Mitochondria Form Factor
H
Long Mitochondria MMP
I
Long vs small Mitochondria Ratio
125
75
25

Figure 127: A comparison of the mitochondrial phenotypes of the four controls used to assess the familial PD patients in high glucose media. A) MMP, **B)** ATP, **C)** Number of mitochondria per cell, **D)** Mitochondrial form factor, **E)** Form factor for the small mitochondria population, **F)** MMP for the small mitochondria population, **G)** Form factor for the long mitochondria population, **H)** MMP for the long mitochondria population, **I)** Long vs small mitochondria ratio. Controls (blue), Parkin patients (grey). Data was normalised to the average of the age- and sex-matched control per repeat and error bars show standard deviation (n = 3/4). The means of each patient were compared to the corresponding age- and sex-matched control by a one-way ANOVA (* $p < 0.05$).

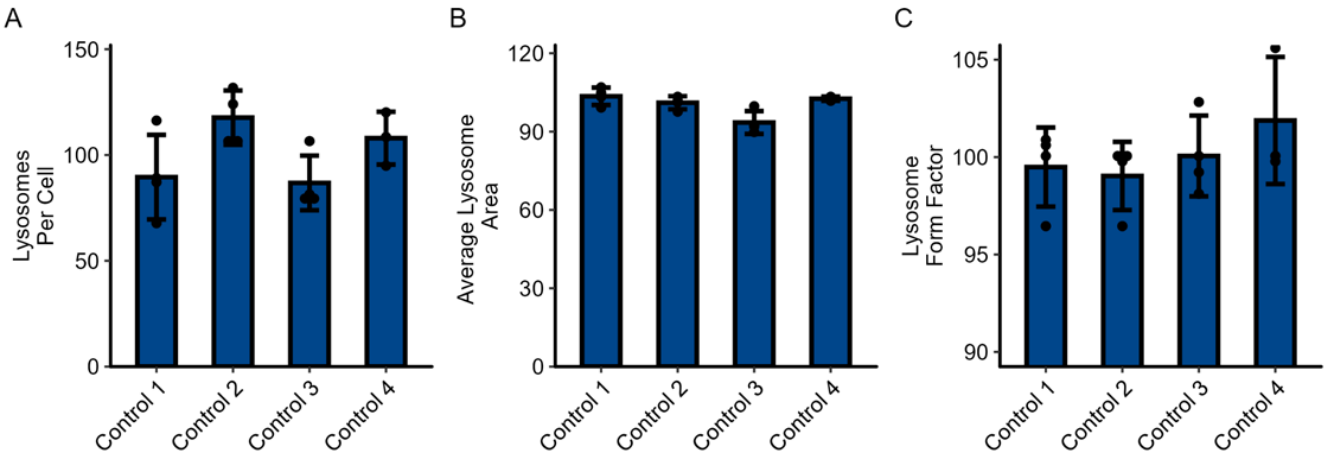

Figure 128: A comparison of the lysosomal phenotypes of the four controls used to assess the familial PD patients in high glucose media. A) MMP, **B)** ATP, **C)** Number of mitochondria per cell, **D)** Mitochondrial form factor, **E)** Form factor for the small mitochondria population, **F)** MMP for the small mitochondria population, **G)** Form factor for the long mitochondria population, **H)** MMP for the long mitochondria population, **I)** Long vs small mitochondria ratio. Controls (blue), Parkin patients (grey). Data was normalised to the average of the age- and sex-matched control per repeat and error bars show standard deviation (n = 3/4). The means of each patient were compared to the corresponding age- and sex-matched control by a one-way ANOVA (* $p < 0.05$).

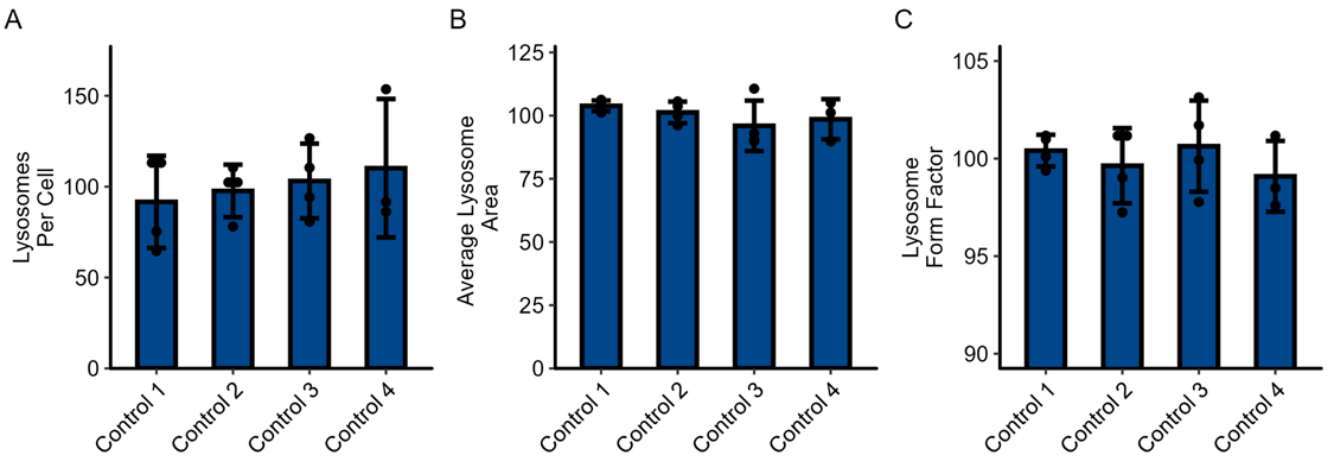

Figure 129: A comparison of the mitochondrial phenotypes of the four controls used to assess the familial PD patients in galactose media. A) MMP, **B)** ATP, **C)** Number of mitochondria per cell, **D)** Mitochondrial form factor, **E)** Form factor for the small mitochondria population, **F)** MMP for the small mitochondria population, **G)** Form factor for the long mitochondria population, **H)** MMP for the long mitochondria population, **I)** Long vs small mitochondria ratio. Controls (blue), Parkin patients (grey). Data was normalised to the average of the age- and sex-matched control per repeat and error bars show standard deviation (n = 3/4). The means of each patient were compared to the corresponding age- and sex-matched control by a one-way ANOVA (* $p < 0.05$).